

THEORY OF CRYSTAL STRUCTURES

Conditions for Stabilization of the Ordered State of Cations in Complex Oxides with Perovskite Structure

A. Yu. Gufan*, Yu. V. Prus*, and V. V. Rumyantseva**

* Research Institute of Physics, Rostov State University,
pr. Stachki 194, Rostov-on-Don, 344090 Russia

e-mail: gufan@mail.ru

** Moscow State Institute of Radio Engineering, Electronics, and Automation (Technical University),
pr. Vernadskogo 78, Moscow, 119454 Russia

Received June 3, 2004

Abstract—Analytical expressions for the coefficients in the Landau potential for six types of ordering of complex oxides with perovskite structure in terms of the sums of ordering energies in different coordination spheres are obtained in the approximation of effective pair interactions. On the basis of the pair interaction potentials of the form $v(r) = -1/r^6 + A \cos(qr)/(qr)^3$, the conditions for q and R are established, which lead to stabilization of the ordered phases. © 2005 Pleiades Publishing, Inc.

The physical properties of complex oxides with perovskite structure correlate strongly with the cation composition of these oxides. The magnetoresistive effect manifests itself almost in all manganates containing rare-earth elements, such as $\text{La}_{2/3}\text{Ca}_{1/3}\text{MnO}_{3-\delta}$ [1]; the high-temperature superconducting state arises in many cuprates containing Ba and a rare earth element R , such as $R_{1/3}\text{Ba}_{2/3}\text{CuO}_{3-\gamma}$ [2]; the relaxor properties manifest themselves in many complex lead-based oxides with perovskite structure, such as $\text{PbMg}_{1/3}\text{Nb}_{2/3}\text{O}_3$ [3]; and so on.

INTRODUCTION

The composition of an oxide is responsible for the specific features of its structure. It is generally accepted to describe the structure of multicomponent oxides with perovskite structure by comparing it with the parent-phase structure. The parent phase of oxides with perovskite structure has the composition ABO_3 and the symmetry O_h^1 . The parent phase structure is determined by the location of A , B , and O ions in regular point systems (RPSs): A ions are located in the RPS 1(b) ($1/2, 1/2, 1/2$), B ions are located in the RPS 1(a) ($0, 0, 0$), and oxygen ions occupy the lattice sites belonging to the RPS 3(d). Multicomponent oxides with perovskite structure have the composition $(A'_{x1}A''_{x2}A'''_{x3}\dots)(B'_{y1}B''_{y2}B'''_{y3}\dots)O_3$; $A^{(i)}$ and $B^{(i)}$ ions are located either in order or randomly in the RPSs 1(b) and 1(a) O_h^1 , respectively. A relationship between the order in the arrangement of cations in the crystal lattice and the oxide composition also clearly manifests itself in complex oxides with perovskite structure. For example,

the structure of all oxides with perovskite structure with the composition $R_{1/3}^{3+}B_{2/3}^{2+}\text{CuO}_{3-\gamma}$ is characterized by the alternation of R and Ba cations located in the A sublattice along the four-fold axis of the parent phase [2] as follows: $\dots R, Ba, Ba, R, Ba, Ba, \dots$. The structure of barium-containing oxides with perovskite structure, which exhibit anomalously high transparency in the millimeter wavelength range (such as $\text{BaMg}_{1/3}\text{Nb}_{2/3}\text{O}_3$ and $\text{BaZr}_{1/3}\text{Ta}_{2/3}\text{O}_3$ [4]), is also characterized by tripling of the parent-phase period due to the ordering of cations in the RPS 1(a) (B sublattice) along the three-fold symmetry axis (O_h^1 symmetry). In lead-containing relaxors (which are characterized by giant electrostriction) of the composition $\text{Pb}B'_{1/3}B''_{2/3}\text{O}_3$, the period is doubled owing to the ordering of cations in the B sublattice along the threefold axis [5]. The question arises: what are the effective interactions that between the cations involved in the ordering and provide the stability of a particular specified ordered structure? Generally, the answer is sought in the reverse order. Interactions between atoms by a certain law are set and then the energies of different, formally allowed, ordered states are calculated for clusters of finite size. The structure with minimum energy is considered to be the most stable one in the set of structures under consideration. Let us analyze the results of some recent studies. In [6], the state of Pb , Zr , Ti , and O ions in $\text{PbZr}_x\text{Ti}_{1-x}\text{O}_3$ was calculated in the one-electron approximation. Both all possible electrostatic interactions (up to the quadrupole–quadrupole one) and short-range repulsive forces were taken into account in the effective pair interaction energy. Then, the minimum energy for nine ordered structures was calculated in this maximally complete

model of interactions by successive decreasing of the energy of clusters $16 \times 16 \times 16$ and $18 \times 18 \times 18 a_0^3$ in size. (Hereinafter, a_0 is the unit-cell parameter of the parent phase.) It was predicted in [6] that the structure with a quadruple period along one of the four-fold axes must have the minimum energy. Purely coulombic interactions between point ions were taken into account in [7]. The charge of the ions was assumed to be equal to their maximum valence, and a cluster $6 \times 6 \times 6 a_0^3$ in size was considered. As a result, the stability of stoichiometrically ordered structures, characteristic of heterovalent ordering cations, was justified. However, the model proposed in [7] made it impossible to explain why $\text{PbMg}_{1/3}\text{Nb}_{2/3}\text{O}_3$ and $\text{BaMg}_{1/3}\text{Nb}_{2/3}\text{O}_3$ are characterized by different ordered structures. The other studies in this line of research [8, 9] have similar drawbacks.

In what follows, we used a phenomenological approach to solve the problem of the most stable ordered structure. As in all studies on the ordering in solid solutions known to us [6–12], we will restrict ourselves to the approximation of effective pair interactions whose form is not specified in deriving the general relations. Within this approximation, we will calculate the coefficients in the Landau potential $\Phi^{(l)}$, which describes the ordering in terms of the pair interaction energies of ions located at different distances.

It should be noted that in the approximation of effective pair interactions the ordered structure formed at the highest temperature ($T = T_{ord}$) remains stable in the entire temperature range from T_{ord} to $T = 0$ [13, 14], which makes all calculations much easier. Thus, our problem is reduced to the calculation of the dependence of the coefficient in the Landau potential for the squared order parameter on the effective pair interactions. It is this coefficient that determines the temperature of the loss of stability of the high-temperature phase with respect to the stabilization of the order in the arrangement of cations in the RPS O_h^1 .

CONDITIONS FOR THE STABILIZATION OF THE ORDERED STATE OBSERVED IN $\text{PbMg}_{1/3}\text{Nb}_{2/3}\text{O}_3$

The ordering of cations of different valence, which occurs in lead-containing relaxors of the $\text{Pb}(B_{1/3}^{+2}B_{2/3}^{+5})\text{O}_3$ type, is characterized by the alternation of B' and B'' ions according to the scheme $1 : 1 (\dots B'B''B'B'' \dots)$ along the three-fold symmetry axis of the parent phase. In terms of the Landau theory, such ordering is characterized by the one-arm star vector $\mathbf{k}_{13} = (\mathbf{b}_1 + \mathbf{b}_2 + \mathbf{b}_3)/2$ [15] and the one-component order parameter, denoted by R according to [16]. The ordering described by R leads to the partition of the B sublattice of perovskite into two equivalent sublattices (1 and 2). The energy of effective pair interactions

between B' and B'' ions, with allowance for the partition into sublattices, can be written as

$$E_2 = \{ V_{B'B'}(P_{B'}^2 + P_{B''}^2) + V_{B'B''}(P_{B'}^2 + P_{B''}^2) + V_{B'B'}P_{B'}P_{B''} + V_{B''B'}P_{B''}P_{B'} + V_{B'B''}(P_{B'}P_{B''} + P_{B''}P_{B'}) \} \frac{N}{2}, \quad (1)$$

where N is the number of sites in the RPS 1(a). Each separate term in (1), for example, $V_{B'B''}P_{B'}P_{B''}$, is a double sum (over all sites of sublattices 1 and 2 and the coordination spheres of each site [17])

$$V_{B'B''}P_{B'}P_{B''} \equiv \frac{4}{N^2} \sum_{i \in 1} \sum_{j \in 2} V_{B'i, B''j}(|\mathbf{r}_{1i} - \mathbf{r}_{2j}|) P_{B'i} P_{B''j} \quad (2)$$

of effective pair interaction energies $V_{B'i, B''j}(|\mathbf{r}_{1i} - \mathbf{r}_{2j}|)$ of B' and B'' atoms located, respectively, in sites $1i$ and $2j$, which belong, respectively, to sublattices 1 and 2. Here, $P_{B'i}$ is the probability of occupation of site i , belonging to the first sublattice, by B' atoms. The approximation used in (1) assumes for all probabilities that $P_{B'i} = P_{B'1l}$ and $P_{B''j} = P_{B''2k}$ at any i, l, j , and k . This circumstance allows us to introduce the concept of a probability for a B' (or B'') atom to be located at any site of sublattice 1 or 2: $P_{B'}P_{B''}P_{B'}P_{B''}$. It is also assumed in (2) that the energy of pair interactions between ions $V_{B'i, B''j}(|\mathbf{r}_{1i} - \mathbf{r}_{2j}|)$ depends only on the distance between them. Thus, $V_{B'B''}$ are averaged and normalized per atom sums of the energies of effective pair interactions of all B' atoms located in sublattice 1 with all B'' atoms located in sublattice 2. Generalization of this consideration to all other terms in (1) is obvious.

The interaction energy of B' and B'' atoms in (2) is given in terms of local (generalized) coordinates of the state of the crystal $P_{B'i}, P_{B''j}, \dots$. In (1), the generalized coordinates $P_{B'}, P_{B''}$ averaged over sublattices 1 and 2, are collective variables. The generalized coordinates $P_{B'}, P_{B''}$ can be related to the symmetric coordinates; i.e., the Landau order parameters R [14, 18] and Frenkel order parameters x [10, 14, 19, 20]:

$$P_{B''2i} = 1 - P_{B'1i}; \quad P_{B''2j} = 1 - P_{B'1j}; \quad (3a)$$

$$P_{B''1} = 1 - P_{B'1}; \quad P_{B''2} = 1 - P_{B'1}; \quad (3b)$$

$$P_{B'1} \equiv P_1; \quad P_{B'2} \equiv P_2;$$

$$x = (P_1 + P_2)/\sqrt{2}; \quad R = (P_1 - P_2)/\sqrt{2}. \quad (3c)$$

In the homogeneous state, $x = \sqrt{2}c$. However, the interaction energy of B' and B'' ions may lead to the decomposition of oxides with perovskite structure into two phases [10, 11, 19, 20]. In the case of the decomposition, the order parameter x determines both the concentration of B' ions in each phase and the fractions of averaged perovskite cells belonging to the new phases

[10, 19, 20]. Substituting designations (3a) into (1) and (2), we can introduce into consideration the ordering energies of B' and B'' ions at each coordination sphere:

$$u_{kk'ij} = V_{B'kiB'k'j}(|\mathbf{r}_i - \mathbf{r}_j|) + V_{B''kiB''k'j}(|\mathbf{r}_i - \mathbf{r}_j|) - 2V_{B'kiB''k'j}(|\mathbf{r}_i - \mathbf{r}_j|), \quad (4)$$

where k and k' are the numbers of sublattices and the value of $|\mathbf{r}_i - \mathbf{r}_j|$ determines the number of the coordination sphere. The local ordering energies (4) are averaged according to designations (2) and yield the effective ordering energies $u(R)$. With $u(R)$, the quadratic part of the Landau potential takes the form

$$\Phi_2^{(1)}(\mathbf{k}_{13}) = \mu_2 x^2 + a_{1R} R^2 = K_1(P_1^2 + P_2^2) + K_2 P_1 P_2. \quad (5)$$

With allowance for the structures of the parent phase and the ordered state, μ_2 and a_{1R} can be written as

$$\mu_2 = 3u(1) + 6u(\sqrt{2}) + 4u(\sqrt{3}) + 3u(2) + 12u(\sqrt{5}) + 12u(\sqrt{6}) + \dots + 4u(2\sqrt{3}) + \dots, \quad (6)$$

$$a_{1R} = -3u(1) + 6u(\sqrt{2}) - 4u(\sqrt{3}) + 3u(2) - 12u(\sqrt{5}) + 12u(\sqrt{6}) + \dots + 4u(2\sqrt{3}) + \dots \quad (7)$$

In (6) and (7), the distance between ions is expressed in terms of the edge lengths a_0 of the parent-phase unit cells. According to (5), it follows from the Landau theory that, at $T \approx 0$, $\mu_2 < 0$, and $a_{1R} > 0$, a complex oxide decomposes into two phases of different composition. If $\mu_2 > 0$ and $a_{1R} < 0$, the ordering of the 1 : 1 type (observed in $\text{PbMg}_{1/3}\text{Nb}_{2/3}\text{O}_3$) occurs in complex oxides with perovskite structure.

CONDITIONS FOR THE STABILIZATION OF THE ORDERED STATE OBSERVED IN $\text{Ba}(\text{Mg}_{1/3}\text{Nb}_{2/3})\text{O}_3$

The ordering of the $\text{Ba}(B_{1/3}^{+2}B_{2/3}^{n+5})\text{O}_3$ type is described by the order parameter whose translational characteristics coincide with those of $\cos[2\pi(\mathbf{b}_1 + \mathbf{b}_2 + \mathbf{b}_3) \cdot \mathbf{r}]/3$ [4]. The ordered structure is characterized by the presence of identical packets consisting of three planes. One of the packet planes contains predominantly (with the probability P_1) B' ions and the other two planes (with equal probabilities $P_2 = P_3$) contain predominantly B'' ions. It is convenient to represent the Landau potential describing such ordering as a function of the two components of the effective order parameter ($\lambda_1 \sim \cos[2\pi(\mathbf{b}_1 + \mathbf{b}_2 + \mathbf{b}_3) \cdot \mathbf{r}]/3$; $\lambda_2 \sim \sin[2\pi(\mathbf{b}_1 + \mathbf{b}_2 + \mathbf{b}_3) \cdot \mathbf{r}]/3$) and x .

Repeating the calculations of the previous section, we obtain the part of the Landau potential quadratic in the components λ_1 and λ_2 in the form

$$\Phi_2^{(2)}(k_9) = \mu_2^1 \xi^2 + a_{1\lambda}(\lambda_1^2 + \lambda_2^2) = Q_1(P_1^2 + P_2^2 + P_3^2) + Q_2(P_1 P_2 + P_2 P_3 + P_3 P_1). \quad (8)$$

Here, the quantity $\xi \equiv (P_1 + P_2 + P_3)/\sqrt{3}$ plays the same role of the nonequilibrium concentration of B' ions as x in (5); accordingly, $\mu_2^1 = \mu_2(u_i(r))$ (6). The relation between the generalized state coordinates P_1 , P_2 , and P_3 averaged over each sublattice and the components of the effective order parameter λ_1 and λ_2 is given by the expressions

$$\lambda_1 = (2P_1 - P_2 - P_3)/\sqrt{6}, \quad \lambda_2 = (P_2 - P_3)/\sqrt{2}. \quad (9)$$

The ordering in $\text{BaMg}_{1/3}\text{Nb}_{2/3}\text{O}_3$ occurs when $\lambda_2 = P_2 - P_3 = 0$. On the basis of (8) and (9), we obtain

$$a_{1\lambda} = Q_1 - \frac{1}{2}Q_2 = -3u(1) + 3u(\sqrt{2}) - u(\sqrt{3}) - 3u(2) + 6u(\sqrt{5}) + \dots - 0.5u(2\sqrt{3}) + \dots \quad (10)$$

CONDITIONS FOR THE STABILIZATION OF THE ORDERED STATE OBSERVED IN $\text{Y}_{1/3}\text{B}_{2/3}\text{CuO}_3$

In the copper-containing oxides with perovskite structure of the $R_{1/3}\text{Ba}_{2/3}\text{CuO}_3$ type, the arrangement of the planes occupied by rare-earth R ions and Ba ions is of the 1 : 2 type: $\text{RBaBaRBaBa} \dots$; these planes are perpendicular to the four-fold axis of the parent phase. The ordered¹ $R_{1/3}\text{Ba}_{2/3}\text{CuO}_3$ state is described by one component of the six-component order parameter [22]:

$$\Delta_1 = \Delta_2 = \dots = \Delta_5 = 0, \quad (11)$$

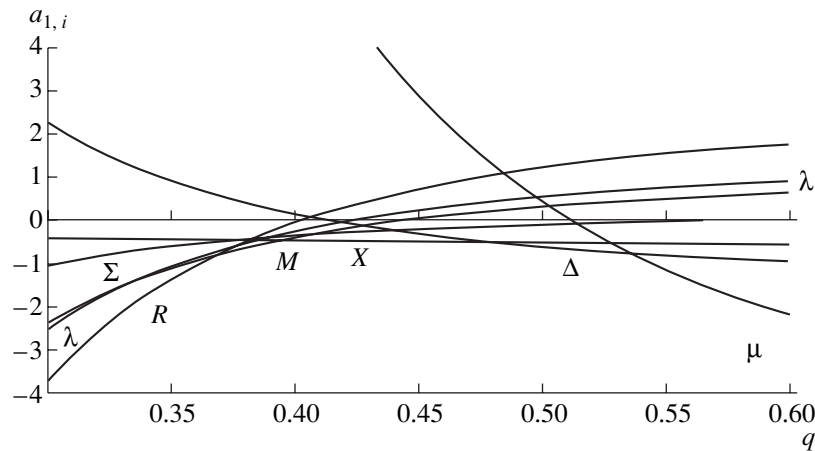
$$\Delta_6 \equiv \Delta \approx \Delta_0(T) \cos(2\pi)\mathbf{b}_1 \mathbf{r}/3.$$

The quadratic part of the effective Landau potential, dependent on

$$\rho = (P_1 + P_2 + P_3)/\sqrt{3}, \quad \Delta_5 = (P_2 - P_3)/\sqrt{2}, \quad (12)$$

$$\Delta_6 = (2P_1 - P_2 - P_3)/\sqrt{6},$$

¹ Real phase transitions to the state of equiprobable distribution of R and Ba ions over the parent phase cell in $R_{1/3}\text{Ba}_{2/3}\text{CuO}_3$ compounds have not been observed. Nevertheless, different models describing various properties of $\text{YBa}_2\text{Cu}_3\text{O}_{7-y}$ on the basis of the concepts about the parent phase in the form of an ideal perovskite have been multiply considered [21, 22]. In the general case, the model of a parent phase or a virtual crystal does not imply necessary realization of real phase transitions [23].



Dependence of a_{1i} ($i = R, M, X, \lambda, \Sigma$, and Δ) and μ on q in the term describing the oscillations of the ordering energy $u(r)$. The model with $u(r) = -1/r^6 + A \cos qr / (qr)^3$ ($A = 0.1$) is used. The value of $a_{1\Sigma}(\mathbf{k}^{(1)} = (\mathbf{b}_2 + \mathbf{b}_3)/2)$ was calculated by summation of the series analogous to (6), (7), and so on.

takes the form

$$\Phi_2^{(3)} = \mu_2'' \rho^2 + a_{1\Delta}(\Delta_5^2 + \Delta_6^2) \quad (13)$$

at $\mu_2'' = \mu_2(6)$ and

$$a_{1\Delta} = [3u(1) - 4u(\sqrt{3}) + 3u(2) + 12u(\sqrt{6}) + \dots - 2u(2\sqrt{3}) + \dots] / 2. \quad (14)$$

The condition for the stabilization of the order observed in $Y_{1/3}\text{Ba}_{2/3}\text{CuO}_3$ is expressed by the inequality $a_{1\Delta} < 0$.

CONDITIONS FOR THE STABILIZATION OF THE SUGGESTED ORDER IN THE ARRANGEMENT OF CATIONS IN THE A SUBLATTICE IN $\text{Ca}_{1/3}\text{La}_{2/3}\text{MnO}_3$

The unit cell parameters of $\text{Ca}_{1/3}\text{La}_{2/3}\text{MnO}_3$ in the ordered state [1] suggest that the stable order is reached as a result of several transitions of different physical nature. Within the theory of ordering based on taking into account only pair interactions, it is impossible to describe sequences of phase transitions. The reason for this is that significant renormalization of effective pair interactions due to the interactions involving more than two particles occurs as a result of each transition [24]. Nevertheless, the structure of $\text{Ca}_{1/3}\text{La}_{2/3}\text{MnO}_3$ can be used to establish two order parameters, which, even in the first-order approximation, determine the difference of all real structures of $A_{1/3}^{2+}A_{2/3}^{3+}\text{MnO}_3$ compounds from the ideal perovskite structure. One of these order parameters is determined by the three-arm vector star $\mathbf{k}_{11}^{(1)} = (\mathbf{b}_2 + \mathbf{b}_3)/2$ and the other order parameter is

determined by the three-arm vector star $\mathbf{k}_{10}^{(1)} = \mathbf{b}_1/2$. In both cases, the symmetry of the order parameter is described by the group $L = C48\alpha$ [14, 25]. The part of the Landau potential (which describes both types of ordering), quadratic in the components of the order parameter, has the form

$$\Phi_2^{(4)} = \mu_2''' x^2 + a_{1x}(X_1^2 + X_2^2 + X_3^2) + a_{1M}(M_1^2 + M_2^2 + M_3^2). \quad (15)$$

Here, $\mu_2''' = \mu_2(6)$, X_i are the components of the order parameter describing the doubling of the parent-phase period along the four-fold axes, and the translational characteristics M_i are determined by the rays of the star $\mathbf{k}_{10}^{(1)}$ [15]. Calculation analogous to the previous one leads to the expressions

$$a_{1x} = u(1) - 2u(\sqrt{2}) - 4u(\sqrt{3}) + 3u(2) + 4u(\sqrt{5}) + \dots + 4u(2\sqrt{3}) + \dots, \quad (16)$$

$$a_{1M} = -u(1) - 2u(\sqrt{2}) + 4u(\sqrt{3}) + 3u(2) - 4u(\sqrt{5}) + \dots + 4u(2\sqrt{3}) + \dots \quad (17)$$

The conditions for the stabilization of each considered type of order in the arrangement of cations at low temperatures follow from (16) and (17).

RESULTS AND DISCUSSION

The analytical expressions for the coefficients in the quadratic parts of the Landau potentials $\Phi_2^{(i)}$, (6), (7), (10), (14), (16), and (17), describing different types of ordering in terms of the ordering energies for different coordination spheres, make it possible to compare the temperatures of the loss of stability of the high-symmetry phase with respect to the formation of each of the

above-considered ordered structures.² In the models taking into account only the effective pair interactions, the highest ordering temperature T_{ord} ensures the stability of this order at all temperatures $T < T_{ord}$ [13, 14]. Thus, to reveal the most stable ordered structure, it is necessary to assume or calculate the dependence $u(r)$. We will restrict ourselves only to an illustration of the noted possibility using the model potentials.

As a pair interaction potential, we chose the sum $(-1/r^6 + A\cos(qr)/(qr)^3)$. The first term can be due to van der Waals forces (the interaction between fluctuations of atomic dipole moments). The second term has the form predicted by the pseudopotential method [26]. We also verified that consideration of the Coulomb potential (q_i/r) , screened at a distance of three coordination spheres, and the renormalization of pair interactions due to the three-particle ones, for which $u(r) \sim 1/r^9$, yield the same results.³ The figure shows the results of summation of series (6), (7), (10), (14), (16), and (17) accurate to 2%. (All terms including 11 coordination spheres are summed.) In this approximation, the error in determining the temperatures of the loss of stability of the high-symmetry phases from (6), (7), (10), (14), (16), and (17) does not exceed 10%. The phenomenological parameter of the interaction energy A in the figure is chosen so as to attain stability of the maximum possible number of ordered phases by varying q . It was found that the dependence $u(r) = 1/r^6 + A\cos qr/(qr)^3$ makes it possible to stabilize only five of the seven ground states under consideration; specifically, $R(7)$, $M(17)$, $X(16)$, $\Delta(14)$, and the two-phase state. The $R(7)$ state and the two-phase state can be implemented as stable at any value of A . With an increase in the role of the pseudopotential term, the Δ , X , and M states successively lose their stability. Furthermore, within the approximation used, the theory predicts that the stability of the ordered state observed in $Y_{1/3}Ba_{2/3}CuO_{3-\delta}$ is always restricted, on the one hand, by the external conditions corresponding to the stability of the two-phase state and, on the other hand, by the conditions for the stabilization of the ordered state (nonstoichiometric for $Y_{1/3}Ba_{2/3}CuO_3$) with a doubled period along one of the four-fold axes. Large values of q always lead to the decomposition of a solid solution into two phases.

None of the pair interaction potentials investigated by us made it possible to obtain the stability of the ordered state observed in $BaMg_{1/3}Nb_{2/3}O_3$ [4]. Apparently, this result indicates that three-particle interac-

tions play a key role in the stabilization of the state described by λ_1 . This suggestion is in agreement with the conclusions of [9] but requires additional calculations that are beyond the scope of this study.

ACKNOWLEDGMENTS

This study was supported by the Russian Foundation for Basic Research, project nos. 02-02-17921 and 02-02-39016. A. Yu. Gufan acknowledges the support of the Foundation of Noncommercial Programs "Dynasty" for the awarding of a scholarship in 2003–2004.

REFERENCES

1. M. B. Salamon, *Rev. Mod. Phys.* **73**, 583 (2001).
2. G. P. Shveikin, V. A. Gubanov, A. A. Fotiev, G. V. Bazuev, and A. A. Evdokimov, *Electron Structure and Physical and Chemical Properties of High-Temperature Superconductors* (Nauka, Moscow, 1990) [in Russian].
3. G. Burns and F. N. Dacol, *Solid State Commun.* **48** (10), 853 (1983).
4. P. K. Davies, J. Tong, and T. Negas, *J. Am. Ceram. Soc.* **80** (7), 1727 (1977).
5. Y. Yan, S. J. Pennycook, Z. Xu, and D. Viehland, *Appl. Phys. Lett.* **72**, 3145 (1998).
6. V. I. Zinenko and S. N. Safronova, *Fiz. Tverd. Tela (St. Petersburg)* **46** (7), 1252 (2004) [*Phys. Solid State* **46**, 1291 (2004)].
7. L. Bellaiche and D. Vanderbilt, *Phys. Rev. Lett.* **81** (6), 1318 (1998).
8. B. P. Burton and E. Cockayne, *Phys. Rev. B* **60** (18), R12542 (1999).
9. B. P. Burton, *Phys. Rev. B* **59** (9), 6087 (1999).
10. M. A. Krivoglaz and A. A. Smirnov, *The Theory of Order-Disorder in Alloys* (Fizmatgiz, Moscow, 1958; Macdonald, London, 1964).
11. A. G. Khachatryan, *The Theory of Phase Transformations and the Structure of Solids Solutions* (Nauka, Moscow, 1974) [in Russian].
12. A. I. Gusev and A. A. Rempel', *Nonstoichiometry, Disorder and Order in Solids* (Ural. Otd. Ross. Akad. Nauk, Yekaterinburg, 2001) [in Russian].
13. J. S. Smart, *Effective Field Theories of Magnetism* (Saunders, London, 1966; Mir, Moscow, 1968).
14. Yu. M. Gufan, *Structural Phase Transitions* (Nauka, Moscow, 1982) [in Russian].
15. O. V. Kovalev, *Representations of the Crystallographic Space Groups: Irreducible Representations, Induced Representations, and Corepresentations* (Nauka, Moscow, 1986; Gordon and Breach, Yverdon, Switzerland, 1993).
16. R. S. Knox and A. Gold, *Symmetry in the Solid State* (Benjamin, New York, 1964; Nauka, Moscow, 1970).
17. A. Yu. Gufan, E. N. Klimova, Yu. V. Prus, and M. B. Stryukov, *Izv. Ross. Akad. Nauk, Ser. Fiz.* **65** (6), 788 (2001).

² In the models with effective pair interaction, the coefficients in the Landau potentials at large powers of the order parameter are found by the approximation of the entropy. These coefficients determine the difference of the ordering temperature from T_{ord} . For the type of the models considered here, this difference is smaller than 0.5% of T_{ord} , which is smaller than the error of these models.

³ The anisotropic part of three-particle interactions may qualitatively change the result of the calculations only when their energy exceeds a fairly high threshold [27].

18. L. D. Landau and E. M. Lifshitz, *Course of Theoretical Physics*, Vol. 5: *Statistical Physics*, 2nd ed. (Nauka, Moscow, 1964; Pergamon, Oxford, 1980).
19. A. Yu. Gufan, *Izv. Ross. Akad. Nauk, Ser. Fiz.* **5**, 651 (2004).
20. Ya. I. Frenkel', *Introduction to the Theory of Metals* (Fizmatgiz, Moscow, 1956) [in Russian].
21. V. P. Dmitriev and P. Toledano, *Kristallografiya* **40** (3), 548 (1995) [*Crystallogr. Rep.* **40**, 502 (1995)].
22. Yu. M. Gufan, *Pis'ma Zh. Éksp. Teor. Fiz.* **8** (5), 271 (1968) [*JETP Lett.* **8**, 167 (1968)].
23. V. I. Torgashev, *Doctoral Dissertation in Physics and Mathematics* (Rostov-on-Don, 1998).
24. J. Jiao, A. N. Sadkov, Yu. V. Prus, and A. Yu. Gufan, *Izv. Ross. Akad. Nauk, Ser. Fiz.* **68** (5) (2004).
25. H. T. Stokes and D. M. Hatch, *Isotropy Subgroups of the 230 Crystallographic Space Group* (World Sci., Singapore, 1988).
26. V. G. Bar'yakhtar, E. V. Zarochentsev, and E. P. Troitskaya, *Methods of Calculation Physics in the Solid-State Theory* (Naukova Dumka, Kiev, 1990) [in Russian].
27. A. Yu. Gufan, Yu. V. Prus, and V. V. Rummyantseva, *Izv. Ross. Akad. Nauk, Ser. Fiz.* (in press).

Translated by Yu. Sin'kov

DIFFRACTION AND SCATTERING OF IONIZING RADIATIONS

Ultimate Volume of a Unit Cell Determined by Powder Diffraction Methods

V. P. Serykh

Kharkov Institute of Physics and Technology, National Science Center,
Akademicheskaya ul. 1, Kharkov, 61108 Ukraine
e-mail: tikhonovsky@kipt.kharkov.ua

Received May 19, 2004; in final form, December 17, 2004

Abstract—The experimental factors limiting the ultimate unit-cell volumes obtained by indexing of powder diffraction patterns are discussed. Relationships for minimum volumes and areas of the reciprocal unit cells are derived. © 2005 Pleiades Publishing, Inc.

The reliability of indexing of powder diffraction patterns can be directly or indirectly evaluated from the following characteristics: the total number of possible diffraction reflections M , which is calculated without regard for extinctions; the number of measured reflections N ; the calculated unit-cell volume V ; and the absolute error Δq in the identification of the complete data array $\{q_i\} = \{1/d_j^2\}$, where d_j stands for the interplanar spacings. Examples of estimates of this type are provided by the de Wolff index [1], which is widely used in practice, and the probability criterion proposed in [2], which can also be reduced to the above index. The correspondence between these two criteria was demonstrated in [3]. In relationship (6) derived in [3], the ultimate volume of a Bravais cell calculated from the results of the indexing is given by

$$V_m = \alpha N / [4\pi \sum \sqrt{q_i \Delta q}], \quad (1)$$

where the summation is taken with respect to all elements of the array $\{q_i\}$ and $a = 48, 24, 16, 8, 4, 2$ for crystals from cubic to triclinic systems, respectively.

At first glance, relationship (1) is consistent with the well-known fact that the unit cell volume V_m increases with an increase in the number of reflections N and a decrease in the experimental error Δq . The role of the quantity $\sqrt{q_i}$ remains unclear, especially as the boundaries of the array $\{q_i\}$ depend on random factors.

Let us rewrite relationship (1) for a single reflection with $q_i = q_n = q_{\max}$. Then, the sum averaged over N reflections in the denominator of relationship (1) is replaced by the maximum term: $V_m = \alpha / [4\pi \sqrt{q_n \Delta q}]$. Substituting $V_m = 1/V_m^*$ (V_m^* is the minimum volume of the reciprocal cell) into the last formula, we obtain

$$4\pi \sqrt{q_n \Delta q} / [\alpha V_m^*] < 1. \quad (2)$$

The left-hand side of expression (2) determines the number of points in the reciprocal lattice map that can occasionally fall in its calculated domain, and the inequality is a necessary condition for identification of the quantity q_n [2].

A necessary tool for correctly indexing the complete array of reflections, as a rule, is the least-squares method. The use of this method requires that the number t of experimental values q_i per refined parameter be large enough. If the number of refined parameters is p , it is necessary to record no less than $N = tp$ diffraction maxima.

The k th part of the points of the reciprocal lattice map that fall inside the sphere of radius $R = \sqrt{q_n}$ is extinguished according to the extinction laws. The total number of points in the calculated domain can be written as

$$M = kN = 4\pi q_n^{3/2} / (3\alpha V_m^*) = 4\pi q_n^{3/2} V_m / (3\alpha). \quad (3)$$

By eliminating the quantity q_n from relationships (2) and (3), we obtain the inequality

$$V_m < \alpha / [\sqrt{48kN\pi} (\Delta q)^{3/2}]. \quad (4)$$

The main difference between relationships (4) and (1) lies in the fact that, according to the former expression, an increase in the number of experimental reflections leads not to an increase but to a decrease in the ultimate unit-cell volume. This volume is limited by the quantities Δq and N , which are opposite to each other in action. In order to increase the number N , thus improving the least-squares statistics, we should narrow the identification range Δq . A reasonable compromise is provided by $t = 4$ (four reflections per parameter).

The coefficient k related to the extinction laws is determined by the most symmetric space group within the crystal system. The calculation performed using a special program with inclusion of the systematic

absences [4] gave the following unit-cell volumes (in \AA^3):

Volume	Cubic	Hexagonal	Rhombohedral	Tetragonal	Orthorhombic	Mono-clinic	Triclinic
$N = tp$	4	8	8	8	12	16	24
$M = kN$	24	14	21	24	71	33	24
V_m	14223	9311	3800	4741	1378	1011	593

Here, the numbers of extinctions correspond to space groups no. 120, 94, 86, 77, 40, 7, and 1, respectively. The last row of the table presents the ultimate unit-cell volumes calculated according to relationship (4) for a typical experimental error $\Delta q = 0.001$ and an optimum number $t = 4$.

Note that the data on the permissible volumes V_m , which are obtained before the indexing, appear to be useful at different stages of this procedure, because it allows us to reject settings of the axes that correspond to extremely large volumes.

During indexing of the diffraction patterns with the $(hk0)$ reflections in the small-angle range, the algorithm operates the maximum permissible area of the reciprocal cell S_m^* [5]. In this case, expressions $\pi\Delta q_n/(\alpha S_m^*) < 1$ and $\pi q_n/(\alpha S_m^*) = kN$ are analogues of relationships (2) and (3), respectively. By combining these expressions, we obtain the formula $S_m^* = 2\pi\Delta q/\alpha$, which is in complete agreement with the results presented in [2]. Hence, in the small-angle range of the diffraction pattern characterized by the $(hk0)$ reflections, the parameter S_m^* does not depend on the number of reflections but is determined by the absolute error Δq .

Finally, when indexing the diffraction patterns with the $(00l)$ reflections in the small-angle range, the algorithm operates a specified parameter z_m (the minimum linear parameter of the reciprocal cell). Taking into account relationship (4) given in [6], we obtain the expressions $\Delta q/(lz_m) < 1$ and $l = kN$ as analogues of formulas (2) and (3). Since only one parameter is refined ($p = 1$), we have $z_m = \Delta q/(kt) = \Delta q/(kN)$. It is seen that the parameter z_m decreases with increasing number of measured reflections. The coefficient k is determined by the screw axes directed along the elongated axis of the cell.

In conclusion, it should be noted that the relationships derived for V_m^* , S_m^* , and z_m^* essentially facilitate the complete automatization of the indexing of X-ray powder diffraction patterns.

REFERENCES

1. O. Kennard, J. D. Hanawalt, A. J. C. Wilson, *et al.*, *J. Appl. Crystallogr.* **4**, 81 (1971).
2. V. P. Serykh, *Kristallografiya* **20** (6), 1170 (1975) [*Sov. Phys. Crystallogr.* **20** (6), 710 (1975)].
3. V. P. Serykh, *Kristallografiya* **24** (5), 1041 (1979) [*Sov. Phys. Crystallogr.* **24** (5), 595 (1979)].
4. L. I. Mirkin, *Handbook of X-ray Analysis of Polycrystalline Materials* (Fizmatgiz, Moscow, 1961; Plenum, New York, 1964).
5. V. P. Serykh, *Kristallografiya* **40** (2), 239 (1995) [*Crystallogr. Rep.* **40** (2), 215 (1995)].
6. V. P. Serykh, *Kristallografiya* **47** (3), 415 (2002) [*Crystallogr. Rep.* **47** (3), 370 (2002)].

Translated by I. Polyakova

STRUCTURE OF INORGANIC COMPOUNDS

Crystal Structure of Golyshevite

K. A. Rozenberg*, R. K. Rastsvetaeva**, N. V. Chukanov***, and I. A. Verin**

* Faculty of Geology, Moscow State University,
Vorob'evy gory, Moscow, 119992 Russia

** Shubnikov Institute of Crystallography, Russian Academy of Sciences,
Leninskii pr. 59, Moscow, 119333 Russia

e-mail: rast@ns.crys.ras.ru

*** Institute of Problems of Chemical Physics, Chernogolovka Branch, Russian Academy of Sciences,
pr. Akademika Semenova 1, Chernogolovka, Moscow oblast, 142432 Russia

Received September 29, 2004

Abstract—The crystal structure of golyshevite,¹ a new calcium- and carbon-rich representative of the eudialyte group, was established by single-crystal X-ray diffraction analysis (sp. gr. $R3m$, $a = 14.231(3)$ Å, $c = 29.984(8)$ Å, $R = 0.062$, 1643 reflections with $F > 3\sigma(F)$). The idealized formula of golyshevite is $(\text{Na}_{10}\text{Ca}_3)\text{Ca}_6\text{Zr}_3\text{Fe}_2\text{SiNb}[\text{Si}_3\text{O}_9]_2[\text{Si}_9\text{O}_{27}]_2(\text{OH})_3(\text{CO}_3) \cdot \text{H}_2\text{O}$. This mineral is characterized by the presence of calcium atoms both in the octahedral positions of six-membered rings and in extraframework positions, where calcium prevails. CO_3 groups are present as the major additional anions. Carbon atoms randomly occupy two positions on the threefold z axis at a distance of 0.75 Å from each other and are coordinated by oxygen atoms arranged around the z axis. © 2005 Pleiades Publishing, Inc.

Most minerals of the eudialyte group contain 9–10 wt % of CaO and are characterized by a Ca/Zr ratio of 2. Representatives with a low calcium content (3–6 wt % of CaO) and Ca/Zr = 1 (oneillite [1], raslakite [2], and some other minerals) are less abundant. Only in calcium-rich feklichevite [3], is the Ca/Zr ratio ~ 3 and the CaO content higher than 15 wt %. Minerals of the eudialyte group can be characterized by the following general formula: $[A(1)A(2)A(3)A(4)A(5)A(6)A(7)]_3A(8)[M(1, 1) \times M(1, 2)]_3[M(2, 1)M(2, 2)M(2, 3)]_{3-6} [M(3)M(4)]Zr_3 \times [\text{Si}_{24}\text{O}_{72}]\text{OH}_{2-6}X_{2-4}$, where $A = \text{Na, Ca, K, Sr, REE, Ba, Mn, H}_3\text{O}$; $[M(1,1), M(1,2)] = \text{Ca, Mn, REE, Na, Sr, Fe}$; $M(2,1) = \text{Fe, Na, Zr, Ta}$; $[M(2,2), M(2,3)] = \text{Fe, Mn, Zr, Ti, Na, K, Ba, H}_3\text{O}$; $[M(3), M(4)] = \text{Si, Nb, Ti, W, Na}$; $Z = \text{Zr, Ti}$; and $X = \text{H}_2\text{O, Cl, F, OH, CO}_3, \text{SO}_4, \text{SiO}_4$. In this study, we established the structure of a new calcium-rich representative of the eudialyte group. Unlike feklichevite, this mineral contains carbon. The new mineral was discovered by one of the authors of this study at the Kovdor massif (the Kola Peninsula).

The chemical composition of this mineral, determined by electron-probe X-ray microanalysis, corresponds to the following empirical formula (calculated for 25 Si, $Z = 3$) with consideration for the microzonality of single crystals: $\text{Na}_{9.1-9.8}\text{Ca}_{9.3-9.9}\text{K}_{0.3-0.4}\text{Ce}_{0-0.1}\text{Zr}_{2.9} \times \text{Nb}_{0.6-0.7}\text{Fe}_{1.9-2.2}\text{Mn}_{0.2-0.3}\text{Al}_{0-0.25}\text{Si}_{25}\text{O}_{72}(\text{CO}_3)_{1-1.1}\text{Cl}_{0.2}$.

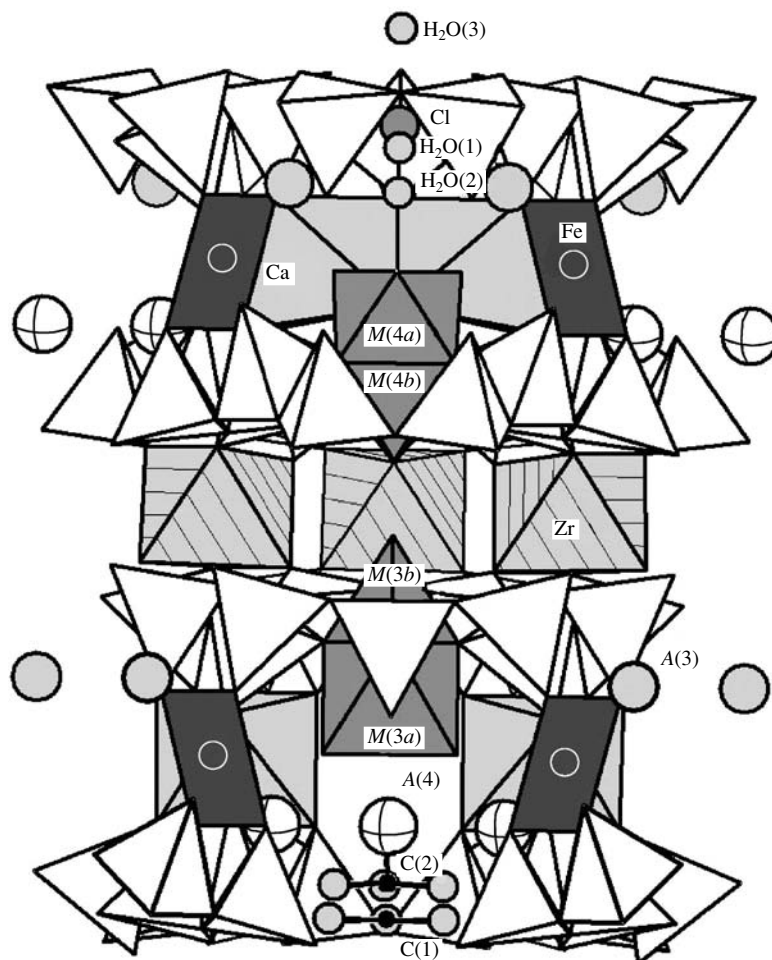
¹ This new mineral and the mineral name were approved by the Commission on New Minerals and Mineral Names of the International Mineralogical Association (CNMMN IMA) on March 21, 2005.

X-ray diffraction data were collected from an isometric single-crystal chip. The characteristics of the crystal and the details of X-ray diffraction study are given in Table 1.

Since the chemical composition of golyshevite is similar to that of feklichevite [3], we used the coordi-

Table 1. Characteristics of the crystal and details of X-ray diffraction study

a , Å	14.231(3)
c , Å	29.984(8)
V , Å ³	5258.9
Sp. gr., Z	$R3m$, 3
Radiation; λ , Å	Mo $K\alpha$; 0.71073
ρ_{calcd} , g/cm ³	2.91
Crystal dimensions, mm	0.3 × 0.25 × 0.4
Diffraction	ENRAF-NONIUS
Ranges of indices of measured reflections	$-20 < h < 17$; $0 < k < 20$; $0 < l < 42$
$\sin \theta / \lambda$	< 0.703
Total number of reflections	4418 $F > 3\sigma(F)$
Number of independent reflections	1643 $F > 3\sigma(F)$
R factor after merging of equivalent reflections	0.062
R factor upon anisotropic refinement	0.062
Program for refinement	AREN [4]
Program for absorption correction	DIFABS [5]

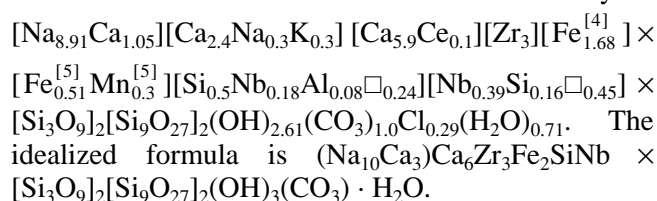


Fragment of the structure of golyshévite projected along the [110] direction.

nates of the framework atoms of the latter as the starting model. Other positions were revealed from a series of difference electron density maps. The coordinates, composition, occupancies of positions, and atomic displacement parameters were refined. A number of positions were refined using mixed atomic scattering curves.

The atomic coordinates and the characteristics of the coordination polyhedra in the golyshévite structure are listed in Tables 2 and 3, respectively.

The main characteristic features of the composition and structure of golyshévite are reflected in its crystal-chemical formula ($Z = 3$), which is in good agreement with the results of chemical analysis:



The golyshévite structure as a whole is analogous to the structures of other representatives of the eudialyte group and consists of three- and nine-membered silicon–oxygen rings and six-membered rings of (Ca,O) octahedra, which are linked to each other by discrete (Zr,O) octahedra to form a heterogeneous framework. The cavities in the framework are occupied by alkali and alkaline-earth cations, impurity transition-metal cations, and additional large anions (see figure).

Golyshévite is characterized by a high calcium content. Calcium atoms are located in octahedral positions of the six-membered rings (as in most minerals of the eudialyte group) and additionally occupy extraframework cation positions. The difference between golyshévite and feklíchevite is that Ca atoms in the latter completely occupy the A(3) position, whereas in the golyshévite structure calcium dominates over sodium in the A(4) position and is located in only one of two split subpositions.

In addition, niobium in golyshévite, in contrast to other structurally characterized minerals of the eudialyte group, is not located in one of two positions in the

Table 2. Atomic coordinates, equivalent atomic displacement parameters, multiplicities (Q), and occupancies (q) of positions

Atom	x/a	y/b	z/c	Q	q	$U_{\text{eq}}, \text{\AA}^2$
Zr	0.3324(2)	0.1662(1)	0.1668(1)	9	1	0.0180(3)
Ca	0.0010(3)	0.2608(2)	0.0001(1)	18	1	0.0119(5)
Si(1)	0.5258(2)	0.2629(1)	0.2502(1)	9	1	0.011(1)
Si(2)	-0.0055(2)	0.6038(2)	0.0970(1)	18	1	0.0134(9)
Si(3)	0.2065(1)	0.4130(2)	0.0770(1)	9	1	0.018(1)
Si(4)	0.0872(3)	0.5436(2)	0.2589(1)	9	1	0.017(1)
Si(5)	0.0585(2)	0.3282(2)	0.2361(1)	18	1	0.0133(9)
Si(6)	0.1400(2)	0.0700(2)	0.0817(1)	9	1	0.013(1)
O(1)	0.4816(9)	0.2408(6)	0.1998(3)	9	1	0.031(5)
O(2)	0.2575(6)	0.0309(7)	0.2089(2)	18	1	0.034(3)
O(3)	0.3991(8)	0.3006(7)	0.1263(3)	18	1	0.029(3)
O(4)	0.6061(4)	0.3939(4)	0.2554(3)	9	1	0.020(5)
O(5)	0.4331(8)	0.2161(5)	0.2875(2)	9	1	0.016(4)
O(6)	0.4128(6)	0.0347(7)	0.0446(2)	18	1	0.028(3)
O(7)	0.0987(6)	0.3761(7)	0.1076(3)	18	1	0.026(3)
O(8)	0.0181(9)	0.5090(7)	0.1149(3)	9	1	0.029(5)
O(9)	0.2734(6)	0.5468(9)	0.0729(9)	9	1	0.044(4)
O(10)	0.1828(4)	0.3656(6)	0.0278(3)	9	1	0.019(4)
O(11)	0.0323(8)	0.5162(6)	0.3061(3)	9	1	0.023(5)
O(12)	0.1760(5)	0.3530(7)	0.2179(3)	9	1	0.026(5)
O(13)	0.0471(6)	0.3028(6)	0.2886(2)	18	1	0.024(3)
O(14)	0.3889(7)	0.4302(7)	0.2277(2)	18	1	0.028(3)
O(15)	0.3937(5)	0.6063(5)	0.2535(4)	9	1	0.034(5)
O(16)	0.0628(3)	0.1256(5)	0.0771(3)	9	1	0.026(5)
O(17)	0.1911(9)	0.0956(6)	0.1302(3)	9	1	0.028(5)
O(18)	0.2250(9)	0.1125(6)	0.0428(3)	9	1	0.021(4)
Fe(1)	0.5195(1)	0.4805(1)	-0.0021(1)	9	0.56(1)	0.0166(4)
Fe(2)	0.0492(6)	0.5246(4)	0.0033(2)	9	0.27(1)	0.0137(8)
<i>M</i> (3 <i>a</i>)	0.3333	0.6667	0.2890(3)	3	0.26(1)	0.022(1)
<i>M</i> (3 <i>b</i>)	0.3333	0.6667	0.2464(4)	3	0.50(2)	0.016(1)
<i>M</i> (4 <i>a</i>)	0.3333	0.6667	0.0410(2)	3	0.39(1)	0.0194(6)
<i>M</i> (4 <i>b</i>)	0.3333	0.6667	0.092(2)	3	0.16(2)	0.017(5)
<i>A</i> (1 <i>a</i>)	0.1094(4)	0.2188(6)	0.1557(3)	9	0.81(1)	0.0248(8)
<i>A</i> (1 <i>b</i>)	0.078(1)	0.156(2)	0.1734(8)	9	0.21(1)	0.015(3)
<i>A</i> (2 <i>a</i>)	0.5658(4)	0.4342(4)	0.1754(3)	9	0.89(1)	0.0308(8)
<i>A</i> (2 <i>b</i>)	0.549(2)	0.099(2)	0.179(2)	9	0.11(2)	0.039(3)
<i>A</i> (3 <i>a</i>)	0.2348(3)	0.4695(4)	-0.0460(2)	9	0.70(1)	0.0297(6)
<i>A</i> (3 <i>b</i>)	0.227(1)	0.114(1)	0.2769(7)	9	0.29(1)	0.023(2)
<i>A</i> (4 <i>a</i>)	0.4528(4)	0.2264(3)	0.0504(1)	9	0.80(1)	0.0261(5)
<i>A</i> (4 <i>b</i>)	0.491(2)	0.245(2)	0.036(1)	9	0.20(1)	0.023(2)
<i>A</i> (5)	0.191(3)	0.595(2)	0.152(1)	9	0.32(2)	0.043(2)
<i>C</i> (1)	0.6667	0.3333	0.108(1)	3	0.55(8)	0.026(5)
<i>C</i> (2)	0.6667	0.3333	0.083(4)	3	0.45(1)	0.022(7)
<i>Oc</i> (1)	0.612(1)	0.388(1)	0.108(1)	9	0.55(4)	0.053(4)
<i>Oc</i> (2)	0.6141(9)	0.3859(9)	0.0869(7)	9	0.45(5)	0.067(2)
Cl	0	0	0.2412(7)	3	0.29(2)	0.028(3)
OH(1)	0.265(1)	0.531(2)	0.324(1)	9	0.33(3)	0.030(5)
OH(2)	0.211(3)	0.606(2)	0.002(1)	9	0.39(3)	0.029(4)
OH(3)	0.3333	0.6667	0.145(8)	3	0.16(1)	0.064(5)
OH(4)	0.3333	0.6667	0.192(2)	3	0.50(6)	0.065(6)
H ₂ O(1)	0	0	0.263(2)	3	0.24(6)	0.034(9)
H ₂ O(2)	0	0	0.293(2)	3	0.23(6)	0.029(8)
H ₂ O(3)	0	0	0.179(3)	3	0.24(6)	0.038(6)

Table 3. Characteristics of the coordination polyhedra

Position	Composition (Z = 3)	Coordination number	Cation–anion distances, Å		
			minimum	maximum	average
Zr	3Zr	6	2.05(1)	2.093(9)	2.07
Ca	5.9Ca + 0.1Ce	6	2.301(7)	2.418(9)	2.365
Fe(1)	1.68Fe	4	2.043(6)	2.138(8)	2.091
Fe(2)	0.51Fe + 0.3Mn	5	2.04(1)	2.22(1)	2.13
<i>M</i> (3 <i>a</i>)	0.18Nb + 0.08Al	6	1.82(1)	1.98(2)	1.90
<i>M</i> (3 <i>b</i>)	0.5Si	4	1.503(2)	1.62(6)	1.53
<i>M</i> (4 <i>a</i>)	0.39Nb	6	1.75(1)	1.89(3)	1.82
<i>M</i> (4 <i>b</i>)	0.16Si	4	1.58(2)	1.60(1)	1.58
A(1 <i>a</i>)	2.4Na	7	2.49(1)	2.73(1)	2.63
A(1 <i>b</i>)	0.6Na	7	2.46(3)	2.91(2)	2.64
A(2 <i>a</i>)	2.67Na	9	2.500(7)	2.94(1)	2.69
A(2 <i>b</i>)	0.33Na	8	2.40(4)	2.71(2)	2.62
A(3 <i>a</i>)	1.05Na + 1.05Ca	7	2.55(1)	2.90(1)	2.69
A(3 <i>b</i>)	0.9Na	9	2.49(2)	2.99(2)	2.67
A(4 <i>a</i>)	2.4Ca	8	2.49(1)	2.81(1)	2.62
A(4 <i>b</i>)	0.3K + 0.3Na	8	2.39(4)	3.28(3)	2.79
A(5)	0.96Na	8	2.40(4)	3.19(5)	2.57
C(1)	0.55C	3	1.34(2)	1.34(2)	1.34
C(2)	0.45C	3	1.29(1)	1.29(1)	1.29

vicinity of the centers of nine-membered Si_9O_{27} rings but is distributed, together with silicon, between the *M*(3) and *M*(4) positions. The *M*(3) position is occupied predominantly by silicon, whereas the *M*(4) position is occupied predominantly by niobium.

Another characteristic feature of golyshvite is the presence of additional occupied anion positions on the threefold axis. In feklchevite, one of these positions is occupied by a water molecule and another position is occupied by chlorine and a water molecule. In the golyshvite structure, the former position is occupied by the (CO_3) group and another position is split into four subpositions. One of these subpositions is occupied by chlorine and the other three subpositions are occupied by water molecules.

Among representatives of the eudialyte group, there are two carbonate-containing minerals, zirsilite-(Ce) and carbokentbrooksite [6]. The composition of the first additional anion position in zirsilite-(Ce) and carbokentbrooksite is described by the formulas $\text{C}_{0.43}\text{Cl}_{0.3}$ and $\text{C}_{0.58}\text{Cl}_{0.27}$, respectively. This position is split in both minerals; carbon atoms occupy one subposition on the threefold axis, and chlorine atoms occupy another subposition. In golyshvite, carbon atoms randomly occupy two positions on the threefold *z* axis at a dis-

tance of 0.75 Å from each other. Oxygen atoms also occupy two positions around the *z* axis and are randomly coordinated to the carbon atoms. Both carbonate groups are almost planar and are coordinated to the split A(4) cation positions through the oxygen atoms, being located at a shorter distance from the A(4*a*) position, where all additional calcium atoms are located.

The IR spectrum of golyshvite shows only asymmetric C–O stretching vibration bands of CO_3 groups at 1418, 1456, 1490, and 1515 cm^{-1} . We cannot say anything about the existence of totally symmetric C–O stretching vibration bands of CO_3 groups in the range 1000–1100 cm^{-1} because this region overlaps with strong Si–O stretching vibration bands. The shift of the main absorption maximum (1490 cm^{-1}) to larger wavelengths as compared to those in the spectra of most carbonates indicates a slight distortion of CO_3 groups. The presence of four asymmetric C–O stretching bands of CO_3 groups is indicative of the nonequivalence of these groups in the golyshvite structure.

To summarize, of all known eudialytes, the mineral golyshvite is characterized by the highest calcium and carbonate contents and its structural features demonstrate the individuality of this new representative of the eudialyte group.

ACKNOWLEDGMENTS

This study was supported by the Russian Foundation for Basic Research (project no. 02-05-64080) and the Grant for Support of Leading Scientific Schools (project nos. NSh-1087.2003.5 and NSh-1642.2003.5).

REFERENCES

1. O. Johnsen, J. D. Grice, and R. A. Gault, *Can. Mineral.* **37**, 1111 (1999).
2. I. A. Ekimenkova, R. K. Rastsvetaeva, and N. V. Chukanov, *Dokl. Akad. Nauk, Khimiya* **374** (3), 352 (2000).
3. R. K. Rastsvetaeva, I. A. Ekimenkova, and I. V. Pekov, *Dokl. Akad. Nauk* **368** (5), 636 (1999).
4. V. I. Andrianov, *Kristallografiya* **32** (1), 228 (1987) [*Sov. Phys. Crystallogr.* **32** (1), 130 (1987)].
5. N. Walker and D. Stuart, *Acta Crystallogr. A* **39** (2), 158 (1983).
6. A. P. Khomyakov, V. D. Dusmatov, Dzh. Ferraris, *et al.*, *Zap. Vseross. Mineral. O–va*, No. 5, 40 (2003).

Translated by T. Safonova

STRUCTURE OF INORGANIC COMPOUNDS

Crystal Structure of Chabazite K

O. V. Yakubovich*, W. Massa**, P. G. Gavrilenko*, and I. V. Pekov*

* Moscow State University, Vorob'evy gory, Moscow, 119992 Russia

e-mail: yakubol@geol.msu.ru

** Philipps University, Marburg, Germany

Received June 30, 2004

Abstract—The crystal structure of the chabazite K with the formula $(K_{1.33}Na_{1.02}Ca_{0.84})[Al_4Si_8O_{24}] \cdot 12.17H_2O$ from late hydrothermalites in the Khibiny alkaline massif (Kola Peninsula) is established by X-ray diffraction analysis (CAD4 four-circle diffractometer, λMoK_α radiation, graphite monochromator, $T = 193$ K, $2\theta_{max} = 70^\circ$, $R_1 = 0.047$ for 4745 reflections) on the basis of experimental data (6265 reflections) obtained from a twin (twinning parameter 0.535(1)): $a = 13.831(3)$ Å, $c = 15.023(5)$ Å, sp. gr. $R\bar{3}m$, $Z = 3$, $\rho_{calcd} = 2.016$ g/cm³. It is shown that cations occupy five independent positions in large cavities of the tetrahedral Al,Si,O anionic framework in potassium-rich chabazite. A comparative crystallochemical analysis of chabazites of different composition and origin is performed. © 2005 Pleiades Publishing, Inc.

INTRODUCTION

Minerals of the chabazite series are wide-pore aluminosilicate zeolites that are the most widely spread in nature. These minerals are characterized by significant variations in the Al/Si ratio in the tetrahedral framework and a large diversity of cationic composition of the framework cavities. The chabazite structure is consistent with the principles of the “Second Chapter of the Crystal Chemistry of Silicates” [1]; i.e., it consists of milarite six-membered two-level rings, which are oriented parallel to each other and perpendicular to the threefold axes, forming a framework of aluminosilicate tetrahedra. In cavities $11 \times 6.6 \times 6.6$ Å³ in size (one cavity per unit cell) of the three-dimensional framework, which are limited by 2 hexagonal and 12 tetragonal rings, windows formed by eight-membered rings about 3.9 Å in diameter are open in six directions [2]. Neighboring cavities are linked to each other through such windows to form a three-dimensional system of channels. The high sorption ability of chabazite is related to

the fact that large cations, including Cs⁺ ions and hydrocarbon ions 4.9 Å in diameter, can easily pass through these channels (Fig. 1).

Milarite six-membered two-level rings $M_{12}O_{30}$ ($M = Si, Al$) are the main silicate building blocks in the chemistry of zeolites. They are generally represented in the form of hexagonal prisms with Si(Al) atoms at vertices. According to [3], chabazite belongs to the ABC family, which includes the crystal structures formed by hexagonal six-member rings without additional tetrahedra. Hexagonal prisms, rhombohedrally arranged at three levels along the c axis (the densest cubic packing), form an anionic tetrahedral framework in chabazite (Fig. 1). Differences in the packing of these prisms and their alternation and sequence along the threefold axis are responsible for the type of a specific structure in the ABC family.

According to the modern nomenclature of zeolites, the chabazite series includes four mineral species differing in the dominant extraframework cation: chaba-

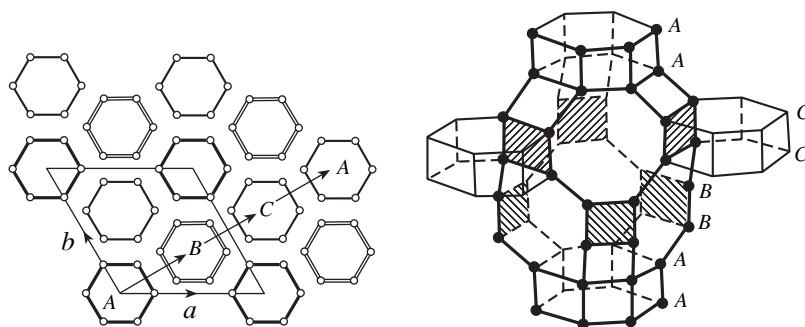


Fig. 1. Schematic diagram of the construction of the chabazite structure from basic structural units: six-membered two-level rings (left) and the crystal structure of chabazite (right); the positions of Si and Al atoms are shown by circles [2].

zite Ca, chabazite Na (previously known as herschelite), chabazite K, and chabazite Sr [4, 5]. Chabazite Ca is most widely spread and best studied. Chabazite K with the formula $(K, Ca_{0.5})_4 Al_4 Si_8 O_{24} \cdot 12H_2O$, which was described for the first time in a composition of hydrothermal mineralization in effusive Vesuvius rocks [6], was considered recently to be a highly rare mineral, although potassium-rich and sodium potassium chabazites can be easily synthesized under laboratory conditions [7]. The crystal structure of this mineral has not been investigated. In recent years, it has been established that chabazite K is one of the basic zeolites in specific calcium-rich late hydrothermalites related to the apatite-containing melteigite–urtite complex in the Khibiny alkaline massif (Kola Peninsula) [8]. A very characteristic feature of chabazite K from hydrothermalites of alkaline rocks is the presence of twins [9]. The sample studied here originates from the underground rock mine in Yukspor Mountain in the southern part of the Khibiny massif. Chabazite K in the form of an aggregate of colorless watery-transparent isometric and flattened grains (up to 1.5 mm in diameter) forms the axial zone in a string 3 mm in size. The selvages in the string are formed by phillipsite K. A string cuts spreusteinized pegmatoid ijolite. The chemical composition of chabazite K is as follows (wt %): Na_2O (2.62), K_2O (7.22), CaO (4.61), SrO (1.44), BaO (0.04), Al_2O_3 (18.75), SiO_2 (46.41), and H_2O (19.35); 100.44 in sum (electron microprobe data for the oxides; the water content was determined by thermogravimetric analysis). The empirical formula calculated for 24 oxygen atoms is $(K_{1.59}Na_{0.88}Ca_{0.85}Sr_{0.14})_{\Sigma 3.46}(Al_{3.82}Si_{8.02})_{\Sigma 11.84}O_{24} \times 11.16H_2O$.

X-RAY EXPERIMENT AND STRUCTURE IDENTIFICATION

The parameters of the trigonal unit cell of chabazite K under normal conditions are $a = 13.840(2)$ Å and $c = 15.100(3)$ Å. Since one of the main problems related to the structural investigation of zeolites is the localization of highly mobile atoms in cavities of the tetrahedral framework, the necessary experimental data for structural interpretation were obtained at low temperatures ($T = 193$ K) on a CAD4 four-circle diffractometer using MoK_{α} radiation (graphite monochromator). The crystallographic characteristics of the chabazite under study, the X-ray data, and the refinement parameters are listed in Table 1.

Analysis of absences in the experimental set of reflections revealed regularities characteristic of a crystal with a rhombohedral lattice that is a so-called obverse/reverse twin formed owing to the action of a twinning axis either parallel or perpendicular to the c axis of the unit cell. In the hexagonal orientation of a rhombohedral crystal, the reflections from the first domain of a twin of this type follow the condition $-h + k + l = 3n$ (obverse orientation) and the reflections from

Table 1. Crystallographic data and the details of X-ray data collection and refinement

Chemical formula	$(K_{0.33}Na_{0.25}Ca_{0.21})[AlSi_2O_6] \times 3.04H_2O$
Space group, Z	$R\bar{3}m, 12$
$a, c, \text{Å}$	13.831(3), 15.023(5)
$V, \text{Å}^3$	2489.3(1)
$\rho_{\text{calcd}}, \text{g/cm}^3$	2.016
Absorption coefficient μ, mm^{-1}	0.866
$\theta_{\text{max}}, \text{deg}$	34.90
Number of independent/collected with $I > 1.96\sigma(I)$ reflections	6265/4745
Refinement method	on F^2
Number of parameters in refinement	107
Absorption correction	semiempirical, using equivalents
$T_{\text{min}}/T_{\text{max}}$	0.667/0.701
Extinction coefficient	0.0009(2)
Twinning parameter	0.535(1)
R_1 (for collected reflections)	0.0470
wR_2 (for all independent reflections)	0.1177
GOF	1.082
$\Delta\rho_{\text{max}}/\Delta\rho_{\text{min}}, e/\text{Å}^3$	0.71/−0.42

the second domain obey the condition $h - k + l = 3n$ (reverse orientation) [10]. The structure was solved directly within the hexagonal orientation of the space group $R\bar{3}m$ and refined on the assumption that Si^{4+} and Al^{3+} cations jointly occupy tetrahedral positions in the ratio 2 : 1, according to the X-ray spectroscopic data. All calculations in the interpretation and structure refinement were carried out using the SHELX97 program package [11, 12]. The values of the atomic-scattering functions and the anomalous-dispersion corrections were taken from [13]. The intensities of the reflections corresponding to the total contribution from both twin individuals were corrected using the TWINXLI program [14]. The location of K, Na, and Ca atoms and water molecules in the framework cavities was established by the method of successive approximations from the difference electron-density maps. The location of most atoms (except for the two oxygen atoms of the water molecules with low occupancy of the corresponding positions) was refined in the anisotropic approximation of thermal vibrations. The refinement results are indicative of the presence of two almost identical domains (the twinning parameter is close to 0.5) in the sample studied. The obtained coordinates of

Table 2. Coordinates of the basic atoms and equivalent thermal displacement parameters for chabazite K

Atom	G^*	x	y	z	U_{eq}
Si	0.6667	0.10485(2)	0.43831(2)	0.06199(1)	0.01161(5)
Al	0.3333	0.10485(2)	0.43831(2)	0.06199(1)	0.01161(5)
K(1)	0.0917(5)	0.6667	0.3333	0.0613(1)	0.0291(4)
K(2)	0.0194(5)	0.6667	0.3333	0.0268(5)	0.025(2)
Ca	0.070(1)	0.1166(3)	-0.1166(3)	-0.0379(4)	0.092(2)
Na(1)	0.059(1)	0	0	0.0998(3)	0.064(2)
Na(2)	0.026(1)	0.6341(26)	0.3170(13)	0.0939(9)	0.077(12)
O(1)	0.5	0.42743(10)	0.21372(5)	-0.03306(8)	0.0307(3)
O(2)	0.5	0.34846(7)	0	0	0.0252(2)
O(3)	0.5	0.07040(8)	0.40374(8)	0.16667	0.0339(2)
O(4)	0.5	0.56780(5)	0.13559(10)	-0.04210(10)	0.0297(2)
O(5) _(H₂O)	0.157(4)	0.343(2)	0.171(1)	0.188(1)	0.119(4)
O(6) _(H₂O)	0.197(4)	0.1380(6)	0	0	0.232(6)
O(7) _(H₂O)	0.003(1)	0.6667	0.3333	-0.1667	0.025(7)**
O(8) _(H₂O)	0.081(6)	0.142(2)	0.071(1)	0.063(4)	0.20(1)
O(9) _(H₂O)	0.142(5)	0.0900(6)	-0.0900(6)	0.1627(10)	0.131(5)
O(10) _(H₂O)	0.328(5)	0.0186(6)	-0.1422(5)	0.1498(6)	0.133(3)
O(11) _(H₂O)	0.094(4)	0.3333	0.1965(6)	0.1667	0.098(7)
O(12) _(H₂O)	0.012(1)	0	0	0.067(3)	0.033(9)**

* Ratio of the number of atoms in a given position to the multiplicity of the general position.

** Isotropic thermal displacement parameters.

Table 3. Interatomic distances in the crystal structure of chabazite K, Å

(Si, Al) tetrahedron		K(1) nine-vertex polyhedron		K(2) nine-vertex polyhedron	
Si-O(3)	1.6434(6)	K(1)-O(9)	2.708(14) × 3	K(2)-O(4)	2.585(3) × 3
O(1)	1.6447(5)		or	O(1)	3.004(3) × 3
O(2)	1.6469(5)	O(10)	2.795(8) × 3	O(9)	3.051(15) × 3
O(4)	1.6482(5)	O(4)	2.833(2) × 3		or
Si-O _{av}	1.646	O(1)	3.197(2) × 3	O(10)	3.159(9) × 3
		K(1)-O _{av}	2.927	K(2)-O _{av}	2.898
			Na(1) prism		Na(2) five-vertex polyhedron
Ca seven-vertex polyhedron		Na-O(9)	2.353(14) × 3	Na-O(10)	2.50(1) × 2
Ca-O(5)	2.314(4)		or		or
	or	O(10)	2.238(7) × 3	O(10)'	2.25(3) × 2
O(11)	2.618(25)	O(6)	2.428(7) × 3		or
O(10)	2.356(9) × 2	Na-O _{av}	2.362	O(9)'	2.30(2) × 2
	or			O(9)	2.79(3)
O(8)	2.467(10) × 2			O(4)	3.00(1) × 2
O(1)	2.562(5)			Na-O _{av}	2.70
O(2)	2.836(3) × 2				
O(9)	3.082(17)				
	or				
O(10)'	3.072(10)				
Ca-O _{av}	2.657				

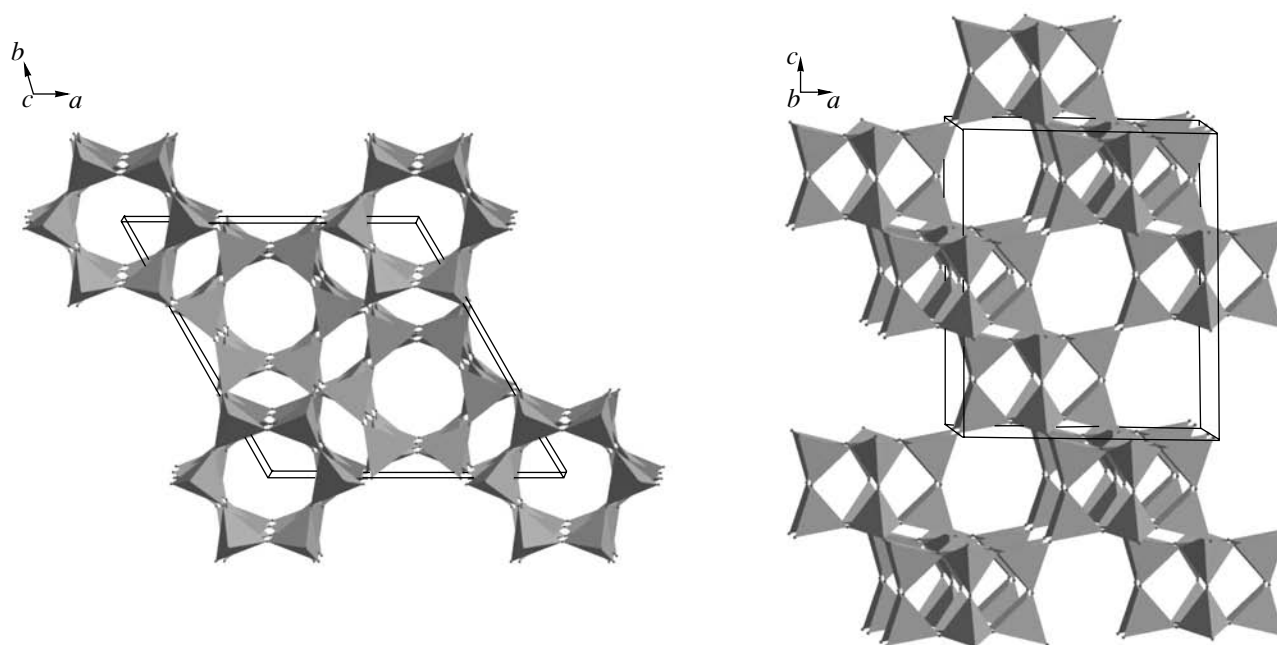


Fig. 2. Tetrahedral framework in the chabazite structure projected onto the *ab* (left) and *ac* (right) planes. The axes correspond to the hexagonal orientation of the space group $R\bar{3}m$.

the basic atoms and the temperature corrections are listed in Table 2. The values of interatomic distances corresponding to these coordinates are given in Table 3. The chabazite formula $(K_{1.33}Na_{1.02}Ca_{0.84})[Al_4Si_8O_{24}] \cdot 12.17H_2O$ found by the structure refinement confirms the quantitative dominance of potassium over sodium and calcium in the mineral from the Khibiny alkaline massif and is in good agreement with the formula obtained from the X-ray spectroscopic and thermogravimetric data.

ANALYSIS OF INTERATOMIC DISTANCES

The cation–oxygen distances in the tetrahedra with intrinsic symmetry C_1 , which form a three-dimensional framework (Fig. 2), lie in the range 1.6434(6)–1.6482(5) Å and are characteristic of polyhedra with mixed Si,Al occupation. Potassium, sodium, and calcium atoms and water molecules are located in the cavities of the tetrahedral framework. Two positions are established for both K and Na atoms, the Ca atom is located in one position, and eight positions are found for the O atoms of water molecules. All cations and water molecules statistically (with different probabilities) occupy corresponding positions in the cavities of the open framework configuration. This distribution of extraframework atoms is typical of zeolites and was established by us, in particular, for the laumontite [15] and merlinoite [16] structures.

Potassium atoms in the positions with symmetry $3m$ are located in nine-vertex polyhedra formed by both framework oxygen atoms and interstitial water mole-

cules. The lengths of K–O distances lie in the range 2.585–3.197 Å (Table 3). The distortion of the oxygen positions corresponding to the positions of the water molecules in the structure leads to the distortion of the coordination polyhedra surrounding K, Na, and Ca atoms. Thus, three of nine vertices of the K(1) polyhedron are occupied by oxygen atoms of water molecules O(9) or O(10). The oxygen atoms of different water molecules are spaced from each other at a distance of 0.905 Å, which forbids their participation in the formation of the same polyhedron. In accordance with the foregoing, the interatomic K(1)–O distances range from 2.708 to 3.197 Å (the average is 2.913 Å) or from 2.795 to 3.197 Å (the average is 2.941 Å). In the nine-vertex polyhedron K(2), the range of K–O distances is 2.585–3.051 Å (the average is 2.880 Å) or 2.585–3.159 Å (the average is 2.916 Å) when the nine-vertex polyhedra are formed by atoms O(9) or O(10), respectively. The K polyhedra are trigonal prisms capped at all lateral faces. When K^+ cations form bonds with atoms O(10) rather than O(9), trigonal prisms are twisted (Fig. 3). The oxygen atoms of the water molecules O(12) and O(7) also enter the first coordination sphere of the K(1) and K(2) atoms, respectively, being located at the distances K(1)–O(12) = 3.077(4) Å and K(2)–O(7) = 2.907(8) Å. However, low statistical occupancies of the O(12) and O(7) positions ($G = 0.012$ and 0.003, respectively) result in very low probabilities of participation of these atoms in the formation of polyhedra around K^+ cations. When the water molecules O(12) and O(7) enter the structure, the K(1) and K(2) polyhedra become ten-vertex ones (Fig. 3).

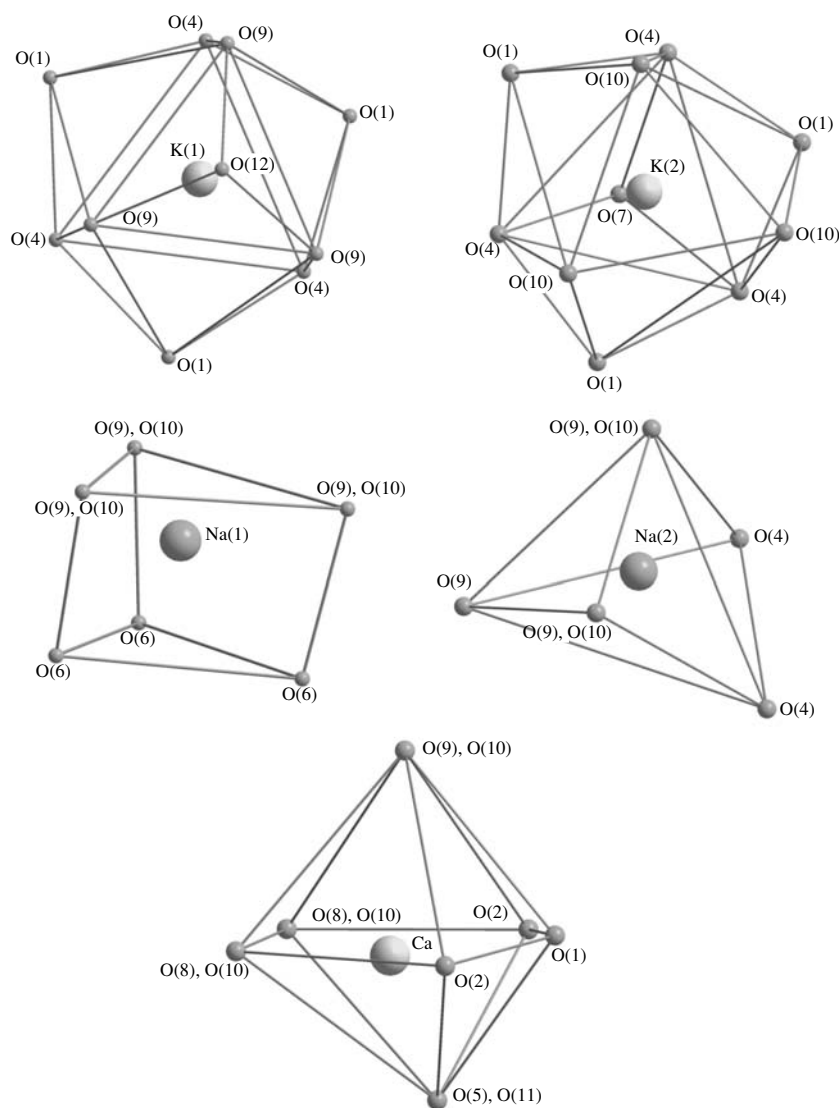


Fig. 3. Environment of cations in framework cavities in the crystal structure of chabazite K.

The coordination polyhedra around the Na atoms are a distorted trigonal prism Na(1) and a five-vertex polyhedron Na(2). The distances between cations and oxygen atoms of water molecules in the six-vertex polyhedron Na(1) range from 2.353 to 2.428 Å when the polyhedron is formed by the water molecules O(9). In the case of coordination of the Na(1) atom by the water molecules O(10), the lower limit of distances in the polyhedron decreases to 2.238 Å (Table 3). In the five-vertex polyhedron Na(2) (Fig. 3), two vertices are statistically occupied by either water molecules O(9) at a distance of 2.30 Å from the Na atoms or by the water molecules O(10) at a distance of 2.25 or 2.50 Å. The framework atoms O(4) coordinating Na(2) are spaced at a distance of 3.00 Å. (The average is 2.70 Å.)

The first coordination sphere of the Ca atom involves three framework oxygen atoms and four water

molecules. The shortened interatomic distances O(5)–O(11) = 0.54 Å, O(8)–O(10) = 1.57 Å, and O(9)–O(10) = 0.905 Å allow for the participation of one oxygen atom from each pair of water molecules in the formation of a pentagonal bipyramid around the Ca atom (Table 3, Fig. 3). The lengths of the Ca–O bonds in the polyhedron range from 2.314 to 3.082 Å. (The average is 2.657 Å.)

DISTRIBUTION OF CATIONS AND WATER MOLECULES IN CAVITIES OF THE TETRAHEDRAL FRAMEWORK AND GENETIC CRYSTAL CHEMISTRY OF CHABAZITES

According to [7], three types of positions in framework cavities applicable for occupation by alkali and alkaline-earth cations are distinguished in the structure

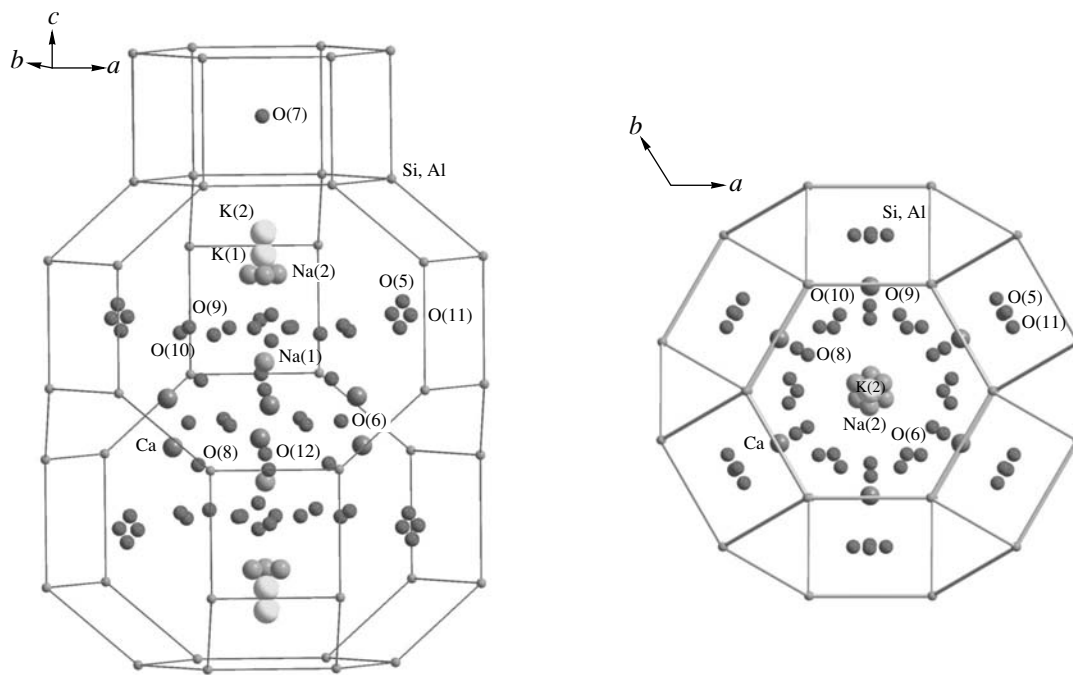


Fig. 4. Arrangement of cations and water molecules in cavities of the tetrahedral framework. Projection along the [001] direction (left) and the side view (right).

of dehydrated chabazite. These are the centers of hexagonal prisms (*S1*); the positions in large lantern-like cavities near six-membered rings (*S2*), shifted from the *S1* position along the threefold axis; and the positions at the internal walls of lantern-like cavities, generally near four-membered or eight-membered rings (*S3*). In hydrated chabazites (natural mineral phases), water molecules, grouping around cations, displace them into cavities. The water molecules that are not bound to framework cations always coordinate interstitial cations in minerals of the chabazite series.

This is specifically the case under consideration. All large cations, coordinated to a greater or lesser extent by water molecules, are located in large lantern-like cavities formed by $(\text{Si,Al})\text{O}_4$ tetrahedra. Two independent positions *S2* (xxx in the rhombohedral coordinates) at a distance of 0.519 \AA from each other under (or above) six-membered rings of tetrahedra are statistically occupied by K atoms with different probabilities. Six oxygen framework atoms and four water molecules surround each K atom. The Na(2) atom is located near the positions of K cations along the direction to the cavity center at distances of 0.62 and 1.08 \AA from K(1) and K(2), respectively (Fig. 4). The displacement of the Na(2) atom from the threefold axis (the xxz position) results in the disordered arrangement of the three atoms at a distance of 0.67 \AA , which are coordinated by both framework oxygen atoms and interstitial water molecules (Table 3). It is noteworthy that the Na(2) position had not been established in minerals of the chabazite series and synthetic species and was found by us for the

first time in the structure of the chabazite from late hydrothermalites in the Khibiny alkaline massif.

Atoms Na(1), which are surrounded by the solvate shell of water molecules and are not bound directly to the framework, are located at the threefold axis near the center of a large cavity at a distance of 2.13 \AA from atoms Na(2) (Fig. 4). Calcium atoms are also located in the central part of the cavity but, in contrast to Na(1), closer to its lateral walls, an arrangement which makes it possible for the framework oxygen atoms to be involved in the formation of coordination polyhedra around Ca atoms along with the oxygen atoms of water molecules.

The formation of a solvate shell around the K^+ , Na^+ , and Ca^{2+} cations leads to their displacement into a large lantern-like cavity, and the *S1* position (at the center of the hexagonal prism) and the *S3* position (at the entrance of the cavity) are occupied by the water molecules O(7) and O(5) (O(11)), respectively (Fig. 4).

It is of interest to compare the character of distribution of K^+ , Na^+ , and Ca^{2+} cations and water molecules in the structural cavities of the chabazite from low-temperature hydrothermalites of an alkaline formation with the arrangement of atoms in the cavities of the tetrahedral anionic framework in the chabazites from rocks of other types and ion-exchange and dehydrated phases (Table 4).

Analysis of the data of Table 4 shows that cations of alkali and alkaline earth metals are generally concentrated in large cavities of the tetrahedral aluminosilicate

Table 4. Comparison of the distributions of atoms in framework cavities in chabazites of different origins

Chabazite K, this study	Wyckoff position, rhombohedral orientation	$x y z^*$	Minerals and ion exchange phases								
			chabazite Ca [17]	** [23]	chabazite Ca [18]	** [18]	** [18]	** [18]	** [18]	chabazite Ca [24]	*** [25]
K(1)	2c	0.228 0.228 0.228	Ca, Sr	K	H ₂ O	H ₂ O	Na, K	H ₂ O	H ₂ O	H ₂ O	
K(2)	2c	0.194 0.194 0.194			Ca, K, Mg, Sr	Na		Ca	Sr		Ca
Ca	6h	0.579 0.579 0.229	H ₂ O	K	Ca, K, Mg, Sr	Na	Na, K	Ca	Sr		
Na(1)	2c	0.400 0.400 0.400	Ca, Sr		Ca, K, Mg, Sr	Na	Na, K	Ca	Sr	H ₂ O	
Na(2)	6h	0.277 0.277 0.228									
O(5) _(H₂O)	6h	0.516 0.516 0.031	H ₂ O	K H ₂ O	H ₂ O	H ₂ O	Na, K H ₂ O	H ₂ O	H ₂ O	H ₂ O	
O(6) _(H₂O)	6g	0.362 -0.362 0.5			H ₂ O	H ₂ O	H ₂ O	H ₂ O	H ₂ O	H ₂ O	
O(7) _(H₂O)	1a	0 0 0	Ca, Sr		Ca, K, Mg, Sr			Ca	Sr		Ca
O(8) _(H₂O)	12i	0.295 0.350 0.508									
O(9) _(H₂O)	6h	0.247 0.247 0.517		H ₂ O	H ₂ O	H ₂ O	H ₂ O	H ₂ O	H ₂ O	H ₂ O	
O(10) _(H₂O)	12i	0.208 0.332 0.511	H ₂ O		H ₂ O	H ₂ O	H ₂ O	H ₂ O	H ₂ O	H ₂ O	
O(11) _(H₂O)	6f	0.470 -0.470 0									
O(12) _(H₂O)	2c	0.433 0.433 0.433									
	6h	x, x, z		H ₂ O 0.447 0.447 0.226							
	6h	x, x, z			H ₂ O 0.585 0.585 0.316	H ₂ O 0.621 0.621 0.386		H ₂ O 0.584 0.584 0.334			
	6h	x, x, z				H ₂ O 0.368 0.368 0.193	H ₂ O 0.370 0.370 0.086				
	12i	x, y, z									Ca 0.093 0.188 0.470
	12i	x, y, z								Ca 0.355 0.478 0.586	
	12i	x, y, z									
	12i	x, y, z									
	12i	x, y, z									

Table 4. (Contd.)

Chabazite K, this study	Wyckoff position, rhombohedral orientation	$x y z^*$	Minerals and ion exchange phases								
			chabazite Ca [19]	chabazite Ca [20]	chabazite Ca [26]	** [21]	** [27]	** [22]	*** [28]	*** [29]	*** [30]
K(1)	2c	0.228 0.228 0.228	Ca(<i>h</i>), Ca(<i>d</i>)		Ca, Na, K	Cs(<i>h</i>)	Ba	H ₂ O			
K(2)	2c	0.194 0.194 0.194		Ca, Fe(<i>d</i>) Ca, Fe(<i>h</i>)		Ca(<i>h</i>)		Cu(<i>d</i>)	Ca	Ca	
Ca	6h	0.579 0.579 0.229	Ca(<i>h</i>)	H ₂ O	Ca, Na, K		Ba				
Na(1)	2c	0.400 0.400 0.400	H ₂ O	H ₂ O	Ca, Na, K		Ba				
Na(2)	6h	0.277 0.277 0.228									
O(5) _(H₂O)	6h	0.516 0.516 0.031	H ₂ O	Ca, Fe(<i>d</i>) Ca, Fe(<i>h</i>)	H ₂ O	Cs(<i>h</i>) Cs(<i>d</i>)	H ₂ O	H ₂ O(<i>h</i>)			
O(6) _(H₂O)	6g	0.362 -0.362 0.5						H ₂ O(<i>h</i>)			
O(7) _(H₂O)	1a	0 0 0	Ca(<i>d</i>)	Ca, Fe(<i>d</i>)		Ca(<i>d</i>)			Ca	Ca	Ca
O(8) _(H₂O)	12i	0.295 0.350 0.508		H ₂ O							
O(9) _(H₂O)	6h	0.247 0.247 0.517	Ca(<i>h</i>)	H ₂ O		H ₂ O	H ₂ O	H ₂ O(<i>h</i>)			
O(10) _(H₂O)	12i	0.208 0.332 0.511	H ₂ O					H ₂ O			
O(11) _(H₂O)	6f	0.470 -0.470 0									
O(12) _(H₂O)	2c	0.433 0.433 0.433									
	6h	x, x, z						Cu(<i>h</i>) 0.426 0.426 0.282	H ₂ O 0.455 0.455 0.179		
	6h	x, x, z									
	6h	x, x, z									
	12i	x, y, z									
	12i	x, y, z		H ₂ O 0.360 0.527 0.615		H ₂ O 0.359 0.530 0.613					
	12i	x, y, z	H ₂ O 0.390 0.083 0.465								
	12i	x, y, z		H ₂ O 0.810 0.504 0.598							
	12i	x, y, z						Cu(<i>h</i>) 0.483 -0.177 0.389			
	12i	x, y, z							CO 0.338 0.403 0.230		

Note: *h* and *d* denote the hydrated and dehydrated forms, respectively.

* The coordinates of atoms from Table 2 are recalculated for the rhombohedral orientation, sp. gr. $R\bar{3}m$.

** Compounds formed by ion exchange.

*** Compounds formed by ion exchange with subsequent dehydration and phases on their basis.

framework of chabazite. The ion exchange data indicate that the same positions can be occupied by cations of different valence, including both small (Na^+ , Ca^{2+}) and large (K^+ , Ba^{2+}) cations. In the structures of some minerals and ion exchange phases on their basis, the S2 position at the threefold axis near the six-membered ring can also be occupied by water molecules.

The position at the center of the hexagonal prism (S1), whose occupancy by water molecules is very low in the case under consideration, is generally occupied by Ca atoms in the structures of dehydrated chabazites. Some researchers [17, 18] believe that this position in parent mineral phases is also occupied by cations.

The positions of water molecules, which are the most significant from the point of view of their participation in the coordination of extraframework cations (specifically, O(10) and O(9)), are present in chabazites of different origin with a rather good stability. However, simultaneous presence of oxygen atoms in both these positions was established (along with the chabazite considered here) only in the mineral studied in [18] and ion exchange phases on its basis. In the chabazite Ca from Zabaykalye [19], a Ca atom is located in one of the noted positions of water molecules (O(9)).

The S3 positions at the entrances of eight-membered windows are mostly occupied by water molecules (O(5) and O(11) in the structure under study) involved in the formation of a solvate shell around the Ca atom. In the structures of chabazites from granite pegmatites from the Kola Peninsula and a Cs-exchanged sample, Ca(Fe) and Cs atoms, respectively, are fixed in these positions [20, 21].

The position of water molecules O(6), coordinating Na(1) near the center of a large cavity, was also established, along with the structure considered here, for the chabazites analyzed in [18, 22].

Summing up this section, we should note that the maximum number of cation positions was established in the structure of the chabazite K from late hydrothermalites in the Khibiny alkaline massif. The changes in the location of water molecules occupying interstitial positions of the tetrahedral framework of chabazites of different origin are due, in particular, to variations in the chemical composition of mobile cations of alkali and alkaline earth metals surrounded by solvate shells and, therefore, to the specific features of the chemical processes occurring in the late stages of formation of rocks of alkaline complexes.

Chabazite is characterized by the lowest framework density (FD = 14.4) among microporous aluminosilicates present in alkaline massifs and is the last term in the associations of zeolites from differentiates of the rocks of this type. It is formed in the final stages of the hydrothermal process under the following conditions: $T \leq 150\text{--}160^\circ\text{C}$ and pH 8.5–9 [9]. The microprobe analysis data on late chabazites show a heterogeneous set of extraframework cations in the absence of regularity in the distribution of regions of different composi-

tion within one sample. With allowance for the well-known ion-exchange properties of chabazites, this type of inhomogeneity in the chemical composition can be interpreted as a result of the postcrystallization cationic exchange [9]. According to [9], the evolutionary transformation of the chemical composition of cations within the framework of zeolites of alkaline hydrothermalites at the coincidence of time coordinates and upon cooling occurs as follows: $\text{Na} \rightarrow \text{Ba} \rightarrow \text{Ca} + \text{Sr} \rightarrow \text{K}$.

It is noteworthy that chabazite K is present not only in the Khibiny massif, with its potassium–sodium geochemical specificity, but also in the neighboring Lovozero massif, very rich in sodium, where the hydrothermal potassium mineralization occurs only in the final stages. Taking into account the foregoing, we cannot exclude that the enrichment in potassium observed in the chabazites from both arrays is, on the whole, due to the secondary natural processes with partial substitution of large K^+ cations with Ca^{2+} and Na^+ cations, these cations being more typical of chabazites.

ACKNOWLEDGMENTS

This study was supported by the Russian Foundation for Basic Research, project no. 02-05-64845; the program “Support of Leading Scientific Schools,” grant no. NSh-1955.2003.5; and the German Academy of Sciences.

REFERENCES

1. N. V. Belov, *Essays on Structural Mineralogy* (Nedra, Moscow, 1976) [in Russian].
2. L. S. Dent and J. V. Smith, *Nature* **181** (4626), 1794 (1958).
3. J. V. Smith and J. M. Bennet, *Am. Mineral.* **66**, 777 (1981).
4. D. S. Coombs, A. Alberti, Th. Armbruster, *et al.*, *Can. Mineral.* **35**, 1571 (1997).
5. I. V. Pekov, A. G. Turchkova, N. V. Chukanov, *et al.*, *Zap. Vseros. Miner. O–va* **129** (4), 54 (2000).
6. M. De Gennaro and E. Franco, *Rend. Accad. Naz. Lincei* **40**, 490 (1976).
7. *Zeolite Molecular Sieves: Structure, Chemistry and Use*, Ed. by D. W. Breck (Wiley, New York, 1974; Mir, Moscow, 1976).
8. E. V. Lovskaya, I. V. Pekov, N. N. Kononkova, and A. G. Turchkova, *Zap. Vseros. Miner. O–va* **131** (2), 17 (2002).
9. I. V. Pekov, A. G. Turchkova, E. V. Lovskaya, and N. V. Chukanov, *Zeolites of Alkaline Massives* (Ékost, Moscow, 2004) [in Russian].
10. R. Herbst-Irmer and G. M. Sheldrick, *Acta Crystallogr., Sect. B: Struct. Sci.* **58**, 477 (2002).
11. G. M. Sheldrick, *SHELXS97. Program for the Solution of Crystal Structures* (Univ. of Göttingen, Göttingen, 1997).

12. G. M. Sheldrick, *SHELXL97. Program for the Refinement of Crystal Structures from Diffraction Data* (Univ. of Göttingen, Göttingen, 1997).
13. *International Tables for Crystallography*, Ed. by T. Hahn, 8th ed. (Kluwer, Dordrecht, 1995).
14. F. Hahn and W. Massa, *TWINXLI, Program for Handling Diffraction Data of Twinned Crystals* (Marburg, 1997).
15. O. V. Yakubovich and M. A. Simonov, *Kristallografiya* **30** (6), 1072 (1985) [*Sov. Phys. Crystallogr.* **30**, 624 (1985)].
16. O. V. Yakubovich, V. Massa, I. V. Pekov, and Ya. V. Kucherinenko, *Kristallografiya* **44** (5), 835 (1999) [*Crystallogr. Rep.* **44**, 776 (1999)].
17. M. Calligaris, G. Nardin, and L. Randaccio, *Acta Crystallogr., Sect. B: Struct. Crystallogr. Cryst. Chem.* **38**, 602 (1982).
18. A. Alberti, E. Galli, G. Vezzalini, *et al.*, *Zeolites*, No. 2, 303 (1982).
19. I. K. Butikova, Yu. F. Shepelev, and Yu. I. Smolin, *Kristallografiya* **38** (4), 68 (1993) [*Crystallogr. Rep.* **38**, 461 (1993)].
20. E. L. Belokoneva, B. A. Maksimov, I. A. Verin, *et al.*, *Kristallografiya* **30** (5), 874 (1985) [*Sov. Phys. Crystallogr.* **30**, 507 (1985)].
21. M. Calligaris, A. Mazzetti, G. Nardin, and L. Randaccio, *Zeolites*, No. 6, 137 (1986).
22. J. J. Pluth and J. V. Smith, *Mater. Res. Bull.* **12**, 1001 (1977).
23. M. Calligaris, G. Nardin, and L. Randaccio, *Zeolites*, No. 3, 205 (1983).
24. J. V. Smith, F. Rinaldi, and L. S. Dent Glasser, *Acta Crystallogr.* **16**, 45 (1963).
25. J. V. Smith, *Acta Crystallogr.* **15**, 835 (1962).
26. F. Mazzi and E. Galli, *Neues Jahrb. Mineral., Monatsh.*, No. 10, 461 (1983).
27. M. Calligaris and G. Nardin, *Zeolites*, No. 2, 200 (1982).
28. W. J. Mortier, J. J. Pluth, and J. V. Smith, *Mater. Res. Bull.* **12**, 103 (1977).
29. W. J. Mortier, J. J. Pluth, and J. V. Smith, *Mater. Res. Bull.* **12**, 97 (1977).
30. W. J. Mortier, *J. Phys. Chem.* **83** (17), 2263 (1979).

Translated by Yu. Sin'kov

**STRUCTURE
OF INORGANIC COMPOUNDS**

Structure and Properties of Antimony-Doped Potassium Titanyl Phosphate Single Crystals

O. A. Alekseeva*, **O. D. Krotova****, **N. I. Sorokina***, **I. A. Verin***, **T. Yu. Losevskaya****,
V. I. Voronkova**, **V. K. Yanovskii****, and **V. I. Simonov***

* *Shubnikov Institute of Crystallography, Russian Academy of Sciences,
Leninskii pr. 59, Moscow, 119333 Russia
e-mail: olalex@ns.crys.ras.ru*

** *Moscow State University, Vorob'evy gory, Moscow, 119992 Russia
Received October 7, 2004*

Abstract—Antimony-doped potassium titanyl phosphate (KTP) crystals of the composition KTiOPO_4 are studied by X-ray diffraction analysis. It is shown that, with an increase of antimony content in KTP crystals, the occupancies of potassium positions change and new additional positions for potassium atoms arise. The formation of additional vacancies and splitting of the potassium-cation positions explain the considerable decrease in the temperature of the ferroelectric phase transition, enhancement of the relaxation phenomena, and an increase in electric conductivity of antimony-doped KTP crystals. Substitution of antimony atoms for titanium is accompanied by elongation of short and shortening of long Ti–O bonds in the TiO_6 octahedra, processes which result in lower intensity of second-harmonic generation in laser-irradiated KTP crystals. © 2005 Pleiades Publishing, Inc.

INTRODUCTION

Potassium titanyl phosphate crystals of the composition KTiOPO_4 (KTP) and other crystals of this family and the solid solutions on their basis are ferroelectrics—

superionics and are promising materials for nonlinear optics [1, 2]. Doping of KTP crystals with various chemical elements allows one to control their physical properties over wide ranges [2, 3].

Table 1. Unit-cell parameters and volume of KTP crystals with different Nb contents

	<i>a</i> , Å	<i>b</i> , Å	<i>c</i> , Å	<i>V</i> , Å ³
KTP [29]	12.819(1)	6.399(1)	10.584(1)	868.2(1)
$\text{K}_{0.99}\text{Ti}_{0.99}\text{Sb}_{0.01}\text{OPO}_4$	12.811(1)	6.4056(4)	10.585(1)	868.6(1)
$\text{K}_{0.93}\text{Ti}_{0.93}\text{Sb}_{0.07}\text{OPO}_4$	12.792(2)	6.4048(5)	10.557(1)	864.9(1)
$\text{K}_{0.83}\text{Ti}_{0.83}\text{Sb}_{0.17}\text{OPO}_4$	12.776(2)	6.4102(9)	10.5027(6)	860.1(1)

Table 2. Conditions of the experiment and refinement for KTB : Sb single crystals with 1, 7, and 17 at % Sb

Single crystals	KTP with 1% Sb	KTP with 7% Sb	KTP with 17% Sb
Chemical composition	$\text{K}_{0.99}\text{Ti}_{0.99}\text{Sb}_{0.01}\text{OPO}_4$	$\text{K}_{0.93}\text{Ti}_{0.93}\text{Sb}_{0.07}\text{OPO}_4$	$\text{K}_{0.83}\text{Ti}_{0.83}\text{Sb}_{0.17}\text{OPO}_4$
Sample size, mm	0.135	0.144	0.125
μ , cm^{-1}	32.31	33.48	36.13
Scanning mode	$\omega/2\theta$		
Sp. gr.	$Pna2_1$		
Ranges of <i>h</i> , <i>k</i> , <i>l</i> variation	$-25 \leq h \leq 25, -12 \leq k \leq 12, 0 \leq l \leq 20$		
θ_{max} , deg	45°		
Total number of measured reflections and structure amplitudes $ F _{hkl}$	13394	13154	11531
Total number of independent reflections with $ F _{hkl} > 3\sigma_{ F _{hkl}}$	3397	3547	2952
$R_{\text{int}}(F _{hkl})$, %	2.23	2.43	2.28
Weighting scheme	$1/\sigma^2$		
Number of parameters to be refined	168	168	168
Reliability factors R/R_w	0.017/0.022	0.020/0.026	0.022/0.026

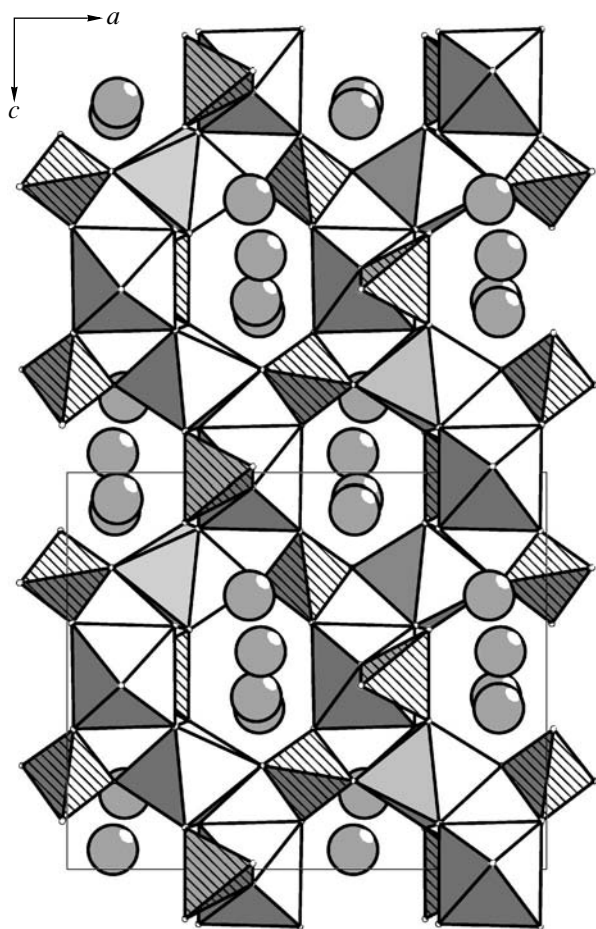


Fig. 1. Fragment of the $K_{1-x}Ti_{1-x}Sb_xOPO_4$ structure projected onto the ac plane. Octahedra are occupied by Ti(Sb) atoms; tetrahedra, by P atoms. Circles indicate the positions of K atoms.

The study of $K_{1-x}Ti_{1-x}Nb_xOPO_4$ ($0 \leq x \leq 0.11$) and $K_{1-x}Ti_{1-x}Sb_xOPO_4$ ($0 \leq x \leq 0.23$) crystals showed that partial substitution of pentavalent niobium or antimony for tetravalent titanium results in reduction of the temperature of the ferroelectric phase transition, an increase in electrical conductivity, and a decrease in the intensity of second-harmonic generation (SHG) in the laser-irradiated crystals [4–7]. However, it was indicated [4, 6–9] that, at certain dopant concentrations, the SHG signal slightly increases. It was established [5, 6] that substitution of Nb^{5+} or Sb^{5+} for Ti^{4+} results in the formation of a limited series of solid solutions with the KTP structure. The maximum x values in niobium-doped $K_{1-x}Ti_{1-x}Nb_xOPO_4$ (KTP:Nb) and antimony doped $K_{1-x}Ti_{1-x}Sb_xOPO_4$ (KTP:Sb) single crystals are 0.11 and 0.23, respectively. At a higher content of these dopants, the phases are crystallized in types different from the KTP type. In a niobium-doped system, a nonstoichiometric monoclinic phase is crystallized with a composition close to $K_2Nb_2TiP_2O_{13}$ [10, 11]. In an antimony-doped system, an increase in the antimony con-

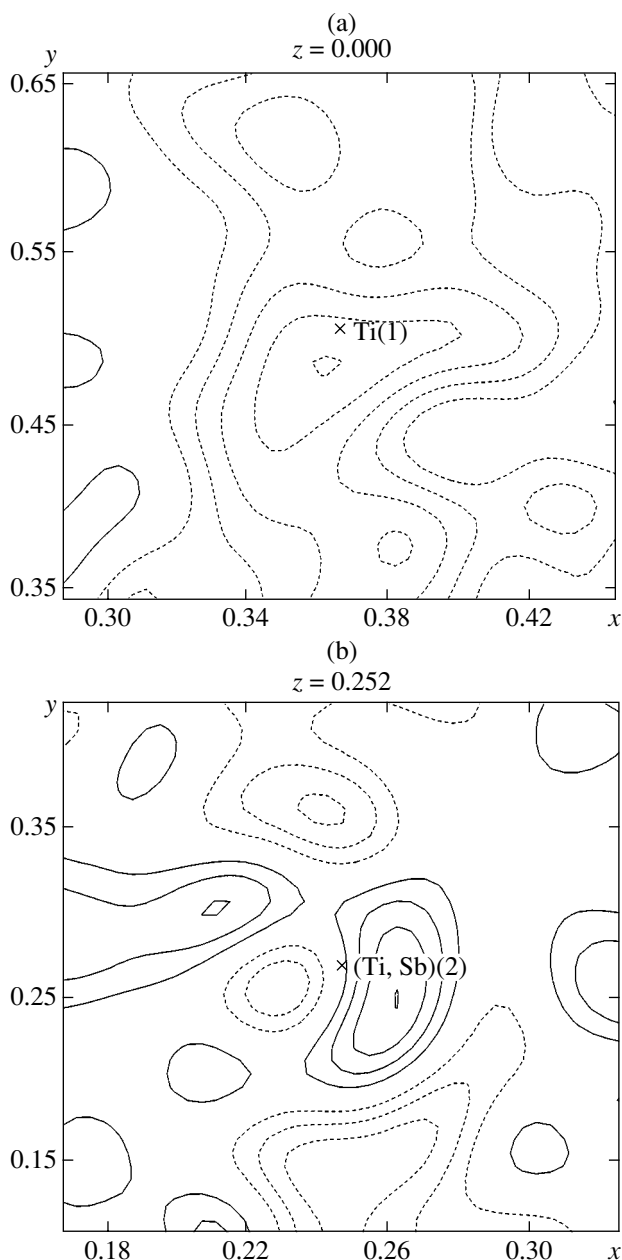


Fig. 2. Difference electron-density maps for the $K_{0.99}Ti_{0.99}Sb_{0.01}OPO_4$ structure. Isolines are spaced by $0.1 \text{ e}/\text{\AA}^3$: (a) section through the Ti(1) atom and (b) section through the (Ti, Sb)(2) atom.

centration results in the formation of hexagonal crystals with the structure of the $K_3Sb_3P_2O_{14}$ type [12, 13]. X-ray diffraction analysis showed that the introduction of Nb atoms into the system increases the number of vacancies in the main crystallographic positions of potassium and gives rise to the formation of additional potassium positions [8, 9, 14–16].

Earlier, the following crystals of the KTP family with titanium substituted for antimony or germanium were studied: $K(Ti_{1-x}Sb_{1-x})O(P_{1-x}Si_{1-x})O_4$ [17],

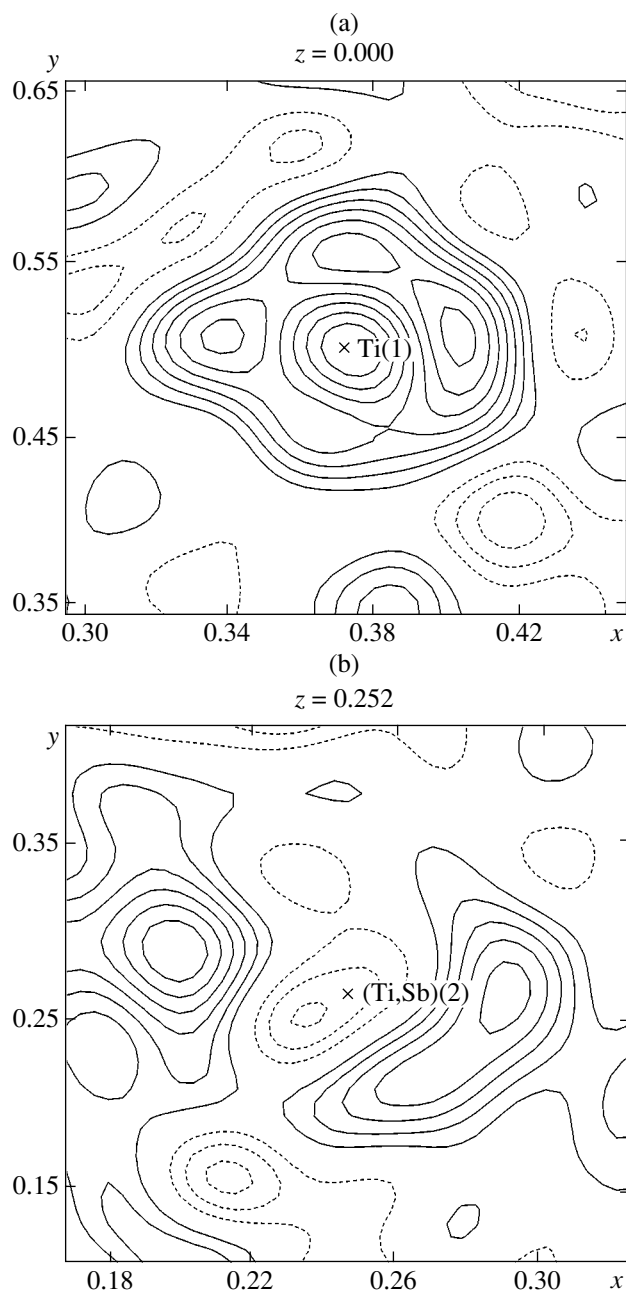


Fig. 3. Difference electron-density maps of the $\text{K}_{0.93}\text{Ti}_{0.93}\text{Sb}_{0.07}\text{OPO}_4$ structure. Isolines are spaced by $0.1 \text{ e}/\text{\AA}^3$. (a) Section through the Ti(1) atom and (b) section through the (Ti,Sb)(2) atom.

RbSbOGeO_4 [18, 19], TiSbOGeO_4 [19, 20–23], AgSbOSiO_4 [23–25], NaSbOGeO_4 [24], $\text{KSb}(\text{Ge}_{0.32}\text{Si}_{0.68})\text{O}_4$ [26], and KSbOSiO_4 [27]. All these crystals are characterized by low values of SHG signals and a high symmetrization degree of octahedra.

Below, we describe the precision X-ray diffraction study of the atomic structure of three single crystals described by the general formula $\text{K}_{1-x}\text{Ti}_{1-x}\text{Sb}_x\text{OPO}_4$

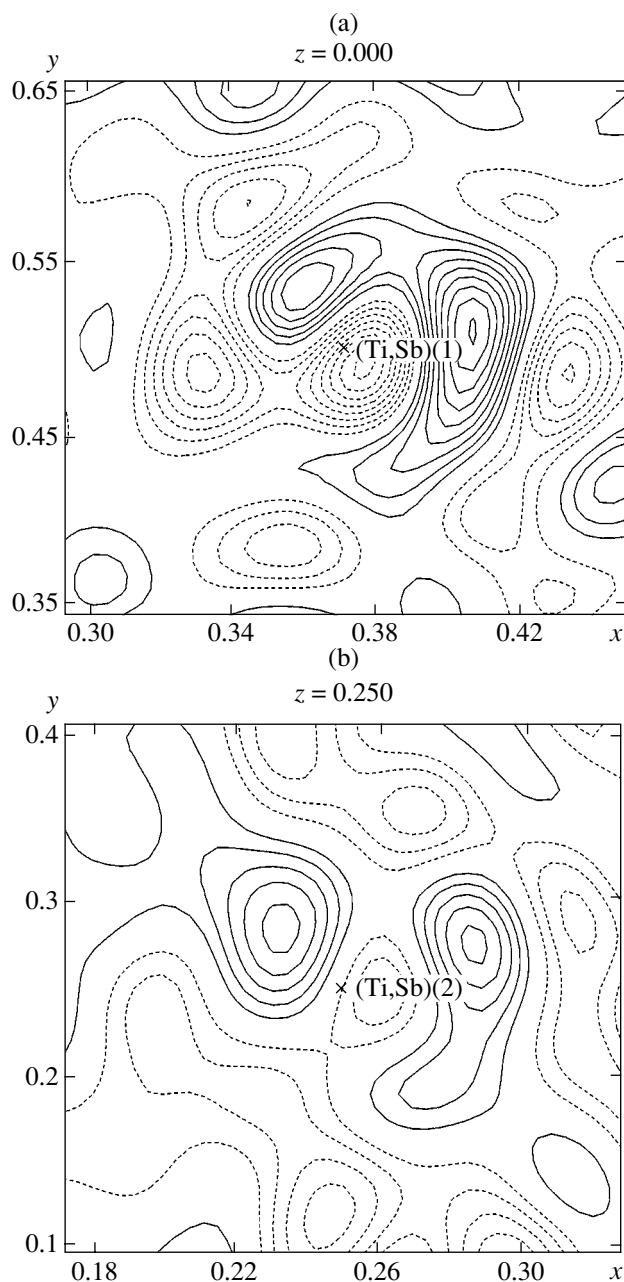


Fig. 4. Difference electron-density maps of the $\text{K}_{0.83}\text{Ti}_{0.83}\text{Sb}_{0.17}\text{OPO}_4$ structure. Isolines are spaced by $0.1 \text{ e}/\text{\AA}^3$. (a) Section through the (Ti,Sb)(1) atom and (b) section through the (Ti,Sb)(2) atom.

with $x = 0.01$ (KTP: 1% Sb), 0.07 (KTP: 7% Sb), and 0.17 (KTP: 17% Sb) and establishment of the relation between their structures and physical properties.

EXPERIMENTAL

Single crystals for X-ray diffraction experiment were grown by spontaneous crystallization from a solution in a $\text{K}_2\text{O}-\text{TiO}_2-\text{P}_2\text{O}_5-\text{Sb}_2\text{O}_5$ system [6]. We

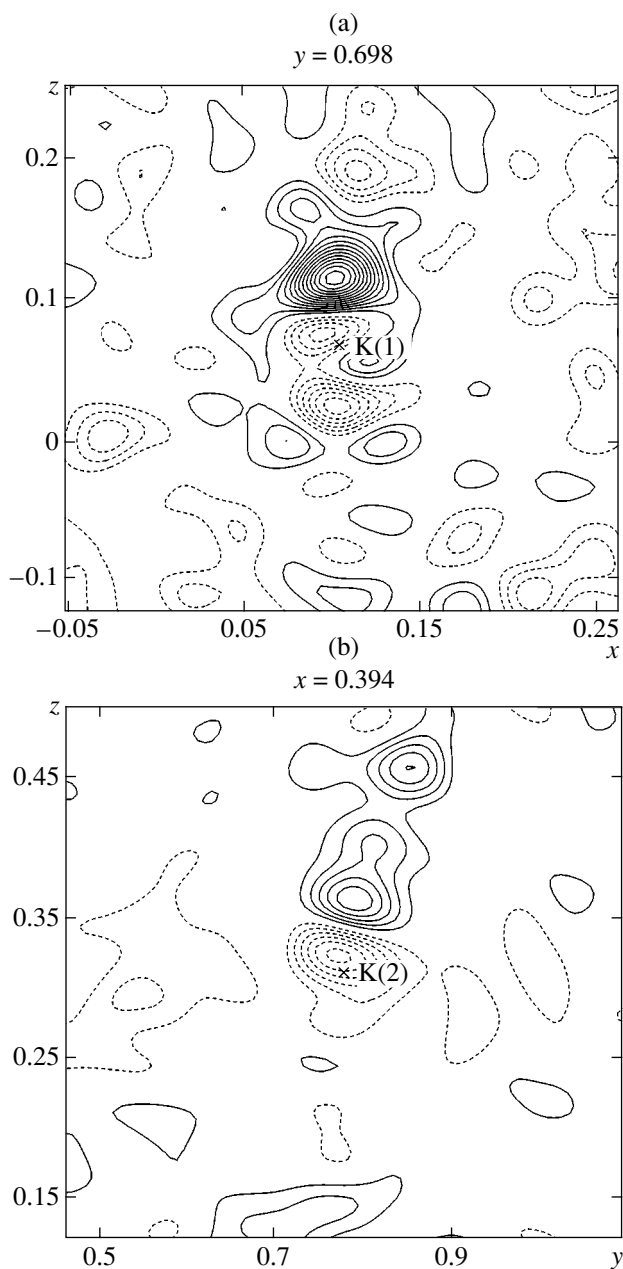


Fig. 5. Difference electron-density maps of the $\text{K}_{0.99}\text{Ti}_{0.99}\text{Sb}_{0.01}\text{OPO}_4$ structure. Isolines are spaced by $0.2 \text{ e}/\text{\AA}^3$. (a) Section through the K(1) atom and (b) section through the K(2) atom.

selected for further experiments only optically homogeneous crystals of different compositions and rolled them into a spherical shape. Of these samples, we used only those whose shape was closest to an ideal sphere and, therefore, gave the best diffraction pattern. The unit-cell parameters of the orthorhombic crystals were refined over 25 reflections (Table 1). The complete set of diffraction intensities was collected on an Enraf-Nonius CAD-4F diffractometer (MoK_α radiation, graphite monochromator). The experimental conditions

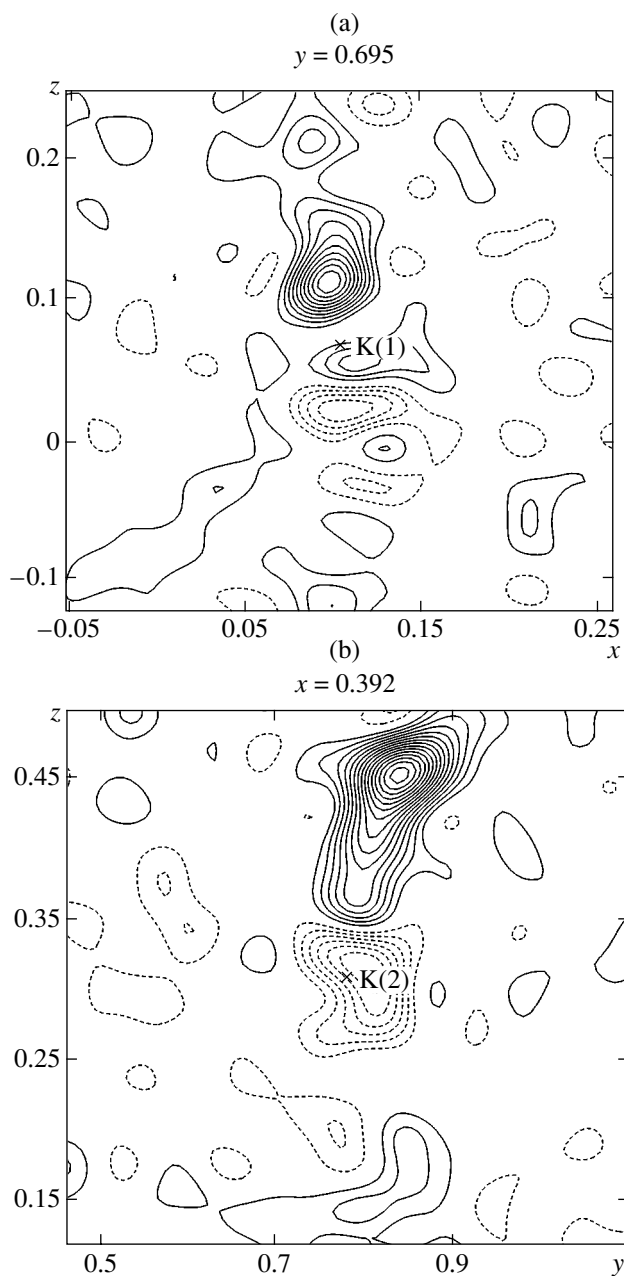


Fig. 6. Difference electron-density maps of the $\text{K}_{0.93}\text{Ti}_{0.93}\text{Sb}_{0.07}\text{OPO}_4$ structure. Isolines are spaced by $0.2 \text{ e}/\text{\AA}^3$. (a) Section through the K(1) atom and (b) section through the K(2) atom.

and the parameters of the refinement procedure are indicated in Table 2.

The structures of KTP:Sb single crystals were refined using the least-squares procedure and the JANA 2000 program [29]. For the initial model, we used the known atomic coordinates of undoped KTP crystals [29]. To take into account extinction, we considered all the possible models in the course of the refinement. The best result was obtained by the Becker–Coppens model

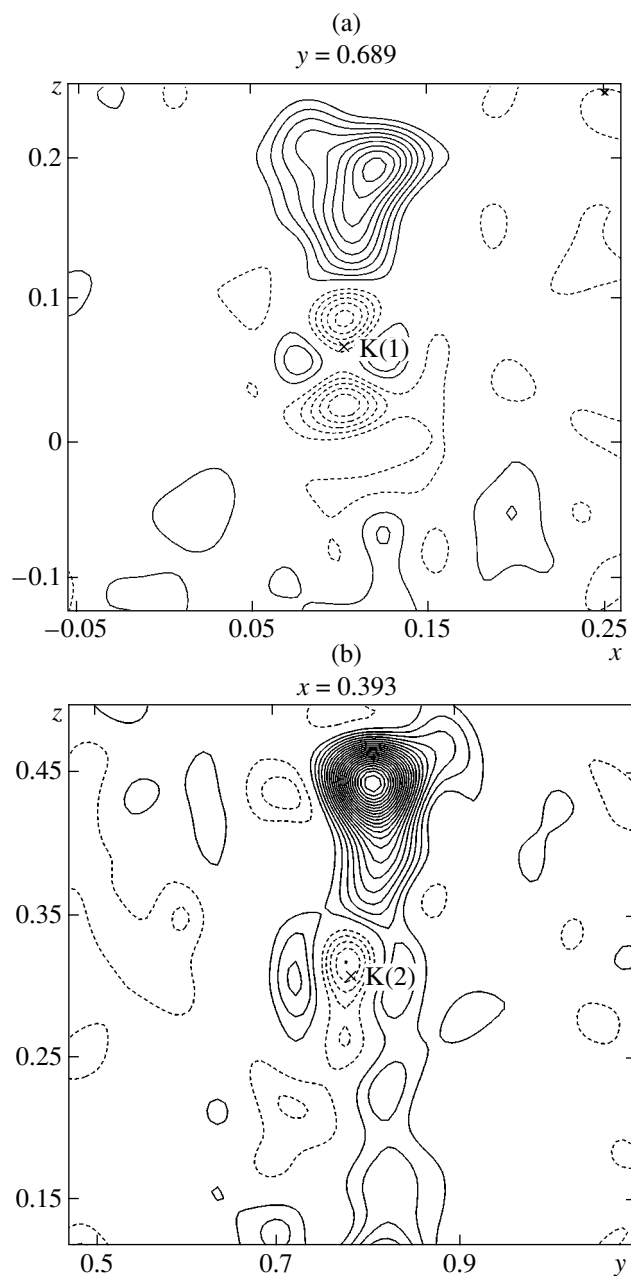


Fig. 7. Difference electron-density maps of the $\text{K}_{0.83}\text{Ti}_{0.83}\text{Sb}_{0.17}\text{OPO}_4$ structure. Isolines are spaced by $0.5 \text{ e}/\text{\AA}^3$. (a) Section through the K(1) atom and (b) section through the K(2) atom.

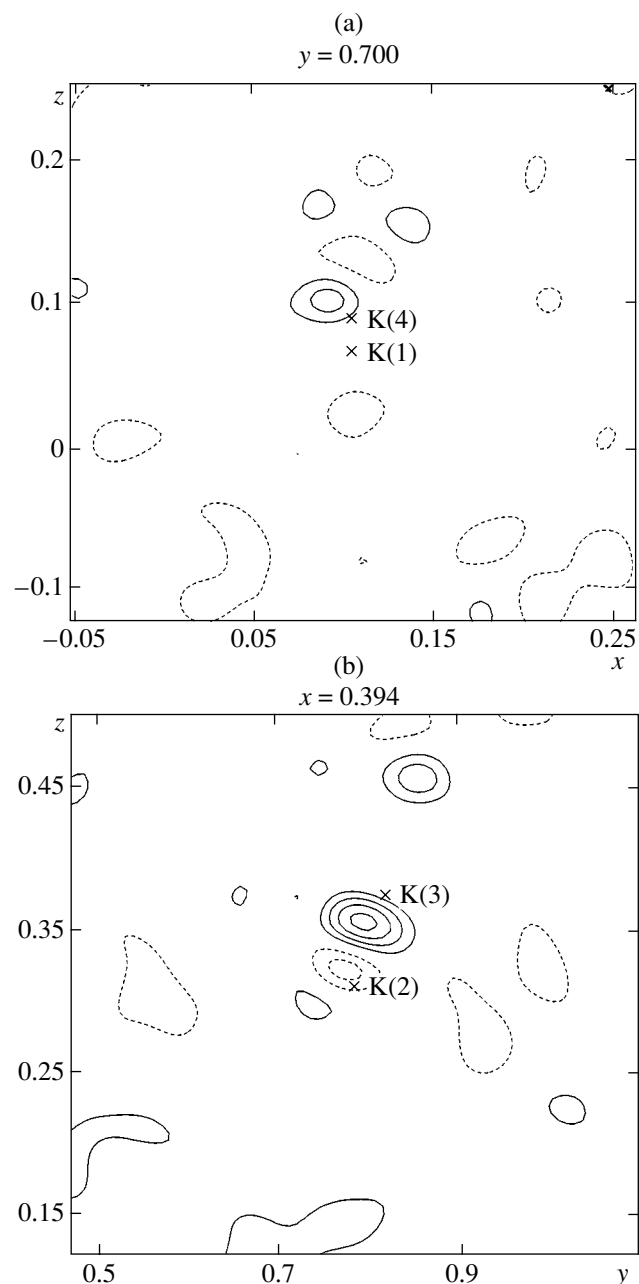


Fig. 8. Difference electron-density maps of the $\text{K}_{0.99}\text{Ti}_{0.99}\text{Sb}_{0.01}\text{OPO}_4$ structure. Isolines are spaced by $0.2 \text{ e}/\text{\AA}^3$. (a) Section through the K(1) and K(4) atoms and (b) section through the K(2) and K(3) atoms.

with the Lorentz distribution of the misoriented mosaic blocks in the crystal.

RESULTS

The structure of the KTP:Nb crystals (Fig. 1) consists of a three-dimensional framework formed by alternating TiO_6 octahedra and PO_4 tetrahedra that share their vertices [14]. The framework channels are occu-

ped by K^+ ions. Titanium atoms in the KTP structure occupy two independent positions with the average distances $(\text{Ti}(1)\text{--O})_{\text{av}} = 1.974 \text{ \AA}$ and $(\text{Ti}(2)\text{--O})_{\text{av}} = 1.970 \text{ \AA}$. Figures 2–4 show the difference electron-density maps which reveal titanium atoms for three structures. At a low antimony content in the structure (KTP: 1% Sb), all the antimony atoms occupy only one “smaller” titanium position, Ti(2) (Fig. 2). The location of antimony in this position is explained by the ionic

Table 3. Values of the maxima and the distances from these maxima to the main potassium positions in KTP crystals with different Sb content

	K(1)		K(2)	
	maximum value, e/Å ³	distance from the maximum to the K(1) position, E	maximum value, e/Å ³	distance from the maximum to the K(2) position, E
K _{0.99} Ti _{0.99} Sb _{0.01} OPO ₄	1.38	0.52	1.16	1.65
K _{0.93} Ti _{0.93} Sb _{0.07} OPO ₄	2.37	0.54	4.14	1.62
K _{0.83} Ti _{0.83} Sb _{0.17} OPO ₄	7.94	1.43	11.55	1.44

Table 4. Occupancies of potassium positions in KTP crystals with different Sb content

	K(1)	K(2)	K(3)	K(4)
K _{0.99} Ti _{0.99} Sb _{0.01} OPO ₄	0.865(9)	0.919(3)	0.097(5)	0.113(8)
K _{0.93} Ti _{0.93} Sb _{0.07} OPO ₄	0.678(7)	0.775(2)	0.162(3)	0.132(7)
K _{0.83} Ti _{0.83} Sb _{0.17} OPO ₄	0.556(5)	0.479(7)	0.423(5)	0.327(6)

Table 5. Distances between potassium positions in KTP structures with different Sb content

Structure	K(1)–K(4)	K(2)–K(3)
KTP with 1% Sb	0.27(2)	0.86(5)
KTP with 7% Sb	0.35(2)	1.583(5)
KTP with 17% Sb	1.372(5)	1.378(5)

Table 6. Atomic coordinates, occupancy of the positions (*q*), and equivalent atomic thermal parameters, *U*_{eq} (Å²), in the K_{0.99}Ti_{0.99}Sb_{0.01}OPO₄ structure

Atom	<i>x</i>	<i>y</i>	<i>z</i>	<i>q</i>	<i>U</i> _{eq}
Ti(1)	0.37280(1)	0.50013(3)	0	1	0.0050(1)
Ti(2)	0.24683(1)	0.26780(2)	0.25152(2)	0.975(1)	0.0052(1)
Sb(2)	0.24683(1)	0.26780(2)	0.25152(2)	0.025(1)	0.0052(1)
P(1)	0.49826(2)	0.33694(4)	0.25970(4)	1	0.0052(1)
P(2)	0.18104(2)	0.50201(4)	0.51206(4)	1	0.0055(1)
K(1)	0.10529(6)	0.6999(1)	0.0653(1)	0.855(8)	0.0179(1)
K(2)	0.37809(3)	0.78097(6)	0.31108(5)	0.909(3)	0.0181(1)
K(3)	0.415(1)	0.817(2)	0.375(4)	0.097(5)	0.4115(11)
K(4)	0.105(1)	0.681(1)	0.087(2)	0.103(8)	0.0679(34)
O(1)	0.4858(1)	0.4864(1)	0.1494(1)	1	0.0093(2)
O(2)	0.5100(1)	0.4661(1)	0.3825(1)	1	0.0091(2)
O(3)	0.4004(1)	0.1993(1)	0.2792(1)	1	0.0079(1)
O(4)	0.5935(1)	0.1936(1)	0.2404(1)	1	0.0086(2)
O(5)	0.1123(1)	0.3110(1)	0.5406(1)	1	0.0083(2)
O(6)	0.1118(1)	0.6919(1)	0.4868(1)	1	0.0095(2)
O(7)	0.2531(1)	0.5394(1)	0.6274(1)	1	0.0090(2)
O(8)	0.2529(1)	0.4615(1)	0.3988(1)	1	0.0093(2)
O(9)	0.2238(1)	0.0416(1)	0.3893(1)	1	0.0087(2)
O(10)	0.2249(1)	−0.0337(1)	0.6426(1)	1	0.0083(2)

radius of antimony (0.62 Å) being smaller than the ionic radius of titanium (0.68 Å). As a result, the average distances in the antimony octahedron determined in [27] are shorter than the average distances in the titanium octahedron determined in [29]. With an increase in the antimony content in the crystal, the Ti(1) position also becomes mixed. The occupancies of the first and second titanium positions in the KTP: 17% Sb structure

studied earlier turned out to be 3.6 at % and 29.7 at %, respectively. In the structure with the intermediate composition (KTP: 7% Sb), antimony also seems to enter both titanium positions (Fig. 3) but the occupancy of the position Ti(1) is so low that we failed to determine it. The difference electron-density maps (Figs. 2–4) show that antimony may also occupy in the octahedron a position different from the titanium position. It is well

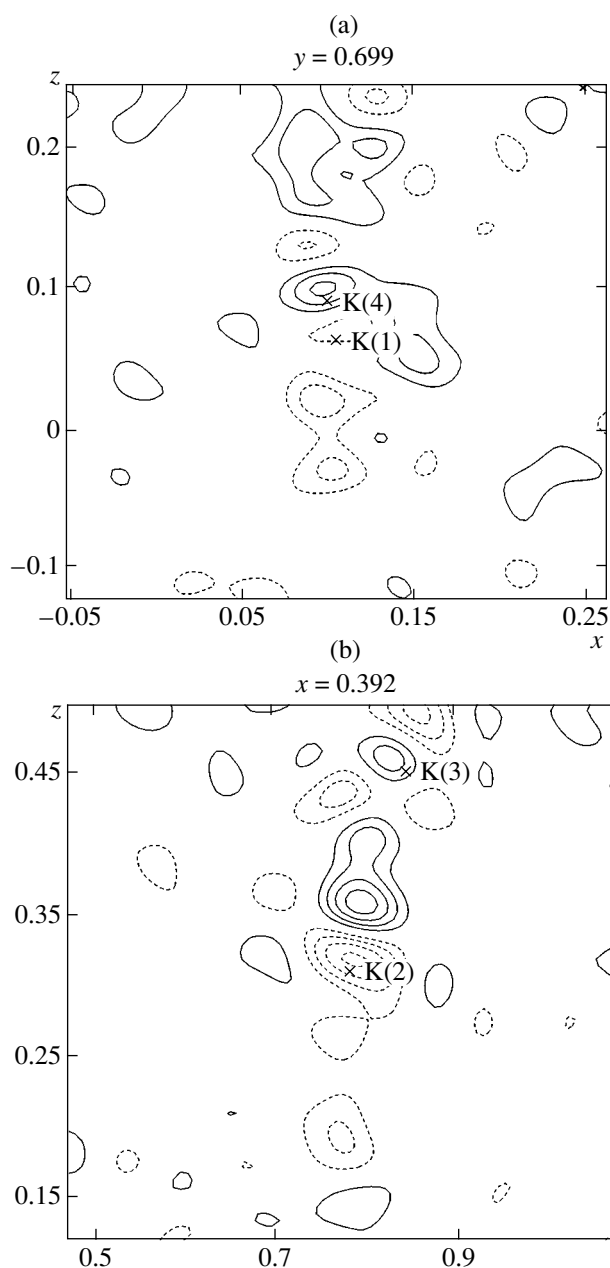


Fig. 9. Difference electron-density maps of the $K_{0.93}Ti_{0.93}Sb_{0.07}OPO_4$ structure. Isolines are spaced by $0.2 e/\text{\AA}^3$. (a) Section through the K(1) and K(4) atoms and (b) section through the K(2) and K(3) atoms.

known that titanium in an octahedron occupies a position somewhat displaced from the octahedron center. On the contrary, antimony usually has symmetric octahedra [18, 24, 27]. However it was impossible to separate the titanium and antimony positions.

There are two main potassium positions in the structures studied: K(1) and K(2). The difference electron-density maps calculated for the model discussed (Figs. 5–7) showed the maxima of the residual electron density in the vicinity of the potassium positions K(1)

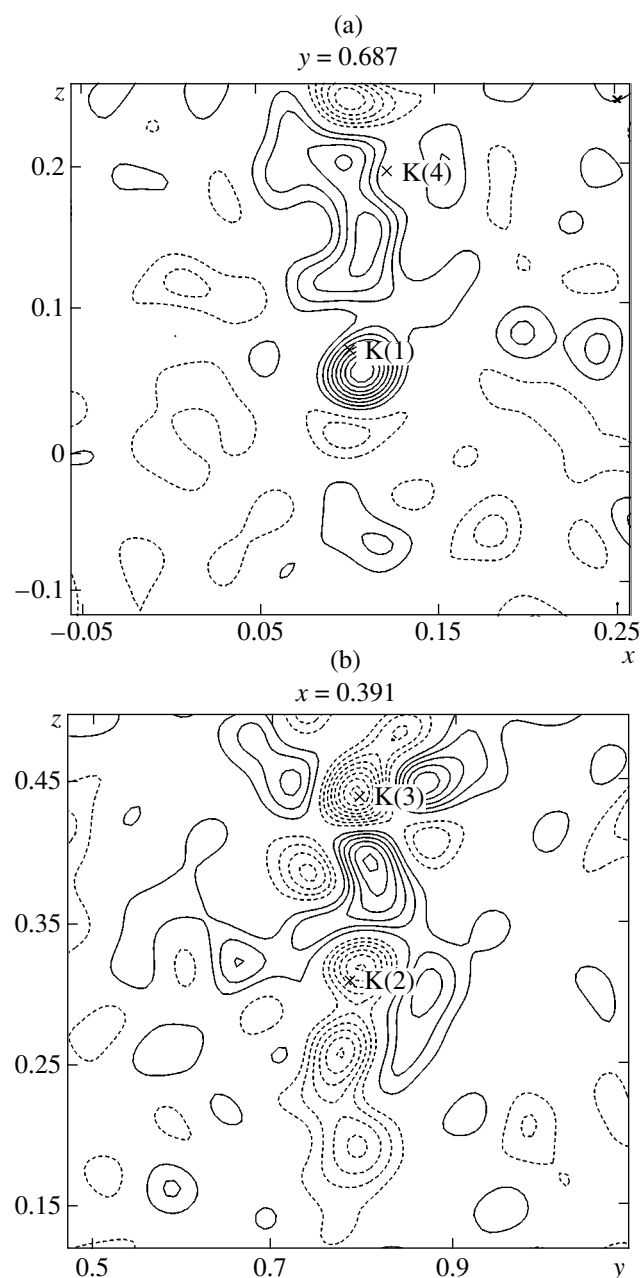


Fig. 10. Difference electron-density maps of the $K_{0.83}Ti_{0.83}Sb_{0.17}OPO_4$ structure. Isolines are spaced by $0.2 e/\text{\AA}^3$. (a) Section through the K(1) and K(4) atoms and (b) section through the K(2) and K(3) atoms.

and K(2) (Table 3). We refined the structural parameters for the models with splitting of the K(1) and K(2) positions. The occupancies of the main and additional potassium positions and the distances between these positions are indicated in Tables 4 and 5. The difference electron-density maps in the vicinity of the potassium positions K(1), K(4) and K(2), K(3) are shown in Figs. 8–10.

In accordance with the determined occupancies (Table 4), the chemical formulas of the compounds

Table 7. Atomic coordinates, occupancy of the positions (q), and equivalent atomic thermal parameter, U_{eq} (\AA^2), in the $\text{K}_{0.93}\text{Ti}_{0.93}\text{Sb}_{0.07}\text{OPO}_4$ structure

Atom	x	y	z	q	U_{eq}
Ti(1)	0.37241(1)	0.50056(3)	0	1	0.0057(1)
Ti(2)	0.24789(1)	0.26218(2)	0.25203(2)	0.853(1)	0.0067(1)
Sb(2)	0.24789(1)	0.26218(2)	0.25203(2)	0.147(1)	0.0067(1)
P(1)	0.49860(2)	0.33882(5)	0.25767(5)	1	0.0062(1)
P(2)	0.18151(2)	0.50193(5)	0.50947(5)	1	0.0065(1)
K(1)	0.10501(6)	0.6986(2)	0.0651(1)	0.678(7)	0.0193(1)
K(2)	0.37010(3)	0.78268(6)	0.30925(7)	0.775(2)	0.0227(1)
K(3)	0.404(1)	0.845(2)	0.451(4)	0.162(3)	0.0408(11)
K(4)	0.100(1)	0.675(2)	0.094(2)	0.132(7)	0.0734(34)
O(1)	0.4857(1)	0.4843(2)	0.1455(1)	1	0.0109(2)
O(2)	0.5107(1)	0.4701(2)	0.3796(1)	1	0.0108(2)
O(3)	0.4011(1)	0.1998(2)	0.2777(1)	1	0.0092(1)
O(4)	0.5941(1)	0.1945(2)	0.2390(1)	1	0.0093(2)
O(5)	0.1129(1)	0.3110(2)	0.5370(1)	1	0.0093(2)
O(6)	0.1123(1)	0.6919(2)	0.4845(1)	1	0.0109(2)
O(7)	0.2537(1)	0.5387(2)	0.6252(1)	1	0.0105(2)
O(8)	0.2541(1)	0.4631(2)	0.3960(1)	1	0.0106(2)
O(9)	0.2246(1)	0.0417(2)	0.3862(1)	1	0.0096(2)
O(10)	0.2253(1)	-0.0353(2)	0.6390(1)	1	0.0095(2)

Table 8. Atomic coordinates, occupancy of the positions (q), and equivalent atomic thermal parameters, U_{eq} (\AA^2), in the $\text{K}_{0.83}\text{Ti}_{0.83}\text{Sb}_{0.17}\text{OPO}_4$ structure

Atom	x	y	z	q	U_{eq}
Ti(1)	0.37158(2)	0.4997(1)	0	0.964(1)	0.0083(1)
Sb(1)	0.37158(2)	0.4997(1)	0	0.036	0.0083(1)
Ti(2)	0.24997(6)	0.2497(1)	0.2500(1)	0.703(1)	0.0083(1)
Sb(2)	0.24997(6)	0.2497(1)	0.2500(1)	0.297	0.0083(1)
P(1)	0.5001(1)	0.3391(2)	0.2510(2)	1	0.0071(1)
P(2)	0.1811(1)	0.4996(2)	0.5009(2)	1	0.0074(1)
K(1)	0.1006(2)	0.6788(4)	0.0718(3)	0.556(5)	0.0559(8)
K(2)	0.3872(3)	0.7884(5)	0.3113(3)	0.479(7)	0.0459(8)
K(3)	0.3950(1)	0.8005(3)	0.4419(2)	0.423(5)	0.0166(3)
K(4)	0.1224(2)	0.7205(4)	0.1971(2)	0.327(6)	0.0162(4)
O(1)	0.4859(4)	0.4776(4)	0.1336(4)	1	0.0132(8)
O(2)	0.5123(3)	0.4762(4)	0.3688(4)	1	0.0125(7)
O(3)	0.4040(2)	0.1951(5)	0.2701(4)	1	0.0109(6)
O(4)	0.5963(2)	0.1977(6)	0.2307(3)	1	0.0102(6)
O(5)	0.1113(2)	0.3108(5)	0.5273(3)	1	0.0100(6)
O(6)	0.1131(2)	0.6918(5)	0.4740(3)	1	0.0122(7)
O(7)	0.2528(3)	0.5393(5)	0.6152(5)	1	0.0129(8)
O(8)	0.2552(3)	0.4637(6)	0.3855(4)	1	0.0106(8)
O(9)	0.2253(3)	0.0396(6)	0.3741(3)	1	0.0109(6)
O(10)	0.2263(4)	-0.0399(6)	0.6274(4)	1	0.0117(8)

Table 9. Interatomic distances (Å) in the $K_{0.99}Ti_{0.99}Sb_{0.01}OPO_4$, $K_{0.93}Ti_{0.93}Sb_{0.07}OPO_4$, and $K_{0.83}Ti_{0.83}Sb_{0.17}OPO_4$ structures

Distances	$KTiOPO_4$	$K_{0.99}Ti_{0.99}Sb_{0.01}OPO_4$	$K_{0.93}Ti_{0.93}Sb_{0.07}OPO_4$	$K_{0.83}Ti_{0.83}Sb_{0.17}OPO_4$
Ti(1)–O(9)	1.716(1)	1.724(1)	1.747(1)	1.829(4)
–O(10)	1.985(1)	1.973(1)	1.942(1)	1.849(5)
–O(1)	2.154(1)	2.146(1)	2.114(1)	2.031(5)
–O(2)	1.955(1)	1.960(1)	1.972(1)	2.030(4)
–O(5)	2.046(1)	2.045(1)	2.035(1)	2.027(4)
–O(6)	1.987(1)	1.989(1)	1.993(1)	2.002(4)
Average	1.974	1.973	1.967	1.961
$\Delta_{\text{long–short}}$	0.438	0.422	0.367	0.202
Ti(2)–O(9)	2.099(1)	2.077(1)	2.022(1)	1.901(4)
–O(10)	1.736(1)	1.753(1)	1.795(1)	1.889(5)
–O(3)	2.042(1)	2.037(1)	2.018(1)	2.010(4)
–O(4)	1.980(1)	1.983(1)	1.992(1)	2.002(4)
–O(7)	1.964(1)	1.966(1)	1.960(1)	1.955(5)
–O(8)	1.998(1)	1.994(1)	1.993(1)	1.978(5)
Average	1.970	1.968	1.963	1.956
$\Delta_{\text{long–short}}$	0.363	0.324	0.227	0.012
K(1)–O(1)	2.675(1)	2.678(1)	2.678(2)	2.724(6)
–O(2)	2.983(1)	2.973(1)	3.008(2)	3.204(6)
–O(3)	3.044(1)	3.030(1)	3.035(2)	3.170(6)
–O(4)	3.117(1)	3.133(1)	3.119(2)	2.936(5)
–O(5)	2.804(1)	2.801(1)	2.804(2)	2.749(5)
–O(7)	2.919(1)	2.907(1)	2.901(2)	3.009(5)
–O(8)	3.047(1)	3.036(1)	3.050(2)	3.249(6)
–O(9)	3.058(1)	3.047(1)	3.054(2)	3.171(6)
–O(10)	2.763(1)	2.764(1)	2.750(2)	2.683(6)
Average	2.934	2.930	2.933	2.988
K(2)–O(1)	2.891(1)	2.897(1)	2.910(2)	3.007(6)
–O(2)	2.763(1)	2.738(1)	2.711(2)	2.632(6)
–O(3)	2.711(1)	2.716(1)	2.706(2)	2.651(5)
–O(5)	2.869(1)	2.871(1)	2.882(2)	2.986(6)
–O(7)	3.055(1)	3.058(1)	3.065(2)	3.167(6)
–O(8)	2.756(1)	2.760(1)	2.761(2)	2.790(6)
–O(9)	2.723(1)	2.717(1)	2.714(2)	2.704(6)
–O(10)	2.994(1)	2.997(1)	3.033(2)	3.203(6)
Average	2.845	2.844	2.845	2.892
K(3)–K(2)	–	0.86(5)	1.583(5)	1.378(5)
–K(1)	–	3.18(4)	2.563(5)	2.783(4)
–O(1)	–	3.32(5)	3.263(5)	3.090(5)
–O(2)	–	2.56(2)	2.866(5)	2.676(5)
–O(3)	–	2.66(3)	2.918(5)	3.109(4)
–O(4)	–	–	3.047(5)	3.035(5)
–O(6)	–	2.79(3)	2.699(4)	2.807(4)
–O(7)	–	–	3.304(5)	3.069(5)
–O(8)	–	3.09(2)	3.164(4)	2.864(5)
–O(9)	–	2.84(2)	2.705(4)	2.749(5)
–O(10)	–	–	3.119(4)	3.080(6)
Average	–	2.877	3.009	2.942

Table 9. (Contd.)

Distances	KTiOPO ₄	K _{0.99} Ti _{0.99} Sb _{0.01} OPO ₄	K _{0.93} Ti _{0.93} Sb _{0.07} OPO ₄	K _{0.83} Ti _{0.83} Sb _{0.17} OPO ₄
K(4)–K(1)	–	0.27(2)	0.35(2)	1.372(5)
–O(1)		2.69(3)	2.68(1)	2.689(6)
–O(2)		3.21(2)	3.27(2)	3.001(5)
–O(3)		3.28(3)	3.35(2)	–
–O(4)		2.89(2)	2.82(1)	2.725(5)
–O(5)		2.84(2)	2.79(1)	3.485(5)
–O(6)		–	–	2.916(5)
–O(7)		2.94(2)	3.01(1)	2.731(6)
–O(8)		3.24(2)	3.36(2)	3.082(6)
–O(9)		3.16(2)	3.26(2)	3.061(5)
–O(10)		2.63(2)	2.65(1)	2.657(6)
Average		2.987	3.021	2.927
P(1)–O(1)	1.518(1)	1.518(1)	1.516(1)	1.529(5)
–O(2)	1.551(1)	1.549(1)	1.545(1)	1.526(5)
–O(3)	1.546(1)	1.546(1)	1.547(1)	1.549(4)
–O(4)	1.541(1)	1.541(1)	1.545(1)	1.542(4)
Average	1.539	1.539	1.538	1.537
P(2)–O(5)	1.538(1)	1.538(1)	1.533(1)	1.528(4)
–O(6)	1.529(1)	1.529(1)	1.527(1)	1.534(4)
–O(7)	1.550(1)	1.550(1)	1.549(1)	1.532(6)
–O(8)	1.535(1)	1.534(1)	1.536(1)	1.555(5)
Average	1.538	1.538	1.536	1.537

studied can be written as K_{0.98}Ti_{0.99}Sb_{0.01}OPO₄, K_{0.87}Ti_{0.93}Sb_{0.07}OPO₄, and K_{0.89}Ti_{0.83}Sb_{0.17}OPO₄. Similar to the case of niobium-doped KTP crystals [14, 15], the number of potassium vacancies in the KTP: 1% Sb and KTP: 7% Sb crystals turns out to be higher than was expected on the basis of the condition of electrical neutrality. The zero electron-density maps (Figs. 7 and 8) show peaks in the vicinity of the potassium positions, which indicates the possible existence of additional positions occupied by potassium which were not taken into account. Moreover, high values of thermal corrections for K(3) and K(4) atoms and the elongated shape of the maxima of these atoms also indicate more pronounced splitting of potassium positions. However, the refinement of the structural parameters of these new additional potassium positions is impossible because of the strong correlation between the parameters of closely located atoms. At the same time, the amount of potassium in the KTP: 17% Sb crystals is somewhat higher than could be expected on the basis of the condition for electrical neutrality. The insufficient accuracy of the data obtained may be explained by a high anti-

mony content in the crystal and the failure of our attempts to separate titanium and antimony positions.

The coordinates of the basis atoms in the structures, the occupancies q of the crystallographic positions, and the equivalent parameters of atomic thermal vibration U_{eq} for all the structures studied are listed in Tables 6–8.

DISCUSSION OF RESULTS

The KTP:Sb crystals are structural analogues of KTiOPO₄ crystals. The incorporation of antimony with partial substitution for titanium atoms in their positions results in a gradual decrease in the lattice parameters a and c and the unit-cell volume. The incorporation of antimony into the structure practically does not change the parameter b (Table 1). Earlier, it was shown that the incorporation of Nb into the crystal lattice of KTP crystals is accompanied by a slight increase in the unit-cell volume [5, 15]. This is associated with different ionic radii of Nb⁵⁺, Sb⁵⁺, and Ti⁴⁺ cations (0.69, 0.62, and 0.68 Å, respectively).

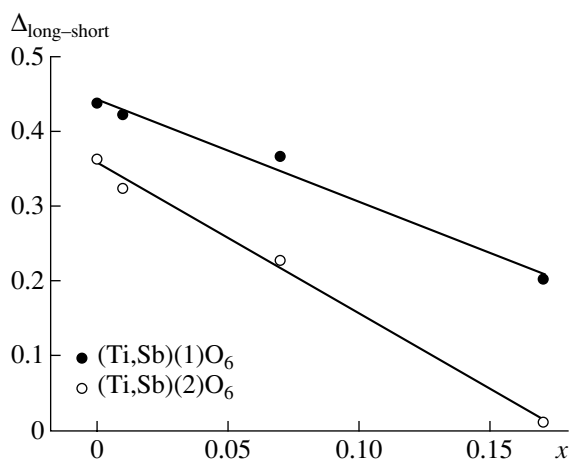


Fig. 11. Difference between the long and short bonds in titanium octahedra as a function of antimony content in $K_{1-x}\text{Ti}_{1-x}\text{Sb}_x\text{OPO}_4$ crystals.

The earlier studies of the physical properties of the crystals considered in this article showed that, with an increase in the antimony content in KTP crystals, the temperature T_C of the ferroelectric phase transition decreases [4, 6, 7]. The concentration dependence of the Curie temperature is of an obvious nonlinear character. Thus, if a crystal contains only 1 at % Sb, the T_C temperature decreases from 934°C (for undoped KTP crystals) to 789°C. Moreover, the temperature dependence of the permittivity of KTP:Sb crystals shows a broad relaxation anomaly which becomes more pronounced with an increase in antimony concentration. Our X-ray diffraction studies showed that, with an increase in antimony content in KTP crystals, the occupancies of the potassium positions also change and some additional potassium positions arise. The occupancies of the main potassium positions, K(1) and K(2), decrease, whereas the occupancies of the positions K(3) and K(4) increase. It is the formation of additional vacancies and splitting of the cationic potassium positions that explain a considerable decrease in the temperature of the ferroelectric phase transition and enhancement of the relaxation phenomena in antimony-doped KTP crystals.

The vacancies in the potassium positions and formation of additional potassium positions give rise to disordering in the potassium sublattice; a higher mobility of potassium cations; and, as a result, an increase in conductivity. The measurements [4, 6, 7] showed that conductivity of the KTP:Sb crystals increases by a factor of 1.5–2.0 in comparison with conductivity in pure KTP crystals (10^{-2} – $10^{-3} \Omega^{-1} \text{cm}^{-1}$ at 300°C).

Doping of KTP crystals with antimony decreases the intensity of the SHG signal during laser irradiation of these crystals [4, 6, 7]. As is well known, nonlinear optical properties of KTP crystals are explained by distortion of titanium octahedra which share their vertices and form chains [3]. Our X-ray diffraction studies

showed that substitution of antimony for titanium atoms results in elongation of short Ti–O distances and shortening of long Ti–O distances in TiO_6 octahedra (Fig. 11, Table 9). This is explained by the fact that an antimony octahedron is more symmetric than a titanium one [18, 24, 27].

ACKNOWLEDGMENTS

This study was supported by the Russian Foundation for Basic Research, project nos. NSh-1642.2003.5 and 04-03-32434, and the Foundation “Universities of Russia,” project no. UR 01.03.069.

REFERENCES

1. M. E. Hagerman and K. R. Poeppelmeier, *Chem. Mater.* **7** (4), 603 (1995).
2. M. N. Satyanarayan, A. Deepthy, and H. L. Bhat, *Crit. Rev. Solid State Mater. Sci.* **24** (2), 103 (1999).
3. G. D. Stucky, M. L. F. Phillips, and T. E. Gier, *Chem. Mater.* **1** (5), 492 (1989).
4. V. I. Voronkova, V. K. Yanovskii, T. Yu. Losevskaya, *et al.*, *Kristallografiya* **49** (1), 131 (2004) [*Crystallogr. Rep.* **49** (1), 123 (2004)].
5. T. Yu. Losevskaya, O. A. Alekseeva, V. K. Yanovskii, *et al.*, *Kristallografiya* **45** (5), 809 (2000) [*Crystallogr. Rep.* **45** (5), 739 (2000)].
6. T. Yu. Losevskaya, V. K. Yanovskii, V. I. Voronkova, and S. Yu. Stefanovich, *Neorg. Mater.* **38** (11), 1377 (2002).
7. V. I. Voronkova, V. K. Yanovskii, T. Yu. Losevskaya, and S. Yu. Stefanovich, *J. Appl. Phys.* **94** (3), 1954 (2003).
8. P. A. Thomas and B. E. Watts, *Solid State Commun.* **73**, 97 (1990).
9. L. T. Cheng, L. K. Cheng, R. L. Harlow, and J. D. Bierlein, *Appl. Phys. Lett.* **64**, 155 (1994).
10. O. A. Alekseeva, N. I. Sorokina, M. K. Blomberg, *et al.*, *Kristallografiya* **46** (2), 215 (2001) [*Crystallogr. Rep.* **46** (2), 176 (2001)].
11. O. A. Alekseeva, N. I. Sorokina, I. A. Verin, *et al.*, *Kristallografiya* **46** (5), 816 (2001) [*Crystallogr. Rep.* **46** (5), 741 (2001)].
12. Y. Piffard, A. Lachgar, and M. Tounoux, *J. Solid State Chem.* **58**, 253 (1985).
13. Y. Piffard, A. Lachgar, and M. Tounoux, *Rev. Chim. Miner.* **22**, 101 (1985).
14. O. A. Alekseeva, M. K. Blomberg, V. N. Molchanov, *et al.*, *Kristallografiya* **46** (4), 710 (2001) [*Crystallogr. Rep.* **46** (4), 642 (2001)].
15. O. A. Alekseeva, N. I. Sorokina, I. A. Verin, *et al.*, *Kristallografiya* **48** (2), 238 (2003) [*Crystallogr. Rep.* **48** (2), 205 (2003)].
16. A. P. Dudka, I. A. Verin, V. N. Molchanov, *et al.*, *Kristallografiya* (in press).
17. J. Ravez, A. Simon, B. Boulanger, *et al.*, *Ferroelectrics* **124**, 379 (1991).
18. E. L. Belokoneva and B. V. Mill', *Zh. Neorg. Khim.* **37** (5), 998 (1992).

19. E. L. Belokoneva, K. S. Knight, W. I. F. David, and B. V. Mill, *J. Phys.: Condens. Matter* **9**, 3833 (1997).
20. E. L. Belokoneva and B. V. Mill', *Zh. Neorg. Khim.* **37** (2), 252 (1992).
21. E. L. Belokoneva, F. M. Dolgushin, M. Yu. Antipin, *et al.*, *Zh. Neorg. Khim.* **38** (4), 631 (1993).
22. E. L. Belokoneva, F. M. Dolgushin, M. Yu. Antipin, *et al.*, *Zh. Neorg. Khim.* **39** (7), 1080 (1994).
23. E. L. Belokoneva, *Usp. Khim.* **63** (7), 559 (1994).
24. E. L. Belokoneva and B. V. Mill', *Zh. Neorg. Khim.* **39** (3), 355 (1994).
25. E. L. Belokoneva and B. V. Mill', *Zh. Neorg. Khim.* **39** (3), 363 (1994).
26. S. T. Norberg, G. Svensson, and J. Albertsson, *Acta Crystallogr., Sect. C: Cryst. Struct. Commun.* **57**, 510 (2001).
27. M.-P. Crosnier, D. Guyomard, A. Verbaere, and Y. Piffard, *Eur. J. Solid State Inorg. Chem.* **27**, 845 (1990).
28. V. Petricek and M. Dusek, in *The Crystallographic Computing System* (Inst. Phys., Praha, 2000).
29. B. V. Andreev, V. A. Dyakov, N. I. Sorokina, and V. I. Simonov, *Solid State Commun.* **80** (10), 777 (1991).

Translated by L. Man

STRUCTURE
OF INORGANIC COMPOUNDS

Structural Transition from Vacancy-Ordered Tetragonal Perovskite to Tetragonal Potassium Tungsten Bronze by the Example of $\text{Na}_4\text{Bi}_2\text{Nb}_{10}\text{O}_{30}$

V. G. Kryshtop, M. F. Kupriyanov, and E. K. Karpenko

Faculty of Physics, Rostov State University, ul. Zorge 5, Rostov-on-Don, 344090 Russia

e-mail: vikr@phys.ras.ru

Received May 26, 2003; in final form, October 1, 2004

Abstract—The phenomenological transition from the perovskite structure type to the potassium tungsten bronze structure type is considered. The structural motif of vacancy-ordered tetragonal perovskite (VOTP) with the space group $P4/m$ is constructed. The atomic coordinates in the unit cell of VOTP and the Madelung energies for the unit cells of VOTP and tetragonal potassium tungsten bronze are calculated. The transition is experimentally observed in $\text{Na}_4\text{Bi}_2\text{Nb}_{10}\text{O}_{30}$ prepared by the solid-state reaction method. The X-ray diffraction pattern measured after the first annealing showed good agreement with the theoretical X-ray diffraction pattern calculated for VOTP $\text{Na}_4\text{Bi}_2\text{Nb}_{10}\text{O}_{30}$. © 2005 Pleiades Publishing, Inc.

INTRODUCTION

Various types of oxygen-octahedral structures are of considerable interest both from the standpoint of their crystal-chemical classification (see, for example, [1–3]) and as a basis of many active materials (ferroelectrics, high-temperature superconductors, ionic conductors, etc.), which are widely used in electronics as crystals, ceramics, and thin films.

Owing to a rather wide range of permissible variations in the chemical composition and various defects within a particular structure type, the production of materials has moderate processing requirements, which makes their production relatively cheap. However, this feature of oxygen-octahedral structures gives rise to the problem of stabilization of structure states and physical parameters of the materials.

Interest in this problem has greatly increased in the past few years owing to, particularly, prospects for constructing and using active nanomaterials [4]. Several studies demonstrated that phase transitions between different structure types may occur during the preparation of materials based on oxygen-octahedral structures. The most well-known examples of these transitions are as follows:

- (1) phase transitions of the ilmenite (calcite) structure type to the perovskite structure type [5, 6],
- (2) transformations of the fluorite (pyrochlore) structure type to the perovskite structure type [7, 8],
- (3) the transformation of the cubic phase of BaTiO_3 to the hexagonal phase [9], and
- (4) transitions between structure types in the Na_xWO_3 and K_xWO_3 series [10, 11].

These phase transitions have commonly been assigned to reconstructive transitions [12], although it remains unclear whether there is a group–subgroup relationship between the structures involved in interconversions. The point is that the octahedral coordination of *B*-type cations remains unchanged in these structures, whereas changes in the coordination of *A*-type cations and the transformation of one packing type (hexagonal) into another (cubic) can, in principle, be described by relatively small displacements. It also seems rather evident that the difference in the energies of the structures related by these transitions is small.

Possible phase transitions between the structure types of potassium tungsten bronzes and perovskite are also among phase interconversions. The crystal-chemical relationship between these structure types has been discussed many times [13]. One of the problems was to reveal the role of structural defects in the formation of stable structures in going from the ReO_3 structure type (defect perovskite of the composition $\square\text{BO}_3$, where \square are vacancies in *A* positions) to the structure types of hexagonal and tetragonal bronzes of the composition $\text{A}_{1-x}\square_x\text{BO}_3$ and then to perovskites of the composition ABO_3 .

The aim of this work was to study experimentally the crystalline phase $\text{Na}_4\text{Bi}_2\text{Nb}_{10}\text{O}_{30}$, whose formula corresponds to the $\text{A}_2''\text{A}_4'\text{B}_{10}\text{O}_{30}$ composition. Previously, this compound has been prepared and reported to have the structure of tetragonal potassium tungsten bronze (TPTB).

In studies of various families of complex oxides, it is important to reveal the relationship between structure types. The fact that oxides belonging to the TPTB type

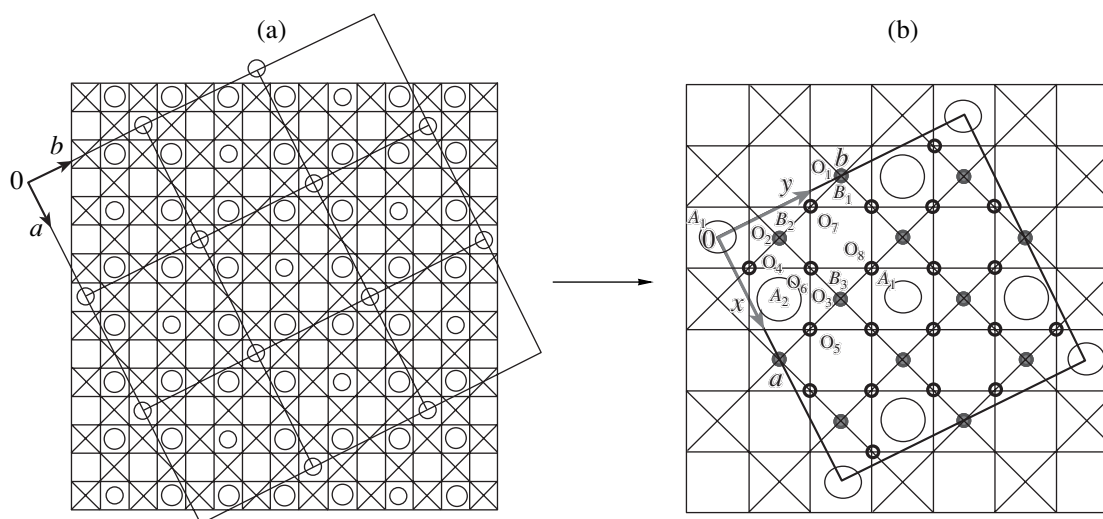


Fig. 1. (a) Structural motif of VOTP projected along the [001] direction and (b) the unit cell of VOTP projected along the [001] direction: (X) oxygen octahedra, (□) empty tetragonal positions, (○) A_1 atoms, and (○) A_2 atoms.

are structurally related to those belonging to the perovskite structure type is particularly promising from the point of view of gaining a deeper insight into the nature of ferroelectricity in oxide ferroelectrics and searching for new ferro- and piezoelectric materials. Oxides belonging to the tetragonal tungsten bronze structure type have been synthesized for many years [14–18]. However, the reproducibility of the results in two- or three-step solid-state reactions is still one of the most complex problems in the preparation of ferroelectric materials. Reproducibility is required when it is necessary to keep track of intermediate results to develop more precise technology. For example, complex oxides, which are often difficult to identify, are formed in the intermediate steps in the synthesis of TPTB.

EXPERIMENTAL

The $\text{Na}_4\text{Bi}_2\text{Nb}_{10}\text{O}_{30}$ compound was synthesized by the solid-state reaction method. First annealing was followed by phase analysis. The X-ray diffraction patterns for phase analysis were measured on a DRON-4.0 dif-

fractometer using $\text{CuK}\alpha$ radiation at a scan rate of 0.5 deg/min. The phase analysis showed a perovskite-like structure with additional lines, which was identified as a tetragonal structure with the unit-cell parameters $a = 12.378 \text{ \AA}$ and $c = 3.914 \text{ \AA}$. (These parameters are similar to those of bronzes.)

EXPERIMENTAL RESULTS

Compounds of the perovskite and TPTB structure types are characterized by similar crystal structures, which are based on a framework of oxygen octahedra (BO_6) linked to each other in a particular fashion. The chemical formulas of perovskite and TPTB are ABO_3 ($\text{A}_{10}\text{B}_{10}\text{O}_{30}$) and $\text{A}_6\text{B}_{10}\text{O}_{30}$, respectively. To explain the experimental results, we hypothesized that the first annealing produces a compound structurally similar to perovskite. However, this compound contains vacancies in A positions in such an amount that the chemical formula of the perovskite structure containing vacan-

Table 1. Atomic coordinates in the unit cell of VOTP

Atom	Multiplicity of position	x/a	y/b	z/c	Atom	Multiplicity of position	x/a	y/b	z/c
A_1	1(a)	0	0	0	O_2	4(j)	0.2	0.9	0
A_1	1(c)	0.5	0.5	0	O_3	4(j)	0.3	0.6	0
A_2	4(j)	1	0.7	0	O_4	4(k)	0.05	0.85	0.5
B_1	2(f)	0	0.5	0.5	O_5	4(k)	0.15	0.55	0.5
B_2	4(k)	0.2	0.9	0.5	O_6	4(k)	0.25	0.75	0.5
B_3	4(k)	0.3	0.6	0.5	O_7	4(k)	0.35	0.95	0.5
O_1	2(e)	0	0.5	0	O_8	4(k)	0.45	0.65	0.5

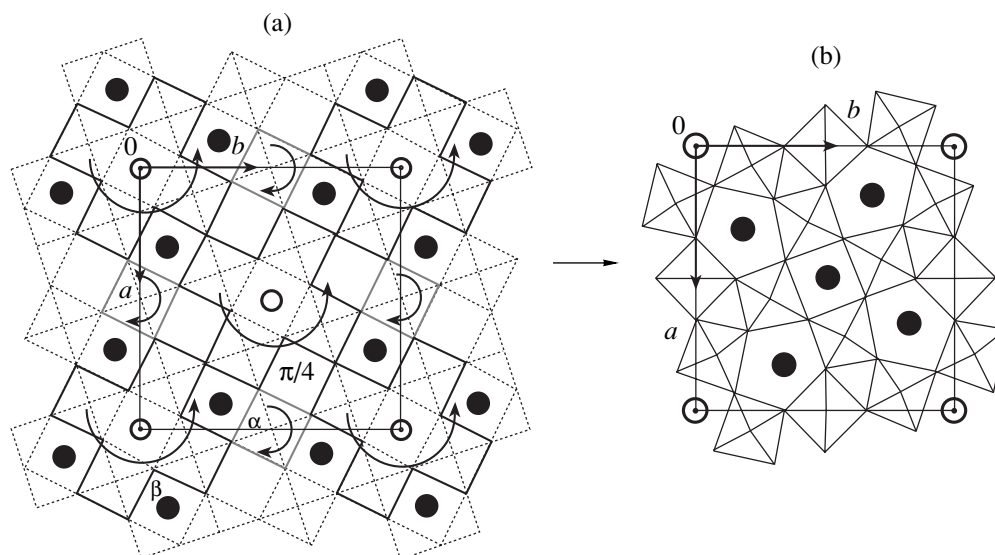


Fig. 2. (a) Fragment of the VOTP structure corresponding to the (b) unit cell of the TPTB structure.

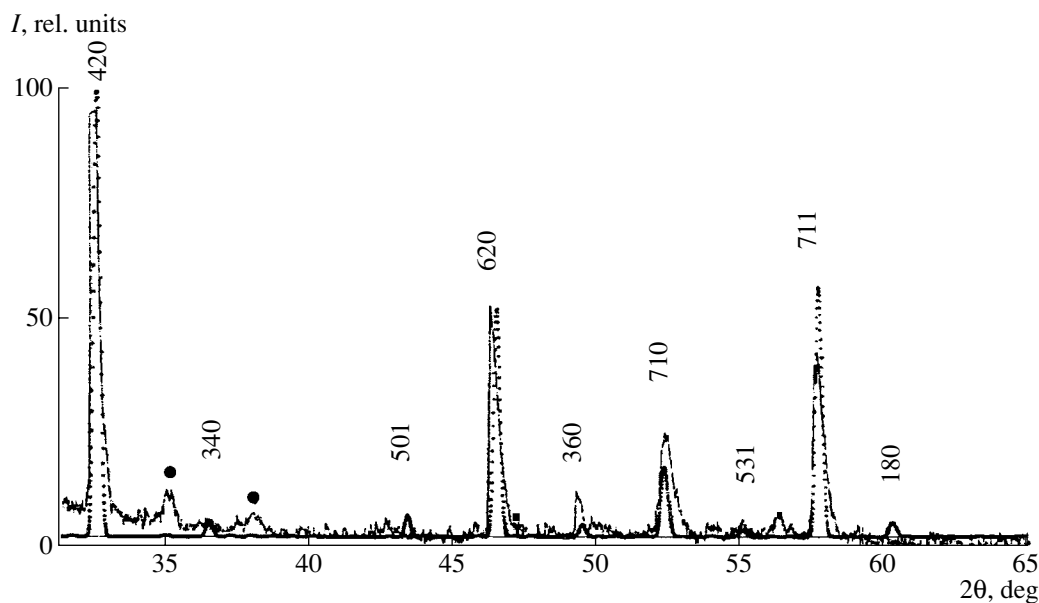


Fig. 3. Comparison of the theoretical (dashed line) and experimental (solid line) X-ray diffraction patterns of $\text{Na}_4\text{Bi}_2\text{Nb}_{10}\text{O}_{30}$ having a VOTP structure.

cies is identical to that of TPTB. We also suggested that vacancies should be ordered.

The vacancy-ordered perovskite structure projected along the [001] direction can be described as a network of oxygen octahedra (a B-type atom is located inside each octahedron) linked together by sharing vertices to form tetragonal cavities. In contrast to perovskite, in which tetragonal (A) positions are completely occupied, vacancy-ordered perovskite has ordered vacancies in A positions. A-type atoms occupy tetragonal positions as follows (Fig. 1a): all A positions are filled in odd rows, whereas only one-fifth of A positions are occupied in even rows in such a way that the occupied

positions (A atoms) are related by a fourfold symmetry axis passing through an A atom in the odd row. The shortest distance between atoms in even rows was chosen as the unit-cell parameter a . Since these atoms are related by the fourfold symmetry axis, $a = b$. The unit-cell parameter c is equal to the body diagonal of the oxygen octahedron. The A atoms located at the corners and at the center of the unit cell are denoted A_1 . All other A atoms are labeled A_2 . It is easily seen that the formula of the unit cell of VOTP is $A_6B_{10}O_{30}$.

The atomic coordinates were calculated from the spatial arrangement of the atoms in the unit cell of VOTP (Fig. 1b). The fractional atomic coordinates are

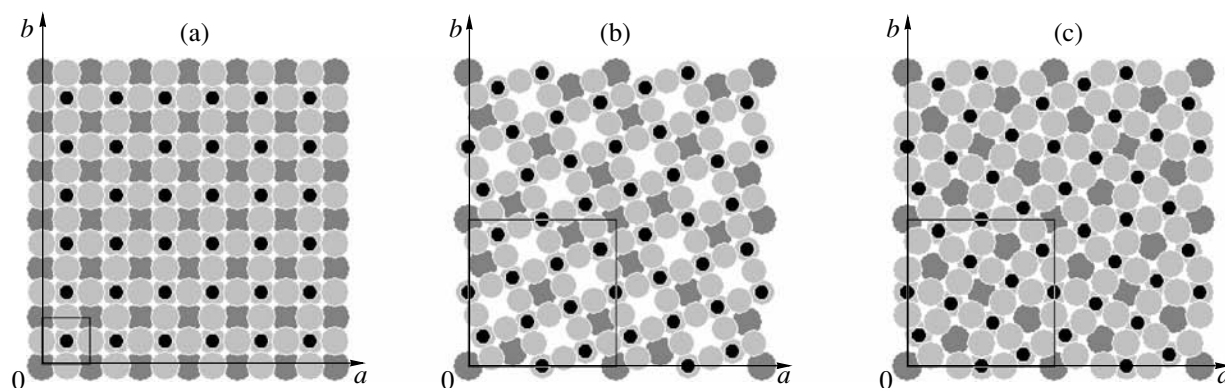


Fig. 4. (a) The NaNbO_3 compound belonging to the perovskite structure type schematically represented as spheres in projection along the $[001]$ direction; (b) $\text{Na}_4\text{Bi}_2\text{Nb}_{10}\text{O}_{30}$ having a VOTP structure schematically represented as spheres in projection along the $[001]$ direction; and (c) $\text{Na}_4\text{Bi}_2\text{Nb}_{10}\text{O}_{30}$ having a TPTB structure schematically represented as spheres in projection along the $[001]$ direction. (●) A, (●) B, and (●) O; unit cells are selected by squares.

given: x (a), y (b), and z (c). The position of the A_1 atom is taken as the origin of coordinates. Figure 1b shows the projection along the $[001]$ direction. The x and y coordinates were obtained by projecting the atoms onto the corresponding axes. The z coordinates of the atoms of the A and B types take the values 0 and 0.5, respectively, and the coordinates of the O atoms are either 0 or 0.5. This is evident from the fact that the atoms in the unit cell of VOTP are located in two planes perpendicular to the c axis. The z coordinates of these planes are 0 and 0.5. The atomic coordinates of the compound corresponding to the general formula $A_6B_{10}O_{30}$ belonging to the VOTP structure type are given in Table 1.

On the basis of the calculated atomic coordinates and the data of [19], we established that the arrangement of the atoms in the unit cell of VOTP is described by the space group $P4/m$.

RESULTS AND DISCUSSION

The relationship between the VOTP and TPTB structure types and their interconversions can be illustrated as follows. Let us consider the VOTP structure projected along the $[001]$ direction (see Fig. 1).

It is reasonable to suggest that a perovskite-type structure containing a large amount of vacancies is unstable. Stabilization accompanied by a decrease in the internal energy can occur as a result of contraction of empty channels and an increase in the number of cation–anion vacancies. This occurs during the transformation of the structure type of perovskite containing vacancies into the TPTB structure type. The latter is energetically more favorable, which is confirmed by comparing the packing coefficients of these structures (Table 2).

The fact that the transformation from VOTP into TPTB (exemplified by $\text{Na}_4\text{Bi}_2\text{Nb}_{10}\text{O}_{30}$) is energetically favorable can be confirmed by calculating the Made-

lung energies for the unit cells of $\text{Na}_4\text{Bi}_2\text{Nb}_{10}\text{O}_{30}$ belonging to the VOTP and TPTB structure types. The energy was calculated using a computer program accurate to 0.144 eV. This program evaluates the Madelung energy for a unit cell by multiplying the ion charge by the electrostatic-field potential at the position of this ion, followed by summation of the energies of all ions forming the unit cell.

The calculated Madelung energies for $\text{Na}_4\text{Bi}_2\text{Nb}_{10}\text{O}_{30}$ belonging to the TPTB and VOTP structure types are $E_{\text{br}} = -4.409$ keV and $E_{\text{VOTR}} = -4.352$ keV, respectively. It can be seen that E_{br} is lower than E_{VOTR} .

The transformation of the defect perovskite structure into the TPTB structure can be represented as rotations of individual octahedra and groups of octahedra about fourfold axes (Fig. 2). The rotation of the groups composed of four octahedra surrounding the A atoms at the corners of the unit cell by the angle $\beta = 8.15^\circ$ is accompanied by the rotation of the linking octahedron by the angle $\alpha = 18^\circ$.

Then, the rotation of a quartet of octahedra located in the center of the unit cell by $\pi/4$ encloses the empty triangular and pentagonal channels occupied by A

Table 2. Packing coefficients of the TPTB and VOTP structures

Unit-cell composition	Packing coefficient of TPTB	Packing coefficient of VOTP
$\text{K}_6\text{W}_{10}\text{O}_{30}$	0.70	0.67
$\text{K}_6\text{Ta}_{10}\text{O}_{30}$	0.69	0.64
$\text{K}_4\text{Bi}_2\text{Nb}_{10}\text{O}_{30}$	0.69	0.62
$\text{Na}_4\text{Bi}_2\text{Nb}_{10}\text{O}_{30}$	0.71	0.60
$\text{Ba}_{1.35}\text{Sr}_{3.75}\text{Nb}_{10}\text{O}_{29}$	0.65	0.58
$\text{Ba}_{1.95}\text{Sr}_{3.05}\text{Nb}_{10}\text{O}_{30}$	0.66	0.60

atoms (positions 4 (*j*)). As a result, A atoms have a coordination number of 15.

The theoretical X-ray diffraction pattern calculated for $\text{Na}_4\text{Bi}_2\text{Nb}_{10}\text{O}_{30}$ having the VOTP structure with the use of the Powder Cell 2.3 program [20] is identical to the experimental X-ray diffraction pattern (Fig. 3). Hence, we can conclude that the first sintering gave rise to a VOTP structure.

For comparison, we give below the structural motifs of some oxygen-octahedral compounds: binary oxide NaNbO_3 having a perovskite structure (Fig. 4a), ternary oxide $\text{Na}_4\text{Bi}_2\text{Nb}_{10}\text{O}_{30}$ having a VOTP structure (Fig. 4b), and ternary oxide $\text{Na}_4\text{Bi}_2\text{Nb}_{10}\text{O}_{30}$ having a TPTB structure (Fig. 4c). It can be seen even visually in Fig. 4 that the packing density of the TPTB structure is higher than that of the VOTP structure.

The foregoing shows that the solid-state synthesis of TPTB involves the formation of a vacancy-ordered perovskite-like structure (VOTP) as the first step. Subsequent annealings lead to the transformation of VOTP into the TPTB structure type.

REFERENCES

1. G. A. Smolenskii, V. A. Bokov, V. A. Isupov, N. N. Kraïnik, R. E. Pasyukov, and M. S. Shur, *Ferroelectrics and Antiferroelectrics* (Nauka, Leningrad, 1971) [in Russian].
2. K. S. Aleksandrov and B. V. Beznosikov, *Perovskite-Like Crystals* (Nauka, Novosibirsk, 1997) [in Russian].
3. F. S. Galasso, *Structure, Properties and Preparation of Perovskite-Type Compounds* (Pergamon, Oxford, 1969).
4. A. I. Gusev and A. A. Rempel', *Nanocrystalline Materials* (Fizmatlit, Moscow, 2000) [in Russian].
5. Yu. V. Kabirov, B. S. Kul'bushev, and M. F. Kupriyanov, *Fiz. Tverd. Tela* (St. Petersburg) **43** (10), 1890 (2001) [*Phys. Solid State* **43**, 1968 (2001)].
6. J. S. Olsen and L. Geward, *Mater. Sci. Forum* **133–136**, 603 (1993).
7. Z. Surovyak, A. B. Panich, and V. P. Dudkevich, *Fine Ferroelectric Films* (Rost. Pedagog. Univ., Rostov-on-Don, 1994) [in Russian].
8. J. F. Scott, *Ferroelectr. Rev.* **1** (1), 1 (1998).
9. N. S. Novosil'tsev and A. L. Khodakov, *Dokl. Akad. Nauk SSSR* **85** (6), 1263 (1952).
10. P. J. Discens and C. Whittinham, *Quart. Rev.* **22** (1), 30 (1968).
11. A. Magneli, *Acta Chem. Scand.* **7** (2), 315 (1953).
12. M. Burger, *Kristallografiya* **16** (6), 1085 (1971) [*Sov. Phys. Crystallogr.* **16**, 959 (1971)].
13. M. A. Poraï-Koshits and L. O. Atovmian, *Crystal Chemistry and Stereochemistry of Coordinated Compounds of Molybdenum* (Nauka, Moscow, 1974) [in Russian].
14. A. Magneli, *Ark. Kemi* **1** (24), 213 (1949).
15. G. A. Smolenskii and N. N. Kraïnik, *Ferroelectrics and Antiferroelectrics* (Nauka, Moscow, 1968) [in Russian].
16. M. H. Francombe, *Acta Crystallogr.* **3**, 349 (1956).
17. F. W. Ainger, W. P. Bickley, and J. V. Smith, *Proc. Br. Ceram. Soc.* **18** (8), 221 (1970).
18. E. N. Sidorenko, I. A. Gurnikovski, and A. V. Turik, *Ferroelectrics* **247** (1–3), 53 (2000).
19. N. N. Matyushenko and Yu. G. Titov, *Structural Analysis in Algorithms and Programs. Generator of Equivalent Points Coordinates* (Khark. Fiz.-Tekh. Univ., Kharkov, 1982) [in Russian].
20. <http://www.ccp14.ac.uk/tutorial/lmgp/>.

Translated by T. Safonova

STRUCTURE
OF ORGANIC COMPOUNDS

Conformational Features and Geometry of Molecules in Crystals of Bridging *ortho,ortho*-Bisphenols and Related Compounds: A Review

L. A. Chetkina and V. K. Belsky

Karpov Institute of Physical Chemistry, ul. Vorontsovo pole 10, Moscow, 103064 Russia

e-mail: vkb@rfbr.ru

Received April 12, 2004

Abstract—This paper generalizes and systematizes the main results of X-ray structure investigations of bridging *ortho,ortho*-bisphenols and related compounds. The conformational characteristics and geometric parameters of molecules and hydrogen bonds in *ortho,ortho*-methylene-bisphenols, their derivatives, polynuclear bridging *ortho*-phenols, *ortho,ortho*-thiobisphenols, dithiobisphenols, and trithiobisphenols are discussed. Structural formulas of 65 compounds, the conformational and selected geometric parameters of the molecules under consideration, and the characteristics of the intramolecular and intermolecular hydrogen bonds are presented in seven tables. © 2005 Pleiades Publishing, Inc.

CONTENTS

1. Introduction
2. Conformations and Geometric Parameters of the Bisphenol Molecules from X-ray Diffraction Data
 - 2.1. *ortho,ortho*-Methylene-Bisphenols and Their Derivatives
 - 2.2. Polynuclear Bridging *ortho*-Phenols
 - 2.3. *ortho,ortho*-Thiobisphenols, Dithiobisphenols, and Trithiobisphenols
3. Conclusions
- References

1. INTRODUCTION

Investigations with the aim of generalizing a large amount of structural data for particular classes of compounds provide deeper insight into the specific features of their structure and structure–property relations. In our previous papers [1–4], we gave surveys of the structures of aromatic quinones and tricyanovinyl compounds. In this paper, we consider the structures of *ortho,ortho*-bisphenols with unsubstituted and substituted methylene bridges; polynuclear bridging *ortho*-phenols; and *ortho,ortho*-bisphenols with thio, dithio, and trithio bridges.

Owing to the unique combination of practically important properties exhibited by bridging *ortho,ortho*-bisphenols, these compounds are widely used in chemistry, biology, etc. This has given further impetus to extensive research in the structures of bridging bisphenols with hydroxyl groups in *ortho* positions, especially because these compounds possess biological activity

[5–9] and are flukicides (vermifuge medicinal) [10–15].

The problems regarding the synthesis, properties, applications, reactivity, and efficiency of phenol stabilizers (including bridging *ortho,ortho*-bisphenols) have been the subject of much investigation [16–23]. Since phenol stabilizers effectively protect polymers against oxidation, do not change the color of polymer products, and are virtually nontoxic, they have found wide application in the production of plastic materials and in the rubber industry [18].

The results obtained in X-ray structure studies are necessary for the elucidation of the mechanism responsible for the inhibiting action exerted by bisphenol compounds, the interpretation of the spectral data, and a correct explanation of the reactivity. In their recent review “Structure and Antioxidant Activity of Some Bisphenols and Trisphenols,” Gurvich *et al.* [23] pursued the question as to how the structure parameters determined in our earlier works [24–33] for stabilizer molecules affect their reactivity and activity in model systems and the question as to which role is played by the structure factors in the mechanism of the antioxidant action. The particular interest expressed by researchers in phenol stabilizers can be judged from the progressively increasing number of works concerned with only one phenol stabilizer, namely, 2,6-di-*tert*-butyl-4-methylphenol (ionol) (see the review [23]), whose structure was described earlier by Maze-Baudet [34].

Among the structure factors, which affect the properties and structure of bisphenol compounds, the conformational features of bisphenol molecules are of the utmost importance and, in many respects, responsible

for their properties. The problems associated with the conformational analysis of organic molecules are considered in the monographs [35–37]. In this review, we used the results of our structural investigations [24–33], bibliographic information available in the Cambridge Structural Database [38, 39], and data taken from periodic scientific journals published up to and including 2002.

2. CONFORMATIONS AND GEOMETRIC PARAMETERS OF THE BISPHENOL MOLECULES FROM X-RAY DIFFRACTION DATA

2.1. *ortho,ortho*-Methylene-Bisphenols and Their Derivatives

Table 1 presents *ortho,ortho*-methylene-bisphenols and their derivatives for which the crystal and molecular structures were determined using X-ray diffraction analysis: compounds **1–19** with unsubstituted methylene bridges $-\text{CH}_2-$; compounds **20–26** with substituted methylene bridges, in which these bridges are replaced by the groups $-\text{CH}(\text{CH}_3)-$ (compound **21**), $-\text{CH}(\text{CH}_3)_2-$ (compounds **20**, **22**), $-\text{CH}(\text{CCl}_3)-$ (compound **23**), $-\text{CH}(\text{OPh})-$ (compound **24**), $-\text{CH}(\text{OCH}_2\text{Ph})-$ (triethylamine adduct **25**), and $-\text{CH}(\text{Bu}^t)-$ (compound **26**); and compounds **27–30**, which belong to the related class of *ortho,ortho*-hydroxybenzophenones (dashed lines indicate intramolecular hydrogen bonds).

In earlier investigations [13, 37, 44, 53–61], primary attention was concentrated on analyzing the conformation of bridging diphenyls. In a series of structural studies (see, for example, [54–57]), X-ray diffraction analysis of substituted bridging diphenyl compounds made it possible to elucidate how the substituents and the nature of bridging groups affect the relative orientation of phenyl rings and the midplane passing through the bridging group. It should be noted that those studies dealt mainly with diphenyl ethers, except for only one compound with methylene bridges [55]. The conformational and geometric parameters determined in the aforementioned works for diphenyl molecules were generalized by Gopal *et al.* [56, 57], who used the nomenclature proposed earlier by van der Heijden *et al.* [54] for describing the conformation of bridging diphenyls. Later, Barnes *et al.* [58] determined the crystal and molecular structures of diphenylmethane—the ancestor of many substituted derivatives whose conformational parameters were found using X-ray diffraction. By analogy with the analysis performed by van der Heijden *et al.* [54], Barnes *et al.* [58] considered the possible conformations of diphenylmethane and determined selected conformational parameters for this compound and its nine derivatives. The data obtained in [58] were used in the monograph by Vereshchagin *et al.* [37], who analyzed the influence of steric and electronic factors on the molecular conformation. The con-

formation of C-bridging diphenyl compounds was also discussed by Cody [59].

In order to describe the conformation of bridging *ortho,ortho*-methylene-bisphenols presented in Table 1, we chose the nomenclature given in [54], which is similar to those proposed in [37, 58, 59, 62]. Bridging diphenyl compounds can adopt four main conformations that are characterized by the dihedral angles Φ_A and Φ_B , which the planes of phenyl rings *A* and *B* make with the midplane: (i) a planar conformation ($\Phi_A = \Phi_B = 0^\circ$, symmetry *mm*); (ii) a butterfly conformation ($\Phi_A = \Phi_B = 90^\circ$, symmetry *mm*) or, according to [58], a tweezer conformation; (iii) a twist conformation ($\Phi_A = \Phi_B = 45^\circ$, symmetry *2* or *m*); and (iv) a skewed conformation ($\Phi_A = 0^\circ$, $\Phi_B = 90^\circ$, symmetry *m*) [54].

The molecular conformation of bridging *ortho,ortho*-bisphenols is governed, to a great extent, by the OH functional groups that are located in *ortho* positions with respect to the methylene bridge and can form both intramolecular and intermolecular hydrogen bonds. Depending on the dihedral angles Φ_A and Φ_B , the diphenylmethylene moiety of the molecules can adopt the following conformations (Table 2): a butterfly conformation for angles $\Phi_A \approx \Phi_B = 80^\circ\text{--}90^\circ$, a twist conformation for angles $\Phi_A \approx \Phi_B = 35^\circ\text{--}55^\circ$, an intermediate twist-skewed conformation for angles $\Phi_A = 15^\circ\text{--}35^\circ$ and $\Phi_B = 60^\circ\text{--}80^\circ$ (a skewed conformation for angles $\Phi_A = 0^\circ\text{--}10^\circ$ and $\Phi_B = 80^\circ\text{--}90^\circ$ is not observed in these compounds), and a twist–butterfly conformation for angles $\Phi_A \approx \Phi_B = 60^\circ\text{--}80^\circ$. Benjamins and Chandler [62] noted that there is no clear-cut distinction between the skewed and twist conformations.

In the C–CH₂–C bridging group, the C–C bond lengths listed in Table 2 are close both to the standard values for carbon atoms in the corresponding hybridization and to the averaged bond lengths in organic compounds [63], whereas the C–C–C bond angles exceed the tetrahedral angle to a varying extent. The C–OH distances are comparable both to the standard length of the C(*sp*²)–O bond (1.397 Å) and to the averaged length of these bonds in phenols (1.362 Å) [63]. For phenol, the initially determined value of the C–OH bond length (1.35 Å) [64] was refined to be 1.372 Å [65], which is the averaged length for three crystallographically independent molecules. The averaged length of the C–OH bonds is equal to 1.384 Å [53] or 1.37 Å [66, 67] in bridging diphenols with hydroxyl groups in *para* positions, 1.366 Å [68] in bridging diphenols with hydroxyl groups in *meta* positions, 1.371–1.402 Å [34, 69–73] in a number of phenol derivatives, and 1.332–1.344 Å [12, 74–77] in phenols with nitro groups in *ortho* positions.

The crystal structure of 2,2'-methylene-bisphenol (compound **1**), which is the ancestor of the compounds presented in Table 1, was determined in the study of linear polynuclear *ortho*-phenol compounds by different methods, as well as in the X-ray structure investigations

Table 1. *ortho,ortho*-Methylene-bisphenols and their derivatives (dashed lines indicate intramolecular hydrogen bonds)

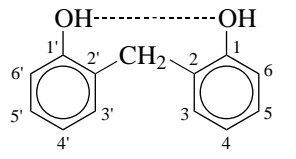
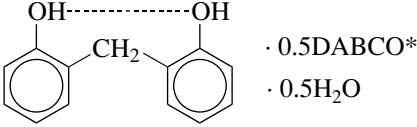
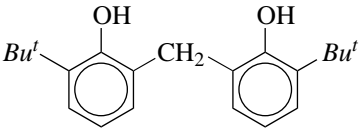
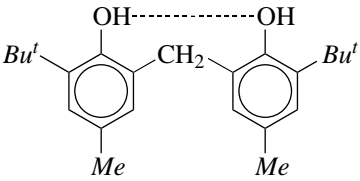
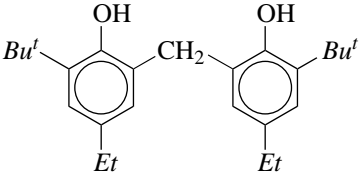
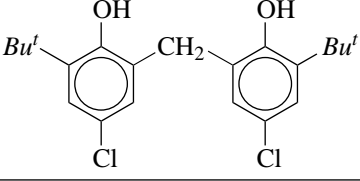
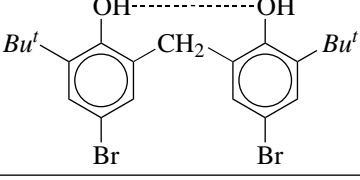
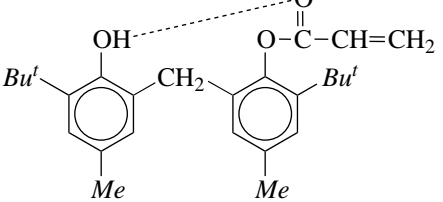
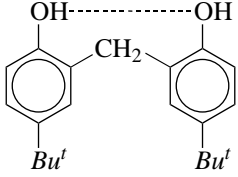
Compound	Formula	Symmetry of the molecule	<i>R</i> factor	Reference
1		1	0.080	[40]
2		1	0.062	[41]
3		1	0.041	[42]
4		1	0.061	[27]
5		2	0.036	[29]
6		2	0.030	[31]
7		1	0.039	[31]
8		1	0.033	[33]
9		1, 1, 1	0.128	[43]

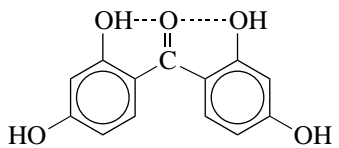
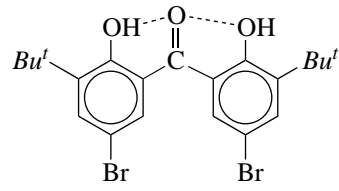
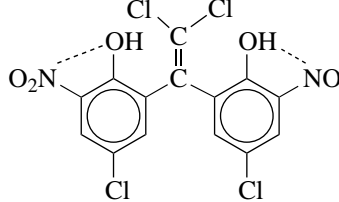
Table 1. (Contd.)

Compound	Formula	Symmetry of the molecule	R factor	Reference
10		1	0.056	[6]
11		1, 1	0.057	[7]
12		1	0.043	[8]
13		1	0.075	[5]
14		1, 1	0.037	[44]
15		1	0.038	[44]
16		1	0.030	[44]
17		1	0.039	[44]
18		1	0.036	[9]

Table 1. (Contd.)

Compound	Formula	Symmetry of the molecule	R factor	Reference
19		1	0.060	[45]
20		1	0.038	[46]
21		1	0.065	[10, 47]
22		2	0.049	[10]
23		1	0.046	[11]
24		1	0.061	[15, 48]
25		1	0.063	[15]
26		1	0.040	[49]
27		1	0.033	[50]

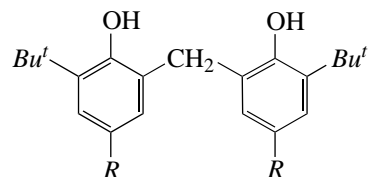
Table 1. (Contd.)

Compound	Formula	Symmetry of the molecule	R factor	Reference
28		1, 1	0.034	[51]
29		1, 1	0.031	[52]
30		2	0.055	[14]

* 1,4-Diazabicyclo[2.2.2]octane.

of trinuclear (compound **31**, see below) and tetranuclear (compound **38**, see below) methylene-bridging oligophenols with OH groups in *ortho* positions [40]. The molecular geometric parameters of compound **1** (see Table 2.1) are close to those of diphenylmethane, in which the C–CH₂ bond lengths are equal to 1.501 and 1.523 Å, the C–CH₂–C bond angle is 112.5°, and the dihedral angles are $\Phi_A = 63.9^\circ$ and $\Phi_B = 71.1^\circ$ [58]. The molecule adopts a *cis* conformation with a moderately strong intramolecular hydrogen bond OH...OH (2.787 Å) (Table 3); the positions of the hydrogen atoms in the hydroxyl groups are not determined. In the crystal, the molecules form zigzag polymer chains owing to the OH...OH intermolecular hydrogen bonds whose lengths are equal to 2.700 and 2.806 Å (the mean-statistic length of these bonds is 2.72 Å [78]). The same molecules in compound **2** crystallize with molecules of water and 1,4-diazabicyclo[2.2.2]octane [41]. In the crystal of compound **2**, the 2,2'-methylene-bisphenol molecules with the OH...OH intramolecular hydrogen bonds (2.673 Å) are related in pairs by the center of symmetry, whereas their hydroxyl groups and the solvent molecules form the intermolecular hydrogen bonds O(1)H...N (2.605 Å) (the mean-statistic length is 2.79 Å [78]) and O(2)H...O(H₂) (2.860 Å). As in structure **1**, these molecules in structure **2** form zigzag chains. The dihedral angle between rings (61.8°) in molecule **2** is less than that in molecule **1**, and molecule **2** has a distorted butterfly conformation [41].

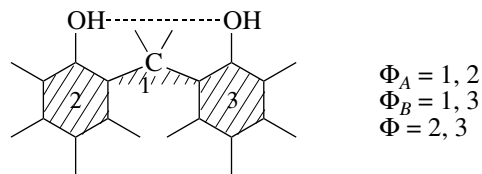
2,2'-Methylene-bisphenols of the general formula



where $R = Me$ or Et , have widespread application as antioxidants [16, 17, 20]. Analysis of the IR spectra of 2,2'-methylene-bisphenols with different *para* substituents ($R = H, Me, Et, t-Bu, Cl, Br$) revealed that the nature of *para* substituents has a substantial effect on the reactivity of bisphenols in radical reactions and on the coexistence of structures with different types of intramolecular hydrogen bonds in solutions [21].

Bohmer *et al.* [42] synthesized and studied different phenol derivatives of calix[4]arene with hydroxyl groups in *exo* positions and performed an X-ray diffraction analysis of bis(2-hydroxy-3-*tert*-butylphenol)methane (compound **3**) and calix[4]arene (compound **51**, see below). In the crystal, molecule **3** has the approximate axis 2 passing through the C central atom of the methylene bridge and the OH groups occupy *trans* positions with the respect to the midplane. Both hydroxyl groups are involved in the OH... π (arene) interactions with the hydroxyl hydrogen atoms directed toward the phenyl carbon atoms of the adjacent rings [the O...C(*sp*²) distances are given in Table 3]. The same type of OH... π intramolecular interaction was revealed in crystals **5**, **6**, and **20**.

Compounds **4–8**, which are extensively used as phenol stabilizers of polymers, have been studied by differ-

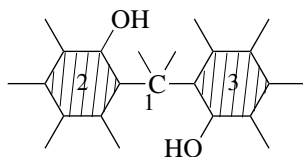
Table 2. Selected geometric parameters of molecules of bridging *ortho,ortho*-bisphenols and their conformation in crystals2.1. *ortho,ortho*-Methylene-bisphenols with a *cis* structure

Compound	Bond lengths (Å) and bridging angle* (deg)			Dihedral angles (deg)			Conformation of the molecule
	C-CH ₂	C-OH	C-CH ₂ -C	Φ _A	Φ _B	Φ	
1	1.510	1.383	113.9	75.1	71.8	71.3	twist-butterfly
4	1.550	1.392	113.0	78	89	62	butterfly
7	1.519	1.387	115.2	82.8	86.8	63.1	butterfly
8	1.519	1.373	114.8	35.8	73.2	87.6	twist-skewed
9	1.54	1.37	110.1	86.6 (I) 86.5 (II) 81.3 (III)	86.7 (I) 89.8 (II) 89.6 (III)		butterfly
10	1.500	1.390	118.6	51.0	65.2	84.4	twist
11	1.51	1.39	116	61 (I) 64 (II)	75 (I) 73 (II)	81 (I) 78 (II)	twist-butterfly
12	1.521	1.374	112.1	79.7	77.7	72.9	butterfly
14	1.515	1.374	112.8	87.7 (I) 83.3 (II)	86.2 (I) 75.9 (II)		butterfly
16	1.511	1.380	113.5	74.2	75.2		twist-butterfly
17	1.521	1.375	114.1	76.6	61.0		twist-butterfly
18	1.520	1.373	113.8	77.3	79.5		butterfly
19	1.517	1.371	116.4	81.5	87.2		butterfly

Substituted methylene group

Compound	C-C \sphericalangle	C-OH	C-C \sphericalangle -C	Φ _A	Φ _B	Φ	Conformation of the molecule
21	1.52	1.35	112.8	34.1	71.0	87.6	twist-skewed
23	1.520	1.341	111.7			73.9	butterfly
24	1.530	1.343	110.7	61.1	71.6	80.1	twist-butterfly
25	1.52	1.31	112	88.0	85.6	61.8	butterfly
26			114.1	79.8	64.2	77.1	twist-butterfly
27	1.472	1.347	121.9			45.7	
28	1.457	1.360	122.9			41.8 (I), 43.3 (II)	

Table 2. (Contd.)

2.2. *ortho,ortho*-Methylene-bisphenols with a *trans* structure

Unsubstituted methylene group

Compound	Bond lengths (Å) and bridging angle* (deg)			Dihedral angles (deg)			Conformation of the molecule
	C-CH ₂	C-OH	C-CH ₂ -C	Φ _A	Φ _B	Φ	
5	1.517	1.386	117.5	64.2	64.2	71.0	twist-butterfly
6	1.516	1.371	117.3	66.3	66.3	70.8	twist-butterfly
13	1.51	1.37	116.1	81.6	81.3	62.1	butterfly
15	1.514	1.367	114.0	77.1	20.1		twist-skewed
Substituted methylene group							
Compound	C-C<	C-OH	C-∠-C	Φ _A	Φ _B	Φ	Conformation of the molecule
20	1.540	1.379	111.9	50.5	50.0	82.3	twist
22	1.541	1.347	113	48.7	48.7	77.4	twist
30	1.483	1.356	117.0	84.2	84.2	67.6	butterfly

* Averaged values for the chemically equivalent bond lengths and angles.

ent physicochemical methods [16, 18–23, 79–81]. The structural characteristics obtained from the X-ray diffraction data for these compounds [27, 29, 31, 33] are compared with their antioxidant activity in the review [23]. In the series of *ortho,ortho*-methylene bisphenols, 2,2'-methylene-bis(4-methyl-6-*tert*-butylphenol) (compound **4**) exhibits an optimum antioxidant activity. The substitution of the ethyl group (compound **5**) or the halogen atom (compounds **6**, **7**) for the methyl group in the *para* position with respect to the hydroxyl group leads to a decrease in the efficiency of polymer-oxidation inhibitors of the bridging bisphenol class [23].

An original method for preparing a highly efficient polymer stabilizer (compound **4**) was devised and brought into commercial practice by Gurvich *et al.* [82]. The results of analyzing the spectra and the reactivity of compound **4** and its analogues [19, 21] allowed us to assume that solutions of these compounds contain a mixture of conformers with intramolecular hydrogen bonds of different types (OH...OH, OH...π), whereas their crystals are characterized by only one conformer with the OH...OH intramolecular hydrogen bond. X-ray diffraction data were necessary to elucidate the mechanism of the inhibiting action exerted by bridging bisphenol compounds. It was established that the conformation of molecule **4** is governed by a moderately strong intramolecular hydrogen bond (O...O, 2.76 Å; O...H, 2.1 Å) between the hydroxyl groups in the *cis* position with respect to the methylene bridge. The dihe-

dral angles Φ_A and Φ_B (Table 2.1) correspond to a butterfly conformation. This conformation of molecule **4** confirms the results of spectral investigations [21] and is consistent with the “cell” mechanism of the inhibiting action exerted by 2,2'-methylene-bisphenols on polymer oxidation: the *cis* conformation provides the most favorable conditions for the interaction with peroxy radicals [19]. The distances between the C atoms of the *tert*-butyl groups and the neighboring oxygen atoms of the hydroxyl groups are relatively short (2.99–3.16 Å). The screening by the *tert*-butyl groups hinders the formation of OH...OH intermolecular hydrogen bonds. This is characteristic of sterically hindered phenols [16].

The X-ray diffraction investigation of 2,2'-methylene-bis(4-ethyl-6-*tert*-butylphenol) (compound **5**), which is a highly efficient noncoloring antioxidant for synthetic rubbers [20], demonstrated that, upon substitution of the ethyl group for the methyl group in the *para* position with respect to the hydroxyl group, the molecule has a twist-butterfly conformation and a *trans* structure with the methylene carbon atom located on the axis 2 (Table 2.2). The bond angle at the methylene carbon atom is increased to 117.5°. The ethyl group is rotated by an angle of 63.6° with respect to the plane of the phenyl ring. With knowledge of the molecular conformation of this compound, it is possible to interpret the spectral data and to explain the reactivity [21]. It was found that, in the structure, the hydroxyl group is

located in the vicinity of the adjacent phenyl ring. The short intramolecular distances H...C (2.39 and 2.51 Å) (the sum of the van der Waals radii of these atoms lies in the range 2.87–2.90 Å [83–87]) suggest the formation of the weak hydrogen bond OH... π due to the interaction of the hydroxyl group with π electrons of the adjacent ring. Apart from the H...C shortened distances, the OH... π hydrogen bond can be characterized by two parameters: (i) the distance r (2.35 Å) from the H[O(1)] atom to the midpoint of the nearest bond C(2')–C(3') in the adjacent ring and (ii) the angle δ (59°) between the H[O(1)]C(2')C(3') plane and the plane of the adjacent ring. As was noted in [88, 89], numerous spectroscopic studies have revealed a small number of crystal structures with OH... π hydrogen bonds. The length of the OH... π intramolecular hydrogen bond in compound **5** is found to be approximately equal to that determined in the structures of 2,6-diphenylphenol (H...C, 2.40 and 2.43 Å) [90], 1,1-diphenylpropanol-1 (H...C, 2.36 and 2.45 Å) [89], 4-nitro-2,6-diphenylphenol (H...C, 2.48 and 2.59 Å; $r = 2.44$ Å) [88], and 2-hydroxy-biphenyl [91].

The reactivity of compounds **6** and **7** with $R = \text{Cl}$ or Br is less than that of compounds **4** and **5**. The IR spectra of crystals **6** (the frequency of stretching vibrations of the OH group is $\nu = 3562 \text{ cm}^{-1}$) indicate that the molecules adopt a *trans* conformation with the OH... π intramolecular hydrogen bond. The IR spectra of crystals **7** ($\nu = 3389$ and 3595 cm^{-1}) suggest that the molecules exhibit a *cis* conformation with the OH...OH intramolecular hydrogen bond [21]. X-ray diffraction analysis of these compounds [31] confirmed the inferences made from the IR spectroscopic data. In the crystal, the molecule of the chlorine derivative (compound **6**) occupies the special position on the axis 2 and has a *trans* structure: the OH groups are located on each side of the methylene bridge. The geometric parameters of molecule **6** (Table 2.2) are close to those in the structure of the ethyl analogue (compound **5**). The OH... π intramolecular hydrogen bonds are also characterized by close parameters (Table 3). For the chlorine derivative, the H...C distances (2.60 and 2.65 Å) (the sum of the van der Waals radii of these atoms is 2.87 Å) indicate the formation of weak hydrogen bonds OH... π ($r = 2.53$ Å, $\delta = 52^\circ$) due to the interaction of the OH group with π electrons of the adjacent ring. The molecule of the bromine analogue (compound **7**) in the crystal occupies the general position and, like molecule **4**, has a *cis* structure in which the OH groups form moderately strong intramolecular hydrogen bonds OH...OH. In this case, polymer stabilizers most efficiently interact with peroxy radicals. Therefore, upon substitution of the bromine atom for the chlorine atom in the *para* position, the molecule in the crystal acquires the *cis* structure rather than the *trans* structure; i.e., the situation is opposite to that observed upon substitution of the ethyl group for the methyl group in the *para* position. In compounds **4** and **7**, there is a certain tendency toward changing the C–OH bond lengths: this bond for the

Table 3. Geometric parameters of intramolecular hydrogen bonds in *ortho*, *ortho*-methylene-bisphenols

Compound	Hydrogen bond type	O...O, Å	O–H...O (deg)
1	OH...OH	2.787	
2	OH...OH	2.673	178.6
4	OH...OH	2.76	149
7	OH...OH	2.717	153
8	OH...O(=C)	2.873	157
9	OH...OH	2.725 (I), 2.685 (II), 2.805 (III)	
10	OH...OH	3.05	
11	OH...OH	2.76 (I), 2.71 (II)	
12	OH...OH	2.827	157
13	OH...O(=C)	2.59, 2.57	
14	OH...OH	2.698 (I), 2.711 (II)	163 (I), 160 (II)
16	OH...OH	2.780	159
17	OH...OH	2.728	155
18	OH...OH OH...O(=C)	2.715 2.633	161 147
19	OH...OH OH...O(=C)	2.703 2.441	
22	OH...O(NO ₂)	2.54	136
23	OH...O(NO ₂)	2.563 2.608	149 151
24	OH...O(NO ₂)	2.554 2.575	152 130
25	OH...O(NO ₂)	2.69, 2.75	
26	OH...OH	2.989	
27	OH...O(=C)	2.602 2.656	148.6 141.7
28	OH...O(=C)	2.616, 2.584 (I) 2.716, 2.516 (II)	148.149 (I) 133.152 (II)
29	OH...O(=C)	2.606, 2.587 (I) 2.624, 2.617 (II)	
30	OH...O(NO ₂)	2.562	160
Compound	Hydrogen bond type	O...C(<i>sp</i> ²), Å	H...C(<i>sp</i> ²), Å
3	OH... π	2.987 2.959	
5	OH... π	3.113 3.331	2.39 2.51
6	OH... π	3.163 3.320	2.60 2.65
20	OH... π	2.88 2.87	2.13, 2.49 2.19, 2.52

donor (1.384 Å in **4** and 1.365 Å in **7**) is shorter than that for the acceptor (1.400 Å in **4** and 1.409 Å in **7**). Compound **7** is the first representative of bridging *ortho* bisphenols with $R = \text{Br}$. The presence of bulky *tert*-butyl groups in *ortho* positions with respect to the OH groups prevents their participation in the formation of intermolecular hydrogen bonds. In the crystal, the molecular packing involves shortened halogen-halogen intermolecular contacts ($\text{Cl}\cdots\text{Cl}'$, 3.323 Å in structure **6** and $\text{Br}\cdots\text{Br}'$, 3.686 Å in structure **7**). These distances are considerably shorter than twice the van der Waals radii of chlorine (3.80 Å) and bromine (3.94 Å) atoms [84, 85] and, according to [92, 93], are smaller than the upper boundaries (3.65 and 3.79 Å, respectively) of the intermolecular specific interactions. The angles $\text{C}-\text{Cl}\cdots\text{Cl}'$ (167.4°) and $\text{C}-\text{Br}\cdots\text{Br}'$ (142.2°) indicate that, unlike the van der Waals interactions, these specific interactions are directional in character [92, 93].

It is known that protection of polymers and polymer products from aging depends on the efficiency of stabilizers. One of the directions of research on the design and use of efficient nonvolatile stabilizers that cannot be washed out of polymers involves grafting of stabilizers to a polymer, thus ensuring their presence in the final product [23, 81]. Such a graft stabilizer is 2,2'-methylene-bis(4-methyl-6-*tert*-butylphenol) monoacrylate (compound **8**). This stabilizer is similar in properties to efficient antioxidants, such as 2,2'-methylene-bis(4-methyl-6-*tert*-butylphenol) (compound **4**) and 2,6-di-*tert*-butyl-4-methylphenol [18, 19]. The crystal structure of the last compound was determined by X-ray diffraction analysis and described in [34]. The study of the antioxidant activity of compound **8** and other acrylate and maleate derivatives of 2,6-di-*tert*-butylphenol in oxidation of poly(isoprene) rubber [94] demonstrated that graft stabilizers hold promise for use in stabilizing elastomers. The ability of antioxidant **8** to bind chemically to polymers is associated with the presence of the $-\text{C}(\text{O})-\text{CH}=\text{CH}_2$ acrylic acid fragment in the molecule. X-ray diffraction investigations revealed that the molecule has a *cis* structure and a twist-skewed conformation and that the intramolecular hydrogen bond ($\text{H}\cdots\text{O}$, 2.02 Å) is formed between the hydroxyl group and the carbonyl oxygen atom of the acrylate fragment. This hydrogen bond is weaker than that observed in compounds **4** and **7** (Table 3). The phenyl rings are mutually perpendicular ($\Phi = 87.6^\circ$), and the planar (within 0.050 Å) acrylic acid fragment $-\text{O}-\text{CO}-\text{C}=\text{C}$ forms an angle of 74.7° with the plane of its own ring. The $\text{C}-\text{OH}$ bond (1.373 Å) of the donor group is considerably shorter than the $\text{C}(\text{Ph})-\text{O}-$ bond (1.422 Å).

Among the most efficient stabilizers of polymer materials used for medical purposes, the stabilizer of most interest is a related compound, namely, 1,3,5-tris(3',5'-di-*tert*-butyl-4'-hydroxybenzyl)mesitylene trisphenol, which has found extensive application in protection of different polymers from aging [16, 20, 23]. The use of spatially loaded phenyl antioxidants, in which the

hydroxyl group is screened by two bulky *tert* butyl groups, strongly hinders the reactions involving the hydrogen atom of the hydroxyl group. In order to determine the molecular and crystal structures of the trisphenol compound, to reveal the conformation of the molecule, and to establish the appropriate conditions for the introduction of trisphenol into polymers, this organic complex ($\text{C}_{54}\text{H}_{78}\text{O}_3$, space group $P2_12_12_1$, $Z = 4$, $R = 0.072$) was studied using X-ray diffraction [24–26]. The trisphenol molecule consists of a completely substituted central mesitylene ring that, in the 1-, 3-, and 5-positions, is bound by the methylene bridges to the three outer rings of the 3',5'-di-*tert*-butyl-4'-hydroxybenzyl fragments. The molecule exhibits a cisoid conformation: all the outer rings are located on one side of the central ring; are nearly orthogonal to this ring; and form angles of 79.7° , 81.9° , and 72.5° . The molecule as a whole has the pseudosymmetry axis 3. The central ring is characterized by an alternation of bond lengths and angles. This is typical of sterically overloaded benzene derivatives. Moreover, a pronounced alternation of bond angles is observed in the outer rings: the bond angles at the carbon atoms bonded to the methylene and *tert*-butyl groups have minimum values. A similar distortion of bond angles was revealed in molecules of other compounds containing *tert*-butyl groups [34, 56]. The mean value of the $\text{C}-\text{OH}$ bond length is equal to 1.381 Å. It should be noted that the lengths of the CH_2-C bonds formed by the methylene group with the central ring (the mean length is 1.544 Å) and with the outer rings (the mean length is 1.516 Å) are not equal to each other. The bond angle at the carbon atom of the methylene bridge is 112.6° . The molecule adopts a basket conformation. In the basket, the bottom is the plane of the mesitylene ring and the walls are formed by 2,6-di-*tert*-butylphenol fragments. The basket serves as a trap, i.e., a pocket for trapping of hydroperoxy radicals and for their rapid deactivation by reactive centers (OH groups) arranged along the rims of the basket walls. The basket structure provides a high antioxidant activity of this stabilizer [23]. The above conformation is determined by the molecular packing in the crystal and is most likely to be one of the possible energetically favorable conformations existing in a solution. The hydroxyl groups are screened by bulk *tert*-butyl groups. As a result, the hydroxyl groups cannot approach each other and intermolecular hydrogen bonds are not formed. The same inference was made by Maze-Baudet [34].

Continuing the studies of polynuclear phenol-formaldehyde oligomers (including compound **1** [40]), Casiraghi *et al.* [43] synthesized binuclear compound **9** (Table 1) and carried out an X-ray diffraction analysis of this oligomer. For three crystallographically independent molecules, only the non-hydrogen atoms were located and one *tert*-butyl group appeared to be disordered. Comparison of the bond lengths and angles in these molecules with those in binuclear compound **1** showed that the *tert*-butyl groups in *para* positions have little if any effect on the molecular geometry. In three

independent molecules, the dihedral angles Φ_A and Φ_B are close to each other (Table 2) and correspond to a butterfly (tweezer [43]) conformation. In compounds **1**, **2**, **9**, **31**, and **38**, the intramolecular and intermolecular hydrogen bonds are the main factors responsible for the conformation and the molecular packing [43]. For structure **9**, the O...O distances between the OH groups in *cis* positions are listed in Table 3. In addition to the intramolecular hydrogen bonds, the hydroxyl groups are involved in the formation of intermolecular hydrogen bonds (the O...O distances are 2.740, 2.702, and 2.767 Å). The 5,5'-di-*tert*-butyl-3-bromo-2,2'-bis(trimethylsiloxy)diphenylmethane compound can be treated as a derivative of compound **9**. The structure of the former compound was determined at 173 K ($R = 0.066$) [95].

Among the first *ortho,ortho*-methylene-bisphenols, whose structure was determined by X-ray diffraction analysis, compounds **10**, **11**, and **12** are characterized by a symmetric arrangement of substituents (chlorine, methyl, isopropyl) in the rings. These compounds exhibit fungicidal and bactericidal activities and have been patented in many countries [6–8]. In all three compounds, the chlorine atoms are located in *para* positions with respect to the hydroxyl groups, whereas the methyl and isopropyl groups occupy different positions. In the crystal, the molecules of these compounds have a *cis* structure with the OH...OH intramolecular hydrogen bonds, among which the bond in structure **10** is the weakest (Table 3). For structure **12**, we calculated the O...O distance and the O–H...O angle according to the data taken from [8]. Judging from the dihedral angles (Table 2), the molecular conformation can be considered a nearly twist conformation for compound **10**, a twist–butterfly conformation for two independent molecules of compound **11**, and a butterfly conformation for compound **12**. An increase in the C–CH₂–C bond angle of the methylene bridge to 118.6° in structure **10**, 116° in structure **11**, and 112.1° in structure **12** with respect to the tetrahedral angle can be caused by the presence of the methyl groups in *ortho* positions with respect to the bridge. As in compounds **4** and **7**, there is a difference between the C–OH bond lengths (the bond for the donor hydroxyl group is shorter): 1.388 and 1.392 Å in structure **10** and 1.370 and 1.379 Å in structure **12**. The isopropyl groups are rotated with respect to their own rings through the following angles: 87.3° and 66.7° in structure **10**; 81° (**I**), 76° (**II**) and 66° (**I**), and 71° (**II**) in structure **11**; and 86.9° and 85.7° in structure **12**. Apart from the OH...OH intramolecular hydrogen bonds, the hydroxyl groups in these compounds can form intermolecular hydrogen bonds due to the presence of isopropyl groups (which are less bulky than the *tert*-butyl groups in structures **4**, **7**, and **8**) in *ortho* positions with respect to the OH groups. In structure **10**, the molecules are joined by weak intermolecular hydrogen bonds (OH...OH, 3.05 Å; the mean-statistic length is 2.72 Å [78]) and form infinite chains. In crystal **11**, two crystallographically independent molecules are linked by

the intermolecular hydrogen bonds (O...O, 2.73 and 2.72 Å) between the OH groups and form dimers; in this case, four oxygen atoms are involved in the formation of intramolecular and intermolecular hydrogen bonds. In structure **12**, the shortest intermolecular distance O...O (3.116 Å) can be considered a very weak intermolecular hydrogen bond.

The crystal structure of compound **13** was determined in the study of biologically active compounds. The molecule in the general position has a *trans* structure and a butterfly conformation in accordance with the dihedral angles Φ_A and Φ_B taken from [58]. The hydroxyl groups and the oxygen atoms of the neighboring acetyl groups form strong intramolecular hydrogen bonds (O...O, 2.59 and 2.57 Å) [5].

In the course of synthesis, individual compounds of tetrachloro-2,2'-methylene-bisphenol with chlorine atoms in the 4-, 4', 5-, and 5'-positions (compound **14**), 3-, 4-, 4', and 5'-positions (compound **16**), and 3-, 3', 4-, and 4'-positions (compound **17**) were isolated from a mixture of three isomers. The structures of these compounds were determined using the NMR spectra and were then confirmed by the X-ray diffraction analysis. Furthermore, the structure of the ethanol solvate of compound **14** (compound **15**) was determined using X-ray diffraction analysis. According to the X-ray diffraction data, the crystal structure and the conformation of solvate **15** in the solid state differ radically from those of bisphenols **14**, **16**, and **17**. The geometric parameters of the molecules of all the isomers are close to each other (Table 2). In molecules **14**, **16**, and **17**, the hydroxyl groups in *cis* positions form OH...OH intramolecular hydrogen bonds with the O...O distances in the range 2.698–2.780 Å (Table 3). The dihedral angles Φ_A and Φ_B (Table 2) correspond to a butterfly conformation for two independent molecules of compound **14** and a twist–butterfly conformation for molecules of compounds **16** and **17**. In the crystal, the molecules of isomers **14**, **16**, and **17** are joined in pairs into centrosymmetric hydrogen-bonded dimers, thus forming eight-membered rings composed of the OH groups linked by the OH...OH intramolecular and intermolecular hydrogen bonds (O...O, 2.721–2.796 Å). The crystal structure of solvate **15** with ethanol does not contain OH...OH intramolecular hydrogen bonds. The hydroxyl groups in *trans* positions interact with the ethanol molecules through the OH...OH intermolecular hydrogen bonds (2.743 Å) with the formation of centrosymmetric dimers consisting of sixteen-membered rings in which ethanol serves as an acceptor and as a donor. The interaction with the ethanol molecule radically changes the orientation of the phenyl rings with respect to the C–CH₂–C central fragment: the molecule adopts a twist-skewed conformation. According to Ferguson *et al.* [44], the absence of centrosymmetric dimers in structures **4**, **5**, **10**, and **12** is explained by the presence of bulky substituents in the 6- and 6'-positions in these molecules.

Compound **18** was prepared in the course of chemical transformations in the study concerned with the problems of fungicide chemistry [9]. The conformation of the molecule is governed by the intramolecular hydrogen bonds [O(1)⋯O(2), 2.715 Å] between the OH groups in *cis* positions. The dihedral angles Φ_A and Φ_B (Table 2) correspond to a butterfly conformation. The second intramolecular hydrogen bond OH⋯O(=C) (O⋯O, 2.633 Å) closes the CO₂Me exocyclic fragment rotated by an angle of 32.5° with respect to the plane of the ring containing two hydroxyl groups. In the crystal, the molecules are linked into chains by the O(1)H⋯O(=C) intermolecular hydrogen bonds (2.896 Å).

Compound **19** is the main constituent of the extract characterized by an inhibiting action in medicinal preparations [45]. The diphenylmethylene fragment of the molecule has a butterfly conformation. The molecular conformation is partially governed by two intramolecular hydrogen bonds: OH⋯OH (O⋯O, 2.703 Å) and O(1)H⋯O(=C) (2.441 Å); i.e., the O(1)H group serves as an acceptor and as a donor of the hydrogen bond. The OH groups at the C(3) atoms are involved in the OH⋯OH intermolecular hydrogen bonds (2.845 Å), thus forming infinite molecular chains.

The crystal structure of *ortho,ortho* bisphenols with substituted methylene bridges, such as disubstituted (compounds **20**, **22**) and monosubstituted (compounds **21**, **23–26**) bisphenols, was determined using X-ray diffraction. Intramolecular hydrogen bonds of the OH⋯ π type (rare in occurrence) were revealed in crystals of 2,2-bis(2-hydroxy-5-methyl-3-*tert*-butylphenyl)propane (compound **20**), initially, on the basis of the IR spectra and, then, from an analysis of the X-ray diffraction data [46]. The geometric parameters of these bonds are given in Table 3, and the mean value of two distances along the perpendicular from the H atoms of the hydroxyl groups to the corresponding π electron-donor ring is equal to 2.09 Å. The OH⋯ π hydrogen bond in compound **20** is stronger than that in compounds **3**, **5**, and **6** with unsubstituted methylene bridges (Table 3). Sterically overloaded molecule **20** with a *trans* structure has a twist conformation and the noncrystallographic symmetry axis 2.

The presence of the nitro groups in *ortho* positions and the chlorine atoms in *para* positions with respect to the hydroxyl groups of the phenol rings are common to compounds **21–25** with substituted methylene bridges. X-ray diffraction analysis of these compounds (bisphenol flukicides) was performed in order to reveal a correlation between the molecular conformation and the biological activity. In biologically active compound **21**, no intramolecular hydrogen bonds occur in the molecule with the OH groups in *cis* positions and only the very weak intermolecular hydrogen bond OH⋯O(NO₂) (3.21 Å) is formed in the structure [10, 47]. In biologically inactive compound **22**, the molecule has a *trans* structure (symmetry 2) and the hydroxyl groups form

intramolecular hydrogen bonds with oxygen atoms of the neighboring nitro groups. The C–O(H) bond length is considerably shortened to 1.35 Å in compound **21** and to 1.347 Å in compound **22**. This is characteristic of phenol derivatives with nitro groups in *ortho* positions that form strong intramolecular hydrogen bonds OH⋯O(NO₂) [12, 74–77]. In molecule **23** (active vermifuge), the equivalent substituents in the ring are located on one side of the plane of the methylene ring. The oxygen atoms of the hydroxyl groups of each *o*-nitrophenol fragment form bifurcated hydrogen bonds, namely, the intramolecular hydrogen bond with the oxygen atom of the neighboring nitro group (the mean O⋯O distance is 2.59 Å) and the weak intermolecular hydrogen bond with the oxygen atom of the nitro group in the neighboring molecule (the mean O⋯O distance is 3.13 Å).

Compounds **24** and **25** are efficient bisphenol flukicides [15, 48]. In molecules of these compounds, the methylene-bisphenol fragments adopt a twist–butterfly conformation in structure **24** (according to [15], it is a twist conformation) or a butterfly conformation in structure **25**. Both structures involve two OH⋯O(NO₂) intramolecular hydrogen bonds: the strong hydrogen bond in molecule **24** (the mean O⋯O distance is 2.565 Å) and a weaker hydrogen bond in the molecule of adduct **25** (the mean O⋯O distance is 2.72 Å). The bond lengths in the hydroxyl groups are shortened to 1.332 and 1.355 Å in compound **24** and 1.29 and 1.33 Å in compound **25**. According to Hay and Mackay [15], an increase in the biological activity of the compounds is associated with the weakening of the steric interaction between the *ortho*-hydroxy substituents and the π -electron system of the adjacent phenol ring.

Compound **26** was prepared during the synthesis of new calix[5]arenes [49]. The intramolecular hydrogen bond between the OH groups is rather weak: the O⋯O distance (2.989 Å) exceeds all the distances given in Table 3. In the crystal, the molecules form hydrogen-bonded dimers with the participation of four hydroxyl groups, as is the case in the crystal structures of isomers **14**, **16**, and **17** [44].

Compounds **27–30** belong to the related class of *ortho,ortho*-dihydroxybenzophenones, in which the transformation of the carbon atom in the bridging group from the *sp*³ state to the *sp*² state leads to a substantial change in the geometric parameters of the molecules (Table 2). In molecules **27–29**, both hydroxyl groups serve as donors of intramolecular hydrogen bonds with respect to the carbonyl oxygen atoms and form strong hydrogen bonds. The O⋯O distances are as follows: 2.629 Å (mean) in structure **27**, 2.516–2.716 Å (in two independent molecules) in structure **28**, and 2.587–2.624 Å in structure **29**. One of the OH groups in molecule **27** forms a weak intermolecular hydrogen bond (3.024 Å) with the carbonyl oxygen atom of the neighboring molecule. All the hydroxyl groups of molecule **28** are involved in the OH⋯O intermolecular hydrogen

bonds (2.756–3.042 Å), and one of these groups forms a bifurcated hydrogen bond. In structure **29**, intermolecular hydrogen bonds are absent owing to the presence of bulky *tert*-butyl substituents in *ortho* positions with respect to the OH groups and the OH...O(=C) intramolecular hydrogen bond is stronger than those in molecules **27** and **28**. Compound **29** is an analogue of compound **7** and differs only by the bridging group (–CO– in molecule **29** and –CH₂– in molecule **7**). Compound **30** is the most active flukicide in the series of bis(4-chloro-6-nitrophenols) (compounds **21–25**) [14]. Molecule with the axis 2 passing through the C=C bond (1.330 Å) of the dichlorovinylidene bridging group has a *trans* structure and a butterfly conformation. According to [14], the conformational features of the molecules correlate with the biological activity of flukicide compounds **21–23** and **30**.

2.2. Polynuclear Bridging *ortho*-Phenols

Table 4 presents linear and cyclic polynuclear bridging *ortho*-phenols for which the crystal and molecular structures were determined by X-ray diffraction analysis. These are linear trinuclear *ortho*-phenols either with methylene bridges (compounds **31–35**) or with the –C(H, Me)– bridging groups (compounds **36, 37**), linear tetranuclear *ortho*-phenols with methylene bridges (compounds **38–45**), and cyclic tetranuclear *ortho*-phenols either with the bridging groups –CH₂– (compounds **46–51**) or with the bridging groups –CH₂– and –CH₂–O–CH₂– (compounds **52–54**). It can be seen from Table 4 that the majority of these compounds form crystal solvates and clathrates.

Linear oligonuclear *ortho*-phenol compounds with methylene bridges are of interest as fragments of methylene-bonded polyphenols and related polymers [40]. In the structure of the benzene clathrate (compound **31**), the bridging trinuclear *ortho*-phenol molecule lies on the axis 2 passing through the central ring and the dihedral angle between the adjacent phenol rings is equal to 68.2°. The C–OH bond lengths of the central and outer rings are equal to 1.372 and 1.385 Å, respectively. The cisoid conformation of the molecule is governed by the system of intramolecular hydrogen bonds (O...O, 2.634 Å) between the hydroxyl groups. In the crystal, the molecules are joined by the OH...OH intermolecular hydrogen bonds (O...O, 2.678 Å) into centrosymmetric dimers that form cavities occupied by the benzene molecules.

In the series of bisphenol flukicides, halogenated bisbenzyl-tri-*ortho*-phenol (compound **32**) exhibits a high biological activity [13]. In the adduct with ethylacetate, the molecule of this compound adopts a skewed conformation in one half of the molecule ($\Phi_A = 19.0^\circ$, $\Phi_B = 85.0^\circ$) and a butterfly conformation in the other half of the molecule ($\Phi_{A'} = 84.8^\circ$, $\Phi_{B'} = 88.8^\circ$). In this half of the molecule, there exists one O(1)H...O(2)H intramolecular hydrogen bond (O...O, 2.74 Å), whereas

the third hydroxyl group forms the O(3)H...O(2)'H intermolecular hydrogen bond (2.79 Å). In the crystal solvate of the acyclic phenol oligomer with the *ortho*-methylene bridge (compound **35**), the asymmetric unit cell consists of two hydrogen-bonded molecules *A* and *B* that forms a cyclic dimer [the O(H)...O(H) distance is equal to 2.639–2.689 Å]. The molecules exhibit a *trans* conformation. In this case, the outer rings are located on each side of the plane of the central ring and the dihedral angles between the outer and central rings are equal to 64.0° and 78.3° in molecule *A* and 72.1° and 71.5° in molecule *B* [41]. According to single-crystal X-ray diffraction analysis of trinuclear *ortho*,*ortho*-ethylidene-bonded phenol diastereomeric compounds **36** and **37**, the molecular conformation is predominantly determined by the system of intramolecular hydrogen bonds in which each hydroxyl group serves as a donor and an acceptor in a regular sequence [97] (the same inference was made in [40]): the O...O distances are equal to 2.739 and 2.751 Å in compound **36** and 2.790 and 2.705 Å in compound **37**. The molecules have a *cis* conformation in structure **36** and a *trans* conformation in structure **37**.

The study of acyclic tetranuclear phenol oligomers **38–45** is closely connected with the investigation into the structure and properties of calixarenes, i.e., phenol macrocycles with methylene bridges in *ortho* positions with respect to the hydroxyl groups [99–102]. The molecule of the tetranuclear phenol oligomer (compound **38**) exhibits an *anti* conformation with three OH...OH intramolecular hydrogen bonds (O...O, 2.647, 2.670, and 2.660 Å). In the crystal, the molecules are linked into zigzag polymer chains by the OH...OH intermolecular hydrogen bonds (O...O, 2.755 and 2.663 Å). Hydrogen bonding (the OH groups serve as donors and as acceptors) with the formation of infinite chains due to a cooperative effect makes a substantial contribution to the stabilization of the system [40]. In the structures of tetranuclear phenol compounds **39–41**, the hydroxyl groups form intramolecular hydrogen bonds in which the mean O...O distance is equal to 2.62 Å in molecule **39**, 2.71 Å in molecule **40**, and 2.64 Å in molecule **41**. The phenol moieties have a *trans–trans* conformation in molecule **39** and a *cis–trans* conformation in molecules **40** and **41**. In the crystal, molecules **39** are joined into chains by the OH...OH intermolecular hydrogen bonds (O...O, 2.708 and 2.753 Å) in head-to-head and tail-to-tail fashions. Molecules **40** or **41** form cyclic dimers through the intermolecular hydrogen bonds (O...O, 2.769 Å in compound **40** and 2.675 Å in compound **41**) in a head-to-tail manner [98].

The molecules of linear tetranuclear phenol oligomers in inclusion complexes with benzene of the 1 : 1 composition in crystal **42** and those of the 1 : 1 composition in crystal **43** adopt different conformations, namely, a *cis–trans* conformation in molecule **42** and a *trans–trans* conformation in molecule **43**. The averaged intramolecular distances O...O (2.695 Å in molecule **42** and 2.681 Å in molecule **43**) are close to the

Table 4. Acyclic and cyclic polynuclear *ortho*-phenols (dashed lines indicate intramolecular hydrogen bonds)

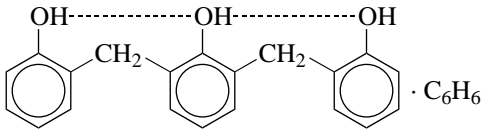
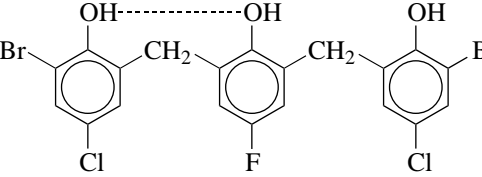
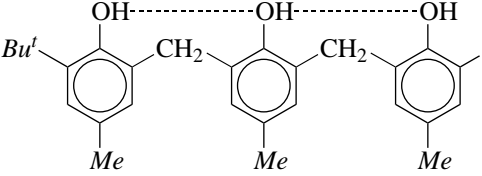
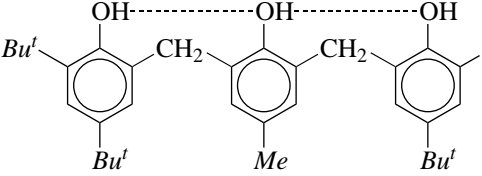
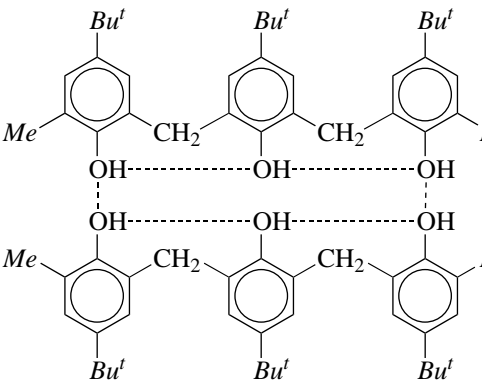
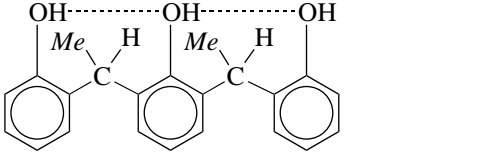
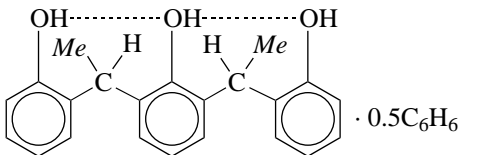
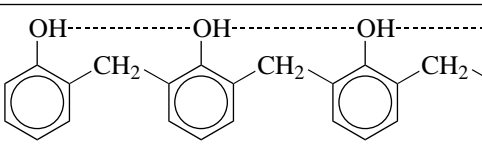
Compound	Formula	Symmetry*	R factor	Reference
31	 $\cdot C_6H_6$	2	0.081	[40]
32	 $\cdot 1/3EtOAc$	1	0.059	[13]
33	 $\cdot 0.29(CH_2Cl_2)$	1, 1, 1	0.086 (173 K)	[96]
34	 $\cdot C_4H_{10}O$	1	0.073 (173 K)	[96]
35	 $\cdot CH_3NO_2$	1	0.082	[41]
36		1	0.049	[97]
37	 $\cdot 0.5C_6H_6$	1	0.070	[97]
38		1	0.079	[40]

Table 4. (Contd.)

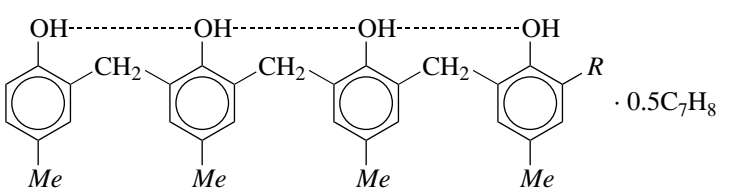
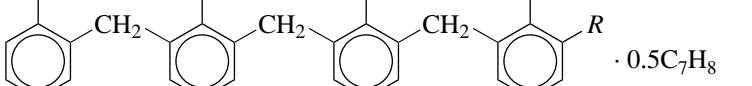
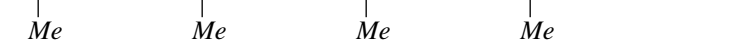
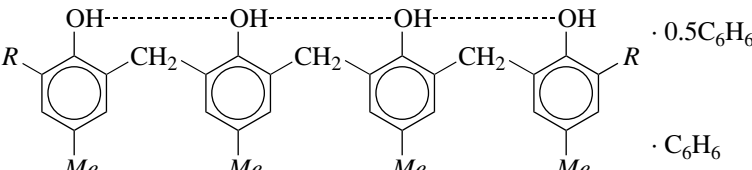

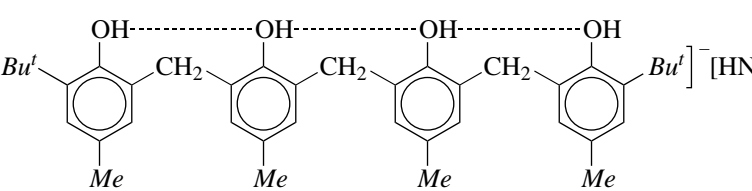
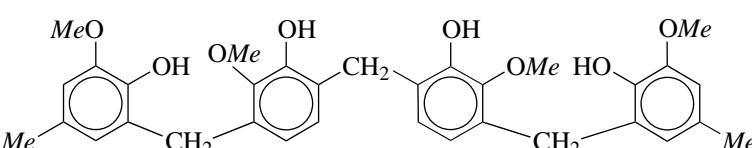
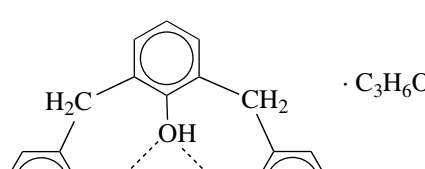
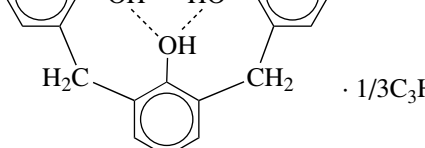
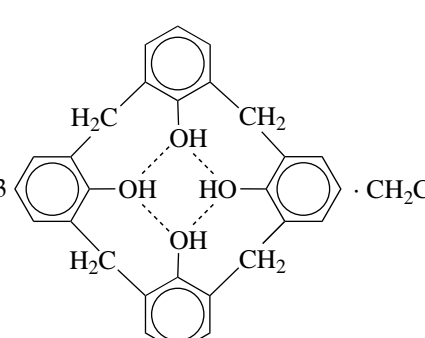
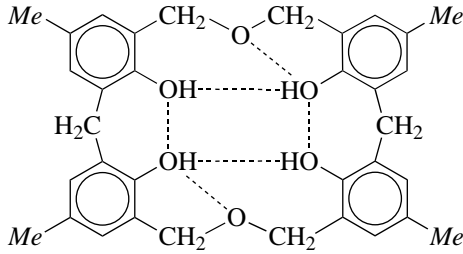
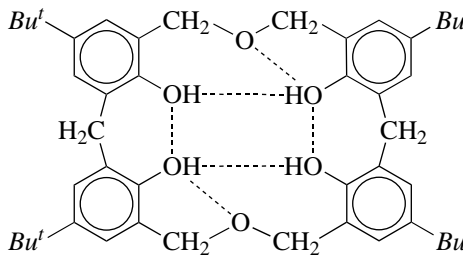
Compound	Formula	Symmetry*	R factor	Reference
39	 $R=H$	1	0.034	
40	 $\cdot 0.5C_7H_8$ $R=Me$	1	0.038	[98]
41	 $R=But'$	1	0.032	
42	 $\cdot 0.5C_6H_6$ $R=H$	1	0.058	
43	 $\cdot C_6H_6$ $R=Br$	1	0.121	[99]
44	 $[But' \dots]^- [HNEt_3]^+ \cdot CH_3CN$	1	0.051 (100 K)	[100]
45		1	0.058	[101]
46	 $\cdot C_3H_6O$	<i>m</i>	0.090	
47	 $\cdot 1/3C_3H_6O$	<i>m</i>	0.070	[102]
48	 $\cdot CH_2Cl_2$	<i>m</i>	0.084	[103]

Table 4. (Contd.)

Compound	Formula	Symmetry*	R factor	Reference
49		4	0.086	[104]
		1	0.108	[105]
50		4	0.132	[106]
51		<i>mm</i>	0.051	[42]
52		<i>m</i>	0.077	[107]

Table 4. (Contd.)

Compound	Formula	Symmetry*	R factor	Reference
53		1	0.077	[108]
54		1	0.078	[109]

* Symmetry of the molecules of bridging *ortho*-phenols.

corresponding distance in calyx[4]arene (2.643 Å) [102]. In structure **42**, the tetramer molecule forms a “partial cone”-type cavity, which is occupied by the centrosymmetric benzene molecule. In the crystal, the molecules form cyclic dimers via the intermolecular hydrogen bonds (O...O, 2.719 Å) in a head-to-tail manner. Thus, the structure of the molecule in crystal solvate **42** with benzene differs from the structure of the same molecule in crystal **39**.

The structure of the dibromo derivative (compound **43**) involves acyclic dimers and weak intermolecular hydrogen bonds due to the presence of bulky bromine atoms in *ortho* positions with respect to the hydroxyl groups. The molecular complex formed by the acetonitrile solvate of the triethylammonium salt (compound **44**) is the first crystal structure of the anionic derivative of acyclic tetraphenol whose conformation can be described as a *cis-trans* conformation. The phenol rings linked by the OH...OH intramolecular hydrogen bonds (O...O, 2.684, 2.499, and 2.666 Å) form a partial cone with the cavity occupied by one of the methyl groups of the triethylammonium cation, which is bonded via the hydrogen atom to the adjacent phenolate fragment (N(H)...O', 2.671 Å) [100].

The cyclic polyphenols are referred to as calixarenes and belong to an interesting class of molecules, which has been extensively studied in recent years. These compounds are used both for preparing different receptor molecules and as frameworks with a wide variety of properties [99, 102, 103, 107, 110, 111]. Calixarenes are synthetic macrocycles that contain phenol residues with bridging methylene groups in *ortho* positions with respect to the hydroxyl groups. They can

form inclusion compounds with different small-sized organic molecules (guests) that are embedded in cavities (in the form of cones, partial cones, etc.) of the host molecules. In this work, we restrict our consideration to several structural studies of calix[4]arenes (compounds **46–54**), which are related to the aforementioned acyclic *ortho*-polyphenols with methylene bridges.

The unsubstituted calix[4]arene crystallizes from acetone in two modifications: the acetone clathrate of the 1 : 1 composition forms orthorhombic crystals (compound **46**), and the acetone clathrate of the 3 : 1 composition forms hexagonal crystals (compound **47**). In both modifications, the cone conformation in the calixarene molecule is stabilized by four intramolecular hydrogen bonds between the OH groups. The molecules have the symmetry plane *m*, which passes through the methylene carbon atoms in molecule **46** and through the O-C...C linear fragment of two *trans*-phenol groups in molecule **47**. The methyl group of acetone is embedded in the calixarene cavity. The geometries of the macrocycles in two modifications differ only slightly: the averaged values of the C-CH₂ and C-OH bond lengths and the C-CH₂-C bond angles in molecule **46** (molecule **47**) are equal to 1.560 Å, 1.344 Å, and 107.3° (1.520 Å, 1.400 Å, and 112.8°), respectively. The dihedral angles between the phenol rings are also different: $\Phi = 57.0^\circ$ and 54.7° in molecule **46** and $\Phi = 64.7^\circ$, 64.5° , and 42.8° in molecule **47** [102]. In the dichloromethane solvate of the 3 : 1 composition (compound **48**), the molecule of unsubstituted calix[4]arene also has symmetry *m* and a cone conformation and forms self-inclusion trimers in the crystal. The solvate molecules are disordered.

The *para-tert*-butylcalix[4]arene clathrate with toluene (compound **49**) forms two crystalline modifications, namely, the tetragonal [104] and monoclinic [105] modifications. Both constituents of the clathrate have the symmetry axis 4 in the tetragonal modification and occupy the general position in the monoclinic modification. In the tetragonal modification, four OH...OH intramolecular hydrogen bonds with an O...O distance of 2.670 Å (according to [103, 112], the mean O...O distance in this molecule is equal to 2.70 Å) stabilize the cone conformation of the macrocycle [104]. In the crystal, the *para-tert*-butylcalix[4]arene molecule in the clathrate with toluene (compound **50**) occupies the special position on the fourfold axis, i.e., retains its symmetry. The molecule exhibits a basket conformation (the calix form), because the hydroxyl groups approach each other upon the formation of the intramolecular hydrogen bond (O...O, 2.65 Å). The OH groups form a planar eight-membered ring that is located perpendicular to the tetragonal axis. This calix[4]arene can include larger-sized guest molecules [106].

Unlike structures **46–50**, in which the OH groups in the calixarene molecule occupy the *endo* positions, the clathrate structure with acetonitrile (structure **51**) contains the OH groups in the *exo* positions. The molecule of the cyclic tetramer has symmetry *mm*, and the mirror planes pass through the carbon atoms of the opposite methylene groups. Each molecule involves two OH...OH intramolecular hydrogen bonds (O...O, 2.657 Å). The acetonitrile molecule is embedded in the calixarene cavity. In the crystal, the molecules are joined together by pairs of the OH...OH intermolecular hydrogen bonds (O...O, 2.712 Å) about the center of symmetry and form infinite zigzag ribbons.

In calixarene structures **52–54**, the phenol groups are linked not only by the methylene bridges but also by the $-\text{CH}_2\text{O}-\text{CH}_2-$ bridges. In the complex with *m*-xylene (compound **52**), the symmetry plane *m* passes through the ether oxygen atom of the bridge and the carbon atom of the opposite CH_2 group. The oxacalix[4]arene molecule adopts the conformation of a cone whose cavity is occupied, to a great extent, by the methyl group of the guest molecule. This suggests a strong guest–host interaction of the $\text{CH}\cdots\text{O}(\text{ether})$, $\text{CH}_3\cdots\pi$, and $\text{CH}_3\cdots\text{CH}_3$ types [107]. Dioxacalix[4]arene with the methyl groups in *para* positions with respect to the OH groups (compound **53**) crystallizes without solvent molecules. The conformation of the macrocycle is a very distorted cone that is stabilized by two simple and two bifurcated intramolecular hydrogen bonds (O...O, 2.689–2.939 Å) involving the phenol and ether oxygen atoms. The molecular fragment containing the ether bond is embedded in the cavity of the neighboring calixarene molecule with the formation of a one-dimensional self-inclusion polymer structure [108]. In the crystal solvate of dioxacalix[4]arene with chloroform and tetrahydrofuran in a 1 : 1 : 1 ratio (compound **54**), the macrocycle also adopts a cone conformation

with the intramolecular hydrogen bonds (O...O, 2.662–2.870 Å) involving the phenol and ether oxygen atoms. Two solvent molecules joined together by the $\text{C}(\text{H})\cdots\text{O}$ hydrogen bond (3.113 Å) are located in either of the two cavities of the calixarene half-cone [109].

2.3. *ortho,ortho*-Thiobisphenols, Dithiobisphenols, and Trithiobisphenols

Table 5 presents *ortho,ortho*-bisphenols with the bridges $-\text{S}-$ (compounds **55–58**), $-\text{S}-\text{S}-$ (compounds **59–61**), and $-\text{S}-\text{S}-\text{S}-$ (compound **62**) and cyclic *ortho*-phenols with a thio bridge (compounds **63, 64**) and a dithio bridge (compound **65**). The structures of these compounds were determined by X-ray diffraction analysis. Table 6 lists the selected geometric parameters of the molecules and the dihedral angles responsible for the molecular conformation in the crystals of acyclic compounds: Φ_A (Φ_B) is the angle formed by the plane of ring *A* (*B*) with the plane of the C–S–C bridging group in compounds **55–58** or with the plane of the neighboring group C–S–S in compounds **59–62**, and the Φ is the angle between the planes of rings *A* and *B*. The conformations of the molecules are given in the last column of Table 6. Molecules **55, 61**, and **62** have a *trans* structure with the OH groups located on each side of the bridging group. By contrast, molecules **56–60** have a *cis* structure with the OH groups located on one side of the bridging group. The dihedral angles Φ_A and Φ_B determine the conformational features of the molecules by analogy with the conformational characteristics of the *ortho,ortho*-methylene-bisphenols considered in Section 2.1. The geometric parameters of OH...S intramolecular hydrogen bonds are listed in Table 7.

It should be noted that, among the phenol stabilizers of polymers, the class of thiobisphenols has attracted particular attention of researchers owing to the specific properties of these compounds, which are efficient inhibitors of polymer oxidation [16, 18]. Examination of the IR spectra and the reactivity of thiobisphenols with different substituents in the 4-position (including compounds **55–57, 59**, and **62**) made it possible to elucidate the influence of the steric and electronic factors on the structure and reactivity of the compounds and to reveal a correlation between these characteristics and the inhibiting action of thiobisphenols [22, 23]. The X-ray structure study of thiobisphenol crystals was performed with the aim of determining the conformations of the molecules and the geometric parameters of the OH...S intramolecular hydrogen bonds, which have a substantial effect on the reactivity of thiobisphenols. Note that the geometric parameters of OH...S intramolecular hydrogen bonds for bridging sulfur atoms were not available in the literature prior to being determined in our works [28, 30, 32]. Based on the spectral data, it was demonstrated that the OH...S intramolecular hydrogen bonds are formed in *ortho*-thiobisphenols when the 6-position is occupied by bulky substituents

Table 5. *ortho,ortho*-Thiobisphenols, dithiobisphenols, and trithiobisphenols and cyclic *ortho,ortho*-phenols with sulfide bridges (dashed lines indicate intramolecular hydrogen bonds)

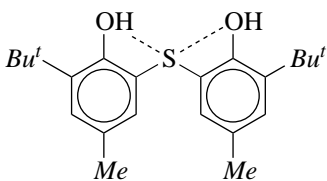
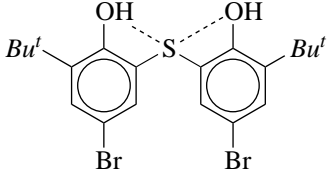
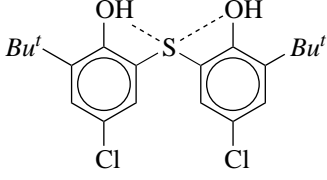
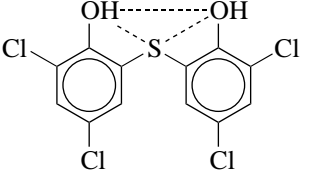
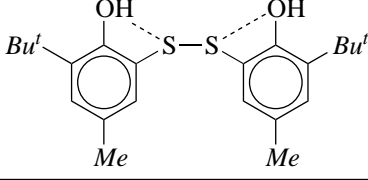
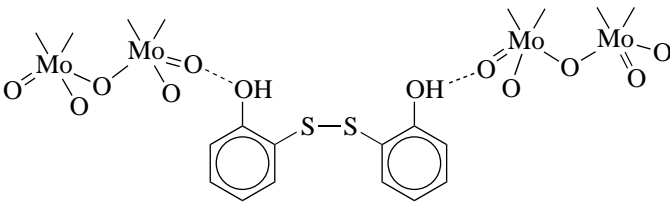
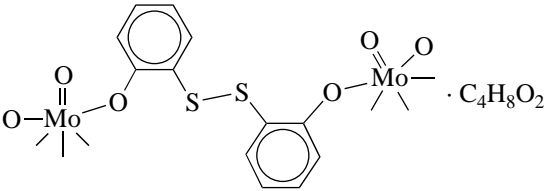
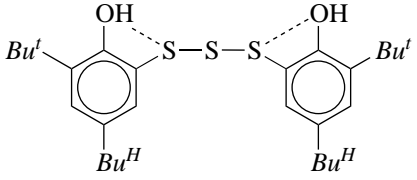
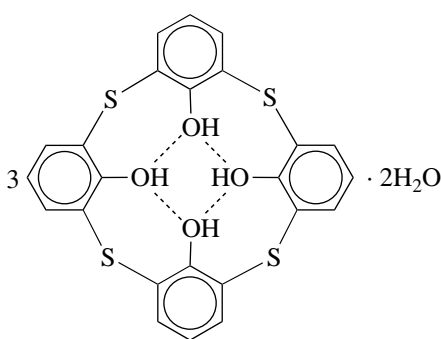
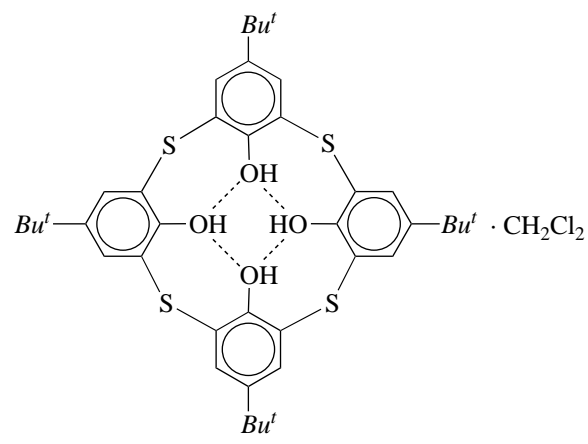
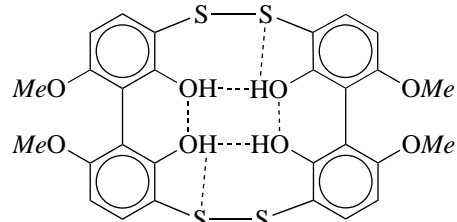
Compound	Formula	Symmetry	<i>R</i> factor	Reference
55		2	0.036	[28]
56		1	0.049	[32]
57		1	*	[32]
58		1	0.036	[113]
59		1	0.032	[30]
60		1, 1	0.050	[114]
61		2	0.062	[115]
62		2	0.030	[30]

Table 5. (Contd.)

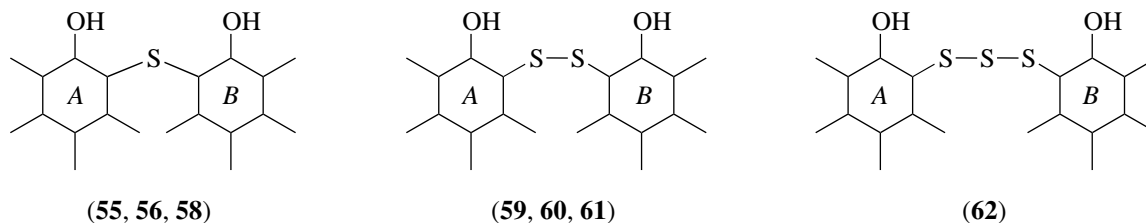
Compound	Formula	Symmetry	R factor	Reference
63		<i>m</i>	0.080	[103]
64		4	0.091	[103]
65		2	0.060	[116]

* For this compound, which is isostructural to the bromine analogue (compound **56**), the structure was not determined.

preventing self-association of molecules and the formation of intermolecular hydrogen bonds [22, 23]. The ability of sulfur atoms to participate in hydrogen bonds and the effect of hydrogen bonding on different physicochemical properties of sulfur-containing compounds are described in the review by Zuřka and Bankovskii [117].

Among the bridging thiobisphenol stabilizers, 2,2'-thiobis(4-methyl-6-*tert*-butylphenol) (compound **55**), which is an analogue of compound **4**, exhibits a high efficiency as an inhibitor of polymer oxidation and has found wide use in practice [16]. In the crystal, the molecule of this compound occupies the special position on the axis 2 and has a *trans* structure. According to the IR spectroscopic data [22], the molecule was assumed to adopt a *trans* conformation both in the crystal state and in solutions. In the $C_{ar}-S-C_{ar}$ bridging group, the C–S

bond length (the standard length of the $C(sp^2)-S$ bond is equal to 1.777 Å, and the averaged length is 1.768 Å [63]) and the bond angle at the sulfur atom (Table 6) are close to those determined in the molecules of diphenyl sulfide [118] and a number of its derivatives (see references in [28]). The C–OH bond length (1.353 Å) is considerably shorter than the standard length of the $C(sp^2)-O$ bond (1.397 Å), smaller than the averaged length of this bond in phenols (1.362 Å) [63], and close to the C–OH shortened distances both in phenols with nitro groups in *ortho* positions [74–77] and in bridging *ortho,ortho*-methylene-bisphenols with *ortho*-nitro groups [10, 11, 15, 48] and with strong intramolecular hydrogen bonds $OH\cdots O(NO_2)$. As in the previous compounds, the decrease in the C–OH bond length can be associated with the $OH\cdots S$ intramolecular interaction. This can be judged from the shortened nonbonded con-

Table 6. Selected geometric parameters of the molecules of *ortho,ortho*-bisphenols with sulfide, dithio, and trithio bridges

Compound	Bond lengths (Å) and bond angles (deg) in bridges					Dihedral angles (deg)			Conformation of the molecule
	C-S	C-OH	S-S	C-S-C	C-S-S	Φ_A	Φ_B	Φ	
55	1.780	1.353		105.5		68.1	68.1	72.3	<i>trans</i> , twist-butterfly
56	1.772 1.785	1.362 1.373		104.2		46.5	67.9	87.6	<i>cis</i> , twist-skewed
58	1.784 1.789	1.354 1.355		99.7		86.2	84.7	81.3	<i>cis</i> , butterfly
59	1.778 1.771	1.369 1.370	2.086	71.4 (C-S-S-C)	103.3 103.1	75.4	86.6	34.6	axial
60	1.772	1.381	2.017	84.3 (C-S-S-C)	106.4			66.8	<i>cis</i>
61			2.016		105.1				<i>trans</i>
62	1.799	1.367	2.057	106.0 (S-S-S)	103.7	82.6	82.6	53.4	<i>trans</i> , butterfly

tacts O...S (3.026 Å) and H(O)...S (2.57 Å) as compared to the sums of the van der Waals radii of these atoms, which are equal to 3.13 Å [83, 84] (3.32 Å according to [86, 87]) and 3.00 Å, respectively. These geometric characteristics of the OH...S intramolecular hydrogen bonds involving the bridging sulfur atom (Table 7) were obtained for the first time. The dihedral angles $\Phi_A (= \Phi_B)$ indicate that the molecule exhibits a twist-butterfly conformation (Table 6). As in other phenols with bulky *tert*-butyl groups in *ortho* positions [16, 27, 46], the crystal structure of compound **55** does not involve OH...OH intermolecular hydrogen bonds. Most likely, this is a specific structural feature of sterically hindered phenols as strong antioxidants.

Compounds **56** and **57** with Br (Cl) atoms in the 4-position turned out to be isostructural, and the crystal structure was solved completely only for the bromine derivative [32]. The molecule occupies the general position and has a *cis* structure and a twist-skewed conformation. The hydroxyl groups are located on one side of the thio bridge and form two OH...S intramolecular hydrogen bonds (2.942, 3.037 Å) with the same sulfur atom. The parameters of these hydrogen bonds (Table 7) are close to those obtained for the methyl analogue (compound **55**). As in crystal **7**, the molecular packing in crystal **56** involves the Br...Br' intermolecular contact (3.541 Å). This contact is considerably shortened as compared to twice the van der Waals radius of the bromine atom (3.94 Å) and corresponds to asymmetric

intermolecular specific interactions of the C-Br...Br-C type [92]. The directional character of this interaction is confirmed by the C-Br...Br' angles (163.0° and 116.9°), which fall in the range of C-Br-Br angles typical of specific interactions [92, 93].

The geometric parameters of molecule **58** in Tables 6 and 7 were calculated in this work from the coordinates taken for the non-hydrogen atoms from the Cambridge Structural Database [38]. The molecule in the general position has a *cis* structure and a butterfly conformation. The lengths of two nonbonded contacts O(H)...S (2.983 and 3.036 Å) suggest the formation of intramo-

Table 7. Geometric parameters of OH...S intramolecular hydrogen bonds in *ortho,ortho*-thiobisphenols, dithiobisphenols, and trithiobisphenols

Compound	O...S, Å	H...S, Å	O-H...S, deg
55	3.026	2.57	118
56	2.942 3.037	2.40 2.51	117 106
58	2.983 3.036		
59	2.990 2.972	2.35 2.49	124 116
62	2.985	2.41	125

lecular hydrogen bonds. Moreover, the hydroxyl groups in *cis* positions form weak intramolecular hydrogen bonds (OH...OH, 2.862 Å). Thus, the hydroxyl groups are involved in bifurcated hydrogen bonds.

Compound **59** belongs to polymer stabilizers of the class of thiobisphenols in which bridging groups contain two sulfur atoms. From analyzing the spectral data, it was concluded that the molecule of compound **59** involves the OH...S intramolecular hydrogen bond [23, 30]. Although numerous studies have been concerned with the crystal structures of aromatic disulfides (see, for example, [38, 119–125]), structural data for *ortho*-dithiobisphenols are not available in the literature. As is known, the molecular conformation of these compounds is determined by the C–S–S–C torsion angles (as a rule, approximately 90°) and the dihedral angles Φ_A and Φ_B , which are formed by the planes of the CSS group with the adjacent phenyl rings and specify the orientation of the S–S bond with respect to the plane of the phenyl ring [126]. The molecule adopts an equatorial conformation when the S–S bond is nearly coplanar to the ring (the angles Φ_A and Φ_B are close to 0°) and exhibits an axial conformation when the angles Φ_A and Φ_B are close to 90° [126]. In the crystal, molecule **59** occupies the general position in the unit cell and adopts an axial conformation (Table 6). In aromatic disulfides, this conformation occurs more rarely than the equatorial conformation. The S–S and S–C bond lengths correspond to standard values, and the mean value of the SSC bond angle is equal to 103.2°. The C–OH bond length exceeds the bond length observed in the monothio analogue (compound **55**) but is considerably shorter than the standard bond length (1.397 Å). This can be explained by the participation of the OH group in the intramolecular hydrogen bond, for which the parameters are listed in Table 7.

For compound **60**, the structural fragment of the complex in which bis(2-hydroxyphenyl) disulfide forms OH...O intermolecular hydrogen bonds (the mean O...O distance is 2.655 Å) with the outer oxo groups of the binuclear molybdenyl anion is presented in Table 5. The averaged values of the parameters for two independent disulfide molecules in a *cis* conformation [114] are given in Table 6. In complex **61** with substituted OH groups, the same disulfide molecule adopts a *trans* conformation. The molecule lies on the axis 2 passing through the midpoint of the S–S bond. The oxygen atoms of the disulfide molecule enter into the coordination sphere of the molybdenum atoms. Compound **61** can be represented as two mononuclear molybdenum complexes linked by a disulfide bond [115].

In the crystal of 2,2'-trithiobis(4-*n*-butyl-6-*tert*-butylphenol) (compound **62**), the molecule occupies the special position with the central sulfur atom on the axis 2, as is the case in monothio analogue **55**. The distance from the hydroxyl hydrogen atom to the central

sulfur atom is equal to 3.14 Å. The trithiophenol molecule exhibits a *trans* butterfly conformation according to the above classification for bridging diphenyl compounds [54]. In the Cambridge Structural Database [38], the structural data for compounds with a trithio bridge are available only for compound **62** and bis(2-nitrophenyl) trisulfide in the triclinic [127] and orthorhombic [128] modifications. The molecules occupy the general position in the triclinic modification and lie on the axis 2 in the orthorhombic modification. The bond lengths and angles in the molecules of these three structures with trithio bridges are close to each other. Using the structure of orthorhombic crystals as an example [128], Zorkii and Zorkaya [129] analyzed the specific features of the molecular arrangement in the rare structural class $P2_12_12$, $Z = 2(2)$. Comparison of the three thio derivatives of *ortho*-bisphenols involving one (compound **55**), two (compound **59**), and three (compound **62**) sulfur atoms in the bridge showed that, upon changing over from structure **55** to structure **59**, the hydrogen bond is somewhat enhanced (the O...S distance is shortened) and the C–OH bond length increases. The parameters of the hydrogen bonds in structures **59** and **62** are close to each other (Table 7). It was shown that an increase in the length of the sulfide bridge between the phenol moieties in thiobisphenols is accompanied by an increase in the reactivity and the antioxidant activity of compounds used as oxidation inhibitors for solid poly(propylene) [23].

ortho,ortho-Thiobisphenols are constituents of cyclic polyphenols, i.e., thiacalixarenes. The structure of the recently synthesized tetranuclear thiacalixarenes (compounds **63**, **64**) was determined by X-ray diffraction analysis [103]. In the structure of the dihydrate (compound **63**), the molecule of the unsubstituted thiacalix[4]arene lies in the symmetry plane *m* and the cone conformation is stabilized by the intramolecular hydrogen bonds between the neighboring hydroxyl groups (the mean O...O distance is 2.64 Å). However, the water molecule is not incorporated into the cavity of the host molecule. In the crystal, this thiacalix[4]arene forms self-inclusion trimers similar to those observed in structure **48** [103]. In the structure of the *p-tert*-butyltetra-thiacalix[4]arene clathrate with dichloromethane (compound **64**), the calixarene molecule in the crystal retains its own symmetry, lies on the fourfold axis, and adopts a cone conformation with a mean distance of 2.85 Å between the neighboring oxygen atoms of the hydroxyl groups involved in the intramolecular hydrogen bonds. The dichloromethane molecule is deeply embedded in the cavity of the cone of the receptor molecule and forms an inclusion complex. In the crystal of this complex, the solvent molecules and the *p-tert*-butyl groups of the calixarene molecule are disordered [103]. It is known that the biphenyl structures with dithio bridges exist in several natural products, which, for the most part, are biologically and pharmacologically active [116]. X-ray diffraction investigations revealed the formation of dimer disulfide (compound **65**) with

the axis 2, which is directed perpendicular to the drawing plane and passes through the center of the molecule. The bond lengths (S–S, 2.061 Å; S–C, 1.749 and 1.730 Å; C–OH, 1.314 and 1.367 Å) slightly differ from those determined in structure **59**. The hydroxyl groups in the *endo* positions form weak intramolecular hydrogen bonds OH...OH (the O...O distances are 3.012 and 3.024 Å). Moreover, one of the two independent hydroxyl groups also participates in the OH...S intramolecular hydrogen bond with parameters (S...OH, 3.023 Å; S...H, 2.43 Å; angle O–H...S, 123°) close to those listed in Table 7. Thus, this hydroxyl group forms a bifurcated hydrogen bond (OH...O and OH...S) as a donor and the third hydrogen bond as an acceptor. The distances and angle reported in this paper were obtained using the Cambridge Structural Database [38].

3. CONCLUSIONS

The structures of 65 bridging *ortho,ortho*-bisphenols and related compounds were considered using X-ray diffraction data. The conformational features and geometric parameters of the molecules and the characteristics of the intramolecular hydrogen bonds OH...OH, OH... π , and OH...S were analyzed for *ortho,ortho*-bisphenols with unsubstituted and substituted methylene bridges, as well as for *ortho,ortho*-bisphenols with thio, dithio, and trithio bridges. The structures of acyclic and cyclic polynuclear bridging *ortho*-phenols were also examined.

It was demonstrated that the hydroxyl functional groups in *ortho* positions with respect to the bridging groups (CH₂, S, S–S, S–S–S) have a substantial effect on the molecular conformation and the formation of intramolecular and intermolecular hydrogen bonds that stabilize the system. In the structures of *ortho,ortho*-bisphenols with unsubstituted and substituted methylene bridges (30 compounds), the majority of molecules in the crystal adopt a *cis* conformation (22 compounds). Among these 22 structures, 14 structures contain hydroxyl groups linked by OH...OH intramolecular hydrogen bonds. Four out of the eight structures with a *trans* conformation of the molecules are characterized by the formation of OH... π intramolecular hydrogen bonds whose nature and structure are poorly understood.

X-ray diffraction investigations of bridging *ortho,ortho*-bisphenols with bulky *tert*-butyl groups in *ortho* positions and different substituents in *para* positions with respect to the hydroxyl groups were motivated by the specific properties of these compounds as stabilizers of polymer materials. As in other sterically hindered phenols, the hydroxyl groups in these compounds do not form intermolecular hydrogen bonds. The molecules of the compounds with unsubstituted methylene groups and *Bu*' groups exhibit either a *cis* conformation with OH...OH intramolecular hydrogen

bonds or a *trans* conformation with OH... π intramolecular hydrogen bonds. In the compounds under consideration, the substitution of the ethyl group for the methyl group in the *para* position with respect to the hydroxyl group leads to a transformation of the *cis* conformation of the molecule into the *trans* conformation. By contrast, the substitution of the bromine atom for the chlorine atom in the *para* position results in a transformation of the *trans* conformation into the *cis* conformation (similar compounds with thio bridges appeared to be isostructural). There is a certain tendency toward changing the C–OH bonds: these bonds in donors are shorter than those in acceptors. It was shown that the antioxidant activity of the compounds whose molecules have a *cis* conformation is higher than the antioxidant activity of the compounds with molecules in a *trans* conformation. Analysis of the structural features revealed by the X-ray diffraction study in the stabilizer molecules made it possible to explain the mechanism of their antioxidant action and to draw a conclusion regarding the controlled synthesis of bridging bisphenol stabilizers with a *cis* conformation of the molecules.

In a number of bisphenols with substituted methylene bridges and nitro groups in the 6-position, the hydroxyl groups form intramolecular hydrogen bonds with the neighboring NO₂ groups. In molecules of these compounds, the C–OH bond is considerably shortened and lies in the range 1.31–1.35 Å. The same shortening of the C–OH bonds was also observed for related *ortho,ortho*-dihydroxybenzophenone compounds with –C(=O)– bridging groups and OH...O(=C) strong intramolecular hydrogen bonds.

The structures of linear and cyclic bridging polynuclear *ortho*-phenols were determined by X-ray diffraction analysis. The majority of these compounds form crystal solvates and clathrates. The study of the acyclic tetranuclear phenol oligomers is closely connected with the investigations into the structure and properties of calixarenes. A number of calix[4]arenes were examined using X-ray diffraction, and the data on the geometry of their macrocycles and selected geometric parameters were analyzed. It was shown that the intramolecular hydrogen bonds between the hydroxyl groups stabilize the cone conformation of the macrocycle. The interaction between the guest and host molecules in crystal solvates and clathrates of cyclic polyphenols was considered.

Among the phenol stabilizers of polymers, compounds of the thiobisphenol class are known as efficient inhibitors of polymer oxidation. X-ray structure studies of the crystals of *ortho,ortho*-bisphenols with thio, dithio, and trithio bridges, as well as with bulky *tert*-butyl substituents in *ortho* positions with respect to the hydroxyl groups, made it possible to determine the molecular conformation in the solid state and the geometric parameters of OH...S intramolecular hydrogen bonds. These characteristics were previously unknown

for crystals, even though they were predicted from the spectral data. As in other phenols with bulky *tert*-butyl groups in *ortho* positions, the crystal structure of *ortho,ortho*-thiobisphenols does not involve OH...OH intermolecular hydrogen bonds. This can serve as one of the structural characteristics of these compounds as strong antioxidants. A decrease in the C–OH bond length as compared to the standard value can be associated with the OH...S intramolecular interaction, which leads to a decrease in the O...S and H(O)...S nonbonded contacts in the molecule. An increase in the length of the sulfide bridge between the phenol rings in thio-bisphenols results in an increase in the strength of the OH...S intramolecular hydrogen bonds and is accompanied by an enhancement of the antioxidant activity of these compounds. The structural data for two thiacalix[4]arenes are presented. In the crystal, one thiacalix[4]arene forms self-inclusion trimers, whereas the other thiacalix[4]arene forms an inclusion complex of the solvent molecule in the cavity of the cone of the receptor molecule.

ACKNOWLEDGMENTS

We would like to thank I.G. Arzamanova for the proposal of the subject matter of this investigation, for growing the crystals, for her unabated interest in this work, and for participation in discussions of the X-ray diffraction data obtained in our collaborative studies.

We also acknowledge the support of the Russian Foundation for Basic Research (project nos. 02-07-90322, 03-03-35001) for the payment of the license to use the Cambridge Structural Database.

REFERENCES

- L. A. Chetkina and V. K. Bel'skiĭ, *Kristallografiya* **40** (5), 941 (1995) [*Crystallogr. Rep.* **40**, 873 (1995)].
- L. A. Chetkina and V. K. Bel'skiĭ, *Kristallografiya* **43** (1), 147 (1998) [*Crystallogr. Rep.* **43**, 137 (1998)].
- L. A. Chetkina and V. K. Bel'skiĭ, *Kristallografiya* **44** (2), 361 (1999) [*Crystallogr. Rep.* **44**, 324 (1999)].
- L. A. Chetkina and V. K. Bel'skiĭ, *Kristallografiya* **47** (4), 638 (2002) [*Crystallogr. Rep.* **47**, 581 (2002)].
- F. Nowshad and Mazhar-Ul-Haque, *J. Chem. Soc., Perkin Trans. 2*, 623 (1976).
- S. Rantsordas, M. Perrin, and A. Thozet, *Acta Crystallogr., Sect. B: Struct. Crystallogr. Cryst. Chem.* **34**, 1198 (1978).
- S. Rantsordas, M. Perrin, A. Thozet, and S. Lecocq, *Acta Crystallogr., Sect. B: Struct. Crystallogr. Cryst. Chem.* **37**, 1253 (1981).
- S. Rantsordas and M. Perrin, *Acta Crystallogr., Sect. B: Struct. Crystallogr. Cryst. Chem.* **38**, 1871 (1982).
- G. Ferguson, B. L. Ruhl, J. Gilmore, *et al.*, *J. Chem. Res., Synop.* 284 (1985); *J. Chem. Res., Miniprint* 3101 (1985).
- D. G. Hay and M. F. Mackay, *Acta Crystallogr., Sect. B: Struct. Crystallogr. Cryst. Chem.* **35**, 2952 (1979).
- D. G. Hay, P. DeMunk, and M. F. Mackay, *Aust. J. Chem.* **33**, 77 (1980).
- D. G. Hay and M. F. Mackay, *Acta Crystallogr., Sect. B: Struct. Crystallogr. Cryst. Chem.* **37**, 463 (1981).
- A. C. Sindt-Josem and M. F. Mackay, *Aust. J. Chem.* **34**, 81 (1981).
- D. G. Hay, P. DeMunk, and M. F. Mackay, *Aust. J. Chem.* **34**, 559 (1981).
- D. G. Hay and M. F. Mackay, *Aust. J. Chem.* **35**, 341 (1982).
- V. V. Ershov, G. A. Nikiforov, and A. A. Volod'kin, *Sterically Hindered Phenols* (Khimiya, Moscow, 1972) [in Russian].
- Ya. A. Gurvich, L. K. Zolotarevskaya, and S. T. Kumok, *Phenol Stabilizers* (TsNIITÉneftkhim, Moscow, 1978) [in Russian].
- N. M. Émanuél', *Usp. Khim.* **48** (2), 2113 (1979); *Usp. Khim.* **54** (9), 1393 (1985).
- Yu. A. Shlyapnikov, *Usp. Khim.* **50** (6), 1105 (1981).
- B. N. Gorbunov, Ya. A. Gurvich, and I. P. Maslova, *Chemistry and Technology of Stabilizers of Polymer Materials* (Khimiya, Moscow, 1981) [in Russian].
- I. G. Arzamanova, M. I. Naĭman, I. P. Romm, *et al.*, *Zh. Fiz. Khim.* **55** (6), 1554 (1981).
- I. G. Arzamanova, M. I. Naĭman, I. P. Romm, *et al.*, *Zh. Fiz. Khim.* **56** (4), 1023 (1982).
- Ya. A. Gurvich, I. G. Arzamanova, and G. E. Zaikov, *Khim. Fiz.* **15** (1), 23 (1996).
- L. A. Chetkina, V. E. Zavodnik, V. I. Andrianov, *et al.*, *Dokl. Akad. Nauk SSSR* **242** (1), 103 (1978) [*Sov. Phys. Dokl.* **23**, 624 (1978)].
- L. A. Chetkina, V. E. Zavodnik, A. N. Sobolev, and V. K. Bel'skiĭ, *Kristallografiya* **29** (2), 389 (1984) [*Sov. Phys. Crystallogr.* **29**, 234 (1984)].
- L. A. Chetkina, V. E. Zavodnik, V. I. Andrianov, *et al.*, *Acta Crystallogr., Sect. A: Cryst. Phys., Diffr., Theor. Gen. Crystallogr.* **34**, S110 (1978).
- L. A. Chetkina, V. E. Zavodnik, V. K. Bel'skiĭ, *et al.*, *Zh. Strukt. Khim.* **25** (6), 109 (1984).
- L. A. Chetkina, V. E. Zavodnik, V. K. Bel'skiĭ, *et al.*, *Zh. Strukt. Khim.* **25** (6), 114 (1984).
- L. A. Chetkina, V. E. Zavodnik, V. K. Bel'skiĭ, *et al.*, *Zh. Strukt. Khim.* **27** (5), 114 (1986).
- L. A. Chetkina, V. E. Zavodnik, V. K. Bel'skiĭ, *et al.*, *Zh. Strukt. Khim.* **27** (6), 112 (1986).
- L. A. Chetkina, V. E. Zavodnik, V. K. Bel'skiĭ, *et al.*, *Zh. Strukt. Khim.* **30** (1), 147 (1989).
- L. A. Chetkina, A. N. Sobolev, I. G. Arzamanova, and Ya. A. Gurvich, *Zh. Strukt. Khim.* **32** (4), 123 (1991).
- L. A. Chetkina, A. N. Sobolev, V. K. Bel'skiĭ, *et al.*, *Zh. Strukt. Khim.* **32** (5), 162 (1991).
- M. Maze-Baudet, *Acta Crystallogr., Sect. B: Struct. Crystallogr. Cryst. Chem.* **29**, 602 (1973).
- V. M. Potapov, *Stereochemistry* (Khimiya, Moscow, 1976) [in Russian].
- V. G. Dashevskiĭ, *Conformational Analysis of Organic Molecules* (Khimiya, Moscow, 1982) [in Russian].
- A. N. Vereshchagin, V. E. Kataev, A. A. Bredikhin, A. P. Timosheva, G. I. Kovylyaeva, and É. Kh. Kazakova, *Conformational Analysis of Hydrocarbons and*

- Their Derivatives* (Nauka, Moscow, 1990), pp. 168–172 [in Russian].
38. *Cambridge Structural Database: Release 2002*.
39. F. H. Allen, *Acta Crystallogr., Sect. B: Struct. Sci.* **58**, 380 (2002).
40. G. Casiraghi, M. Cornia, G. Sartori, *et al.*, *Makromol. Chem.* **183**, 2611 (1982).
41. P. Thuery, M. Nierlich, Z. Asfari, and J. Vicent, *J. Chem. Soc., Dalton Trans.* 1297 (2000).
42. V. Bohmer, R. Dorrenbacher, M. Frings, *et al.*, *J. Org. Chem.* **61**, 549 (1996).
43. G. Casiraghi, M. Cornia, G. Ricci, *et al.*, *Makromol. Chem.* **184**, 1363 (1983).
44. G. Ferguson, R. McCringle, and A. D. McAllees, *Can. J. Chem.* **67**, 779 (1989).
45. J. R. Cole, S. J. Torrance, R. M. Wiedhopf, *et al.*, *J. Org. Chem.* **41**, 1852 (1976).
46. A. D. U. Hardy and D. D. MacNicol, *J. Chem. Soc., Perkin Trans. 2*, 1140 (1976).
47. D. G. Hay and M. F. Mackay, *Acta Crystallogr., Sect. B: Struct. Crystallogr. Cryst. Chem.* **36**, 2508 (1980).
48. D. G. Hay, M. F. Mackay, and A. C. Sindt-Josem, *Acta Crystallogr., Sect. A: Cryst. Phys., Diffr., Theor. Gen. Crystallogr.* **37**, C62 (1981).
49. V. Bohmer, I. Columbus, G. Ferguson, *et al.*, *J. Chem. Soc., Perkin Trans. 2*, 2261 (1998).
50. E. O. Schlemper, *Acta Crystallogr., Sect. B: Struct. Crystallogr. Cryst. Chem.* **38**, 1619 (1982).
51. E. O. Schlemper, *Acta Crystallogr., Sect. B: Struct. Crystallogr. Cryst. Chem.* **38**, 554 (1982).
52. V. Sharma, B. Bachand, M. Simard, and J. D. Wuest, *J. Org. Chem.* **59**, 7785 (1994).
53. V. K. Bel'skiĭ, N. Yu. Chernikova, V. K. Rotaru, and M. M. Kruchinin, *Kristallografiya* **28** (4), 685 (1983) [*Sov. Phys. Crystallogr.* **28**, 405 (1983)].
54. S. P. N. van der Heijden, E. A. H. Griffith, W. D. Chandler, and B. E. Robertson, *Can. J. Chem.* **53**, 2084 (1975).
55. S. P. N. van der Heijden, W. D. Chandler, and B. E. Robertson, *Can. J. Chem.* **53**, 2121 (1975).
56. R. Gopal, W. D. Chandler, and B. E. Robertson, *Can. J. Chem.* **57**, 2767 (1979).
57. R. Gopal, W. D. Chandler, and B. E. Robertson, *Can. J. Chem.* **58**, 658 (1980).
58. J. C. Barnes, J. D. Paton, J. R. Damewood, and K. Mislow, *J. Org. Chem.* **46**, 4975 (1981).
59. V. Cody, *Acta Crystallogr., Sect. B: Struct. Crystallogr. Cryst. Chem.* **37**, 763 (1981).
60. V. K. Bel'skiĭ, V. K. Rotaru, and M. M. Kruchinin, *Kristallografiya* **28** (4), 695 (1983) [*Sov. Phys. Crystallogr.* **28**, 411 (1983)].
61. L. A. Chetkina, A. N. Sobolev, V. K. Bel'skiĭ, *et al.*, *Kristallografiya* **36** (4), 902 (1991) [*Sov. Phys. Crystallogr.* **36**, 506 (1991)].
62. H. Benjamins and W. D. Chandler, *Can. J. Chem.* **52**, 597 (1974).
63. F. H. Allen, O. Kennard, D. G. Watson, *et al.*, *J. Chem. Soc., Perkin Trans. 2*, No. 12, S1 (1987).
64. H. Gillier-Pandraud, *Bull. Soc. Chim. Fr.*, 1988 (1967).
65. V. E. Zavodnik, V. K. Bel'skiĭ, and P. M. Zorkiĭ, *Zh. Strukt. Khim.* **28** (5), 175 (1987).
66. Yu. A. Simonov, Yu. M. Cheban, V. K. Rotaru, and V. K. Bel'skiĭ, *Kristallografiya* **31** (2), 397 (1986) [*Sov. Phys. Crystallogr.* **31**, 232 (1986)].
67. J. Eriksson and L. Eriksson, *Acta Crystallogr., Sect. C: Cryst. Struct. Commun.* **57**, 1308 (2001).
68. M. Nakamura, K. Fukuyama, T. Tsukihara, and Y. Katsube, *Acta Crystallogr., Sect. C: Cryst. Struct. Commun.* **39**, 268 (1983).
69. R.-W. Jiang, D.-S. Ming, P. P. H. But, and T. C. W. Mak, *Acta Crystallogr., Sect. C: Cryst. Struct. Commun.* **56**, 594 (2000).
70. M. Shibakami and A. Sekiya, *Acta Crystallogr., Sect. C: Cryst. Struct. Commun.* **50**, 1152 (1994).
71. M. Perrin, C. Bavoux, and A. Thozet, *Acta Crystallogr., Sect. B: Struct. Crystallogr. Cryst. Chem.* **33**, 3516 (1977).
72. G. V. Gridunova, N. G. Furmanova, Yu. T. Struchkov, *et al.*, *Kristallografiya* **27** (2), 267 (1982) [*Sov. Phys. Crystallogr.* **27**, 164 (1982)].
73. M. Perrin, S. Rantsordas, and A. Thozet, *Cryst. Struct. Commun.* **7**, 59 (1978).
74. F. Iwasaki and Y. Kawano, *Acta Crystallogr., Sect. B: Struct. Crystallogr. Cryst. Chem.* **33**, 2455 (1977).
75. Z. A. Starikova, T. M. Shchegoleva, V. K. Trunov, *et al.*, *Zh. Strukt. Khim.* **20** (3), 514 (1979).
76. S. K. Bhattacharjee and H. L. Ammon, *Acta Crystallogr., Sect. B: Struct. Crystallogr. Cryst. Chem.* **37**, 2082 (1981).
77. F. Iwasaki, M. Sato, and A. Aihara, *Acta Crystallogr., Sect. B: Struct. Crystallogr. Cryst. Chem.* **32**, 102 (1976).
78. L. N. Kuleshova and P. M. Zorkii, *Acta Crystallogr., Sect. B: Struct. Crystallogr. Cryst. Chem.* **37**, 1363 (1981).
79. I. G. Arzamanova, Ya. A. Gurvich, L. A. Chetkina, *et al.*, in *Abstracts of All-Union Meeting on New Potentialities of Diffraction Methods* (Moscow, 1987), p. 77.
80. I. G. Arzamanova, Ya. A. Gurvich, L. A. Chetkina, *et al.*, in *Abstracts of All-Union Meeting on Diffraction Methods in Chemistry* (Suzdal, 1988), p. 31.
81. Ya. A. Gurvich, S. T. Kumok, and O. F. Starikova, *Graft and Oligomer Stabilizers for Protection of Rubbers for Medical and Food Applications* (TsNIITÉneftkhim, Moscow, 1989), No. 2, p. 40 [in Russian].
82. Ya. A. Gurvich, A. E. Grinberg, A. G. Liakumovich, *et al.*, US Patent No. 4,087,469 (1978).
83. Yu. V. Zefirov and P. M. Zorkiĭ, *Zh. Strukt. Khim.* **15** (1), 118 (1974); *Zh. Strukt. Khim.* **17** (4), 745 (1976).
84. Yu. V. Zefirov and P. M. Zorkiĭ, *Usp. Khim.* **58** (5), 713 (1989); *Usp. Khim.* **64** (5), 446 (1995).
85. Yu. V. Zefirov, *Kristallografiya* **42** (1), 122 (1997) [*Crystallogr. Rep.* **42**, 111 (1997)].
86. A. Bondi, *J. Phys. Chem.* **68**, 441 (1964).
87. R. S. Rowland and R. Taylor, *J. Phys. Chem.* **100**, 7384 (1996).
88. S. Ueji, K. Nakatsu, H. Yoshioka, and K. Kinoshita, *Tetrahedron Lett.* **23**, 1173 (1982).

89. B. Yu. Sultanov, A. N. Shnulin, and Kh. S. Mamedov, *Zh. Strukt. Khim.* **26** (2), 187 (1985).
90. K. Nakatsu, H. Yoshioka, K. Kunimoto, *et al.*, *Acta Crystallogr.*, Sect. B: *Struct. Crystallogr. Cryst. Chem.* **34**, 2357 (1978).
91. M. Perrin, K. Bekkouch, and A. Thozet, *Acta Crystallogr.*, Sect. C: *Cryst. Struct. Commun.* **43**, 980 (1987).
92. Yu. V. Zefirov and M. A. Porai-Koshits, *Zh. Strukt. Khim.* **27** (2), 74 (1986).
93. Yu. V. Zefirov, *Kristallografiya* **42** (5), 936 (1997) [*Crystallogr. Rep.* **42**, 865 (1997)].
94. Ya. A. Gurvich, I. G. Arzamanova, A. G. Shingareeva, and R. M. Popova, *Abstracts of VIII All-Union Conference on Aging and Stabilization of Polymers* (Dushanbe, 1989), p. 70 [in Russian].
95. U. Hagenau, J. Heck, W. Kaminsky, and A.-M. Schawienold, *Z. Anorg. Allg. Chem.* **626**, 1814 (2000).
96. B. W. F. Gordon and M. J. Scott, *Inorg. Chim. Acta* **297**, 206 (2000).
97. G. Casiraghi, M. Cornia, G. Ricci, *et al.*, *Macromolecules* **17**, 19 (1984).
98. E. Paulus and V. Bohmer, *Makromol. Chem.* **185**, 1921 (1984).
99. S. Usui, K. Deyama, Y. Fukazawa, *et al.*, *Chem. Lett.*, 1387 (1991).
100. P. C. Leverd, D. Weber, W. D. Habicher, and M. Nierlich, *Acta Crystallogr.*, Sect. C: *Cryst. Struct. Commun.* **56**, 997 (2000).
101. F. Xi, D. W. Reeve, A. B. McKague, and A. J. Lough, *Z. Kristallogr.* **211**, 281 (1996).
102. R. Urgaro, A. Pochini, G. D. Andreotti, and V. Sandermano, *J. Chem. Soc., Perkin Trans. 2*, 1979 (1984).
103. H. Akdas, L. Bringel, E. Graf, *et al.*, *Tetrahedron Lett.* **39**, 2311 (1998).
104. G. D. Andreotti, R. Urgano, and A. Pochini, *J. Chem. Soc., Chem. Commun.*, 1005 (1979).
105. A. Arduini, R. Caciuffo, S. Geremia, *et al.*, *Supramol. Chem.* **10**, 125 (1998).
106. S. A. Talipov, A. M. Yuldashev, Kh. L. Gapparov, *et al.*, *Zh. Org. Khim.* **33** (8), 1249 (1997).
107. A. E. Arman, K. Suzuki, S. Fujii, *et al.*, *Acta Crystallogr.*, Sect. C: *Cryst. Struct. Commun.* **48**, 1474 (1992).
108. P. Thuery, M. Nierlich, J. Vicens, and B. Masci, *Acta Crystallogr.*, Sect. C: *Cryst. Struct. Commun.* **57**, 833 (2001).
109. P. Thuery, M. Nierlich, J. Vicens, and B. Masci, *Acta Crystallogr.*, Sect. C: *Cryst. Struct. Commun.* **57**, 70 (2001).
110. V. I. Kal'chenko, J. Lipkowski, Yu. A. Simonov, *et al.*, *Zh. Obshch. Khim.* **65** (8), 1311 (1995).
111. L. G. Kuz'mina, G. G. Sadikov, J. A. K. Howard, *et al.*, *Kristallografiya* **48** (2), 267 (2003) [*Crystallogr. Rep.* **48**, 233 (2003)].
112. G. Mislin, E. Graf, M. W. Hosseini, *et al.*, *J. Chem. Soc., Chem. Commun.*, 1345 (1998).
113. H. Song, E. Kim, and H. Shin, *Bull. Korean Chem. Soc.* **11**, 19 (1990).
114. X.-J. Wang, Z.-F. Chen, B.-S. Kang, *et al.*, *Polyhedron* **18**, 647 (1999).
115. S. A. Roberts, G. P. Darsey, W. E. Cleland, Jr., and J. H. Enemark, *Inorg. Chim. Acta* **154**, 95 (1988).
116. G. Capozzi, G. Delogu, M. A. Dettori, *et al.*, *Tetrahedron Lett.* **40**, 4421 (1999).
117. I. V. Zúika and Yu. A. Bankovskii, *Usp. Khim.* **42** (1), 39 (1973).
118. B. Rozsondai, J. H. Moore, D. C. Gregory, and I. Hargittai, *Acta Chim. Acad. Sci. Hung.* **94**, 321 (1977).
119. J. L. Wardell, J. N. Low, and C. Glidewell, *Acta Crystallogr.*, Sect. C: *Cryst. Struct. Commun.* **56**, 679 (2000).
120. D. Cannon, C. Glidewell, J. N. Low, and J. L. Wardell, *Acta Crystallogr.*, Sect. C: *Cryst. Struct. Commun.* **56**, 1267 (2000).
121. C. Glidewell, J. N. Low, and J. L. Wardell, *Acta Crystallogr.*, Sect. B: *Struct. Sci.* **56**, 893 (2000).
122. N. Ueyama, T. Okamura, and Y. Yamada, *J. Org. Chem.* **60**, 4893 (1995).
123. C. Glidewell, J. N. Low, J. M. S. Skakle, and J. L. Wardell, *Acta Crystallogr.*, Sect. C: *Cryst. Struct. Commun.* **58**, 0485 (2002).
124. V. R. Vangala, G. R. Desiraju, R. K. R. Jetti, *et al.*, *Acta Crystallogr.*, Sect. C: *Cryst. Struct. Commun.* **58**, 0635 (2002).
125. J. R. Anaconda, J. Gomez, and D. Lorono, *Acta Crystallogr.*, Sect. C: *Cryst. Struct. Commun.* **59**, 0277 (2003).
126. E. Shefter and T. I. Kalman, *J. Chem. Soc., Chem. Commun.*, 1027 (1969).
127. R. A. Howie and J. L. Wardell, *Acta Crystallogr.*, Sect. C: *Cryst. Struct. Commun.* **52**, 1533 (1996).
128. P. J. Cox and J. L. Wardell, *Acta Crystallogr.*, Sect. C: *Cryst. Struct. Commun.* **53**, 122 (1997).
129. P. M. Zorkii and O. N. Zorkaya, *Zh. Strukt. Khim.* **42** (1), 3 (2001).

Translated by O. Borovik-Romanova

STRUCTURE
OF ORGANIC COMPOUNDS

Synthesis and Crystal Structure of a Two-Dimensional Silver(I)-Hexamethylenetetramine Coordination Polymer (*hmt*)¹

L.-Y. Kong*, Z.-H. Zhang*, W.-Y. Sun*, T.-A. Okamura**, and N. Ueyama**

* Coordination Chemistry Institute, State Key Laboratory of Coordination Chemistry,
Nanjing University, Nanjing 210093, China

e-mail: sunwy@nju.edu.cn

** Department of Macromolecular Science, Graduate School of Science, Osaka University,
Toyonaka, Osaka 560-0043, Japan

Received March 30, 2004

Abstract—A novel two-dimensional coordination polymer [Ag(μ_3 -hexamethylenetetramine)(H₂O)](BF₄) was synthesized and characterized by X-ray crystallography. It crystallized in the orthorhombic space group *Pnmm* with $a = 15.561(7)$ Å, $b = 10.754(5)$ Å, $c = 6.514(3)$ Å, and $Z = 4$. Each Ag center is four-coordinated in a slightly distorted tetrahedral geometry. The structure consists of 2D wavy layers of hexagonal units; these 2D layers are further connected to form a 3D network by O–H...F, C–H...F hydrogen bonds with counter anions BF₄[−] in the layers. © 2005 Pleiades Publishing, Inc.

1. INTRODUCTION

In recent years considerable attention has been focused on rational design materials with specific structures and useful properties, such as magnetism, spectroscopy, catalysis, and nonlinear optical activity [1–3]. A great number of 1D chains, 2D networks, and 3D frameworks have been obtained by self-assembly of various metal salts with rationally designed organic ligands [4, 5]. In the practice of crystal engineering, the main strategy for design and construction of supramolecules is selecting suitable organic ligands and metal ions according to their structures and coordination geometries. Hexamethylenetetramine (*hmt*) has been used as a multidentate ligand to assemble with Ag(I) to produce various Ag-*hmt* frameworks. Most of these were made up of stable, 2D infinite [Ag(μ_3 -*hmt*)] layers comprising hexagonal units [6–10]. Other interesting topologies have also been obtained, such as the 0D cage, 1D ribbons, and 3D interpenetration networks, by varying the counter ions, lateral ligands, and the Ag/*hmt* ratio [6, 11, 12]. Here we report the preparation and crystal structure of a new coordination polymer, [Ag(μ_3 -*hmt*)(H₂O)](BF₄).

2. EXPERIMENTAL

2.1. Materials and Physical Measurements

Solvents and starting materials were purchased commercially and used as received without further purification. Elemental analyses for C, H, and N were

Table 1. Summary of crystal data and refinement results for [Ag(μ_3 -*hmt*)(H₂O)](BF₄)

Empirical formula	C ₆ H ₁₄ BAgF ₄ N ₄ O
Formula weight	352.89
Crystal system	orthorhombic
Space group, <i>Z</i>	<i>Pnmm</i> , 4
<i>a</i> , Å	15.561(7)
<i>b</i> , Å	10.754(5)
<i>c</i> , Å	6.514(3)
<i>V</i> , Å ³	1090.0(8)
<i>T</i> , K	200
<i>D_c</i> , g cm ^{−3}	2.150
<i>F</i> (000)	696
μ (MoK α), cm ^{−1}	18.94
Collection range, deg	6.46 < 2 θ < 54.98
Range of <i>h</i> , <i>k</i> , <i>l</i>	−20 to 20, −13 to 13, −8 to 7
No. of Reflections Collected	10903
No. of Independent Reflections	1361 (<i>R</i> _{int} = 0.0383)
<i>RI</i> (<i>I</i> > 2 σ (<i>I</i>)) on <i>F</i> ₂	0.0209
<i>wRI</i> (<i>I</i> > 2 σ (<i>I</i>)) on <i>F</i> ₂	0.0504
<i>RI</i> (all data) on <i>F</i> ₂	0.0309
<i>wRI</i> (all data) on <i>F</i> ₂	0.0525
Goodness of fit	0.963
$\Delta\rho_{\max}$, $\Delta\rho_{\min}$, e Å ^{−3}	0.74, −0.77

¹ The text was submitted by the authors in English.

Table 2. Selected bond distances (Å) and angles (deg) for the title complex

Bond	<i>d</i>	Angles	ω
Ag(1)–N(1)	2.330(3)	N(1)–Ag(1)–N(3)*	120.27(5)
Ag(1)–N(3)*	2.3713(19)	N(1)–Ag(1)–O(1)	96.19(12)
Ag(1)–O(1)	2.480(3)	N(3)*–Ag(1)–N(3)**	116.95(9)
		N(3)*–Ag(1)–O(1)	94.80(7)

* The symmetry transformations used to generate equivalent atoms are $-x + 3/2, y - 1/2,$ and $-z + 3/2$.

** The symmetry transformations used to generate equivalent atoms are $-x + 3/2, y - 1/2,$ and $z + 1/2$.

Table 3. Hydrogen bond data for the title complex

<i>D</i> –H... <i>A</i>	Distance of <i>D</i> ... <i>A</i> , Å	Angle of <i>D</i> –H... <i>A</i> , deg
O(1)–H(1w)...F(3)*	2.6933(19)	149
C(1)–H(1)...F(1)**	3.4077(19)	155
C(1)–H(1)...F(3)**	3.2493(19)	134
C(3)–H(3A)...F(3)	3.4249(19)	174

* The symmetry transformations used to generate equivalent atoms are $-x + 3/2, y - 1/2,$ and $-z + 3/2$.

** The symmetry transformations used to generate equivalent atoms are $-x + 3/2, y - 1/2,$ and $z + 1/2$.

made on a Perkin-Elmer 240C elemental analyzer at the Analysis Center of Nanjing University. The IR spectrum was recorded on a Bruker Vector22 FT-IR spectrophotometer using KBr discs.

C 20.28; H 4.09; N 15.75%. IR (KBr, cm^{-1}): 3441 (s), 1238 (s), 1123 (m), 1084 (vs), 1038 (m), 1008 (vs).

2.2. Preparation of $[\text{Ag}(\mu_3\text{-hmt})(\text{H}_2\text{O})](\text{BF}_4)$

The title complex was prepared by the layering method. A methanol solution (15 ml) of AgBF_4 (31.4 mg, 0.1 mmol) was carefully layered over a solution of hmt (6.5 mg, 0.05 mmol) in water (10 ml). Colorless block crystals were obtained after 7 d in ca. 45% yield. Calculated elemental analysis for $\text{C}_6\text{H}_{14}\text{BAgF}_4\text{N}_4\text{O}$: C 20.42; H 4.00; N 15.88%. Found:

2.3. Crystal Structure Determination

The X-ray diffraction measurement for the title complex was carried out on a Rigaku RAXIS-RAPID Imaging Plate diffractometer using graphite-monochromated $\text{MoK}\alpha$ radiation ($\lambda = 0.7107 \text{ \AA}$) at 200 K. The structure was solved by the direct method with SIR92 [13] and expanded using Fourier techniques [14]. All data were refined anisotropically by the full-matrix least-squares method on F^2 in Shelxl. The hydrogen atoms were found from the difference Fourier

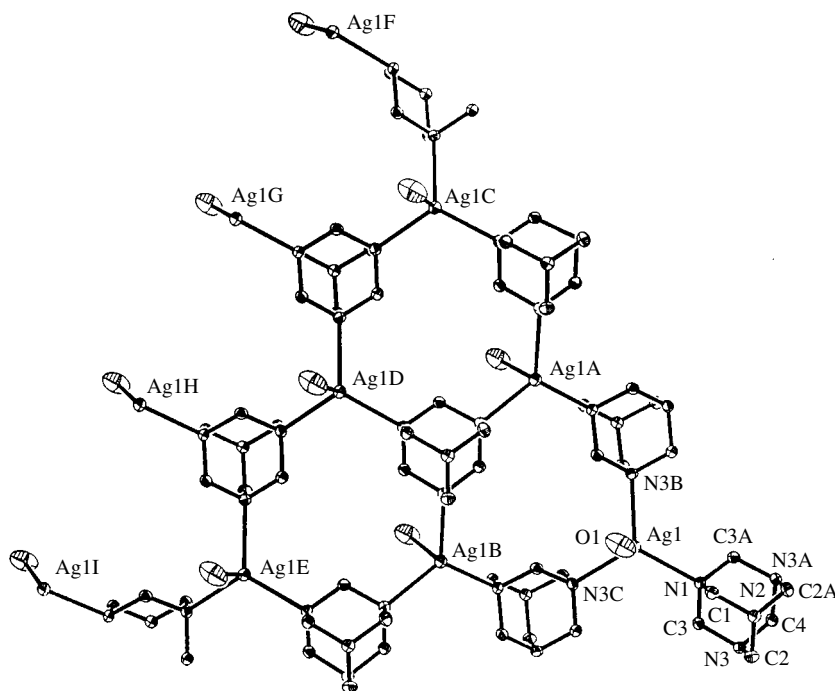


Fig. 1. Top view of the 2D wavy layer structure with hexagonal units of $[\text{Ag}(\mu_3\text{-hmt})(\text{H}_2\text{O})](\text{BF}_4)$ (hydrogen atoms and BF_4^- units were omitted for clarity).

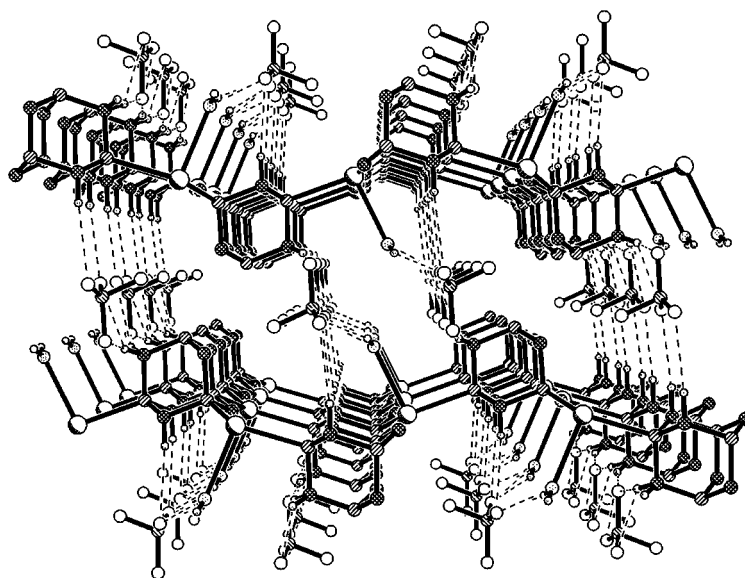


Fig. 2. The 3D network formed by O–H...F and C–H...F hydrogen bonds (shown by the dashed line) as viewed along the *b* axis.

map directly, and the positions were refined using a fixed B factor ($1.2 B_{\text{eq}}$ of the connected atom). One F atom of BF_4^- disordered into two positions with site occupancy factors of 0.506(18) and 0.494(18). All calculations were carried out on an SGI workstation using the teXsan crystallographic software package (Molecular Structure Corporation) [15]. The significant crystal data, details of data collection, and structure refinement for the complex are summarized in Table 1, and selected bond lengths and angles with their estimated standard deviations are given in Table 2. Further details are provided in the supporting information. Crystallographic data (excluding structure factors) for the structure reported in this paper have been deposited with the Cambridge Crystallographic Data Center as supplementary publication no. CCDC-231288. Copies of the data can be obtained free of charge by application to CCDC, 12 Union Road, Cambridge CB2 1EZ, UK (fax: (+44) 1223 336-033; e-mail: deposit@ccdc.cam.ac.uk).

3. RESULTS AND DISCUSSION

3.1. Description of Crystal Structure

The crystal structure of the complex is shown in Fig. 1. Each Ag(I) is four-coordinated by three N atoms from three different hmt molecules and one O atom from a water molecule in a slight distorted tetrahedral geometry. Herein the solvent water molecules are not lattice molecules as in the Ag-hmt networks reported previously [8] but coordinated to Ag(I) centers. The bond lengths of Ag–N are 2.330(3) and 2.3713(19) Å, while the bond length of Ag–O is 2.480(3) Å. An hmt molecule serves as a tridentate ligand, so each Ag(I) ion is coordinated by three hmt molecules and each hmt

molecule coordinates to three Ag(I) ions. Such a coordination manner makes the complex a 2D infinite layer structure consisting of hexagonal units in a boat conformation (see Fig. 2), which are common in the reported $[\text{Ag}(\text{hmt})]\text{X}$ ($\text{X} = \text{ClO}_4^-, \text{PF}_6^-, \text{CF}_3\text{SO}_3^-$) networks [6, 7, 12]. The BF_4^- counter ions are located between two layers and held there by hydrogen bonds between the coordinated water molecules O–H...F, methylene C–H...F from hmt molecules, and F atoms from BF_4^- anions (see Fig. 2). So the 2D layers were further connected together to form a 3D network by the BF_4^- anions through hydrogen bonds. The hydrogen-bonding data are summarized in Table 3.

ACKNOWLEDGMENTS

The authors are grateful to the National Natural Science Foundation of China (grant no. 20231020) for financial support of this work.

REFERENCES

1. C. Janiak, *J. Chem. Soc. Dalton Trans.*, 2781 (2003).
2. B. Q. Ma, S. Gao, G. Su, and G. X. Xu, *Angew. Chem., Int. Ed. Engl.* **113**, 448 (2001).
3. X. R. Meng, Y. L. Song, Y. W. Hou, *et al.*, *Inorg. Chem.* **42**, 1306 (2003).
4. S. R. Batten and R. Robson, *Angew. Chem., Int. Ed. Engl.* **37**, 1460 (1998).
5. B. Moulton and M. J. Zaworotko, *Chem. Rev.* **101**, 1629 (2001).
6. L. Carlucci, G. Ciani, D. W. Gudenberg, *et al.*, *Chem. Commun.*, 631 (1997).

7. L. Carlucci, G. Ciani, D. M. Proserpio, and S. Rizzato, *J. Solid State Chem.* **152**, 211 (2000).
8. L. M. Tong, S. L. Zheng, and X. M. Chen, *Chem. Commun.*, 561 (1999).
9. S. L. Zheng, M. T. Tong, R. M. Fu, *et al.*, *Inorg. Chem.* **40**, 3562 (2001).
10. A. Michelet, B. Voissat, P. Khodadad, and N. Rodier, *Acta Crystallogr., Sect. B: Struct. Sci.* **37**, 2171 (1981).
11. L. Carlucci, G. Ciani, D. M. Proserpio, and A. Sironi, *Inorg. Chem.* **36**, 1736 (1997).
12. L. Carlucci, G. Ciani, D. M. Proserpio, and A. Sironi, *J. Am. Chem. Soc.* **117**, 12861 (1995).
13. A. Altomare, M. C. Burla, M. Camalli, *et al.*, *J. Appl. Crystallogr.* **27**, 435 (1994).
14. P. T. Beurskens, G. Admiraal, G. Beurskens, *et al.*, in *The DIRFID-94 Program System* (Tech. Rep. Crystallogr. Labor. Univ. Nijmegen, Netherlands, 1994).
15. *Crystal Structure Analysis Package* (Molecular Structure Corporation, 1999).

STRUCTURE OF ORGANIC COMPOUNDS

Synthesis, Crystal Structure, and Conducting Properties of a New Molecular Metal, $(BEDO)_4Ni(CN)_4 \cdot 4CH_3CN$

A. D. Dubrovskii, N. G. Spitsina, G. V. Shilov, O. A. D'yachenko, and É. B. Yagubskii

Institute of Problems of Chemical Physics, Russian Academy of Sciences, pr. Akademika Semenova 1,
Chernogolovka, Noginskii raion, Moscow oblast, 142432 Russia

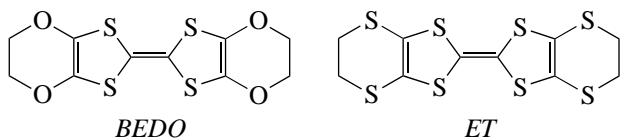
e-mail: spitsina@icp.ac.ru

Received May 19, 2004

Abstract—A new radical cation salt based on bis(ethylenedioxy)tetrathiafulvalene (*BEDO*) with the plane-square anion $Ni(CN)_4^{2-}$ is synthesized. The molecular and crystal structures of the radical cation salt are determined, and the conducting properties are investigated. In the structure, the *BEDO* radical cations have a β'' -type packing. It is shown that the temperature dependence of the conductivity of $(BEDO)_4Ni(CN)_4 \cdot 4CH_3CN$ crystals exhibits metallic behavior. © 2005 Pleiades Publishing, Inc.

INTRODUCTION

Bis(ethylenedioxy)tetrathiafulvalene (*BEDO*) is an oxygen-containing analogue of bis(ethylenedithio)tetrathiafulvalene (*ET*).



A large number of radical cation salts based on *BEDO* with different anions have been synthesized and their structures and conducting properties have been investigated to date [1–8]. The majority of *BEDO* salts are molecular metals, except for only two salts, $(BEDO)_3Cu_2(SCN)_3$ and $(BEDO)_2ReO_4 \cdot H_2O$, which undergo a superconducting transition [5–7]. The crystal structure of *BEDO* salts with linear [1, 2], tetrahedral [2, 5, 6], planar [3, 8], and octahedral [4] anions differs from that of the corresponding *ET*-based salts. For example, crystals of the $(BEDO)_4Pt(CN)_4 \cdot H_2O$ salt have a structure with an α'' -type packing and possess metallic conductivity down to liquid-helium temperature (4.2 K) [8], whereas crystals of the *ET*-based salt of similar composition have a structure with a β'' -type packing and undergo a transformation into the dielectric state at a temperature of 100 K [9]. It was of interest to synthesize and investigate new *BEDO*-based salts with a tetracyanonickelate anion and to compare them with the corresponding *ET*-based salts.

EXPERIMENTAL

Synthesis. Crystals of the $(BEDO)_4Ni(CN)_4 \cdot 4CH_3CN$ salt (**I**) were prepared through electrochemical oxidation of neutral *BEDO*. A solution containing

BEDO (10 mg, $C = 1.3 \times 10^{-3}$ mol/l) and $(Ph_4P)_2Ni(CN)_4$ (42 mg, $C = 3 \times 10^{-3}$ mol/l) in acetonitrile (25 ml) with an additive of absolute ethanol (10 vol %) was subjected to electrochemical oxidation at a platinum anode under dc conditions ($I = 0.5 \mu A$) at a temperature of 25°C. Crystals grew on the anode for 10–15 days in the form of well-faceted black plates with a characteristic metallic luster. Then, the crystals were filtered off, washed with acetone, and dried in air.

X-ray diffraction analysis. The composition and structure of compound **I** were determined by X-ray diffraction analysis. The main crystal data are presented in Table 1. The experimental set of diffraction data was collected on a Kuma Diffraction KM-4 automated four-circle diffractometer (CuK_α radiation, $\lambda = 1.5418 \text{ \AA}$, graphite monochromator). The structure was solved by direct methods with the SHELXS97 program package [10]. The intensities of the Bragg reflections were corrected for X-ray absorption in the crystal according to the DIFFABS program [11]. The hydrogen atoms in the *BEDO* radical cations were located from difference Fourier syntheses. The positions of all the non-hydrogen atoms were refined using the full-matrix least-squares procedure in the anisotropic approximation, and the positions of the hydrogen atoms were refined by the least-squares method in the isotropic approximation with the SHELXL97 program package [12].

The crystal data on the structure of salt **I** have been deposited with the Cambridge Structural Database (CCDC no. 243316).

RESULTS AND DISCUSSION

Crystals of salt **I** have a layered structure in which layers formed by the *BEDO* radical cations alternate with the anion layers along the *b* axis of the unit cell

Table 1. Main crystal data, data collection, and refinement parameters for the structure of the $(C_{10}H_8O_4S_4)_4Ni(CN)_4 \cdot 4CH_3CN$ compound

Empirical formula	$C_{52}H_{44}N_8O_{16}S_{16}Ni$
M	1608.6
Space group, Z	$P\bar{1}, 1$
a , Å	7.127(1)
b , Å	19.098(4)
c , Å	12.535(3)
α , deg	87.03(3)
β , deg	71.53(3)
γ , deg	87.70(3)
V , Å ³	1615.6(6)
ρ_{calcd} , g/cm ³	1.65
$\mu(\text{CuK}\alpha)$, mm ⁻¹	5.90
Sample size, mm	0.65 × 0.45 × 0.10
Scan mode	$\omega/2\theta$
$2\theta_{\text{max}}$, deg	161.12
Number of unique reflections/Number of observed reflections with $I \geq 2\sigma(I)$	6481/2613
R	0.076
S	0.841

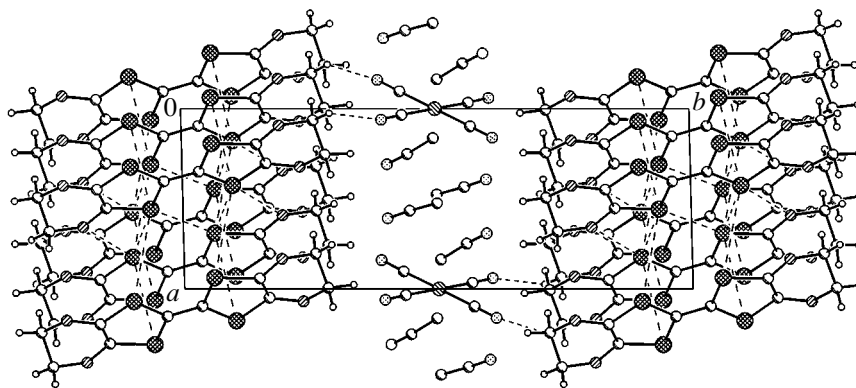
(Fig. 1). The asymmetric part of the unit cell involves two crystallographically independent *BEDO* radical cations (hereafter, these cations will be denoted as *A* and *B*), two acetonitrile molecules, and 1/2 of the $Ni(CN)_4^{2-}$ anion. In the crystallographically independent $Ni(CN)_4^{2-}$ anion, the nickel atom is located at the center of symmetry. The *BEDO* radical cations each have a formal charge of +1/2.

The $Ni(CN)_4^{2-}$ centrosymmetric anion has a plane-square configuration typical of Ni(II) complexes. In this configuration, the Ni(1)–C(1) bond length

[1.870(6) Å] differs from the Ni(1)–C(2) bond length [1.838(6) Å], whereas the Ni(1)–C(1)–N(1) bond angle [178.3(7)°] is approximately equal to the Ni(1)–C(2)–N(2) bond angle [177.3(8)°] (Fig. 2). On the whole, the bond lengths and the bond angles in the $Ni(CN)_4^{2-}$ anion are in close agreement with those determined earlier for the $(ET)_4Ni(CN)_4$ and $(ET)_4Ni(CN)_4 \cdot H_2O$ salts [9]. In structure **I**, there are three C–H···N intermolecular contacts between the anions and cations: N(1)···H(1A), 2.554 Å (x, y, z); N(1)···H(8A), 2.734 Å ($1-x, -y, -z$); and N(2)···H(1B), 2.433 Å ($x, y, 1+z$). These contacts each do not exceed the sum of the van der Waals radii of the nitrogen and hydrogen atoms (1.55 and 1.20 Å, respectively [13, 14]).

In the previously synthesized radical cation salts based on *ET* with tetracyanometalate anions, the planes of these anions are nearly perpendicular to the organic layer formed by the *ET* radical cations. An interesting feature of the structure of the anion layer in crystal **I** is that the anion plane is rotated with respect to the radical cation layer aligned parallel to the *ac* plane of the unit cell. The angle of rotation of the $Ni(CN)_4^{2-}$ anion plane with respect to the *ac* plane is equal to 88.3°. The rotation of the anion plane can be explained by the fact that the anion layer (Fig. 2) involves solvent (acetonitrile) molecules. The acetonitrile molecules and the *BEDO* radical cations are linked by the C–H···N hydrogen bonds: N(3)···H(8B), 3.678 Å ($-x, -y, -1-z$).

As in the structures of $(ET)_4M(CN)_4$ and $(ET)_4M(CN)_4H_2O$ ($M = Ni, Pd, Pt$) [9, 15], the radical cation layer in the structure of $(BEDO)_4Ni(CN)_4 \cdot 4CH_3CN$ is formed by the *BEDO* stacks with a β'' -type packing according to the structural classification of *ET* salts and their analogues [16]. The packing of the *BEDO* molecules in the organic layer is depicted in Fig. 3. The stack axis is approximately aligned along the [101] direction. In the stack, the *BEDO* radical cations alternate in the following manner: ...*A*...*A*...*B*...*B*... The distances between the midplanes of the radical cat-

**Fig. 1.** Projection of crystal structure **I** onto the *ab* plane.

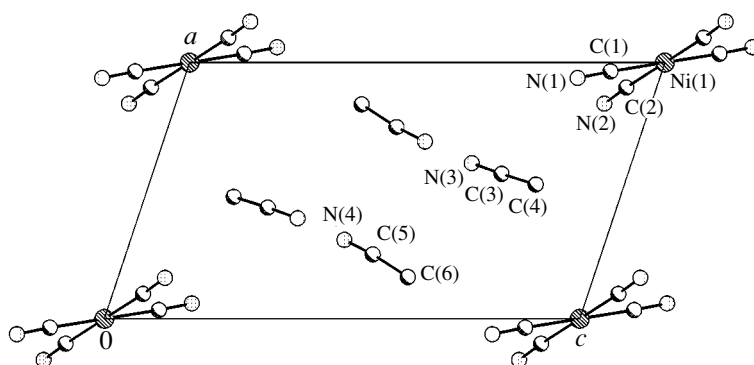


Fig. 2. Projection of the anion layer in structure **I** onto the *ab* plane.

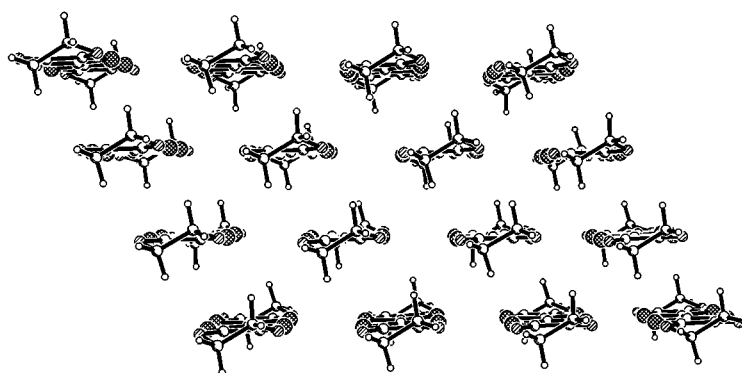


Fig. 3. Packing of the *BEDO* radical cations in the organic layer.

ions in the stack (the planes pass through the *TTF* central fragment and the oxygen atoms) are as follows: $A \cdots A$, 3.52(1) Å; $A \cdots B$, 3.57(1) Å; and $B \cdots B$, 3.52(1) Å. In the structure of the *BEDO* salt with a β'' -type packing, the interplanar distances between the cations are approximately identical and do not exceed 3.6 Å [1–7]. The midplanes of the *BEDO* radical cations in the stack are aligned parallel to each other [the angle between the midplanes does not exceed 1.08(6)°]. Inside the stacks, there are shortened intermolecular contacts C–H \cdots O (2.642–2.737 Å). The *BEDO* radical cations of the adjacent stacks are joined together into ribbons through shortened intermolecular contacts in a side-to-side manner. Cations *A* and *B* each have ten shortened contacts of the S \cdots S and S \cdots O types (Fig. 4, Table 2). The lengths of these contacts are less than the sum of the van der Waals radii of the sulfur and oxygen atoms (1.8 and 1.6 Å, respectively [14]). In the ribbons, the *BEDO* molecules alternate in the following manner: $\cdots A \cdots B \cdots$.

In structure **I**, the *BEDO* radical cations, on the whole, have a planar structure. The atoms of the *TTF* fragment and the oxygen atoms deviate from the midplane of the molecule by no more than 0.021(2) Å. The carbon atoms of the terminal ethylene groups are located on each side of the midplane of the molecule

and form the so-called eclipsed conformation. The maximum deviation of the terminal carbon atoms from the midplane of the molecule can be as large as 0.386(3) Å.

The bond lengths and the bond angles are in good agreement with those determined earlier for the (*BEDO*)^{+1/2} salts. The C=C central bonds [C(1A)–C(2A), 1.372(6) Å; C(1B)–C(2B), 1.373(5) Å] are longer than the corresponding bond [1.342(9) Å] in the neutral molecule (*BEDO*)⁰ [2] but are shorter than the bond [1.398(5) Å] in the (*BEDO*)⁺¹ radical cation in the structure of the (*BEDO*)₃ salt [17].

Table 2. Shortened intermolecular contacts between *BEDO* radical cations in ribbons

Contact	<i>r</i> , Å	Contact	<i>r</i> , Å
S(1A) \cdots S(1B) ⁱ	3.414	S2(A) \cdots S(4B) ⁱⁱ	3.359
S(1A) \cdots S(3B) ⁱ	3.393	S2(A) \cdots O(4B) ⁱⁱ	3.268
S(3A) \cdots S(1B) ⁱ	3.389	S4(A) \cdots S(2B) ⁱⁱ	3.363
S(3A) \cdots O(1B) ⁱ	3.187	S4(A) \cdots S(4B) ⁱⁱ	3.479
O(1A) \cdots S(3B) ⁱ	3.195	O4(A) \cdots S(2B) ⁱⁱ	3.270

Symmetry codes: (i) $-x, -y, -z$; (ii) $1-x, -y, -1-z$.

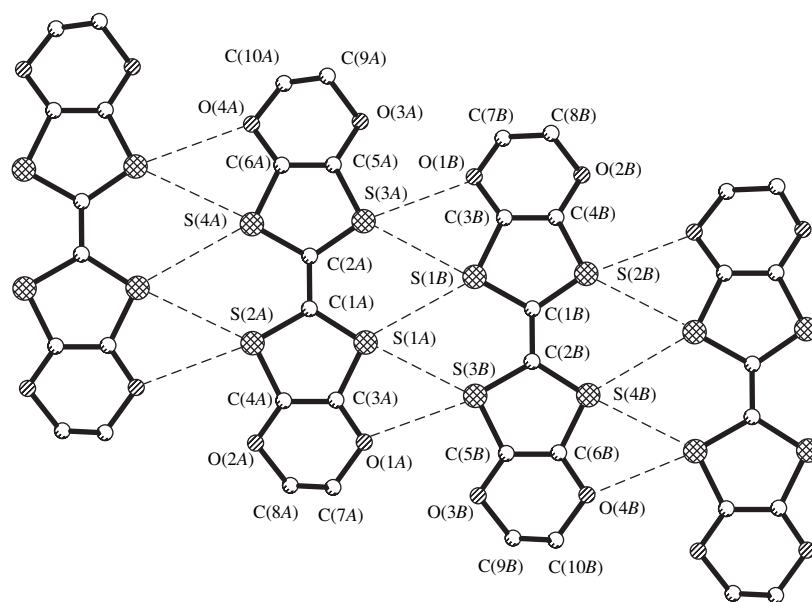


Fig. 4. Environment of the $BEDO^{+1/2}$ radical cation in the organic layer of the structure.

The conductivity of crystals **I** was measured by the standard four-point probe method in the *ac* plane. The conductivity at room temperature was found to be $6.5\text{--}13.0\ \Omega^{-1}\ \text{cm}^{-1}$. It should be noted that the *ET* salts with the $\text{Ni}(\text{CN})_4^{2-}$ anion undergo a metal–insulator phase transition at low temperatures [9]. By contrast, the β'' -($BEDO$) $_4\text{Ni}(\text{CN})_4 \cdot 4\text{CH}_3\text{CN}$ salt is a stable metal over a wide range of temperatures from 300 to 4.2 K (Fig. 5). The majority of radical cation salts based on *BEDO* have a β'' -type packing and possess metallic properties irrespective of the anion type [1–7, 18]. Therein lies a substantial difference between the *BEDO* radical cation salts and the *ET* salts whose packing type and conducting properties depend significantly on the nature and the geometry of the anion. The *BEDO* cations, unlike

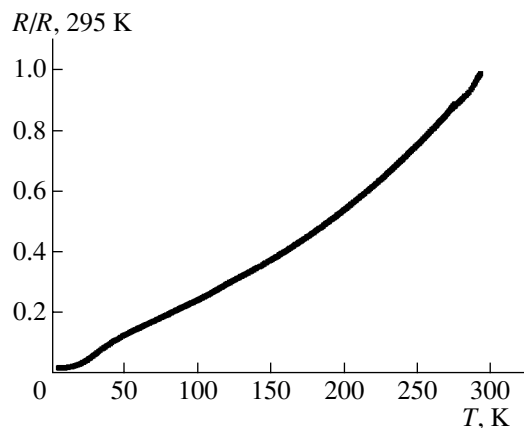


Fig. 5. Temperature dependence of the resistance for crystals **I**.

the *ET* cations, exhibit a strong tendency toward β'' -type packing in the organic layer, because the energy of the $\text{C}\text{--}\text{H}\cdots\text{O}$ and $\text{O}\cdots\text{S}$ intermolecular interactions in the *BEDO* salt is higher than the energy of the $\text{C}\text{--}\text{H}\cdots\text{S}$ and $\text{S}\cdots\text{S}$ intermolecular interactions in the *ET* salt [19]. It is this β'' -type packing that is responsible for metallic conductivity of the *BEDO* salts.

ACKNOWLEDGMENTS

We would like to thank L.I. Buravov and V.A. Tkacheva for their assistance in the conductivity measurements.

This work was supported by the International Association of Assistance for the Promotion of Cooperation with Scientists from the New Independent States of the Former Soviet Union (project INTAS no. 2001-2212) and the Russian Foundation for Basic Research (project nos. 02-03-32794, 02-03-33218).

REFERENCES

1. F. Wudl, H. Yamochi, T. Suzuki, *et al.*, *J. Am. Chem. Soc.* **112**, 2461 (1990).
2. M. A. Beno, H. H. Wang, K. D. Carlson, *et al.*, *Mol. Cryst. Liq. Cryst.* **181**, 145 (1990).
3. H. Yamochi, S. Horiuchi, G. Saito, *et al.*, *Synth. Met.* **55–57**, 2096 (1993).
4. L. V. Zorina, S. S. Khasanov, R. P. Shibaeva, *et al.*, *J. Mater. Chem.* **10**, 2017 (2000).
5. M. A. Beno, H. H. Wang, A. M. Kini, *et al.*, *Inorg. Chem.* **29**, 1599 (1990).
6. S. Kahlich, D. Schweitzer, I. Heinen, *et al.*, *Solid State Commun.* **80**, 191 (1991).

7. L. I. Buravov, A. G. Khromenko, N. D. Kushch, *et al.*, J. Phys. I **2**, 529 (1992).
8. E. I. Zhilyaeva, R. N. Lyubovskaya, S. A. Torunova, *et al.*, Synth. Met. **80**, 93 (1996).
9. H. Mori, I. Hirabayashi, S. Tanaka, *et al.*, Synth. Met. **55–57**, 2044 (1993).
10. G. M. Sheldrick, *SHELXS97: Program for Crystal Structure Determination* (Univ. of Göttingen, Germany, 1997).
11. N. Walker and D. Stuart, Acta Crystallogr., Sect. A: Found. Crystallogr. **39**, 158 (1983).
12. G. M. Sheldrick, *SHELXL97: Program for the Refinement of Crystal Structures* (Univ. of Göttingen, Germany, 1997).
13. S. S. Batsanov, Zh. Neorg. Khim. **36**, 3015 (1991).
14. S. S. Batsanov, Izv. Akad. Nauk, Ser. Khim., No. 1, 24 (1995).
15. R. M. Lobkovskaya, N. D. Kushch, R. P. Shibaeva, *et al.*, Kristallografiya **34** (6), 1158 (1989) [Sov. Phys. Crystallogr. **34**, 698 (1989)].
16. T. Mori, Bull. Chem. Soc. Jpn. **71**, 2509 (1998).
17. S. Horiuchi, H. Yamochi, G. Saito, and K. Matsumoto, Mol. Cryst. Liq. Cryst. **284**, 357 (1996).
18. S. Horiuchi, H. Yamochi, and G. Saito, J. Am. Chem. Soc. **118**, 8604 (1996).
19. J. M. Williams, J. R. Ferraro, R. J. Thorn, K. D. Carlson, U. Geiser, H. H. Wang, A. M. Kini, and M.-H. Whangbo, *Organic Superconductors (Including Fullerenes): Synthesis, Structure, Properties, and Theory* (Prentice Hall, Englewood Cliffs, N.J., 1992), pp. 270–275.

Translated by O. Borovik-Romanova

STRUCTURE
OF ORGANIC COMPOUNDS

Crystal Structure of [N-(2-Aminoethyl)iminodiacetato](1,10-Phenanthroline)copper(II) Tetrahydrate,
[Cu(Aeida)(Phen)] · 4H₂O

A. L. Poznyak*, A. S. Antsyshkina**, G. G. Sadikov**, V. S. Sergienko**,
and L. V. Stopolyanskaya*

* Institute of Molecular and Atomic Physics, Belarussian Academy of Sciences,
pr. Frantsiska Skoriny 70, Minsk, 220072 Belarus

** Kurnakov Institute of General and Inorganic Chemistry, Russian Academy of Sciences,
Leninskiĭ pr. 31, Moscow, 119991 Russia

e-mail: sadgg@igic.ras.ru

Received April 17, 2004

Abstract—Crystals of [N-(2-aminoethyl)iminodiacetato](1,10-phenanthroline)copper(II) tetrahydrate, [Cu(Aeida)(Phen)] · 4H₂O (**I**), are obtained, and their structure is determined. Crystals **I** are triclinic, and the unit cell parameters are as follows: $a = 8.341(1)$ Å, $b = 9.424(1)$ Å, $c = 13.864(2)$ Å, $\alpha = 74.23(1)^\circ$, $\beta = 79.25(1)^\circ$, $\gamma = 82.67(1)^\circ$, $Z = 2$, and space group $P1$. The structural units of the crystal are [Cu(Aeida)(Phen)] molecular complexes and crystallization water molecules. The coordination polyhedron of the copper atom is a tetragonal bipyramid with four nitrogen atoms in the equatorial plane (mean Cu–N, 2.05 Å) and two oxygen atoms of the acetate groups in axial positions (Cu–O, 2.264 and 2.426 Å; O–Cu–O angle, 148.8°). The *Aeida* and *Phen* ligands fulfill the tetradentate (2N + 2O) chelate and bidentate (2N) chelate functions, respectively. The complexes are joined into dimer associates in which the interplanar spacing between *Phen* molecules is equal to 3.54 Å and the Cu...Cu distance is 7.02 Å. © 2005 Pleiades Publishing, Inc.

INTRODUCTION

This study continues our investigations into the structure of mixed-ligand copper(II) complexes that contain both derivatives of iminodiacetic acid RN(CH₂CO₂H)₂ and heterocyclic nitrogen-containing ligands (such as 2,2'-bipyridyl (*Bipy*), 1,10-phenanthroline (*Phen*), or two imidazole (*Im*) molecules) [1–3]. In this work, we determined the crystal structure of a compound that, according to the X-ray diffraction analysis, has the composition [Cu(Aeida)(Phen)] · 4H₂O (**I**), where *Aeida* is the *N*-(2-aminoethyl)iminodiacetate ion NH₂CH₂CH₂N(CH₂CO₂)₂.

EXPERIMENTAL

Synthesis of compound I. *N*-(2-Aminoethyl)iminodiacetate ions were obtained in a solution using iminodiacetic acid. A solution of iminodiacetic acid and acrylamide (in a 1 : 1 molar ratio) was allowed to stand under basic conditions at a temperature of 40°C for a few hours. The reaction resulted in *N*-(2-carbamoylethyl)iminodiacetate ions NH₂COCH₂CH₂N(CH₂CO₂)₂. After the reaction mixture was cooled in an ice bath, a solution of sodium hypobromite (prepared from sodium hydroxide and bromine) was added to the cold mixture in an amount required to perform the Hofmann reaction according to the standard procedure (oxidative destruc-

tion of the CH₂CH₂CONH₂ propionamide group into the CH₂CH₂NH₂ aminoethyl group.) After the reaction was completed, cupric chloride CuCl₂ · 2H₂O (equivalent) was added to the mixture. The excess alkali was neutralized with some amount of an HCl solution. Colored Cu(II) complexes necessary for further experiments were isolated from the resultant solution through gel filtration on a Sephadex G10 column and, thus, purified from salt impurities. Then, Cu(*Aeida*) neutral complexes were separated from charged impurities of Cu(II) complexes. For this purpose, the solution was passed through columns packed with an anionite and a cationite. Then, the solution was once more purified on a Sephadex G10 column. Evaporation of the final solution resulted in a Cu(*Aeida*) powder (its exact composition was not determined). Slow evaporation of an aqueous solution containing this compound and 1,10-phenanthroline (*Phen*) yielded blue crystals suitable for X-ray diffraction analysis.

X-ray diffraction analysis. The unit cell parameters and the three-dimensional set of intensities of reflections were obtained for compound **I** in the form of a single crystal 0.12 × 0.15 × 0.18 mm in size on an Enraf–Nonius CAD4 diffractometer (MoK_α radiation, graphite monochromator, 2θ/ω scan mode, 2θ = 60°) at a temperature of 293 K.

Table 1. Selected bond lengths (d , Å) and angles (ω , deg) in the structure of compound **I**

Bond	d	Bond	d	Angle	ω	Angle	ω
Cu(1)–O(1)	2.264(2)	Cu(1)–O(3)	2.426(2)	Cu(1)N(1)C(6)	111.8(2)	O(3)Cu(1)N(4)	89.88(7)
Cu(1)–N(1)	2.150(2)	Cu(1)–N(2)	1.988(2)	C(1)N(1)C(6)	108.8(2)	N(1)Cu(1)N(3)	158.06(8)
Cu(1)–N(3)	2.040(2)	Cu(1)–N(4)	2.043(2)	Cu(1)N(2)C(2)	109.6(2)	N(2)Cu(1)N(3)	94.46(9)
O(1)–C(3)	1.245(3)	O(2)–C(3)	1.248(3)	Cu(1)N(3)C(18)	112.6(2)	N(3)Cu(1)N(4)	81.09(8)
O(3)–C(5)	1.248(3)	O(4)–C(5)	1.248(3)	Cu(1)N(4)C(16)	130.1(2)	Cu(1)N(1)C(4)	111.4(2)
N(1)–C(1)	1.487(3)	N(1)–C(4)	1.474(3)	C(16)N(4)C(17)	117.5(2)	C(1)N(1)C(4)	110.8(2)
N(1)–C(6)	1.467(4)	N(2)–C(2)	1.476(3)	N(2)C(2)C(1)	107.3(2)	C(4)N(1)C(6)	111.4(2)
N(3)–C(7)	1.326(3)	N(3)–C(18)	1.353(3)	O(1)C(3)C(4)	119.0(2)	Cu(1)N(3)C(7)	128.9(2)
N(4)–C(16)	1.326(4)	N(4)–C(17)	1.359(3)	N(1)C(4)C(3)	114.4(2)	C(7)N(3)C(18)	118.1(2)
C(1)–C(2)	1.501(4)	C(3)–C(4)	1.533(4)	O(3)C(5)C(6)	117.1(2)	Cu(1)N(4)C(17)	112.4(2)
C(5)–C(6)	1.531(4)			N(1)C(6)C(5)	112.4(2)	N(1)C(1)C(2)	111.1(2)
C(17)–C(18)	1.435(3)			N(4)C(16)C(15)	122.8(3)	O(1)C(3)O(2)	125.5(2)
Angle	ω	Angle	ω	N(4)C(17)C(18)	116.7(2)	O(2)C(3)C(4)	115.4(2)
O(1)Cu(1)N(1)	77.46(7)	N(1)Cu(1)N(2)	85.21(9)	N(3)C(18)C(10)	123.6(2)	O(3)C(5)O(4)	126.0(3)
O(1)Cu(1)N(3)	124.47(7)	N(1)Cu(1)N(4)	102.22(8)	O(1)Cu(1)N(2)	87.65(8)	O(4)C(5)C(6)	116.9(2)
O(3)Cu(1)N(1)	72.73(7)	N(2)Cu(1)N(4)	170.14(9)	O(1)Cu(1)N(4)	87.66(8)	N(3)C(7)C(8)	121.9(3)
O(3)Cu(1)N(3)	85.68(7)	Cu(1)N(1)C(1)	102.3(2)	O(3)Cu(1)N(2)	98.60(8)	N(3)C(18)C(17)	116.7(2)

Crystals **I**, $[\text{Cu}(\text{C}_6\text{H}_{10}\text{N}_2\text{O}_4)(\text{C}_{12}\text{H}_8\text{N}_2)] \cdot 4\text{H}_2\text{O}$, are triclinic, and the unit cell parameters are as follows: $a = 8.341(1)$ Å, $b = 9.424(1)$ Å, $c = 13.864(2)$ Å, $\alpha = 74.23(1)^\circ$, $\beta = 79.25(1)^\circ$, $\gamma = 82.67(1)^\circ$, $V = 1027.0(3)$ Å³, $\rho_{\text{calcd}} = 1.585$ g/cm³, $\mu = 1.12$ mm⁻¹, $Z = 2$, and space group $P\bar{1}$. A total of 4717 reflections were collected (index ranges: $-11 < h < 6$, $-12 < k < 12$, $0 < l < 18$), of which 4587 reflections were unique ($R_{\text{int}} = 0.018$).

The structure was solved by direct methods and refined in the anisotropic (isotropic for H atoms)

approximation according to the full-matrix least-squares procedure. The final parameters of the refinement are as follows: $R_1 = 0.0300$, $wR_2 = 0.0769$ for 3136 reflections with $I > 2\sigma(I)$; $R_1 = 0.0704$, $wR_2 = 0.0940$ for all reflections; 384 parameters refined; and $GOF = 0.941$. The maximum and minimum residual electron densities are 0.364 and -0.480 e Å⁻³, respectively.

All the calculations were performed with the SHELXS86 [4] and SHELXL93 [5] program packages.

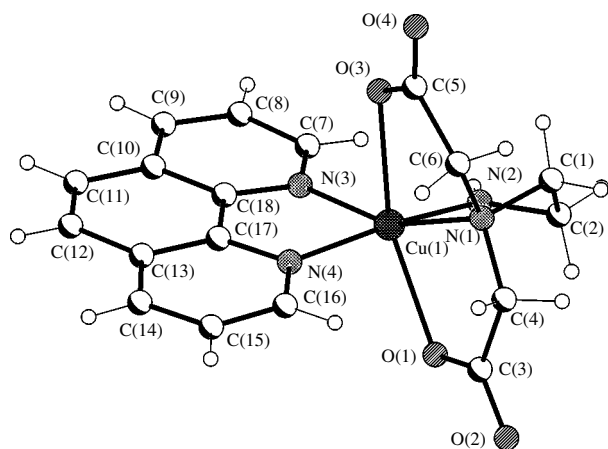
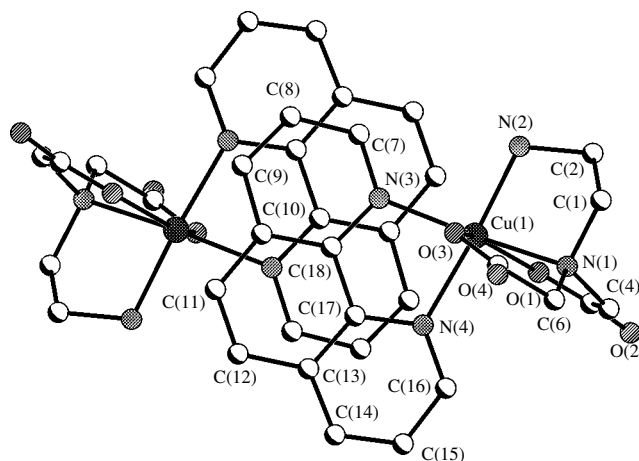
**Fig. 1.** Structure of molecular complex **I**.**Fig. 2.** Dimer associates formed through the overlapping of *Phen* molecules.

Table 2. Geometric parameters of hydrogen bonds in the structure of compound **I**

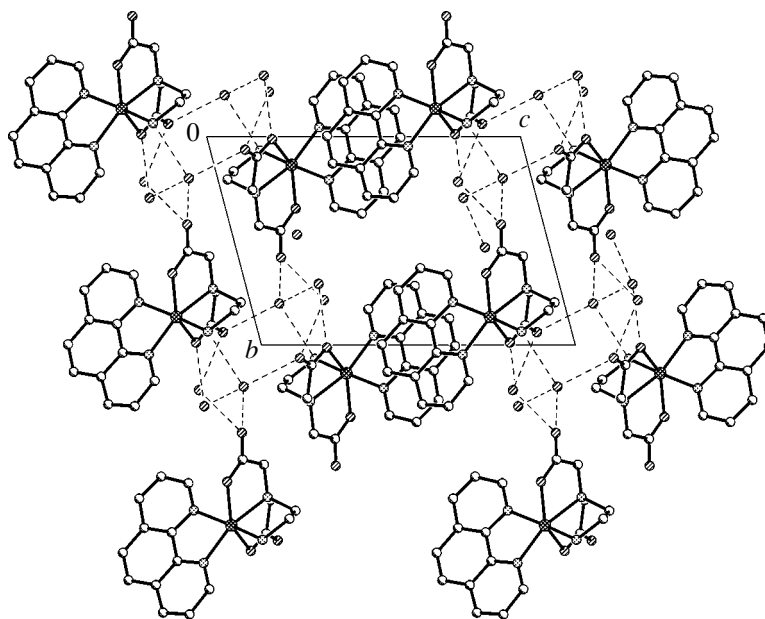
<i>D</i> –H... <i>A</i> bond	Distances, Å			$\angle DHA$, deg	Position of atom <i>A</i>
	<i>D</i> ... <i>A</i>	<i>D</i> –H	H... <i>A</i>		
O(<i>w</i> 1)–H(1 <i>w</i> 1)...O(4)	2.776(3)	0.83(4)	1.95(4)	176(4)	<i>x</i> , <i>y</i> , <i>z</i>
O(<i>w</i> 1)–H(2 <i>w</i> 1)...O(2)	2.756(3)	0.64(4)	2.13(4)	166(4)	– <i>x</i> , 1 – <i>y</i> , 2 – <i>z</i>
O(<i>w</i> 2)–H(1 <i>w</i> 2)...O(2)	2.834(4)	0.85(4)	2.01(4)	164(5)	<i>x</i> , <i>y</i> , <i>z</i>
O(<i>w</i> 2)–H(2 <i>w</i> 2)...O(4)	2.899(4)	0.82(6)	2.10(6)	166(6)	<i>x</i> + 1, <i>y</i> – 1, <i>z</i>
O(<i>w</i> 3)–H(1 <i>w</i> 3)...O(3)	2.831(4)	0.69(6)	2.20(6)	153(6)	<i>x</i> , <i>y</i> , <i>z</i>
O(<i>w</i> 3)–H(2 <i>w</i> 3)...O(<i>w</i> 1)	2.808(5)	0.75(7)	2.07(7)	167(7)	– <i>x</i> , 2 – <i>y</i> , 2 – <i>z</i>
O(<i>w</i> 4)–H(1 <i>w</i> 4)...O(<i>w</i> 3)	2.781(3)	0.95(6)	1.87(6)	160(5)	<i>x</i> + 1, <i>y</i> – 1, <i>z</i>
O(<i>w</i> 4)–H(2 <i>w</i> 4)...O(2)	3.127(4)	0.83(6)	2.33(6)	159(5)	<i>x</i> , <i>y</i> , <i>z</i>
N(2)–H(2N2)...O(<i>w</i> 1)	2.949(4)	0.84(4)	2.13(4)	166(4)	– <i>x</i> , 2 – <i>y</i> , 2 – <i>z</i>

The bond lengths and angles are listed in Table 1. The CIF file has been deposited with the Cambridge Structural Database (CCDC no. 235802).

RESULTS AND DISCUSSION

The structural units of crystal **I** are [Cu(*Aeida*)(*Phen*)] molecular complexes and crystallization water molecules. The coordination polyhedron of the copper atom is an elongated tetragonal bipyramid (4 + 2), whose base is formed by four nitrogen atoms of the *Aeida* and *Phen* ligands and in which the axial positions are occupied by oxygen atoms of the acetate groups. Thus, the carboxyl groups of the *Aeida* ligand occupy mutually *trans* positions (Fig. 1). This arrangement is responsible for the considerable deviation of

the O(1)–Cu–O(3) angle [148.8(8)°] from 180°. The coordination of the tetradentate chelate *Aeida* ligand to the metal atom results in the closure of three five-membered metallocycles, namely, one CuN₂C₂ and two CuONC₂ metallocycles. The bidentate chelate *Phen* ligand and the copper atom form the CuN₂C₂ five-membered ring. It should be noted that the lengths of two Cu–N(*Aeida*) bonds differ significantly [Cu–N(1), 2.150(2) Å; Cu–N(2), 1.988(2) Å]. The mean Cu–N(*Phen*) bond length is equal to 2.042(2) Å, and the Cu–O distances are 2.264(2) and 2.426(2) Å. Note also that, unlike compound **I**, the related bipyramidal complexes [Cu(*Apida*)(*Phen*)] (**II**) [3], [Cu(*Heida*)(*Phen*)] [1], [Cu(*Heida*)(*Bipy*)] [2], and [Cu(*Heida*)(*Im*)₂] [2] (where *Apida* is the *N*-(3-aminopropyl)iminodiacetate ion and *Heida* is the *N*-(2-hydroxyethyl)iminodiacetate

**Fig. 3.** Columns of dimer supramolecular ensembles and channels occupied by H₂O molecules.

ion) contain the carboxyl groups in mutually *cis* positions.

In crystal **I**, the complexes are joined into compact centrosymmetric dimer associates involved in a strong π - π stacking interaction due to the overlapping of *Phen* molecules (Fig. 2). The interplanar spacing between the *Phen* ligands is equal to 3.54 Å, and the Cu...Cu distance between the central atoms of the complexes is 7.02 Å.

In a similar manner, the dimers are packed into columns aligned along the *a* axis. However, in this case, the π - π stacking interaction between the dimers is less efficient because the *Phen* ligands of different dimers overlap to a significantly lesser extent and, hence, the interplanar spacing is equal to only 3.61 Å. The Cu...Cu distance between the nearest neighbor dimers is 9.17 Å.

In the supramolecular ensemble, the dimers are linked by hydrogen bonds (Table 2) involving crystallization water molecules (thus strengthening the ensemble), which are located along channels formed by four columns of supramolecular ensembles (Fig. 3).

The structures of compounds **I** and **II** are similar to each other in the mode of formation of dimers and supramolecular ensembles, as well as in the function of the aqua component of the crystal. However, these structures differ in the mode of complex formation. For example, in compound **I**, the acetate groups occupy

mutually *trans* positions. In compound **II**, the acetate groups are located in mutually *cis* positions and N atoms of the propionediamine and phenanthroline metallocycles serve as their *trans* partners. Moreover, in **I**, all H₂O molecules are bonded to the terminal O atoms of the complexes, whereas in **II**, the additional (compared to **I**), fifth H₂O molecule participates in hydrogen bonding only with H₂O molecules, thus forming a more complex structure of the aqua system.

REFERENCES

1. O. P. Gladkikh, A. L. Poznyak, T. N. Polynova, and M. A. Porai-Koshits, *Koord. Khim.* **23** (3), 181 (1997).
2. I. N. Polyakova, A. L. Poznyak, and V. S. Sergienko, *Zh. Neorg. Khim.* **46** (4), 633 (2001).
3. A. S. Antsyshkina, G. G. Sadikov, A. L. Poznyak, *et al.*, *Zh. Neorg. Khim.* **47** (6), 924 (2002).
4. G. M. Sheldrick, *SHELXS86: Program for the Solution of Crystal Structures* (Univ. of Göttingen, Germany, 1986).
5. G. M. Sheldrick, *SHELXL93. Program for the Refinement of Crystal Structures* (Univ. of Göttingen, Germany, 1993).

Translated by I. Polyakova

STRUCTURE
OF ORGANIC COMPOUNDS

X-ray Mapping in Heterocyclic Design:
16. X-ray Diffraction Study of 1-(4-Chlorophenacyl)-4-Methyl-
1,5,6,7-Tetrahydro-2H-Cyclopenta[*b*]pyridin-2-one

D. V. Albov, V. B. Rybakov, E. V. Babaev, and L. A. Aslanov

Faculty of Chemistry, Moscow State University, Leninskie gory, Moscow, 119992 Russia

e-mail: albov@biocryst.phys.msu.su

Received September 24, 2004

Abstract—The structure of 1-(4-chlorophenacyl)-4-methyl-1,5,6,7-tetrahydro-2H-cyclopenta[*b*]pyridin-2-one is studied using single-crystal X-ray diffraction. The structure ($a = 37.006(8)$ Å, $b = 8.967(3)$ Å, $c = 27.911(3)$ Å, $\beta = 96.52(2)^\circ$, $Z = 24$, space group $P2_1/c$) is solved by direct methods and refined to $R_1 = 0.0608$ and $wR_2 = 0.1170$. Six crystallographically independent molecules differ in the dihedral angle between the phenyl and heterocycle planes. The formation of Cl...Cl aggregates is discussed. © 2005 Pleiades Publishing, Inc.

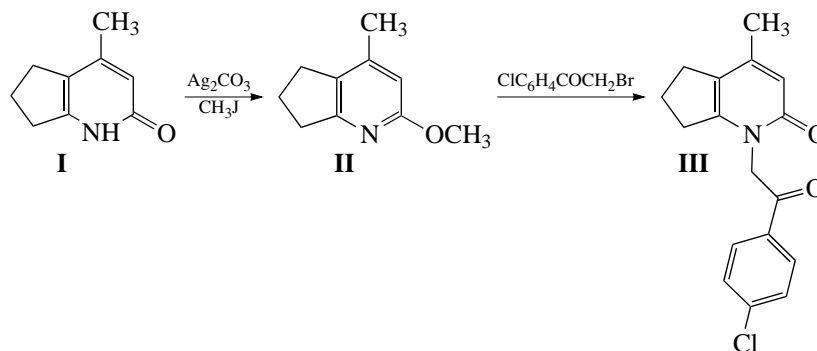
INTRODUCTION

This study continues a series of structural investigations of heterocyclic compounds that are able to undergo different transformations, including cyclization reactions [1–10]. As was done in our previous works, we perform the step-by-step structure determination of all the intermediates and final products of multistage cyclization reactions and rearrangements. In particular, substituted pyridones are characterized by a high reactivity and, therefore, serve as objects of interest in our investigations. In this work, we determined the structure of 1-(4-chlorophenacyl)-4-methyl-1,5,6,7-

tetrahydro-2H-cyclopenta[*b*]pyridin-2-one. Data on the molecular and crystal structure of this compound are not available in the Cambridge Structural Database (version 11.03) [11].

EXPERIMENTAL TECHNIQUE

The initial compound **I** was prepared and studied earlier in [2]. 1-(4-Chlorophenacyl)-4-methyl-1,5,6,7-tetrahydro-2H-cyclopenta[*b*]pyridin-2-one (**III**) was synthesized according to the procedure developed earlier in [3]:



The intermediate product **II** was a liquid. Its structure was confirmed by ^1H NMR spectroscopy. The ^1H NMR spectra were recorded on a Bruker AM-360 spectrometer (field strength, 8.46 T; operating frequency, 360.14 MHz for protons; $\text{DMSO}-d_6$; internal standard, TMS). The signals in the NMR spectra were assigned taking into account the data available in the literature. The atomic numbering in both compounds corresponds

to that used in Fig. 1 (see below). For compound **II** (δ , ppm): 2.12 [m, 2H, C(7)H₂], 2.27 [s, 3H, C(10)H₃], 2.67 [t, 2H, C(6)H₂], 2.86 [t, 2H, C(8)H₂], 3.65 [s, 3H, OCH₃], 6.09 [s, 1H, C(3)H]. For compound **III** (δ , ppm): 2.10 [m, 2H, C(7)H₂], 2.15 [s, 3H, C(10)H₃], 2.75 [m, 4H, C(6)H₂ + C(8)H₂], 5.34 [s, 2H, C(11)H₂], 6.03 [s, 1H, C(3)H], 7.55, 8.07 (dd, 4H, Ar).

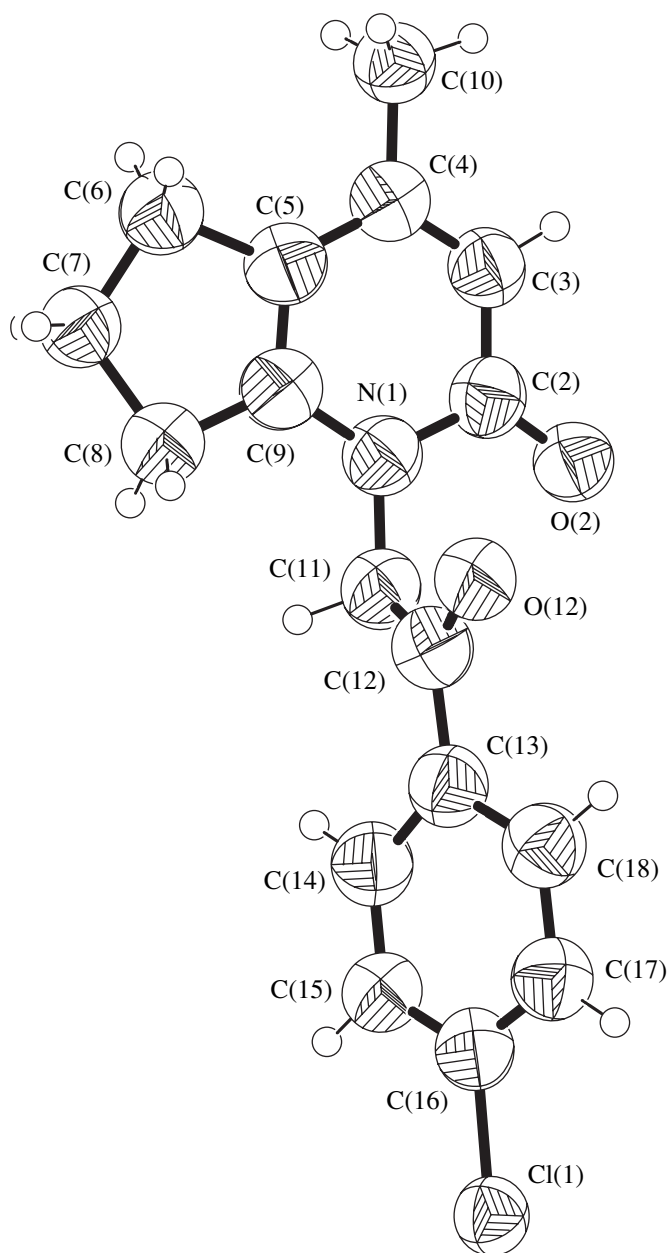


Fig. 1. Molecular structure and atomic numbering for compound **III**.

The experimental intensities of diffraction reflections were obtained for compound **III** on a CAD4 diffractometer [12] ($\text{CuK}\alpha$ radiation, graphite monochromator, ω scan mode) at room temperature. The unit cell parameters were determined and refined using 25 reflections in the θ range 22° – 25° . The main experimental parameters and crystal data for compound **III** are summarized in Table 1. No absorption correction was introduced because of the small linear absorption coefficient of the compound under investigation and the small sizes of its crystals. The primary processing of the experimental data set was performed with the

Table 1. Main crystal data, details of the X-ray diffraction experiment, and refinement parameters for the structure of compound **III**

Empirical formula	$\text{C}_{17}\text{H}_{16}\text{NO}_2\text{Cl}$
M	301.76
Crystal system	Monoclinic
Space group, Z	$P2_1/c$, 24
a , Å	37.006(8)
b , Å	8.967(3)
c , Å	27.911(5)
β , deg	96.52(2)
V , Å ³	9202(4)
ρ_{calcd} , g/cm ³	1.307
$\mu(K\alpha)$, mm ⁻¹	2.333
θ range, deg	1.20–69.99
h, k, l index range	$-44 \leq h \leq 45, 0 \leq k \leq 10, 0 \leq l \leq 34$
Crystal size, mm	$0.22 \times 0.20 \times 0.18$
Number of reflections measured	17437
Number of unique reflections	17437
Number of reflections with $I \geq 2\sigma(I)$	15846
Number of reflections in the refinement/Number of parameters refined	17437/1142
S	1.408
R_1/wR_2 [$I \geq 2\sigma(I)$]	0.0608/0.1170
$\Delta\rho_{\text{max}}/\Delta\rho_{\text{min}}$, e/Å ³	0.384/–0.332

WinGX98 program package [13]. All the subsequent calculations were carried out with the SHELX97 program package [14]. The crystal structure was solved by direct methods. All the non-hydrogen atoms were refined in the anisotropic approximation. The hydrogen atoms were introduced into the calculated positions and refined in the isotropic approximation. The linear molecular parameters were averaged over all the crystallographically independent molecules; therefore, only one set of interatomic distances and angles is given in Tables 2 and 3, respectively. The crystal data for compound **III** have been deposited with the Cambridge Structural Database (deposition no. 268723). The molecular structure of compound **III** with the atoms depicted as thermal ellipsoids and the atomic numbering are shown in Fig. 1, which was drawn using the ORTEP program [15]. The arrangement of molecules in the asymmetric part of the unit cell is given in Fig. 2, which was obtained with the PLUTON96 program [16].

RESULTS AND DISCUSSION

Crystals of compound **III** contain six crystallographically independent molecules *A*–*F* (Fig. 2). These molecules differ in the dihedral angles between the

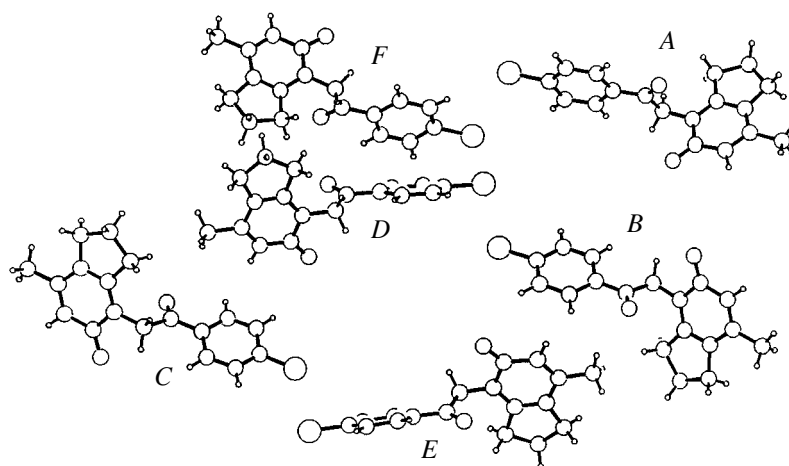


Fig. 2. Spatial arrangement of crystallographically independent molecules of compound **III**.

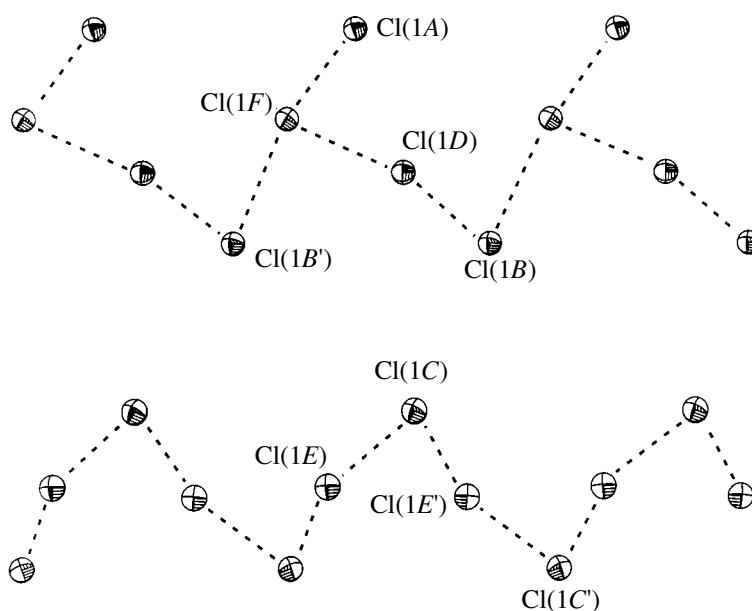


Fig. 3. Structure of *Hal* aggregates in the crystal of compound **III**.

phenyl and heterocycle planes. The dihedral angles are equal to $88.05(4)^\circ$, $66.58(4)^\circ$, $65.72(4)^\circ$, $62.21(5)^\circ$, $58.79(5)^\circ$, and $80.39(4)^\circ$, respectively. The large number of independent molecules evoked our interest in the packing. We found that the Cl atoms are located close to one another (Fig. 3). Such contacts have been described in the literature [17–20], and the formation of similar *Hal* aggregates in the compounds with a low halogen content has been explained by the chlorophobic interaction [19]. The Cl...Cl distances in these aggregates amount to 4.3 \AA [20]. In compound **III**, the Cl(1A), Cl(1F), Cl(1D), and Cl(1B) atoms form a cluster chain in which the distances between the neighbor-

ing atoms are equal to $3.889(2)$, $4.350(2)$, and $3.962(2) \text{ \AA}$, respectively. The Cl(1A)...Cl(1F)...Cl(1D) and Cl(1F)...Cl(1D)...Cl(1B) angles are $64.17(8)^\circ$ and $140.02(9)^\circ$, respectively. The shortest Cl(1F)...Cl(1B') distance between the clusters is significantly larger and equal to $5.151(2) \text{ \AA}$. The Cl(1C) and Cl(1E) atoms, together with their symmetrically equivalent atoms Cl(1C') and Cl(1E'), form a zigzag chain along the twofold screw axis. The Cl(1E)...Cl(1C) and Cl(1C)...Cl(1E') distances are equal to $4.125(2)$ and $3.943(2) \text{ \AA}$, respectively; and the Cl(1E)...Cl(1C)...Cl(1E') and Cl(1C)...Cl(1E')...Cl(1C') angles are $68.91(7)^\circ$ and $156.12(9)^\circ$, respectively.

Table 2. Average bond lengths d (Å) in structure of compound **III**

Bond	d	Bond	d
C1(1)–C(16)	1.7435(8)	C(7)–C(8)	1.5408(10)
N(1)–C(9)	1.3631(9)	C(8)–C(9)	1.4734(10)
N(1)–C(2)	1.4178(9)	C(11)–C(12)	1.5188(10)
N(1)–C(11)	1.4510(9)	C(12)–O(12)	1.2273(9)
C(2)–O(2)	1.2484(9)	C(12)–C(13)	1.4758(9)
C(2)–C(3)	1.4207(9)	C(13)–C(14)	1.3878(10)
C(3)–C(4)	1.3498(10)	C(13)–C(18)	1.4077(10)
C(4)–C(5)	1.3924(10)	C(14)–C(15)	1.3760(10)
C(4)–C(10)	1.5095(10)	C(15)–C(16)	1.3496(10)
C(5)–C(9)	1.3456(9)	C(16)–C(17)	1.3696(10)
C(5)–C(6)	1.5071(10)	C(17)–C(18)	1.3794(10)
C(6)–C(7)	1.4904(10)		

Table 3. Selected bond angles ω (deg) in molecule **III**

Angle	ω	Angle	ω
C(9)–N(1)–C(2)	121.78(7)	C(5)–C(9)–C(8)	115.03(7)
C(9)–N(1)–C(11)	121.43(7)	N(1)–C(9)–C(8)	124.42(7)
C(2)–N(1)–C(11)	116.36(7)	N(1)–C(11)–C(12)	112.13(7)
O(2)–C(2)–N(1)	118.88(7)	O(12)–C(12)–C(13)	120.25(7)
O(2)–C(2)–C(3)	126.76(8)	O(12)–C(12)–C(11)	120.57(7)
N(1)–C(2)–C(3)	114.23(7)	C(13)–C(12)–C(11)	118.85(7)
C(4)–C(3)–C(2)	124.05(8)	C(14)–C(13)–C(18)	116.64(7)
C(3)–C(4)–C(5)	117.77(7)	C(14)–C(13)–C(12)	120.83(7)
C(3)–C(4)–C(10)	120.45(8)	C(18)–C(13)–C(12)	122.46(7)
C(5)–C(4)–C(10)	121.49(8)	C(15)–C(14)–C(13)	122.02(8)
C(9)–C(5)–C(4)	121.24(7)	C(16)–C(15)–C(14)	119.54(8)
C(9)–C(5)–C(6)	109.42(7)	C(15)–C(16)–C(17)	121.11(8)
C(4)–C(5)–C(6)	129.16(7)	C(15)–C(16)–Cl(1)	119.65(7)
C(7)–C(6)–C(5)	104.61(6)	C(17)–C(16)–Cl(1)	118.98(6)
C(6)–C(7)–C(8)	109.25(7)	C(16)–C(17)–C(18)	119.75(8)
C(9)–C(8)–C(7)	101.64(6)	C(17)–C(18)–C(13)	120.77(8)
C(5)–C(9)–N(1)	120.54(7)		

In all the molecules, the N(1)–C(9) six-membered ring is planar within 0.036 Å. In molecules *A*, *C*, and *D*, the O(2), C(6), C(7), C(8), C(10), and C(11) atoms lie in the plane of this ring. In molecule *B*, the C(6) atom deviates from the plane by 0.120(2) Å. In molecules *E* and *F*, the C(7) atom deviates by 0.129(3) and 0.200(2) Å, respectively. It is interesting to note that the cyclopentene fragments are actually planar, as is the case in the crystal of compound **I** [2].

Our further studies will concentrate on the reactivity of compound **III** and the X-ray structure analysis of the products obtained.

ACKNOWLEDGMENTS

We acknowledge the support of the Russian Foundation for Basic Research in the payment of the license for using the Cambridge Structural Database, project no. 02-07-90322.

REFERENCES

- D. V. Al'bov, V. B. Rybakov, E. V. Babaev, and L. A. Aslanov, *Kristallografiya* **48** (2), 315 (2003) [*Crystallogr. Rep.* **48** (2), 280 (2003)].
- D. V. Al'bov, O. S. Mazina, V. B. Rybakov, *et al.*, *Kristallografiya* **49** (2), 208 (2004) [*Crystallogr. Rep.* **49** (2), 158 (2004)].
- D. V. Albov, V. B. Rybakov, E. V. Babaev, and L. A. Aslanov, *Kristallografiya* **49** (3), 495 (2004) [*Crystallogr. Rep.* **49** (3), 430 (2004)].
- D. V. Albov, V. B. Rybakov, E. V. Babaev, *et al.*, *Acta Crystallogr. E* **60**, 892 (2004).
- D. V. Albov, V. B. Rybakov, E. V. Babaev, and L. A. Aslanov, *Acta Crystallogr. E* **60**, 894 (2004).
- D. V. Albov, V. B. Rybakov, E. V. Babaev, and L. A. Aslanov, *Acta Crystallogr. E* **60**, 922 (2004).
- D. V. Albov, V. B. Rybakov, E. V. Babaev, and L. A. Aslanov, *Acta Crystallogr. E* **60**, 1096 (2004).
- D. V. Albov, V. B. Rybakov, E. V. Babaev, and L. A. Aslanov, *Acta Crystallogr. E* **60**, 1098 (2004).
- D. V. Albov, V. B. Rybakov, E. V. Babaev, and L. A. Aslanov, *Acta Crystallogr. E* **60**, 1219 (2004).
- D. V. Albov, V. B. Rybakov, E. V. Babaev, and L. A. Aslanov, *Acta Crystallogr. E* **60**, 1301 (2004).
- F. H. Allen, *Acta Crystallogr., Sect. B: Struct. Sci.* **58**, 380 (2002).
- Enraf–Nonius CAD4 Software: Version 5.0* (Enraf–Nonius, Delft, The Netherlands, 1989).
- L. J. Farrugia, *WinGX98: X-ray Crystallographic Programs for Windows* (Univ. of Glasgow, UK, 1998).
- G. M. Sheldrick, *SHELXS97 and SHELXL97* (Univ. of Göttingen, Germany, 1997).
- M. N. Burnett and C. K. Johnson, *ORTEP: Report ORNL 6895* (Oak Ridge National Laboratory, Tennessee, USA, 1996).
- A. L. Spek, *PLUTON96: Molecular Graphics Program* (Univ. of Utrecht, The Netherlands, 1996).
- P. M. Zorkiĭ, *Russ. Khim. Zh.* **40** (3), 5 (1996).
- O. V. Grineva and P. M. Zorkiĭ, *Zh. Strukt. Khim.* **43** (6), 1073 (2002).
- O. V. Grineva and P. M. Zorkiĭ, *Zh. Fiz. Khim.* **72** (4), 714 (1998).
- O. V. Grineva and P. M. Zorkiĭ, *Zh. Fiz. Khim.* **74** (11), 1937 (2000).

Translated by I. Polyakova

STRUCTURE OF MACROMOLECULAR COMPOUNDS

Formation of Langmuir–Blodgett Films in Solutions of Comblike Polymers

N. D. Stepina*, V. V. Klechkovskaya*, L. G. Yanusova*, L. A. Feigin*, A. L. Tolstikhina*,
V. P. Sklizkova**, A. K. Khripunov**, Yu. G. Baklagina**, and V. V. Kudryavtsev**

* *Shubnikov Institute of Crystallography, Russian Academy of Sciences,
Leninskii pr. 59, Moscow, 119333 Russia
e-mail: stepina@ns.crys.ras.ru*

** *Institute of Macromolecular Compounds, Russian Academy of Sciences,
Bol'shoi pr. 31, St. Petersburg, 199004 Russia*

Received December 22, 2004

Abstract—The structures have been analyzed of the monolayers of comblike precursor polymers of polyimides and mixed cellulose esters formed at the water/air interface and of the Langmuir–Blodgett films obtained by transfer of these condensed monolayers onto solid substrates. The important factors that ensure the structure control and supramolecular organization of these monolayers and films are established. © 2005 *Pleiades Publishing, Inc.*

INTRODUCTION

Langmuir–Blodgett films are molecular ensembles consisting of monolayers of amphiphilic molecules successively transferred onto a solid substrate from the water/air interface. The molecules consisting of hydrophilic and hydrophobic parts are organized in a certain way on the surface of the aqueous subphase. Under a certain surface pressure created by a movable barrier in a Langmuir trough, it is possible to form a condensed monolayer and then transfer it onto a solid substrate [1]. The use of the Langmuir–Blodgett technique for producing thermally and chemically resistant ultrathin (nanometer-thick) polymer films ensures these films' wide use in modern membrane technologies—micro-, nano-, and optoelectronics—and other fields [1, 2]. The introduction of various substituents into the backbone or side chains of polymers allows one to vary over wide ranges the photosensitive, nonlinear optical, and electrical properties of the initial polymer.

It is obvious that optimization of the properties of ultrathin polymer films obtained by the Langmuir–Blodgett technique requires the detailed knowledge of the macromolecular and supramolecular structure because, in a number of instances, the useful properties of these films are irreproducible and may be deteriorated by the formation of a defect structure [3]. Amphiphilic polymers that can form a monolayer on the subphase are produced by grafting of the polymer backbone with side groups. The specific feature of thus obtained macromolecules (comblike polymers) is the combination in one chain of portions having different polarities, which increases the ability of macromolecules for ordering and crystallization via inter- and intramolecular interactions [4].

Below, we generalize the results of our studies of the conditions necessary for the formation of Langmuir–Blodgett films based on comblike polymers: polymer precursors of polyimides (PI) and cellulose derivatives [5–13]. The focus is on the estimation of the effects of the macrochain structure, solvent nature, and number and structure of side groups on the structure of the Langmuir–Blodgett films prepared. All the successive stages of producing Langmuir–Blodgett films (from preparation of solutions deposited onto the subphase in a Langmuir trough up to the formation of multilayer Langmuir–Blodgett films) are analyzed. The complicated structural organization of Langmuir–Blodgett polymer films, i.e., their small thicknesses (5- to 25-Å-thick monolayers); possible formation of various defects during packing of backbone and side chains; and the specific characteristics of the interaction of the X-ray and electron radiation with organic materials resulted in the development of the methods increasing the contrast of scattering from multilayer organic films. The film structure was studied by a complex of methods including X-ray and electron diffraction, X-ray reflectometry, and atomic force microscopy (AFM) [6, 10].

EXPERIMENTAL

The objects were polymer precursors of polyimides (PI): long-chain alkylammonium polyamic acid (PAA) salts, long-chain PAA esters, the corresponding polyimides [5, 10, 11, 13], and mixed cellulose esters [7, 9, 12]. The comblike polymers were synthesized on the basis of the following two approaches. The PAA and cellulose esters were obtained by multistage synthesis. The salts were obtained by neutralization with the tertiary amine of preliminarily synthesized polyamic acids

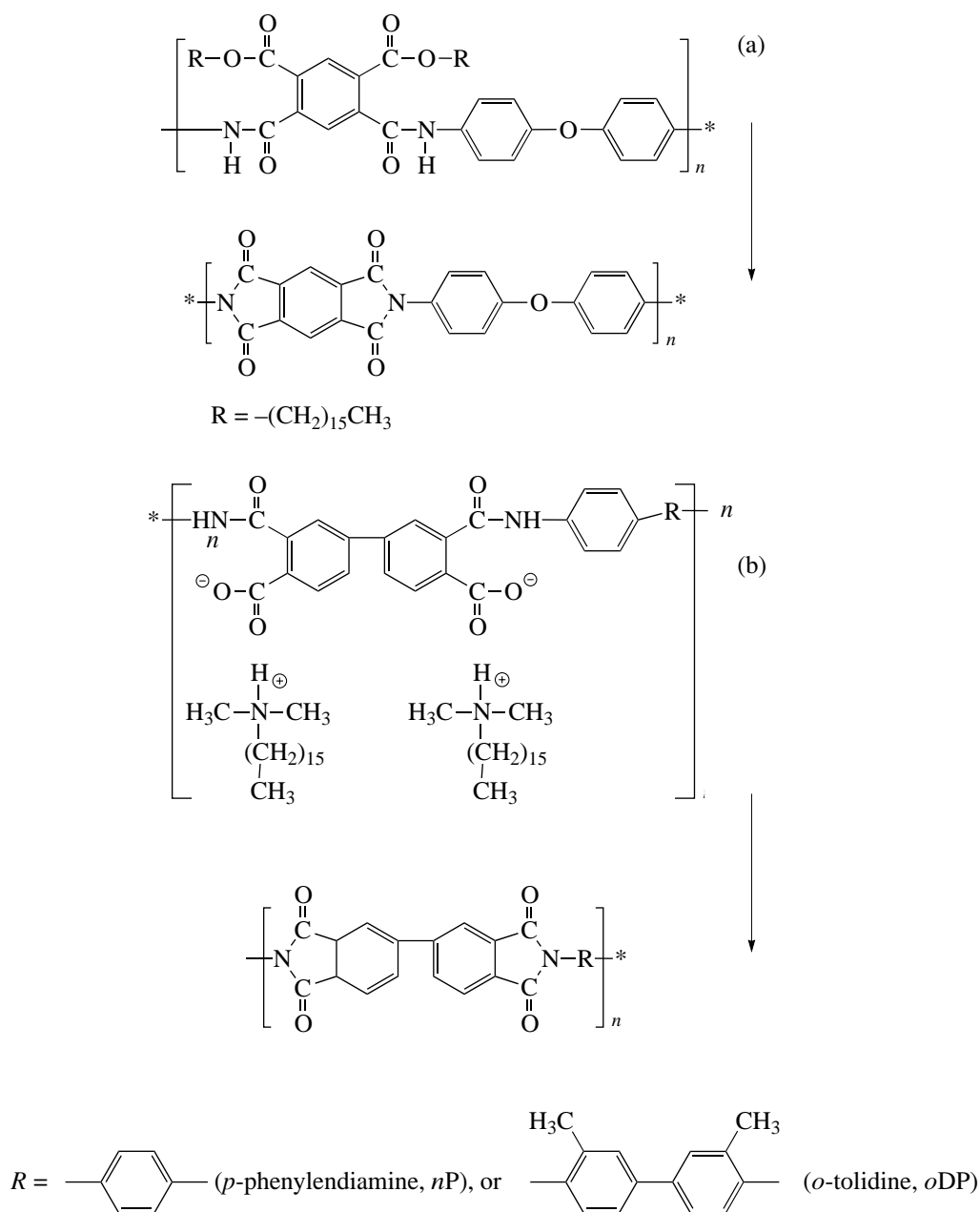


Fig. 1. Schematics illustrating synthesis of polyimides: (a) PM and (b) DP-P and DP-T.

directly before transferring the polymer onto the substrate. To obtain a PI film, the Langmuir–Blodgett film of a polymer precursor was subjected to thermal imidization [11].

We studied the following objects:

1. Cetyl ester of polyamic acid based on pyromellitic dianhydride and 4,4'-diaminodiphenyl ether (hereafter referred to as PAA PM- C_{16} ester) and the respective polyimide (PI PM) (Fig. 1a).

2. Amphiphilic alkylammonium salts of polyamic acid based on 3,3',4,4'-diphenyltetracarboxylic acid

and *p*-phenyldiamine (PAA DP-*nP*) or *o*-tolidine (PAA DP-*oT*) with *N,N*-dimethylhexadecylamine (C_{16}), hereafter referred to as PAA DP-P- C_{16} and PAA DP-T- C_{16} , and the respective polyimides PI (Fig. 1b).

3. Homologous series of cellulose acetomyristate (CAM) with the substitution degrees of 290/10, 275/25, 250/50, 200/100, 150/150, 100/200, 50/250, and 10/290 (where the numerator indicates the degree of substitution of hydroxyl groups by the myristic acid and the denominator indicates the degree of substitution of hydroxyl groups by the acetic acid); cellulose

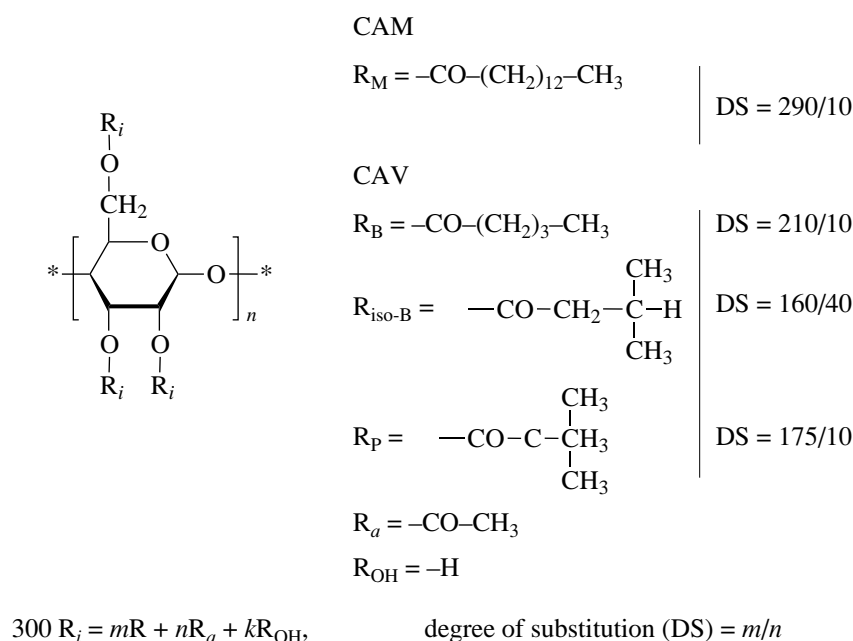


Fig. 2. Structural formulas of mixed cellulose esters CAM and CAV.

acetoveralates based on the structural isomers of valeric acid (*n*-valeric and *iso*-valeric acids, CANV and CAiV, respectively) and pivalic acid (CAP) with the degrees of substitution of 210/10 in CANV, 160/40 in CAiV, and 175/10 in CAP (where the numerator indicates the degree of substitution of hydroxyl groups in isomers of the valeric acid and the denominator indicates the degree of substitution of hydroxyl groups of acetic acid (Fig. 2).

Langmuir monolayers and multilayer films were prepared and studied in a Joyce-Loebl Langmuir Trough 4. The behavior of monolayers on the subphase surface was controlled using π -A isotherms (the curves of surface pressure versus area occupied by a repeat polymer unit in a monolayer). The subphase was triply distilled water with a pH of 6.4. Langmuir-Blodgett films were prepared by the techniques of horizontal and vertical lift.

The X-ray diffraction studies were performed on an Amur-K diffractometer with a position-sensitive detector with an angular resolution of 0.02° ($\text{CuK}\alpha$ radiation, Ni filter, 40 kV voltage). The arrangement of molecules in the plane of the monolayer and in the bulk of Langmuir-Blodgett films was studied by methods of transmission and reflection electron diffraction in an EMR-102 electron diffraction camera. The surface structure of the films was studied in P4-SPM-MDT and P47-SPM-MDT scanning atomic force microscopes (NT-MDT, Moscow) in air both in contact and resonance modes. The maximum scanning area was $4 \times 4 \mu\text{m}$.

RESULTS AND DISCUSSION

As a rule, polyimide macrofilms are prepared from solutions of polyamic acid (PAA) in amide solvents. However, we failed to obtain stable monolayers on the subphase from the solutions of polyimide polymer precursors. Stable Langmuir PAA monolayers on the water surface were obtained only with the aid of mixed solvents such as dimethylacetamide (DMAA)-benzene in the volume ratio 1 : 1 and N-methylpyrrolidone (MP)-benzene in the volume ratio 1 : 1. In this case, the area per repeating unit *A* evaluated by extrapolating the π -A isotherm to the zeroth surface pressure π was equal to 32 and 56 \AA^2 for PAA DP-P and PAA DP-T, respectively, and did not depend on the solvent nature and the time of keeping a monolayer before its compression. However, we failed to transfer the monolayers thus obtained onto a solid substrate. Therefore, in our study we used various amphiphilic PAA derivatives forming stable Langmuir monolayers that could readily be transferred onto solid substrates.

Analysis of the compression isotherms of the PAA DP-P- C_{16} salt shows that the area *A* per repeating unit in a monolayer depends on the solvent nature (Fig. 3). In the transition from the DMAA-benzene solvent to the MP-benzene solvent, the *A* area decreased from 140 to 120 \AA^2 , which could be caused by the deterioration of the solvent quality and an increase in macromolecule aggregation [14]. Analysis of the compression isotherms for monolayers of the PAA DP-T- C_{16} salt also confirms a decrease in the area of the repeating unit from 180 to 140 \AA^2 with the change of the solvent from DMAA-benzene to the MP-benzene.

It was shown [15] that the process of self-organization of the precursor polymers of polyimides in diluted solutions also depended on the solvent quality. In the case of MP-based solvent, macromolecule aggregation in the solution is more pronounced than in the case of the DMAA-based solvent. The effects observed are explained by the mechanisms of intermolecular interactions between the main and side fragments of macromolecules with the participation of the molecules of the mixed solvent. In this case, the primary order in the solution can considerably affect the structure and physical–chemical properties of the polymer material [4]. These data on the structural state of the polymer in the solution are consistent with the X-ray diffraction and AFM data obtained for these films. The small-angle X-ray scattering curves of the Langmuir–Blodgett films of the PAA DP-T-C₁₆ salt prepared from the DMAA–benzene solution (as opposed to the similar curves from the Langmuir–Blodgett films prepared from MP–benzene solution) show Kiessig oscillations, which indicate that the films thus obtained have a smoother surface [11]. The topographs from the surface of the PAA DP-T-C₁₆ films obtained by horizontal lift (Fig. 4) show that the surface of the polymer precursor film prepared with the use of the DMAA–benzene solvent is rather smooth. The roughness height ranges within 6–9 nm, whereas the roughness height of the surface of the precursor polymer prepared with the use of the MP–benzene solvent is much larger, 70 nm [10]. It is seen from Fig. 4 that the transverse size of the aggregates in the films obtained with the use of different solvents are considerably different. It should also be indicated that the monolayers of polyimide precursors obtained with the use of the MP–benzene solvent can be transferred onto the substrate only by horizontal lift.

With further compression of a monolayer on the subphase, the macromolecular packing becomes denser. Depending on the structure and chemical composition of the polymer chain, the contacting macrochains may form bonds facilitating the formation of an ordered structure. In this case, structure formation is essentially dependent on the time of keeping of the monolayer on the aqueous subphase prior to its compression when natural molecular diffusion at the water surface may give rise to the formation of stable hydrogen bonds. Thus, in the monolayers of the PAA PM-C₁₆ ether [5, 13], compression results in the formation of a stable intermolecular order because of the formation of rather large ordered domains and a network of hydrogen bonds between the backbones. On the contrary, the monolayers of the PAA DP-T-C₁₆ salt, where the diamine component of the polymer chain has two methyl groups hindering the formation of a dense packing of macrochains, form a less ordered structure [11].

Hydrophobic side chains also play an important role in the organization of a Langmuir monolayer on the subphase. These chains influence the orientation of macrochains at the interface and the degree of their

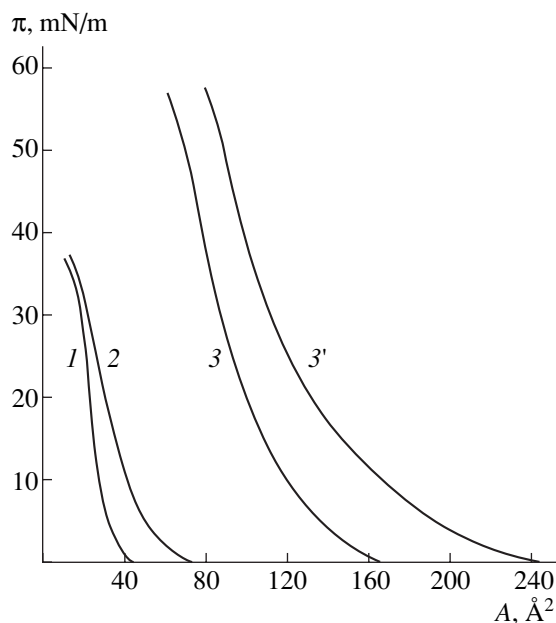


Fig. 3. π - A isotherms from the monolayers of PAA DP-P (curve 1), dimethylhexadecyl amine (C₁₆) (curve 2), and PAA DP-P-C₁₆ salt in MP–benzene (curve 3) and in DMAA–benzene (curve 3') solvents.

interactions because intra- and intermolecular contacts of the side chains also stabilize the structural order. The dense packing of hydrophobic side groups increases the polymer-chain stiffness, promotes the ordered arrangement of macromolecules on the subphase surface and, thus, facilitates the formation of a network of hydrogen bonds between polymer chains in the condensed monolayer, which, in turn, promotes the formation of domains having a mesomorphic structure. Such a close-packed layer may readily be transferred onto the substrate, whereas the surface of the deposited layer becomes smoother. If a monolayer is transferred onto the substrate by vertical lift (each following layer is formed at the subphase/monolayer interface), the structure of a floating monolayer with a certain degree of freedom can be accommodated to the structure of the monolayer already existing on the substrate. Thus, in the PAA PM-C₁₆ polyimide ester precursor, two-dimensional unit-cell fragments are formed, which, in the process of subsequent thermal imidization, facilitate the formation of three-dimensional crystal packings in the Langmuir–Blodgett polyimide film (Fig. 5) [5, 13]. The formation of stable monolayers and the uniform structure of the final Langmuir–Blodgett polyimide film were also formed with an increase of the side-chain length from C₁₀ to C₁₆ in the PAA DP-P- and PAA DP-T-based alkylammonium salts [11].

When preparing Langmuir polymer monolayers, one may also introduce into the solution to be deposited onto the subphase some amphiphilic compounds such as fatty acids or alcohols. To obtain stable ordered PAA

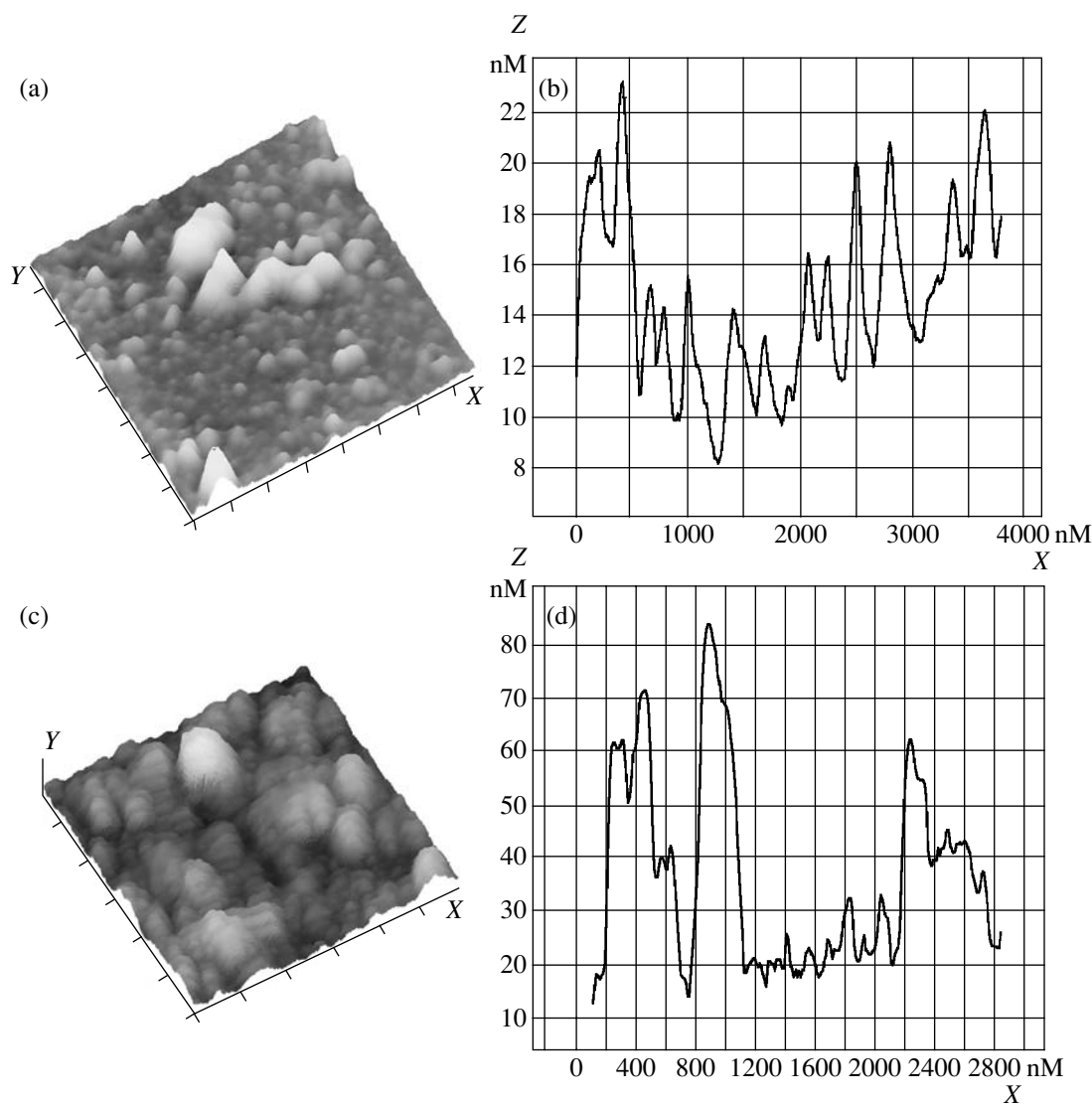


Fig. 4. (a) Topographic image of the surface of the PAA DP-T-C₁₆ polymer precursor prepared with the use of the DMAA–benzene solvent; (b) characteristic surface profile of this film in the direction parallel to the X axis at Y = 700 nm; (c) topographic image of the same film obtained with the use of the MP–benzene solvent; (d) characteristic surface profile of this film in the direction parallel to the X axis at Y = 1000 nm. The scale division along the X and Y axes is 500 nm in (a) and (c).

PM-C₁₆ ester monolayers, we added to the solution to be deposited onto the subphase some cetyl alcohol (in the molar ratio 1 : 1). It was established that, in the formation of a condensed monolayer, cetyl alcohol molecules are incorporated into the space between the side groups attached to the polymer chain by covalent bonds. Thus, the aliphatic comblike layer becomes denser and, as a result, the polymer-chain stiffness increases, thus facilitating the forced orientation of the precursor-polymer segments with respect to the subphase surface. This, in turn, increases the density of macrochain packing in the polymer layer because of the formation of a network of hydrogen bonds (Figs. 6a, 6b). The electron diffraction patterns from the Langmuir–Blodgett films of the polymer precursor have three characteristic diffuse halos with the interplanar

spacings of 5.8–6.2, 3.9–4.1, and 3.2–3.5 Å, which indicate the formation of a stable intermolecular order first in monolayers and, as a result, also in the bilayer.

All the above facts are also characteristic of mixed cellulose esters [7, 9, 12]. The area per repeating unit of a polymer increases after long keeping of the monolayer on the subphase prior to its compression. The respective isotherms depend on the rate of monolayer compression, its initial density, and the length of the chain of the alkyl substituent in a glucoside unit. We believe that this dependence may be explained by conformational rearrangements associated with the macrochain rotation at the air/water interface and ordering of hydrophobic side chains above the subphase. Figure 7a shows the π -A isotherms for the CAM on the subphase

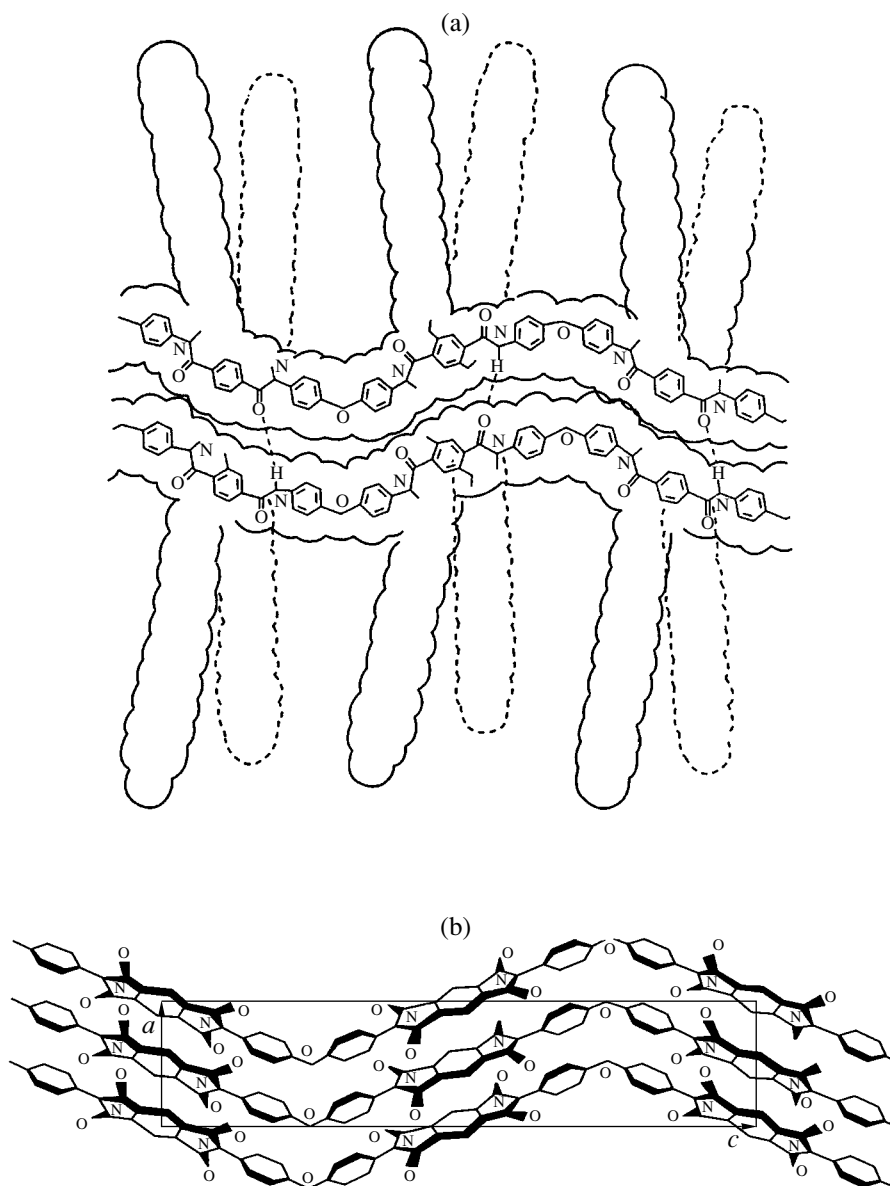


Fig. 5. (a) Illustration of the formation of a bilayer of the polymer precursor PAA PM-C₁₆ ester with hydrogen bonds between the layers. (b) Illustration of the arrangement of molecules in the orthorhombic PI PM unit cell having the parameters $a = 6.31$ Å, $b = 3.97$ Å, and $c = 32.0$ Å and formed in the process of its thermal imidization.

(with a ratio of myristinoyl and acetyl groups of 290/10). Under a surface pressure of about 18 mN/m, a characteristic plateau was formed, which was accompanied by the change of the area per glucoside ring from 106 to 55 Å². The isotherm has three clearly seen regions. In region I (low pressures), the isotherm is fully reversible. In region II, reversibility disappears. Extending a monolayer compressed to 18.5 mN/m and then subjecting it to the compression again, we observed shortening of the isotherm plateau. Then, the curve starts rising at a lower value of the monolayer area (probably, because of the already-formed stable bonds between some macromolecules). In region III,

the secondary compression of the monolayer primarily compressed to 35 mN/m gives rise to disappearance of the plateau and formation of a weak bend instead. The Langmuir–Blodgett CAM-based films form one-dimensional periodic domains along the substrate normal with two different periodicity values. This fact may readily be explained in terms of the conformational polymorphism of CAM chains. Depending on the angle of internal rotation around glucoside bonds, the conformational maps of dimer fragments of cellulose esters show two conformational regions with the energy minimum [9]. These two regions of stable conformational states are predicted theoretically for a number of cellu-

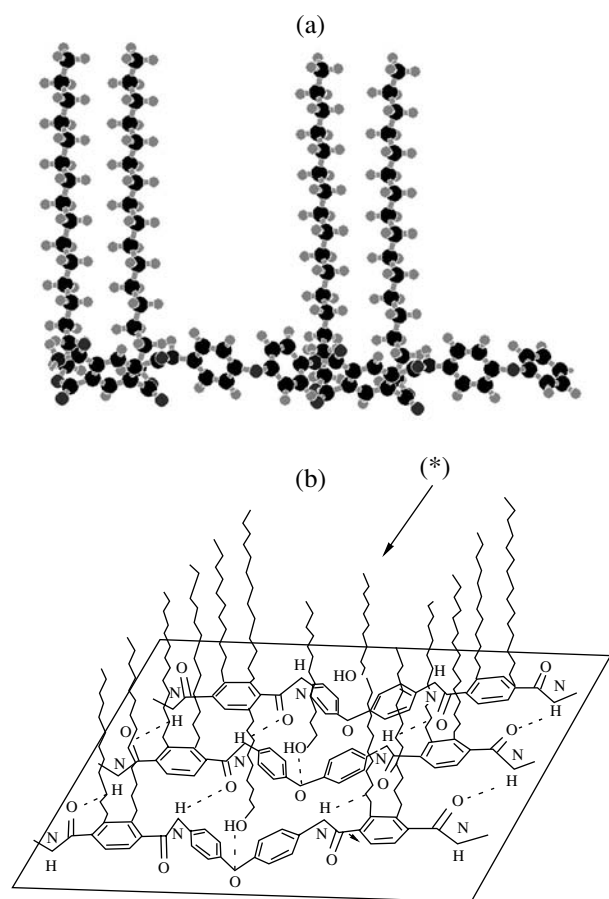


Fig. 6. (a) Model of a dimer in the PAA PI-C₁₆ ester and (b) schematic of formation of intermolecular hydrogen bonds in ordered domains of the monolayer (the asterisk indicates the incorporated cetyl alcohol molecules).

lose esters but still have not been revealed even for the highly oriented fibers that were formed in the process of forced organization of two-dimensional structure of CAM molecules on the water surface.

In this case, an important factor that influences the conformational rearrangements of molecules on the subphase and stabilization of the monolayer during the subsequent compression is the presence of free hydroxyl groups in the glucoside chain which may participate in the formation of hydrogen bonds between the chains.

The influence of the length and structure of hydrophobic side chains on the order of the comblike cellulose-based polymers (Fig. 2) can be evaluated by analyzing the π -A isotherms of the monolayers of mixed CAM esters with long side chains (C₁₄) (Fig. 7a) and three isomers of acetovalerate (hereafter referred to as CAnV, CAiV, and CAP) with short alkyl side chains (C₅) (Fig. 7b). Computer simulation of the CAV and CAM isomers (by the Alchemy-III program) also showed that the area per glucoside unit is essentially dependent on the steric positions of the side groups and

their structure. Electron diffraction data from Langmuir–Blodgett CAV films show that the CAP films are amorphous, whereas the CAnV and CAiV films have mesomorphic structure. Electron diffraction patterns (Fig. 8) show a broad halo, indicating the existence in the films of regions with a mesomorphic structure. The same effect was also observed for macrosamples of a number of CAMs with different degrees of substitution. In the range of the ratio from 50/250 to 10/290, the samples underwent amorphization [9]. Comparison of the transmission electron diffraction patterns from the Langmuir–Blodgett CAnV and CAiV films showed that the structure of multilayer films also depends on the method of monolayer transfer onto the substrate. Thus, the electron diffraction patterns from the films obtained by horizontal lift are characterized by uniform intensity distribution over the diffraction ring, which indicates the isotropic distribution of ordered domains in the Langmuir–Blodgett film plane. The electron diffraction patterns from the films obtained by vertical lift are quite different: the region of reflections along the direction parallel to the substrate motion during monolayer transfer onto the substrate consists of more intense reflections (Fig. 8). The interface periodicity in this direction equals 1.036 Å, which coincides with the length of the repeating unit of the cellulose polymer [9]. Thus, macromolecules in the films prepared by vertical lift acquire the preferable orientation. This is schematically shown in Fig. 9. The phenomenon of forced orientation during transfer by vertical lift was also observed in the Langmuir–Blodgett *iso*-pentylcellulose films [16]. The AFM study revealed the characteristic topographic features of the CAV-film surface [7]. The main elements of the supramolecular structure are the oriented domains having different lengths and the widths ranging from 50 to 300 nm. The length and width of these domains and the character of the domain arrangement on the film surface of all the studied CAV films vary depending on the method of monolayer transfer from the subphase onto the solid substrate. The films obtained by vertical lift show the obvious preferred orientation of the ordered domains parallel to the direction of the substrate motion during monolayer transfer onto the substrate (Figs. 10b and 10d). The films obtained by horizontal lift show no preferable domain orientation (Figs. 10a and 10c). It should also be noted that the roughness of Langmuir–Blodgett films obtained by vertical lift is more pronounced than the roughness of the films prepared by horizontal lift. The above features are weakest in the CAP films with the amorphous structure of the condensed monolayer. In all the cases, the structure of the cellulose ester surfaces is not uniform: the ordered regions are adjacent to less ordered ones, which is also confirmed by the respective electron diffraction data.

The X-ray and electron diffraction data obtained and computer simulation lead to the conclusion that the Y-type structures are formed in all the Langmuir–Blodgett polymer films considered above. However, the

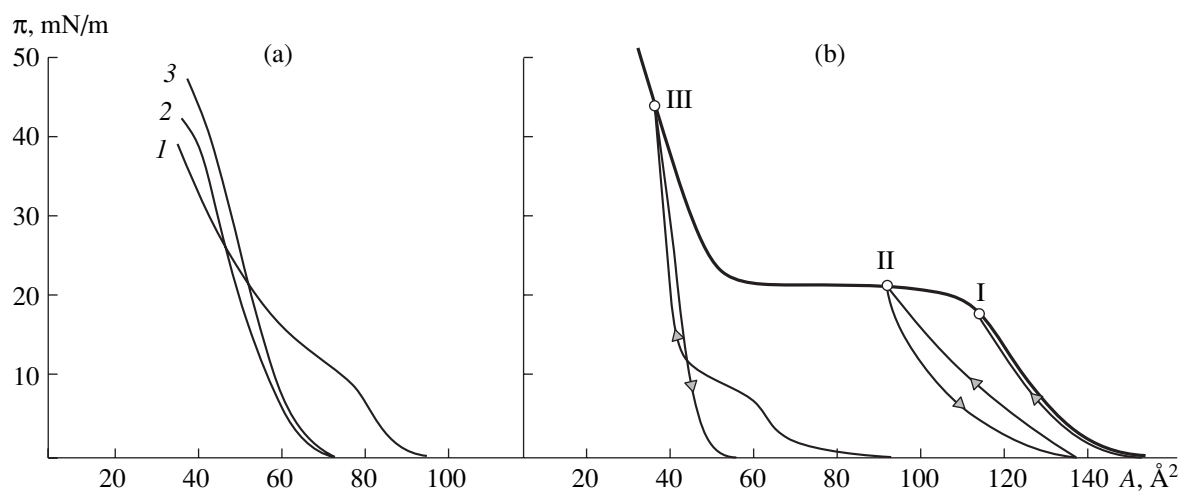


Fig. 7. π - A isotherms of (a) CAM (290/90) and (b) (1) cellulose aceto-*n*-valerate (CA*n*V), (2) cellulose aceto-*iso*-valerate (CA*i*V), and (3) cellulose acetopivalinate (CAP).

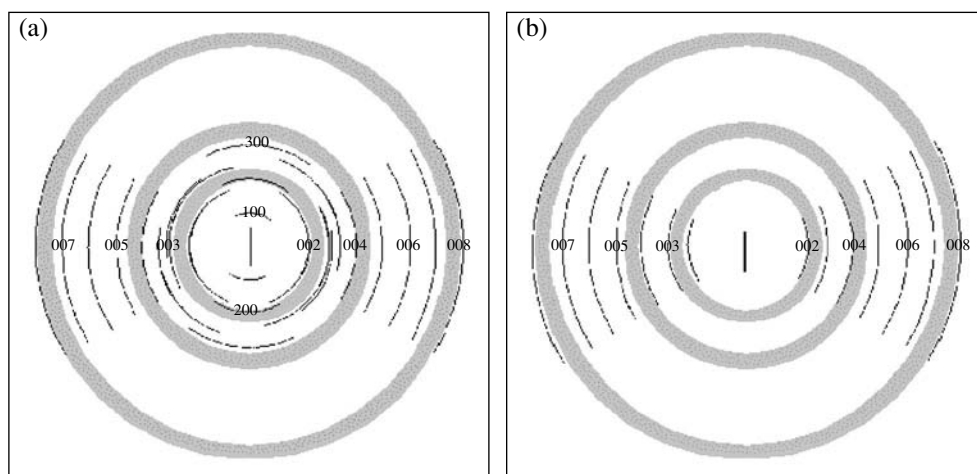


Fig. 8. Schematic transmission electron diffraction patterns from the Langmuir-Blodgett (a) CA*i*V and (b) CA*n*V films obtained by vertical lift. Amorphous halos indicate the formation along with the ordered regions also of a mesomorphic packing of polymer chains.

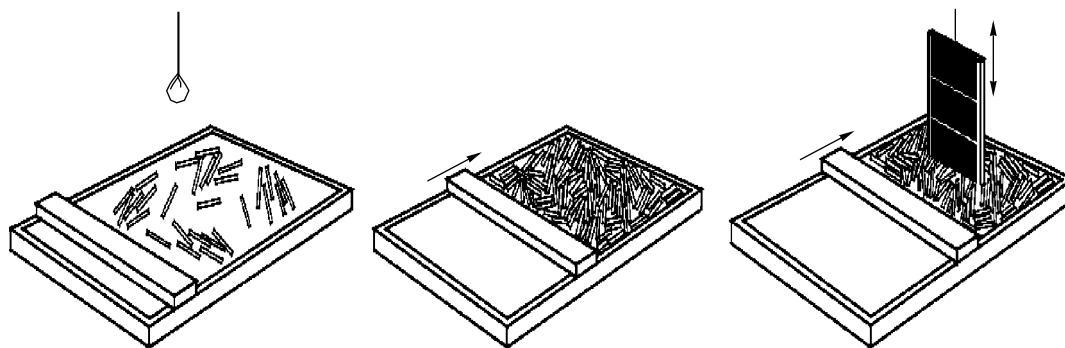


Fig. 9. Schematics illustrating the appearance of forced orientation during transfer of monolayers with stiff chains onto the substrate by vertical lift [16].

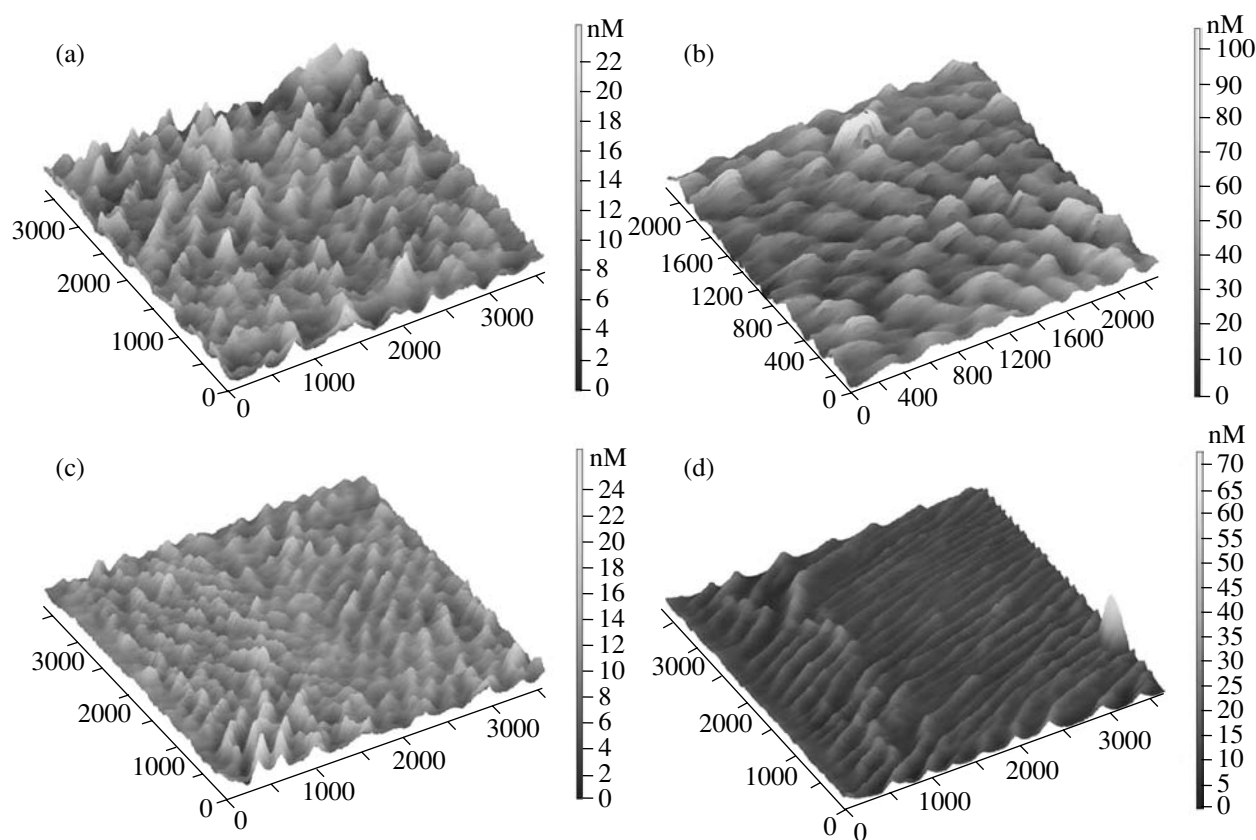


Fig. 10. Topographic images of the surfaces of the Langmuir–Blodgett CAnV and CAiV films obtained by different techniques. (a) CAnV films, horizontal lift, $3600 \times 3600 \text{ nm}^2$ scanning area, scale division along the X and Y axes is 500 nm and that along the Z axis is 100 nm; (b) CAnV films, vertical lift, $2300 \times 2300 \text{ nm}^2$ scanning area, scale division along the X, Y, and Z axes is 100 nm; (c) CAiV films, horizontal lift and (d) CAiV films, vertical lift; $3600 \times 3600 \text{ nm}^2$ scanning area, scale division along the X and Y axes is 500 and along the Z axis is 100 nm.

hydrophobic chains in bilayers may form the contacts either in the butt mode or by interpenetrating one another, depending on the density of the arrangement of the hydrophobic side chains along the backbone and the size of the amphiphilic regions along the polymer chain (Fig. 11). The repetition periods of bilayers are also considerably different. The most important factor in this case is the ratio of the projection of the polymer repeating unit to the area per hydrocarbon side chain. Thus, in the amphiphilic PAA DP-P-C₁₆ polymer precursor with the area per repeating link 140 \AA^2 , the Y-type structure is formed with a layer period of 34 \AA , whereas in the PAA DP-T-C₁₆ polymer precursor having a larger transverse dimension of the repeat unit equal to 180 \AA^2 , the side chains interpenetrate for a larger depth, which is accompanied by a side-chain tilt. The bilayer period in this case equals 27 \AA (Fig. 11b). The introduction of cetyl alcohol promoting an increase in the density of hydrocarbon-tail packing, the bilayer period increases up to 53 \AA (Fig. 11a).

Small-angle X-ray scattering patterns from multilayer Langmuir–Blodgett films are the main instrument for characterization of the order and periodicity of a

layer film. However, because of a low X-ray contrast from polymer films, these patterns often show only one diffuse reflection corresponding to the layer period. The more reliable data on packing of monolayers in a Langmuir–Blodgett film (more reliable data on the layer period) are obtained from superlattices consisting of alternating layers of the polymer under consideration and contrasting layers of the salts of fatty acid. Thus, preparing a superlattice of the PAA MP-C₁₆ ester, we transferred onto the substrate first five cadmium behenate bilayers (*B*) and then seven tetralayers consisting of a polymer precursor (*P*) and a cadmium behenate (*B*) bilayer (Figs. 12a and 12b). The diffraction data from the samples thus obtained contained not only a number of Bragg reflections from the superlattice with the period 102 \AA but also the reflections from the cadmium behenate sublayer with a period of 59 \AA , which, in this case, were used as the reference reflections for evaluating the period of the polymer-precursor bilayer.

Thus, the following conclusions can be drawn:

High molecule stiffness ensures a better contact between molecule segments and the water/air interface

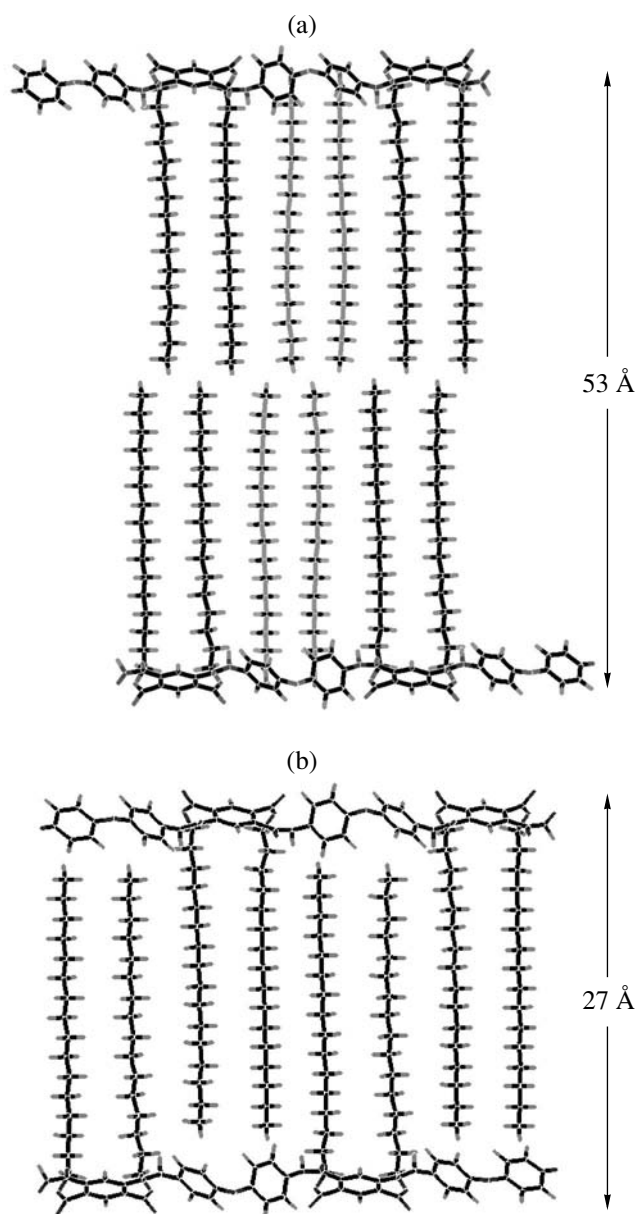


Fig. 11. Packing of bilayers of the PAA DP-T-C₁₆ salt: (a) with addition of cetyl alcohol to the solution in order to increase the density of the packing of hydrocarbon tails and (b) without addition of cetyl alcohol.

without formation of loops (formed in polymers with flexible chains).

The appropriately chosen solvent reduces the aggregation of macromolecules in the solution during the formation of a Langmuir layer of the polymer, which is reflected in the supramolecular structure of the monolayer and allows one to evaluate with a high precision the area per repetition link in the monolayer.

Under the conditions of formation of Langmuir–Blodgett films, the molecular ensembles at the interfaces are formed owing to hydrogen bonding and pos-

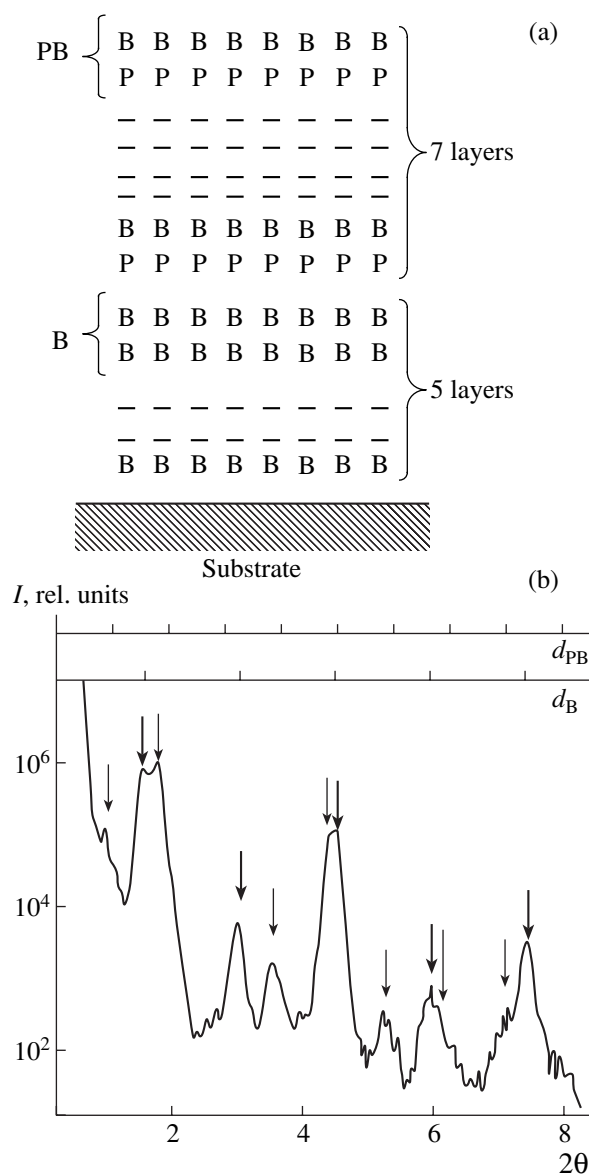


Fig. 12. (a) Illustration of the formation of a superlattice consisting of PAA PM-C₁₆ ester (P) and cadmium behenate (B) bilayers and (b) of the corresponding X-ray small-angle scattering pattern. Thin arrows indicate the reflections formed owing to the bilayer period of the polymer precursor, d_{PB} ; thick arrows, the reflections formed owing to cadmium behenate period d_B .

sible conformational transformations of macrochains. Packing of such rodlike molecules in a compressed monolayer is best described in terms of a two-dimensional liquid-crystal phase [9, 11].

The structure of the hydrophobic component of the monolayer (structure of the hydrocarbon side chains, their number, the methods of their attachment, and their steric arrangement) determines the variety of possible packings of monolayers in Langmuir–Blodgett films; that is, the degree of mutual interpenetration of hydrocarbon chains in a bilayer and their possible tilt. In

other words, the structure determines the repetition period of a bilayer and the degree of film crystallinity.

The possibility of the polymer chains to be oriented in the monolayer plane (the principal axes of rodlike backbones show the preferable orientation parallel to the direction of substrate immersion) allows one to create oriented molecular ensembles.

The use of the Langmuir technology in the studies of comblike polymers may be very useful for solving the important problem of the organization of a supramolecular structure in the solutions of comblike polymers under the conditions close to those observed at the deposition point and the transformation of a primary order into a crystalline phase.

ACKNOWLEDGMENTS

This study was supported by the Russian Foundation of Basic Research, project nos. 05-03-33194, 04-03-32607, 04-02-17211, NSh-1824.2003.3, and NSh-1404.2003.2.

REFERENCES

1. V. K. Srivastava, *Physics of Thin Films* (Mir, Moscow, 1977), Vol. 7, p. 340 [in Russian].
2. A. A. Arslanov, *Usp. Khim.* **63** (1), 3 (1994).
3. T. Kubota, S. Kuragasaki, and M. Iwamoto, *Jpn. J. Appl. Phys.* **37**, 4428 (1998).
4. N. A. Platé and V. P. Shibaev, *Comblike Polymers and Liquid Crystals* (Khimiya, Moscow, 1980) [in Russian].
5. Yu. G. Baklagina, V. P. Sklizkova, V. V. Kudryavtsev, *et al.*, *Vysokomol. Soedin., Ser. A* **37** (8), 1361 (1995).
6. V. V. Klechkovskaya and L. A. Feigin, *Kristallografiya* **43** (6), 975 (1998) [*Crystallogr. Rep.* **43** (6), 917 (1998)].
7. N. D. Stepina, A. L. Tolstikhina, V. V. Klechkovskaya, *et al.*, *Izv. Ross. Akad. Nauk, Ser. Fiz.* **62** (3), 492 (1998).
8. L. A. Feigin and V. V. Klechkovskaya, *Poverkhnost*, No. 12, 25 (1999).
9. A. K. Khripunov, Yu. G. Baklagina, N. D. Stepina, *et al.*, *Kristallografiya* **45** (2), 352 (2000) [*Crystallogr. Rep.* **45** (2), 318 (2000)].
10. N. D. Stepina, R. V. Gañutdinov, V. V. Klechkovskaya, *et al.*, *Poverkhnost*, No. 8, 79 (2001).
11. V. V. Kudryavtsev, V. P. Sklizkova, Yu. G. Baklagina, *et al.*, *Vysokomol. Soedin., Ser. A* **43** (7), 1211 (2001).
12. L. Feigin, V. Klechkovskaya, N. Stepina, *et al.*, *Colloids Surf. A: Physicochem. Eng. Aspects* **198–200**, 13 (2002).
13. V. P. Sklizkova, V. V. Kudryavtsev, Yu. G. Baklagina, *et al.*, *Polyimides: Trends in Materials and Applications* (Plenum Press, New York, 1996), p. 367.
14. M. M. Koton, O. V. Kallistov, V. V. Kudryavtsev, *et al.*, *Vysokomol. Soedin., Ser. A* **21** (3), 532 (1979).
15. N. A. Kalinina, V. P. Sklizkova, I. G. Silinskaya, *et al.*, in *Proceedings of 2nd International Conference on Chemistry of Highly Organized Materials and Scientific Foundations of Nanotechnology* (St. Petersburg, 1998), p. 99.
16. M. Schaub, C. Fakirov, A. Schmidt, *et al.*, *Macromolecules* **28** (4), 1221 (1995).

Translated by L. Man

REAL STRUCTURE OF CRYSTALS

Macroscopic Localization of Plastic Flow in Zinc Single Crystals Oriented for Basal Slip

V. I. Danilov, K. V. Gonchikov, and L. B. Zuev

*Institute of Strength Physics and Materials Science, Siberian Division, Russian Academy of Sciences,
Akademicheskii pr. 2/1, Tomsk, 634021 Russia*

e-mail: dvi@ispms.tsc.ru

Received April 7, 2004

Abstract—The patterns of plastic-flow localization in hcp Zn single crystals oriented for slip in the $\{0001\}$ $\langle 2110 \rangle$ systems are investigated. The main spatial and temporal regularities of the flow localization are established for all portions of the three-stage curve of such crystals. The relationship between the type of localization patterns and the regularities of strain-hardening of single crystals is traced for each stage. The role of the kinking in the formation of the observed macroscopic-flow distributions is estimated. © 2005 Pleiades Publishing, Inc.

INTRODUCTION

Quantitative investigations of the macroscopic localization of plastic flow in metal single crystals carried out from the mid-1990s [1–4] made it possible to determine the spatial and kinetic parameters of this process and to establish its dependence on the type of the stress–strain curve for the corresponding material. It was shown in [1–4] that macroscopic-localization patterns are always ordered. Within the yield plateau, where the deformation occurs through the propagation of a Chernov–Luders band, a single localization front moves with a constant velocity along the axis of an object under load. There are several such fronts in the stages of easy glide. They can move in either the same or the opposite directions, but each element of a sample is passed through only once during their motion. In the stages of linear hardening, synchronous motion of series of equidistant deformation fronts occurs, and these fronts successively pass through the sample several (up to five) times. In going to the stages of parabolic hardening, the localization patterns become randomized, and during the parabolic stages a system of stationary spatially periodic localization regions is formed.

The above systematization was established for single crystals of pure fcc metals and doped fcc alloys and then confirmed for bcc materials. Similar investigations have not been performed for hcp single crystals. At the same time, with superficial similarity of the alternation of stages in the stress–strain curves, the microscopic mechanisms of plastic flow in hcp materials radically differ from analogous mechanisms in fcc and bcc single crystals [5–7].

MATERIALS AND EXPERIMENTAL TECHNIQUE

Single-crystal zinc plates of the 99.997% purity grade were used as the object of study. The sizes of the working part of the samples were $25 \times 4 \times 2$ mm³. The longitudinal axis coincided with the $[\bar{1}2\bar{1}4]$ direction and the wide face lay in the (0443) plane. These crystallographic parameters ensure basal slip in the (0001) $[\bar{1}2\bar{1}0]$ and (0001) $[1\bar{2}10]$ systems, which are characterized by Schmid factors ± 0.48 , respectively. These systems yield slip traces on the working face of a sample with the $[2\bar{1}10]$ orientation, which make an angle of 90° with the extension axis (Fig. 1).

The samples prepared were subjected to active extension with the strain rate $\dot{\epsilon} = 6.7 \times 10^{-5}$ s⁻¹ at room temperature. Note that we first measured diagrams in the coordinates σ (arbitrary tensile stress) and ϵ (arbitrary elongation strain), which were then recalculated into the τ – γ coordinates, where τ is the shear stress in

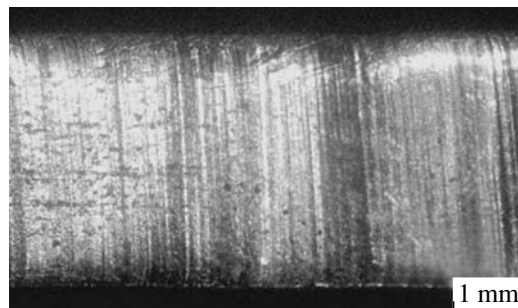


Fig. 1. Slip traces on the working face (0443) of a single-crystal zinc sample.

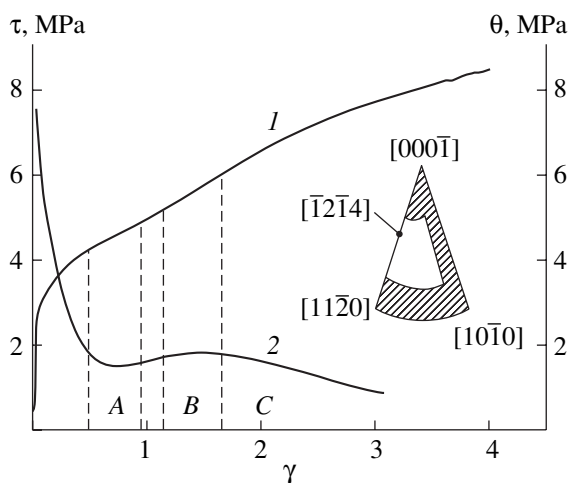


Fig. 2. (1) Stress–strain diagram of a zinc single crystal oriented for basal slip and (2) the dependence of the hardening coefficient on strain. The point on the stereographic triangle indicates the orientation of the longitudinal axis of the sample; the region of orientations of purely basal slip is unshaded.

the slip plane and γ is the corresponding shear strain [5]. As one would expect [5], a stress–strain curve was obtained with all three clearly pronounced stages of basal slip in hcp single crystals (A, B, and C) (Fig. 2). The critical shear stress was $\tau_0 = 3.5$ MPa. The ranges of stages A and B were $\Delta\gamma_A = 0.48$ and $\Delta\gamma_B = 0.5$, respectively; stage C ranged from $\gamma = 1.68$ to the sample fracture. In going from the elastic stage to stage A ($e \rightarrow A$) and between stages A and B, wide transition ranges were observed: $\gamma_{e-A} = 0.5$ and $\Delta\gamma_{A-B} = 0.18$. The transition from stage B to stage C occurred gradually. The curve portions corresponding to stages A and B are straight, with the hardening coefficients $\theta_A = 1.4$ MPa and $\theta_B = 1.7$ MPa, respectively. (Here $\theta = d\tau/d\gamma$.) In stage C, the hardening coefficient monotonically decreases, which gives grounds to consider this stage a parabolic one.

In each of the above stages, the method of double-exposure speckle interferometry was used to investigate the evolution of the fields of displacement vectors of points on the working surface and, then, the fields of distributions of local elongations ϵ_{xx} [1, 3]. The strain fields was measured with a step $\Delta\epsilon_{tot} = 0.2\%$ for each speckle pattern. Thus, any current speckle pattern contained information on the displacements with respect to the previous pattern and the regions with larger values of ϵ_{xx} corresponded to strain-localization zones.

EXPERIMENTAL RESULTS

After going from elasticity to developed plastic flow (beginning of stage A), three localization zones are formed in a sample, where the strain-accumulation rate exceeds the increase in $\Delta\epsilon_{tot}$ by an order of magnitude

(Fig. 3). These zones are located normally to the extension axis of the sample; i.e., they are regions of preferred emergence of basal dislocations to the surface. We have observed previously such a situation for the easy-glide stage in fcc single crystals, for example, copper and nickel [2], where localization zones were oriented along the traces of slip in the primary system. In Fig. 3a, the localization zones are shown as distributions of local elongations ϵ_{xx} and local rotations ω_z along the axis of the working surface of a sample. It can be seen that the zones under consideration are distributed over the sample length as follows: they are concentrated at both clamps (1 and 3) and in the middle (2). Analysis of the distributions of local elongations shows that the strain-localization zone in the middle (2) has a complex structure. In the beginning of stage A, this zone consists of two linked maxima. Then, 260 s after the beginning of the analysis of localization patterns, three linked maxima arise, the spacing between which slightly exceeds 2 mm. During deformation, this central zone is expanded owing to the motion of one of the three maxima, which is located closer to the mobile clamp of the testing machine. Localization zone 3 (near the mobile clamp) also moves as a whole. Analysis of the distributions of local rotations shows that their sign changes within each of the noted localization zones (1–3). In this case, the extreme rotation corresponds to the immobile zone 1 and local rotations change their signs in the zones of the mobile maxima of elongations, 2 and 3 (Fig. 3a). Figure 4 shows the positions of the localization zones as functions of the load time. On the basis of these data, the expansion rates of the localization zone near the mobile clamp 3 and the central localization zone 2 were estimated: $v_3 = 2.6 \times 10^{-6}$ m/s and $v_2 = 2.3 \times 10^{-6}$ m/s, respectively. We failed to observe the motion of localization zone 1 at the immobile clamp within the observation time interval shown in Fig. 4. The motion of zones 2 and 3 cannot be explained by simple elongation of the sample, since the velocity of the mobile clamp of the testing machine was maintained constant: $V_m = 1.67 \times 10^{-6}$ m/s (see above). The true velocity of the deformation fronts can be estimated as

$$V_{fr} = V_n - \dot{\epsilon}X_n, \quad (1)$$

where X_n is the position of the corresponding front at the beginning of stage A, when the sample can be considered unstrained, and v_n is the front velocity obtained from Fig. 4. This estimation gives identical velocities of motion of both zones (1.5×10^{-6} m/s). If we take into account that the duration of stage A is about 4500 s, both fronts will pass a distance of about 7 mm for this time. This fact indicates that the middle zone 2 will reach the initial position of zone 3 by the end of stage A and zone 3 will shift to the end of the working part of the sample.

In going to the linear stage B, the character of the strain distribution changes. The pattern of strain distri-

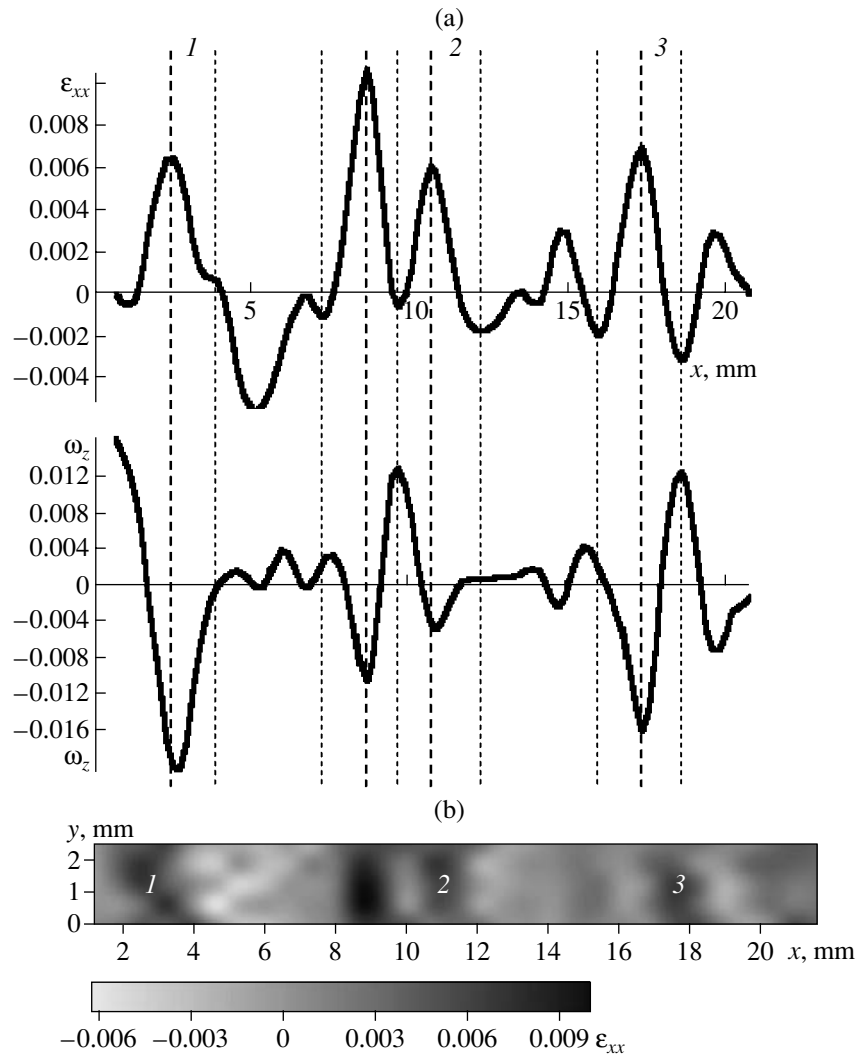


Fig. 3. (a) Positions of the strain-localization zones in stage A and (b) their half-tone image. The total strain $\gamma_{\text{tot}} = 0.023$ and $t = 130$ s.

bution over the sample in stage *B* shows three pronounced strain-localization zones (Fig. 5a). These zones seem to be caused by the transformations and motion of the localization zones even in the previous stage *A*. During the entire stage *B*, these strain-localization zones are immobile; however, there are small-amplitude maxima of local elongations between these zones, which move in the course of time.

Consideration of the kinetics of the strain-localization zones in stage *B* shows that small-amplitude maxima ϵ_{xx} move at a velocity of 3.6×10^{-5} m/s from zone 2 to zone 1 and at a velocity of 2×10^{-5} m/s from zone 3 to zone 2 (Fig. 5b). Thus, in stage *B*, small-amplitude maxima move only between stationary zones where strain is mainly concentrated. This means that the motion of localization zones occurs when the hardening coefficient significantly differs from the average value calculated from the load curve. The local hardening coefficient can be found from the following consid-

erations. Actually, large-amplitude localization zones also do not remain completely immobile but the velocities of their displacements are very small and depend on their positions with respect to the mobile clamp. The closer a zone to the mobile clamp, the higher its velocity. As follows from Fig. 5b, the velocities of zone 2 with a coordinate of 29 mm and zone 1 with a coordinate of 18 mm are -2.4×10^{-7} and -5.3×10^{-7} m/s, respectively. The coordinates are given for the beginning of stage *B*. According to (1), the true velocities of these zones are $V_2 = -2.4 \times 10^{-7} - 3.4 \times 10^{-5} \times 29 \times 10^{-3} = -1.226 \times 10^{-6}$ m/s and $V_1 = -5.3 \times 10^{-7} - 3.4 \times 10^{-5} \times 18 \times 10^{-3} = -1.138 \times 10^{-6}$ m/s.¹ Here, it is taken into account that the sample had been elongated by the beginning of stage *B* and, therefore, the average total strain rate decreased from 6.7×10^{-5} to 3.4×10^{-5} s⁻¹.

¹ The negative values of the velocities mean that the zones move opposite to the extension direction.

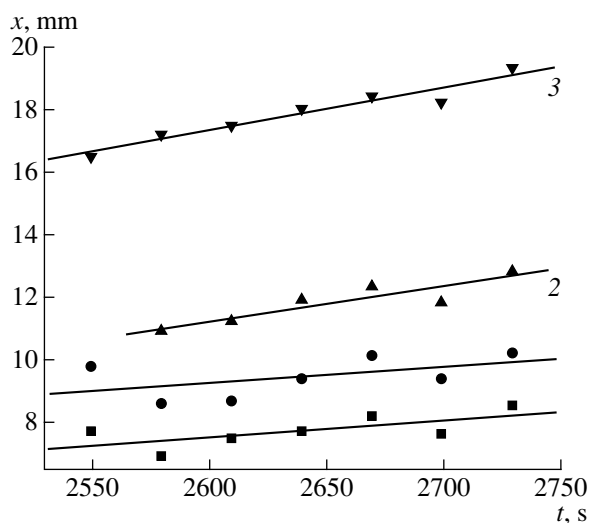


Fig. 4. Motion of deformation fronts in stage A in a zinc single crystal. The designations 2 and 3 are the same as in Fig. 3. The positions of three different maxima in zone 2 are denoted as \blacktriangle , \bullet , and \blacksquare .

Then, for the time interval $t = 400$ s (the observation time of localization patterns), the distance between the zones will change by $(V_2 - V_1)t = (1.226 - 1.138) \times 10^{-6} \times 400 = 3.52 \times 10^{-5}$ m that corresponds to the strain $\Delta\varepsilon = 3.52 \times 10^{-2}/(29 - 18) = 0.0032$. Since $\Delta\varepsilon$ is small, the changes in the arbitrary and true strains² are almost the same ($\Delta\varepsilon \sim \Delta e$). The change in the true stresses in this load range (taken from the stress–strain curve for the instants of time 10500 and 10896 s) $\Delta s = 0.85$ MPa. Then, $\theta = \Delta s/\Delta\varepsilon = 265$ MPa. According to the data of [8], for zinc single crystals, $E = 34.92$ GPa, $\nu = 0.24$, $G = E/2(1 + \nu) = 13.8$ GPa, and the ratio $G/\theta = 52$. In this case, the value of the velocity of maxima between zones 1 and 2 (Fig. 5) $V_{aw} = 3.6 \times 10^{-5}$ m/s is in good agreement with the generalized inversely proportional dependence $V_{aw} \sim (G/\theta)$, described in [1], for the linear stage of deformation of fcc single crystals. When stage B comes to an end, this motion ceases and the stationary zones lose their stability.

In the parabolic stage C, the stationary stable zones 1–3, which exist in stage B, lose their spatial periodicity and gradually shift to the mobile clamp of the sample (Fig. 6). It should be noted that the analysis of the localization patterns of the single crystal in stage C was performed 5 h after the beginning of the deformation and lasted 740 s. By the beginning of stage C, the sample was elongated by 125%; therefore, the positions of the localization zones significantly differed from their positions at the beginning of stage B, and, all the more, in stage A. The maximum amplitude of the accumulation rate of plastic strain was observed in zone 3 with a coordinate of 55 mm. This maximum was imple-

mented by the relatively fast motion of the localization zone, which had a coordinate of 45 mm at the beginning of measurement of shear fields in stage C; such a fast motion lasted 80 s. It can be seen that the motion of zones 2 and 3 is irregular, but the variations in their velocities are not very large and, in this stage of investigations, we can only speak about a trend of their motion to the mobile clamp. Random formation of localization zones with small amplitudes in different regions of the sample is superimposed on this main trend. Furthermore, after 35 min, the sample was fractured in the zone with the maximum amplitude of local elongation.

DISCUSSION

Comparing all the results presented here with the analogous data on the localization of plastic flow in fcc single crystals, we can conclude the following. Stages A, B, and C in hcp single crystals can be regarded as analogs of, respectively, stages I (easy-glide stage), II (linear stage), and III (parabolic stage) in fcc materials [5]. Indeed, in the easy-glide stage and stage A, dislocation slip occurs in one operational system. In hcp crystals, these are basal dislocations in the systems $\{0001\} \langle \bar{2}110 \rangle$. Stage II in fcc materials is caused by the action of secondary systems, the intersection of mobile dislocations, and the formation of Lomer–Cottrell locks. Therefore, this stage is characterized by a high constant hardening coefficient. The increase in the hardening coefficient in stage B is explained by the retardation of basal dislocations at prismatic loops, which are formed during the previous stage and play the same role as Lomer–Cottrell locks. Finally, both stage III in fcc single crystals and stage C in hcp materials are due to the transverse slip, which makes it possible to overcome locks. Therefore, the hardening coefficient monotonically decreases and one would expect similarity of evolution of the patterns of macroscopic flow localization in the corresponding stages. Moreover, a strict correspondence between the localization type and the law of plastic flow, independent of the crystallographic structure, has been established for polycrystalline materials (see, for example, [1]). However, it has not been observed that the previously found regularity is absolutely valid for stage A. Indeed, by the beginning of the portion of the load curve corresponding to stage A for a zinc single crystal, three strain-localization zones had already been formed, which were then observed during the entire stage A. Apparently, these localization zones were formed during the $e \rightarrow A$ transition, which is characterized (see above) by $\Delta\gamma_{e-A} = 0.5$. The boundaries of these zones are clearly visible kink bands (Fig. 7). Such bands were observed in the experiments with extension of zinc single crystals by Washburn [9] and Regel' [10]. The existence of kink bands is also confirmed by the characteristic behavior of the rotational components of the distortion tensor at the bound-

² The true strains are $e = \ln(1 + \varepsilon)$ and the true stresses are $s = \sigma(1 + \varepsilon)$.

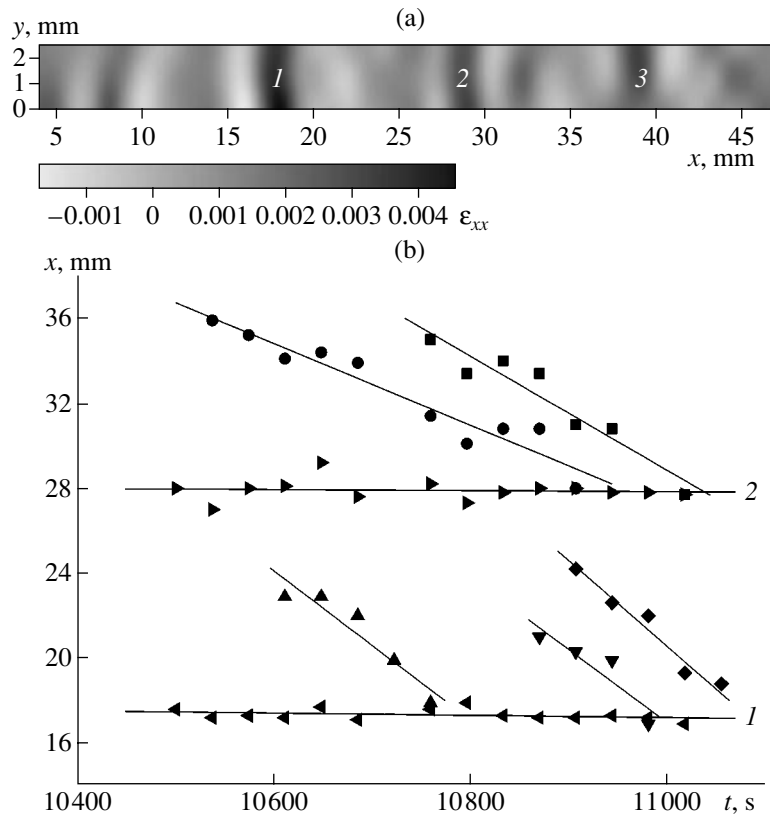


Fig. 5. Stationary zones (*1, 2, 3*) and mobile strain-localization zones in a zinc single crystal in stage *B*. (a) Halftone image (total strain $\gamma_{tot} = 1.168$, $t = 10910$ s) and (b) the kinetics of the motion of localization zones to stationary zones *1* and *2*.

aries of large-amplitude localization zones (see Fig. 3a and, especially, Fig. 8).

If we consider the distributions of local elongations and local rotations, as was done in Fig. 3a for the region of the sample working part covering zones *1* and *2* in Fig. 5 and the region between them at the instant of time $t = 10910$ s, some important features can be noted. First, maximum rotations correspond to the maximum local elongations (Figs. 8a, 8b). Second, on the right descending branch of the peak of elongations *1* and on the left ascending branch of peak *2*, local rotations change their signs to opposite. Third, when the elongations in both zone *1* and zone *2* become minimum, local rotations become zero. In the adjacent regions of the gap between zones *1* and *2*, they take extreme values again but with different signs. Local maxima of rotations ω_z correspond to the small-amplitude maxima ϵ_{xx} in the intermediate region; however, on the whole, the values of rotations gradually vary from negative to positive here. A similar situation develops between zones *2* and *3*. (The latter is not shown in Fig. 8.)

Thus, as one should expect, at the boundaries of the regions with maximum strain accumulation, local rotations have extreme values and different signs for conjugate kink bands (Fig. 8c). This effect is noteworthy since Fig. 7 shows kinks along the direction of the sample thickness; i.e., the components of complete rota-

tions in the material related to these kinks should correspond to rotation around the *y* axis. The rotations ω_z observed from the patterns of displacement vectors (Figs. 3a and 8b) are implemented around the *z* axis; i.e., normally to the wide face. Naturally, these components of complete rotations ω are much smaller and can

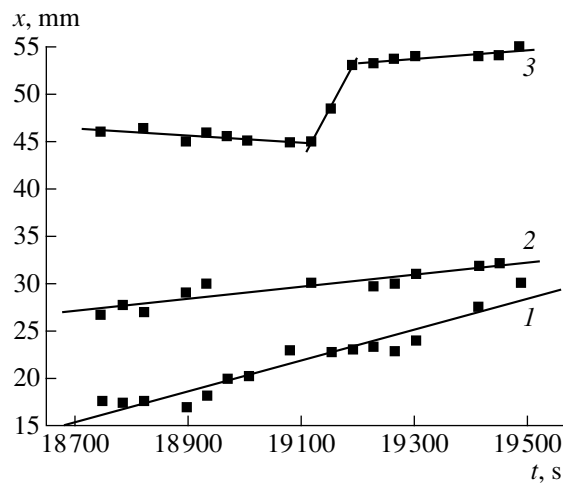


Fig. 6. Kinetics of the motion of strain-localization zones in a zinc single crystal in stage *C*.

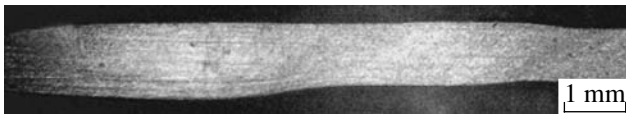


Fig. 7. Kinking at the end surface of an extended zinc single crystal in the end of stage A. The total strain $\gamma_{\text{tot}} = 0.46$ and $t = 1850$ s.

only be detected by other methods immediately before the fracture.

Returning to stage A, it should be noted that in this case only the fronts of localization zones turn out to be mobile rather than the entire zones. However, the fronts, as in other materials, moved with constant and identical velocities and passed through the sample volume once during the stage under consideration. The long duration of stage A resulted in very low velocities of the front motion. Nevertheless, similar kinetics of localization patterns was previously observed by us in single crystals of high-manganese austenite oriented for single twinning [4].

In stage B, the differences in the evolution of the flow-localization patterns of zinc single crystals are

even more pronounced. Wide stationary strain zones limited by kink bands are observed. The regions between these zones are deformed much weaker; however, equidistant motion of smaller maxima of localized elongations at constant velocities occurs in these regions. The velocities are of the same order of magnitude as those detected in fcc single crystals [1–4].

Finally, in the parabolic stage C, one should expect the existence of stationary spatially periodic localization zones [3]. However, the opposite situation is observed in zinc single crystals: the zones that were previously stationary now move (Fig. 6). Averaging the velocity of zone 1 ($V = 1.6 \times 10^{-5}$ m/s), we find that, for the time preceding the fracture, this zone should pass 34 mm and reach the fracture region, i.e., zone 3. Apparently, this is not a coincidence. As was shown in [11], in the parabolic stage of the load curve for a hexagonal polycrystalline alloy Zr–1%Nb, a stationary system of strain-localization fronts is observed only at the parabolicity exponent $n \geq 0.5$. At $n < 0.5$ (up to $n \sim 0.3$), the localization maxima move synchronously. At low strain-hardening exponents ($n < 0.3$), the synchronism is lost and the strain-localization maxima merge to form a single zone (the future fracture zone). Such

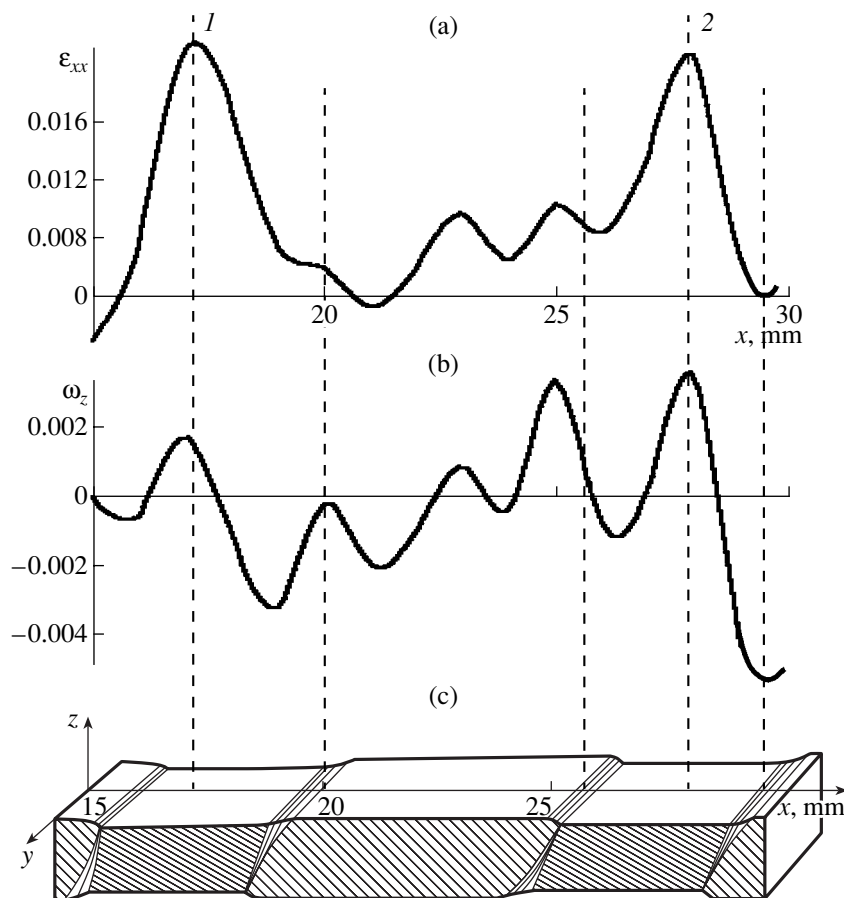


Fig. 8. Distributions of the components (a) ϵ_{xx} and (b) ω_z of the distortion tensor in the middle of a sample between the stationary localization zones 1 and 2 in stage B; $t = 10910$ s. (c) Schematic diagram of this region with kink bands.

behavior is not a specific feature of hcp materials but is, obviously, related to the value of the strain-hardening exponent since we observed a similar situation in the parabolic stage for bcc single-crystal and polycrystalline samples. Moreover, it was shown for silicon iron [12] that, moving in this way, all localization zones also tend to be associated in the region of future fracture.

CONCLUSIONS

The specific features of the evolution of macroscopic localization patterns of plastic flow in zinc single crystals are due primarily to the kinking at the transition from elasticity to developed plastic flow (stage *A*). As a result, a sample becomes divided into regions with a very high strain-accumulation rate and regions in which this parameter is an order of magnitude lower. Large-amplitude strain-localization zones, which are stationary in stages *A* and *B*, arise first. These zones are limited by kink bands of opposite signs. They gradually expand at rates comparable with the rate set by the loading machine. Material rotation and almost all plastic flow are concentrated in these zones. According to the models of kinking, the regions between the strain-localization zones should not be distorted. However, it is shown in this study that deformation also occurs in these regions; its development is localized and the localization zones move synchronously.

Thus, the evolution of the local-flow distributions in single-crystal zinc, having some significant differences, corresponds on the whole to the previously established regularities of plastic-flow localization:

- (i) single passage of deformation fronts through the sample volume in the single-slip stage (stage *A*);
- (ii) synchronous motion of localization zones in the linear stage, in which the hardening coefficient is controlled by the interaction between dislocations of different systems (stage *B*); and

- (iii) motion of previously stationary localization zones to the zone of future fracture in the parabolic stage *C*.

REFERENCES

1. L. B. Zuev, V. I. Danilov, and B. S. Semukhin, *Usp. Fiz. Met.* **3** (3), 237 (2002).
2. V. I. Danilov, K. V. Gonchikov, L. B. Zuev, *et al.*, *Crystallogr. Rep.* **47**, 672 (2002).
3. L. B. Zuev and V. I. Danilov, *Philos. Mag. A* **79** (1), 43 (1999).
4. V. I. Danilov, S. A. Barannikova, and L. B. Zuev, *Zh. Tekh. Fiz.* **73** (11), 69 (2003) [*Tech. Phys.* **48**, 1429 (2003)].
5. R. Berner and H. Kronmüller, *Plastische Verformung von Einkristallen* (Springer, Berlin, 1965; Mir, Moscow, 1969), in *Moderne Probleme der Metallphysik*, Ed. by A. Seeger.
6. R. W. K. Honeycombe, *The Plastic Deformation of Metals* (Arnold, London, 1968; Mir, Moscow, 1972).
7. V. I. Startsev, V. Ya. Il'ichev, and V. V. Pustovalov, *Plasticity and Strength of Metals and Alloys at Low Temperatures* (Metallurgiya, Moscow, 1975) [in Russian].
8. I. N. Frantsevich, *Elastic Constants and Elastic Moduli of Metals and Nonmetals* (Naukova Dumka, Kiev, 1982) [in Russian].
9. J. Washburn and E. Parker, *J. Met.* **4** (10), 1076 (1952).
10. V. V. Regel' and V. G. Govorkov, *Kristallografiya* **3** (11), 376 (1958) [*Sov. Phys. Crystallogr.* **3**, 377 (1958)].
11. T. M. Poletika, V. I. Danilov, L. B. Zuev, *et al.*, *Zh. Tekh. Fiz.* **72** (9), 57 (2002) [*Tech. Phys.* **47**, 1125 (2002)].
12. V. I. Danilov, L. B. Zuev, M. A. Kunavina, *et al.*, in *Proceedings of All-Russian School-Seminar on Modern Problems in Mechanics of Deformed Solids* (Novosib. Gos. Tekh. Univ. Novosibirsk, 2003), p. 77.

Translated by Yu. Sin'kov

LATTICE DYNAMICS AND PHASE TRANSITIONS

Reversible Low-Temperature Transition in $\text{LaMnO}_{3+\delta}$

V. Sh. Shekhtman, N. S. Afonikova, V. D. Sedykh,
A. V. Dubovitskii, and V. I. Kulakov

*Institute of Solid State Physics, Russian Academy of Sciences,
Chernogolovka, Moscow oblast, 142432 Russia*

e-mail: shekht@issp.ac.ru

Received April 20, 2004

Abstract—The evolution with a decrease in temperature of the basic rhombohedral structure of the $\text{LaMnO}_{3+\delta}$ compound having a specified constant oxygen concentration is considered. The X-ray diffraction analysis shows that a transition from rhombohedral to monoclinic phase begins at a temperature close to 200 K. The important feature of the revealed low-temperature phase transition is its reversibility with heating to room temperature. A deformation mechanism of structural phase transitions based on uniform distortions of a perovskite block with a doubled lattice parameter is proposed. The results of the analysis of the symmetry of atomic positions are in favor of two-step routes of phase transitions through dilatation and twinning. © 2005 Pleiades Publishing, Inc.

INTRODUCTION

In our previous study [1], we considered possible mechanisms of structural transitions in undoped lanthanum manganite. The emphasis was on the transitions from the rhombohedral modification $R\bar{3}c$ to the orthorhombic phases $Pnma$ I and $Pnma$ II with a change in the oxygen concentration. A two-step scheme of the noted diffusionless transitions through a virtual cubic configuration ($\bar{3}m \rightarrow m\bar{3}m \rightarrow mmm$) was discussed. In addition, it was noted that the experimental investigation of the structural processes occurring with a decrease in temperature had begun.

The subject of this study is the evolution of the basic rhombohedral structure of the $\text{LaMnO}_{3+\delta}$ compound having a specified constant oxygen concentration with a decrease in temperature.

EXPERIMENTAL

The technique of preparation of powder samples of oxides of specified composition was described in [2]. The excess of oxygen δ (or the ratio of Mn^{3+} and Mn^{4+} ions) was determined by either direct weighting or titration with potassium iodide. It was found that the value of δ depends not only on the synthesis temperature and the type of gas atmosphere but also on the rate of sample cooling. The rhombohedral phase (sp. gr. $R\bar{3}c$) was obtained by cooling a sample from 1100°C at a rate of 10 K/h. The composition of the sample grown under these conditions was $\text{LaMnO}_{3.13}$ (29.5 and 70.5% of Mn^{4+} and Mn^{3+} ions, respectively).

The X-ray diffraction analysis was performed on a SIEMENS D500 diffractometer ($\text{CuK}\alpha$ radiation); a

continuous-flow liquid-helium cryostat, designed and fabricated at the Institute of Solid-State Physics of the Russian Academy of Sciences, served as a low-temperature attachment. The cryostat design ensures precise measurements of diffraction patterns in a wide angular range. The accessible temperature range is 4.2–300 K, the rate of sample cooling can be varied in a specified range, and a specified temperature is stabilized accurate to 0.1 K [3, 4]. The cryostat was installed on the goniometer of the X-ray diffractometer. The sample holder was mounted on a rod, which was installed in the cryostat well. In the working cell, powder samples were tightened up by a thin polyethylene film to retain a planar surface. (This amorphous film gave rise to a halo reflection at $2\theta \sim 25^\circ$ in the diffraction patterns in Fig. 1.) Varying temperature step by step, we reached a specified temperature, after which a diffraction pattern was measured with thermal stabilization of the sample during the measurement.

The X-ray diffraction experiments were carried out in the temperature range 93.4–300 K in the cooling mode; the design of the measuring system also made it possible to use, when necessary, heating and thermal-cycling modes.

RESULTS AND DISCUSSION

The X-ray diffraction pattern of a powder sample of $\text{LaMnO}_{3+\delta}$ measured at room temperature is shown in Fig. 1a. Analysis shows that the diffraction lines at room temperature correspond to the rhombohedral phase with the lattice parameters $a_{\text{rhom}} = 5.455 \text{ \AA}$ and $\alpha = 60.74^\circ$. The diffraction pattern at 93.4 K is shown in Fig. 1b. The additional splitting of some lines (beginning with 200 K) is indicative of a decrease in the sym-

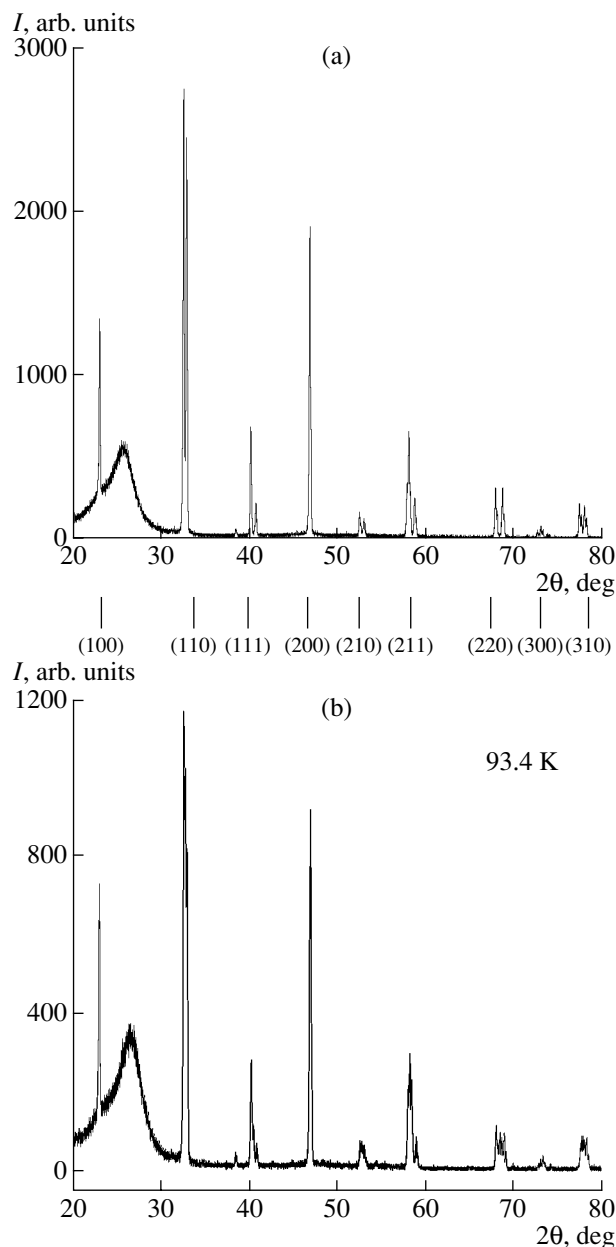


Fig. 1. X-ray powder diffraction pattern of the $\text{LaMnO}_{3+\delta}$ compound at (a) room temperature and (b) the lowest stabilized temperature (93.4 K).

metry of the crystal structure at the phase transition. The most characteristic changes in the diffraction pattern were observed in the angle ranges near $2\theta = 32.5^\circ$ and $2\theta = 68^\circ$ – 69° . Figure 2 shows as an example an additional reflection arising between the $(2\bar{2}0)$ and (422) peaks. The intensity of this reflection increases with a decrease in temperature. Heating a sample led, accordingly, to the disappearance of this line and the recovery of the initial pattern. This fact indicates that a reversible low-temperature phase transition occurs in lanthanum manganite crystals.

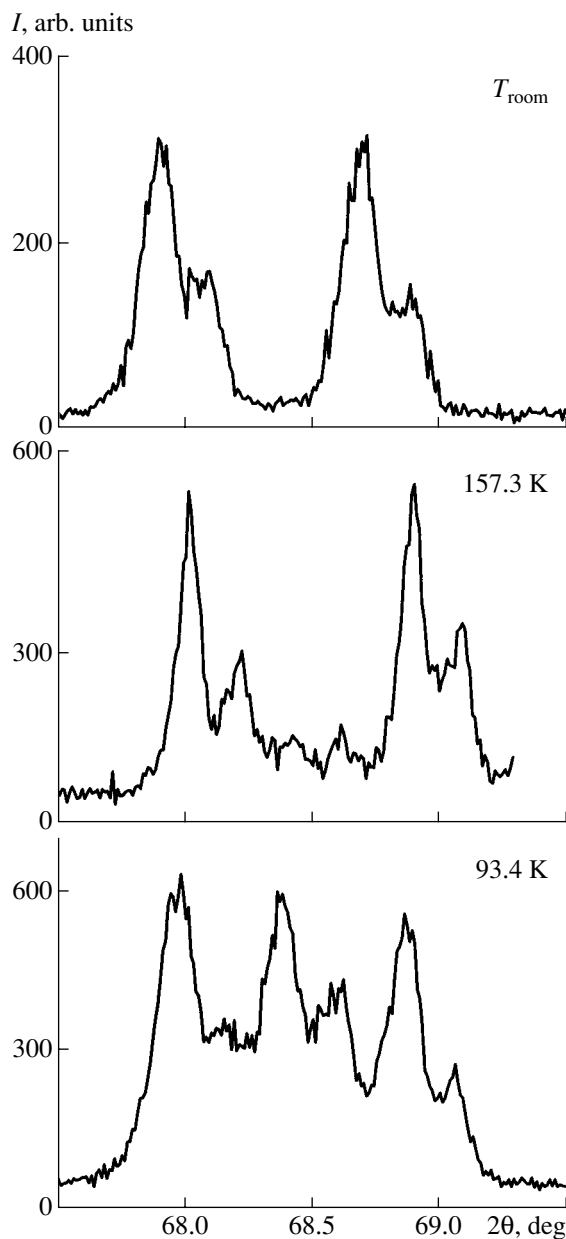


Fig. 2. Transformations of the diffraction lines $(2\bar{2}0)_{\text{rhom}}, (422)_{\text{rhom}} \Rightarrow (004)_{\text{mon}}, (\bar{2}42)_{\text{mon}}, (400)_{\text{mon}}$ recorded during the cooling from room temperature to 93.4 K.

Table 1 contains the experimental and calculated data on the characteristic groups of lines in the X-ray diffraction patterns recorded at two temperatures according to Figs. 1a and 1b. To understand the genesis of crystalline modifications, we found it useful to add to Table 1 the calculated values of the positions of the lines corresponding to a “virtual” cubic phase ($Pm\bar{3}m$). The lattice constants of this perovskite configuration were calculated from the experimental data on the structures of other modifications. The relationship

Table 1. Summary data on d_{calcd} (Å), d_{exper} (Å), and I_{exper} (%) for the diffraction patterns of rhombohedral ($R\bar{3}c$) and monoclinic ($P112_1/a$) modifications in comparison with the data on the virtual cubic $Pm\bar{3}m$ phase

$Pm\bar{3}m$		$R\bar{3}c$				$P112_1/a$			
hkl	d_{calcd}	hkl	d_{calcd}	d_{exper}	I_{exper}	hkl	d_{calcd}	d_{exper}	I_{exper}
(1)	(2)	(3)	(4)	(5)	(6)	(7)	(8)	(9)	(10)
100	3.870	110	3.879	3.871	38	101	3.865	3.861	44
						020	3.860		
110	2.737	$1\bar{1}0$	2.758	2.753	100	002	2.752	2.749	100
						$1\bar{2}1$	2.741	2.734	70
		211	2.727	2.724	96	200	2.715	2.717	60
111	2.234					112	2.336	2.337	2
		200	2.248	2.245	27	022	2.241	2.241	24
						$2\bar{2}0$	2.231	2.229	9
		222	2.215	2.215	7	220	2.210	2.208	5
200	1.935	220	1.939	1.938	77	202	1.933	1.935	73
						040	1.930		
210	1.731	$2\bar{1}1$	1.742	1.742	5	103	1.738	1.740	5
		321	1.727	1.728	4	$1\bar{4}1$	1.732	1.731	3
						141	1.724	1.723	3
211	1.580	$2\bar{1}1$	1.592	1.593	14	$1\bar{2}3$	1.587	1.589	14
		310	1.586	1.587	23	042	1.580	1.583	14
		$22\bar{1}$	1.569	1.570	11	$3\bar{2}1$	1.576	1.578	11
						240	1.566	1.565	6
220	1.368	$2\bar{2}0$	1.379	1.379	14	004	1.376	1.378	10
						$2\bar{4}2$	1.371	1.369	8
		422	1.366	1.365	14	400	1.357	1.362	8

between these structures will be discussed in the next section.

The data of Table 1 make it possible to quantitatively characterize the low-temperature modification of undoped manganite as the monoclinic phase. The monoclinic lattice constants ($a = 5.430$ Å, $b = 7.721$ Å, $c = 5.504$ Å, $\gamma = 90.56^\circ$) are in satisfactory agreement with the known data in the literature [5].

A significant result, characterizing the nature of the phase transition revealed, is the phase transition's reversibility in thermal cycles in the range 93.4–300 K. If we consider that the process under consideration implies the that the oxygen concentration remains constant, the main factor is the effect of temperature on the structural characteristic of undoped lanthanum manganite. In this interpretation, the structural changes at high temperatures are determined to a greater extent by possible deviations from stoichiometry with respect to oxygen.

Two-step Structural Transformations

The X-ray diffraction data obtained in situ and comparison with the complete set of crystalline modifications can be used for summary representation of the structural processes occurring in undoped manganite.

Taking into account the data considered in [1, 2], we use the representation of all known modifications of manganite as derivatives of cubic phase (parent phase) with a perovskite cell of a virtual cube. In the logical sequence of considerations, we assume a cell in rhombohedral axes to be the initial configuration. A virtual perovskite cell with the period $a_{\text{cub}} \sim 3.870$ Å is related to these parameters. It is also assumed that the period of a rhombohedral cell $a_{\text{rhomb}} = a_{\text{cub}}\sqrt{2}$; i.e., a_{rhomb} reproduces the length of the cubic cell diagonal. The cubic block composed of eight such cells has the lattice constant $2a_{\text{cub}} = 7.740$ Å.

The above scheme makes it possible to construct a successively justified system of structural transitions on

the basis of uniform distortions of the noted perovskite unit with a doubled lattice parameter. In this scheme, the reconstruction of a cubic cell is determined by the dilatation along the body diagonal of the rhombohedral cell. The repetition period $(I_{111})_{\text{rhomb}} = 13.287 \text{ \AA}$ should increase by $\sim 0.9\%$ to 13.406 \AA for the body diagonals of the cube $2(I_{111})_{\text{cub}}$. This distortion also sets the decrease in the angle between the rhombohedron edges $\alpha = 60.74^\circ \Rightarrow 60^\circ$, i.e., to the value of the angle between the directions of the $[101]/[011]/[110]$ type, which is characteristic of the cubic cell.

In this consideration, we can represent the increase in the symmetry from the point group $\bar{3}m$ to its supergroup $m\bar{3}m$ as the first stage of mutual phase transitions in this system. This is illustrated in Fig. 3 by a hierarchical scheme of mutual subordination of crystallographic point groups.

The geometric schematic diagram of the known transition to the orthorhombic phase is given in [1]. In this generalized model, in terms of the return to the parent-phase axes with subsequent twinning, a point group is formed, which is a subgroup of cubic rather than the initial rhombohedral phase. As was noted in [2], the model suggests that twinning of a virtual perovskite cell in the $(100)/[011]$ system by specified characteristic angles is necessary for the formation of the $Pnma$ I and $Pnma$ II orthorhombic phases.

To extend this model for the transition to a monoclinic modification, let us use the scheme $\bar{3}m \rightarrow m\bar{3}m \rightarrow 2/m$, in which the symmetry of the final phase is the general subgroup for the groups $m\bar{3}m$ and $\bar{3}m$. For quantitative estimation, it is useful to compare the values of the lattice constants $a_{\text{mon}} \approx c_{\text{mon}} \approx (I_{101})_{\text{cub}}$, $b_{\text{mon}} \approx 2a_{\text{cub}}$, and $\gamma = 90.56^\circ$.

According to Fig. 4, we can assume a correspondence between the basis vectors for the monoclinic and cubic lattices: $[101]_{\text{cub}} \Rightarrow [001]_{\text{mon}}$, $[10\bar{1}]_{\text{cub}} \Rightarrow [100]_{\text{mon}}$, and $[010]_{\text{cub}} \Rightarrow [010]_{\text{mon}}$. In this consideration, the following system of twinning in the axes of the cubic lattice is used: the invariant plane $(101)_{\text{cub}}$, the shear direction $[10\bar{1}]_{\text{cub}}$, and a twinning angle of 0.56° .

Transformation of the Symmetry of Atomic Positions

In accordance with [1], note that the transition from a virtual cube to actually observed phases can also be characterized by the number of atoms in the unit cell. The interpreted X-ray diffraction data (see, for example, [2]) listed in Table 2 make it possible to write the structural formula for the entire series of the modifications: LaMnO_3 ($Pm\bar{3}m$), $\text{La}_2\text{Mn}_2\text{O}_6$ ($R\bar{3}c$), and $\text{La}_4\text{Mn}_4\text{O}_{12}$ ($Pnma$ or $P112_1/a$).

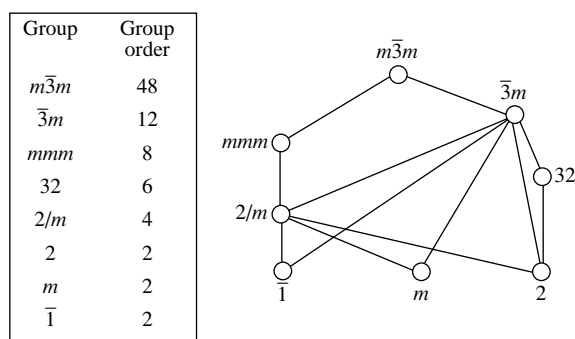


Fig. 3. Hierarchy of the symmetries of crystallographic point groups.

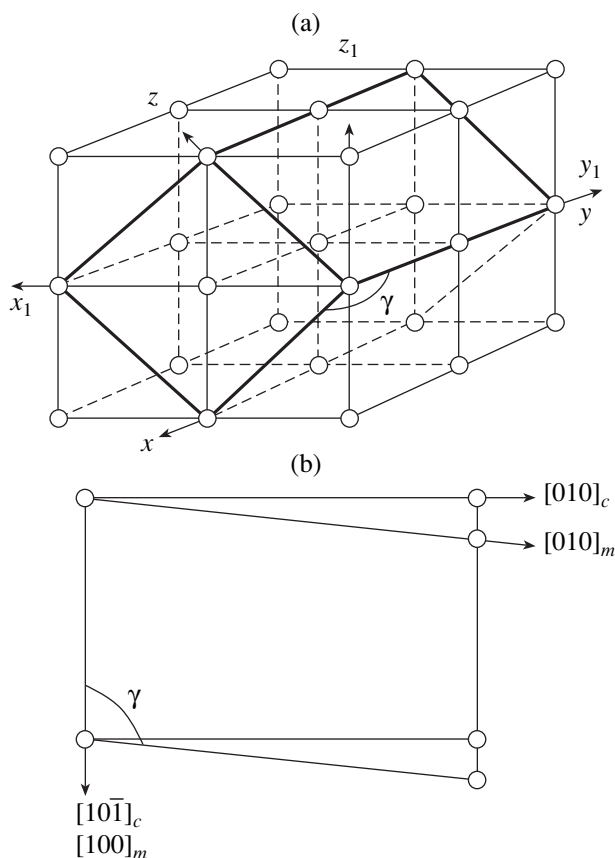


Fig. 4. (a) Mutual orientation of the coordinate axes of the cubic and monoclinic cells and (b) the directions of shear distortions at the transition from cubic to monoclinic phase.

The increase in the number of formula units in the cell is accompanied by changes in the nearest environment and the symmetry of atomic positions. For example, the symmetry of the position of Mn atoms significantly changes. The rhombohedral cell contains two equivalent Mn atoms: at the vertex and at the center of the cell; the symmetry of a particular position is the threefold inversion axis. In the orthorhombic cell, four equivalent Mn atoms are located at the midpoints of the

Table 2. Positions of atoms in the unit cells of the manganite modifications

Group	Element	Position	Point symmetry	Coordinates
$R\bar{3}c$	La	2(<i>a</i>)	32	1/4, 1/4, 1/4
	Mn	2(<i>b</i>)	$\bar{3}$	0, 0, 0
	O	6(<i>e</i>)	2	<i>x</i> , 1/2 - <i>x</i> , 1/4
<i>Pnma</i>	La	4(<i>c</i>)	<i>m</i>	<i>x</i> , 1/4, <i>z</i>
	Mn	4(<i>b</i>)	$\bar{1}$	0, 0, 1/2
	O(1)	4(<i>c</i>)	<i>m</i>	<i>x</i> , 1/4, <i>z</i>
	O(2)	8(<i>d</i>)	1	<i>x</i> , <i>y</i> , <i>z</i>
$P112_1/a$	La	4(<i>e</i>)	1	<i>x</i> , <i>y</i> , <i>z</i>
	Mn(1)	2(<i>c</i>)	$\bar{1}$	0, 0, 1/2
	Mn(2)	2(<i>d</i>)	$\bar{1}$	1/2, 0, 1/2
	O(1)	4(<i>e</i>)	1	<i>x</i> , <i>y</i> , <i>z</i>
	O(2)	4(<i>e</i>)	1	<i>x</i> , <i>y</i> , <i>z</i>
	O(3)	4(<i>e</i>)	1	<i>x</i> , <i>y</i> , <i>z</i>

edges *a* and *c* and at the centers of the faces *Oyz* and *xy0*; the symmetry of the position is the inversion center. In the monoclinic cell, the numerical values of the coordinates formally coincide with those in the previous variant and the symmetry of each position is the inversion center. In this case, four Mn atoms are shared between two twofold particular positions. In one of the positions, a Mn atom is located at the twofold screw axis and, in the other position, a Mn atom lies in the glide-reflection plane.

For the atoms of the other metal component, lanthanum, the sequence of modifications is characterized by a change in the symmetry from 32 (rhombohedral cell) to *m* (orthorhombic cell); when a monoclinic cell is formed, four La atoms are in the same common position (symmetry 1).

The symmetry of the positions of O atoms significantly changes at structural transitions. In the rhombohedral cell, they are located at the twofold axis. In the orthorhombic cell, a particular position with the symmetry *m* arises for O atoms. In the monoclinic cell, all O atoms are in three positions of common location.

Note that only the positions of Mn atoms at all transitions acquire the symmetry of the subgroup of the initial rhombohedral modification. In contrast, the symmetry *m* of the positions of La and O atoms cannot be described (according to the hierarchical scheme in

Fig. 3) by the transition from $R\bar{3}c$ to the subgroup. Thus, it turns out that analysis of the symmetry of atomic positions can also be in favor of two-stage routes of phase transitions. In this context, the proposed model of virtual return to the general supergroup of the cubic parent phase as a real stage of a cooperative phase transition seems to be quite natural.

CONCLUSIONS

The evolution with a decrease in temperature of the basic rhombohedral structure of the $\text{LaMnO}_{3+\delta}$ compound having a specified constant oxygen concentration was considered. X-ray diffraction analysis showed that at a temperature of about 200 K a transition from the rhombohedral to the monoclinic phase begins. This transition is reversible with respect to temperature.

A deformation mechanism of structural phase transitions based on uniform distortions of a perovskite unit with a doubled lattice parameter is proposed. The results of the analysis of the symmetry of atomic positions can be in favor of two-stage routes of phase transitions through dilatation and twinning. In this context, the proposed model of virtual return to the general supergroup of the cubic parent phase as a real stage of a cooperative phase transition seems to be natural.

ACKNOWLEDGMENTS

We are grateful to I.M. Shmyt'ko for his help in carrying out experiments and useful discussions.

This study was supported by the Russian Foundation for Basic Research, project no. 03-02-17232.

REFERENCES

1. V. Sh. Shekhtman, I. S. Smirnova, V. D. Sedykh, *et al.*, *Kristallografiya* **49** (1), 45 (2004) [*Crystallogr. Rep.* **49**, 40 (2004)].
2. V. D. Sedykh, I. S. Smirnova, B. Sh. Bagautdinov, *et al.*, *Poverkhnost*, No. 12, 9 (2002).
3. L. S. Kruts, G. S. Med'ko, and I. M. Shmyt'ko, USSR Inventor's Certificate No. 993220 (October 1, 1982).
4. I. M. Shmyt'ko, N. Ya. Donchenko, S. S. Klimyuk, *et al.*, USSR Inventor's Certificate No. 1148452 (December 1, 1984).
5. Q. Huang, *Phys. Rev. B* **55**, 14 987 (1997).

Translated by Yu. Sin'kov

LATTICE DYNAMICS
AND PHASE TRANSITIONS

Competition between Rotational and Polar Structural Distortions in Perovskites

V. I. Torgashev*, V. B. Shirokov*, A. S. Prokhorov**, and L. A. Shuvalov***†

* Rostov State University, ul. Zorge 5, Rostov-on-Don, 344090 Russia

e-mail: victor@ip.rsu.ru

** General Physics Institute, Russian Academy of Sciences, ul. Vavilova 38, Moscow, 119991 Russia

e-mail: prokhor@ran.gpi.ru

*** Shubnikov Institute of Crystallography, Russian Academy of Sciences,
Leninskii pr. 59, Moscow, 119333 Russia

Received September 7, 2004

Abstract—Symmetrically admissible structural distortions are analyzed in terms of the group theory under the assumption that the order parameter is transformed according to the direct sum of irreducible representations $M_5 \oplus R_8 \oplus \Gamma_{10}$ consisting of the M , R , and Γ points of the Brillouin zone in a primitive cubic lattice. As a result, a set of 92 low-symmetry phases is obtained. The order parameter describes the rotational and polar distortions of the perovskite structure. The topology of the arrangement of the equilibrium phases on phenomenological phase diagrams is considered within the Landau theory of second-order phase transitions. Different variants of the change of the phase states are discussed. The possible existence of several polar states (and their changes) as “final products” of successive structural distortions is substantiated. © 2005 Pleiades Publishing, Inc.

INTRODUCTION

One of the widespread types of structural distortions in the perovskite family described by the general formula ABX_3 (sp. gr. $Pm\bar{3}m-O_h^1$) is caused by lattice instability with respect to small rotations of constituent octahedra considered as rigid structural units (rotational phase transitions) [1, 2]. Cowley [3] and Cochran and Zia [4] seem to have been the first to show the relation of these distortions to the phonon modes of the M and R points of the Brillouin zone. Glaser [5] considered geometrically admissible rotation types of octahedra located in two conjugated layers and obtained 23 variants of possible low-symmetry phases [5, 6]. In order to identify the type of structural distortion, Glaser [5] introduced the $a^\pm b^\pm c^\pm$ notation, where a , b , and c are proportional to the angles of rotation about the respective orthogonal axes of the cubic reference system. The superscript's \pm determine the direction of rotations (in-phase rotations indicated by + and antiphase rotations indicated by –) about the axis common for the adjacent octahedra.

The phase transitions observed at the superposition of the rotational and polar distortions were first considered by Aleksandrov [1, 2], who used the method of enumeration of the subgroups of those groups which were obtained as a result of only rotational distortions. Recently, Stokes *et al.* [7] solved a similar problem by the group-theory methods and obtained a set of 60 low-symmetry groups. They also criticized the geometrical approach. However, it should be noted that Stokes *et al.*

[7] considered only simple types of rotations and, therefore, the list given in [7] is incomplete. In particular, they did not take into account the possibility that rotations of different types (+ and –) may simultaneously take place around the same axis. This detail was also indicated by Aleksandrov [1, 2].

Below, we use the group-theoretical methods of enumeration of admissible distortions of the cubic perovskite lattice in the case where both types of instabilities—rotation of octahedra and displacements of B ions from their octahedral positions in the structure—are superimposed. We also take into account possible simultaneous rotations of different types around the one axis and compare the results obtained with the results obtained in [7]. We also consider, within the Landau theory of second-order phase transitions, the general topology of the arrangement of stable equilibrium phases in the phase diagrams constructed and the specificity of the changes of the phase states caused by the variation of the constants in the Landau potential.

GROUP-THEORETICAL ANALYSIS OF ADMISSIBLE STRUCTURAL DISTORTIONS

Centers of octahedra in the perovskite structure occupy the b position ($1/2, 1/2, 1/2$). To describe the rotation of these octahedra, it is possible to limit the problem to the consideration of some of the singular points in the Brillouin zone of a cubic unit cell [3, 4]: $\mathbf{k}_{10} = 1/2\mathbf{b}_1$ (X point), $\mathbf{k}_{11} = 1/2(\mathbf{b}_1 + \mathbf{b}_2)$ (M point), $\mathbf{k}_{13} = 1/2(\mathbf{b}_1 + \mathbf{b}_2 + \mathbf{b}_3)$ (R point), and $\mathbf{k}_{12} = \mathbf{0}$ (Γ point). Here

† Deceased.

\mathbf{b}_i are the basis vectors of the reciprocal lattice. We borrow the notation for vectors and the respective irreducible representations from [8]. It was shown [9] that the following irreducible representations may correspond to the order parameter for structures of rotation: $\mathbf{k}_{10} : \tau_{10}$, $\mathbf{k}_{11} : \tau_5$, $\mathbf{k}_{11} : \tau_9$, and $\mathbf{k}_{13} : \tau_8$. The corresponding large representations for $\mathbf{k}_{10} : \tau_{10}$ and $\mathbf{k}_{11} : \tau_9$ are six-dimensional; the remaining representations are three-dimensional. Traditionally, when analyzing octahedron rotations, one usually considers the $\mathbf{k}_{11} : \tau_5$ and $\mathbf{k}_{13} : \tau_8$ representations [1–4], which are sufficient for the description of the majority of concrete situations [9]. The condition of equivalence of octahedra at distortions arising in dissymmetric phases is satisfied only in 35 structures of all 122 symmetrically admissible ones [9]. The parameters of these structures are determined and listed in [9] together with all the secondary order parameters. The soft mode $\mathbf{k}_{12} : \tau_{10}$ (or F_{1u} type) of the symmetry from the Γ point ensures the displacement of B cations from their octahedral positions, which results in the formation of polar structural distortions.

Thus, the combined consideration of the rotational and polar distortions includes the consideration of the order parameter, which is transformed according to the reducible representation $\mathbf{k}_{11} : \tau_5 \oplus \mathbf{k}_{13} : \tau_8 \oplus \mathbf{k}_{12} : \tau_{10}$ (or, shortly, $M_5 \oplus R_8 \oplus \Gamma_{10}$).

Not going into the details of the group-theoretical method, which may be found in [10, 11], we only give here the tabulated results of our calculations. All the phases indicated in [7] are also listed in our table, but the total number of various low-symmetric phases is thrice larger than in [7] and amounts to 92 phases. (In the table, new phases are indicated by asterisks.) The $\boldsymbol{\eta}$ column, which indicates the order-parameter component (symmetry solution of the equations of state for the Landau potential), is divided into three subcolumns indicating the components of the primary order parameters condensed into the corresponding phase: $M_5(m_i)$, $R_8(r_i)$, and $\Gamma_{10}(g_i)$ ($i = 1, 2, 3$). All the solutions are grouped into eight blocks with different types of distortions.

Solution no. 0 (all the values of the order parameter are zeroes) corresponds to the cubic perovskite. Solutions nos. 1–6 give all the phases arising in condensation of the polar Γ_{10} mode [12]. Solutions nos. 7–12 determine the symmetry of the phases formed only owing to condensation of the R_8 mode [10], whereas solutions nos. 13–16 determine only that of the M_5 mode [10]. The simultaneous condensation of the M_5 and R_8 modes is described by solutions nos. 17–30; of the R_8 and Γ_{10} modes, by solutions nos. 31–44; and that of the M_5 and Γ_{10} modes, by solutions nos. 45–58. Solutions nos. 59–92 describe the situations of simultaneous condensation of all three modes under study. We would like to single out the situation arising during the simultaneous condensation of those modes, which give different variants of low-symmetry phases in different

combinations (“enclosures”) of the same numbers of condensed order-parameter components (e.g., $(m_1 00 00r_3 000)$ in sp. gr. $P4/mbm$ and $(00m_3 00r_3 000)$ in sp. gr. $Cmcm$, etc.). It is difficult to follow all these situations using mere geometric methods and, therefore, not all of them are indicated in [7]. Thus, the first solution in the above example is not indicated in [7], as well as some other important phases, e.g., $(m_1 m_1 m_1 r_3 r_3 r_3 000)$ in sp. gr. $R\bar{3}$, $(00m_1 r_3 00 g_1 00)$ in sp. gr. $P4bm$, etc. It will be shown below that the allowance for these phases is very important for constructing appropriate phase diagrams.

PHASE STATES AND TRANSITION SEQUENCES

For displacive phase transitions, the atomic displacements $\psi_i^{(j)}(\mathbf{r})$ in the phonon modes $\mathbf{q}j$ (\mathbf{q} is the wave vector) serve as a canonical basis of the j th irreducible representation of the sp. gr. G_0 . The phonon basis functions $\psi_i^{(j)}(\mathbf{r})$ determine the direction and relative amplitude of the atomic displacements participating in the mode under study.

In our case, j corresponds to the M_5 ($\mathbf{q} = (1/2 1/2 0)$), R_8 ($\mathbf{q} = (1/2 1/2 1/2)$), and Γ_{10} ($\mathbf{q} = (000)$) modes and the order parameter $\boldsymbol{\eta}$ has nine components $[(m_1, m_2, m_3)(r_1, r_2, r_3)(g_1, g_2, g_3)]$. In this case, the free energy is written in the form

$$\begin{aligned} \delta F' = & \alpha_2' J_1 + \alpha_4' J_1^2 + A_4 J_4 + \beta_2' J_2 + \beta_4' J_2^2 \\ & + B_4 J_7 + \gamma_2' J_3 + \gamma_4' J_3^2 + \Gamma_4 J_{10} + \delta_{22}' J_1 J_2 + \Delta_{22} J_5 \\ & + \varepsilon_{22}' J_1 J_3 + E_{22} J_6 + \eta_{22}' J_2 J_3 + H_{22,1} J_9 + H_{22,2} J_8 + \dots, \end{aligned} \quad (1)$$

where

$$\begin{aligned} J_1 &= m_1^2 + m_2^2 + m_3^2, & J_2 &= r_1^2 + r_2^2 + r_3^2, \\ J_3 &= g_1^2 + g_2^2 + g_3^2, \\ J_4 &= m_1^2 m_2^2 + m_1^2 m_3^2 + m_2^2 m_3^2, \\ J_5 &= m_1^2 r_3^2 + m_3^2 r_1^2 + m_2^2 r_2^2, \\ J_6 &= m_1^2 g_3^2 + m_3^2 g_1^2 + m_2^2 g_2^2, \\ J_7 &= r_1^2 r_2^2 + r_1^2 r_3^2 + r_2^2 r_3^2, \\ J_8 &= r_1^2 g_2^2 + r_1^2 g_3^2 + r_2^2 g_3^2 + r_2^2 g_1^2 + r_3^2 g_1^2 + r_3^2 g_2^2, \\ J_9 &= r_1 r_2 g_1 g_2 + r_2 r_3 g_2 g_3 + r_1 r_3 g_1 g_3, \\ J_{10} &= g_1^2 g_2^2 + g_1^2 g_3^2 + g_2^2 g_3^2 \end{aligned} \quad (2)$$

are constructed in such a way that all the operations of the cubic symmetry leave them invariant in the respective transformations. The Greek letters in (1) are the

Subgroups of the space group $Pm\bar{3}m$ for the $M_5 \oplus R_8 \oplus \Gamma_{10}$ representation

Mode type	η			Sp. gr.	$\frac{V'}{V''}$	Basis vectors			Distortion type
	m_i	r_i	g_i			a	b	c	
0	000	000	000	$Pm\bar{3}m$ (N221)	1	\mathbf{a}_1	\mathbf{a}_2	\mathbf{a}_3	0)
1	000	000	100	$P4mm$ (N99)	1	$-\mathbf{a}_3$	\mathbf{a}_2	\mathbf{a}_1	3)
2	000	000	10 $\bar{1}$	$Amm2$ (N38)	1	\mathbf{a}_2	$\mathbf{a}_1 + \mathbf{a}_3$	$\mathbf{a}_1 - \mathbf{a}_3$	
3	000	000	1 $\bar{1}$ 1	$R3m$ (N160)	1	\mathbf{a}_1	\mathbf{a}_2	\mathbf{a}_3	
4	000	000	012	Pm (N6)	1	\mathbf{a}_1	\mathbf{a}_2	\mathbf{a}_3	
5	000	000	121	Cm (N8)	1	$\mathbf{a}_1 + \mathbf{a}_3$	$\mathbf{a}_1 - \mathbf{a}_3$	\mathbf{a}_2	
6	000	000	123	$P1$ (N1)	1	\mathbf{a}_1	\mathbf{a}_2	\mathbf{a}_3	
7	000	100	000	$I4/mcm$ (N140)	2	$\mathbf{a}_2 - \mathbf{a}_3$	$\mathbf{a}_2 + \mathbf{a}_3$	$2\mathbf{a}_1$	2)
8	000	10 $\bar{1}$	000	$Imma$ (N74)	2	$\mathbf{a}_1 - \mathbf{a}_3$	$2\mathbf{a}_2$	$\mathbf{a}_1 + \mathbf{a}_3$	
9	000	1 $\bar{1}$ 1	000	$R\bar{3}c$ (N167)	2	$\mathbf{a}_2 + \mathbf{a}_3$	$\mathbf{a}_1 + \mathbf{a}_3$	$\mathbf{a}_1 + \mathbf{a}_2$	
10	000	012	000	$C2/m$ (N12)	2	$-\mathbf{a}_2$	$2\mathbf{a}_1$	$\mathbf{a}_1 + \mathbf{a}_3$	
11	000	121	000	$I2/a$ (N15)	2	$2\mathbf{a}_2$	$\mathbf{a}_3 - \mathbf{a}_1$	$\mathbf{a}_1 + \mathbf{a}_3$	
12	000	123	000	$P\bar{1}$ (N2)	2	$\mathbf{a}_2 + \mathbf{a}_3$	$\mathbf{a}_1 + \mathbf{a}_3$	$\mathbf{a}_1 + \mathbf{a}_2$	
13	100	000	000	$P4/mbm$ (N127)	2	$\mathbf{a}_1 - \mathbf{a}_2$	$\mathbf{a}_1 + \mathbf{a}_2$	\mathbf{a}_3	1)
14	011	000	000	$I4/mmm$ (N139)	4	$2\mathbf{a}_1$	$2\mathbf{a}_2$	$2\mathbf{a}_3$	
15	111	000	000	$Im\bar{3}m$ (N204)	4	$2\mathbf{a}_1$	$2\mathbf{a}_2$	$2\mathbf{a}_3$	
16	123	000	000	$Immm$ (N71)	4	$2\mathbf{a}_1$	$2\mathbf{a}_2$	$2\mathbf{a}_3$	
17*	100	002	000	$P4/mbm$ (N127)	4	$\mathbf{a}_1 - \mathbf{a}_2$	$\mathbf{a}_1 + \mathbf{a}_2$	$2\mathbf{a}_3$	4)
18	001	002	000	$Cmcm$ (N63)	4	$2\mathbf{a}_2$	$2\mathbf{a}_3$	$2\mathbf{a}_1$	
19	001	022	000	$Pnma$ (N62)	4	$\mathbf{a}_2 + \mathbf{a}_3$	$2\mathbf{a}_1$	$\mathbf{a}_2 - \mathbf{a}_3$	
20	001	023	000	$P2_1/m$ (N11)	4	$\mathbf{a}_2 - \mathbf{a}_3$	$\mathbf{a}_2 + \mathbf{a}_3$	$2\mathbf{a}_3$	
21*	001	23 $\bar{3}$	000	$P2_1/b$ (N14)	4	$2\mathbf{a}_3$	$\mathbf{a}_2 - \mathbf{a}_3$	$\mathbf{a}_2 + \mathbf{a}_3$	
22*	001	234	000	$P\bar{1}$ (N2)	4	$2\mathbf{a}_1$	$\mathbf{a}_2 + \mathbf{a}_3$	$2\mathbf{a}_3$	
23*	001	230	000	$B2/m$ (N12)	4	$-2\mathbf{a}_2$	$2\mathbf{a}_1$	$2\mathbf{a}_3$	
24	01 $\bar{1}$	002	000	PA_2/nmc (N137)	8	$2\mathbf{a}_1$	$2\mathbf{a}_2$	$2\mathbf{a}_3$	
25*	1 $\bar{1}$ 0	02 $\bar{2}$	000	$Cmcm$ (N63)	8	$2(\mathbf{a}_2 - \mathbf{a}_3)$	$2(\mathbf{a}_2 + \mathbf{a}_3)$	$2\mathbf{a}_1$	
26*	101	232	000	$B2/b$ (N15)	8	$2(\mathbf{a}_1 + \mathbf{a}_3)$	$-2\mathbf{a}_2$	$2(\mathbf{a}_1 - \mathbf{a}_3)$	
27*	123	004	000	$Pmmm$ (N59)	8	$2\mathbf{a}_1$	$2\mathbf{a}_2$	$2\mathbf{a}_3$	
28*	1 $\bar{1}$ $\bar{1}$	222	000	$R\bar{3}$ (N148)	8	$2\mathbf{a}_1$	$2\mathbf{a}_2$	$2\mathbf{a}_3$	
29*	123	045	000	$P2_1/m$ (N11)	8	$2\mathbf{a}_2$	$2\mathbf{a}_1$	$-2\mathbf{a}_3$	
30*	123	456	000	$P\bar{1}$ (N2)	8	$2\mathbf{a}_1$	$2\mathbf{a}_2$	$2\mathbf{a}_3$	
31	000	100	200	$I4cm$ (N108)	2	$\mathbf{a}_2 - \mathbf{a}_3$	$\mathbf{a}_2 + \mathbf{a}_3$	$2\mathbf{a}_1$	6)
32	000	100	002	$Fmm2$ (N42)	2	$2\mathbf{a}_1$	$2\mathbf{a}_2$	$2\mathbf{a}_3$	
33	000	100	022	$Ima2$ (N46)	2	$2\mathbf{a}_1$	$\mathbf{a}_3 - \mathbf{a}_2$	$-(\mathbf{a}_2 + \mathbf{a}_3)$	
34	000	01 $\bar{1}$	022	$Imm2$ (N44)	2	$2\mathbf{a}_1$	$\mathbf{a}_3 - \mathbf{a}_2$	$-(\mathbf{a}_2 + \mathbf{a}_3)$	
35	000	10 $\bar{1}$	020	$Ima2$ (N46)	2	$\mathbf{a}_1 - \mathbf{a}_3$	$-(\mathbf{a}_1 + \mathbf{a}_3)$	$2\mathbf{a}_2$	
36	000	011	022	$Ima2$ (N46)	2	$2\mathbf{a}_1$	$\mathbf{a}_3 - \mathbf{a}_2$	$-(\mathbf{a}_2 + \mathbf{a}_3)$	
37	000	100	023	Cm (N8)	2	$2\mathbf{a}_1$	$2\mathbf{a}_2$	$2\mathbf{a}_3$	
38	000	120	003	$C2$ (N5)	2	$2\mathbf{a}_1$	$\mathbf{a}_1 + \mathbf{a}_2$	$2\mathbf{a}_3$	
39	000	121	30 $\bar{3}$	$C2$ (N5)	2	$2\mathbf{a}_2$	$\mathbf{a}_1 + \mathbf{a}_3$	$\mathbf{a}_1 - \mathbf{a}_3$	
40	000	10 $\bar{1}$	232	Cm (N8)	2	$\mathbf{a}_1 + \mathbf{a}_3$	$\mathbf{a}_1 - \mathbf{a}_3$	$2\mathbf{a}_2$	
41	000	012	034	Fm (N8)	2	$2\mathbf{a}_1$	$2\mathbf{a}_2$	$2\mathbf{a}_3$	
42	000	123	456	$P1$ (N1)	2	$\mathbf{a}_1 + \mathbf{a}_2$	$\mathbf{a}_1 + \mathbf{a}_3$	$\mathbf{a}_2 + \mathbf{a}_3$	
43	000	1 $\bar{1}$ 1	2 $\bar{2}$ 2	$R3c$ (N161)	2	$\mathbf{a}_2 + \mathbf{a}_3$	$\mathbf{a}_1 + \mathbf{a}_3$	$\mathbf{a}_1 + \mathbf{a}_2$	
44	000	121	343	Cc (N9)	2	$\mathbf{a}_1 + \mathbf{a}_3$	$\mathbf{a}_1 - \mathbf{a}_3$	$2\mathbf{a}_2$	
45	100	000	002	$P4bm$ (N100)	2	$\mathbf{a}_1 - \mathbf{a}_2$	$\mathbf{a}_1 + \mathbf{a}_2$	\mathbf{a}_3	5)
46	001	000	002	$Amm2$ (N38)	2	\mathbf{a}_1	$2\mathbf{a}_2$	$2\mathbf{a}_3$	
47	001	000	022	$Pmc2_1$ (N26)	2	\mathbf{a}_1	$\mathbf{a}_2 - \mathbf{a}_3$	$\mathbf{a}_2 + \mathbf{a}_3$	
48	001	000	230	Cm (N8)	2	$2\mathbf{a}_2$	$2\mathbf{a}_3$	\mathbf{a}_1	
49	001	000	023	Pm (N6)	2	$\mathbf{a}_2 - \mathbf{a}_3$	$\mathbf{a}_2 + \mathbf{a}_3$	\mathbf{a}_1	

Table. (Contd.)

Mode type	η			Sp. gr.	$\frac{V'}{V''}$	Basis vectors			Distortion type
	m_i	r_i	g_i			a	b	c	
50	0 0 1	0 0 0	2 3 $\bar{3}$	<i>Pb</i> (N7)	2	$\mathbf{a}_2 + \mathbf{a}_3$	$\mathbf{a}_3 - \mathbf{a}_2$	\mathbf{a}_1	7)
51	0 1 $\bar{1}$	0 0 0	0 0 2	<i>I4mm</i> (N107)	4	$2\mathbf{a}_1$	$2\mathbf{a}_2$	$2\mathbf{a}_3$	
52	1 0 1	0 0 0	2 0 $\bar{2}$	<i>Fmm2</i> (N42)	4	$2(\mathbf{a}_1 + \mathbf{a}_3)$	$2\mathbf{a}_2$	$2(\mathbf{a}_3 - \mathbf{a}_1)$	
53	1 0 1	0 0 0	2 3 2	<i>Bm</i> (N8)	4	$\mathbf{a}_1 + \mathbf{a}_2 + \mathbf{a}_3$	$2\mathbf{a}_2$	$2(\mathbf{a}_1 - \mathbf{a}_3)$	
54	1 $\bar{1}$ $\bar{1}$	0 0 0	2 2 2	<i>R3</i> (N146)	4	$2(\mathbf{a}_1 - \mathbf{a}_3)$	$2(\mathbf{a}_2 - \mathbf{a}_1)$	$\mathbf{a}_1 + \mathbf{a}_2 + \mathbf{a}_3$	
55	1 2 3	0 0 0	4 0 0	<i>Imm2</i> (N44)	4	$2\mathbf{a}_2$	$2\mathbf{a}_3$	$2\mathbf{a}_1$	
56	0 0 1	0 0 0	2 3 4	<i>P1</i> (N1)	2	\mathbf{a}_1	$\mathbf{a}_2 + \mathbf{a}_3$	$2\mathbf{a}_3$	
57	1 2 3	0 0 0	0 4 5	<i>Im</i> (N8)	4	$-2\mathbf{a}_2$	$2\mathbf{a}_1$	$2\mathbf{a}_3$	
58	1 2 3	0 0 0	4 5 6	<i>P1</i> (N1)	4	$\mathbf{a}_1 + \mathbf{a}_2 + \mathbf{a}_3$	$2\mathbf{a}_2$	$2\mathbf{a}_3$	
59	1 0 0	2 $\bar{2}$ 0	3 $\bar{3}$ 0	<i>Pmc2₁</i> (N26)	4	$2\mathbf{a}_3$	$\mathbf{a}_1 + \mathbf{a}_2$	$\mathbf{a}_2 - \mathbf{a}_1$	
60	0 0 1	0 2 $\bar{2}$	0 3 3	<i>Pmn2₁</i> (N31)	4	$2\mathbf{a}_1$	$\mathbf{a}_2 - \mathbf{a}_3$	$\mathbf{a}_2 + \mathbf{a}_3$	
61	0 0 1	0 2 $\bar{2}$	3 0 0	<i>Pna2₁</i> (N33)	4	$\mathbf{a}_2 - \mathbf{a}_3$	$\mathbf{a}_2 + \mathbf{a}_3$	$2\mathbf{a}_1$	
62	0 0 1	0 2 3	4 0 0	<i>P2₁</i> (N4)	4	$\mathbf{a}_2 - \mathbf{a}_3$	$\mathbf{a}_2 + \mathbf{a}_3$	$2\mathbf{a}_1$	
63	0 0 1	0 2 3	0 4 5	<i>Pm</i> (N6)	4	$\mathbf{a}_3 - \mathbf{a}_2$	$-2\mathbf{a}_1$	$\mathbf{a}_2 + \mathbf{a}_3$	
64	1 0 0	2 $\bar{2}$ 0	3 3 4	<i>Pn</i> (N7)	4	$2\mathbf{a}_3$	$\mathbf{a}_1 - \mathbf{a}_2$	$\mathbf{a}_2 + \mathbf{a}_1$	
65*	0 0 1	2 0 0	0 3 3	<i>Pmc2₁</i> (N26)	4	$2\mathbf{a}_1$	$\mathbf{a}_3 - \mathbf{a}_2$	$-(\mathbf{a}_2 + \mathbf{a}_3)$	
66*	0 0 1	2 0 0	3 0 0	<i>P4bm</i> (N100)	4	$\mathbf{a}_2 - \mathbf{a}_3$	$\mathbf{a}_2 + \mathbf{a}_3$	$2\mathbf{a}_1$	
67*	0 0 1	2 0 0	0 3 4	<i>Pm</i> (N6)	4	$2\mathbf{a}_1$	$\mathbf{a}_2 + \mathbf{a}_3$	$2\mathbf{a}_3$	
68*	1 0 0	2 2 3	4 $\bar{4}$ 0	<i>P2₁</i> (N4)	4	$2\mathbf{a}_3$	$\mathbf{a}_1 - \mathbf{a}_2$	$\mathbf{a}_1 + \mathbf{a}_2$	
69*	1 0 0	2 2 3	4 4 5	<i>Pc</i> (N7)	4	$2\mathbf{a}_3$	$\mathbf{a}_1 - \mathbf{a}_2$	$\mathbf{a}_1 + \mathbf{a}_2$	
70*	1 0 0	2 0 0	3 0 0	<i>Amm2</i> (N38)	4	$-2\mathbf{a}_3$	$2\mathbf{a}_2$	$2\mathbf{a}_1$	
71	0 0 1	0 0 2	3 0 0	<i>Cmc2₁</i> (N36)	4	$2\mathbf{a}_2$	$2\mathbf{a}_3$	$2\mathbf{a}_1$	
72	1 0 0	0 0 2	3 0 0	<i>Amm2</i> (N38)	4	$2\mathbf{a}_3$	$2\mathbf{a}_2$	$2\mathbf{a}_1$	
73	0 1 0	0 0 2	3 0 0	<i>Ama2</i> (N40)	4	$2\mathbf{a}_2$	$2\mathbf{a}_3$	$2\mathbf{a}_1$	
74	0 1 1	0 0 2	0 0 3	<i>P4₂mc</i> (N105)	8	$2\mathbf{a}_1$	$2\mathbf{a}_2$	$2\mathbf{a}_3$	
75	1 $\bar{1}$ 0	2 0 0	0 3 3	<i>Aba2</i> (N41)	8	$2\mathbf{a}_1$	$2(\mathbf{a}_2 - \mathbf{a}_3)$	$2(\mathbf{a}_2 + \mathbf{a}_3)$	
76*	1 $\bar{1}$ 0	0 2 2	3 0 0	<i>Cmc2₁</i> (N36)	8	$2(\mathbf{a}_2 + \mathbf{a}_3)$	$2(\mathbf{a}_3 - \mathbf{a}_2)$	$2\mathbf{a}_1$	
77*	0 1 1	2 $\bar{2}$ 0	3 $\bar{3}$ 0	<i>Ama2</i> (N40)	8	$2\mathbf{a}_3$	$2(\mathbf{a}_1 + \mathbf{a}_2)$	$2(\mathbf{a}_2 - \mathbf{a}_1)$	
78*	1 $\bar{1}$ 0	0 2 $\bar{2}$	0 3 3	<i>Amm2</i> (N38)	8	$2\mathbf{a}_1$	$2(\mathbf{a}_2 - \mathbf{a}_3)$	$2(\mathbf{a}_2 + \mathbf{a}_3)$	
79*	1 1 1	2 2 2	3 3 3	<i>R3</i> (N146)	8	$2\mathbf{a}_1$	$2\mathbf{a}_2$	$2\mathbf{a}_3$	
80	0 1 0	2 0 0	0 3 4	<i>Cc</i> (N9)	4	$2\mathbf{a}_3$	$2\mathbf{a}_1$	$2\mathbf{a}_2$	
81*	0 1 0	0 2 3	4 0 0	<i>C2</i> (N5)	4	$2\mathbf{a}_3$	$2\mathbf{a}_1$	$2\mathbf{a}_2$	
82*	0 1 $\bar{1}$	2 $\bar{2}$ 0	3 3 4	<i>Cm</i> (N8)	8	$2(\mathbf{a}_1 - \mathbf{a}_2)$	$2(\mathbf{a}_1 + \mathbf{a}_2)$	$2\mathbf{a}_3$	
83*	0 1 $\bar{1}$	2 2 3	4 $\bar{4}$ 0	<i>C2</i> (N5)	8	$2(\mathbf{a}_1 + \mathbf{a}_2)$	$2(\mathbf{a}_2 - \mathbf{a}_1)$	$2\mathbf{a}_3$	
84*	1 0 0	0 2 3	0 4 5	<i>Cm</i> (N8)	4	$-2\mathbf{a}_2$	$2\mathbf{a}_1$	$2\mathbf{a}_3$	
85*	0 1 1	2 2 3	4 4 5	<i>Cc</i> (N9)	8	$2(\mathbf{a}_1 + \mathbf{a}_2)$	$2(\mathbf{a}_2 - \mathbf{a}_1)$	$2\mathbf{a}_3$	
86*	1 2 3	4 0 0	5 0 0	<i>Pmm2</i> (N25)	8	$2\mathbf{a}_2$	$2\mathbf{a}_3$	$2\mathbf{a}_1$	
87*	1 2 3	0 4 0	5 0 0	<i>Pmn2₁</i> (N31)	8	$2\mathbf{a}_3$	$-2\mathbf{a}_2$	$2\mathbf{a}_1$	
88*	1 2 3	4 0 0	0 5 6	<i>Pn</i> (N7)	8	$-2\mathbf{a}_2$	$2\mathbf{a}_1$	$2\mathbf{a}_3$	
89*	1 2 3	0 4 5	6 0 0	<i>P2₁</i> (N4)	8	$2\mathbf{a}_3$	$2\mathbf{a}_1$	$2\mathbf{a}_2$	
90*	1 2 3	0 4 5	0 6 7	<i>Pm</i> (N6)	8	$2\mathbf{a}_3$	$2\mathbf{a}_1$	$2\mathbf{a}_2$	
91*	1 0 0	2 3 4	5 6 7	<i>P1</i> (N1)	4	$\mathbf{a}_1 - \mathbf{a}_2$	$\mathbf{a}_1 + \mathbf{a}_2$	$2\mathbf{a}_3$	
92*	1 2 3	4 5 6	7 8 9	<i>P1</i> (N1)	8	$2\mathbf{a}_1$	$2\mathbf{a}_2$	$2\mathbf{a}_3$	

Note: The value of the order parameter η , the space group of the low-symmetry phase (and its sequential number), and the unit-cell basis (in terms of the basis vectors \mathbf{a}_i of the unit-cell described by the sp. gr. *Pm3m*) are indicated for each subgroup. As a rule, the lattice vectors are given for the main settings of the space groups. Numbering of the irreducible representations and wave vectors is made in accordance with [8]. Numerically different indices (rows in table) in the component column η indicate different values of these condensed-mode components. Index 0 indicates that the corresponding order-parameter component is identical to zero. The column V'/V'' shows the change in the unit-cell volume of the low-symmetry phase with respect to the perovskite unit cell. The asterisks in the first column indicate the phases not considered in [7].

coefficients dependent on the external conditions. Writing (1), we limited ourselves to the fourth-order expansion, although it is necessary to emphasize that the integer rational basis of invariants in Eqs. (2) is incomplete and should be continued up to the sixth order with respect to r and g and up to the ninth order with respect to the order parameter m [10]. However, at the present stage, the model with allowance for higher degrees is beyond our interest: we are interested only in the qualitative results associated with the determination of the stability conditions for most symmetric phases indicated in the table.

The equilibrium state at an arbitrary temperature is determined by minimizing $\delta F'$ with respect to m_i , r_i , and g_i . The exhaustive study of the extrema of the function $\delta F'$ in a multidimensional parametric space is a very cumbersome problem. However, some characteristics of the phase diagram can be obtained under some model simplifications. This is motivated by the following. First, the solutions of equations of state for all the symmetrically admissible phases with the order parameter $M_5 \oplus R_8 \oplus \Gamma_{10}$ have already been obtained by the direct group-theoretical method (table). Second, at the beginning, we are interested only in those situations where each of the phase states considered differs from another phase state only by the presence (absence) of at least one structural distortion (but of a different type). In other words, we are interested in the topology only of those phases in which the distortions are caused by different types of structural instabilities (+ and – rotations or polar displacement of a B cation). It is possible to solve this problem in the model with three nondegenerate order parameters. Third, the intrinsic three-fold degeneracy of each individual mode can be taken into account in each particular phenomenological situation.

Thus, first of all, we consider only distortions of different types for the model of an effective potential with three one-component order parameters,

$$F = \alpha_2 m^2 + \alpha_4 m^4 + \beta_2 r^2 + \beta_4 r^4 + \gamma_2 g^2 + \gamma_4 g^4 - \delta_{22} m^2 r^2 - \epsilon_{22} m^2 g^2 - \eta_{22} r^2 g^2 + \dots \quad (3)$$

Here, similar to (1), the Greek letters indicate the coefficients but have different values. It is assumed in (3) that the interaction between different modes reduces the system's energy; i.e., $\delta_{22} > 0$, $\epsilon_{22} > 0$, and $\eta_{22} > 0$, and the inequalities $4\alpha_4\beta_4 - \delta_{22}^2 > 0$, $4\beta_4\gamma_4 - \eta_{22}^2 > 0$, and $4\alpha_4\gamma_4 - \epsilon_{22}^2 > 0$ are valid. These conditions predetermine the existence in the phase diagrams of the maximum number of stable phases. Then, as is usual in the Landau theory [13], we assume that only α_2 , β_2 , and γ_2 are the linear functions of temperature and pressure (but with different values of the respective critical tem-

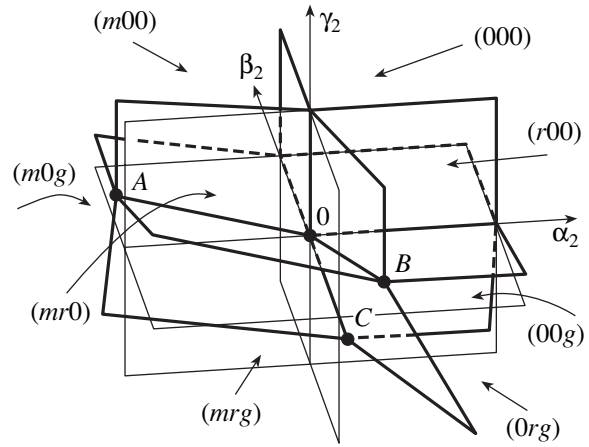


Fig. 1. Three-dimensional phase diagram for the model described by (3). The AO , BO , and CO straight lines are the lines of multiphase points. The regions with symbols in parentheses correspond to solutions (5).

peratures T_j and pressures p_j):

$$\begin{aligned} \alpha_2 &= \alpha_{mT}(T - T_M) + \alpha_{mp}(p - p_M), \\ \beta_2 &= \beta_{rT}(T - T_R) + \beta_{rp}(p - p_R), \\ \gamma_2 &= \gamma_{gT}(T - T_\Gamma) + \gamma_{gp}(p - p_\Gamma). \end{aligned} \quad (4)$$

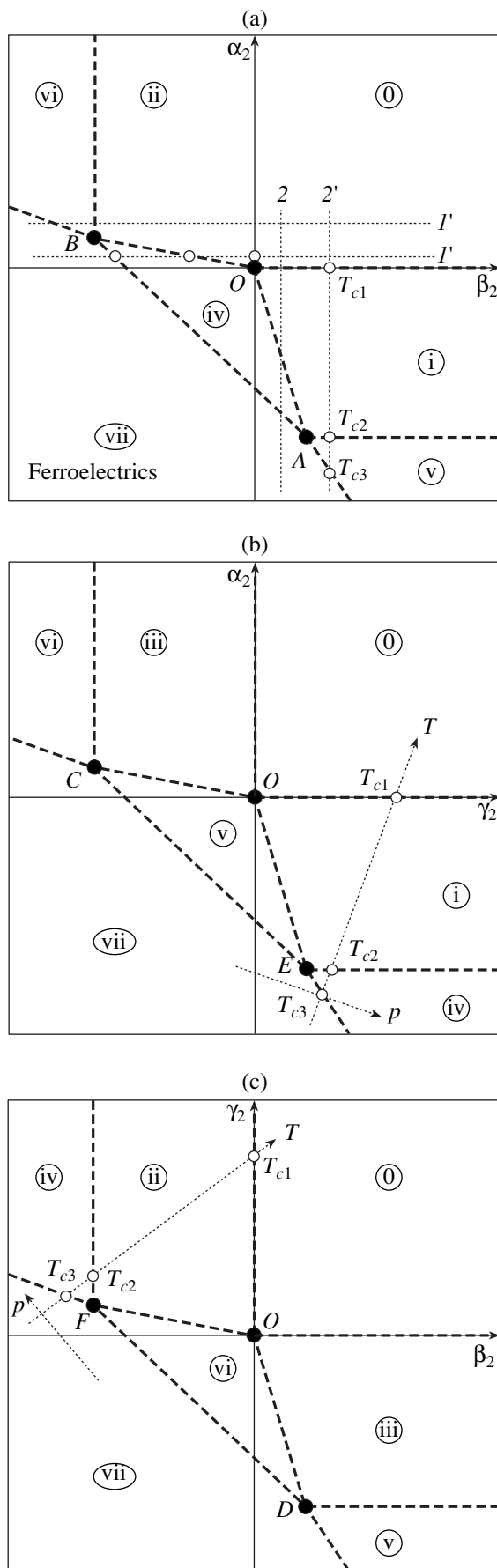
The remaining coefficients in (3) are constants. The conditions $\alpha_4 > 0$, $\beta_4 > 0$, and $\gamma_4 > 0$ ensure the potential stability with respect to infinitely large fluctuations of the order parameters \mathbf{m} , \mathbf{r} , and \mathbf{g} .

The equations of state for the model described by (3) are $\partial F/\partial m = \partial F/\partial r = \partial F/\partial g = 0$. They admit the following eight solutions:

$$\begin{aligned} (0) \quad & m = r = g = 0, & (i) \quad & m \neq 0, r = 0, g = 0, \\ (ii) \quad & m = 0, r \neq 0, g = 0, & (iii) \quad & m = 0, r = 0, g \neq 0, \\ (iv) \quad & m \neq 0, r \neq 0, g = 0, & (v) \quad & m \neq 0, r = 0, g \neq 0, \\ (vi) \quad & m = 0, r \neq 0, g \neq 0, & (vii) \quad & m \neq 0, r \neq 0, g \neq 0. \end{aligned} \quad (5)$$

Analyzing the positive definiteness of the Hessian corresponding to (3) and requiring that all solutions (5) be real, we arrive at the phase diagram shown in Fig. 1. The planes determining the stability of the neighboring phases coincide and, thus, in this case, all the transitions are of the second order. It follows from Fig. 1 that there exist several sequences of phase transitions depending on the numerical values of the coefficient ratios in (3).

In that case, where only the individual modes are soft, which corresponds to the change of only one of the coefficients α_2 , β_2 , or γ_2 in (3) (in the phase diagram, this corresponds to thermodynamic paths parallel to the coordinate axes), the following sequences of the phase states are admissible. The phase sequence (0) \rightarrow (ii) \rightarrow (iv) \rightarrow (vii) is implemented if the coefficient β_2 decreases. (Only the mode R_8 is soft.) However, in



this case, the conditions $\gamma_2 > 0$ and $0 < \alpha_2 < \gamma_2 \delta_{22} / \eta_{22}$ should be fulfilled. If $\alpha_2 > \gamma_2 \delta_{22} / \eta_{22}$, then, as earlier, $\gamma_2 > 0$ and a decrease in the coefficient β_2 results in the sequence (0) \rightarrow (ii) \rightarrow (vi) \rightarrow (vii). If the M_5 mode is soft, which corresponds to the change of only the coefficient α_2 , whereas all the other modes considered are rigid, then two phase sequences are also possible: (0) \rightarrow (i) \rightarrow (iv) \rightarrow (vii) at $\gamma_2 > 0$ and $0 < \beta_2 < \gamma_2 \delta_{22} / \epsilon_{22}$ or (0) \rightarrow (i) \rightarrow (v) \rightarrow (vii) if $\gamma_2 > 0$ and $\beta_2 > \gamma_2 \delta_{22} / \epsilon_{22}$. Finally, if only the polar mode Γ_{10} is soft, which signifies only the change of the coefficient γ_2 , two different sequences of second-order phase transitions analogous to those indicated above are possible: (0) \rightarrow (iii) \rightarrow (v) \rightarrow (vii) at $0 < \alpha_2 < \beta_2 \epsilon_{22} / \eta_{22}$ or (0) \rightarrow (iii) \rightarrow (vi) \rightarrow (vii) if $\beta_2 > 0$ and $\alpha_2 > \beta_2 \epsilon_{22} / \eta_{22}$.

The statement above is illustrated by Fig. 2, which shows three typical sections of the diagram shown in Fig. 1. It should be noted that the type of every second (and third!) phase transition in the above sequences may be classified as a trigger one [14] because of the *appearance* in more low-symmetry phases of distortions not corresponding to the symmetry of the soft mode which initiated the first phase transition of the sequence. Note also that, unlike [14], in our case, the expansion degree with respect to the rigid mode is lower than that used in [14], because of the existence of three interacting order parameters and not only two as in [14]. Pairwise mode softening (to which there correspond the tilted thermodynamic paths in Fig. 1 indicated as T axes for one of these paths) gives no new sequence of the phase states for the model described by (3). It should also be emphasized that the phase transition from the highly symmetric phase (0) to one of the phases (iv), (v), or (vi) may proceed only through the point O , which is hardly probable. As a result, the three-phase sequences (0) \rightarrow (iv) \rightarrow (vii), (0) \rightarrow (v) \rightarrow (vii), and (0) \rightarrow (vi) \rightarrow (vii) are unlikely.

Fig. 2. Three characteristic sections of the diagram shown in Fig. 1. (The third variate not variable within the section is positive.) The encircled Roman numerals correspond to solutions (5). Dashed lines correspond to second-order phase transitions. Dotted lines indicate the thermodynamic paths for the dependences of type (4) (T and p axes). The coordinates of the multiphase points are as follows: the O

point $(0, 0)$, the A point $(\beta_2^A = \frac{\delta_{22}}{\epsilon_{22}} \gamma_2, \alpha_2^A = -\frac{2\alpha_4}{\epsilon_{22}} \gamma_2)$, the

B point $(\beta_2^B = -\frac{2\beta_4}{\eta_{22}} \gamma_2, \alpha_2^B = \frac{\delta_{22}}{\eta_{22}} \gamma_2)$, the C point $(\gamma_2^C =$

$-\frac{2\gamma_4}{\eta_{22}} \beta_2, \alpha_2^C = \frac{\epsilon_{22}}{\eta_{22}} \beta_2)$, the D point $(\beta_2^D = \frac{\eta_{22}}{\epsilon_{22}} \alpha_2, \gamma_2^D =$

$-\frac{2\gamma_4}{\epsilon_{22}} \alpha_2)$, the E point $(\gamma_2^E = \frac{\epsilon_{22}}{\delta_{22}} \beta_2, \alpha_2^E = -\frac{2\alpha_4}{\delta_{22}} \beta_2)$, and

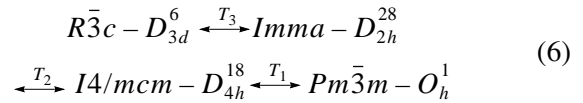
the F point $(\beta_2^F = -\frac{2\beta_4}{\delta_{22}} \alpha_2, \gamma_2^F = \frac{\eta_{22}}{\delta_{22}} \alpha_2)$.

Of course, one has to remember that, under real thermodynamic conditions, only a part of the indicated sequence will be implemented. Thus, in calcium titanate, the transition to the ferroelectric state may take place only at a temperature considerably lower than absolute zero ($T_C \approx -150$ K) and, therefore, CaTiO_3 is considered to be only an *incipient* ferroelectric [15]. In our approach, this signifies that the transition to phase (vii) (if one or the other of the above sequences takes place) is not attained under the conditions of a real experiment. Such a transition may take place, although along a thermodynamically different path of the phase diagram, only owing to the change of the composition or owing to doping with some impurities. Thus, in the $\text{Ca}_{1-x}\text{Pb}_x\text{TiO}_3$ solid solution, *incipient ferroelectricity* is really observed only if $x > 0.3$ [15]. The corresponding phenomenological model is considered elsewhere [16].

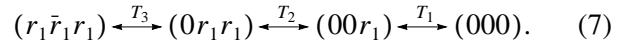
We would like to emphasize once again the specific nature of the phase diagrams shown in Figs. 1 and 2. This specificity concerns the relation between the potential described by Eq. (1), which takes into account three-fold degeneracy of soft modes, and the potential described by (3) with the nondegenerate order parameters. Within the model accepted, each of the solutions described by (5) corresponds to sets of phases grouped into eight blocks in the table. In each of the sets, only one type of distortions is possible: only in-phase distortions for the M_5 mode (type 1), only antiphase rotations for the R_8 mode (type 2), and only polar shifts for the Γ_{10} mode (type 3) or their joint combinations (types 4–7). Therefore, generally speaking, each of the regions in Figs. 1 and 2 is a specific *phase container* of distortions of one type. The contents of such a container depend on the numerical values of the constants in the initial potential described by Eq. (1). In the transition to a symmetrically correct model described by Eq. (1), the regions of “one-type phase states” are “divided” into components and form a specific phase mosaic with distortions of one type. In this case, straight lines of the phase transitions in Fig. 2 become broken lines. Several examples of such “correct” phase diagrams are shown in Fig. 3.

If only one of the rotational modes considered above is soft, whereas all the other modes are rigid, then the condensation of only one its component at the positive value of the corresponding anisotropy coefficient (A_4 or B_4) in Eq. (1) always results in the formation of a tetragonal structure, i.e., D_{4h}^5 in the case of the M_5 mode as the “primary” one or D_{4h}^{18} in the case of the R_8 mode as the first structural distortion (see table). If in this case the anisotropy coefficient (e.g., B_4 in Eq. (1)) changes its value and sign for some reason, then the sequence of phase transitions may also include some other low-symmetry phases related to this mode. Thus, the condensation of each additional component in any of the rotational modes is equivalent to freezing of the dis-

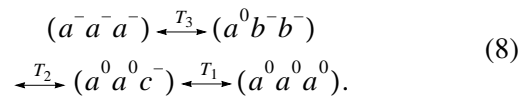
placements around another axis (with respect to the first one). Then the corresponding structural distortion is described by an orthorhombic space group. Thus, the sequence of the phase transitions of the type



may take place only owing to the mode R_8 as a successive condensation of equal antiphase rotations of octahedra around one, two, or three cubic axes at the temperatures T_1 , T_2 , and T_3 :



This is equivalent to the following expressions in the Glaser notation [4]:



However, in this case, the coefficient B_4 in Eq. (1) should be strongly dependent on temperature. However, it should be noted that this sequence may really take place only in the models with a high degree of expansion of the free energy (1) in the order parameter r [10]. Therefore, region (ii) (as well as regions (i) and (iii)) in the diagram shown in Fig. 3 remains a one-phase region. Obviously, the further structural distortions are due to the addition of distortions caused by other modes. The regions of the mixed states with respect to the type of distortion are divided into smaller parts and form a specific phase mosaic with distortions of only one type (which is most clearly seen in Fig. 3f).

However, model (3) reflects the gradual complication of total distortions of the structure arising with lowering of the temperature qualitatively correctly (Aleksandrov's criterion [1, 2]) irrespective of the phase participating in the sequence of phase transitions. It is only important that each following phase transition in the given model may be considered as a triggering one, because a low-symmetric phase spontaneously acquires distortions not corresponding to the symmetry of the “leading” soft mode. It is the triggering nature of the phase transition that imposes certain limitations on the sequence of phase transformations, whereas the choice of a concrete “phase representative” in the sequence depends on the numerical value of the ratio of the constants in the Landau potential.

Figure 3 shows several variants of phase diagrams corresponding to potential (1). If the sign of the coefficient B_4 and the numerical coefficients are varied with allowance for the intermode interactions δ'_{22} , Δ_{22} , etc., in Eq. (1), it is possible to implement different phase sequences, including those with the first-order phase transitions. We would like to indicate once again that the allowance for the three-dimensional character of the modes results in the transformation of straight lines in

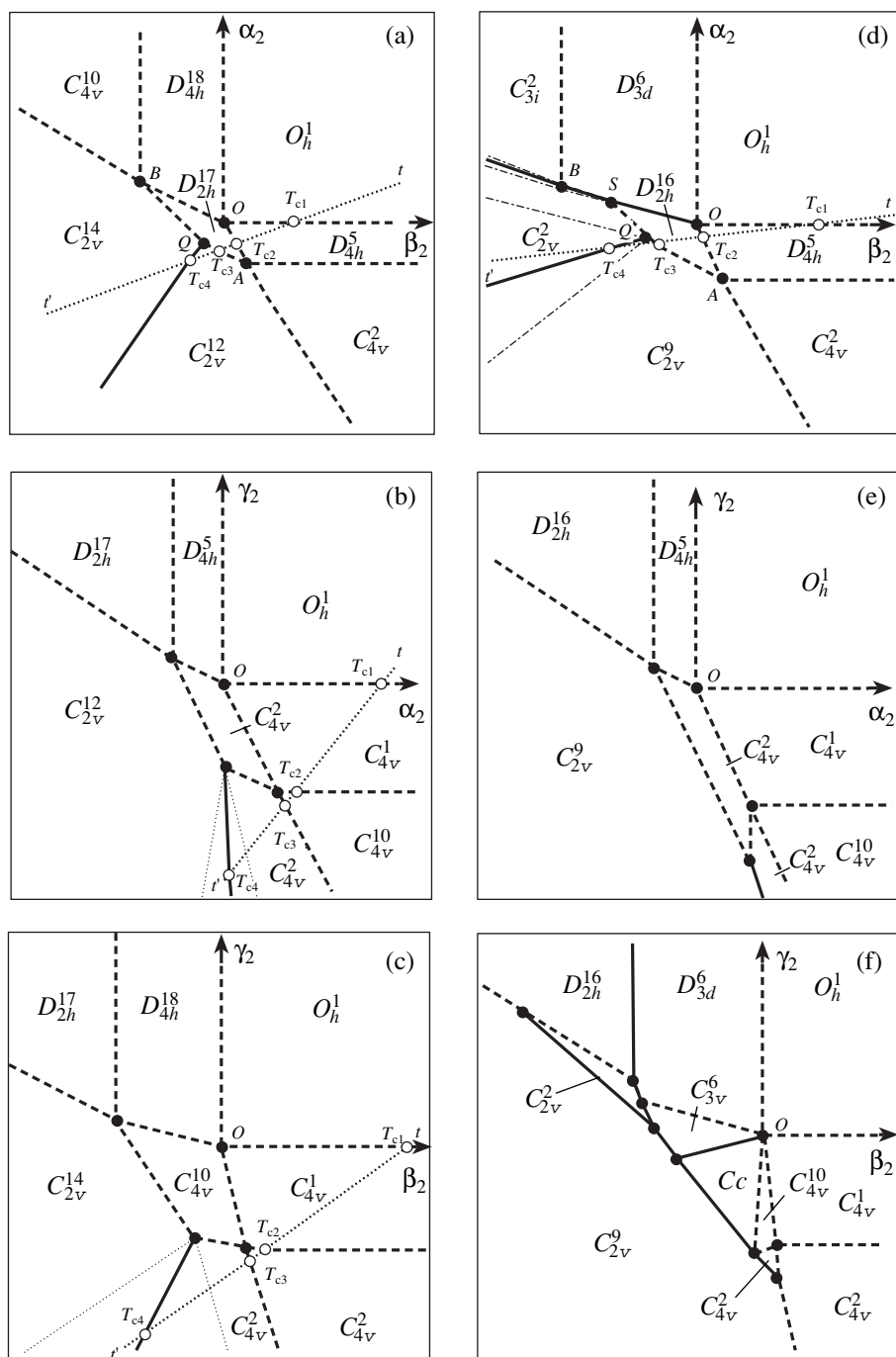


Fig. 3. the α_2 - β_2 - γ_2 sections of the variants of the phase diagrams for model (1). Dashed lines correspond to the second-order phase transitions; solid lines, to first-order phase transitions. Thin dashed-dotted lines are spinodals of the conjugated phases of the first-order phase transitions. Dotted lines indicate thermodynamic paths. Closed circles indicate multiphase points. Open circles indicate the points of phase transitions during the change of phase states along the thermodynamic path. The selection of the symmetry groups from the table in panels (a)–(f) is associated with the selection of the numerical values of the constants in the potential described by Eq. (1). In all cases $\alpha_4 > 0$, $\beta_4 > 0$, $\Gamma_4 > 0$, $-\delta_{22} = \Delta_{22} > 0$, $\epsilon_{22} = E_{22} < 0$, and $-\eta_{22} = -H_{22,1} = H_{22,2} > 0$. For (d)–(f) $A_4 > 0$, $B_4 < 0$, $\Gamma_4 > 0$, $-\delta_{22} \neq \Delta_{22} > 0$, $\epsilon_{22} = E_{22} < 0$, and $\eta_{22} = H_{22,1} < 0 < H_{22,2} < -H_{22,1}$.

Fig. 2 into broken lines in Fig. 3, because, now, the “container regions” of the model described by (3) may be in several phase states with the structural distortions of one type. However, in the free-energy expansion of

the low degree (1), only regions (iv)–(vii) can “decompose” into the constituent regions.

Analysis of the table shows that all the phases of set (vii) may be ferroelectrics. Therefore, the change of the

polarization vector is probable in some perovskite representatives when the thermodynamic path passes through region (vii). This change is generically predetermined, above all, because of the interactions described by the terms $H_{22,1}J_9$ and $H_{22,2}J_8$ in the potential described by Eq. (1).

Concluding the article, we would like to indicate that it is also important for further analysis of various concrete situations to take into account the studies dedicated to the problems close to those considered above [16–18].

CONCLUSIONS

The symmetries of 92 different variants of distortions in the ideal perovskite structure are determined by group-theoretical analysis in the presence of interactions between two rotational (R_8 and M_5) and one polar (Γ_{10}) soft modes.

The global picture of the changes of the phase states is considered within the framework of a simple Landau model of second-order phase transitions for the three three-component order parameters. The change of the phase states in the chains of phase transitions is explained by the trigger mechanism. Unlike the Holakovskiy model [14], our model of three interacting order parameters considers the fourth-order expansion in the rigid mode and the corresponding phase transformation may be a second-order phase transition. It is also shown that the change of the polarization-vector direction in some perovskites necessarily follows from the specific character of the interaction between the R_8 and Γ_{10} modes.

ACKNOWLEDGMENTS

The study was supported by the Russian Foundation for Basic Research, project nos. 04-02-16228 and 03-02-16720, and the Presidential Foundation “Scientific Schools,” project NSh-1415.2003.2.

REFERENCES

1. K. S. Aleksandrov, A. T. Anistratov, B. V. Beznosikov, *et al.*, *Phase Transitions in ABX_3 Haloid Crystals* (Nauka, Novosibirsk, 1981) [in Russian].
2. K. S. Aleksandrov and J. Bartolome, *Phase Transit.* **74**, 255 (2001).
3. R. A. Cowley, *Phys. Rev.* **134**, A981 (1964).
4. W. Cochran and A. Zia, *Phys. Status Solidi* **25**, 273 (1968).
5. A. M. Glaser, *Acta Crystallogr., Sect. B: Struct. Crystallogr. Cryst. Chem.* **28**, 3384 (1972).
6. A. M. Glaser, *Acta Crystallogr., Sect. A: Cryst. Phys., Diffr., Theor. Gen. Crystallogr.* **31**, 756 (1975).
7. H. T. Stokes, E. H. Kisi, D. M. Hatch, *et al.*, *Acta Crystallogr., Sect. B: Struct. Sci.* **58**, 934 (2002).
8. O. V. Kovalev, *Irreducible Representations of the Space Groups* (Akad. Nauk Ukr. SSR, Kiev, 1961; Gordon and Breach, New York, 1965).
9. V. B. Shirokov and V. I. Torgashev, *Kristallografiya* **49** (1), 25 (2004) [*Crystallogr. Rep.* **49**, 20 (2004)].
10. Yu. M. Gufan, *Structural Phase Transitions* (Nauka, Moscow, 1982) [in Russian].
11. J. C. Toledano and P. Toledano, *The Landau Theory of Phase Transitions* (World Sci., Singapore, 1987).
12. É. B. Vinberg, Yu. M. Gufan, V. P. Sakhnenko, and Yu. I. Sirotnin, *Kristallografiya* **19**, 21 (1974) [*Sov. Phys. Crystallogr.* **19**, 10 (1974)].
13. L. D. Landau, *Phys. Z. Sowjetunion* **11**, 26 (1937).
14. J. Holakovskiy, *Phys. Status Solidi B* **56**, 616 (1973).
15. V. V. Lemanov, A. V. Sotnikov, E. P. Smirnova, *et al.*, *Appl. Phys. Lett.* **81**, 886 (2002).
16. A. A. Volkov, G. A. Komandin, B. P. Gorshunov, *et al.*, *Fiz. Tverd. Tela (St. Petersburg)* **46**, 899 (2004) [*Phys. Solid State* **46**, 927 (2004)].
17. M. P. Ivliev, *Kristallografiya* **47** (6), 1065 (2002) [*Crystallogr. Rep.* **47**, 996 (2002)].
18. M. P. Ivliev, M. P. Raevskii, L. A. Reznichenko, *et al.*, *Fiz. Tverd. Tela (St. Petersburg)* **45**, 1886 (2003) [*Phys. Solid State* **45**, 1984 (2003)].

Translated by L. Man

PHYSICAL PROPERTIES OF CRYSTALS

Zinc Oxide Single Crystals: Influence of Temperature and Orientation of Crystals on Their Mechanical Properties

L. N. Demyanets, N. L. Sizova, and L. E. Li

*Shubnikov Institute of Crystallography, Russian Academy of Sciences,
Leninskiĭ pr. 59, Moscow, 119333 Russia*

e-mail: demianets@mail.ru

Received August 11, 2003

Abstract—Zinc oxide single crystals are grown hydrothermally and their microhardness is measured on different $\{hkil\}$ faces in the temperature range from liquid nitrogen temperature to 900°C. The coefficient K_{1C} of fracture roughness and the surface energy γ of fracture are estimated. The (0001) plane of a positive monohedron is characterized by the maximum hardness and plasticity over the whole temperature range studied. The shape of indenter prints and dislocation rosettes on the planes of monohedra, hexagonal prisms, and the pyramid are studied. The indenter print on the basal plane has an isotropic shape, whereas on the planes of prisms and the pyramid the prints indicate the first-kind anisotropy of mechanical properties. The first-kind anisotropy coefficient k equal to H_{\max}/H_{\min} increases with an increase in the temperature for the $\{10\bar{1}0\}$, $\{11\bar{2}0\}$, and $\{10\bar{1}1\}$ planes. For the $\{10\bar{1}0\}$ plane, the coefficient k varies from ~ 1.4 at room temperature to ~ 2 at 900°C.
© 2005 Pleiades Publishing, Inc.

INTRODUCTION

Zinc oxide is a high-energy gap semiconductor of the $A^{II}B^{VI}$ group that possess a number of unique physical and chemical properties and is widely used in various fields of modern science and technology from ultraviolet light diodes to piezoelectric technologies. Such a popularity of this material explains the large number of studies dedicated to synthesis of ZnO single crystals, crystalline ZnO films, and low-dimensional crystalline ZnO powders. The successful use of this material in various devices requires clear understanding of the behavior of its main characteristics under the action of varying external factors such as temperature, irradiation, etc. One of such important material characteristics is its mechanical properties. The mechanical properties of zinc oxide crystals were studied only in a small number of works [1–5] and mainly on ZnO ceramics. The mechanical properties of crystals with the wurtzite structure (including ZnO) were studied in details on CdS crystals by the group headed by Osip'yan. Thus, this group was the first to study the photoplastic properties of CdS crystals [6]. Carlsson [7] showed that zinc oxide single crystals also possess the photoplastic effect.

The present study is dedicated to growth of specially oriented zinc oxide single crystals, the crystallochemical analysis of their structure, and the study of their mechanical properties over a wide temperature range.

EXPERIMENTAL

Growth of ZnO Single Crystals

Zinc oxide single crystals were obtained by hydrothermal synthesis in the ZnO–KOH–LiOH–H₂O system by the method described in detail elsewhere [8]. The KOH concentration was 5.5 mol/l and the LiOH concentration was 1.4 mol/l. The temperature in the growth zone ranged within 230–300°C, the temperature gradient Δt between the dissolution and growth zones ranged within ~ 15 –55°C, and the pressure ranged within ~ 10 –50 MPa. The growth experiments were performed in 1000-cm³-autoclaves with silver containers of the floating type and a 500-cm³ working volume. The seeds were single-crystal ZnO plates cut out from hydrothermally grown ZnO single crystals parallel to their basal plane. The growth mechanism of ZnO crystals was discussed in detail elsewhere [8–11].

Mechanical Properties

The samples in the form of $10 \times 10 \times 2$ -mm³ plates were cut out from the grown single crystals in such a way that the plane having the maximum area was parallel to one of the main simple crystallographic forms of zinc oxide crystals: to the positive (0001) and negative (000 $\bar{1}$) planes of monohedra, the first- and second-kind $\{10\bar{1}0\}$ and $\{11\bar{2}0\}$ planes of prisms, and $\{10\bar{1}1\}$ planes of the pyramid. The plates were first polished and finished mechanically, then polished chemically, and finally indented by a Vickers pyramid

under loads up to 1.5 N on a high-temperature microhardness tester in the temperature range -196 to 900°C [12]. The indenter was oriented in a such a way that one its diagonal was brought into coincidence with the $\langle 11\bar{2}0 \rangle$ or $\langle 10\bar{1}0 \rangle$ glide directions in ZnO crystals. For monohedra, the indenter diagonals were parallel to the $\langle 10\bar{1}0 \rangle$ and $\langle 11\bar{2}0 \rangle$ directions. For the first-kind prisms, the indenter diagonals were parallel to the $[0001]$ and $\langle 11\bar{2}0 \rangle$ directions, while for the second-kind prism $\{11\bar{2}0\}$, the indenter diagonals were parallel to the $[0001]$ and $\langle 10\bar{1}0 \rangle$ directions, respectively. On the pyramid face $\{10\bar{1}0\}$, one diagonal coincided with the glide direction $\langle 11\bar{2}0 \rangle$, whereas the other coincided with the projection of the $[0001]$ direction onto the pyramid plane c' .

Surface Morphology

The microstructure of deformed samples was revealed by chemical etching in the etchants specially selected for each face: a 5-mol KOH solution at 110°C for the basal plane, a saturated KOH solution at 110°C for the $\{10\bar{1}1\}$ plane of the pyramid, and a boiling mixture of nitric and hydrofluoric acids in a 2 : 1 ratio for the $(10\bar{1}0)$ plane of the prism.

RESULTS AND DISCUSSION

Main Crystallographic Characteristics of ZnO Crystals

Zinc oxide crystallizes in the polar sp. gr. $P6_3mc$ (wurtzite structure type) with the unit-cell parameters $a = 3.249 \text{ \AA}$, $c = 5.207 \text{ \AA}$, and $Z = 2$. Chemical bonding in ZnO is of the mixed covalent–ionic nature with $\sim 60\%$ ionicity [13]. The structure framework is built by $[\text{ZnO}_4]$ tetrahedra sharing their vertices (Fig. 1a). The structure has no center of inversion, which indicates its polar nature along the $[0001]$ direction.

Consider the structure of the faces of the main crystallographic forms of zinkite crystals. A detailed structure analysis was made in [9]. The structure may be described as a packing of elementary layers characteristic of each $(hkil)$ face. Some structural characteristics of the main simple crystallographic forms of zinc oxide are indicated in Table 1. Figure 1b illustrates the obvious polar nature of the structure and shows the plane nets of atoms of one species forming the face of the positive monohedron (alternation of plane nets occupied by atoms of one species), the first-kind prisms (alternation of the plane nets of the mixed composition), and the first-kind pyramids (corrugated nets occupied by atoms of one species).

The surface of the (0001) face terminates with Zn^{2+} ions, whereas the surface of the negative monohedron terminates with O^{2-} ions. Thus, the main difference

Table 1. Composition, calculated thickness Δ_{hkil} , and reticular density ρ_{hkil} of elementary layers for the main crystallographic simple forms of ZnO single crystals

$\{hkil\}$ face	d_{hkil} , \AA	Δ_{hkil} , \AA	ρ_{hkil} , \AA	Composition of the nets forming ele- mentary layer
(0001) monohedron	5.207	2.60	2	Zn/O/Zn
$(000\bar{1})$ monohedron	5.207	2.60	2	O/Zn/O
$\{10\bar{1}0\}$ prism	2.817	2.82	2.17	(Zn, O)/(Zn, O)
$\{11\bar{2}0\}$ prism	1.626	1.62	1.25	(Zn, O)/(Zn, O)
$\{10\bar{1}1\}$ pyramid	2.476	2.47	1.90	$\text{Zn}^*/\text{O}^*/\text{Zn}^*$
$\{10\bar{1}2\}$ pyramid	1.911	1.91	1.47	$(\text{Zn, O})^*/\text{O}/\text{Zn}$

* Corrugated planes.

between these two faces reduces to different effective charges at their surfaces, which can manifest itself in different properties of the positive and negative monohedra. The faces of both prisms $\{10\bar{1}0\}$ and $\{11\bar{2}0\}$ are built by the nets of the mixed composition. Such structures and the polar axis located in the prismatic planes should give rise to close physical characteristics and to anisotropy along the polar axis.

Analysis of the structure of individual faces allowed us to draw some preliminary conclusions on the relative crystallization rates along different crystallographic directions. In accordance with the simple empiric rule formulated in [14], the maximum growth rates have the faces whose coordination polyhedra enter the interface with their vertices, whereas the minimum growth rates have the $\{hkil\}$ planes whose coordination polyhedra enter the interface with their faces. The intermediate growth rates are characteristics of the faces of simple crystallographic forms looking at the interface with polyhedron edges. This simple consideration applied to ZnO crystals gives the following sequence of growth rates V of various faces:

$$V(000\bar{1}) < V\{11\bar{2}0\} < V\{10\bar{1}0\} \\ < V\{10\bar{1}1\} < V(0001).$$

Growth of Single Crystals

Under the selected conditions, crystallization on the seeding plates parallel to the (0001) plane results in the formation on the plate surface mainly of growth pyramids of the positive monohedron. Crystal faceting is characterized by the following simple forms: the positive (0001) monohedron, negative $(000\bar{1})$ monohedron, first-kind $\{10\bar{1}0\}$ prism, second-kind $\{11\bar{2}0\}$ prism, and $\{10\bar{1}1\}$ pyramid. The habit of grown crystals clearly reflects the polarity of zinc oxide crystals. The growth rate along the $[0001]$ direction is higher by a factor of 1.5–2.0 than the growth rate along the

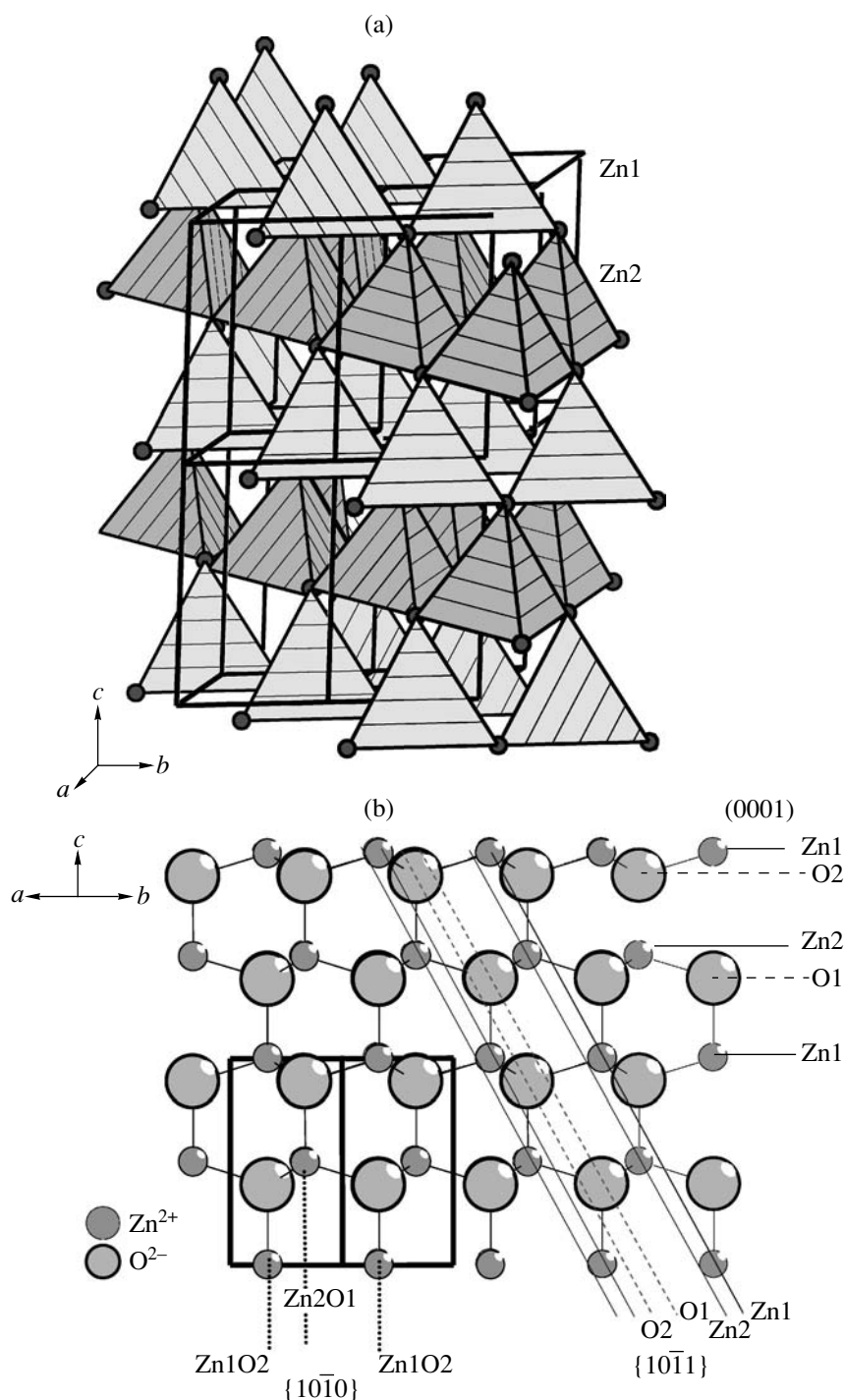


Fig. 1. Crystal structure of zinc oxide: (a) ZnO structure in polyhedra and (b) ZnO structure projected onto the $(11\bar{2}0)$ plane. One can see the composition of the elementary layers on the (0001) , $(10\bar{1}0)$, and $(10\bar{1}1)$ faces.

$[000\bar{1}]$ direction. The sequence of the experimentally established growth rates coincides with the above sequence:

$$V(000\bar{1}) \ll V\{11\bar{2}0\} \approx V\{10\bar{1}0\} \\ < V\{10\bar{1}1\} < V(0001).$$

The growth rate $V(0001)$ ranged within 0.35–0.1 mm/day for various Δt values, whereas the $V(000\bar{1})$ rate ranged only within 0.11–0.04 mm/day. The $V(0001)/V(000\bar{1})$ ratio varied within 1.5–2.3 depending on the solution supersaturation.

The grown crystals had lithium impurities, which, because of the close ionic radii of Li and Zn (r_{Li^+} 0.73 Å and $r_{\text{Zn}^{2+}}$ 0.74 Å) could either replace Zn^{2+} (Li_{Zn}) or occupy the interstices (Li_{Zn}^i). The lithium content in the grown crystals ranged within 10^{17} – 10^{18} cm^{-3} . The dislocation density in the samples cut from the growth pyramid of the positive monohedron ranged within 10^2 – 10^4 cm^{-2} .

The growth mechanism was considered in detail elsewhere [10, 11].

Temperature Dependence of Microhardness

Microhardness on different $\{hkl\}$ faces of the crystals was determined in kgf/mm^2 by the formula $H = 1854P/d^2$, where P is the load applied to the indenter in grams and d is the diagonal of the indenter print in microns. Figure 2 shows the dependence of the Vickers microhardness of the (0001), $\{10\bar{1}0\}$, and $\{10\bar{1}1\}$ planes as function of temperature in the temperature range -196 to 900°C .

Analyzing the structure of individual faces of the grown ZnO crystals, we expected that hardness of the faces of the first- and second-kind prisms would have close values because of their similar structure (in both cases, the faces consist of atomic nets formed by different species) and would considerably differ for the positive and negative monohedra. As the tests showed, the hardness values of the planes of the $\{10\bar{1}0\}$ and $\{11\bar{2}0\}$ prisms were in fact equal within experimental error (3%); therefore, Fig. 2 shows only the data obtained for the first-kind prism $\{10\bar{1}0\}$. At the same time, despite the considerably different structures and compositions of the plane nets forming the positive and negative (0001) and $(000\bar{1})$ monohedra, the microhardness values of both faces are also equal within measurement error. Thus, despite the fact that the $(000\bar{1})$ plane was polished and finished more easily than the (0001) plane, microindentation did not reveal any difference between the (0001) and $(000\bar{1})$ planes within experimental error. Therefore, it is reasonable to solve this problem by the method of nanoindentation.

Comparison of hardness H of different planes at various temperatures shows that the basal (0001) plane has the highest hardness in the whole temperature range measured. In the range from the temperature of liquid nitrogen to room temperature, the value of $H(0001)$ was more than twice as high as the H values for prisms and pyramids. The hardness of the pyramid is higher by ~6% than the hardness of prism. Analyzing the plot, we may divide it into three characteristic temperature ranges: (i) from -196 to 300°C , (ii) from 300 to 600°C , and (iii) from 600 to 900°C . The first range is charac-

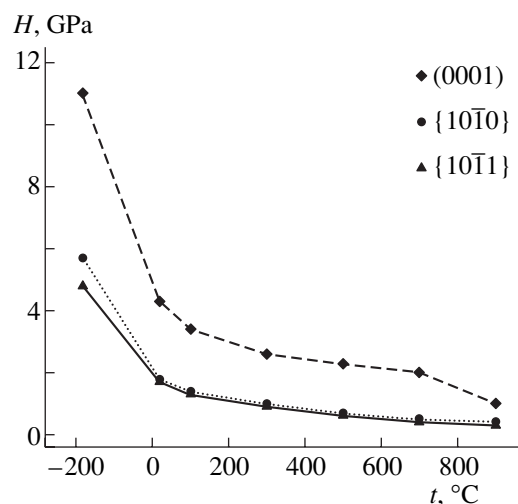


Fig. 2. Microhardness of the (0001), $\{10\bar{1}0\}$, and $\{10\bar{1}1\}$ faces of a ZnO crystals as a function of temperature.

terized by a dramatic decrease in microhardness with an increase in the temperature for all the planes studied. Thus, the hardness of the (0001) face decreases from ~10 to ~5 GPa and the hardness of the faces of the $\{10\bar{1}0\}$ prism decreases from ~5 to ~2 GPa. In the second temperature range, hardness smoothly decreases with temperature. Finally, in the third temperature range, hardness only slightly depends on temperature for the planes of the prism and pyramid, but the microhardness of the (0001) planes decreases with a rise in temperature. Microhardness at 900°C is ~1.0 and ~0.5 GPa for the (0001) and $\{10\bar{1}0\}$ planes, respectively.

Note also that the indentation depths at room temperature correspond to an increase in the hardness and are equal to ~6, 5, and 3 μm for the $\{10\bar{1}0\}$ plane of a prism, $\{10\bar{1}1\}$ plane of a pyramid, and (0001) plane of a monohedron, respectively.

Print Shape: Its Dependence on Plane Orientation and Temperature

The print shape as well as the shape of a dislocation rosette is determined by the indenter shape (square pyramid), the characteristic of the surface analyzed (crystallographic orientation of face and its structure), and some external factors (temperature, etc.).

The (0001) and $(000\bar{1})$ Monohedra

The images of the prints obtained in an optical microscope show that the prints on the (0001) and $(000\bar{1})$ planes repeat the indenter shape (undistorted square). In the whole temperature range studied, no

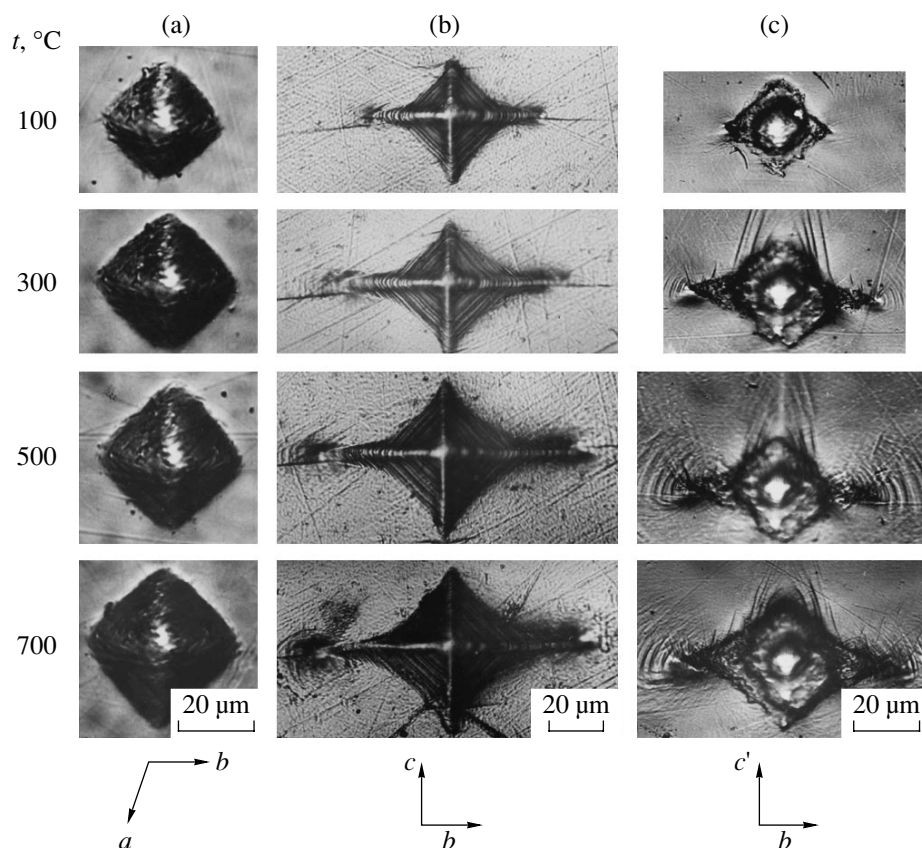


Fig. 3. Indenter prints on the faces of a (a) positive (0001) monohedron, (b) $\{10\bar{1}0\}$ hexagonal prism, and (c) $\{10\bar{1}1\}$ pyramid at different temperatures; c' is the projection of the [0001] direction onto the pyramid plane.

cracks around the print were observed (Fig. 3a). It should be noted that the atomic force microscope (AFM) study of the (0001) ZnO plane at room temperature revealed no cracks around the print either [2]. No crack formation was observed at the liquid nitrogen temperature either. With an increase in the temperature, the print shape left on the basal plane did not change.

The $\{10\bar{1}0\}$ and $\{11\bar{2}0\}$ Prisms

On the planes of the $\{10\bar{1}0\}$ and $\{11\bar{2}0\}$ prisms, the hardness values were the same as were the print shapes (Fig. 3b). Unlike prints on the basal planes, the prints observed on these planes were not symmetric in accordance with the face symmetry and the presence of a polar axis. The shapes of these prints allow one to draw a conclusion about first-kind anisotropy of these faces (different hardness values along different directions on a face). The large diagonal of the print and, hence, the minimum hardness of the $\{10\bar{1}0\}$ planes corresponded to the $\langle 11\bar{2}0 \rangle$ directions, whereas on the $\{11\bar{2}0\}$ planes, they corresponded to the $\langle 10\bar{1}0 \rangle$ directions. Both above directions coincide with glide

directions in zinc oxide. The small diagonal of the indenter print on the planes of both prisms coincided with the [0001] direction. The anisotropy coefficient of the first-kind microhardness $k = H_{\max}/H_{\min}$ was equal to ~ 1.4 at room temperature. With an increase in temperature, k increased and attained a value of ~ 2 at 900°C .

On the planes of the prism of a zinc oxide crystal, radial cracks formed at the print vertices and propagated along the glide direction (Fig. 3b). Their length C depended on the applied load and temperature. Measuring the crack length and using the Evans method [15], one may determine the fracture-toughness coefficient K_{1C} . The K_{1C} value on the $\{10\bar{1}0\}$ plane at room temperature was $\sim 0.09 \text{ MPa m}^{1/2}$.

It is also possible to calculate the fracture surface energy $\gamma = K_{1C}^2/2E$, where E is Young's modulus of ZnO [5]. The E , K_{1C} , and γ values for zinc oxide are listed in Table 2. For comparison, the analogous characteristics for a number of other well-known oxide compounds, quartz, langasite, and tellurium oxide are also indicated.

Table 2. Young's modulus E , microhardness H , viscous-fracture coefficient K_{1C} , and surface energy of fracture γ of ZnO, AlPO₄, La₃Ga₅SiO₁₄, quartz, and TeO₂ crystals at room temperature

Compound	Plane orientation	Direction of crack propagation	E , GPa	H , GPa	K_{1C} , MPa m ^{1/2}	γ , J/m ²
ZnO	{10 $\bar{1}$ 0}	$\langle 11\bar{2}0 \rangle$	47.7	1.7	0.09	0.085
				4.2		
AlPO ₄ [16]	X-cut	$\langle 0001 \rangle$		6	0.34	0.9
La ₃ Ga ₅ SiO ₁₄ [17]	(0001)	$\langle 10\bar{1}0 \rangle$	113	10	0.4	0.64
Natural quartz [18, 19]	(0001)	$\langle 11\bar{2}0 \rangle$	102		1.15	6.14
Synthetic quartz [18, 19]	(0001)	$\langle 11\bar{2}0 \rangle$			1.17	6.38
					1.24	7.17
TeO ₂ [20]	(001)	$\langle 110 \rangle$	112.36	3.4	0.15	0.2
				(100)		

The {10 $\bar{1}$ 1} Pyramid

As in the case of prisms, the prints on faces of the pyramid are elongated in the glide directions $\langle 11\bar{2}0 \rangle$. This pattern is equivalent to the section of the pyramid plane by the (0001) plane (Fig. 3c). With an increase in temperature, the print becomes more anisotropic.

Using the measured hardness data, we constructed the indentation diagrams $P(d)$ and $P(C)$, where C is the crack length in the logarithmic coordinates (Fig. 4). It is seen that indentation of the ZnO samples yields results consistent with the laws of elastic-plastic deformation and brittle fracture for a Vickers pyramid, $P \sim d^2$ and $P \sim C^{3/2}$ [15]. The indentation diagrams allowed us to calculate the minimum size d^* of the print and the minimum load P^* of the beginning of the crack propagation. The d^* value for the {10 $\bar{1}$ 0} plane at room temperature, $\sim 18 \mu\text{m}$, corresponds to the load $P \sim 0.26 \text{ N}$.

Dislocation Rosettes: Their Dependence on Face Orientation and Temperature

Selective etching of the indented (0001) and (000 $\bar{1}$) planes show that they are quite different. On the plane of the positive (0001) monohedron, dislocation rosettes are formed around the indenter print. It is also possible to distinguish individual etch pits and block boundaries. The etched face of the negative (000 $\bar{1}$) monohedron has numerous etching figures, which are explained by a very high etching rate of this face due to the specific features of its structure: oxygen ions having dangling bonds with two electrons at the surface emerge to the interface and ensure their strong reaction with the electron-containing etchant [21].

The dislocation rosettes on the (0001) face obtained at the liquid-nitrogen temperature are characteristic six-ray figures with the rays aligned in the glide $\langle 11\bar{2}0 \rangle$ direction. At higher temperatures (from room temperature to $\sim 200^\circ\text{C}$), the rosettes are transformed into hex-

agonal stars (Fig. 5) with the vertices located along the $\langle 11\bar{2}0 \rangle$ directions. With a further increase in temperature, the rosettes are transformed into circles. The evolution of the rosette shape may be explained by polygonization taking place at elevated temperatures during annealing of ZnO crystals.

Figure 6a shows the dislocation rosettes in the {10 $\bar{1}$ 0} planes at different test temperatures. After the first short etching process, the length of the rosette rays

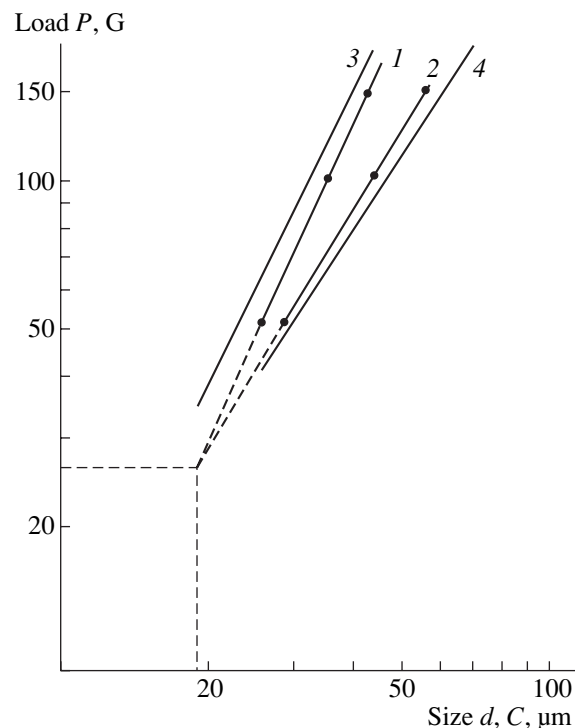


Fig. 4. Experimental indentation diagrams (1) $P(d)$ and (2) $P(C)$ on the {10 $\bar{1}$ 0} planes of a ZnO crystal at room temperature. The corresponding theoretical curves (3) $P(d) \sim d^2$ and (4) $P(C) \sim C^{3/2}$.

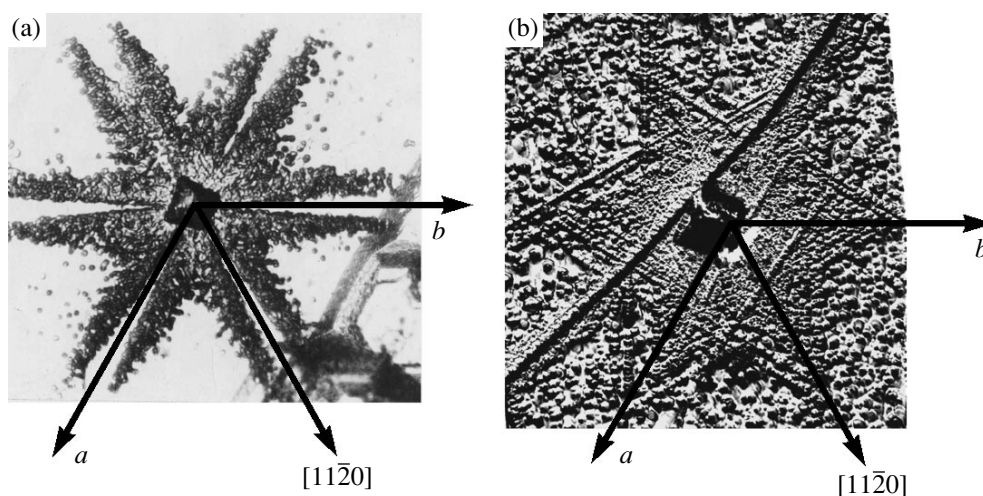


Fig. 5. Dislocation rosettes on the (0001) plane (a) at the liquid-nitrogen temperature and (b) at 300°C.

along [0001] direction becomes somewhat larger than along the $[000\bar{1}]$ direction. However, during the considerable duration of the etching process, the rosette starts elongating in the [0001] direction, i.e., in the direction of the maximum growth of a ZnO crystal.

In the $\{10\bar{1}1\}$ plane, the dislocation rosette is elongated along the projection of the polar [0001] axis onto the c' plane of the pyramid.

CONCLUSIONS

Zinc oxide single crystals are grown by the method of hydrothermal synthesis on the seeding (0001) ZnO plates under conditions of a constant temperature gradient.

The structure of zinc oxide single crystals is analyzed crystallochemically. The simple nets forming the zinc oxide structure are singled out.

Microhardness of ZnO single crystals is measured in the temperature range from the temperature of liquid nitrogen to 900°C on the planes of monohedra, hexagonal prisms, and the pyramid. The monohedron (0001) and $(000\bar{1})$ planes are characterized by the maximum hardness and are plastic over the whole temperature range studied. Around the print on the planes of prisms and the pyramid, radial cracks are formed, which makes it possible to determine the coefficient K_{1C} of fracture toughness. This coefficient for the $\{10\bar{1}0\}$ plane at room temperature is $K_{1C} \sim 0.09 \text{ MPa m}^{1/2}$.

The print shapes are analyzed on the basal plane and on the planes of the pyramid and prisms. The print on the basal plane has an isotropic shape, whereas the prints on the planes of prisms and pyramid are characteristic of the first-kind anisotropy of mechanical properties. The first-kind anisotropy coefficient k , equal to H_{\max}/H_{\min} , increases with an increase in temperature for the $\{10\bar{1}0\}$, $\{11\bar{2}0\}$, and $\{10\bar{1}1\}$ planes. For the $\{10\bar{1}0\}$ plane, k varies from ~ 1.4 at room temperature to ~ 2 at 900°C.

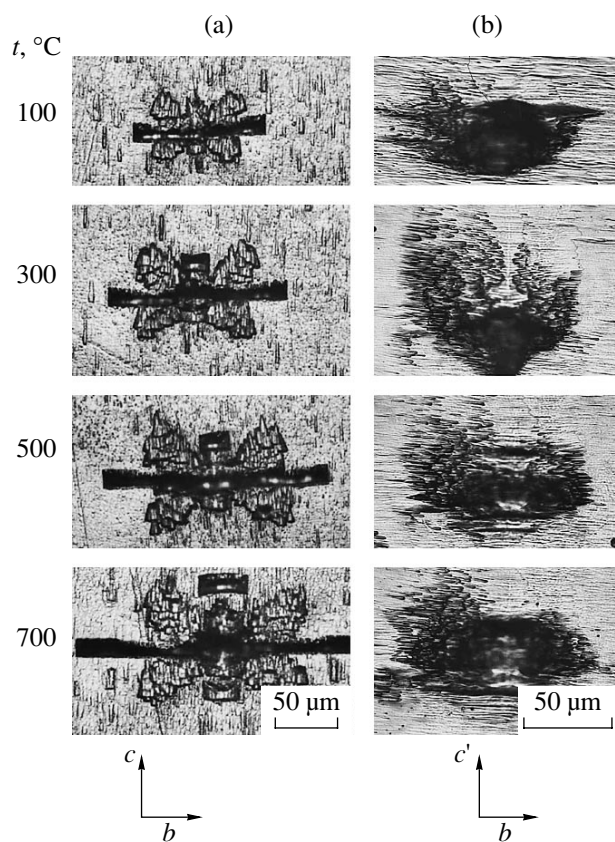


Fig. 6. Dislocation rosettes on the faces of the (a) $\{10\bar{1}0\}$ prism and (b) $\{10\bar{1}1\}$ pyramid at different temperatures.

The shapes of dislocation rosettes are studied on the planes of monohedra, prisms, and the pyramid. On the (0001) plane, a symmetric six-ray rosette corresponding to the symmetry of the plane is observed. On the planes of prisms and the pyramid, asymmetric dislocation rosettes are observed along the [0001] polar axis.

The mechanical properties of the first- and second-kind prisms are the same, which follows from the crystallochemical analysis of these pyramids. The macroindentation method did not reveal any differences in the microhardness of the positive and negative monohedra, which could have been expected on the basis of the crystallochemical analysis. It seems that this problem should be solved by the nanoindentation method.

ACKNOWLEDGMENTS

This study was supported by the Russian Foundation for Basic Research, project nos. 03-02-17308, and 04-02-17195, and the Council of the President of the Russian Federation for Support of Leading Schools, grant no. NSh-1954.2003.2.

REFERENCES

1. V. R. Regel, N. L. Sizova, M. A. Chernysheva, *et al.*, *Cryst. Res. Technol.* **17** (12), 1579 (1982).
2. S. O. Kucheev, J. E. Bradly, J. S. Williams, *et al.*, *Appl. Phys. Lett.* **80** (6), 956 (2002).
3. J. S. Ahearn, J. J. Mills, and A. R. C. Westwood, *J. Appl. Phys.* **49**, 96 (1978).
4. V. I. Vladimirov, I. P. Kuzmina, A. A. Loshmanov, *et al.*, *Cryst. Res. Technol.* **21** (8), 1055 (1986).
5. I. M. Silvestrova, Yu. V. Pisarevsky, V. A. Skuratov, *et al.*, *J. Phys. (Paris)* **4** (111), C2-211 (1994).
6. Yu. A. Osip'yan and I. B. Savchenko, *Pis'ma Zh. Éksp. Teor. Fiz.* **7**, 130 (1968) [*JETP Lett.* **7** (4), 100 (1968)].
7. L. Carlsson, *J. Appl. Phys.* **42** (2), 676 (1971).
8. I. P. Kuz'mina and V. A. Nikitenko, *Zinc Oxide. Synthesis and Optical Properties* (Nauka, Moscow, 1984) [in Russian].
9. L. N. Dem'yanets, D. V. Kostomarov, and I. P. Kuz'mina, *Neorg. Mater.* **38**, 171 (2002).
10. L. N. Demianets and D. V. Kostomarov, *Ann. Chim. Sci. Mat. (Paris)* **26**, 193 (2001).
11. L. N. Demianets, D. V. Kostomarov, I. P. Kuz'mina, and C. V. Pushko, *Kristallografiya* **47** (1), 93 (2002) [*Crystallogr. Rep.* **47** (1), 86 (2002)].
12. N. L. Sizova and V. R. Regel', *Fiz. Tverd. Tela (Leningrad)* **27** (12), 3693 (1985) [*Sov. Phys. Solid State* **27** (12), 2226 (1985)].
13. W. Kieber and R. Mlodoch, *Krist. Tech.* **1**, 249 (1966).
14. W.-J. Li, E.-W. Shi, and Z.-W. Yin, *J. Cryst. Growth* **208**, 546 (2000).
15. A. Evans and A. Charles, *J. Am. Ceram. Soc.* **59**, 731 (1976).
16. N. L. Sizova, G. S. Mironova, and E. P. Kostyukova, *Kristallografiya* **35** (3), 787 (1990) [*Sov. Phys. Crystallogr.* **35** (3), 461 (1990)].
17. A. M. Aronova, G. V. Berezhkova, A. V. Butashin, and A. A. Kaminskiĭ, *Kristallografiya* **35** (4), 933 (1990) [*Sov. Phys. Crystallogr.* **35** (4), 550 (1990)].
18. M. Iwada and R. C. Bradt, *Mater. Res. Bull.* **22**, 1241 (1987).
19. E. Breval and G. C. Dodds, *Mater. Res. Bull.* **20**, 413 (1985).
20. A. V. Vinogradov, V. A. Lomonov, Yu. A. Pershin, and N. L. Sizova, *Kristallografiya* **47** (6), 1105 (2002) [*Crystallogr. Rep.* **47** (6), 1036 (2002)].
21. A. N. Mariano and R. E. Hanneman, *J. Appl. Phys.* **34** (2), 384 (1963).

Translated by L. Man

PHYSICAL PROPERTIES OF CRYSTALS

Piezo-optic Properties of TGS Crystals Doped with *D*-Serine

V. I. Stadnik

Lviv State University, ul. Kirilla i Mefodiya 8, Lviv, 79005 Ukraine

e-mail: staves@mail.ru

Received October 16, 2003

Abstract—The effect of uniaxial mechanical pressure along the main crystallophysical axes on the principal values of birefringence Δn_i in TGS crystals doped with 5% *D*-serine is investigated. It is ascertained that the values of Δn_i are rather sensitive to the action of uniaxial stresses. The temperature shift coefficients $\partial T_c / \partial \sigma_m$ are determined for the phase-transition points. The temperature and spectral dependences of the combined piezo-optic constants π_{im}^0 are calculated. The contribution of the secondary electro-optic effect to the changes in the birefringence and the piezo-optic constants of doped crystals is determined. It is found that the piezo-optic constants π_{23}^0 and π_{12}^0 have the same values, which indicates a decrease in the anisotropy of the optical indicatrix of doped crystals under the action of uniaxial stress. The optical and deformation contributions to the relaxation effect of piezo-optical birefringence in doped TGS crystals are found. © 2005 Pleiades Publishing, Inc.

INTRODUCTION

Triglycine sulfate $(\text{NH}_2\text{CH}_2\text{COOH})_3 \cdot \text{H}_2\text{SO}_4$ (TGS) belongs to the series of ferroelectric isomorphous molecular compounds of glycine and inorganic acids and salts. Doping of a TGS crystal with organic impurities leads to fixation of one of the polarizations ($+P_c$ or $-P_c$) and generation of a bias field E_b in the crystal [1]. As a result, the dielectric parameters of doped TGS crystals slightly change during spontaneous aging, which is of great importance for the practical use of these crystals. Previously, the effect of *L*- and *D*-alanine impurities on the physical properties of TGS crystals was studied [2–5]. In this paper, we report the results of the investigation of doping with *D*-serine on the birefringence and piezo-optic properties of TGS crystals.

D-Serine is a protein amino acid, which contains an oxyl group and has the chemical formula $\text{NH}_2\text{CHCH}_2\text{OHCOOH}$ [6, 7].

Serine-doped crystals grow asymmetrically with respect to the seed along the *b* axis [8]. It was found in [8] that serine is distributed nonuniformly in grown crystals: the impurity impedes the crystal growth in the *b* direction. The Curie temperature of a serine-doped crystal is lower than that of pure TGS crystals [9, 10]. Introduction of serine makes the structure asymmetric in such a way that hysteresis loops shift along the *E* axis by a value equal to the bias field, as it was established for the *L*- α -alanine impurity [11, 12].

Measurement of the piezo-optic constants of pure TGS crystals by the half-wave stress method has revealed temperature anomalies of π_{km}^0 near the phase transition: when temperature approaches T_c , the values

of π_{km}^0 sharply increase in the polar phase and stepwise decrease in the paraelectric phase [13]. It is shown that isomorphous substitution in TGS crystals leads to significant changes in the piezo-optic constants: the temperature anomalies of the constants π_{km}^0 of triglycine selenate crystals are several times larger than for TGS crystals. Triglycine fluoroberyllate crystals, along with quantitative differences, are also characterized by significant qualitative differences in the piezo-optic constants [14]. Isotopic substitution (deuteration) in TGS crystals, significantly shifting the Curie point, almost does not change the piezo-optic constants of the crystals, including the vicinity of T_c . The reason for this is the approximate equality of the coefficients of the Curie point shift under uniaxial compression and the spontaneous increments in the path differences for pure and deuterated TGS crystals. Changes in the piezo-optic properties of TGS crystals caused by the introduction of *L*- α -alanine and X-ray irradiation have the same character: with an increase in the impurity concentration and the irradiation dose, the peaks of π_{km}^0 decrease, become somewhat diffused, and are located at temperatures somewhat below T_c of the corresponding crystals. This behavior is in good agreement with the specific features of the dependences $P_c(T)$ for doped and irradiated crystals. Isotopic substitution, doping, and irradiation almost do not affect the piezo-optic properties of TGS crystals far from the phase-transition point [14, 15].

The temperature and spectral dependences of the birefringence of the crystals under study were measured by the interference method. Uniaxial stress was

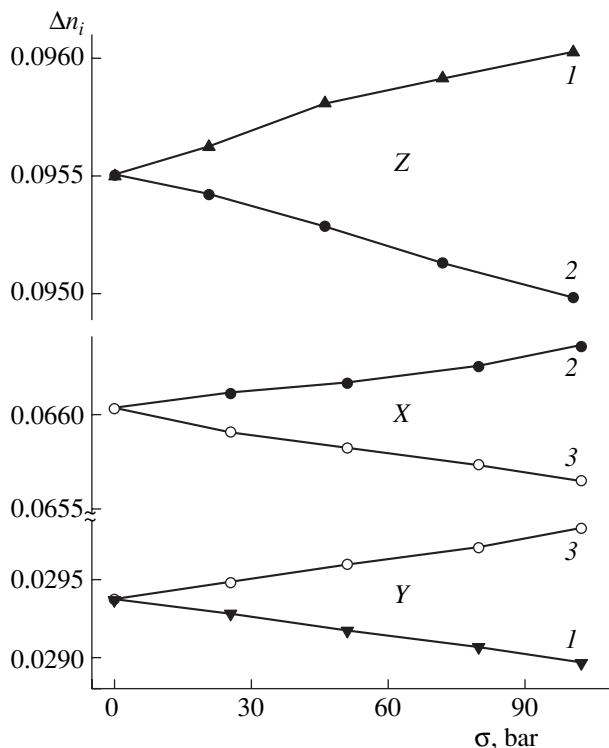


Fig. 1. Baric dependences of the birefringence of TGS crystals with 5% *D*-serine at room temperature for $\lambda = 500$ nm.

obtained using a special attachment providing stresses up to ~ 200 bar, although much lower stresses were used here ($\sigma_m \sim 100$ bar). The change in the birefringence of a crystal under the action of a stress field is determined by the expression

$$\Delta n_i(\sigma_m) = k(\sigma_m)\lambda/d_i(\sigma_m), \quad (1)$$

where Δn_i is the birefringence, k is the interference order, λ is the light wavelength, and d_i is the crystal thickness along the light-propagation direction. Under the simultaneous action of thermal and stress fields, the birefringence is determined as

$$\Delta n_i(T, \sigma_m) = k(T, \sigma_m)\lambda/d_i(T, \sigma_m). \quad (2)$$

Changing one of the parameters (T or σ_m) with the other parameter fixed, one can unambiguously determine the temperature or baric dependence of Δn_i from the shift of interference orders.

EXPERIMENTAL RESULTS AND DISCUSSION

Baric Changes in the Birefringence

Figure 1 shows the baric dependence of the birefringence of a TGS crystal with 5% *D*-serine (DSTGS) at room temperature for $\lambda = 500$ nm. It can be seen that the value of Δn_i linearly increases up to stresses $\sigma_i \sim$

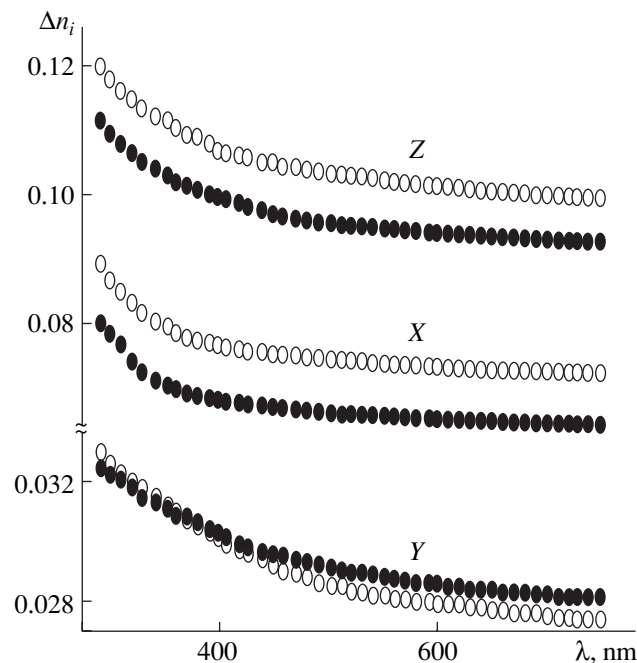


Fig. 2. Dispersion of the birefringence of pure (open symbols) and *D*-serine-doped (filled symbols) TGS crystals at room temperature.

100 bar. Uniaxial stresses σ_x , σ_y , and σ_z lead to changes in Δn_i that are different in magnitude and sign: $\delta\Delta n_z = 5.3 \times 10^{-4}$ ($\sigma_x = 100$ bar) and -5.2×10^{-4} ($\sigma_y = 100$ bar); $\delta\Delta n_y = -4.1 \times 10^{-4}$ and 4.8×10^{-4} for $\sigma_x = \sigma_z = 100$ bar; and $\delta\Delta n_x = 6.1 \times 10^{-4}$ and -6.3×10^{-4} for $\sigma_y = \sigma_z = 200$ bar. Generally, one of the stresses applied normally to the observation direction always leads to an increase in Δn_i , whereas the other stress acts oppositely; in addition, these changes are different in magnitude.

The birefringence of a doped TGS crystal (Fig. 2), as compared with a pure crystal, decreases in two crystallophysical directions: $\Delta n_z^p - \Delta n_z^D = 6.57 \times 10^{-3}$ and $\Delta n_x^p - \Delta n_x^D = 7.82 \times 10^{-3}$. In the polar *Y* direction, the sign of the birefringence of a doped crystal changes in comparison with a pure crystal: $\delta(\Delta n_y) = \Delta n_y^p - \Delta n_y^D = 5.59 \times 10^{-4}$ and -7.32×10^{-4} . In this case, at room temperature and $\lambda \sim 365$ nm, the birefringences of pure and doped TGS crystals become equal: $\Delta n_y^p = \Delta n_y^D = 0.030888$. With a decrease in temperature, the wavelength at which $\Delta n_y^p = \Delta n_y^D$ decreases. A similar situation was observed in a TGS crystal doped with *L*-threonine; however, in this case, the birefringences are equal to each other in the *Z* direction [16].

It was ascertained that the changes in Δn_i in the paraelectric phase of a doped TGS crystal are linear in all three crystallophysical directions: $d\Delta n_y/dT =$

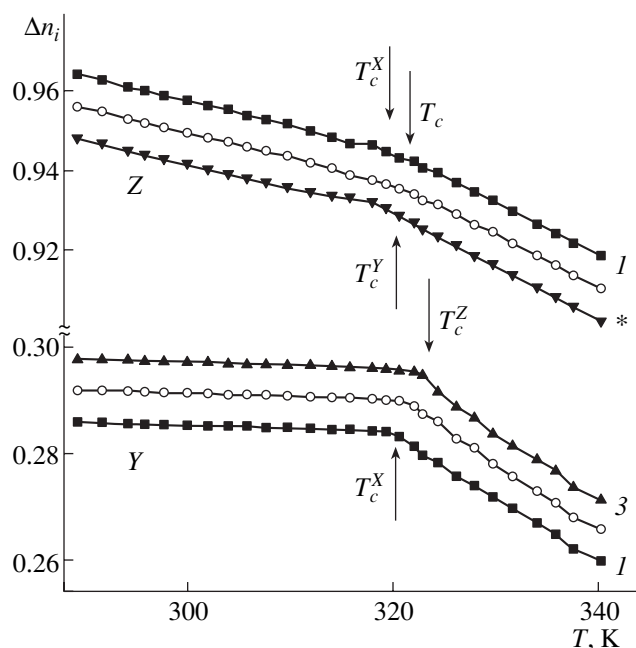


Fig. 3. Temperature dependences of the birefringence of TGS crystals with 5% *D*-serine for different directions of uniaxial pressure at $\lambda = 500$ nm: a mechanically free crystal (open symbols) and crystals loaded with stresses (1) σ_x , (2) σ_y , and (3) σ_z ($\sigma_m = 100$ bar, $m = X, Y, Z$).

$13.23 \times 10^{-5} \text{ K}^{-1}$, $d\Delta n_z/dT = 19.44 \times 10^{-5} \text{ K}^{-1}$, and $d\Delta n_x/dT = 0.65 \times 10^{-5} \text{ K}^{-1}$. A slight nonlinearity of the changes in the birefringence was revealed for the ferroelectric phase. Pronounced changes in $\Delta n_i(T)$ were observed at the Curie point in the *Z* and *Y* directions, whereas these changes were insignificant in the *X* direction.

In the ferroelectric phase, the values of Δn_i of a doped crystal depend very weakly on temperature: $d\Delta n_y/dT = 0.42 \times 10^{-5} \text{ K}^{-1}$, $d\Delta n_z/dT = 6.14 \times 10^{-5} \text{ K}^{-1}$, and $d\Delta n_x/dT = 6.15 \times 10^{-5} \text{ K}^{-1}$ (Fig. 3).

Figure 3 shows also the temperature changes in the principal values of the birefringence of loaded DSTGS samples. The general features are as follows: the changes in Δn_i are proportional to temperature; the derivative $\partial\Delta n_i/\partial T$ changes at the transition through the Curie point; uniaxial stresses, changing the magnitude of Δn_i , do not radically change the temperature behavior of Δn_i ; and the application of stress leads to a shift of the phase-transition point. Under the action of the stresses σ_x and σ_y (~ 100 bar), the phase-transition point shifts to lower temperatures: $T_c^X = 320.3 \text{ K}$ and $T_c^Y = 320.2 \text{ K}$, whereas the stress σ_z shifts the phase-transition point to higher temperatures: $T_c^Z = 322.8 \text{ K}$ ($T_c^0 = 321 \text{ K}$). In this case, the temperature coefficients of the phase-transition shift are $\partial T_c/\partial\sigma_x = -0.007 \text{ K/bar}$, $\partial T_c/\partial\sigma_y = -0.008 \text{ K/bar}$, and $\partial T_c/\partial\sigma_z = 0.018 \text{ K/bar}$. The

hydrostatic coefficient of the phase-transition shift under the action of uniaxial stresses in all crystallographic directions is $\partial T_c/\partial p = \sum_{i=1}^3 \partial T_c/\partial\sigma_i = +0.003 \text{ K/bar}$. On the one hand, these results are in good agreement with the data for pure TGS crystals obtained in [17, 18]: $\partial T_c/\partial\sigma_x = -7 \text{ K/kbar}$, $\partial T_c/\partial\sigma_y = -8.5 \text{ K/kbar}$, and $\partial T_c/\partial\sigma_z = 20 \text{ K/kbar}$. The values for doped TGS crystals are somewhat smaller, which confirms the increase in the hardness of TGS crystals as a result of the doping. On the other hand, similar results were obtained for LiKSO_4 , RbNH_4SO_4 , and $(\text{NH}_4)_2\text{BeF}_4$ crystals, as well as for Rochelle salt and KDP crystals [19–21], in which, depending on the pressure direction, the point T_c shifted to higher or lower temperatures. In this case, the hydrostatic shift coefficient for T_c was negative. These phase-transition shifts were attributed to the influence of temperature and pressure on the displacement of elements of the structure characteristic of this phase transition. The obtained small differences can be caused by the complex structure of TGS crystals and the ambiguity of the incorporation of serine impurities into the crystal structure. During the growth of a crystal doped with serine, the latter, being incorporated into the TGS crystal structure, may substitute only glycine. Glycines I–III are planar in the paraelectric phase, whereas glycine I becomes nonplanar in the ferroelectric phase. When a serine molecule substitutes glycine I, the spontaneous polarization P_c becomes fixed and a bias field arises, which changes all measured dielectric parameters of the crystal and shifts the phase-transition point. The substitution of glycine by serine is more likely when a crystal grows in the ferroelectric phase. In addition, it is obvious that a significant shift of the phase-transition point to higher temperatures is related to the action of uniaxial pressure on ferroelectric domains, which have the shape of tubes with an oval cross section extended in the direction perpendicular to the *c* axis in TGS crystals. The reason for smaller shift coefficients of DSTGS as compared with a pure crystal is that domains in doped crystals are larger in size but have an irregular shape and diffuse boundaries; in addition, their concentration decreases during spontaneous aging of samples.

Piezo-optic Properties of Doped TGS Crystals

The combined difference of the piezo-optic constants was calculated by the formula

$$\pi_{im}^0 = 2\delta\Delta n_i/\sigma_m - 2\Delta n_i s_{im}, \quad (3)$$

where $\delta\Delta n_i$ is the induced change in the birefringence for the light-propagation direction along the crystallographic axis *i* and a pressure applied to a sample along the *m* axis. The second term takes into account the change in the sample size along the *i* axis, where s_{im} is the elastic compliance constant. Figure 4 shows the temperature dependences of the piezo-optic constants

of DSTGS crystals. Most piezo-optic constants π_{im}^0 very rapidly increase on approaching the phase-transition point from the side of the ferroelectric phase, step-wise decrease during the transition to the paraelectric phase, and then are almost independent of temperature.

The piezo-optic constant π_{31}^0 changes in another way: it decreases on approaching the point T_c in the polar phase.

Comparison of the results obtained here with analogous results for pure TGS crystals [14] shows the following. The piezo-optic constants π_{21}^0 , π_{32}^0 , and π_{13}^0 are negative, which corresponds to a decrease of the birefringences Δn_y , Δn_z , and Δn_x under the action of the stresses σ_x , σ_y , and σ_z , respectively. The step changes in all piezo-optic constants during the phase transition in doped crystals are much smaller than those for pure crystals: for example, $\delta\pi_{13}^0 = 11.8 \times 10^{-12}$ and $19.3 \times 10^{-12} \text{ m}^2/\text{N}$ for DSTGS and TGS crystals, respectively.

The piezo-optic effect in TGS crystals is determined by the actual piezo-optic and secondary electro-optic contributions $d\Delta n_i/dP_c$. The electro-optic contribution has the following origin. As a result of the temperature dependence of the spontaneous polarization and the shift of the function $P_c(T)$ along the temperature axis under the action of a uniaxial stress σ_m , the spontaneous polarization changes by some value δP_c , which, in turn, leads to an additional electro-optic change in the birefringence:

$$\pi_{im}^* = 2 \frac{d\Delta n_i}{d\sigma_m} = 2 \left[\left(\frac{d\Delta n_i}{d\sigma_m} \right)_{\text{act}} + \frac{d\Delta n_i}{dP_c} \frac{dP_c}{d\sigma_m} \right], \quad (4)$$

where $(d\Delta n_i/d\sigma_m)_{\text{act}}$ is the contribution of the actual piezo-optic effect to the combined difference π_{im}^* and, since

$$\pi_{im}^0 = \pi_{im}^* + 2\Delta n_i s_{im}, \quad (5)$$

to the value of π_{im}^0 .

Let us estimate the contribution of the electro-optic effect. To this end, using the known temperature dependence of the spontaneous polarization of a TGS crystal with 5% *D*-serine [5] and the above experimental results on the baric shift of the phase-transition point $dT_c/d\sigma_m$, we calculated the temperature dependence of the spontaneous polarization in a crystal subjected to uniaxial pressure (Fig. 5). In this case, we took into account that the shape of the curve $P_c(T)$ is independent of σ_m , which is in agreement with the corresponding investigations of the spontaneous polarization of TGS crystals subjected to hydrostatic pressure [22]: pressures up to 6 kbar do not affect the molecular mechanism of polarization of TGS crystals but only shift the Curie point to higher temperatures owing to the

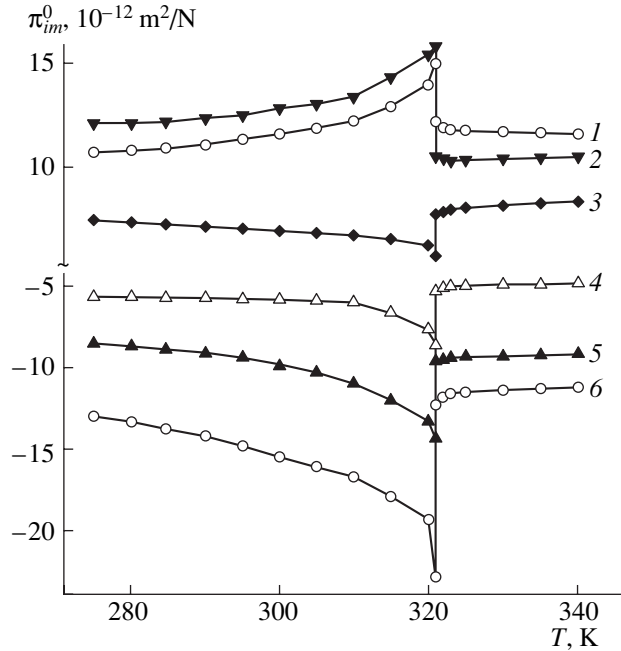


Fig. 4. Temperature dependences of the piezo-optic constants (1) π_{23}^0 , (2) π_{12}^0 , (3) π_{31}^0 , (4) π_{21}^0 , (5) π_{32}^0 , and (6) π_{13}^0 of TGS crystals with 5% *D*-serine for $\lambda = 500 \text{ nm}$.

increase in the number of dipoles per unit volume. The temperature dependences of P_c of mechanically free and loaded DSTGS crystals reported here make it possible to determine the increments of the spontaneous polarization δP_c and δP_c^2 (since the spontaneous electro-optic effect in TGS crystals is quadratic) at certain stresses σ_m . The found values of $d\Delta n_i/dP_c^2$ and δP_c^2 were used to determine the increments of the secondary electro-optic birefringence $\delta\Delta n_i = d\Delta n_i/dP_c^2 \delta P_c^2$. Formula (4) was used to calculate the secondary electro-optic contribution to the piezo-optic constants of DSTGS crystals (Table 1).

It has been ascertained that the electro-optic effect makes the largest contribution to the changes in the piezo-optic constants π_{23} and π_{21} near the phase transition. On going away from the phase-transition point into the ferroelectric phase, the contribution of the electro-optic effect becomes insignificant (~10–15%). These results are in good agreement with the data on the differences between the values of π_{23}^0 and π_{21}^0 in the ferroelectric phase and the extrapolated data for the paraelectric phase.

Comparison of pure and doped TGS crystals shows that the step changes in the piezo-optic constants (the discontinuity of the function $\pi_{im}^0(T)$) at the phase tran-

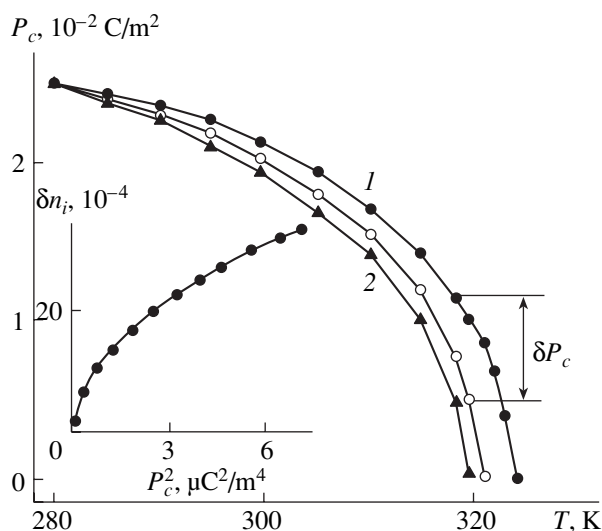


Fig. 5. Temperature dependences of the spontaneous polarization of mechanically free (open symbols) and loaded (filled symbols, (1) $\sigma_z = 100$ bar and (2) $\sigma_x = 100$ bar) TGS crystals with 5% *D*-serine. The inset shows the dependence of the birefringence increment on the squared spontaneous polarization.

sition are much smaller for doped crystals (Table 2). The reason for this is that the factor $dP_c/d\sigma_m$, which is proportional to δP_c , is smaller for doped crystals in comparison with pure ones owing to smaller values of $dT_c/d\sigma_m$ and lower spontaneous polarization.

Anisotropy of the coefficients $\delta\pi_{im}^0$ for doped crystals is determined mainly by the difference in the mag-

Table 1. Magnitudes of the increments $\delta\pi_{im}^0$ (in 10^{-12} N/m²) and the secondary electro-optic contributions (in %) to the piezo-optic constants of DSTGS crystals for $\lambda = 500$ nm

<i>T</i> , K	$\delta\pi_{23}^0$	Contribution	$\delta\pi_{21}^0$	Contribution
321	1.51	71	1.03	73
320	1.06	54	0.69	57
319	0.79	39	0.48	42
318	0.58	31	0.36	33
317	0.42	27	0.28	27
316	0.37	22	0.28	24
315	0.29	21	0.26	22

Table 2. Magnitudes of the step increments $\delta\pi_{im}^0$ at the phase transitions in pure and doped TGS crystals

Crystal	$\delta\pi_{12}^0$	$\delta\pi_{13}^0$	$\delta\pi_{21}^0$	$\delta\pi_{23}^0$	$\delta\pi_{31}^0$	$\delta\pi_{32}^0$
TGS	7.5	20	2.5	8	3.5	7
DSTGS	5.25	10.5	2.3	2.8	2.0	4.7

nitudes of $dT_c/d\sigma_m$. For example, for pure and doped crystals, $\delta\pi_{32}^0 > \delta\pi_{31}^0$ because $|dT_c/d\sigma_2| > |dT_c/d\sigma_1|$ and $\delta\pi_{23}^0 > \delta\pi_{21}^0$ because $|dT_c/d\sigma_3| > |dT_c/d\sigma_1|$. Obviously, the anisotropy of the coefficients $\delta\pi_{im}^0$ at the same *m* and different values of *i* is determined by the anisotropy of the coefficients of the spontaneous electro-optic effect $d\Delta n_i/dP_c^2$: the inequality $\delta\pi_{32}^0 > \delta\pi_{31}^0$ corresponds to $|d\Delta n_2/dP_c^2| > |d\Delta n_1/dP_c^2|$ and the inequality $\delta\pi_{23}^0 > \delta\pi_{21}^0$ corresponds to $|d\Delta n_3/dP_c^2| > |d\Delta n_1/dP_c^2|$.

This qualitative correspondence between the values of $\delta\pi_{im}^0$, $dT_c/d\sigma_m$, and $d\Delta n_i/dP_c^2$ confirms the suggestion that the contribution of the secondary electro-optic effect to the anomalies of π_{im}^0 is fairly large in comparison with the contribution of the elastic constants.

It should be noted that for doped TGS crystals the temperature coefficients of the changes in the piezo-optic constants in the paraelectric and ferroelectric phases far from the Curie point ($T < T_c - 20$ K) are small and have approximately the same values $d\pi_{im}^0/dT \sim (2-9) \times 10^{-14}$ m² (N K)⁻¹ and the piezo-optic constants are weakly anisotropic.

Thus, only when approaching T_c , the secondary electro-optic effect and, possibly, the anomalies of the elastic constants (unfortunately, the data on the latter are absent) lead to a significant anisotropy of the piezo-optic constants and their magnitudes significantly increase.

Figure 6 shows the dispersion dependences of the piezo-optic constants of DSTGS crystals at room temperature. As can be seen, the piezo-optic constants of doped crystals have a small dispersion in the spectral range under study. The character of their dispersion reproduces that of the birefringence dispersion $|\partial\pi_{im}^0/\partial\lambda| < 0$. The piezo-optic constants π_{23}^0 and π_{21}^0 change most significantly with a change in the wavelength, which corresponds to the change in the birefringence in the polar direction Δn_y under the action of stresses σ_z and σ_x , respectively ($\partial\pi_{23}^0/\partial\lambda \approx \partial\pi_{21}^0/\partial\lambda \approx 1.48 \times 10^{-5}$ m²/N nm), although the dispersion Δn_y of a mechanically free crystal is the smallest.

It is noteworthy that $\pi_{23}^0 = \pi_{12}^0 = 9.97 \times 10^{-12}$ m²/N at $\lambda = 725$ nm. This fact indicates that, under the action of stresses σ_z and σ_y , the birefringences Δn_z and Δn_y are equal to each other, which leads to a decrease in the anisotropy of the optical indicatrix of a doped crystal. Since the inequality $n_x > n_z > n_y$ is valid for TGS crys-

tals, the equality $\Delta n_z = \Delta n_y$ means averaging of the refractive index: $n_z = (n_x + n_y)/2$.

Let us consider the relaxation of the piezo-optic birefringence. It is well known that the piezo-optic relaxation is a change with time in the optical parameters of a sample subjected to strictly constant stress [23, 24]. It was shown in [25] that the relaxation changes in the birefringence $\delta\Delta_{km}^r$ induced by a stress σ_m are determined by the optical contribution (the relaxation change in the birefringence $\delta\Delta n_{km}^r$) and the deformation contribution, which is caused by the relaxation change in the sample thickness along the light-propagation direction $\delta\Delta d_{km}^r$. The optical and deformation contributions to the photoelastic relaxation are related to the relaxation change in the optical path difference as follows:

$$\delta\Delta_{km}^r = \delta(\Delta n_k d_k)_m^r = \delta\Delta n_{km}^r d_k + \Delta n_k \delta d_{km}^r, \quad (6)$$

where d_k is the sample size and Δn_k is the birefringence along the light-propagation direction.

The relaxation of linear sizes (δd_{km}^r) has an essentially piezocaloric nature since the possible strain relaxation due to plastic effects is absent. The absence of plastic strains is confirmed by the fact that residual effects were absent after the stress was removed and the relaxation $\delta\Delta n_{km}^r$ ceased.

The contribution $\delta\Delta n_{km}^r$ was calculated on the basis of the temperature changes in the optical path difference:

$$\delta\Delta_k(T) = \delta\Delta n_k d_k + \Delta n_k \delta d_{km}(T). \quad (7)$$

Subtracting the second term from formula (7), we obtain the temperature dependences $\delta\Delta_k(T)$ and, correspondingly, the derivative $d\Delta n_k(T)/dT$. Using the values of this derivative and the relaxation temperature change ($-\delta T_{km}^r$), we determine the birefringence relaxation for each temperature:

$$\delta\Delta n_{km}^r(T) = (d\Delta n_k(T)/dT)(-\delta T_m^r). \quad (8)$$

The optical and deformation contributions calculated per unit length are listed in Table 3.

Comparison of the results obtained with the corresponding data for pure crystals [26] shows that the photoelastic relaxation is smaller for doped crystals. In addition, the optical contribution increases in the ferroelectric phase, whereas the deformation contribution decreases, although it also has different signs for different geometries of experiment. When passing through the phase-transition point, the deformation contribution changes its sign in both experiment geometries.

Thus, we investigated the effect of uniaxial mechanical pressure applied along the main crystallophysical

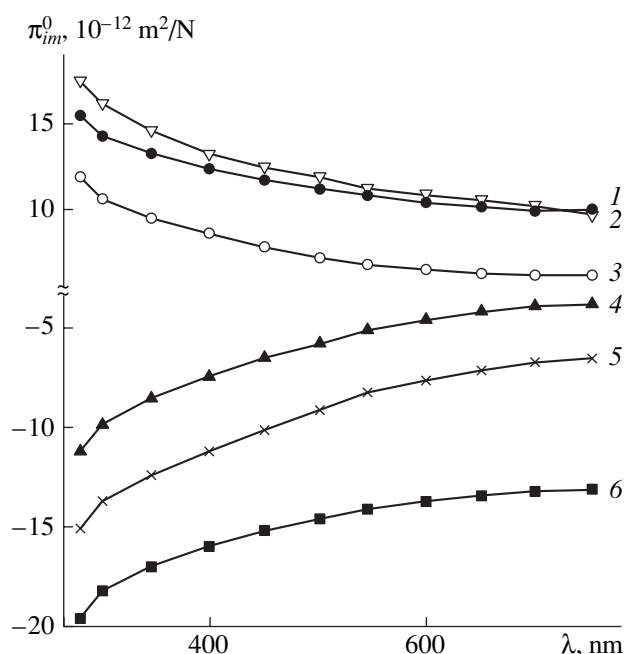


Fig. 6. Spectral dependences of the piezo-optic constants (1) π_{23}^0 , (2) π_{12}^0 , (3) π_{31}^0 , (4) π_{21}^0 , (5) π_{32}^0 , and (6) π_{13}^0 of TGS crystals with 5% *D*-serine at room temperature.

axes on the principal values of the birefringence of TGS crystals with 5% *D*-serine. It is ascertained that the value of Δn_i is rather sensitive to the action of uniaxial pressures. One of the stresses normal to the observation direction leads to an increase in Δn_i , whereas the other stress leads to a decrease in Δn_i . In addition, these increments are different in magnitude and, for DSTGS crystals, $\delta\Delta n_x > \delta\Delta n_y \geq \delta\Delta n_z$. With a decrease in wavelength, the birefringences Δn_i of both free and mechanically strained samples decrease. The temperature shift coefficients $\partial T_c / \partial \sigma_m$ were determined for the phase-transition point. They turned out to be somewhat smaller than for pure TGS crystals, which confirms the increase in the hardness of TGS crystals as a result of doping. The hydrostatic coefficient of the shifts of the phase-transition point under the action of uniaxial pressures is determined.

The temperature and spectral dependences of the combined piezo-optic constants π_{im}^0 are calculated. It is shown that the magnitudes of π_{im}^0 for doped crystal are somewhat larger than for pure crystals at $T < 320$ K. When approaching the phase transition, the temperature dependences of doped crystals become much weaker. The step changes in all piezo-optic constants at the phase transition are much smaller for doped crystals as compared with pure crystals. The increments of the spontaneous polarization, δP_c and δP_c^2 , are determined, as well as the contribution of the secondary

Table 3. Optical and deformation contributions (in %) calculated per unit length and the relaxation of the optical path difference $\delta\Delta_{km}^r/d_k \times 10^{-6}$

Geometry	T = 294 K			T = 320 K			T = 325 K		
	$\delta\Delta_{km}^r/d_k$	optical contribution	deformation contribution	$\delta\Delta_{km}^r/d_k$	optical contribution	deformation contribution	$\delta\Delta_{km}^r/d_k$	optical contribution	deformation contribution
$k = 1, m = 3$	1.8	97.4	2.6	12.2	95.1	4.9	-1.2	101	-1
$k = 3, m = 1$	2.4	111	-11	7.3	122	-22	2.8	97.9	2.1

electro-optic effect to the changes in the birefringence and the piezo-optic constants of DSTGS crystals. It is shown that the electro-optic effect makes the largest contribution to the changes in the piezo-optic constants near the phase-transition. In the ferroelectric phase far from the phase transition point, the contribution of the electro-optic effect is insignificant (~10–15%). It is established that the piezo-optic constants π_{23}^0 and π_{12}^0 are equal to each other, which is indicative of the decrease in the anisotropy of the optical indicatrix of doped crystals subjected to uniaxial pressure.

ACKNOWLEDGMENTS

I am grateful to N.A. Romanyuk for helpful discussions and valuable remarks and J. Stankowska (Poland) for supplying the crystals for study.

REFERENCES

1. K. L. Bye, P. W. Whips, and E. T. Keve, *Ferroelectrics* **4**, 235 (1972).
2. J. Stankowska and A. Czarnecka, *Ferroelectrics* **98**, 95 (1989).
3. M. Koralewski, T. Stankowska, and T. Jasinski, *Jpn. J. Appl. Phys.* **26**, 383 (1987).
4. B. Brezina and M. Havrankova, *Cryst. Res. Technol.* **20**, 787 (1985).
5. J. Stankowska, S. Mielcarek, A. Czarnecka, and M. Musial, *Ferroelectrics* **158**, 169 (1994).
6. G. V. Gurskaya, *The Molecular Structure of Amino Acids* (Nauka, Moscow, 1966; Consultants Bureau, New York, 1968).
7. J. Stankowska, Z. Bochynski, A. Czarnecka, and L. Dejnea, *Ferroelectrics* **124**, 55 (1991).
8. J. Stankowska and T. Jasinski, *Acta Phys. Pol. A* **71**, 959 (1987).
9. M. Koralewski, J. Stankowska, and T. Jasinski, *Jpn. J. Appl. Phys.* **26**, 3831 (1987).
10. S. R. Fletcher, E. T. Keve, and A. C. Skapski, *Ferroelectrics* **8**, 479 (1973).
11. J. Stankowska, A. Czarnecka, and S. Mielcarek, *Ferroelectrics* **172**, 221 (1995).
12. J. Stankowska, A. Czarnecka, and S. Mielcarek, *Ferroelectrics* **108**, 325 (1990).
13. N. A. Romanyuk, B. G. Mytsyk, and V. M. Varikash, *Izv. Akad. Nauk BSSR, Ser. Fiz.*, No. 6, 105 (1980).
14. B. G. Mytsyk and N. A. Romanyuk, *Ukr. Fiz. Zh.* **28**, 538 (1983).
15. N. A. Romanyuk and B. G. Mytsyk, *Ukr. Fiz. Zh.* **27**, 1206 (1982).
16. V. Ā. Stadnik, V. I. Kardash, M. O. Romanyuk, and J. Stankowska, *Ukr. Fiz. Zh.* **41**, 940 (1996).
17. N. A. Romanyuk, B. G. Mytsyk, and V. M. Varikash, *Fiz. Tverd. Tela (Leningrad)* **25**, 1670 (1983) [*Sov. Phys. Solid State* **25** (6), 962 (1983)].
18. B. G. Mytsyk and N. A. Romanyuk, *Izv. Akad. Nauk SSSR* **47**, 674 (1983).
19. M. O. Romanjuk and V. Yo. Stadnyk, *Condens. Matter Phys.* **2** (20), 711 (1999).
20. V. I. Stadnik, N. A. Romanyuk, and R. G. Chervonyĭ, *Opt. Spektrosk.* **84**, 317 (1998).
21. V. Ā. Stadnik, *Ukr. Fiz. Zh.* **43**, 213 (1998).
22. K. Imai, *J. Phys. Soc. Jpn.* **36**, 1069 (1974).
23. B. G. Mytsyk and N. M. Dem'yanishin, *Fiz. Tverd. Tela (St. Petersburg)* **40**, 318 (1998) [*Phys. Solid State* **40**, 290 (1998)].
24. B. G. Mytsyk and N. M. Dem'yanishin, *Ukr. Fiz. Zh.* **43**, 479 (1998).
25. N. O. Romanjuk and B. H. Mytsyk, *Ferroelectrics* **203**, 101 (1997).
26. N. M. Dem'yanishin and B. G. Mytsyk, *Fiz. Tverd. Tela (St. Petersburg)* **44** (1), 144 (2002) [*Phys. Solid State* **44** (1), 149 (2002)].

Translated by Yu. Sin'kov

PHYSICAL PROPERTIES
OF CRYSTALS

Effect of the Vacancy Composition of GaAs Single Crystals on Optical Quenching of Luminescence through *EL2* Defects

M. B. Litvinova

*Institute of Semiconductor Physics, National Academy of Sciences of Ukraine,
Kherson, 73008 Ukraine*

e-mail: lmb@ist.com.ua

Received March 3, 2003

Abstract—Optical quenching of luminescence through *EL2* defects in single crystals of undoped semi-insulating gallium arsenide is investigated. It is shown that the minimum energy of light photons providing the transition of such defects into the metastable state depends on the vacancy composition of the crystals. It is suggested that the nature of the effect revealed is related to the existence of a set of *EL2* defects with different configurations. An optical method is proposed to determine the vacancy composition of undoped semi-insulating GaAs crystals. © 2005 Pleiades Publishing, Inc.

INTRODUCTION

Semi-insulating properties of single crystals of undoped gallium arsenide, which is widely used in modern microelectronics as a substrate material, are determined by the presence of the deep donor level *EL2*. This level is related to antisite defects formed as a result of the incorporation of As atoms into the Ga sublattice (As_{Ga}). These defects can be either in positively charged (*EL2*⁺) or neutral (*EL2*⁰) states [1, 2]. Radiative trapping of free electrons by *EL2*⁺ defects (transition 1 in Fig. 1) and free holes by *EL2*⁰ defects (transition 2 in Fig. 1) leads to the formation of Gaussian luminescence bands peaked at $h\nu_m = 0.63$ and 0.68 eV, respectively, in the photoluminescence (PL) spectra of undoped semi-insulating GaAs crystals (inset in Fig. 1) [1, 3]. As a result of the superposition of these bands, an emission band at $h\nu_m = 0.645$ – 0.66 eV is formed.¹

It is known [1–5] that light with the photon energy $h\nu_{\text{ex}} \sim 0.9$ – 1.5 eV transforms *EL2* defects into the electrically inactive metastable state *EL2*^{*} (Fig. 1); as a result, the intensity of the PL band related to the radiative transitions through the *EL2* level significantly decreases. However, the data in the literature on the boundary (maximum and minimum) values of $h\nu_{\text{ex}}$ providing the optical quenching of this band under the same temperature conditions are significantly different [1–4].

In this paper, we report the results of the investigation of the optical quenching of luminescence through *EL2* defects in GaAs single crystals with different vacancy compositions. The change in the boundary values of $h\nu_{\text{ex}}$ for such crystals is analyzed. An optical

method is proposed to determine the vacancy composition of undoped semi-insulating GaAs crystals.

EXPERIMENTAL TECHNIQUE

We investigated undoped semi-insulating *n*-GaAs(100) crystals with the resistivity $\rho = 7 \times 10^7$ – 2×10^8 Ω cm grown by the Czochralski method in a unified manufacturing cycle. The concentration of *EL2* centers in the grown crystals, found by absorption of photons with the energy $h\nu = 1.04$ eV [3], was $N = (1.2$ – $1.8) \times 10^{16}$ cm^{-3} . Selective photoluminescence excitation was performed using a conventional technique [7]. A compact quartz halogen KGM lamp with a continuous spectrum and a power of 60 W served as an excitation source. Selective extraction of excitation bands with a half-width $w_{\text{ex}} \leq 0.8$ meV and a power of 4–6 mW in the range $h\nu_{\text{ex}} = 0.8$ – 1.6 eV was performed by an MDR-2 monochromator. The photoluminescence intensity I_{PL} was measured at a sample temperature of 77 K using an FÉU-68 photomultiplier. To eliminate the effects related to the nonlinearity of the dependence of I_{PL} on the excitation light intensity I_{ex} at different energies $h\nu_{\text{ex}}$, a reverse filter was installed behind the KGM lamp. Thus, a change in the excitation light intensity with a change in the energy $h\nu_{\text{ex}}$ was compensated for by the corresponding change in the transmission of the optical filters chosen for certified values. As a result, the deviation of the excitation light intensity from the spectrum-averaged value did not exceed 15% in the entire measurement range.

When the optical quenching of luminescence through *EL2* centers was investigated, the sample was initially heated to $T = (155 \pm 5)$ K and kept at this temperature for 10–11 min. Then the sample was rapidly cooled to 77 K. The value of I_{PL} was measured after

¹ The position of the maximum of this band is determined by the ratio of the intensities of the bands at $h\nu_m = 0.63$ and 0.68 eV [3, 6].

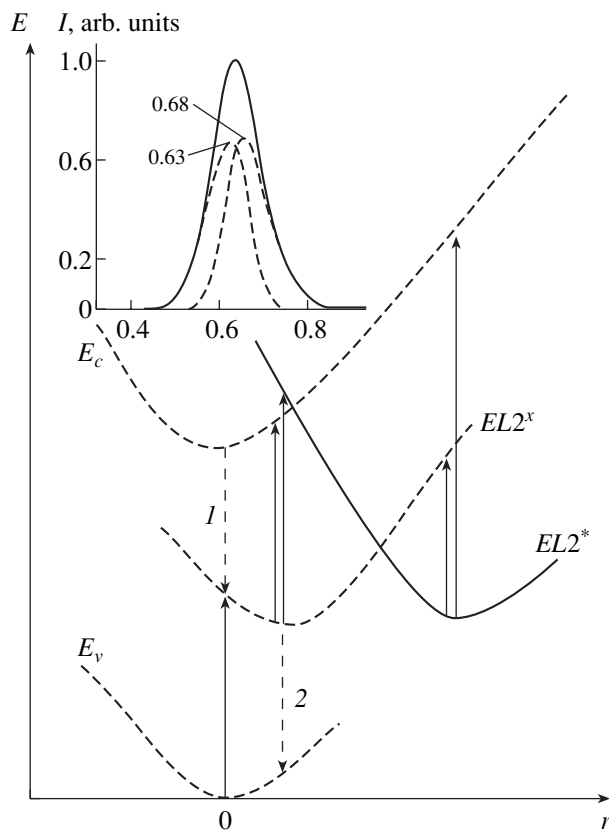


Fig. 1. Configuration-coordinate model of the $EL2$ center in gallium arsenide; $EL2^x$ and $EL2^*$ are the ground and metastable states, respectively; dotted and solid arrows indicate, respectively, the radiative and optical transitions in the $EL2^x$ and $EL2^*$ centers [1–3]. The inset shows the band of luminescence through $EL2$ centers at $T = 77$ K in the PL spectrum of undoped semi-insulating GaAs crystals. Dotted lines are the Gaussian band components with the maximum energies $h\nu_m = 0.63$ and 0.68 eV (arrows 1 and 2, respectively).

complete stabilization of the luminescence intensity. This procedure was repeated before determining each new value of $I_{PL}(h\nu_{ex})$; the energy step was $\Delta h\nu_{ex} = 2$ meV.

The vacancy composition of the crystals under study was determined as the concentration ratio of gallium and arsenic vacancies: $Z = [V_{As}]/[V_{Ga}]$. The value of Z was found from the ratio of the intensities of the edge PL band ($T = 77$ K) and the band related to the radiative transition from the conduction band to the acceptor level of carbon in the As sublattice [8, 9]. This method can be applied when a stable source of background carbon impurity (charge, graphite furnace elements, and so on) is used during the crystal growth, i.e., when a constant concentration of background carbon impurity at the crystallization front is provided from process to process. In this study, this requirement was satisfied owing to the unified manufacturing cycle of crystal growth. On the basis of the results obtained, a luminescence method is proposed, which makes it possible to

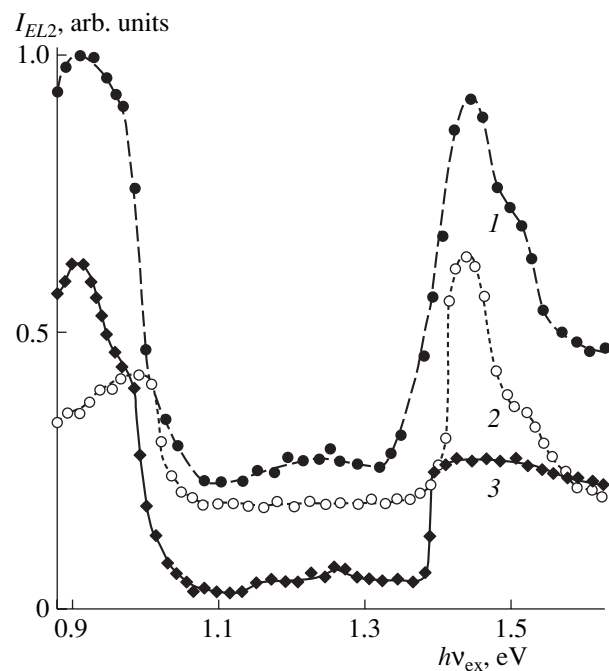


Fig. 2. (1) Spectrum of excitation of luminescence through $EL2$ defects and the spectral components with maxima at $h\nu_m = (2) 0.63$ and (3) 0.68 eV; $Z = 80$.

determine the vacancy composition of undoped semi-insulating GaAs crystals independent of the changes in the carbon background during the crystal growth.

EXPERIMENTAL RESULTS

The selective luminescence excitation spectra with bands peaked at $h\nu_m = 0.63$ and 0.68 eV (intensities $I_{0.63}$ and $I_{0.68}$, respectively) are shown in Fig. 2 (curves 2, 3). In the range $h\nu_{ex} = 1.0$ – 1.4 eV, almost complete quenching of the luminescence signal $I_{0.68}$ can be seen. The luminescence signal $I_{0.63}$ is quenched partially (to 70%).² Note that the ratio $k = I_{0.63}/I_{0.65}$ at $h\nu_{ex} > 1.4$ eV differs from k at $h\nu_{ex} < 1.0$ eV, this difference corresponding to a change in the cross sections of capture through $EL2^0$ and $EL2^+$ defects in these ranges of photon energies [1]. As a result, the position of the maximum of the resulting luminescence through $EL2$ defects (the peak intensity $I_{EL2} = I_{0.63} + I_{0.68}$) in the range of excitation energies under study shifts from 0.648 to 0.692 eV.³ In what follows, the optical quenching is regarded as a change in the value of I_{EL2} . The dependence $I_{EL2} = \varphi(h\nu_{ex})$ is shown in Fig. 2 (curve 1).

² The residual (after the optical quenching) intensity of the band at $h\nu_m = 0.63$ eV is determined by the radiative transitions through oxygen centers. The optical quenching of this luminescence band is much weaker than the quenching of the luminescence through $EL2$ defects [10].

³ This effect was investigated in [11] and will not be considered here.

For crystals of different vacancy composition, the short- and long-wavelength maxima in the dependence $I_{EL2} = \varphi(h\nu_{ex})$ shift with a change in Z ; i.e., the boundary values of $h\nu_{ex}^b$, at which the intensity I_{EL2} sharply decreases, change. However, the position of the short-wavelength maximum can be affected by the concentration of residual oxygen (see Footnote 2). Therefore, we will consider here only the change in the position of the long-wavelength maximum ($h\nu_{ex}^b$), for which this effect is absent [10]. The dependences $I_{EL2} = \varphi(h\nu_{ex})$ near the long-wavelength maximum for several crystals with different Z are shown in Fig. 3. As can be seen, with an increase in Z , i.e., with an increase in the deficit in arsenic, the value of $h\nu_{ex}^b$ shifts to larger energies.

DISCUSSION

It is known that the optical quenching of luminescence through $EL2$ defects is caused by their transition into the electrically inactive metastable state $EL2^*$. The shift of $h\nu_{ex}^b$ with a change in the ratio Z (Fig. 3) indicates that the boundary energy of the $EL2 \rightarrow EL2^*$ transition depends on the vacancy composition of the crystals. The most likely reason for this dependence is as follows.

It was shown in [5] that at $T < 125$ K the activation energy of the transition of the $EL2$ defect from the metastable to the ground state ($EL2^* \rightarrow EL2$) is different for different undoped semi-insulating GaAs single crystals. It was suggested in [5] that this phenomenon is caused by the existence of a set of $EL2$ defects with different configurations. Presently, all models considering $EL2$ centers assume that they are antisite defects As_{Ga} [6, 12–16]. There are different opinions about the nature of these defects: they are considered to be isolated substitutional defects As_{Ga} [11] or complexes of As_{Ga} with interstitial arsenic atoms As_i ($As_{Ga}As_i$) [12], gallium vacancies V_{Ga} ($As_{Ga}V_{Ga}$) [13], or vacancy associates $V_{As}V_{Ga}$ ($As_{Ga}V_{As}V_{Ga}$) [14]. However, there are also data suggesting that $EL2$ centers form a set of defects of the $As_{Ga} + X$ type [5, 14, 15], which can change their composition with respect to the element X .

A similar conclusion about the structural modification of this defect was drawn by us in [16].⁴ It was suggested that a change in the concentration of intrinsic point defects in a crystal leads to a corresponding change in the structure of complexes composed of As_{Ga} and intrinsic point defects in favor of the dominant defect or the absence of a particular defect near As_{Ga} .

⁴This conclusion is based on the data on the passivation of $EL2$ defects during the formation of $EL2-Cd_{Ga}$ and $EL2-Se_{As}$ complexes in crystals of different vacancy composition.

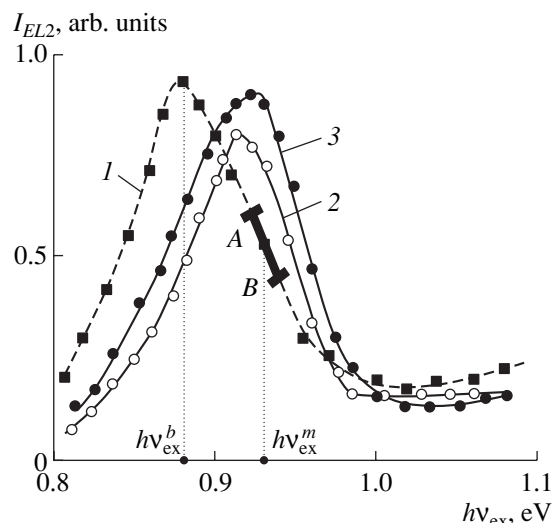


Fig. 3. Long-wavelength range of the dependence $I_{EL2} = \varphi(h\nu_{ex})$ for undoped semi-insulating GaAs crystals with $Z = (1) 2$; (2) 8; and (3) 80.

On the basis of the aforesaid, it is most likely that the shift of the position of $h\nu$ in Fig. 3 with a change in Z occurs as a result of structural changes in complexes composed of As_{Ga} and intrinsic point defects. In other words, an increase in the concentration of As vacancies or Ga vacancies leads to an increase in the relative number of $As_{Ga}V_{As}$ or $As_{Ga}As_i$ complexes, respectively. (The increase in the number of intrinsic defects in one of the GaAs sublattices is accompanied by an increase in the number of interstitial defects in the other sublattice [17].) The difference in the activation energies of the $EL2 \rightarrow EL2^*$ transitions [5] for different modifications of complexes composed of As_{Ga} and intrinsic point defects leads to the dependence of the position of the maximum $h\nu_{ex}^b$ on the vacancy composition of crystals.

It should be noted that the dependence obtained in [18] of the quenching of the luminescence through $EL2$ centers on the concentration of background carbon impurity has the same nature. It was shown in [18] that the increase in the concentration of background carbon impurity N_C in undoped semi-insulating GaAs (in our experiments, $N_C = (1.8-14.3) \times 10^{15} \text{ cm}^{-3}$) leads to an increase in the quenching of the luminescence through $EL2$ defects (from 5 to 85%). This result is in complete agreement with the data obtained here. Indeed, during the growth of a single crystal, an increase in the concentration of electrically active carbon, which occupies As vacancies in some region at the crystallization front, is directly proportional to the general increase in $[V_{As}]$. According to the law of mass action ($[V_{As}][V_{Ga}] = \text{const}$ [17]), $[V_{Ga}]$ decreases with an increase in $[V_{As}]$. Therefore, the concentration N_C depends on the ratio

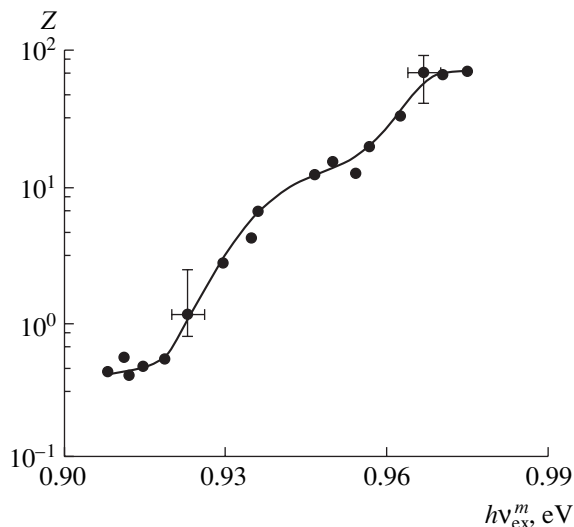


Fig. 4. Calibration dependence for determination of the vacancy composition of undoped semi-insulating GaAs crystals.

$[V_{As}]/[V_{Ga}]$ in undoped semi-insulating GaAs [8]. Thus, in contrast to the conclusions drawn in [18], the change in the optical quenching of the luminescence through $EL2$ defects (i.e., the probability of the $EL2 \rightarrow EL2^*$ transitions) should be related primarily to different compositions (including the vacancy composition) of the ensembles of intrinsic point defects in crystals.⁵

A METHOD FOR DETERMINING THE VACANCY COMPOSITION OF UNDOPED SEMI-INSULATING GAAS CRYSTALS

On the basis of the existence of the relation between the boundary energy of the $EL2 \rightarrow EL2^*$ transitions and the vacancy composition of undoped semi-insulating GaAs, one can plot a calibration dependence to determine the ratio of the concentrations of gallium and arsenic vacancies in such crystals. However, we propose another approach to this problem, which is more reasonable in our opinion. The slope of the short-wavelength wing of the dependence $I_{EL2} = \varphi(h\nu_{ex})$ in Fig. 3 is statistically determined by the number of centers undergoing transitions to the metastable state at the corresponding excitation energies on the abscissa axis. The largest value of the parameter

$$\zeta = dI_{EL2}/d(h\nu_{ex}) \quad (1)$$

corresponds to the maximum probability of such transitions. At the same time, a change in the vacancy com-

⁵ The energy level located at 70–80 meV above the top of the valence band, whose charge state, according to [18], determines the efficiency of the transition of $EL2$ defects to the metastable state, in undoped GaAs, is generally related to defects in the As sublattice [3]. Thus, the existence of this level is determined by the defect composition (and, therefore, the vacancy composition) of a crystal.

position of a crystal leads to a change in the structure of $EL2$ defects (see previous section). Therefore, the energy $h\nu_{ex}^m$, at which the value of the parameter (1) is maximum, corresponds to the transition to the metastable state of dominant complexes composed of As_{Ga} and intrinsic point defects. The value of this energy is related to the parameter $Z = [V_{As}]/[V_{Ga}]$. On the basis of this fact, a segment with the maximum slope to the $h\nu_{ex}$ axis (segment AB in curve 1, Fig. 3) is chosen on the noted portion of the curve $I_{EL2} = \varphi(h\nu_{ex})$. A perpendicular dropped from the middle of this segment on the abscissa axis gives the desired value of $h\nu_{ex}^m$. The obtained dependence of Z on $h\nu_{ex}^m$ is shown in Fig. 4. It can be used as a calibration dependence to determine the vacancy composition of undoped semi-insulating GaAs single crystals.

The method considered above is nondestructive. Its advantage over the existing luminescence method for determining the vacancy composition of similar crystals [8, 9] is that the data obtained are independent of the growth conditions and, in particular, the presence of background carbon impurity.

CONCLUSIONS

There is a dependence between the vacancy composition of undoped semi-insulating GaAs crystals and the boundary (minimum) value of the excitation light energy $h\nu_{ex}^b$, which causes the transition of $EL2$ defects to the metastable state: $EL2 \rightarrow EL2^*$. An increase in the deficit in arsenic leads to a shift of $h\nu_{ex}^b$ to higher energies. The most probable reason for this shift is the corresponding change in the composition of complexes composed of As_{Ga} and intrinsic point defects in favor of dominant intrinsic point defects of the crystal structure, which changes the activation energy of the $EL2 \rightarrow EL2^*$ transition. A calibration dependence is obtained, which makes it possible to estimate the vacancy composition of undoped semi-insulating GaAs crystals by analyzing the spectra of selective excitation of luminescence through $EL2$ defects.

REFERENCES

1. M. Tajima, Jpn. J. Appl. Phys. **26** (6), L885 (1987).
2. G. M. Martin and S. Makram-Ebeid, *Deep Centers in Semiconductors*, Ed. by S. T. Pantelides (Gordon and Breach, New York, 1986), p. 399.
3. K. D. Glinchuk, V. I. Guroshv, and A. V. Prokhorovich, *Optoelektronnaya i Poluprovodnikovaya Tekhnika*, No. 24, 66 (1992).
4. J. Dabrowski and M. Scheffler, Phys. Rev. B **40** (15), 10391 (1989).
5. David W. Fischer, Phys. Rev. B **37** (6), 2968 (1988).

6. M. Tajima, T. Iino, and K. Ishida, *Jpn. J. Appl. Phys.* **26** (6), L1060 (1987).
7. G. P. Peka, V. F. Kovalenko, and V. N. Kutsenko, *Luminescent Methods of Control of the Parameters of Semiconductor Materials and Devices* (Tekhnika, Kiev, 1986) [in Russian].
8. V. F. Kovalenko, M. B. Litvinova, and V. A. Krasnov, *Optoelektronnaya i Poluprovodnikovaya Tekhnika*, No. 37, 202 (2002).
9. V. F. Kovalenko and M. B. Litvinova, U Patent No. 57444A (2002).
10. M. Tajima and I. Takayuki, *Jpn. J. Appl. Phys.* **28** (5), L841 (1989).
11. Q. M. Zhang and J. Bernholc, *Phys. Rev. B* **47** (3), 1667 (1993).
12. H. E. Ruda, Q. Liu, M. Ozawa, *et al.*, *Appl. Phys.* **25**, 1538 (1992).
13. R. A. Morrow, *J. Appl. Phys.* **78** (8), 5166 (1995).
14. Chao Cheng, M. A. Bykovskii, and M. I. Tarasik, *Fiz. Tekh. Poluprovodn. (St. Petersburg)* **28**, 35 (1994).
15. Hoon Young Cho, Eun Kyu Kim, and Suk-Ki Min, *Phys. Rev. B* **39** (14), 10 376 (1989).
16. M. B. Litvinova, *Fiz. Tekh. Poluprovodn. (St. Petersburg)* **38** (1), 44 (2004) [*Semiconductors* **38**, 42 (2004)].
17. M. G. Mil'vidskii and V. B. Osvenskiĭ, *Structural Defects in Single Crystals of Semiconductors* (Metalurgiya, Moscow, 1984) [in Russian].
18. M. Suemitsu, H. Takahashi, Y. Sagae, and N. Miyamoto, in *Materials Science Forum. Trans. Techn. Publ.* (Switzerland, 1995), p. 1037.

Translated by Yu. Sin'kov

LIQUID
CRYSTALS

Molecular Aspects of the Main Phase Transition in Lipid Systems as a Weak First-Order Phase Transition: 2. Fluctuation Phenomena and the Role of Molecule Conformation in the Behavior of Lipid Films

S. A. Pikin

*Shubnikov Institute of Crystallography, Russian Academy of Sciences,
Leninskii pr. 59, Moscow, 119333 Russia*

e-mail: pikin@ns.crys.ras.ru

Received January 20, 2005

Abstract—The influence of molecule “softness” on the thermodynamic behavior of membranes, on the character of the main phase transition, and on an anomalous increase in the distance between bilayers in the film (swelling) above the phase-transition temperature is studied. The formation of the so-called ripple phase in multilayer films (modulation in the membrane plane) below the phase-transition temperature and the role of such factors as the molecule parameters and the lipid-film thickness are considered. It is shown that swelling of a lipid film is caused by the fluctuation-induced tilt of the molecules and the corresponding decrease in the number of “soft” molecules, whereas the formation of the ripple phase is caused by fluctuations of the order parameter in the gel phase and the corresponding increase in the number of soft molecules. © 2005 Pleiades Publishing, Inc.

INTRODUCTION

The first part of this study [1] was dedicated to the thermodynamics of a weak first-order phase transition in one- and multilayer lipid membranes with pronounced fluctuations in the vicinity of the phase-transition temperature T_M . The specific features of the thermodynamics behavior of this phase transition were explained by the interactions between the fluctuations of orientations of the molecules and their density at a low shear modulus μ in the low-temperature gel phase (of the smectic-C or smectic-G type). The average tilt of the molecules (the deviation θ from the normal z to the lipid bilayer or the membrane plane xy along the separated direction) was considered as an order parameter. It was shown that, if the shear modulus has a non-zero value in the gel phase, the interaction between the tilted molecules proceeding via the phonon exchange cannot fully compensate the compressibility effect resulting in a first-order phase transition. Such compensation is observed if the characteristic parameter $\lambda \sim \mu$ goes to zero, which results in a second-order phase transition accompanied by the corresponding fluctuation effects. The fluctuation phenomena in the thermodynamics of one- and multilayer vesicles of dipalmitoyl-phosphatidylcholine (DPPC or di16PC) were interpreted within the framework of the first approximations of the theory of a self-consistent field.

Below, we consider the effects of molecule ordering which may experience some conformational changes such that the fluctuation and conformational phenom-

ena are interrelated. We discuss the role of this relation in the behavior of lipid membranes in the vicinity of T_M . Lipid molecules with flexible hydrocarbon tails (relatively easily changing their shape under the action of various factors) are conditionally considered as soft and impurity molecules in comparison with the rigid rod-like molecules prevalent at low temperatures. We also consider the influence of softness of the molecule shape on the thermodynamic behavior of membranes, the character of the main phase transition, an anomalous increase in the distance between bilayers in a film (swelling), the appearance of the so-called ripple phase in multilayer films (modulations in the membrane plane) below the phase-transition temperature, and the role of such factors as the molecule structure and lipid-film thickness.

ROLE OF DEFECTS AND IMPURITIES IN LIPID SYSTEMS

Weakening of Singularity of a Thermodynamic Potential

It was shown [2, 3] that a sufficiently high impurity concentration can change a first-order phase transition to a second-order phase transition and damp large-scale fluctuations in the system, thus weakening the singularity of the thermodynamic potential of the system. Qualitatively, this effect may be considered by assuming that a molecular system at the fixed chemical potential of the impurity, ζ , undergoes a second-order phase transi-

tion at the point $T_c(\zeta)$ at which the heat capacity has an infinite value. Physically, this assumption signifies that fluctuations of the impurity concentration, n , at $\zeta = \text{const}$ may be arbitrarily large and, therefore, cannot prevent the appearance of the critical fluctuations in the order parameter. The density of the free energy $F(T, n)$ in the vicinity of the transition point is written in the form

$$F(T, n) = -T_c(\zeta)f\left(\frac{T - T_c(\zeta)}{T_c(\zeta)}\right) + \Omega(\zeta) + \zeta n, \quad (1)$$

$$\frac{\partial F}{\partial \zeta} = 0,$$

where f is the singular function and $T_c(\zeta)$ and $\Omega(\zeta)$ are smooth functions. Taking into account small deviations of the chemical potential from the value ζ_0 determined by the equation $n = -\partial\Omega/\partial\zeta|_{\zeta=\zeta_0}$, we may rewrite Eq. (1) in the following form:

$$F = F_0 + \tilde{T}_c \left[-f(x) + \frac{1}{2} \tilde{\lambda} (f'(x))^2 \right], \quad (2)$$

$$T - \tilde{T}_c = \tilde{T}_c (x - \tilde{\lambda} f'(x)), \quad \tilde{T}_c = T_c(\zeta_0),$$

$$\tilde{\lambda} = \frac{1}{\tilde{T}_c} \left(\frac{\partial \tilde{T}_c}{\partial \zeta_0} \right)^2 \left(\frac{\partial^2 \Omega}{\partial \zeta_0^2} \right)^{-1}, \quad (3)$$

$$\zeta - \zeta_0 \approx -\frac{\partial \tilde{T}_c}{\partial \zeta_0} \frac{f'(x)}{\partial^2 \Omega / \partial \zeta_0^2}. \quad (4)$$

Equations (2)–(4) differ from analogous Eqs. (6) in [1] by the sign of the coefficient $\tilde{\lambda}$; the coefficient $\tilde{\lambda}$ is negative because the derivative $\partial^2 \Omega / \partial \zeta_0^2$ is negative, which corresponds to an increase in the chemical potential with an increase in the number of impurity particles. This fact can dramatically change the thermodynamic properties of the system with a fixed average number of impurities per unit volume, n . Indeed, in accordance with Eqs. (2)–(4), the transition point corresponds to $x = 0$, in other words, the transition temperature equals \tilde{T}_c , because $T(x)$ is a monotonic function and $x(T)$ and $F(x(T))$ are single-valued functions. As a result, a quantity such as, heat capacity C_p remains continuous and finite at the transition point: $C_p(\tilde{T}_c) = C_p^0 + |\tilde{\lambda}|^{-1}$.

Effects of Molecular Length

Various structural defects (dislocations, disclinations, etc.) may play the role of impurities that may readily arise in a soft matter (lipid membranes). In this case, the molecular properties should influence the

parameters considered, e.g., the value of $\tilde{\lambda}$. As was shown in the first part of this study [1], intermolecular van der Waals interactions result in the dependence of F , Ω , and other quantities on the molecular length l . The defect concentration n should increase with weakening of these interactions; i.e., it is possible to write in a crude approximation that $n = n_0 - \zeta l^2$, where the parameter ζ is positive and its derivative $\partial\zeta/\partial\zeta$ is negative. In this case, the derivative $\partial^2 \Omega / \partial \zeta_0^2 = -\partial n / \partial \zeta_0 = l^2 \partial \zeta / \partial \zeta_0$ and the parameter $\tilde{\lambda} \propto -l^{-2}$ are negative. Now, using the relationship $|\tilde{\lambda}| A (\Delta T / \tilde{T}_c)^{-\alpha} \sim 1$, we can estimate the temperature region $\Delta T_{\text{damp}}(l)$ in the vicinity of the phase-transition point \tilde{T}_c (or T_M), at which the critical fluctuations are damped by impurities. Thus, we arrive at the relationships

$$\Delta T_{\text{damp}}(l) \sim |\tilde{\lambda}|^{1/\alpha} \sim l^{-2/\alpha}, \quad (5)$$

$$(C_p(\tilde{T}_c) - C_p^0) \sim |\tilde{\lambda}|^{-1} \sim l^2.$$

In other words, this temperature region should dramatically increase with a decrease in the molecular length at $\alpha < 1$. The experimentally measured anomalies in the behavior of heat capacity in the transition from the gel state to the smectic-A-type phase (second-order phase transition in one-layer vesicles in phosphatidylcholines [4]) show that, in expressions (5), $\Delta T_{\text{damp}}(l)$ increases and $(C_p(\tilde{T}_c) - C_p^0)$ decreases with a decrease in the molecular length.

In the general case, the parameter λ responsible for the character of the phase transition can be written as

$$\lambda = a l^2 - b_1 l^{-2} - b_2, \quad (6)$$

where the coefficients a and $b_{1,2}$ are positive. In fact, the first term in Eq. (6) is the quantity λ determined in the first part of this study (Eq. (7) in [1]) associated with a certain shear rigidity of the gel. The second term in Eq. (6) is determined by Eq. (3) and is associated with possible existence of some defects or impurities in the film. The third term reflects the effect of a finite thickness of the film on possible nucleation of defects. The quantities a and b_2 should depend on the film thickness D . At $D \approx 2l$, the coefficient a is determined by the shear modulus in the film plane. Proceeding from dimensionality consideration, we can relate (qualitatively) the shear modulus in the film plane to the shear modulus in the bulk multiplied by the molecular length as $a \sim l$. With a decrease in D , the volume effects become weaker but the fluctuations in the plane become more pronounced and, as a result, the coefficient a should decrease, whereas the coefficient b_2 (which depends on the ratio l/D and reflects the appearance of structural defects) should increase. At $D \sim 2l$, the coefficient b_2 does not depend on l . For one-layer DC12PC (di12PC), DC13PC (di13PC), and DC14PC (di14PC) samples,

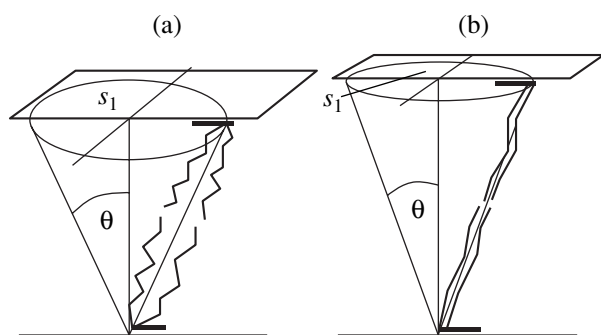


Fig. 1. Molecular model of a smectic monolayer (lipid bilayer) with consideration for possible orientational fluctuations and conformational changes: (a) pronounced orientational disorder and conformational changes far from the phase-transition temperature and (b) an increase in bilayer thickness in the vicinity of T_M caused by strong orientational correlations and weak conformational changes.

the interval $\Delta T_{\text{damp}}(l)$ evaluated in [4] may be approximated by the following formula, ignoring the first term in Eq. (6): $\Delta T_{\text{damp}}(l) \sim [0.03 + (2.47 + \kappa)^{-2}]^2$, where $\kappa = 0, 1$, and 2 for the aboveindicated molecules, respectively.

Equation (6) shows that, for relatively short molecules and very thin films, the main transition may change its character— from the first-order to the second-order phase transition. In the latter case, the temperature region of the noticeable fluctuation behavior for shorter molecules should be narrower because of a weaker singularity of the molecular systems with short-range interactions. In the vicinity of the value l^* , where $\lambda(l^*) = 0$, we arrive at the linear dependence $\lambda(l) \sim 4al^*(l - l^*)$ and the corresponding dependence for enthalpy, $\Delta H \sim (l - l^*)^{1/\alpha}$. The experiments with multilayer vesicles of phosphatidyl ethanolamines [5–7] showed that the measured ΔH value extrapolated to small lengths of molecular chains could have went to zero at nine hydrocarbons in the chain, whereas in actual fact these materials did not demonstrate clearly pronounced pretransition behavior. At low positive λ values, this fact may be qualitatively explained by a weak singularity (low α values) characteristic of shorter molecules over rather wide temperature ranges in the vicinity of T_M [5].

ANOMALOUS SWELLING OF LIPID FILMS

Model of Thickness Variation of a Lipid Layer

Usually, because of a molecule tilt, the thickness of a smectic monolayer is less than the doubled molecular length l . In the case under study, membrane thickening observed with an approach to T_M from the side of high temperatures may be explained by the specific features of the ordering mechanism of molecules which, in the vicinity of T_M , may undergo both conformational changes and orientational fluctuations. Two important

processes can take place in this temperature region: (1) conformational changes in the course of which a zigzag shape of the molecules in a lipid layer (Fig. 1) acquires a more pronounced rigidity and rectilinearity, so that the molecular length increases with lowering of the temperature and (2) fluctuation ordering of these zigzag molecules in the course of which the temporary local groups of molecules with a certain tilt $\Delta\theta$ are formed, with the mean square deviation from the layer normal being $\langle(\Delta\theta)^2\rangle \propto \chi \propto \tau^{-\gamma}$ (fluctuations similar to those in a C-smectic). The first process should be considered as an activation process because the change of a molecule shape is associated with the necessity to give a thermal push to a molecule to overcome a certain energy barrier W . The barrier W is somewhat lower for molecules that can freely rotate around the normal to the membrane plane. In the fluctuation groups (of smectic-C-type) of locally ordered molecules, the change of the conformation of tilted molecules is somewhat hindered; in other words, in this case, the barrier W is higher and, therefore, the probability of such conformational change becomes lower with lowering of the temperature and the appearance of the orientational fluctuations in a high-temperature phase (smectic-A-type).

Another cause of anomalous swelling is usually considered to be thickening of water interlayers between smectic layers in a membrane. Experimentally, these effects may be separated so that the role of each of the above factors can be studied separately [5]. We qualitatively studied the roles played by the above processes in swelling of a lipid membrane.

Let us write the thickness d of a layer in a membrane as

$$d = d_{\text{rigid}}(1 - v_{\text{soft}}), \quad (7)$$

where d_{rigid} is the thickness of a layer of rectilinear rigid molecules and v_{soft} is a relative fraction of soft molecules in the form

$$v_{\text{soft}} \sim \exp(-W/k_B T), \quad W = W_0 + w(\tau), \quad (8)$$

where W_0 is a positive constant and the function $w(\tau)$ is a fluctuation addition increasing with an approach to the temperature of the main phase transition. Thus, the thickness d should also increase with an approach to the point T_M . A decrease in d with lowering of the temperature below T_M is explained by an increase of the order parameter (an increase in the molecule tilt θ and the respective decrease in the layer thickness).

In fact, Eq. (8) describes the thermodynamic probability of conformational changes in an equilibrium lipid system, which is quite justified within the framework of the thermodynamic approach used here. However, strictly speaking, the process of conformational changes does not correspond to a stable statistical equilibrium. The evolution of the system up to the attainment of a stable equilibrium requires kinetic consideration. The above description is only valid for relatively

short times shorter than the time necessary for the attainment of an equilibrium tilt angle and the respective film thickness. (The latter increases in the vicinity of T_M approximately as $|T_M - T|^{-1}$.) Far from T_M , the equilibrium film thickness is attained relatively quickly and the conformational changes only follow the temperature changes.

*Fluctuation Change of Area
per Molecule Above
the Phase-Transition Temperature*

Another interesting feature of the main phase transition is the experimentally observed change in the area s_1 per molecule in the xy plane: the s_1 area noticeably decreases with an approach to the point T_M from the side of high temperatures [8]. For zigzag-like tilted molecules in the fluctuation regions of the radii $r_c \propto |\tau|^{-\eta}$, this decrease in the area s_1 can indicate that the two-dimensional rotators (ξ_1, ξ_2) [1] in such fluctuating molecular groupings have a preferential orientation in the xy plane. Therefore, we may write the following qualitative expression:

$$s_1 \approx s_{\max} - \sigma s_0, \quad (9)$$

where s_0 is a certain molecular parameter and the quantity s_{\max} corresponds to the condition of absolutely free molecule rotation at high temperatures. The σs_0 quantity characterizes the area per molecule in the xy plane in which no free molecule rotations in this plane are possible (Fig. 2) because of correlations: in the vicinity of the transition point and below T_M , this area is rather large (its maximum value is of the order of $(s_{\max} - s_0)$), whereas at high temperatures, this area is minimal and close to zero. Now, let us evaluate the coefficient σ proceeding from dimensionality. This coefficient is proportional to the squared correlation radius,

$$\sigma \sim (r_c^2 / N s_0), \quad (10)$$

where N is the number of molecules. Thus, the minimum s_1 value is of the order s_0 ; the minimum r_c^2 / N ratio equals $s_0 / N \approx 0$; and σs_0 , being a function of temperature, is characterized by the dependence $\sigma s_0 \sim r_c^2(T) \sim |\tau|^{-2\eta}$.¹

One may think that larger areas of orientationally correlated molecules would result in more pronounced hindrances of conformational changes. In other words, with an approach to T_M from the side of higher temperatures, the barrier W should increase proportionally to the area in which no free molecular rotations can take place, $\sigma s_0 \sim r_c^2(T) / N \sim |\tau|^{-2\eta} / N$. Moreover, the quantity

¹ The above consideration is only qualitative. In fact, the fluctuation contribution to $\sigma(\tau)$ may be of a more complicated nature with the critical exponent being only approximately equal to 2η . The reliable determination of this exponent requires a more rigorous theoretical and experimental consideration.

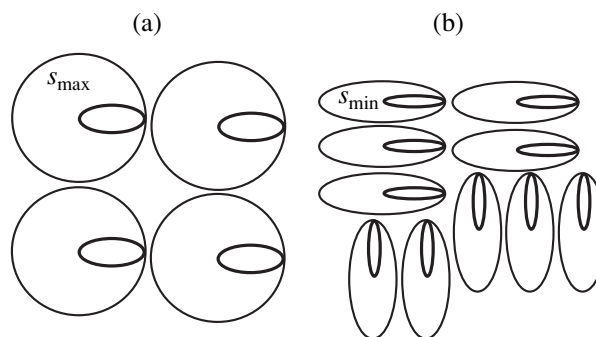


Fig. 2. Area per pair of molecules having the same tilt in the fluctuational groupings in a lipid bilayer of the disordered smectic-A type phase (thin lines show the probability ellipsoids of molecular orientations): (a) pronounced disorder far from the phase-transition point, (b) weak disorder (large correlation regions) in the vicinity of the transition temperature; instantaneous positions of the molecules are shown by solid lines; far from the transition point, the soft molecules occupy a larger area.

W_0 in Eq. (8) should also depend on the molecular length l , e.g., as $W_0 = w'l^2$, because, as was indicated above, the concentration v_{soft} of soft molecules should increase with weakening of intermolecular interactions ($n = n_0 - \zeta l^2$). If these correlation effects are weak enough, the d value in the vicinity of T_M is equal to

$$d \approx d_0 + B l^2 - d' l^2 |\tau| + d'' |\tau|^{-2\eta}, \quad (11)$$

where $d_0 \sim l$, B , d' , and d'' are positive quantities, with the constant d'' having a low value proportional to $1/N$. Thus, above T_M , the thickness d decreases almost linearly with an increase in temperature. In the direct vicinity of T_M (in the region ΔT), d increases nonlinearly with a decrease in τ , because of the fluctuations in molecule orientations.

Temperature Region of Anomalous Swelling

The temperature region ΔT should depend on the molecular length l . Comparing the third and fourth terms in expression (11), we see that the fourth term is prevalent in the interval

$$\Delta T_{\text{swel}}(l) \sim l^{-2/(1+2\eta)}. \quad (12)$$

In other words, the region of the so-called anomalous swelling should decrease with an increase in the molecular length l . Since the critical exponent is equal to $\eta = 1/2$ for the first correlation correction to the Landau approximation and to $\eta \approx 2/3$ for the two-component order parameter in the scaling theory, the dependence $\Delta T_{\text{swel}}(l)$ discussed here should be intermediate between two close dependences l^{-1} and $l^{-6/7}$.

At $T = T_M$, the quantity r_c is finite for a first-order phase transition ($r_c(T_c) \propto (A\lambda)^{-\eta/\alpha}$, see also Eqs. (10) and (11) in [1]) and, moreover, the quantity $v_{\text{soft}} = 0$ if the barriers W are high (strong fluctuations). Therefore,

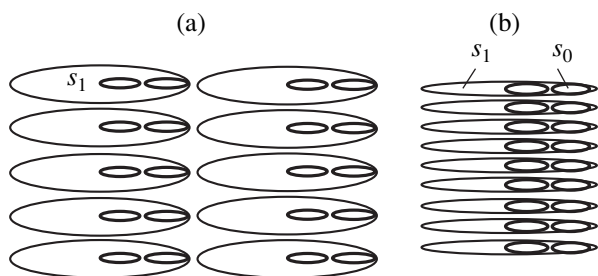


Fig. 3. Areas per pairs of molecules with a considerable tilt in the bilayer of an ordered smectic-C type gel phase: (a) in the vicinity of the temperature T_M and (b) far from the temperature T_M , where $s_1 \sim s_0$.

if the value $W(T_M)$ is less than $k_B T_M$, the thickness d at $T = T_M$ (with an approach from the side of high temperatures) should have a finite maximum,

$$d_{\max} \approx d_0 + d'' |x_c^+|^{-2\eta} \approx d_0 + d'' \left(\frac{\alpha}{2 - \alpha} \right)^{-2\eta} (\lambda A)^{-2\eta/\alpha}. \quad (13)$$

In a first-order phase transition, d_{\max} undergoes a jump at the transition point. If $W(T_M)$ is much larger than $k_B T_M$, the maximum d value at the transition point T_M is equal to d_{rigid} . For very low l values, the function $d(T)$ has a smooth maximum at $T = T_M$ and the derivative $\partial d / \partial T|_{T_M} = 0$. In the experiments on DBPC (di22PC) [5], an almost linear dependence of d on τ was observed over a rather wide interval of temperatures in the vicinity of T_M , whereas an anomalous increase in d took place only in a narrow range of τ values, with the maximum of $d(T_M)$ being relatively smooth [5]. In accordance with Eq. (11), a fluctuation-induced increase in bilayer thickness is practically independent of the molecular length. This fact was also observed in [5].

INSTABILITY OF THE GEL PHASE IN THE VICINITY OF THE MAIN PHASE TRANSITION

Deformations Caused by Conformation Changes in the Gel Phase

Below T_M (negative τ values), a certain linear decrease in d with lowering of the temperature is observed because of the effect associated with an increase in the tilt angle of the molecules in the gel phase (an effect analogous to the effect observed in smectic C). In the direct vicinity of T_M , the equilibrium d value should increase as $d_{\max}(1 - \theta^2)$ because of a decrease in the tilt angle θ with an approach to T_M . On the other hand, below T_M , the quantity r_c^2/N is the area σs_0 (per molecule) of possible fluctuations breaking the orientational order in the xy plane (Fig. 3). In turn, an increase in σ corresponds to lowering of the barrier W in the vicinity of T_M (proportional to σs_0), i.e., to an

increase in the number of soft molecules and the corresponding decrease in d (the fourth term in expression (11) taken with a minus sign). Thus, below the transition point, these two effects compete with one another. In actuality, no decrease in the lipid-layer thickness is observed with an approach to T_M from the side of low temperatures, because relatively fast conformational changes observed at the deceleration of the establishment of the equilibrium parameters of the film may give rise only to the formation of mechanical stresses in the film (at practically constant equilibrium film thickness). For example, in order to compensate the above-mentioned decrease in thickness d due to an increase in the concentration of soft molecules, this competition should give rise to the tensile deformation along the normal to the film plane. This tensile deformation in the layer film over the given temperature range should reach the value u_{zz}^0 proportional to the contribution $|\tau|^{-2\eta}$ discussed above. Relaxation of this deformation can be accompanied by appearance of nonuniform modulations in the film plane.

Above T_M , the change in the soft-molecule concentration n and the corresponding change in d are the only processes determining the attainment of the equilibrium film thickness. Therefore, in this case, the time necessary for the attainment of a stable equilibrium is equal to the time necessary for the attainment of the equilibrium concentration n . Therefore, the compression deformations in the film caused by a fast increase in the number of straightened molecules relax without film modulations.

Factors that Influence the Formation of Ripples in the Gel Phase

The physical consequence of the reduction of the system stability in the vicinity of a weak first-order phase transition is the existence in the vicinity of $T_c \equiv T_M$ (in the case considered here, below T_c) of the temperature region, where the film structure can readily be distorted. This situation can correspond to the formation in a certain temperature interval below T_M of a certain phase with the characteristic modulation or ripples: the so-called ripple phase dependent on the length l of a lipid molecule and some other factors. This modulated phase is usually interpreted as a wavy smectic structure of the gel phase considered here. The smectic phases of liquid crystals often demonstrate the formation of wavy bending of smectic layers in those cases, where the homogeneous deformation u_{zz}^0 corresponding to film extension along the film normal z exceeds a certain critical value [3, 9, 10]. Compression deformation of the film along the normal z cannot give rise to such an instability. A similar mechanical instability may also arise in the layered lipid system under consideration. As was indicated above, the homogeneous ten-

sile deformation u_{zz}^0 proportional to $|\tau|^{-2\eta}$ may also appear in a certain vicinity of the temperature lower than T_M , because of the fluctuation-induced orientational disorder and the corresponding increase in the number of soft molecules. Above T_M , the fluctuation-induced orientational order in molecular groupings and the corresponding decrease in the number of soft molecules can give rise to compression deformation in the film, which does not result in film instability. In this case, one may draw the following qualitative conclusions: the critical deformation $(u_{zz}^0)_c$ is proportional to the ratio l/D and the critical length of the bending wave X_c is proportional to $(lD)^{1/2}$, where D is the film thickness [3]. Thus, the wavy structure may exist in a certain temperature interval ΔT_{ripple} below T_M if $|\tau|^{-2\eta}$ exceeds the l/D ratio (with a certain proportionality coefficient). In other words, if the parameter $|\tau|$ is less than $(lD)^{-1/2\eta}$,

$$\Delta T_{\text{ripple}} \sim (lD)^{-1/2\eta}, \quad X_{\text{ripple}} \sim (lD)^{1/2}. \quad (14)$$

For the multilayer lipid film considered above (a three-dimensional system with the critical exponent $\eta \approx 1/2$), the dependence $\Delta T_{\text{ripple}}(l/D)$ determined can be close to the inverse dependence $\Delta T_{\text{ripple}}(l/D)^{-1}$ [1]. The region ΔT_{ripple} should be larger for short molecules and smaller for longer lipid molecules. The characteristic period X_{ripple} should increase with an increase in molecular length. The thinner the lipid film (the smaller the thickness D), the narrower the temperature region of the existence of the modulated phase, because of a very large critical value $(u_{zz}^0)_c$ in very thin films.

In a lipid system, the situation with the wavy flexural instability can be more complicated because of the polar heads of lipid molecules and the water molecules between the lipid bilayers. Under these conditions, the existence of a modulated gel phase may be essentially dependent on the so-called flexoelectric phenomena. It was shown [11, 12] that elastic stresses arising in such films can give rise to electric fields E that increase, e.g., because of an increase in the density of the surface electric charge during reduction of the surface area occupied by the polar heads of the molecules. Flexoelectricity exists because of a certain relation between various nonuniform perturbations (e.g., material density and elastic deformation) and orientational deformations in the electric field \mathbf{E} . The modulations in the plane of a smectic C may be energetically favorable because of the following contribution to the free energy

$$\Xi E_z \Delta \rho \left(\frac{\partial \langle \xi_1 \rangle}{\partial x} + \frac{\partial \langle \xi_2 \rangle}{\partial y} \right), \quad (15)$$

where Ξ is the flexoelectric coefficient, $\Delta \rho$ is the fluctuation of density, $\langle \xi_1, \xi_2 \rangle$ is the parameter of the orientational order, $\Xi \sim (p/\rho_0 l^2)$, p is the dipole moment of the molecule, and ρ_0 is the average density. The field E is

related to the elastic deformation Σ as

$$\Xi' E = \Xi' \Sigma, \quad (16)$$

where the flexoelectric coefficient is described as $\Xi' \sim (\bar{\omega} p / \rho_0 l^2)$ and $\bar{\omega}$ is the density of the surface charge.

It is possible to write the change in the density of the free energy for the model of modulations along the x axis in the form

$$\Delta F = \frac{1}{2} K_{\text{orient}} \left(\frac{\partial \langle \xi_1 \rangle}{\partial x} \right)^2 + g \left[(\Delta \rho)^2 + \frac{1}{2} x_0^2 \left(\frac{\partial \Delta \rho}{\partial x} \right)^2 \right] + \Xi E_z \Delta \rho \frac{\partial \langle \xi_1 \rangle}{\partial x}, \quad (17)$$

where $K_{\text{orient}} \sim l^2$ is the modulus of the orientational elasticity and g and x_0 are the parameters of the density modulations. Minimizing ΔF with respect to the variables $\langle \xi_1 \rangle \sim \sin qx$ and $\Delta \rho \sim \cos qx$ and the wave number $q \sim \partial/\partial x$, we obtain

$$q = \frac{\sqrt{2}}{x_0} \sqrt{\frac{\Xi E}{2gK_{\text{orient}}}}, \quad E_c = \frac{\sqrt{2gK_{\text{orient}}}}{\Xi}, \quad (18)$$

where the critical energy is $E_c \sim l^3$ and the period of the x modulation is $1/q \sim l^{3/2}$ at the fixed E value exceeding the critical value E_c . Using Eqs. (16) and (18), we obtain the dependences of the main modulation characteristics on the molecular parameters in the form

$$\Sigma_c \sim \frac{l^3}{\bar{\omega} p}, \quad X_{\text{ripple}} \sim 1/q \sim \frac{l^{3/2}}{\sqrt{\bar{\omega} p}}. \quad (19)$$

Thus, in the presence of electric fields and electric charges, the threshold value of the film deformation Σ_c and the ripple length X_{ripple} depend on the length of hydrocarbon chains l (stronger than in Eq. (17)), the polar characteristics of the molecules, and on surface charges. Experimentally, the well pronounced dependence $X_{\text{ripple}}(l)$ was observed in [5]: in fully hydrated di14PC, di16PC, and di20PC, this period increased with an increase in the length of a hydrocarbon chain almost by a factor of 2. It seems that an increase in the water content results in an increase in the surface-charge density $\bar{\omega}$ and, therefore, in a decrease in the experimentally observed ripple period [13]. A similar modulated phase cannot be formed in lipid systems consisting of molecules that are too long, because of a dramatic increase in the threshold Σ_c . This was confirmed experimentally on phosphatidylcholine with 22 carbon atoms (di22PC) and with larger numbers of carbon atoms in the tail chain of the molecule [5].

It should also be indicated that the swelling region $\Delta T_{\text{swel}}(l) \sim l^{-2/(1+2\eta)}$ (above T_M) and the region of formation of the ripple phase $\Delta T_{\text{ripple}} \sim \Sigma_c^{-1/2\eta} \sim l^{-3/2\eta}$ (below T_M) increase for shorter molecules; however, as was indicated in [5], the above phenomena are not related.

CONCLUSIONS

According to the model suggested above, the main role in the behavior of lipid membranes in the vicinity of the main phase transition is played by mutually dependent conformational changes of the molecules and their orientational fluctuations. This fact becomes very important at very low values of the shear modulus of the gel phase. In this case, the soft molecules formed as a result of the conformational changes, which are usually considered as impurities or defects, may change the order and the nature of the main phase transition. In very thin films consisting of short lipid molecules, such a transformation becomes a second-order phase transition. In the latter case, the pretransitional fluctuation effects become relatively weak because of weakening of the singularities in the temperature behavior of the thermodynamic derivatives.

Anomalous swelling of a lipid film above the temperature of the main phase transition may be a consequence of an increase in the number of rectilinear molecules in the vicinity of the transition point. Swelling is also enhanced by the fluctuations in the formation of the C-smectic order. Qualitatively, the temperature region of anomalous swelling may be described as a function of the length of a lipid molecule. This region should become larger with a decrease in the molecular length.

The structure of the gel phase in the vicinity of the transition temperature is unstable because of the formation of mechanical deformations during film extension at pronounced fluctuations in the molecule orientations (break of the C-smectic order) and an increase in the number of soft molecules. Such instability may manifest itself in the formation of ripples, a wavy modulation of lipid bilayers. The temperature region of the ripple phase should become larger with a shorter length of the molecule. The threshold value of the deformation above which the smectic structure becomes modulated dramatically increases with an increase in the molecular length and a decrease in the total film thickness. Moreover, this value should also be sensitive to the polar characteristics of the molecules and the surface charges of lipid bilayers because of possible flexoelectric instability of the films. The ripple wavelength should depend on the water content in the film, which

influences the threshold of the flexoelectric instability. In this case, the threshold of formation of modulations and their period should considerably decrease with an increase in the concentration of water molecules in the lipid film. These conclusions are in good qualitative agreement with the known experimental data.

ACKNOWLEDGMENTS

I am grateful to D.P. Kharakoz, P. Lagner, G. Pabst, and M. Rappolt for fruitful discussions of the results. This study was supported by INTAS, project no. 01-0105.

REFERENCES

1. S. A. Pikin, D. P. Kharakoz, L. I. Tiktopulo, and E. S. Pikina, *Kristallografiya* **50** (2), 344 (2005) [*Crystallogr. Rep.* **50**, 308 (2005)].
2. S. A. Pikin, *Zh. Éksp. Teor. Fiz.* **58**, 1406 (1970) [*Sov. Phys. JETP* **31** (4), 753 (1970)].
3. S. A. Pikin, *Structural Transformations in Liquid Crystals* (Nauka, Moscow, 1981; Gordon and Breach, New York, 1991).
4. K. Uchida, Y. Haruhiko, and K. Ema, *Phys. Rev. E* **56**, 661 (1997).
5. G. Pabst, H. Amenitsch, D. P. Kharakoz, *et al.*, *Phys. Rev. E* **70**, 021908 (2004).
6. R. Koynova and M. Caffrey, *Biochim. Biophys. Acta* **1376**, 91 (1998).
7. R. Koynova and M. Caffrey, *Chem. Phys. Lipids* **69**, 1 (1994).
8. G. Pabst, J. Katsaras, V. F. Raghunathan, and M. Rappolt, *Langmuir* **19**, 1716 (2003).
9. N. Clark and R. B. Meyer, *Appl. Phys. Lett.* **22**, 493 (1973).
10. F. Kahn, *Appl. Phys. Lett.* **22**, 111 (1973).
11. E. I. Demikhov, E. Hoffmann, H. Stegemeyer, *et al.*, *Phys. Rev. E* **51**, 5954 (1995).
12. S. Pikin, A. Sparavigna, and A. Strigazzi, *Mol. Mater.* **6**, 7 (1996).
13. D. C. Wack and W. W. Webb, *Phys. Rev. A* **40**, 2712 (1989).

Translated by L. Man

SURFACE
AND THIN FILMS

Spectrum of Natural Electromagnetic Waves in a Periodic Ferromagnet–Dielectric Structure

S. V. Eliseeva and D. I. Sementsov

Ul'yanovsk State University, ul. L'va Tolstogo 42, Ul'yanovsk, 432700 Russia

e-mail: sementsovdi@ulsu.ru

Received November 29, 2004; in final form, February 10, 2005

Abstract—The specific features of propagation of natural TE waves in a periodic ferromagnet–dielectric structure are investigated in the following geometry: a bias magnetic field is parallel to the ferromagnet/dielectric interface and perpendicular to the wave propagation direction. The transformation matrix for the period of the structure, the dispersion relation, and the energy reflection coefficient are obtained for the case of normal incidence of a wave on a semi-infinite periodic medium by solving the boundary-value problem. It is shown that an external field can be used to control the spectrum and characteristics of reflected waves. © 2005 Pleiades Publishing, Inc.

INTRODUCTION

Multilayered periodic structures based on various materials have attracted much attention for a long time [1, 2]. In the absence of external fields, these structures have the properties of a uniaxial crystal with the symmetry axis perpendicular to the interface between the layers. The most promising materials for developing periodic structures, from the point of view of effective control of their electromagnetic properties, are semiconductors [3, 4] and magnets [5, 6]. These materials are used as active gyrotropic layers, which can easily change their characteristics in an external magnetic field. A bias magnetic field, depending on its orientation, generally changes the structural symmetry and the character of the frequency dependence of the effective material parameters of the structure. One of the most important characteristics of a periodic structure is its band energy spectrum, which determines the relation between the frequency and the wave vector of natural waves propagating through the structure. There is a direct analogy between electromagnetic waves in periodic structures and electron density waves in a periodic field of a crystal, this field being based on the translational symmetry and, hence, on the similarity of the dispersion relations. Therefore, such specific features as forbidden and allowed energy (frequency) bands are typical of the propagation of both electron and electromagnetic waves [6].

For periodic semiconductor–dielectric structures, the features of the band energy spectrum were investigated in detail in [7, 8]. For helical, helicoidal, and multidomain magnetogyrotropic periodic structures, the spectral features were widely investigated in the optical range, where the gyrotropy of a magnet is determined

by its permittivity [9–11]. For planar layered ferromagnet–dielectric structures, the general dispersion relation for microwaves was investigated only in the thin-layer approximation [12], in which the period of a structure is much smaller than the wavelength in the media composing the structure ($d \ll \lambda$). In this study, the specific features of the spectrum of natural polariton waves in a layered structure are investigated in the linear approximation with respect to the ac magnetization component under the conditions when the band structure of the spectrum manifests itself ($d \sim \lambda$). The structure under study, consisting of alternating layers of ferromagnetic and nonmagnetic dielectric materials, is placed in an external bias magnetic field lying in the interface plane and oriented perpendicular to the wave propagation direction. An expression for the reflection coefficient is obtained by solving the boundary-value problem and the frequency spectrum of this coefficient is plotted.

GENERAL EQUATIONS

Let us consider a multilayered periodic structure composed of layers of a magnet and a nonmagnetic dielectric with thicknesses d_1 and d_2 , respectively. The OZ axis of the Cartesian coordinate system is directed perpendicular to the interface plane. An external bias magnetic field is oriented along the OX axis and an electromagnetic wave of the polariton type propagates parallel to the interface plane (along the OY axis) and perpendicular to the bias magnetic field. The specific features of the interaction of the magnetization of ferromagnetic layers with the microwave field are described by the magnetic permeability, which is generally a tensor. It is well known that the tensor properties of mag-

nets related to magnetogyrotropy manifest themselves in the microwave range [13]. For the chosen coordinate system and the bias-field direction, when the magnetic relaxation is neglected, the nonzero components of the magnetic permeability of an isotropic magnet depend on frequency as follows:

$$\begin{aligned}\mu_{yy} = \mu_{zz} &= 1 + \frac{\omega_M \omega_H}{\omega_H^2 - \omega^2}, \\ \mu_{yz} = -\mu_{zy} &= \frac{i\omega \omega_M}{\omega_H^2 - \omega^2},\end{aligned}\quad (1)$$

and $\mu_{xx} = 1$. Here, the parameters $\omega_M = 4\pi\gamma M$ and $\omega_H = \gamma H$; M is the saturation magnetization, H is the external static magnetic field, and γ is the gyromagnetic ratio. Concerning the electrical properties, a magnet is also an isotropic medium; therefore, the permittivity tensor has a diagonal form with the components ϵ_f . For dielectric layers, the permittivity and permeability tensors are also assumed to be diagonal with the corresponding components ϵ_d and μ_d .

Solution of the Maxwell equations for each layer, with allowance for the propagation direction and the form of the material parameters of the layers, leads to two natural waves: a TE wave with the field components (e_x, h_y, h_z) and a TM wave with the components (h_x, e_y, e_z) . Furthermore, we will perform analysis only for the TE wave, which is driven by the external magnetic field. The time dependences of all components of the wave field will be chosen in the form $\exp(i\omega t)$ and the dependence on the coordinate along the wave propagation direction is determined by the factor $\exp(-iky)$, where k is the longitudinal component of the wave vector; i.e., the propagation constant. Omitting the exponential factors, which determine the above-mentioned dependences on time and coordinate y , we can write the expressions for the dependence of the corresponding field amplitudes of the wave propagating in magnet layers on the transverse coordinate z :

$$\begin{aligned}e_{xf} &= A_1 \exp(iv_f z) + A_2 \exp(-iv_f z), \\ h_{yf} &= \frac{i}{k_0 \mu_{\perp}} \frac{de_{xf}}{dz} + \frac{k \mu_{yz}}{k_0 \mu_{\perp} \mu_{zz}} e_{xf}, \\ h_{zf} &= -\frac{k \mu_{yy}}{k_0 \mu_{zz} \mu_{\perp}} e_{xf} - \frac{i \mu_{zy}}{k_0 \mu_{zz} \mu_{\perp}} \frac{de_{xf}}{dz},\end{aligned}\quad (2)$$

where $k_0 = \omega/c$ and ω and c are, respectively, the frequency and the velocity of a wave in a vacuum. Similarly, we have for dielectric layers:

$$\begin{aligned}e_{xd} &= B_1 \exp(iv_d z) + B_2 \exp(-iv_d z), \\ h_{yd} &= \frac{i}{k_0 \mu_d} \frac{de_{xd}}{dz}, \quad h_{zd} = -\frac{k}{k_0 \mu_d} e_{xd}.\end{aligned}\quad (3)$$

Here, the transverse components of the wave vector in each layer of a period are introduced. These components are determined by the relations

$$v_f^2 = k_0^2 \epsilon_f \mu_{\perp} - k^2, \quad v_d^2 = k_0^2 \epsilon_d \mu_d - k^2, \quad (4)$$

where the effective permeability of magnetic layers $\mu_{\perp} = \mu_{yy} - \mu_{yz} \mu_{zy} / \mu_{zz}$. Analysis of this expression, with allowance for (1), shows that the characteristic frequencies for magnetic layers are the ferromagnetic resonance frequency $\omega_f = \sqrt{\omega_H(\omega_H + \omega_M)}$, at which, without allowance for the magnetic relaxation, $\mu_{\perp} \rightarrow \infty$, and the antiresonance frequency $\omega_a = \omega_H + \omega_M$, at which $\mu_{\perp} = 0$.

TRANSFORMATION MATRIX AND DISPERSION RELATION

To determine the field distribution in an infinite periodic layered structure, we will introduce the transformation matrix \hat{m} for two layers making the period of the structure. This matrix relates the tangential components of the wave field at the beginning and the end of the period. For example, the relation between the field amplitudes at the boundary of the n th layer with the amplitudes at boundary of the $(n-2)$ th layer has the form:

$$\begin{aligned}e_{xn} &= m_{11} e_{xn-2} + m_{12} h_{yn-2}, \\ h_{yn} &= m_{21} e_{xn-2} + m_{22} h_{yn-2}.\end{aligned}\quad (5)$$

Taking into account the continuity of the tangential field components at the interface between the layers and the periodicity conditions

$$\begin{aligned}e_{xf}(d_1) &= e_{xd}(d_1), \quad h_{yf}(d_1) = h_{yd}(d_1), \\ e_{xd}(d) &= e_{xf}(0) \exp(iv_{ef} d), \\ h_{yd}(d) &= h_{yf}(0) \exp(iv_{ef} d),\end{aligned}\quad (6)$$

we obtain the expressions for the transformation matrix components:

$$\begin{aligned}m_{11} &= C_1 C_2 - i \frac{k \mu_{yz}}{v_f \mu_{zz}} S_1 C_2 - \frac{\mu_{\perp} v_d}{\mu_d v_f} S_1 S_2, \\ m_{22} &= C_1 C_2 - i \frac{k \mu_{yz}}{v_f \mu_{zz}} S_1 C_2 + \frac{\mu_d}{v_d \mu_{\perp}} \left(\frac{k^2 \mu_{yz}^2}{v_f \mu_{zz}^2} - v_f \right) S_1 S_2, \\ m_{12} &= -\frac{k_0 \mu_d}{i v_d} C_1 S_2 + \frac{k \mu_{yz}}{v_f \mu_{zz}} \frac{k_0 \mu_d}{v_d} S_1 S_2 - \frac{k_0 \mu_{\perp}}{i v_f} S_1 C_2, \\ m_{21} &= \frac{i v_d}{k_0 \mu_d} C_1 S_2 - \frac{k \mu_{yz}}{v_f \mu_{zz}} \frac{v_d}{k_0 \mu_d} S_1 S_2\end{aligned}\quad (7)$$

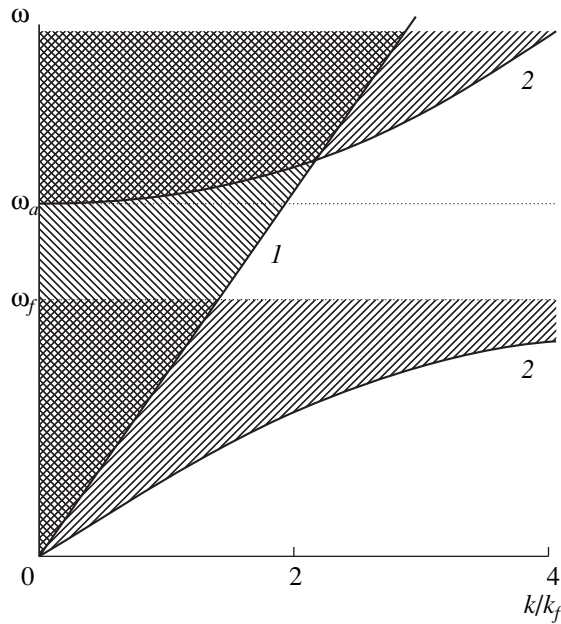


Fig. 1. Frequency-propagation-constant diagram determining the domains of existence of bulk and surface waves; curves 1 and 2 correspond to Eqs. (9).

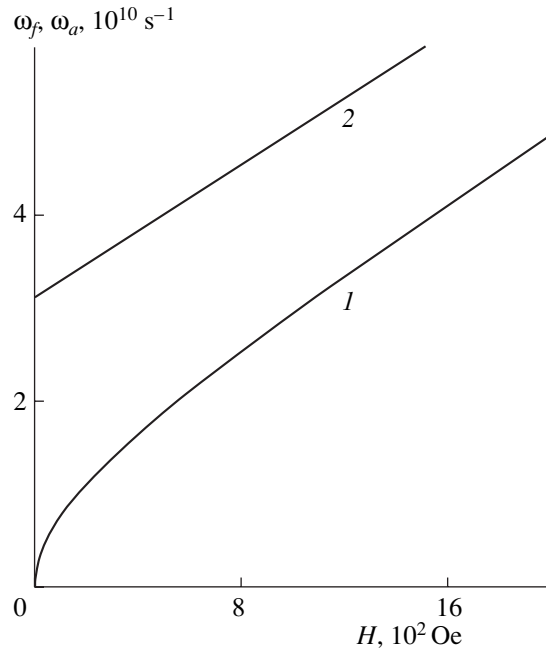


Fig. 2. Dependences of the ferromagnetic (1) and antiferromagnetic (2) resonance frequencies on the bias magnetic field.

$$-i \frac{1}{k_0 \mu_{\perp}} \left(\frac{k^2 \mu_{yz}^2}{v_f \mu_{zz}^2} - v_f \right) S_1 C_2,$$

where the following designations are introduced: $C_1 = \cos v_f d_1$, $C_2 = \cos v_d d_2$, $S_1 = \sin v_f d_1$, and $S_2 = \sin v_d d_2$. The dispersion relation for electromagnetic waves in an infinite medium consisting of alternating magnetic and dielectric layers is obtained from the expressions for the diagonal components of the \hat{m} matrix. This relation has the form

$$\begin{aligned} \cos d v_{ef} &= \frac{m_{11} + m_{22}}{2} \\ &= C_1 C_2 - \frac{\mu_d}{2 \mu_{\perp}} \left(\frac{\mu_{\perp}^2 v_d}{\mu_d^2 v_f} + \frac{v_f}{v_d} - \frac{k^2 \mu_{yz}^2}{v_f v_d \mu_{zz}^2} \right) S_1 S_2, \end{aligned} \quad (8)$$

where v_{ef} is the transverse component of the wave vector of a wave propagating in the structure. This component plays the role of the Bloch wave number. The imaginary part of the Bloch wave number determines the effective penetration depth of the microwave field in the structure; specifically, $\delta_{ef} = (\text{Im} v_{ef})^{-1}$.

In analysis of the dispersion relation (8), the dependences $\omega(k)$, corresponding to the relations

$$k_1 = \frac{\omega}{c} \sqrt{\epsilon_d \mu_d}, \quad k_2 = \frac{\omega}{c} \sqrt{\epsilon_f \mu_{\perp}(\omega)}, \quad (9)$$

are important because at $k > k_{1,2}$ the transverse wave numbers v_d and v_f are imaginary and the polariton waves arising in this case are surface waves. Figure 1 shows the dependences of the frequency on the normalized wave number determined from the above relations (curves 1, 2). The hatched areas correspond to real values of the parameters v_d and v_f and bulk waves, while the unhatched areas correspond to imaginary values of the parameters v_d and v_f and surface waves, which are localized at the interface between the media. In the cross-hatched areas, the waves are bulk from the sides of both media, whereas in the single-hatched areas we have bulk waves from the side of the corresponding medium and surface waves from the side of the other medium. The propagation constant $k_f = \omega_f/c$, where ω_f is the ferromagnetic resonance frequency.

The characteristic frequencies shown in Fig. 1 depend strongly on the bias magnetic field, which serves as a basis for controlling the type and the parameters of the waves propagating in magnetogyrotropic structures. The field dependences of the ferromagnetic resonance and antiresonance frequencies, determined by the above expressions, are shown in Fig. 2. Hereinafter, we will use for numerical analysis the following values of the layer parameters: $\epsilon_f = 5.5$, $4\pi M = 1767$ G, $\gamma = 1.76 \times 10^7 \text{ s}^{-1} \text{ oE}^{-1}$, $\epsilon_d = 2$, and $\mu_d = 1$. It can be seen that an increase in the field leads to an increase in the

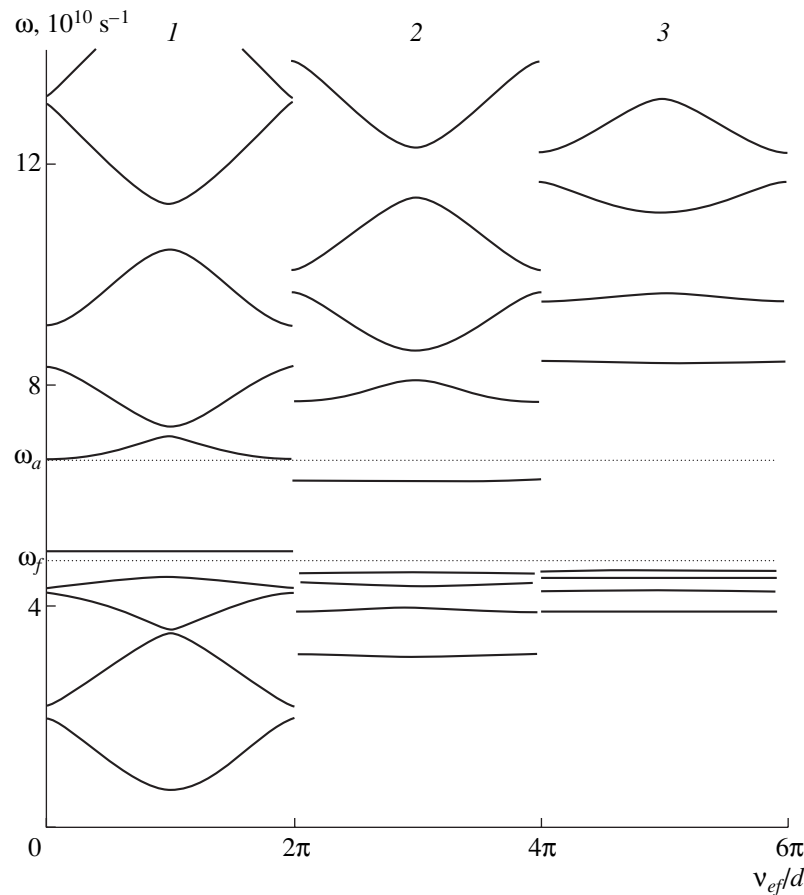


Fig. 3. Dependences of the frequency on the effective Bloch wave number of a periodic structure; $k/k_f = (1) 0.31$, $(2) 1.86$, and $(3) 3.10$.

frequencies ω_f and ω_a and, therefore, to a shift of the boundaries of the regions of propagation of collective bulk and surface waves.

ANALYSIS OF THE DISPERSION RELATION

Dispersion relation (8) has solutions at both real and imaginary values of v_f and v_d , which corresponds to bulk and surface polariton waves. Relation (8) takes the simplest form in the thin-layer approximation when the conditions $v_{ef}d, v_f d_1, v_d d_2 \ll 1$ are satisfied. In this case, the effective Bloch wave number is given by the expression

$$v_{ef} = \frac{1}{1 + \theta} \left[v_f^2 \theta^2 \left(1 + \frac{\mu_d}{\theta \mu_{\perp}} \right) + v_d^2 \left(1 + \frac{\theta \mu_{\perp}}{\mu_d} \right) - \frac{\mu_{yz}^2 \mu_d}{\mu_{zz} \mu_{\perp}} \theta k^2 \right]^{1/2}, \quad (10)$$

where the parameter $\theta = d_1/d_2$ and the parameters $\theta/(1 + \theta)$ and $1/(1 + \theta)$ determine the contribution to the period of the structure $d = d_1 + d_2$ of the magnetic and dielectric layers, respectively. At frequencies $\omega \sim 10^{10} \text{ s}^{-1}$, for multilayered structures based on a ferroelectric, relation (10) is valid for the period of the structure $d < 10^2 \mu\text{m}$. It follows from (10) that the characteristics of a layered medium may change in a wide range owing to the change in the parameter θ , i.e., the ratio of the thicknesses of dielectric and magnetic layers. A detailed analysis of relation (10) was performed in [12] and the wave characteristics of a layered medium were obtained in the above-mentioned approximation. At thicknesses of magnetic layers $d_1 \geq 10^2 \mu\text{m}$, the thin-layer approximation is not valid and relation (8) must be calculated more exactly. Let us perform a numerical analysis of the general dispersion relation for a symmetric structure with $d_1 = d_2 = d/2$ and the above-mentioned material parameters.

Figure 3 shows the dependences of the frequency $\omega(k)$ on the parameter v_{ef} for three values of the propagation constant k/k_f , 0.31, 1.86, and 3.10 (regions 1–3), corresponding to different areas in the diagram $\omega(k)$.

These dependences, obtained on the basis of (8), indicate the band character of the spectrum of collective waves in the structure. The spectrum is periodic with respect to the Bloch wave number with the period $2\pi/d$. Therefore, this spectrum is shown for each value of k in the interval of values of v_{ef} related to one of the Brillouin zones. The allowed bands, for which the propagation of collective bulk and surface waves is possible, are located between the frequencies corresponding to the Bloch wave numbers $v_{ef} = 2\pi n/d$ and $v_{ef} = \pi(2n + 1)$, where $n = 0, 1, 2, \dots$. In the range $\omega < \omega_f$, as frequency increases, crowding of allowed bands is observed, which is accompanied by a decrease in the widths of both allowed and forbidden bands. The reason for this is that, when the frequency approaches the value of the ferromagnetic resonance frequency, $\mu_{\perp} \rightarrow \infty$ and the optical thickness of ferromagnet layers also tends to infinity, which leads to fast oscillations of trigonometric functions in dispersion relation (8) and the formation of numerous transmission and nontransmission bands. With an increase in the propagation constant, the bands with the same numbers shift to higher frequencies. In the frequency range $\omega > \omega_f$, a single narrow band arises, which corresponds to the surface polariton mode. For small k , this mode is a surface wave from the side of a magnetic layer and a bulk wave from the side of a dielectric layer. At $k > k_1(\omega)$, the mode becomes a surface wave from the dielectric side as well. At $\omega > \omega_a$, bands corresponding to bulk waves arise again. They are enumerated as follows: $n' = 1, 2, 3, \dots$

Figure 4 shows the dependence of the frequency on the propagation constant, which is also plotted on the basis of dispersion relation (8) and accounts for the band character of the spectrum. Several first allowed bands in the ranges $\omega < \omega_f$ and $\omega > \omega_a$, in which collective bulk waves can propagate, are hatched. Near the ferromagnetic resonance frequency at $\omega < \omega_f$, the bands with numbers $n \geq 5$ are not shown owing to the spectrum crowding, as well as the bands with $n' \geq 5$ in the range $\omega > \omega_a$. A single narrow band is shown in the range $\omega > \omega_f$, which corresponds to the collective surface polariton mode. The curves in Fig. 4, which correspond to the band boundaries, indicate that the width of the allowed and forbidden bands depends on the propagation constant. With an increase in the propagation constant, the width of the allowed bands corresponding to the bulk modes decreases. For the bands in the range $\omega < \omega_f$, the bandwidth decreases with an increase in k fairly rapidly, whereas for the bands in the range $\omega > \omega_a$ this decrease is less pronounced. The width of the single narrow band in the range $\omega > \omega_f$, which corresponds

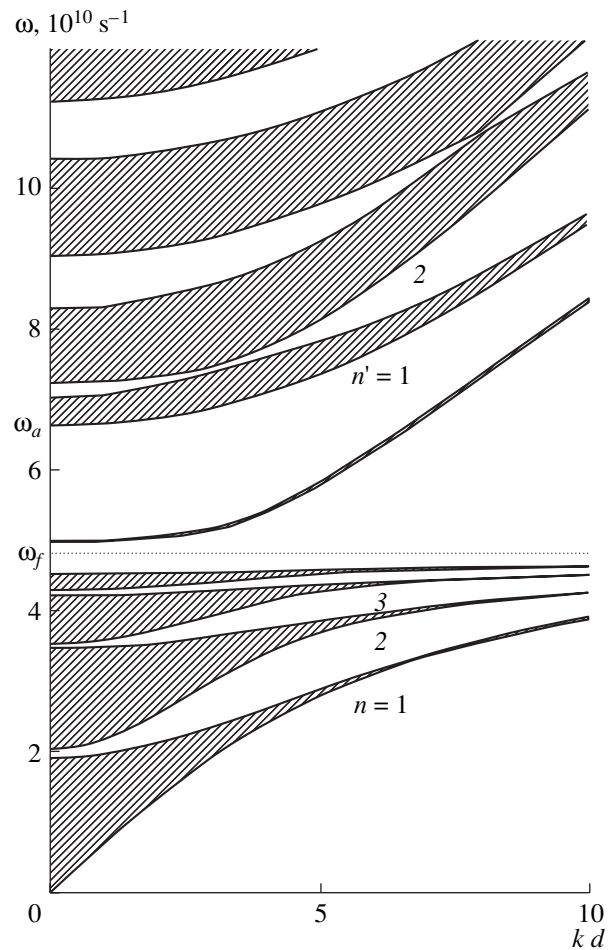


Fig. 4. Dependences of the frequency on the propagation constant for the boundaries between the allowed and forbidden bands, these bands corresponding to the values of $v_{ef}d = n\pi$ at $\omega < \omega_f$ and $v_{ef}d = n'\pi$ at $\omega > \omega_a$.

to the surface mode, slowly increases with an increase in k .

SPECTRUM OF THE REFLECTION COEFFICIENT

The specific features of the spectrum of natural waves in the periodic structure under study can be revealed most completely in experiments with reflection of an electromagnetic wave incident on the structure from a homogeneous medium. In this context, let us determine the reflection coefficient for the periodic structure under consideration and analyze the dependence of the reflection coefficient on the parameters of the structure and the wave. Let a plane wave with a frequency ω and a wave number $k_i = k_0 \sqrt{\epsilon \mu}$ be incident from the region $z < 0$ occupied by a nonmagnetic medium with a permittivity ϵ and a permeability μ on a periodic structure occupying the region $z > 0$ normal to the interface between layers in the structure. In this

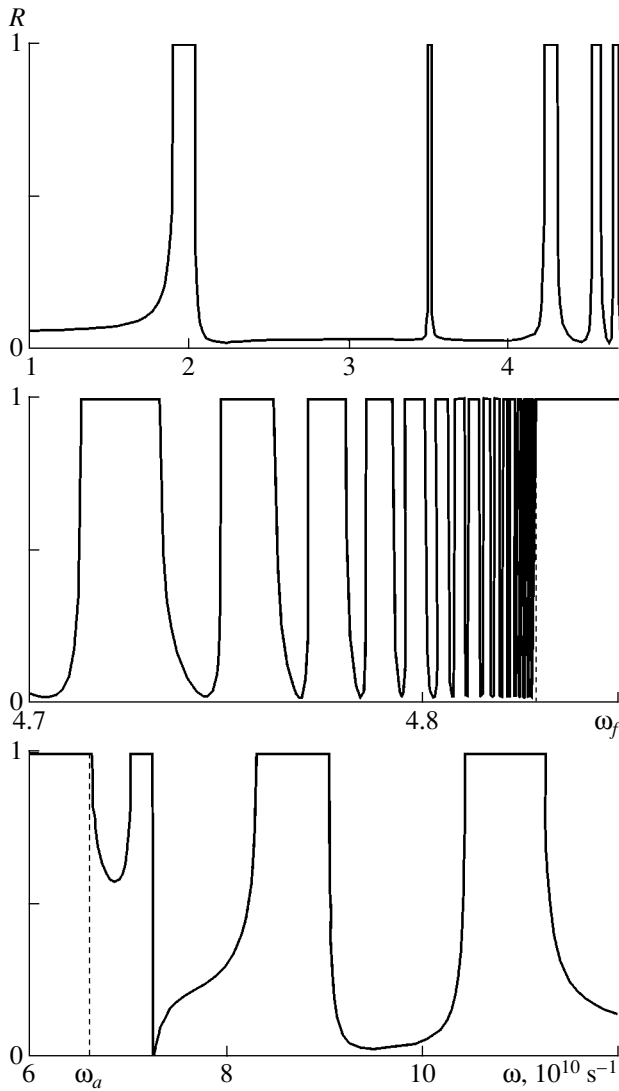


Fig. 5. Frequency dependence of the reflection coefficient at normal incidence of a wave on a periodic structure ($k = 0$).

case, the total wave field in the region $z < 0$ is the sum of the fields of the incident and reflected waves. Taking into account the relation between the electric and magnetic tangential field components determined by one of Eqs. (3) (which is valid for a nonmagnetic dielectric medium), we can write

$$\begin{aligned} e_x &= e_x^{(i)} [\exp(ik_i z) + r \exp(-ik_i z)], \\ h_y &= -\sqrt{\epsilon/\mu} e_x^{(i)} [\exp(ik_i z) - r \exp(-ik_i z)], \end{aligned} \quad (11)$$

where $r = e_x^{(r)}/e_x^{(i)}$ is the complex amplitude reflection coefficient and $e_x^{(r)}$ and $e_x^{(i)}$ are the amplitudes of the reflected and incident waves, respectively. To determine the reflection coefficient, let us use the expressions for the fields in the ferromagnetic (2) and dielec-

tric (3) layers, the boundary and periodicity conditions (6), and the boundary conditions at the interface between the uniform half-space and the ferromagnet:

$$e_x(0) = e_{xf}(0), \quad h_y(0) = h_{yf}(0). \quad (12)$$

Solving the obtained system, we derive the expression for the energy reflection coefficient $R = |r|^2$:

$$R = \left| \frac{\exp(iv_{ef}d) - m_{22} - m_{12}\sqrt{\epsilon/\mu}}{\exp(iv_{ef}d) - m_{22} + m_{12}\sqrt{\epsilon/\mu}} \right|^2. \quad (13)$$

Here, in accordance with the normal incidence of a wave on the periodic structure, k should be assumed to be zero in the elements m_{12} and m_{22} of the transfer matrix of the structure under study.

In the limiting cases $d_1 \rightarrow 0$ or $d_2 \rightarrow 0$ we derive from (13) the known expressions for the reflection coefficient at the interface either between two different dielectrics or between a dielectric and a magnet:

$$R_d = \left| \frac{\sqrt{\epsilon_d \mu} - \sqrt{\mu_d \epsilon}}{\sqrt{\epsilon_d \mu} + \sqrt{\mu_d \epsilon}} \right|^2, \quad R_f = \left| \frac{\sqrt{\epsilon_f \mu} - \sqrt{\mu_{\perp} \epsilon}}{\sqrt{\epsilon_f \mu} + \sqrt{\mu_{\perp} \epsilon}} \right|^2. \quad (14)$$

Figure 5 shows the frequency dependences of the reflection coefficient obtained from (13). In the forbidden bands, the reflection coefficient takes the value $R = 1$. In the transmission bands for bulk waves in the ferromagnet, frequencies are observed at which the reflection coefficient $R \rightarrow 0$ and the incident wave propagates through the layered medium with almost no energy losses. Taking into account that the relaxation is neglected, the energy of the wave passed through the structure is determined by the transmittance $T = 1 - R$. In the frequency range $\omega_f < \omega < \omega_a$, total reflection is observed; i.e., $R = 1$, although there is a narrow band corresponding to the surface mode. This fact indicates that collective surface modes cannot be excited at normal incidence of a wave on a periodic structure.

In summary, we investigated the dispersion properties of a periodic ferromagnet–dielectric structure. The dispersion relation and the conditions for the existence of bulk and surface polariton waves are analyzed. A change in the ratio of the thicknesses of the layers forming the period of a structure leads to changes in the width and the number of transmission and nontransmission bands, the penetration depth of a high-frequency field in the structure, and the reflection coefficient. A change in an external bias magnetic field shifts the characteristic frequencies and the frequency ranges

corresponding to allowed and forbidden bands in the spectrum of collective bulk and surface waves.

REFERENCES

1. A. Yariv and P. Yeh, *Optical Waves in Crystals: Propagation and Control of Laser Radiation* (Wiley, New York, 1984; Mir, Moscow, 1987).
2. C. Elashi, Proc. IEEE **64**, 1666 (1976).
3. F. G. Bass, A. A. Bulgakov, and A. P. Tetervov, *High-Frequency Properties of Semiconductors with Superlattices* (Nauka, Moscow, 1989) [in Russian].
4. R. S. Brazhe and L. S. Safonova, Fiz. Tekh. Poluprovodn. (Leningrad) **22** (2), 320 (1988).
5. A. A. Bulgakov and O. V. Shramkova, Fiz. Tekh. Poluprovodn. (St. Petersburg) **34** (6), 712 (2000) [Semiconductors **34**, 686 (2000)].
6. A. Ielon, in *Physics of Thin Films: Advances in Research and Development*, Ed. by G. Haas and R. Toon (Academic, New York, 1963; Mir, Moscow, 1973), Vol. 6.
7. S. B. Borisov, N. N. Dodoenkova, and I. L. Lyubchanskiĭ, Kristallografiya **36** (6), 1358 (1991) [Sov. Phys. Crystallogr. **36** (6), 769 (1991)].
8. O. V. Ivanov and D. I. Sementsov, Kristallografiya **41** (5), 791 (1996) [Crystallogr. Rep. **41** (5), 749 (1996)].
9. M. Sh. Erukhimov and V. V. Tyurnev, Fiz. Tverd. Tela (Leningrad) **17** (8), 2440 (1975) [Sov. Phys. Solid State **17** (8), 1618 (1975)].
10. D. I. Sementsov and A. M. Morozov, Fiz. Tverd. Tela (Leningrad) **20** (9), 2591 (1978) [Sov. Phys. Solid State **20** (9), 1498 (1978)].
11. D. I. Sementsov, Izv. Vuzov, Fiz., No. 3, 84 (1982).
12. S. V. Eliseeva and D. I. Sementsov, Fizika Volnovykh Protseessov i Radiotekhnicheskie Sistemy **6** (3), 19 (2003).
13. A. G. Gurevich and G. A. Melkov, *Magnetic Oscillations and Waves* (Nauka, Moscow, 1994; CRC, New York, 1996).

Translated by Yu. Sin'kov

**SURFACE
AND THIN FILMS**

Determination of Anisotropic Optical Parameters of Thin Films with Allowance for Multiple Reflections

A. F. Konstantinova*, **K. B. Imangazieva****, **E. A. Evdishchenko***,
and K. K. Konstantinov***

* *Shubnikov Institute of Crystallography, Russian Academy of Sciences,
Leninskiĭ pr. 59, Moscow, 119333 Russia*

e-mail: afkonst@ns.crys.ras.ru

** *Issyk-Kul State University, ul. Tynystanova 103, Karakol, 722360 Kyrgyzstan*

*** *JFC Service, ul. Shabolovka 2, Moscow, 119049 Russia*

Received January 31, 2005

Abstract—The intensity of light transmitted through a system consisting of a polarizer, a sample, and an analyzer is calculated with due regard for multiple reflections at the sample boundaries. The intensities of the transmitted light calculated with and without allowance for multiple reflections are compared in the presence and the absence of absorption. It is shown that multiple reflections considerably change the transmitted-light characteristics. The computational errors are evaluated for sample birefringence and dichroism with due regard for multiple reflection. © 2005 Pleiades Publishing, Inc.

The determination of anisotropic optical parameters of thin films, such as birefringence and dichroism, is characterized by some specific features. This is associated with the fact that, in thick samples, multiple reflections may be ignored, whereas neglect of multiple reflections in thin films may result in considerable errors in the measured intensities of the transmitted light. Despite the fact that the effect of multiple reflections of light in a sample has been known for a long time, no analytical expressions for its contribution to the transmitted-light parameters have been derived as yet. Below, we show in what instances one should take into account multiple light reflection in the determination of the anisotropic optical parameters of thin films and derive the respective relationships.

The method for determining birefringence and dichroism in crystalline plates from the intensity of light $J(\alpha)$ transmitted by a system consisting of a polarizer, a sample, and an analyzer was suggested in [1]. However, the formulas derived in [1] did not take into account multiple reflections and were written for the parallel geometry of the polarizer and analyzer.

Let us consider with allowance for multiple reflections $J(\alpha)$ on the basis of the exact solution of the problem of transmission by a sample of linearly polarized light with the azimuth α [1, 2]. The refractive indices are $N_{1,2} = n_{1,2} + i\kappa_{1,2}$ for an anisotropically absorbing sample, n_i for an ambient medium, and n_t for a substrate.

The vector of the electric-field strength, \mathbf{E}_t , of a wave transmitted through the sample is written in the

form [1, 2]

$$\mathbf{E}_t = (E_s \mathbf{c}_1 + E_p \mathbf{c}_2) e^{i\varphi}, \quad (1)$$

where E_s and E_p are the projections of the complex amplitude of the transmitted wave onto the directions \mathbf{c}_1 and \mathbf{c}_2 , where \mathbf{c}_1 and \mathbf{c}_2 are the orthogonal unit vectors parallel to the directions of polarization of two linearly polarized eigenwaves propagating in the crystal ($\mathbf{c}_1 \mathbf{c}_2 = 0$).

In the above formula, one may use the E_s and E_p values obtained for the problem of light propagation through an isotropic sample with due regard for multiple reflections and the refractive-index values N_1 for E_s and N_2 for E_p [1, 2]. Thus, ignoring the phase factor $e^{i\varphi}$ for E_s and E_p , we may write

$$\begin{aligned} E_s &= \frac{|t_1| e^{-\eta_1} e^{i(\varphi_1 + \xi_1)}}{1 - |r_1| e^{-2\eta_1} e^{2i(\varphi_1 + \zeta_1/2)}} E_0 \sin \alpha, \\ E_p &= \frac{|t_2| e^{-\eta_2} e^{i(\varphi_2 + \xi_2)}}{1 - |r_2| e^{-2\eta_2} e^{2i(\varphi_2 + \zeta_2/2)}} E_0 \cos \alpha. \end{aligned} \quad (2)$$

In the above equations, the following notation was used:

$$\varphi_{1,2} = 2\pi d n_{1,2} / \lambda, \quad \eta_{1,2} = 2\pi d \kappa_{1,2} / \lambda,$$

$$t_{1,2} = 4n_i N_{1,2} / [(N_{1,2} + n_i)(N_{1,2} + n_t)]$$

$$= t'_{1,2} + i t''_{1,2} = |t_{1,2}| e^{i\xi_{1,2}},$$

$$t'_{1,2} = 4n_i[n_{1,2}(n_{1,2} + n_i)(n_{1,2} + n_t) \quad (3) \quad \text{where}$$

$$+ \kappa_{1,2}^2(n_{1,2} + n_i + n_t)]/\mu_{1,2},$$

$$t''_{1,2} = 4n_i\kappa_{1,2}[n_{1,2}n_t - n_{1,2}^2 - \kappa_{1,2}^2]/\mu_{1,2},$$

$$\xi_{1,2} = \arctan(t''_{1,2}/t'_{1,2}),$$

$$\begin{aligned} & r_{1,2} \\ = & -[(N_{1,2} - n_i)(N_{1,2} - n_t)]/[(N_{1,2} + n_i)(N_{1,2} + n_t)] \\ & = r'_{1,2} + ir''_{1,2} = |r_{1,2}|e^{i\xi_{1,2}}, \\ r'_{1,2} = & -[(n_{1,2}^2 - n_i^2 + \kappa_{1,2}^2)(n_{1,2}^2 - n_t^2 + \kappa_{1,2}^2) \\ & - 4n_in_t\kappa_{1,2}^2]/\mu_{1,2}, \end{aligned} \quad (4)$$

$$r''_{1,2} = -[2\kappa_{1,2}(n_i + n_t)(n_{1,2}^2 - n_in_t + \kappa_{1,2}^2)]/\mu_{1,2},$$

$$\zeta_{1,2} = \arctan(r''_{1,2}/r'_{1,2}),$$

$$\mu_{1,2} = [(n_{1,2} + n_i)^2 + \kappa_{1,2}^2][(n_{1,2} + n_t)^2 + \kappa_{1,2}^2].$$

Light with the vector \mathbf{E}_t transmitted by the sample is incident onto the analyzer. It leaves the analyzer as a linearly polarized wave with the azimuth β . The vector of this wave \mathbf{E} may be written in the same form as \mathbf{E}_r , i.e.,

$$\mathbf{E} = (E_s \sin \alpha \sin \beta + E_p \cos \alpha \cos \beta) \mathbf{P} e^{i\varphi_i}, \quad (5)$$

where \mathbf{P} is the unit vector of the direction of the maximum transmission in the analyzer.

Using Eq. (5), we may write the intensity of light transmitted through the system consisting of a polarizer with the azimuth α , an oriented film (sample) on the substrate, and an analyzer with the azimuth β in the form

$$\begin{aligned} J = |\mathbf{E}|^2 = & |E_s|^2 \sin^2 \alpha \sin^2 \beta + |E_p|^2 \cos^2 \alpha \cos^2 \beta \\ & + (E_p E_s^* + E_p^* E_s) \sin^2 \alpha \cos^2 \beta. \end{aligned} \quad (6)$$

If the polarizer and analyzer are parallel to one another ($\alpha = \beta$) (then the angle α is the angle of the sample rotation around the surface normal or the angle of the simultaneous rotation of the polarizer and analyzer with respect to the immobile sample, Eq. (6) yields $J(\alpha)$ in the form of a Fourier series with due regard for multiple reflections:

$$J(\alpha) = T[a + b \cos 2\alpha + c \cos 4\alpha], \quad (7)$$

$$T = (e^{-(\eta_1 + \eta_2)} |t_1| |t_2|) / 4z_1 z_2,$$

$$\begin{aligned} z_{1,2} = & 1 - 2e^{-2\eta_{1,2}} |r_{1,2}| \cos 2(\varphi_{1,2} + \zeta_{1,2}/2) \\ & + e^{-4\eta_{1,2}} |r_{1,2}|^2, \end{aligned} \quad (8)$$

$$a = a_0 + 1.5p + q, \quad b = b_0 + 2s,$$

$$c = c_0 + 0.5p - q,$$

$$a_0 = 3 \cosh \delta_0 + \cos \Delta_0, \quad b_0 = 4 \sinh \delta_0,$$

$$c_0 = \cosh \delta_0 - \cos \Delta_0,$$

$$p = e^{\delta_0} z_2 (|t_1|/|t_2|) + e^{-\delta_0} z_1 (|t_2|/|t_1|) - 2 \cosh \delta_0,$$

$$s = e^{\delta_0} z_2 (|t_1|/|t_2|) - e^{-\delta_0} z_1 (|t_2|/|t_1|) - 2 \sinh \delta_0,$$

$$q = [\cos(\Delta_0 + \tau) - \cos \Delta_0]$$

$$+ e^{-2(\eta_1 + \eta_2)} |r_1| |r_2| \cos(\Delta_0 - \tau + t)$$

$$- e^{-2\eta_1} |r_1| \cos(\varphi_1 + \varphi_2 + \tau + \zeta_1)$$

$$- e^{-2\eta_2} |r_2| \cos(\varphi_1 + \varphi_2 - \tau + \zeta_2),$$

$$\tau = \xi_2 - \xi_1, \quad t = \zeta_2 - \zeta_1.$$

$$\Delta_0 = \varphi_2 - \varphi_1 = 2\pi d(n_2 - n_1)/\lambda$$

$$= 2\pi d \Delta n_0 / \lambda = 2\pi \Gamma / \lambda, \quad (9)$$

$$\delta_0 = \eta_2 - \eta_1 = 2\pi d(\kappa_2 - \kappa_1)/\lambda = 2\pi d \delta \kappa_0 / \lambda.$$

Here $\Gamma = d\Delta n_0$ is the path difference, $\Delta n_0 = (n_2 - n_1)$ is true birefringence, $\delta \kappa_0 = (\kappa_2 - \kappa_1)$ is true dichroism, and a_0 , b_0 , and c_0 are the Fourier coefficients without allowance for multiple reflections [2]. The quantities p , q , and s are the terms taking into account multiple reflections in the Fourier coefficients a , b , and c .

As a rule, the samples are thin films on the substrates which also multiply reflect light. Thus, a medium with the refractive index n_t has a finite thickness, and multiple reflections also takes place in the substrate. Then light multiply reflected in the substrate goes out into a medium with a different refractive index (usually, into air with the refractive index $n_i = 1$). Comparison of the dependences $J(\alpha)$ for this case and also for the case where multiply reflected light goes out into a semi-infinite medium with the refractive index n_t shows that these dependences are similar and that the ratio of their minimum and maximum values, $J_{\min}(\alpha)/J_{\max}(\alpha)$, is constant in all cases. This is very important for further calculation of anisotropic optical parameters of the sample.

It is convenient to determine birefringence and dichroism [2] on a sample placed between the oriented polarizer and the analyzer of a spectropolarimetric modular complex [3, 4] in which both the polarizer and

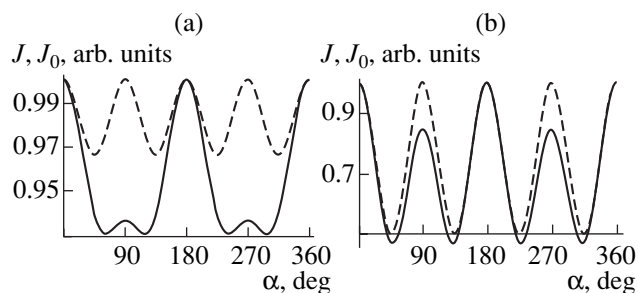


Fig. 1. Dependences of the light intensity $J(\alpha)$ and $J_0(\alpha)$ at $\lambda = 0.6 \mu\text{m}$. $\Delta n_0 = 0.116637$ and $\delta\kappa_0 = 0$. (The solid line indicates the intensity with allowance for multiple reflections; the dashed line, the intensities without allowance for multiple reflections.) (a) $d = 0.3 \mu\text{m}$, $\Delta_0 = 20.9947^\circ$, (b) $d = 1.286 \mu\text{m}$, and $\Delta_0 = 90^\circ$.

analyzer may simultaneously be rotated at a certain angular step.

The light intensity $J_0(\alpha)$ in Eq. (7) without allowance for multiple reflections has the form [2]

$$J_0(\alpha) = T_0[a_0 + b_0 \cos 2\alpha + c_0 \cos 4\alpha], \quad (10)$$

where

$$T_0 = (1/4)e^{-(\eta_1 + \eta_2)}.$$

Once the Fourier coefficients a_0 , b_0 , and c_0 are determined, we can also determine the Δ_{00} and δ_0 parameters from the following relationships:

$$\cos \Delta_{00} = (a_0 - 3c_0)/[(a_0 + c_0)^2 - b_0^2]^{1/2}, \quad (11)$$

$$e^{2\delta_0} = (a_0 + c_0 + b_0)/(a_0 + c_0 - b_0). \quad (12)$$

Now, it is also possible to determine birefringence Δn_0 and dichroism $\delta\kappa_0$. It is important to take into account that $\Delta_0 = 2\pi l \pm \Delta_{00}$, ($l = 0, 1, 2, 3, \dots$) depending on the path difference Γ . It is important that, in this case, the coefficient T_0 may be ignored.

It was shown [2] that neglect of multiple reflections in the calculation of the dependence of light intensity $J_0(\alpha)$ for a transparent films ($\delta_0 = 0$ and, therefore, $b_0 = 0$) has four equivalent maxima. In absorbing films, b_0 has a nonzero value and, therefore, the maximum values of $J_0(\alpha)$ are different. For transparent films and with due regard for multiple reflections in Eq. (7), the coefficient b of the second harmonic has a nonzero value because $s \neq 0$. Therefore, the dependence $J(\alpha)$ for a transparent film has the same form as for an absorbing film. This is illustrated by Fig. 1, which shows curves obtained with allowance for multiple reflections, $J(\alpha)$, and without them, $J_0(\alpha)$, for transparent films with different thicknesses. For the sake of easier comparison, the intensities are indicated in arbitrary units. In all the calculations, it was assumed that $n_i = n_t = 1$. Now, we evaluate all the above quantities for different wave-

lengths λ . In our calculations, we used the dispersion in refractive indices n_1 and n_2 and the absorption coefficient κ_1 and κ_2 of porous silicon [5], namely:

$$n_1^2 = 1.827 + 0.056/(\lambda^2 - 0.034) + (-4.5 \times 10^{-4})\lambda^2,$$

$$n_2 = n_1 + \Delta n_0,$$

$$\Delta n_0 = 8.6264 - 49.64543\lambda + 109.77752\lambda^2$$

$$- 108.68486\lambda^3 + 40.38208\lambda^4.$$

$$\kappa_1 = 0.05 - 0.1223\lambda + 0.0749\lambda^2, \quad \kappa_2 = \kappa_1 + \delta\kappa_0,$$

$$\delta\kappa_0 = 0.02409 - 0.05893\lambda + 0.03693\lambda^2.$$

In this case, $\Delta n_0 \sim 10^{-1}$ and $\delta\kappa_0 \sim 10^{-3}$.

At such $\delta\kappa_0$ values, the intensity dependences $J(\alpha)$ for thin absorbing films ($d = 0.3$ and $1.2861 \mu\text{m}$) are practically the same as the analogous dependences for transparent films. At the Δn_0 and $\delta\kappa_0$ values used, considerable differences between $J(\alpha)$ and $J_0(\alpha)$ are observed only at d of the order of several wavelengths. Figures 2a and 2b show these dependences at $d = 10 \mu\text{m}$. Figures 2c and 2d show the $T(\lambda)$ and $T_0(\lambda)$ dependences.

To illustrate the variation of all the quantities depending on the wavelength λ , Fig. 3 shows the Fourier coefficients a , b , and c and Fig. 4 shows the quantities p , q , and s . It is seen that, with the change in the wavelength, the quantities T , a , b , c , p , q , and s oscillate. It is also seen that, if multiple reflections are ignored, the T_0 , a_0 , and c_0 curves are the average curves of the oscillating ones. It should be indicated that the values of p , q , and s are lower (by an order of magnitude) than the value of the coefficient a . For thick samples, the coefficients a , b , and c coincide with the coefficients a_0 , b_0 , and c_0 , respectively.

Now, we calculate the values of $\cos \Delta$, with due regard for multiple reflections, by Eq. (11) with the substitution of a , b , and c for a_0 , b_0 , and c_0 , respectively. We obtain

$$\begin{aligned} \cos \Delta &= \frac{a - 3c}{\sqrt{(a + c)^2 - b^2}} \\ &= \frac{\cos \Delta_0 + 4q/(a_0 + c_0)}{(1 + 2p/(a_0 + c_0))\sqrt{1 - (b_0 + 2s)^2/(a_0 + c_0 + 2p)^2}}. \end{aligned} \quad (13)$$

Then, we may write the following approximate relationship

$$\begin{aligned} \cos \Delta &= \left(\cos \Delta_0 + \frac{4q}{a_0 + c_0} \right) \left(1 - \frac{2p}{a_0 + c_0} \right) \\ &\times \left(1 + \frac{1}{2} \frac{(b_0 + 2s)^2}{(a_0 + c_0 + 2p)^2} \right). \end{aligned} \quad (14)$$

With due regard for the fact that p , q , and s are small quantities in comparison with $(a_0 + c_0)$, we may write,

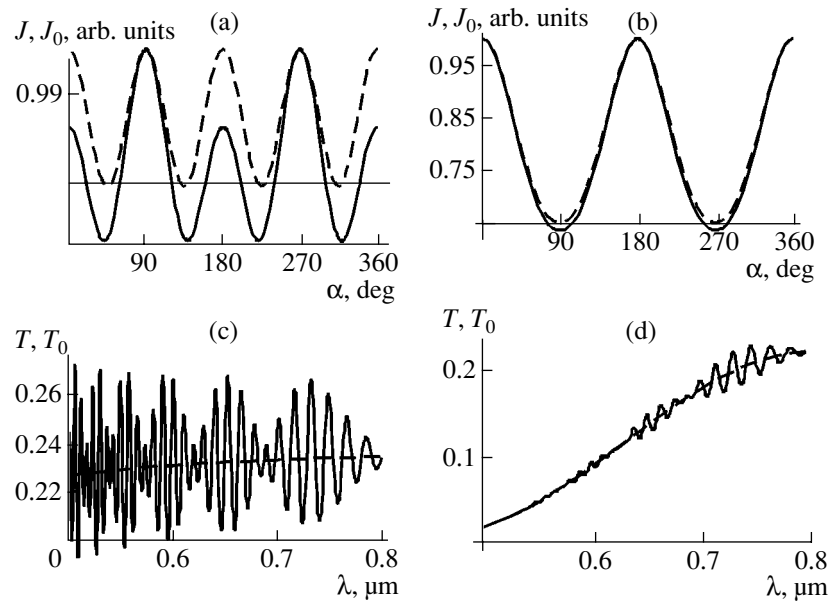


Fig. 2. (a, b) Light intensities $J(\alpha)$ and $J_0(\alpha)$ at $\lambda = 0.6 \mu\text{m}$, $\Delta n_0 = 0.116637$, $\Delta_0 = 360^\circ + 339.822^\circ$, and $d = 10 \mu\text{m}$. (c, d) Coefficients $T(\lambda)$ and $T_0(\lambda)$ at $d = 10 \mu\text{m}$. Solid lines are obtained with allowance for multiple reflections, dashed lines, without allowance for multiple reflections. (a, c) Curves for transparent film at $\delta\kappa_0 = 0$; (b, d) curves for absorbing films at $\delta\kappa_0 \sim 10^{-3}$.

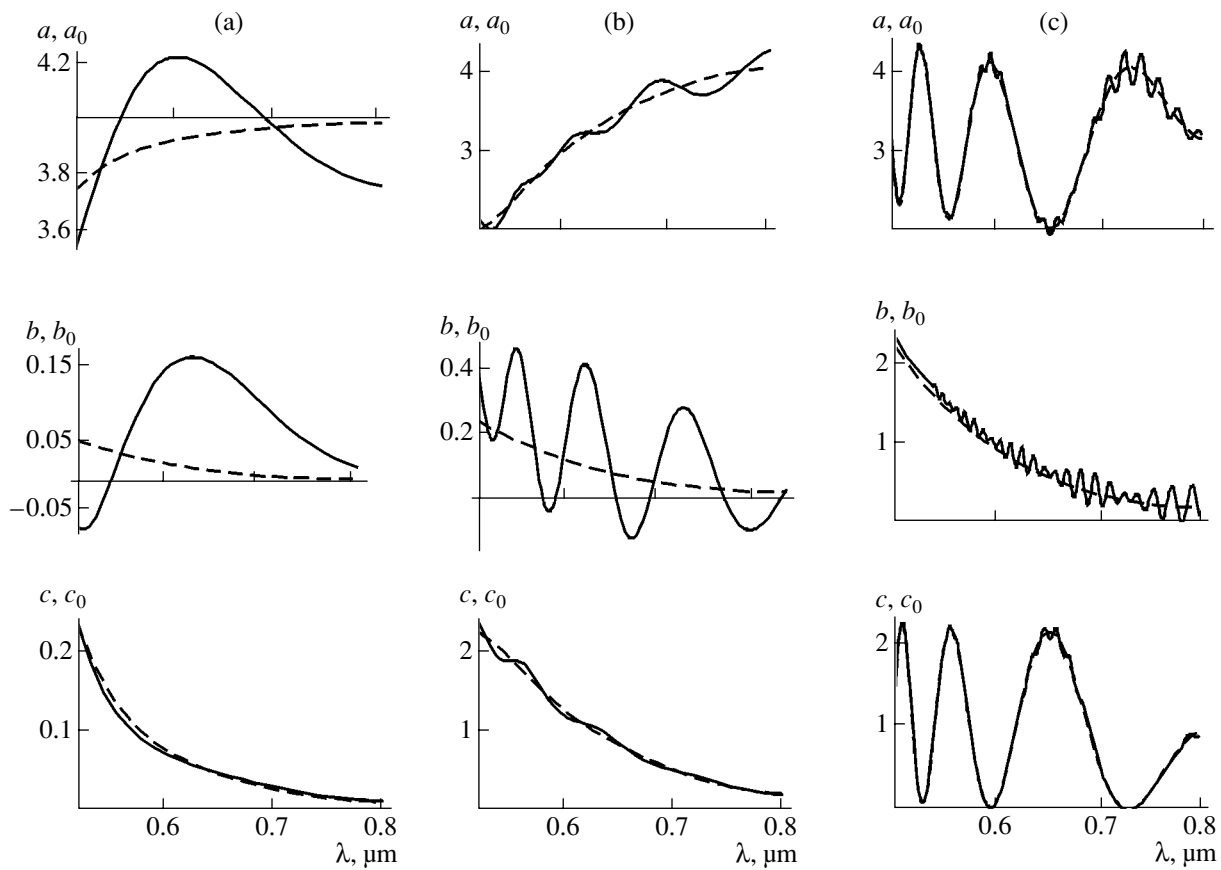


Fig. 3. Fourier coefficients as functions of wavelength λ at $\delta\kappa_0 \sim 10^{-3}$ with (solid line) and without (dashed line) multiple reflections; $d =$ (a) 0.3, (b) 1.286, and (c) 10.0 μm .

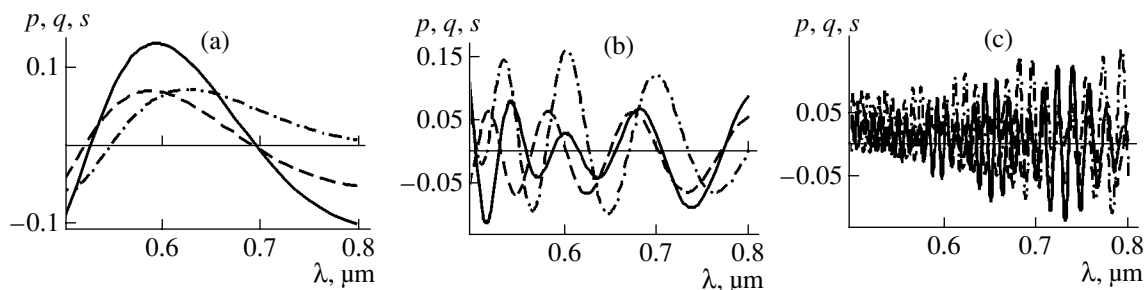


Fig. 4. p (solid line), q (dashed line), and s (dash-dotted line) as functions of wavelength λ at $\delta\kappa_0 \sim 10^{-3}$. $d =$ (a) 0.3, (b) 1.286, and (c) 10.0 μm .

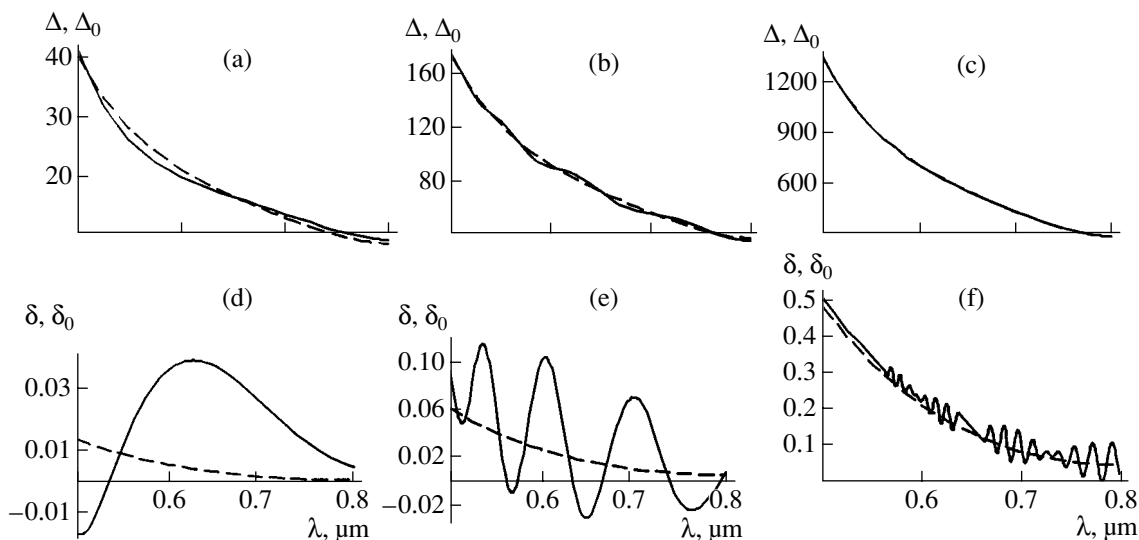


Fig. 5. Δ and Δ_0 and δ and δ_0 as functions of wavelength λ at $\delta\kappa_0 \sim 10^{-3}$ with (solid line) and without (dashed line) allowance for multiple reflections. $d =$ (a, d) 0.3, (b, e) 1.286, and (c, f) 10.0 μm .

within the accuracy of the second-order terms, that

$$\cos\Delta = \cos\Delta_0 + 2(2q - p\cos\Delta_0)/(a_0 + c_0). \quad (15)$$

In a similar way, substituting a , b , and c into Eq. (12), we have for $e^{2\delta}$

$$e^{2\delta} = \frac{a + c + b}{a + c - b} = e^{2\delta_0} \left(\frac{z_2}{z_1} \right) \frac{|t_1|^2}{|t_2|^2}; \quad (16)$$

whence, we have

$$2\delta = 2\delta_0 + \ln \left[\frac{z_2 |t_1|^2}{z_1 |t_2|^2} \right]. \quad (17)$$

Taking into account that for transparent samples $\delta_0 = 0$ and, therefore, $b_0 = 0$, we obtain

$$e^{2\delta} = \frac{1 + 2s/(a + c)}{1 - 2s/(a + c)} = \frac{z_2}{z_1} \left(\frac{t_1}{t_2} \right)^2 \quad (18)$$

and, therefore,

$$2\delta = \ln \left[\frac{z_2}{z_1} \left(\frac{t_1}{t_2} \right)^2 \right]. \quad (19)$$

It is seen from Eq. (18) that, within the accuracy of the terms of the second-order smallness, we may take that in transparent films $\delta \approx 2s/(a + c)$.

It is seen that, in the determination of Δ by Eq. (15), it is the quantity $[2(2q - p\cos\Delta_0)/(a_0 + c_0)]$ that is the error due to multiple reflections, whereas in the determination of δ by Eq. (17), the error is described by the

term $\ln \left[\frac{z_2 |t_1|^2}{z_1 |t_2|^2} \right]$.

Figure 5 illustrates the dependences Δ and δ at $\delta\kappa_0 \sim 10^{-3}$ calculated by Eqs. (13) and (16) and, for comparison, also the true values of Δ_0 and δ_0 calculated by Eq. (9). In this case, birefringence Δn is determined quite reliably. Even if the path difference $\Gamma \sim 0.05 \mu\text{m}$, the error in birefringence determination does not

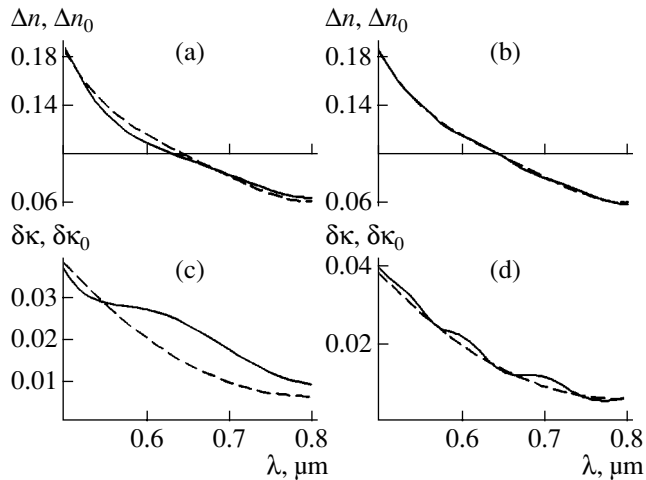


Fig. 6. Comparison of calculated birefringence Δn and dichroism $\delta\kappa$ with true birefringence and dichroism, Δn_0 and $\delta\kappa_0$ depending on the wavelength λ at $\delta\kappa_0 \sim 10^{-2}$ with allowance (solid line) and without allowance (dashed line) for multiple reflection. (a, c) $d = 0.3$, (b, d) $d = 1.286 \mu\text{m}$.

exceed 5%. Obviously, the higher the Γ value, the lower the error in birefringence. The situation is much worse with determination of dichroism, because at small thicknesses, the oscillations due to multiple reflections become comparable with or even exceed the value of δ_0 (Figs. 5d and 5e). At high values of path differences (beginning with $\Gamma \sim 1 \mu\text{m}$), the value of δ may be determined using Eq. (16) because the true δ_0 value is the average δ value (Fig. 5f). In this case, it is necessary to measure $J(\alpha)$ at small steps slowly varying the wavelength. Obviously, the larger the thickness, the more precise the determination of δ and, therefore, of $\delta\kappa$.

If $\delta\kappa_0 \sim 10^{-2}$ and, therefore, absorption is of the same order of magnitude as for the samples with $\Gamma \sim 1 \mu\text{m}$, the intensity of the transmitted light $J(\alpha)$ is very low, so it is impossible to measure $J(\alpha)$ at such absorption. At lower Γ values, the values of Δ and, therefore, Δn are determined with an accuracy no lower than 5% (Figs. 6a and 6b). The value of δ can be determined even if $\Gamma \sim 0.01 \mu\text{m}$ (Fig. 6d).

Thus, we derived the equation for the intensity of light transmitted by the system consisting of a polarizer, a sample, and an analyzer with due regard for multiple reflections. In this equation, the terms responsible for multiple reflections are in the explicit form. The Fourier coefficients in the equations for intensity with and without allowance for multiple reflections are compared. It is shown that all the coefficients a_0 , b_0 , and c_0

calculated without allowance for multiple reflections, are the average values of the coefficients a , b , and c calculated with allowance for multiple reflections. It is also shown that the phase difference Δ can be calculated by the equation

$$\cos\Delta = \frac{a - 3c}{\sqrt{(a + c)^2 - b^2}}.$$

The accuracy of the determination of birefringence Δn in this case is not worse than 5% even for the samples with a phase difference of $\Gamma \sim 0.05 \mu\text{m}$. At higher Γ values, the accuracy of the Δn determination is even higher.

The value of δ can be calculated from the equation

$$e^{2\delta} = \frac{a + c + b}{a + c - b}.$$

If dichroism is of the order of $\delta\kappa_0 \sim 10^{-3}$, this formula is quite applicable at $\Gamma \sim 1 \mu\text{m}$ or higher values. If $\delta\kappa_0 \sim 10^{-2}$, dichroism is determined from this formula quite reliably beginning with the values $\Gamma \sim 0.1 \mu\text{m}$.

For thick samples, the dependences of transmitted-light intensity and Fourier coefficients with and without allowance for multiple reflections are practically the same. Thus, they allow one to reliably calculate Δ and δ values and, respectively, Δn and $\delta\kappa$ values.

ACKNOWLEDGMENTS

This study was supported by the Russian Foundation for Basic Research, project no. 03-02-16871.

REFERENCES

1. R. M. Azzam and N. M. Bashara, *Ellipsometry and Polarized Light* (North-Holland, Amsterdam, 1977; Mir, Moscow, 1981).
2. A. F. Konstantinova, B. N. Grechushnikov, B. V. Bokut', and E. G. Valyashko, *Optical Properties of Crystals* (Nauka Tekh., Minsk, 1995) [in Russian].
3. A. F. Konstantinova, E. A. Evdishchenko, B. V. Nabatov, *et al.*, in *Proceedings of 2nd National Conference on Application of X-rays, Synchrotron Radiation, Neutrons, and Electrons to Studies of Materials (RSNÉ, 1999)* (Inst. Crystallogr. RAN, Moscow, 1999), p. 410.
4. G. I. Utkin, S. V. Alekseev, U. V. Volnov, *et al.*, in *Proceedings of SPIE Lightmetry, 2000*, Vol. 42, p. 178.
5. L. A. Golovan', A. F. Konstantinova, and K. B. Imangazieva, *Kristallografiya* **49** (1), 151 (2004) [*Crystallogr. Rep.* **49** (1), 143 (2004)].

Translated by L. Man

SURFACE
AND THIN FILMS

Boundary Conditions for the Formation of a Ferromagnetic Phase during the Deposition of $\text{Ti}_{1-x}\text{Co}_x\text{O}_{2-\delta}$ Thin Films

L. A. Balagurov*, E. A. Gan'shina**, S. O. Klimonskiĭ*, S. P. Kobeleva*, A. F. Orlov*,
N. S. Perov**, and D. G. Yarkin*

* *Institute of Rare Metals, Bol'shoĭ Tolmachevskii per. 5, Moscow, 119017 Russia*
e-mail: rmdp@girnet.ru

** *Faculty of Physics, Moscow State University, Vorob'evy gory, Moscow, 119899 Russia*

Received September 1, 2004

Abstract—The conditions and the mechanism of the formation of a ferromagnetic phase in a $\text{Ti}_{1-x}\text{Co}_x\text{O}_{2-\delta}$ oxide semiconductor are studied. It is found that the ferromagnetism manifests itself at room temperature in the films of Co-doped $\text{TiO}_{2-\delta}$ oxide deposited on SrTiO_3 (100) substrates only within a limited range of charge carrier densities: 2×10^{18} – 3×10^{22} cm^{-3} . The minimum concentration of charge carriers corresponding to the formation of the ferromagnetic phase increases with a decrease in the cobalt content in the material under study. The ferromagnetism in $\text{Ti}_{1-x}\text{Co}_x\text{O}_{2-\delta}$ thin films can be attributed to Co-enriched clusters with above critical sizes. © 2005 Pleiades Publishing, Inc.

INTRODUCTION

The discovery of ferromagnetism at room temperature in the anatase phase of $\text{Ti}_{1-x}\text{Co}_x\text{O}_2$ oxide [1, 2] attracted much attention to this semiconductor, which may be a promising material for spin electronics. Later, the ferromagnetic phase was found at room temperature in the rutile phase of this compound [3–5]. However, the nature of the ferromagnetism and the conditions of its formation in these *n*-type semiconductors are still far from being well understood. There are experimental indications in favor of both the exchange mechanism of the ferromagnetism via charge carriers in a homogeneous material [6, 7, 8] and the formation of the ferromagnetic phase as a result of the formation of Co clusters [4, 5, 9, 10]. At the same time, these indications are of great importance from the point of view of possible effective spin polarization in such materials. The formation of second-phase inclusions consisting of Co or, at least, highly enriched in Co during the growth of ferromagnetic TiO_2 :Co films under certain conditions was unambiguously demonstrated in the recent studies of two research groups [9, 11]. In [9, 11], the existence of ferromagnetism was attributed to such inclusions. In this study, ferromagnetism at room temperature was observed in Co-doped samples of the anatase tetragonal phase of TiO_2 and in the TiO cubic phase. It was found that the indirect exchange between magnetic ions via charge carriers cannot be the reason for the ferromagnetism, while ferromagnetic clusters can be formed during the deposition of thin films only when the charge-carrier concentration exceeds some threshold value.

RESULTS AND DISCUSSION

We studied the structure and magnetic properties of $\text{Ti}_{1-x}\text{Co}_x\text{O}_{2-\delta}$ films (where $0 \leq \delta \leq 2$ and the cobalt content *x* is either 4 or 8%) deposited on SrTiO_3 (100) substrates by magnetron sputtering of a metallic-alloy target in an argon–oxygen mixture at different partial oxygen pressures from 2×10^{-6} to 2×10^{-4} Torr. The substrate temperature during the deposition was 550°C, the film growth rate was 0.05–0.09 nm/s, and the film thickness was 0.2–0.3 μm . The Co content in the films, determined by the target composition, was monitored by local X-ray spectral analysis.

X-ray diffraction analysis of the films demonstrated that at low oxygen partial pressures they consist of an amorphous metallic phase, whereas an increase in the oxygen content in the gas mixture leads to the formation of polycrystalline films having initially the structure of the cubic phase of TiO and the tetragonal phases of TiO_2 : anatase and rutile. Under these conditions, single-phase samples with rutile structure were not obtained. It is known that the anatase and rutile phases are semiconducting and their band gaps are 3.2 and 3.0 eV, respectively. At the same time, according to [12], TiO oxide is an ionic crystal with metallic conductivity. The X-ray diffraction patterns of the films with cubic and tetragonal structures are shown in Fig. 1. The reflections from the second-phase inclusions (metallic or oxidized Co) were not observed. The peaks observed in the X-ray diffraction patterns correspond to the normal orientation of the *c* axis of the film with respect to the substrate plane. The large width of the peaks can be

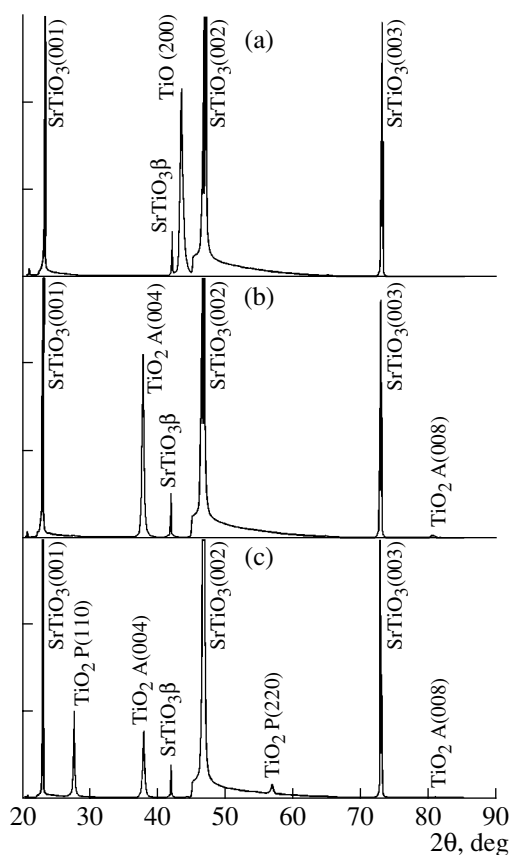


Fig. 1. X-ray diffraction patterns of the $\text{Ti}_{0.92}\text{Co}_{0.08}\text{O}_{2-\delta}$ films deposited on $\text{SrTiO}_3(100)$ substrates: (a) cubic TiO structure, (b) tetragonal anatase (A) structure of TiO_2 , (c) mixture of the anatase and rutile (R) phases.

related to the decrease in the lattice constant c caused by the enrichment of some regions of the film with Co impurities.

The magnetic characteristics of the films were measured by the methods of vibrating sample magnetometry and magneto-optics. We demonstrated [13] that ferromagnetism in $\text{Ti}_{0.92}\text{Co}_{0.08}\text{O}_{2-\delta}$ films exists only within a limited range of carrier densities. Figure 2 shows the relative remanent magnetization M_0 in a zero field (in percent of the saturation magnetization) for the films with different cobalt contents as a function of the carrier density n . The magnetization was measured by a vibrating sample magnetometer and the value of n was calculated from the measured values of resistivity and the Hall coefficient. At room temperature, the films exhibit ferromagnetic behavior with a clearly pronounced magnetic hysteresis loop when the film resistivity changes by more than four orders of magnitude. The carrier densities at the limits of the range of existence of the ferromagnetic phase for the composition with 8% of Co are 2×10^{18} and $3 \times 10^{22} \text{ cm}^{-3}$, when the carrier mobility is $0.3 \text{ cm}^2 \text{ V}^{-1} \text{ s}^{-1}$. At a Co content of 4%, the minimum carrier density corresponding to the

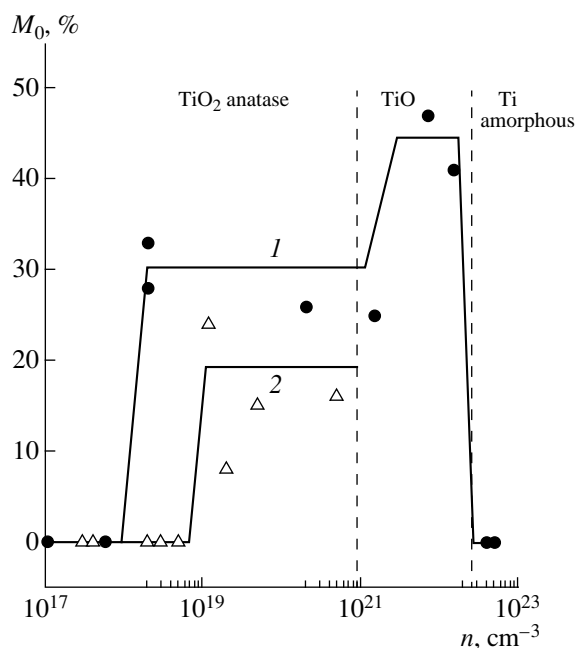


Fig. 2. Dependence of the relative remanent magnetization M_0 in a zero field on the carrier density n for the $\text{Ti}_{1-x}\text{Co}_x\text{O}_{2-\delta}$ films with different Co contents: (1) 8 and (2) 4%.

onset of ferromagnetism is higher ($6 \times 10^{18} \text{ cm}^{-3}$). The magnetic moment calculated from the saturation magnetization is $0.87 \mu_B$ per Co atom for the cubic TiO phase and $0.57 \mu_B$ for the anatase phase at nearly stoichiometric phase compositions. These values are in good agreement with the level of M_0 for these phases shown in Fig. 2.

Note that the values of the magnetic parameters drop to zero at the limits of the aforementioned range. The room-temperature ferromagnetism is absent in both metallic $\text{Ti}_{1-x}\text{Co}_x$ films and high-resistivity semiconducting $\text{Ti}_{1-x}\text{Co}_x\text{O}_2$ films. The absence of ferromagnetism in the metallic Ti-Co phase seems to be related to the amorphization of the material. The existence of a sharp lower limit for the carrier density in the magnetic material allowed us to suggest that the mechanism of ferromagnetism is more likely related to the exchange interaction between magnetic ions via charge carriers [14] than to the existence of magnetic Co clusters. An additional indication that supports for this suggestion is the data obtained by X-ray absorption and photoelectron emission spectroscopy [2, 13, 15], which demonstrate that all cobalt in the ferromagnetic samples exists only in the oxidized Co^{2+} state. (The energy of the Co $2p_{3/2}$ line in the photoelectron spectra is $781.0 \pm 0.5 \text{ eV}$.) However, the additional investigations performed by us unambiguously rule out the indirect exchange between magnetic ions as a possible cause of the ferromagnetism in the material under study.

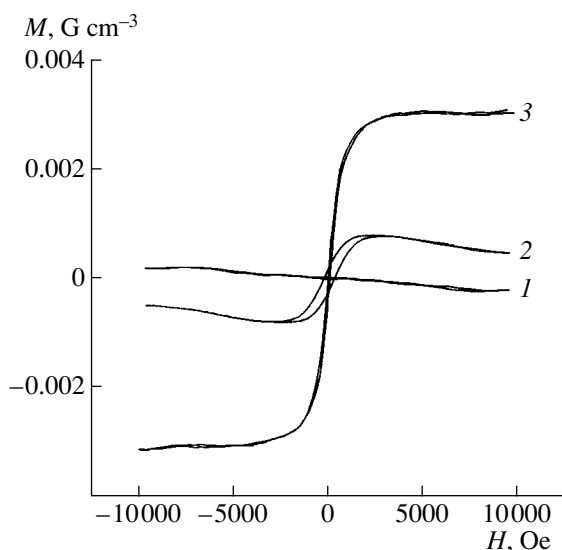


Fig. 3. The magnetic-field dependence of the magnetization M at room temperature for the $\text{Ti}_{0.96}\text{Co}_{0.04}\text{O}_{2-\delta}$ films prepared under different conditions: (1) as-deposited at 560°C and partial oxygen pressure $P_{\text{O}_2} = 1 \times 10^{-4}$ Torr, (2) the same as (1) with additional annealing for 15 min at 525°C and $P_{\text{O}_2} = 1 \times 10^{-6}$ Torr, and (3) the same as (2) with additional annealing in air for 1 h at 525°C . The carrier density in the film is lower than 10^{12} cm^{-3} .

The measurements performed (not shown here), as well as those reported in [3], demonstrate that below room temperature the temperature dependence of the resistivity of all ferromagnetic films is typical of semiconductors; i.e., the resistivity rapidly increases with a decrease in temperature. Taking this into account, one would expect that, in the case of the exchange mechanism of the ferromagnetism, in the films with a carrier density only slightly exceeding the lower limit in Fig. 2, a decrease in temperature should reduce the carrier density below the allowable limit and, thus, lead to the disappearance of ferromagnetism (or, at least, to a decrease in magnetization). We measured the temperature dependence of magnetization in the range 300–40 K for the films with 4% of Co, which exhibit a pronounced hysteresis loop at room temperature and have carrier densities of 8×10^{18} and $2 \times 10^{19} \text{ cm}^{-3}$. Upon cooling to 40 K, the carrier density in these films decreases to about $5 \times 10^{16} \text{ cm}^{-3}$. The available vibration-sample magnetometer did not provide the necessary sensitivity at low temperatures. Therefore, we measured the equatorial Kerr effect at a magnetic field of 3.5 kOe applied in the film plane. In these experiments, we measured the relative change in the intensity of light reflected from the film in the energy range from 0.5 to 3.5 eV. We compared the intensities measured in the applied magnetic field and without the field. We did not observe any difference between the Kerr spectra at 300 and 40 K. This suggests the absence of changes in

the magnetization even for significant changes in the carrier density. This excludes the mechanism of indirect exchange between magnetic ions via charge carriers as a possible cause of ferromagnetic ordering in the material under study.

The films deposited in low vacuum, which have a low carrier density and show no ferromagnetic ordering, can be easily transformed to the ferromagnetic state by subsequent annealing at sufficiently high temperatures. Figure 3 shows the magnetic-field dependence of the relative magnetization of the $\text{Ti}_{0.96}\text{Co}_{0.04}\text{O}_{2-\delta}$ films obtained under different conditions. Curve 1 corresponds to the as-deposited film with a carrier density of $5 \times 10^{18} \text{ cm}^{-3}$. After short annealing for 15 min at 525°C (i.e., below the condensation temperature) and a partial pressure of O_2 equal to 1×10^{-6} Torr, the carrier density increased to $1.2 \times 10^{19} \text{ cm}^{-3}$ and the film became ferromagnetic (curve 2). Additional annealing of the films at temperatures above 500°C both in vacuum and in air leads only to an increase in the magnetization of the films (curve 3).

These observations confirm the suggestions put forward in [9, 11] that the ferromagnetism in $\text{TiO}_2:\text{Co}$ films is related to Co-enriched clusters. During the deposition in high vacuum, the concentration of oxygen vacancies in the growing film become sufficiently high for enhanced diffusion and coalescence of Co impurities with the formation of the ferromagnetic phase. In the opposite case, the ferromagnetic phase (clusters) is formed only during subsequent high-temperature annealing of the films. As was shown in [11], small-size clusters in $\text{Ti}_{1-x}\text{Co}_x\text{O}_{2-\delta}$ films are superparamagnetic and transform to the ferromagnetic state only after reaching a certain critical size on the order of several nanometers. One can expect that the limiting carrier density observed in Fig. 2 corresponds to the minimum density of oxygen vacancies necessary for the formation of ferromagnetic clusters having the critical size. At lower contents of magnetic cobalt impurities in the material, the formation of the ferromagnetic phase requires a higher concentration of oxygen vacancies. The Co-enriched clusters formed in the films are thermodynamically stable because of the low solubility limit of Co in the TiO_2 matrix. Therefore, clusters do not decompose upon subsequent oxidation annealing. During the annealing, the film magnetization increases to the values characteristic of the magnetic moment in metallic cobalt ($1.71 \mu_B$) and the coercive force significantly decreases (Fig. 3, curves 2, 3) owing to the processes of further agglomeration of Co impurities in ferromagnetic clusters and healing of defects in the crystal structure during the annealing.

It was shown in [1] that Co atoms substitute Ti in the anatase lattice. Hence, the clusters formed have the composition $\text{Ti}_{1-x}\text{Co}_x\text{O}_{2-\delta}$, where x far exceeds the average Co content in the material. This was experimentally confirmed in [9]. At low concentrations of oxygen vacancies, $\delta = x$ [9] and the film is a semicon-

ductor with the anatase or rutile lattice, containing inclusions in the form of magnetic clusters. At large values of δ , the material has metallic conductivity and undergoes a phase transition to the structure of cubic oxide TiO.

Thus, we demonstrated that the room-temperature ferromagnetism in the $\text{Ti}_{1-x}\text{Co}_x\text{O}_{2-\delta}$ films deposited on $\text{SrTiO}_3(100)$ substrates occurs only within a limited range of carrier densities. The films deposited in low vacuum become ferromagnetic after high-vacuum annealing at temperatures above 500°C . The main cause of the ferromagnetism in these films is the formation of Co-enriched ferromagnetic clusters reaching a certain critical size rather than the indirect exchange between magnetic atoms via charge carriers.

ACKNOWLEDGMENTS

We are grateful to Yu.B. Patrikeev for preparing the targets for magnetron sputtering and to O.P. Sideleva for determining the film composition by local X-ray spectral analysis.

REFERENCES

1. Y. Matsumoto, M. Murakami, T. Shono, *et al.*, *Science* **291**, 854 (2001).
2. S. A. Chambers, S. Thevuthasan, R. F. C. Farrow, *et al.*, *Appl. Phys. Lett.* **79**, 3467 (2001).
3. W. K. Park, R. J. Ortega-Hertogs, J. S. Moodera, *et al.*, *J. Appl. Phys.* **91**, 8093 (2002).
4. A. Punnoose, M. S. Seehra, W. K. Park, and J. S. Moodera, *J. Appl. Phys.* **93**, 7867 (2003).
5. P. A. Stampe, R. J. Kennedy, Yan Xin, and J. S. Parker, *J. Appl. Phys.* **93**, 7864 (2003).
6. T. Dietl, H. Ohno, F. Matsukura, *et al.*, *Science* **287**, 1019 (2000).
7. K. Nishizawa and O. Sakai, *Physica B* **281–282**, 468 (2000).
8. J. Schliemann, J. König, and A. H. MacDonald, *Phys. Rev. B* **64**, 165 201 (2001).
9. S. A. Chambers, T. Droubay, C. M. Wang, *et al.*, *Appl. Phys. Lett.* **82**, 1257 (2003).
10. J. Y. Kim, J. H. Park, B. J. Park, *et al.*, *Phys. Rev. Lett.* **90**, 017 401 (2003).
11. J. R. Simpson, H. D. Drew, S. R. Shinde, *et al.*, *cond-mat/0205626* (2002), Vol. 1.
12. T. Suzuki and R. Souda, *Surf. Sci.* **445**, 506 (1999).
13. L. A. Balagurov, S. O. Klimonskiĭ, S. P. Kobeleva, *et al.*, *Pis'ma Zh. Éksp. Teor. Fiz.* **79**, 111 (2004) [*JETP Lett.* **79**, 98 (2004)].
14. S. A. Chambers, *Mater. Today* **5** (4), 34 (2002).
15. B.-S. Jeong, Y. W. Heo, D. P. Norton, *et al.*, *Appl. Phys. Lett.* **84**, 2608 (2004).

Translated by K. Kugel

Microacoustic Study of Anisotropy in Optically Isotropic Pyrolytic Nanocarbon

Yu. S. Petronyuk and V. M. Levin

*Emanuel Institute of Biochemical Physics, Russian Academy of Sciences,
ul. Kosygina 4, Moscow, 119991 Russia*

e-mail: julia@sky.chph.ras.ru

Received August 5, 2004

Abstract—Elastic anisotropy was observed experimentally in pyrolytic nanocarbon, which is characterized by optical methods as an isotropic material. It is shown by methods of acoustical microscopy that, when an ultrashort pulse of focused ultrasound passes through a plate of such a material, splitting of the probe pulse occurs, which is caused by the excitation of longitudinal and both modes of transversal elastic waves in the volume of the material. Measurements of the sound velocity showed that pyrolytic nanocarbon has orthotropy and layered distribution of bulk elastic characteristics. The results obtained show a high efficiency of microacoustic methods for detection of anisotropy in weakly anisotropic textured materials, whose anisotropy is difficult to characterize by other methods. © 2005 Pleiades Publishing, Inc.

INTRODUCTION

Attention of researchers has been focused on nanostructured carbon for a long time. In recent years, along with the traditional objects (nanocluster structures in the form of fullerenes or nanotubes), interest in other (macroscopic) forms of nanocarbon has arisen. In particular, the so-called isotropic pyrolytic carbon has become the object of increasing attention [1]. One of the reasons for this interest is unusual mechanical (elastic, plastic, strength) properties of this carbon modification, which differ principally from those of a crystalline graphite owing to the nanostructural organization of isotropic pyrocarbon [2]. The isotropic pyroelectric carbon is one of possible products of pyrolysis of natural hydrocarbon. As a result of pyrolysis, submicron graphite particles forming a bulk material are deposited on a graphite substrate [3, 4]. Although the graphite particles are anisotropic, a natural misorientation of graphite planes is attained owing to the fine-grained structure resulting in the anisotropy of the material as a whole.

Traditionally, the anisotropy of pyrocarbon is evaluated by optical methods: the structure of optically isotropic pyroelectric nanocarbon is not contrasted in polarized light [1–3]. However, it is well known that the optical anisotropy of graphite crystallites is weaker than the anisotropy of their elastic properties [5, 6]. In this context, it seems to be more reasonable to characterize the pyrographite nanostructure by evaluation of its elastic anisotropy. This proves to be especially effective since the elastic properties are often decisive in practical application of isotropic pyrocarbon, for example, in cardio prosthetics [2].

In this work, the elastic properties and anisotropy of pyroelectric nanocarbon are studied experimentally by

the microacoustic methods based on application of short pulses of focused ultrasound. In contrast to conventional ultrasonic methods, in which plane beams are used and the integrated values of elastic constants are measured, the use of convergent ultrasonic beams allows one to measure local elastic parameters of materials, depending on the length of the focal range (20–100 μm) and the operating frequency (50–100 MHz). A high-frequency focused ultrasound proves to be a powerful measuring tool to obtain the data on elastic properties of small samples and inclusions and low-dimensional systems (films, fibers, and so on), as well as to study nano- and microstructured, nonhomogeneous, multiphase, and gradient materials. The microacoustic methods were successfully used to measure the elastic characteristics of the initial states and high-pressure phases of fullerites C_{60} and C_{70} [7, 8], bulk metal glasses [9], and polymer films [10]. Up to now, the field of the method application was limited to isotropic materials. In this work, we show that the method described can be successfully used to characterize isotropic objects. Another goal of this work is to demonstrate a high efficiency in use of the microacoustic technique for revealing and studying the elastic anisotropy, especially in textured and nonhomogeneous materials, where a presence of anisotropy is not evident and its detection and characterization by other methods proves to be difficult.

EXPERIMENTAL

Method

The schematic diagram of studying the elastic properties by spherically focused ultrasound is as follows [7–10]. A spherical beam is induced by an acoustic

objective in an immersion liquid and interacts with a plane-parallel object placed near the beam focal area. The signal reflected from the object is recorded by the same focusing system. The received signal consists of a series of echo signals caused by the reflection of a probe pulse from the front and rear sample surfaces, as well as signals caused by multiple rereflections in the sample. If the sample either has an internal microstructure or contains rather extended defects, the recorded signal should include additional echoes caused by the reflection by these elements. Ultrashort probe pulses are used in this method; therefore, the echo signals formed owing to the propagation of different types of ultrasound oscillations in the sample are separated in time (Fig. 1). Measurement of the time intervals between echo signals from the front and rear surfaces of a plane-parallel sample allows one to determine the velocities of propagation of elastic waves through a sample. Because the angular spectrum of a convergent beam contains both normal and oblique components with respect to the interface, different types of elastic waves are induced in the sample.

The pulse *B* reflected from the front sample surface is used as reference pulse. A group of pulses arising due to the propagation of different types of ultrasonic oscillations through the sample includes *L* and *T* signals caused by the passage of longitudinal and transverse waves through the sample, as well as an *LT* signal formed owing to the conversion of elastic modes during the reflection from the rear sample surface.

Low-aperture long-focus acoustic lenses are used, whose length of focal waist is comparable with the thickness of the object studied. The field inside the focal area of such beams is a restricted plane wave; therefore, it may be considered that the delay times τ_L , τ_{LT} , and τ_T between the reference *B* signal and the pulses *L*, *T*, and *LT* are determined with good accuracy by the travel times of different types of elastic waves across the plate [11]:

$$\tau_L = \frac{2d}{c_L}, \quad \tau_{LT} = \frac{d}{c_L} + \frac{d}{c_T}, \quad \tau_T = \frac{2d}{c_T}, \quad (1)$$

where *d* is the sample thickness at the point of measurement. The first of these relations is used to determine the velocity c_L of longitudinal waves from the measured values of *d* and τ_L . The velocity c_T of transverse waves is found from the interval τ_{LT} using the calculated value of the velocity c_L . The third expression in (1) is usually used to check the interpretation of echo pulses on the oscillograms; the delay times for a correct triad *L*, *T*, and *LT* of echo signals follow the relation

$$\tau_{LT} - \tau_L = \tau_T - \tau_{LT}. \quad (2)$$

In the case of elastic anisotropy of a material studied, additional *LT* and *T* signals formed during the propagation of the second transverse mode through a sample should be observed on the oscillogram of echo pulses.

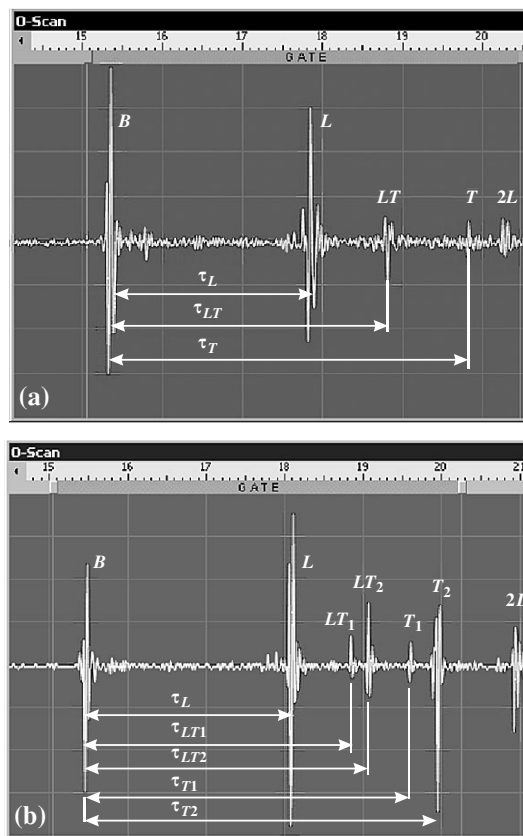


Fig. 1. Oscillograms of echo pulses caused by the interaction of focused sound with a plate of isotropic pyrolytic nanocarbon for the (a) *Z* orientation and (b) *X* and *Y* orientations of the sample.

Materials

To study the elastic properties of pyrocarbon, samples of isotropic pyrolytic graphite (carbon pyroceram) [4] produced by the Kirov–Chepets chemical plant were used. The samples were bars with a $5 \times 5 \text{ mm}^2$ cross section and cubes $5 \times 5 \times 5 \text{ mm}^3$ in size. The samples were oriented so that the normal to one of the faces coincided with the direction of the carbon deposit growth, i.e., the direction of possible preferred orientation of the pyrocarbon texture.

Observation of the samples in polarized light in an optical microscope (Leica, Germany) revealed no anisotropy and no specific microstructure features.

Experimental Apparatus

The elastic anisotropy was observed on a ShIAM wide-field pulse acoustic microscope (Laboratory of Acoustic Microscopy, Institute of Biochemical Physics of the Russian Academy of Sciences). A short ultrasonic pulse at the operating frequency $f = 50 \text{ MHz}$ and a width of $\sim 50 \text{ ns}$ was used as a probe pulse. The angular aperture θ_m of the focused beam (a half of the opening angle of the microscope acoustic lens) was 11° in

Elastic characteristics of transversally isotropic pyrolytic nanocarbon measured by microacoustic methods

Property	Orientation	Value
Velocity of longitudinal waves c_L , km/s	Z	3990
	X	3670
Velocity of fast transverse waves, c_{Tf} , km/s	Z	2220
	X	2220
Velocity of slow transverse waves, c_{Ts} , km/s	Z	–
	X	2070
Elastic moduli C_{ij} , GPa	C_{11}	25.7
	C_{12}	9.3
	C_{13}	8.8
	C_{33}	30.4
	C_{44}	9.4
	C_{66}	8.2
Young modulus E , GPa	ZZ	25.9
	XX, YY	21.1
Shear modulus G , GPa	XY	8.2
	XZ, YZ	9.4
	Poisson ratio μ	0.29
Poisson ratio μ	XY, YX	0.29
	XZ, YZ	0.21
	ZX, ZY	0.25

Note: The measurement error of the velocity of transverse waves is 2.5%.

water. These data allow one to evaluate the diameter of the focal waist of the focused beam $a_f \sim (0.67/\theta_m)\lambda$ and the length of the focal waist $l_f = (4/\theta_m^2)\lambda$ [12]. The

diameter of the focal spot ($\sim 100 \mu\text{m}$) determines the lateral resolution and is taken to be a measure of the locality of the data obtained. The length of the focal waist $l_f \sim 3 \text{ mm}$ defines the optimal sample thickness ($\sim 3\text{--}6 \text{ mm}$).

Experimental Results

The anisotropy of carbon pyroceram was studied on 28 samples. In the first stage, the sound velocities were measured along the direction of carbon deposit growth. One of the obtained echograms is shown in Fig. 1a. The echogram contains a conventional set of echo signals (B , L , LT , and T signals) characteristic for any isotropic sample. Measurement of the sample thickness d and the time intervals τ_L , τ_{LT} , and τ_T allows one to determine from relations (1) the velocities of propagation of longitudinal and transverse elastic waves in pyrocarbon along the direction of deposit growth (the Z -direction). The measurement data are listed in the table.

The structure of ultrasonic echograms changes significantly with a change in the sample orientation. The oscillogram of echo pulses obtained for the sample orientation at which the axis of the probe is parallel to the deposition surface and normal to the direction of carbon deposit growth (the X orientation) is shown in Fig. 1b. It can be seen from the echogram that the following changes occur as compared with the case of the Z orientation.

(i) The position of the L pulse caused by the propagation of transverse waves changed; i.e., the transverse sound velocity changed. The velocities for the Z and X orientations differ by about 10% ($c_{Lz} = 3.99 \text{ km/s}$ and $c_{Lx} = 3.67 \text{ km/s}$).

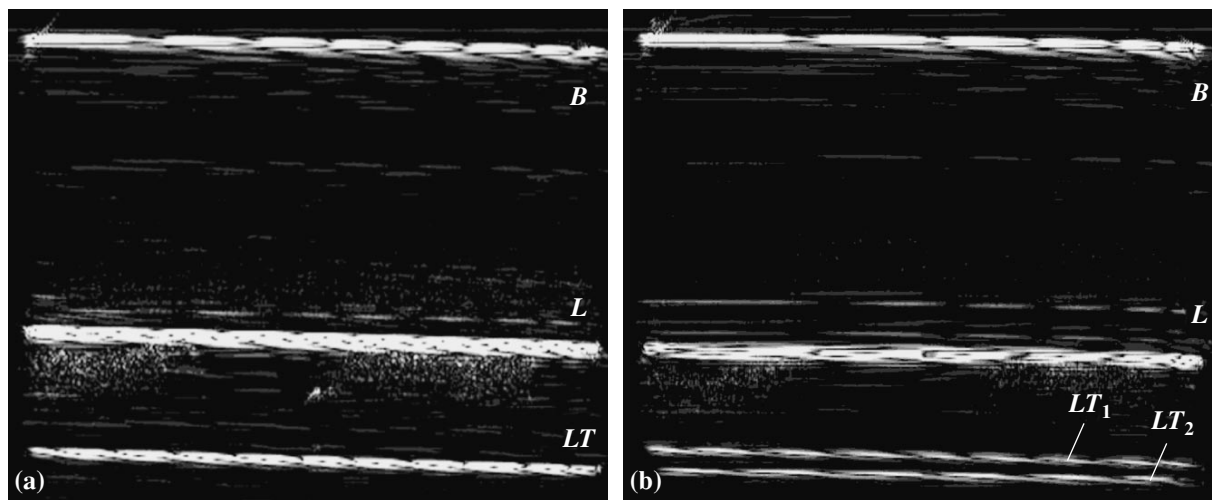


Fig. 2. Acoustic images (B scans) showing splitting of the LT signal due to the elastic anisotropy of the sample of pyrolytic nanocarbon: the axis of the probe beam (a) coincides with the direction of carbon deposit growth (the Z orientation) and (b) is normal to the direction of carbon deposit growth and parallel to the deposition surface (the X orientation). B is the signal reflected from the surface, L corresponds to the reflection of longitudinal waves from the bottom of the sample, and LT is the signal caused by the combined propagation of longitudinal and transverse waves through the sample.

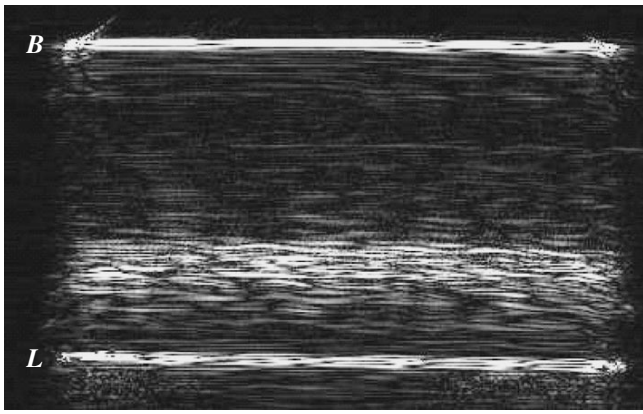


Fig. 3. Layered microstructure in the volume of a sample of isotropic nanocarbon. *B* is the echo signal from the sample surface and *L* is the echo signal from the bottom of the sample formed by a longitudinal wave.

(ii) The *LT* and *T* signals are split into two groups of closely spaced pulses (LT_1, LT_2 and T_1, T_2 , respectively). Two pairs of the *LT* and *T* signals are caused by the propagation of transverse elastic waves with two polarizations having different velocities through the sample.

(iii) For each pair of the *LT* and *T* signals, relation (2) is satisfied, which confirms the correctness of the interpretation of the echogram peaks (Fig. 1b). The results of measurements of the velocities of transverse sound along the deposit plane are listed in the table.

(iv) The sound velocity of one of transverse elastic modes remains constant for both *X* and *Z* orientations, which indicates the presence of a preferred symmetry direction in the material.

The echograms for cubic samples can be obtained along the third direction (*Y* orientation) when the axis of the probe beam lies in the deposition plane and is normal to the growth direction (as for the *X* orientation), but is oriented along another orthogonal direction *Y*. The experiments showed that the *X* and *Y* orientations are equivalent.

The above-listed specific features typical of the carbon pyroceram echograms (Fig. 1) give grounds to conclude that the material studied has elastic anisotropy. Comparison of the sound velocities for different orientations suggests the existence of orthotropy (the symmetry class C_{∞}): the velocity of transverse waves observed for the *Z* orientation coincides with the velocity of one of transverse modes for the *X* and *Y* orientations, which in turn prove to be equivalent. The anisotropy axis C_{∞} coincides with the direction of carbon deposit growth; hence, the material demonstrates the presence of a texture.

In the case of one-dimensional scanning of the lens system, the signals received from different depths form so-called *B* scans, which are spatial scans of echograms along the scanning direction. The coordinate axis along the scanning direction is plotted on the abscissa and the ordinate is the travel time of the probe pulse to an obstacle and back. The echo-signal amplitude is mapped in

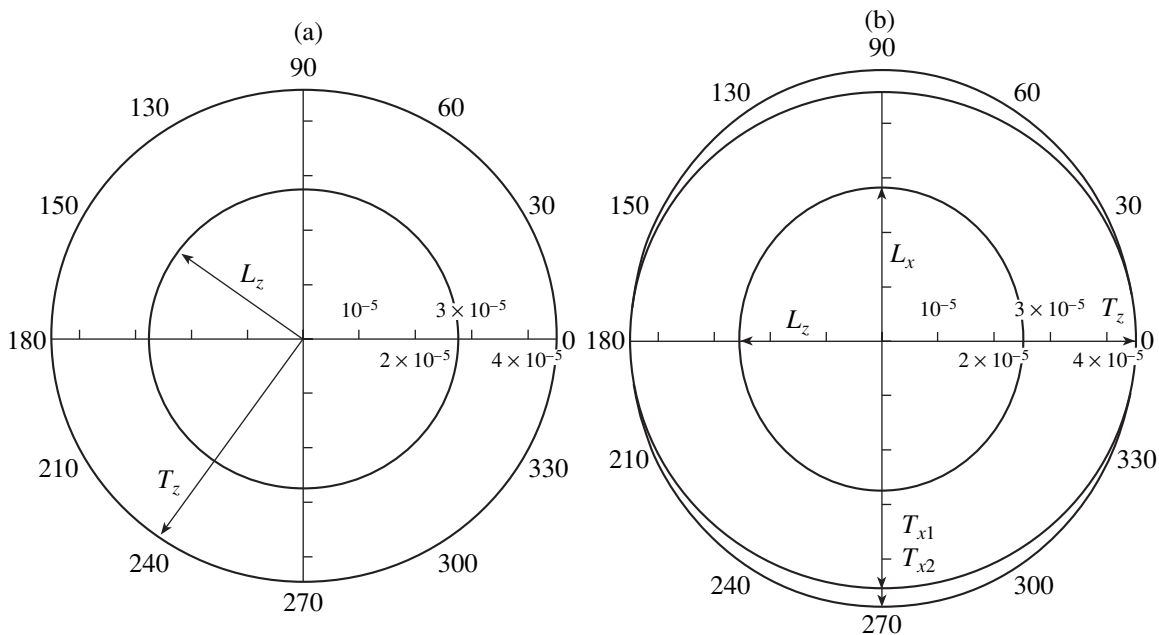


Fig. 4. Surfaces of inverse velocities k/ω for the transversally isotropic pyrolytic nanocarbon obtained experimentally by microacoustic methods: (a) propagation of longitudinal *L* and transverse *T* sound waves in the isotropic *XY* plane (the plane of carbon deposit growth) and (b) the same for the *XZ* plane. The sound velocities for the directions noted by arrows are $c_{Lz} = \sqrt{C_{33}/\rho}$, $c_{Tz} = \sqrt{C_{44}/\rho}$, $c_{Lx} = \sqrt{C_{11}/\rho}$, $c_{Tx2} = \sqrt{C_{44}/\rho}$, and $c_{Tx1} = \sqrt{C_{66}/\rho}$.

gray shades. The B scans for the Z and X orientations including the B , L , and LT signals are shown in Fig. 2. Displacement of the L signal and the splitting of the LT signal are clearly visible on the B scans in going from the Z to X orientation. The presence of texture in pyrocarbon is confirmed by the observation of a layered microstructure of the material in the B scans (Fig. 3).

On the basis of the measured values of the sound velocities, the elastic coefficients were determined. For the case of C_{∞} symmetry, the matrix contains nine non-zero components, five of which are independent:

$$C_{11} = C_{22}, \quad C_{12}, \quad C_{13} = C_{23}, \quad C_{33}, \\ C_{66} = 1/2(C_{11} - C_{12}), \quad C_{44} = C_{55}.$$

The experimental data on the sound velocities listed in the table allow one to obtain the values of seven non-zero components: the moduli C_{11} , C_{22} , C_{12} , C_{33} , C_{44} , C_{55} , and C_{66} . The moduli C_{13} and C_{23} were found from an additional measurement (orientation at an angle of 45° to the C_{∞} axis). The data on the density of carbon pyroceram, which is necessary for calculations, were obtained by hydrostatic weighing accurate to $\pm 3\%$; the obtained value is $\rho = 1.92 \text{ g/cm}^3$. The values of elastic moduli found for carbon pyroceram are listed in the table.

To evaluate the degree of elastic anisotropy of optically isotropic pyrolytic nanocarbon, the slowness surfaces for the X and Z orientations of the material (Fig. 4) were constructed on the basis of the measured values of sound velocities. It can be seen from the plot that optically isotropic nanographite has a moderate anisotropy of elastic properties, which is generally typical of textured and noncrystalline materials

CONCLUSIONS

Focused high-frequency ultrasound is sensitive even to a moderate anisotropy of not only crystalline but also both textured and inhomogeneous solids. This is most clearly pronounced for carbon materials, whose elastic properties and anisotropy are widely varied and are

closely connected with their nanostructure organization.

For optically isotropic pyrolytic nanocarbon, the bulk elastic characteristics were measured, which indicate the presence of anisotropy (orthotropy) caused by a preferred orientation of structural elements of the material, i.e., graphite nanoparticles. Microlayers observed in the acoustic images of the material cross section (B scans) confirm the occurrence of a texture.

Apparently, due to the strong anisotropy of interatomic interaction characteristic of carbon, a partial ordering of nanoparticles is observed in the pyrolytic nanocarbon structure. The formation of a texture leads to a noticeable anisotropy of elastic properties, but this anisotropy is insufficient for observation by optical methods.

REFERENCES

1. A. Oberlin, *Carbon* **40**, 1 (2002).
2. J. C. Bocros, *Chem. Phys. Carbon* **9**, 103 (1973).
3. J. C. Bocros, *Chem. Phys. Carbon* **5**, 62 (1969).
4. T. M. Volkov, in *Carbon Material for Artificial Cardiac Valves* (Nauka, Moscow, 1962) [in Russian].
5. S. Ergun, *Chem. Phys. Carbon* **3**, 45 (1968).
6. O. L. Blakslee, D. G. Proctor, and E. J. Seldin, *J. Appl. Phys.* **41** (8), 3373 (1970).
7. V. D. Blank, V. M. Levin, and V. M. Prokhorov, *JETP* **87** (4), 741 (1998).
8. V. M. Levin, V. D. Blank, and V. M. Prokhorov, *J. Chem. Phys. Solids* **61**, 1017 (2000).
9. V. Levin, Y. Petronyuk, and I. Ponevazh, *Acoust. Imaging* **27**, 69 (2004).
10. V. Levin, Y. S. Petronyuk, and Wang Limin, *Acoust. Imaging* **27**, 229 (2004).
11. Y. S. Petronyuk, O. V. Priadilova, and V. M. Levin, *Mater. Res. Soc. Symp. Proc.* **740** (2003).
12. M. Born and E. Wolf, *Principles of Optics*, 4th ed. (Pergamon, Oxford, 1969; Nauka, Moscow, 1973).

Translated by T. Dmitrieva

Growth and Defect Structure of CdF_2 and Nonstoichiometric $\text{Cd}_{1-x}\text{R}_x\text{F}_{2+x}$ Phases ($R = \text{Rare Earth or In}$): 4. Ion Transport in $\text{Cd}_{0.9}\text{R}_{0.1}\text{F}_{2.1}$ Crystals

N. I. Sorokin, E. A. Sul'yanova, I. I. Buchinskaya, and B. P. Sobolev

Shubnikov Institute of Crystallography, Russian Academy of Sciences,
Leninskij pr. 59, Moscow, 119333 Russia

e-mail: sorokin1@mail.ru

Received November 22, 2004

Abstract—Ion transport in the isoconcentration series of the $\text{Cd}_{0.9}\text{R}_{0.1}\text{F}_{2.1}$ solid solutions ($R = \text{La–Lu or Y}$) is studied in the temperature range from 360 to 730 K. With a change of an RE cation along the series (from La to Lu and Y), the anionic conductivity increases from 6×10^{-6} to 6×10^{-5} S/cm at 500 K. The relation between the conductivity parameters and the structural characteristics of the $\text{Cd}_{0.9}\text{R}_{0.1}\text{F}_{2.1}$ solid solutions is discussed. For a $\text{Cd}_{0.9}\text{R}_{0.1}\text{F}_{2.1}$ crystal, the concentration and mobility of anionic carriers are equal to $2 \times 10^{21} \text{ cm}^{-3}$ and $2 \times 10^{-7} \text{ cm}^2/(\text{V s})$ at 500 K. © 2005 Pleiades Publishing, Inc.

Heterovalent solid solutions described by the general formula $M_{1-x}\text{R}_x\text{F}_{2+x}$ ($M = \text{Ca, Sr, Ba, Cd, or Pb}$ and $R = \text{La–Lu, Y, or Sc}$) with the fluorite structure (sp. gr. $Fm\bar{3}m$) possess high ionic conductivity caused by migration of defects in the anionic sublattice [1–4]. The possible substitution of R^{3+} ions for a considerable number of the M^{2+} ions of the matrix (up to 50 at % under normal pressure) explains the pronounced nonstoichiometry of the fluorite MF_2 phases and formation in these phases of defect complexes (clusters) [5]. Clusters accumulate both cationic and anionic defects (R^{3+} ions, various types of interstitial F_{int} ions, and anionic vacancies V_{F}). Unlike in MF_2 -based solid solutions with $M = \text{Ca, Sr, or Ba}$, the ionic conductivity and evolution of the defect structure in the cadmium fluoride-based fluorite $\text{Cd}_{1-x}\text{R}_x\text{F}_{2+x}$ phases have not been studied as yet. The present article continues the series of publications on the growth and defect structure of the nonstoichiometric $\text{Cd}_{1-x}\text{R}_x\text{F}_{2+x}$ [6–8] phases and is dedicated to their electric conductivity, one of the most structure-sensitive characteristics of the nonstoichiometric fluorite phases and, in particular, of the isoconcentration $\text{Cd}_{0.9}\text{R}_{0.1}\text{F}_{2.1}$ crystals ($R = \text{La–Lu or Y}$). The data on the electrolytic properties of the $\text{Cd}_{1-x}\text{R}_x\text{F}_{2+x}$ solid solutions were studied earlier [4, 9, 10].

EXPERIMENTAL

We studied 14 crystals of the $\text{Cd}_{0.9}\text{R}_{0.1}\text{F}_{2.1}$ solid solutions with $R = \text{La, Ce, Pr, Nd, Sm, Gd, Tb, Dy, Ho, Er, Tm, Yb, Lu, or Y}$. The starting materials for crystal growth were extra pure CdF_2 and chemically pure RF_3 . The growth conditions for $\text{Cd}_{0.9}\text{R}_{0.1}\text{F}_{2.1}$ single crystals

were considered elsewhere [6]. The crystalline boules grown were 20–30 mm in length and 10–12 mm in diameter. The UV absorption spectrum of the $\text{Cd}_{0.9}\text{R}_{0.1}\text{F}_{2.1}$ ($R = \text{Sm, Yb}$) crystals had no bands corresponding to Sm^{2+} and Yb^{2+} , which indicated that the Sm^{3+} and Yb^{3+} cations were not reduced during crystal growth.

The crystalline plates for the further study were cut out from the middle portions of the crystalline boules normally to the growth direction. Their optical properties were studied in [6]. The plates thus cut were divided into three parts to prepare the samples for electrophysical measurements, determination of the chemical composition, and X-ray diffraction analysis. The RF_3 content in the $\text{Cd}_{0.9}\text{R}_{0.1}\text{F}_{2.1}$ crystals with $R = \text{Sm, Gd, Tb, Ho, or Lu}$ was determined by atomic emission spectroscopy with inductively coupled plasma (ICP-AES). The crystal composition thus determined turned out to be close to the composition determined in the starting charge within ± 1 mol % RF_3 .

The samples studied had an area of $\sim 30 \text{ mm}^2$ and a thickness of 3 mm. We used graphite electrodes (DAG-580 paste). The conductivity (σ) measurements were performed by the method of impedance spectroscopy in the frequency and resistance ranges $5\text{--}5 \times 10^5 \text{ Hz}$ and $1\text{--}1 \times 10^6 \Omega$, respectively, on a Tesla BM-507 instrument in a $\sim 10^{-1} \text{ Pa}$ vacuum in the temperature range 360–730 K. The error in σ measurements was less than 5%. The activation enthalpy of ion transport, ΔH , was determined from the equation $\sigma T = A \exp(-\Delta H/kT)$, where A is the preexponential factor of conductivity.

The $\text{Cd}_{0.9}\text{R}_{0.1}\text{F}_{2.1}$ crystals show an obvious propensity for pyrohydrolysis (reaction with water vapor) at

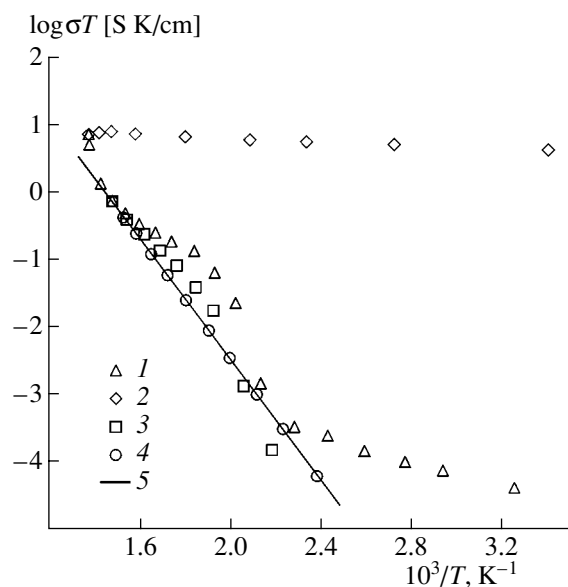


Fig. 1. Conductivity of $\text{Cd}_{0.9}\text{R}_{0.1}\text{F}_{2.1}$ crystals in four different temperature modes: (1) first heating (weakly hydrolyzed crystal), (2) first cooling (strongly hydrolyzed crystal), (3) second heating, and (4) second cooling. Curve (5) shows the true crystal conductivity.

the time of heating during measurement of conductivity. The electrophysical characteristics of partly hydrolyzed samples can considerably differ from the conductivity of oxygen-free crystals. Figure 1 shows the conductivity of the $\text{Cd}_{0.9}\text{Ce}_{0.1}\text{F}_{2.1}$ crystals subjected to different degrees of pyrohydrolysis. Pyrohydrolysis taking place in continuous high-temperature experi-

Table 1. Parameters of ionic conductivity of $\text{Cd}_{0.9}\text{R}_{0.1}\text{F}_{2.1}$ crystals

<i>R</i>	<i>T</i> , K	log <i>A</i> , S K/cm	ΔH , eV
La	425–726	6.52	0.89
Ce	420–703	6.46	0.89
Pr	453–703	6.31	0.87
Nd	446–650	6.73	0.92
Sm	449–648	6.36	0.85
Gd	446–650	6.74	0.89
Tb	449–726	6.74	0.87
Dy	412–729	6.67	0.85
Ho	449–726	6.67	0.83
Er	434–626	6.37	0.77
Tm	438–726	6.26	0.77
Yb	520–648	7.11	0.86
Lu	554–725	6.73	0.82
Y	359–649	6.45	0.78

ments on $\text{Cd}_{0.9}\text{R}_{0.1}\text{F}_{2.1}$ crystals resulted in the formation of a conductive film. During sample cooling, this film masked the true sample resistance. Therefore, we were forced to take special measures to prevent strong pyrohydrolysis of crystals during their heating up to 730 K and developed a special procedure for determining their true sample conductivity from the complex-impedance spectra of partly hydrolyzed crystals.

RESULTS AND DISCUSSION

Temperature curves of ionic conductivity of $\text{Cd}_{0.9}\text{R}_{0.1}\text{F}_{2.1}$ ($R = \text{La-Lu}$ or Y) crystals are shown in Fig. 2. Conductometric data indicate the same conductivity mechanism in all the solid solutions in the temperature range studied. The preexponential factor A and the activation enthalpy ΔH are indicated in Table 1. The conductometric data showed close σ values for four groups of neighboring rare earth elements (Fig. 2). Therefore, we decided divide the $\text{Cd}_{0.9}\text{R}_{0.1}\text{F}_{2.1}$ crystals into four groups depending on their ionic conductivity: the first group with $R = \text{La, Ce, Pr, or Nd}$; the second groups with $R = \text{Sm or Gd}$; the third groups with $R = \text{Tb, Dy, or Ho}$; and the fourth group with $R = \text{Y, Er, Tm, Yb, or Lu}$.

The division of the $\text{Cd}_{0.9}\text{R}_{0.1}\text{F}_{2.1}$ solid solutions into groups depending on their conductivity is similar to the division of the series of RF_3 trifluorides into four groups depending on the morphotropic transformations and reflects the nonmonotonic character of the variation of many properties of RE compounds, the so-called secondary periodicity or the tetrad effect [11, 12]. The average characteristics of ion transport for four groups of $\text{Cd}_{0.9}\text{R}_{0.1}\text{F}_{2.1}$ crystals are indicated in Table 2.

Figure 3 shows the variation of ionic conductivity in the family of $\text{Cd}_{0.9}\text{R}_{0.1}\text{F}_{2.1}$ (present article) and $M_{0.9}\text{R}_{0.1}\text{F}_{2.1}$ phases ($M = \text{Ca, Sr, or Ba}$) [1]. The preexponential factor A of the $\text{Cd}_{0.9}\text{R}_{0.1}\text{F}_{2.1}$ crystals in the passage along the RE series from La to Lu and Y remains practically unchanged (with the average value being $\log A = 6.58 \pm 0.19$), whereas the activation enthalpy ΔH decreases from 0.9 to 0.8 eV. In turn, this results in an increase in σ (within an order of magnitude) along the series in the passage from La to Lu. An analogous effect was observed earlier [9] on another somewhat shortened isoconcentration series of $\text{Cd}_{0.78}\text{R}_{0.22}\text{F}_{2.22}$ ($R = \text{Nd, Dy, Ho, Tm}$).

Analysis of the changes in ionic conductivity in the $\text{Cd}_{0.9}\text{R}_{0.1}\text{F}_{2.1}$ crystals with the change of R is closely related to their defect structure. Earlier, an analogous relation was also observed for the isoconcentration series $M_{0.8}\text{R}_{0.2}\text{F}_{2.2}$ ($M = \text{Ca, Sr, or Ba}$) [1, 2]. The chemical inhomogeneity of the $M_{1-x}\text{R}_x\text{F}_{2+x}$ crystals, including $\text{Cd}_{0.9}\text{R}_{0.1}\text{F}_{2.1}$, is explained by the tendency toward the differentiation of the M^{2+} and R^{3+} cations in the structure. Highly charged cations and anionic defects (interstitial fluoride ions and anionic vacancies) form

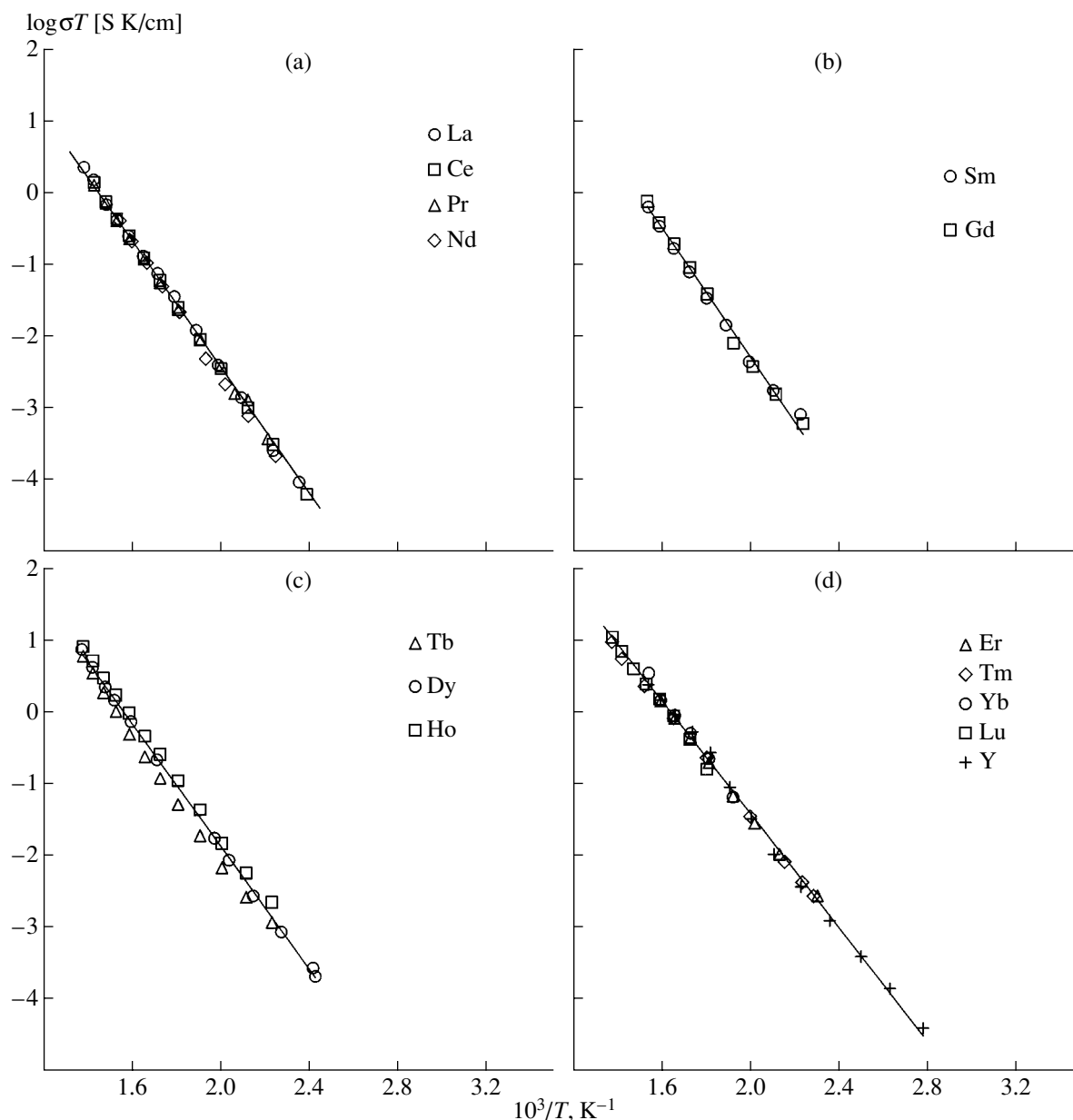


Fig. 2. Ionic conductivity of $\text{Cd}_{0.9}\text{R}_{0.1}\text{F}_{2.1}$ crystals; $R =$ (a) La, Ce, Pr, or Nd; (b) Sm or Gd; (c) Tb, Dy, or Ho; and (d) Er, Tm, Yb, Lu, or Y.

certain groupings or clusters. These defect clusters are statistically distributed over the $M_{1-x}R_xF_{2+x}$ solid solutions.

The cationic composition and the configuration of these groupings may be directly determined in the structural studies of the ordered phases with the structures derived from the fluorite structure, where RE clusters become structural elements whose arrangement in the structure is characterized by a certain long-range order. However, no ordered phases are formed in the $\text{CdF}_2\text{-RF}_3$ systems [13]. Thus, the only available information on a possible cluster structure in these systems

is the averaged defect structure of the nonstoichiometric disordered $\text{Cd}_{1-x}R_xF_{2+x}$ phases.

Structural studies of the $\text{Cd}_{0.9}\text{R}_{0.1}\text{F}_{2.1}$ ($R = \text{Sm-Lu}$ or Y) crystals [7, 8] showed that, according to the notation suggested in [8], the fluoride ions are distributed over the following positions in the sp. gr. $Fm\bar{3}m$: $F_{(8c)}$ fluoride ions are located in the main $8c$ position with the coordinates (0.25, 0.25, 0.25); $F_{\text{int}(32f)1}$ interstitial fluoride ions occupy the $32f$ position with the coordinates (u, u, u), with u ranging from 0.289 to 0.305; $F_{\text{int}(32f)2}$ interstitial fluoride ions occupy the $32f$ position with the coordinates (v, v, v), with v ranging from

Table 2. Characteristics of ion transport for four groups of $\text{Cd}_{0.9}\text{R}_{0.1}\text{F}_{2.1}$ crystals

R	$\log A$, S K/cm	ΔH , eV	σ , 10^{-6} S/cm	μ_{mob} , 10^{-8} $\text{cm}^2/(\text{V s})$
			$T = 500$ K	
La, Ce, Pr, Nd	6.51 ± 0.20	0.89 ± 0.03	0.6 ± 0.1	1.9 ± 0.3
Sm, Gd	6.55 ± 0.19	0.87 ± 0.02	1.0 ± 0.1	3.1 ± 0.3
Tb, Dy, Ho	6.69 ± 0.05	0.85 ± 0.02	2.5 ± 0.5	7.8 ± 1.6
Er, Tm, Yb, Lu, Y	6.58 ± 0.53	0.80 ± 0.06	6 ± 1	19 ± 3

0.339 to 0.359; $\text{F}_{\text{int}(32f)3}$ interstitial fluoride ions are located in the $32f$ position with the coordinates (w, w, w) , with w ranging from 0.411 to 0.422; $\text{F}_{\text{int}(48g)}$ interstitial fluoride anions occupy the $48g$ position with the coordinates $(y, 0.25, 0.25)$ and $y = 0.17$; and $\text{F}_{\text{int}(48i)}$ interstitial fluoride ions occupy the $48i$ position with the coordinates $(r, r, 0.25)$ and $r = 0.40$. The interstitial defects $\text{F}_{\text{int}(48i)}$, $\text{F}_{\text{int}(32f)}$, and $\text{F}_{\text{int}(48g)}$ occupy the positions on the two-, three-, and fourfold symmetry axes, respectively.

Interstitial anions are divided into two groups in accordance with the positions they occupy in the structure. The first group consists of $\text{F}_{\text{int}(32f)3}$ and $\text{F}_{\text{int}(48i)}$ defects formed in the fluorite structure as a result of the compensation of the excessive positive charge of R cations. The second group consists of the $\text{F}_{\text{int}(32f)1}$, $\text{F}_{\text{int}(32f)2}$, and $\text{F}_{\text{int}(48g)}$ defects, i.e., the anions relaxed from the main $8c$ positions.

In $\text{Cd}_{1-x}\text{R}_x\text{F}_{2+x}$ crystals, we established for the first time that the interstitial fluoride ions of the second group prevail over the fluoride ions of the first group, which is characteristic of the CdF_2 -based solid solutions in comparison with other families of fluorite

phases of the composition $M_{1-x}\text{R}_x\text{F}_{2+x}$ ($M = \text{Ca}, \text{Sr}$, or Ba and $R = \text{La-Lu}$ or Y). In other words, the anionic sublattice of the $\text{Cd}_{0.9}\text{R}_{0.1}\text{F}_{2.1}$ phases is characterized by a more pronounced structural relaxation than in the $M_{1-x}\text{R}_x\text{F}_{2+x}$ phases. This may be explained by a decrease in the unit-cell parameter in the BaF_2 - SrF_2 - CaF_2 - CdF_2 sequence and a much more pronounced covalent bonding in CdF_2 . The formation of structural defects in these crystalline matrices proceed against different "chemical" backgrounds, which can explain the specific cluster structure of the $\text{Cd}_{1-x}\text{R}_x\text{F}_{2+x}$ compounds.

The determination of the positions of the interstitial fluoride ions and anion vacancies in $\text{Cd}_{1-x}\text{R}_x\text{F}_{2+x}$ confirms that they have defect structures. The coordinates and the occupancies of interstitial anions obtained allow one to draw conclusions about the structure of defect clusters in $\text{Cd}_{1-x}\text{R}_x\text{F}_{2+x}$. The presence of interstitial F_{int} defects in the $32f$ position are established in all the $\text{Cd}_{0.9}\text{R}_{0.1}\text{F}_{2.1}$ ($R = \text{Sm-Lu}$ or Y) crystals studied. The main grouping of the anionic F_{int} defects in the $\text{Cd}_{0.9}\text{R}_{0.1}\text{F}_{2.1}$ crystals is a tetrahedral anionic grouping formed by $\text{F}_{\text{int}(32f)3}$ with the maximum displacement relative to the main anionic $8c$ position formed in the following way. One $\text{F}_{(8c)}$ ion leaves its position; then a group of four $\text{F}_{\text{int}(32f)3}$ ions adjacent to this vacant position are incorporated into four empty cubes and occupy the tetrahedron vertices. One of these ions compensates the $\text{F}_{(8c)}$ ion which left its position, whereas three other fluoride ions should compensate the difference between the valences of the cations of the Cd^{2+} matrix and the R^{3+} ion. The formation of a tetrahedral anionic grouping is illustrated by Fig. 3 in [7].

All the above facts allow one to assume that the preferable formation of tetrahedral A_4F_{26} type ($A = R$ or M) [14] clusters (named tetrahedral because of the arrangement of cations) in the $\text{Cd}_{0.9}\text{R}_{0.1}\text{F}_{2.1}$ phases. In the ordered phases with the structure derived from the fluorite structure, no tetrahedral A_4F_{26} groupings were revealed. However, in the nonstoichiometric fluorites of the composition $M_{1-x}\text{R}_x\text{F}_{2+x}$ ($M = \text{Ca}, \text{Sr}$, or Ba), the interstitial anions in the $32f$ position with the coordinates (w, w, w) and $w \sim 0.4$ were repeatedly observed. Four cationic polyhedra around the cluster core can

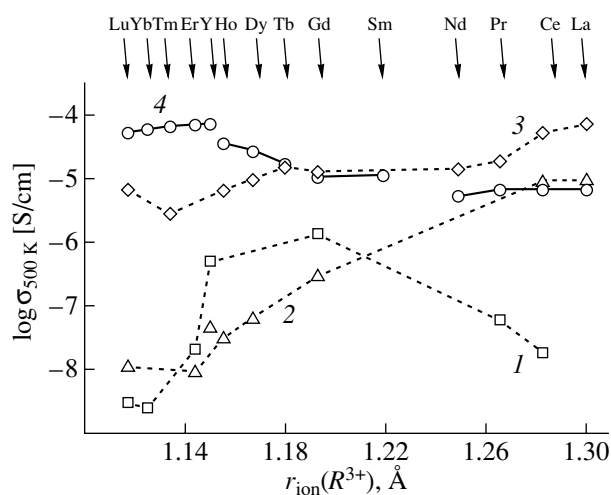
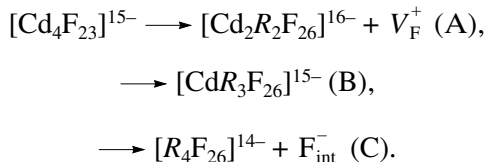


Fig. 3. Isoconcentration curves of conductivity σ of $M_{0.9}\text{R}_{0.1}\text{F}_{2.1}$ solid solutions ($R = \text{La-Lu}, \text{Y}$) at 500 K; $M =$ (1) Ca, (2) Sr, (3) Ba, and (4) Cd.

incorporate from two to four R^{3+} ions. With due regard for this possibility, the schemes of heterovalent substitutions may be written as follows:



Studying ion transport in nonstoichiometric fluorite phases, one may ask the question about the structural defects responsible for anionic conductivity. The formation of defect clusters in solid solutions manifests itself in a pronounced difference between the number of charge carriers responsible for ionic conductivity and the number of formal structural defects. Obviously, some fluoride ions and anionic vacancies only indirectly participate in ion transport. It is most probable that these are relaxed $\text{F}_{\text{int}(32f)1}$, $\text{F}_{\text{int}(32f)2}$, and $\text{F}_{\text{int}(48g)}$ fluoride ions and the corresponding vacancies.

Proceeding from the structural considerations [7, 8], one may assume that the charge carriers are those fluoride-ion vacancies which were not incorporated into the tetrahedral $[\text{Cd}_2\text{R}_2\text{F}_{26}]^{16-}$ clusters and that they compensate the excess negative charge with respect to the $[\text{Cd}_4\text{F}_{23}]^{15-}$ matrix group (scheme A). However, it is well known [15] that the activation enthalpies of the interstitial and vacancy mechanisms of ion transport pronouncedly differ and are equal to ~ 1 and ~ 0.5 eV, respectively.

In accordance with the experimental value of the activation enthalpy of migration of anionic defects (0.8–0.9 eV), it is possible to draw the conclusion that the role of the carriers of ionic conductivity in the heterovalent $\text{Cd}_{0.9}\text{R}_{0.1}\text{F}_{2.1}$ solid solutions is played by interstitial F_{int}^- ions and not anionic vacancies. This is also confirmed by the ^{19}F NMR [16] and dielectric spectroscopy [17] studies of the $\text{Cd}_{1-x}\text{R}_x\text{F}_{2+x}$ solid solutions.

Since anion defects entering the cluster do not participate in ion transport [18], it was suggested to interpret the ionic conductivity of the $M_{1-x}\text{R}_x\text{F}_{2+x}$ solid solutions within the model of “defect regions” suggested in [1]. According to this model, the $M_{1-x}\text{R}_x\text{F}_{2+x}$ solid solutions consist of a matrix having the cubic fluorite lattice and defect regions incorporated into the matrix. The defect regions contain clusters at the center, which, being enriched with rare earth elements, are interpreted as microscopic chemical inhomogeneities. The important characteristic of the atomic structure of the $M_{1-x}\text{R}_x\text{F}_{2+x}$ clusters is the isotopic coherent structures of the defect regions and the matrix. The most probable charge carriers in the fluorite-type solid solutions are interstitial F_{mob}^- fluoride ions located in the vicinity of the clusters at the periphery of the defect regions.

In the $M_{1-x}\text{R}_x\text{F}_{2+x}$ solid solutions, the interstitial anion displaces the main anion to the neighboring interstitial position and occupies its position (the so-called indirect (noncollinear) interstitial mechanism of ion transport) [15]. Fluoride ions may also jump into vacant fluoride positions in such a sequence: interstitial position – vacancy – interstitial position. The presence of a considerable number of fluoride vacancies outside the structural clusters favors the noncollinear mechanism of conductivity via interstitial anions in the $\text{Cd}_{0.9}\text{R}_{0.1}\text{F}_{2.1}$ solid solutions.

In the temperature range studied, the mechanism of ionic conductivity is of the “impurity nature” and is not thermally activated. Therefore, the concentration of the charge carriers (n_{mob}) in the $\text{Cd}_{0.9}\text{R}_{0.1}\text{F}_{2.1}$ phases does not depend on temperature. The concentration n_{mob} of ion carriers was determined experimentally as $n_{\text{mob}} = 2 \times 10^{21} \text{ cm}^{-3}$ [19]. Under the assumption that the concentration n_{mob} only slightly varies along the isoconcentration series of $\text{Cd}_{0.9}\text{R}_{0.1}\text{F}_{2.1}$ structures, we calculated the average mobilities of anionic carriers for the four groups of crystals indicated above (Table 2).

Now, we consider the possible structural mechanisms of formation of mobile interstitial anions. First, the role of mobile F_{mob} defects may be played by some $\text{F}_{\text{int}(32f)3}$ defects not incorporated into $[\text{R}_4\text{F}_{26}]^{14-}$ clusters and located at the periphery of the defect regions (scheme C). Within the model of defect regions [1], it is possible to determine the defect-region volume as $V_{dr} = yb_{\text{per}}a^3/4x_{\text{per}}$, where y is the number of rare earth ions in the defect region, a is the unit-cell parameter, b_{per} is the volume fraction of the defect regions in the solid solution during percolation, and x_{per} is the percolation threshold.

For the tetrahedral R_4F_{26} clusters, the average volume of the defect region in the $\text{Cd}_{0.9}\text{R}_{0.1}\text{F}_{2.1}$ solid solutions was determined using the following values: $y = 4$, $a = 5.45 \text{ \AA}$, $b_{\text{per}} = 0.25\text{--}0.3$ [20], and $x_{\text{per}} = 0.05\text{--}0.10$ [1, 4, 16, 19]. This average volume ranges within $V_{dr} = (5 \times 10^{-22})\text{--}(1 \times 10^{-21}) \text{ cm}^3$. Assuming that there is only one charge carrier in the defect region, we may determine the concentration of free charge carriers as $n_{\text{mob}} = (1 \times 10^{21})\text{--}(2 \times 10^{21}) \text{ cm}^{-3}$, which satisfactorily coincides with the concentration of ion carriers in a $\text{Cd}_{0.9}\text{Er}_{0.1}\text{F}_{2.1}$ crystal experimentally found in [19].

If the $[\text{Cd}_2\text{R}_2\text{F}_{26}]^{16-}$ (scheme A) and $[\text{CdR}_3\text{F}_{26}]^{15-}$ (scheme B) clusters are formed in the $\text{Cd}_{0.9}\text{R}_{0.1}\text{F}_{2.1}$ solid solutions without the necessary formation of any interstitial anions outside clusters [7, 8], the mechanism can be different. It is not excluded that the distorted fluorite structure at the periphery of the defect regions may contain some amount of impurities which may generate some interstitial anions such as, e.g., $[\text{R}_{\text{Cd}}\text{F}_i]_r$ dipoles. The establishment of the structural mechanism of formation of mobile interstitial anions requires additional study.

Thus, the ion transport in $\text{Cd}_{0.9}\text{R}_{0.1}\text{F}_{2.1}$, as well as in other fluorite phases of the composition $M_{1-x}\text{R}_x\text{F}_{2+x}$, seems to be determined by the interstitial fluoride F_{mob} anions located outside clusters. Change of R along the series from La to Lu and Y in $\text{Cd}_{0.9}\text{R}_{0.1}\text{F}_{2.1}$ practically does not change the carrier concentration. At the same time, the enthalpy of activation of carrier migration decreases, which results in an increase of their mobility.

Comparison of the ion-transport characteristics of different families of the fluorite $M_{0.9}\text{R}_{0.1}\text{F}_{2.1}$ solid solutions shows that the conductivity of the fourth group of $\text{Cd}_{0.9}\text{R}_{0.1}\text{F}_{2.1}$ compounds ($R = \text{Er-Lu, Y}$) is higher than the conductivity σ of all the other groups of $\text{Ca}_{0.9}\text{R}_{0.1}\text{F}_{2.1}$ and $\text{Sr}_{0.9}\text{R}_{0.1}\text{F}_{2.1}$ ($R = \text{La-Lu, Y}$) compounds. The conductivity of $\text{Cd}_{0.9}\text{R}_{0.1}\text{F}_{2.1}$ in the second, third, and fourth groups exceeds the conductivity of $\text{Ba}_{0.9}\text{R}_{0.1}\text{F}_{2.1}$ ($R = \text{Sm-Lu, Y}$) and coincides only with the conductivity σ of the first group $\text{Ba}_{0.9}\text{R}_{0.1}\text{F}_{2.1}$ ($R = \text{La-Nd}$). This allows one to use the cadmium fluoride-based solid solutions with the fluorite structure in various electrochemical devices operating at moderate temperatures (up to 500 K).

ACKNOWLEDGMENTS

This study was supported by the Russian Foundation for Basic Research, project nos. 04-02-16241, NSh-1642.2003.2, and NSh-1954.2003.2, and MNTTs, project no. 2136.

REFERENCES

1. A. K. Ivanov-Shitz, N. I. Sorokin, P. P. Fedorov, and B. P. Sobolev, *Solid State Ionics* **31**, 253 (1989).
2. N. I. Sorokin and M. W. Breiter, *Solid State Ionics* **99**, 241 (1997).
3. N. I. Sorokin, P. P. Fedorov, and B. P. Sobolev, *Neorg. Mater.* **33** (1), 5 (1997).
4. N. I. Sorokin, B. P. Sobolev, and M. Braüter, *Fiz. Tverd. Tela* (St. Petersburg) **44** (8), 1506 (2002) [*Phys. Solid State* **44** (8), 1579 (2002)].
5. A. K. Cheetham, B. E. F. Fender, D. Steele, *et al.*, *Solid State Commun.* **8** (3), 171 (1970).
6. I. I. Buchinskaya, E. A. Ryzhova, M. O. Marychev, and B. P. Sobolev, *Kristallografiya* **49** (3), 544 (2004) [*Crystallogr. Rep.* **49** (3), 500 (2004)].
7. E. A. Ryzhova, V. N. Molchanov, A. A. Artyukhov, *et al.*, *Kristallografiya* **49** (4), 668 (2004) [*Crystallogr. Rep.* **49** (4), 591 (2004)].
8. E. A. Sul'yanova, V. N. Molchanov, A. P. Shcherbakov, *et al.*, *Kristallografiya* **50** (2), 210 (2005) [*Crystallogr. Rep.* **50** (2), 203 (2005)].
9. N. I. Sorokin, P. P. Fedorov, A. K. Ivanov-Shitz, and B. P. Sobolev, *Fiz. Tverd. Tela* (Leningrad) **30** (5), 1537 (1988) [*Sov. Phys. Solid State* **30** (5), 890 (1988)].
10. N. I. Sorokin, I. I. Buchinskaya, E. A. Ryzhova, and B. P. Sobolev, in *Proceedings of the 7th Meeting on Fundamental Problems of Solid State Ionics* (Chernogolovka, 2004), p. 8 [in Russian].
11. F. Peppard, G. W. Mason, and S. Lewey, *J. Inorg. Nucl. Chem.* **31** (7), 2271 (1969).
12. I. Fidelis and S. Siekerski, *J. Inorg. Nucl. Chem.* **33** (9), 3191 (1971).
13. B. P. Sobolev, in *Rare Earth Trifluorides* (Inst. d'Estudis Catalans, Barcelona, 2000), Vols. 1–2.
14. L. A. Muradyan, B. A. Maksimov, and V. I. Simonov, *Koord. Khim.* **12** (10), 1398 (1986).
15. A. B. Lidiard, *Crystals with the Fluorite Structure*, Ed. by W. Hayes (Clarendon, Oxford, 1974), p. 101.
16. S. Kyung-Soo, J. Senegas, J. M. Reau, and P. Hagenmuller, *Solid State Ionics* **93** (2), 469 (1991).
17. D. P. Almond, B. Vainas, and N. F. Uvarov, *Solid State Ionics* **111**, 253 (1998).
18. A. V. Chadwick, *Solid State Ionics* **8** (3), 209 (1983).
19. E. F. Hairetdinov, N. F. Uvarov, J. M. Reau, and P. Hagenmuller, *Physica A* **244**, 201.
20. S. Kirkpatrick, *Novosti Fiz. Tverd. Tela*, No. 7, 249 (1977).

Translated by L. Man

Physical and Physicochemical Processes Accompanying Powder Synthesis, Growth of PbMoO_4 Crystals, and Their Annealing in Various Media:

III. Methods of Controlling the Crystallization Front Shape

V. T. Gabrielyan^{1,2}, O. S. Grunskii¹, A. A. Gukasov², A. V. Denisov¹, and S. V. Paturyan²

¹ Russian Center of Laser Physics, St. Petersburg State University, St. Petersburg, 198504 Russia
e-mail: tigran@home.rclph.spbu.ru

² Institute for Physical Research, Academy of Sciences of Armenia, Ashtarak, 138410 Armenia

Received November 20, 2003; in final form, December 23, 2004

Abstract—Different methods of controlling the crystallization front shape are considered: variation in a crucible position in a heater, rotation of a crystal, introduction of impurities absorbing melt radiation, and formation of forced convection under dominant free convection in the melt. © 2005 Pleiades Publishing, Inc.

INTRODUCTION

The crystallization front shape is directly related to the character of hydrodynamic flows in a melt and depends on which of the interacting flows is dominant in the crucible: either the flow near the crystal, which descends owing to the superheating of the crucible walls, or the flow under the crystal, which ascends owing to the crystal rotation. To determine the possibility of growing crystals with a crystallization front close to planar, we investigated the degree of the front convexity depending on the character of the crucible heating, the rotation speed of the crystal, the presence of impurities in the crystal that absorb melt radiation, and other growth parameters. As a parameter characterizing the crystallization front convexity, we considered the ratio H/D , where H is the height of the tapered protrusion and D is the diameter of the growing crystal. The dimensionless parameter H/D determines changes in the character of the growth front under different growth conditions. It is evident that we should consider the dependence of specifically this quantity rather than H on the process parameters: the temperature gradient G , the pulling rate V_{pull} , and the rotation speed V_{rot} . Indeed, when these parameters are constant, only an increase in the crystal diameter D leads to the corresponding elongation of the tapered protrusion in the melt (Fig. 1). It should also be noted that, all other factors being equal, the value of H/D only slightly (<0.1) varies within the limited range of V_{pull} [1].

CHARACTER OF CRUCIBLE HEATING

In order to control heat flows in the melt, we used ceramic stands to install the crucible in different positions with respect to the inductor [1, 2]. Heating of the

crucible was characterized by the temperature distribution on its lateral wall measured by a Pt/Pt–Rh thermocouple for three positions of the crucible (Fig. 2).

The thermocouple was moved along the crucible wall from bottom to top with a step of 5 mm by a pulling mechanism and kept at each point for 20–30 min before the measurement. The results of the measurements are shown in Fig. 2 (bottom). In the bottom, middle, and top crucible positions with respect to the inductor (Figs. 2a, 2b, and 2c, respectively), the top, middle, and bottom parts of the wall, respectively, are superheated. The maximum temperature gradients for the bottom, middle, and top positions are 150, 170, and 170 K/cm, respectively. To establish the effect of the character of crucible heating on the crystallization front shape, several series of crystals (four in each) were

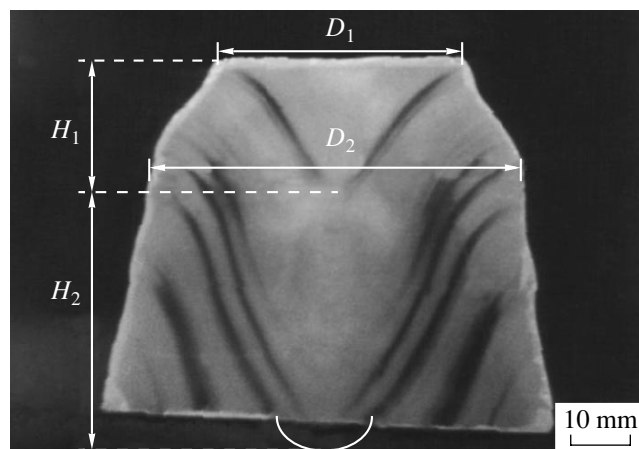


Fig. 1. Height H of the tapered protrusion depending on the crystal diameter D .

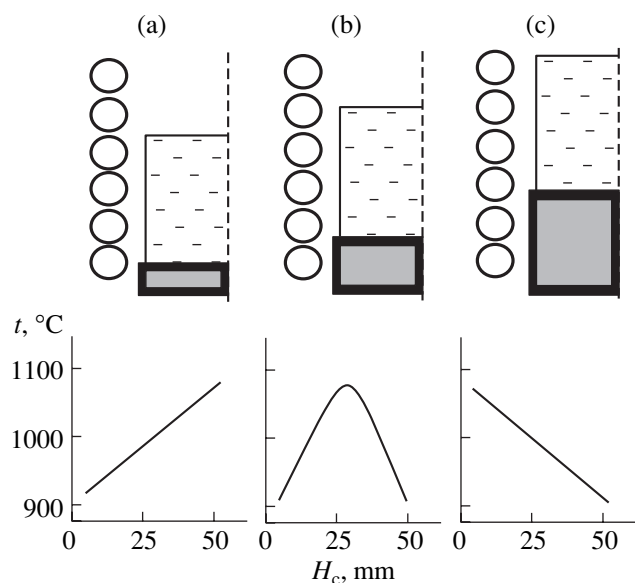


Fig. 2. Different positions of the crucible in the inductor for different heights of the ceramic stand (top) and the temperature distributions on the lateral crucible wall (bottom): $h =$ (a) 5, (b) 14, and (c) 29 mm; H_c is the height of the lateral crucible wall.

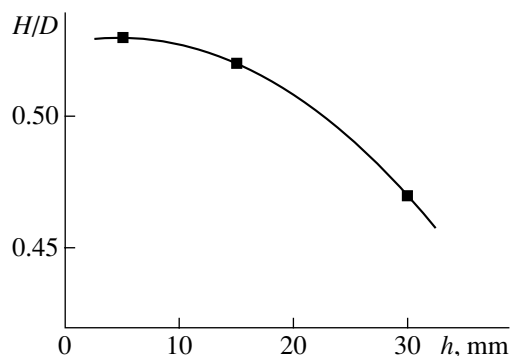


Fig. 3. Dependence of the ratio H/D on the crucible position in the inductor (height h of the ceramic stand).



Fig. 4. Change in the character of the growth front (the ratio H/D) with a change in the rotation speed of a crystal: (from left to right $V_{rot} = 3, 15, 30,$ and 50 rpm). The temperature gradient above the melt is $G = 70$ K/cm.

grown in each of the three crucible positions. The average diameter and the length of the crystals were 12 and 40 mm, respectively; the pulling rate was 3 mm/h; and the rotation speed was 30 rpm. A standard statistical treatment was performed for each series: the mean $\overline{H/D}$ and the mean variance $S_{H/D}$ were calculated. The dependence of the mean $\overline{H/D}$ on the stand height h (Fig. 3) demonstrates that the minimum value of H/D is obtained at the top position, when the bottom part of the crucible wall is superheated, whereas the use of thinner stands results in a higher convexity of the front towards the melt. Hence, to decrease the crystallization front convexity, the geometry of the inductor–crucible system should be chosen in such a way to ensure the location of the bottom part of the crucible in the hottest zone of the heating unit.

CRYSTAL ROTATION SPEED

Figure 4 shows the crystals grown at different rotation speeds: from 3 to 50 rpm. It can be seen that, in order to obtain a planar (or close to planar) crystallization front, one has to increase the rotation speed. However, we should note that, owing to the high plasticity of PbMoO_4 (resulting from a very perfect cleavage in the (001) plane), deformation twisting of a crystal occurs when the rotation speed increases to some critical value (depending on the values of D and axial G) (Fig. 5a). This phenomenon is accompanied by the formation of mosaic blocks and strains in the crystal bulk (Fig. 5b). The deformation of crystals whose diameter is close to or exceeds the crucible radius occurs at much lower rotation speeds, which is related to the larger difference in the linear and angular velocities (V_{rot} and ω_s , respectively).

The experimental data [3] and the results of mathematical modeling [4] show that the value of axial G above the melt significantly affects the dependence of H/D on the rotation speed V_{rot} . Figure 6 shows the experimental dependences of H/D on V_{rot} for two different values of G (200 and 70 K/cm) (Fig. 6a, PbMoO_4 [3]) and the dependences of H (at $D = \text{const}$) on ω_s calculated for YAG at three temperatures t of the top heat shields of the growth system (i.e., in fact, the values of G): (1) 1121.5, (2) 2000.0, and (3) 2333.0°C. (Fig. 6b [4]). As can be seen, the curves are steeper at smaller values of axial G , and, all other factors being equal, high rotation speeds and, correspondingly, large values of axial G should be used to obtain a planar crystallization front. Such good agreement between the experimental and calculated curves indicates adequacy of the mathematical model proposed in [4]. In both cases, as can be seen from the plots, the curves for large values of G terminate and do not intersect the abscissa. In the first case (Fig. 6a), such behavior is caused by the above-mentioned deformation twisting of the crystal at high V_{rot} . In the second case (Fig. 6b), as was stated in [4],

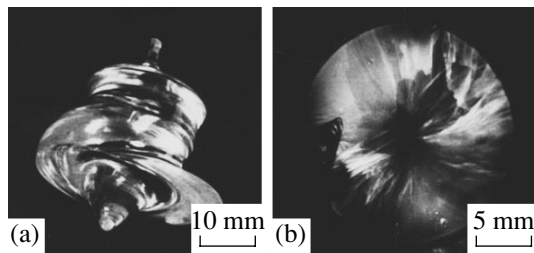


Fig. 5. (a) Deformation twisting and (b) mosaic block pattern of a crystal grown at $V_{\text{rot}} = 70$ rpm.

the reason for this behavior is the computational difficulties associated with large values of G .

CONTROL OF THE CRYSTALLIZATION FRONT SHAPE THROUGH RADIATIVE HEAT TRANSFER

When optical crystals are grown, more than 80% of heat is removed from the crystal/melt interface in the form of radiation passing through the growing crystal. In the case of supercooling on the melt surface caused by melt evaporation, radiative heat losses through the growing crystal cause even higher supercooling, which, as was noted in [5], leads to a more pronounced penetration of the tapered protrusion into the melt as a result of the decrease in the level corresponding to the melting isotherm of the grown material. Thus, the problem is to provide conditions under which the melt radiation is absorbed by the growing crystal and thus decreases the degree of supercooling.

According to the Stefan–Boltzmann law, the total emissive power of a blackbody is $\epsilon_T = \sigma T^4$, where $\sigma = 5.67 \times 10^{-8} \text{ W m}^{-2} \text{ K}^{-4}$ is the Stefan–Boltzmann constant and T is the absolute temperature. On the basis of the Wien displacement law, one can find the wavelength

at which the emissive power of a heated body is maximum: $\lambda_{\text{max}} = B/T$, where $B = 2.898 \times 10^{-3} \text{ m K}$ is the Wien constant. Hence, disregarding the supercooling, we have, for a melt of PbMoO_4 , $t_{\text{melt}} = 1065^\circ\text{C}$ and $\lambda_{\text{max}} = 2.1 \mu\text{m}$. Then, taking into account the transmission band of PbMoO_4 ($\lambda = 0.42\text{--}5.5 \mu\text{m}$), we conclude that the crystal is in fact transparent for the greater part of the melt thermal radiation; i.e., it operates as a light guide removing the radiative energy from the crystal/melt interface.

It is known [6–8] that ions of rare earth elements (REEs) in optical crystals are responsible for strong absorption in the range 1.5–2.2 μm . The results of our experiments showed that these impurities in PbMoO_4 crystals give rise to absorption bands near $\lambda = 2.2 \mu\text{m}$. Thus, a significant part of radiation is absorbed in the crystal. Figure 7 shows the crystals grown at different concentrations of Ho_2O_3 in a melt, all other parameters being the same: G above the melt is $\sim 70 \text{ K/cm}$, $V_{\text{pull}} = 3 \text{ mm/h}$, and $V_{\text{rot}} = 15 \text{ rpm}$. (The process was carried out in the same crucible loaded with equivalent volumes of melts and installed at the same height in the heating unit.) It can be seen that, with an increase in the impurity concentration from 0 to 1.35 wt %, the crystallization front shape changes from tapered to almost planar. Thus, analysis of the crystallization conditions for PbMoO_4 , which determine the morphological features of its growth, suggests that, among the factors affecting the shape of the crystal/melt interface, the impurity, as a tool for controlling the radiative heat transfer, plays an important role. It is likely that the control of the radiative heat transfer upon doping a melt (and, correspondingly, the crystal) to a large extent solves the problem of obtaining a planar crystallization front, which gives rise to uniform dopant distribution over the length and cross section of the crystal. Indeed, PbMoO_4 crystals doped with REE ions can be used as matrices for solid-state lasers with low excitation thresholds and as a

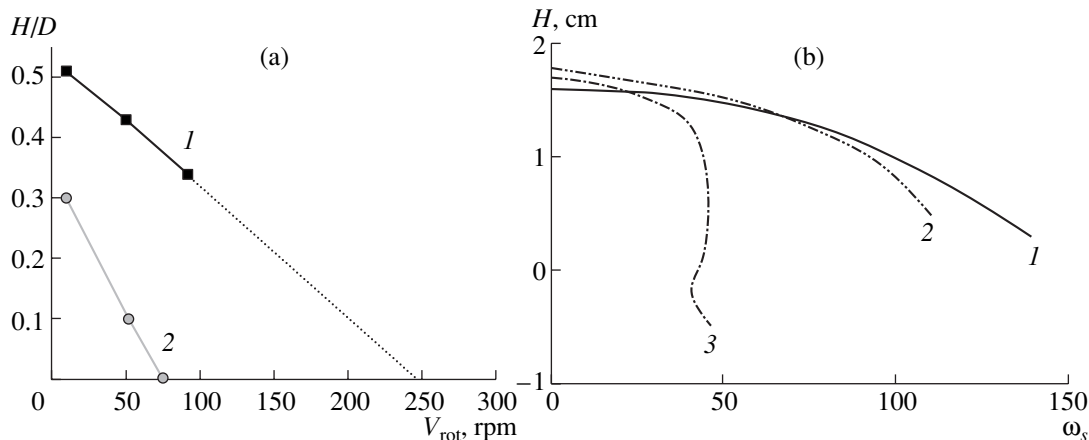


Fig. 6. (a) Dependences of the ratio H/D on V_{rot} for PbMoO_4 crystals grown at different values of G above the melt: (1) 200 and (2) 70 K/cm [3]. (b) The results of simulation of the dependence of H on ω_s for three values of t of the heat shields, calculated for YAG crystals: $t =$ (1) 1121.5, (2) 2000.0, and (3) 2333.0 $^\circ\text{C}$ [4].

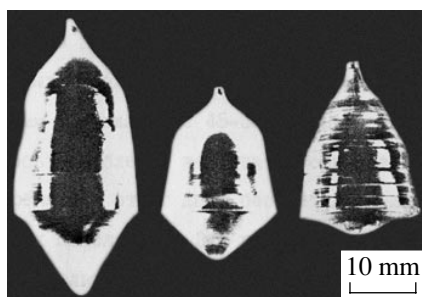


Fig. 7. Change in the character of the growth front (the ratio H/D) for the crystals grown at different dopant concentrations c in the melt (from left to right: $c = 0, 0.5,$ and 1.35 wt % of Ho_2O_3); $V_{\text{rot}} = 15$ rpm.

promising material for tunable lasers [8]. From this point of view, the above-described method of controlling the crystallization front shape is in fact expedient and even necessary. Taking into account the main purpose of this crystal—to be used in acoustooptics as the most promising (after TeO_2) material—we should note that doped crystals are very inferior to their nominally pure analogs in the figure of merit M_2 . The matter is that materials with high optical transparency at the operating wavelength are required to design devices with high diffraction efficiency [9]. Therefore, to obtain pure PbMoO_4 crystals of high quality with a planar shape of the crystallization front, other ways of controlling hydrodynamic flows in a melt should be sought compared to.

FORCED CONVECTION UNDER DOMINANT FREE CONVECTION IN A MELT

The combination of natural experiments and mathematical modeling [1] made it possible to determine the effect of hydrodynamic flows and heat transfer in a melt on crystal growth. On the basis of the shapes of thermal fields obtained experimentally and numerically [1, 2], an important conclusion was made about the possibility

of optimizing the growth conditions by controlling the radial temperature gradient G in the region of the melt directly adjacent to the crystallization front. The structure of the flow in the melt is determined primarily by the character of the crucible heating rather than variation in V_{rot} , although attempts have been made to affect the melt hydrodynamics by changing the rotation speed of a crystal. At the same time, the results of the numerical analysis show that heating of the bottom part of the crucible is the most favorable factor for decreasing the crystallization front convexity. In this case, the boundary separating the forced and natural convection flows is located at the largest distance from the region under a melt. Therefore, it is no coincidence that, in order to change the character of crucible heating, along with the above-described method of changing the crucible position in the inductor, additional bottom heating is often used. This makes it possible to control the crystallization front shape at relatively lower V_{rot} and thus to avoid undesirable deformation twisting of crystals.

In view of the above considerations, the modification of the Czochralski method, which radically changes both the structure of the melt flow and the shapes of the crystal/melt interface occurring in this case, is of even greater interest. We mean the use of a hydrodynamic insertion of particular configuration made of the same material as the crucible (Fig. 8a). The hydrodynamic insertion I facilitates the temperature equalization by mixing the portion of the melt superheated at the crucible wall with the portion cooled in the central part. This distribution of flows in the melt in the crucible is in fact the forced convection under dominant free convection. The hydrodynamic insertion, along with its main purpose, to form necessary thermal distribution in the melt at relatively small values of V_{rot} , has a number of details that significantly improve the growth conditions for volatile crystals. For example, the ring diaphragm 2, which is used to fasten the insertion to the crucible, impedes the melt evaporation, thus excluding the probability of formation of phase inclusions and significantly decreasing the radial G in the

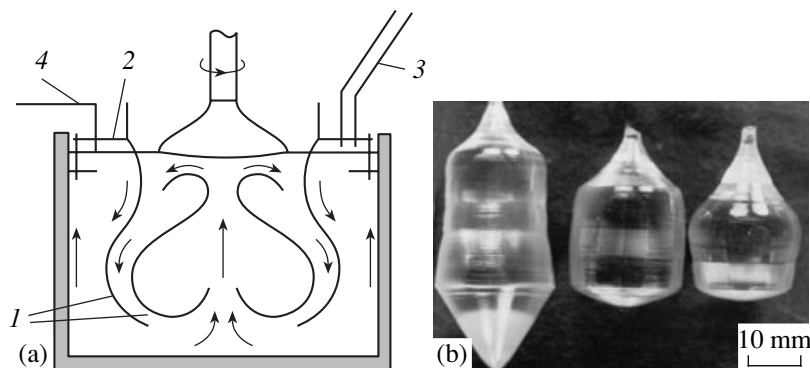


Fig. 8. (a) Schematic of the crystallization unit with a hydrodynamic insertion in the crucible with melt: (1) hydrodynamic insertion, (2) ring diaphragm, (3) feeding mechanism, and (4) melt-level sensor. (b) Crystals grown without an insertion at $V_{\text{rot}} = 18$ rpm (left) and with insertion at $V_{\text{rot}} = 18$ and 22 rpm (middle and right, respectively).

melt. At the same time, the insertion can be used only in combination with the feeding mechanism 3 and the melt-level sensor 4. The reason for this is as follows: as the melt level decreases during the crystal growth, the top part of the insertion emerges from the melt and becomes a serious obstacle for further growth.

Figure 8b shows the crystals grown at the same values of G above the melt (~ 70 K/cm) and $V_{\text{pull}} = 3$ mm/h without and with the insertion. The crystals were grown at $V_{\text{rot}} = 18$ rpm (left and middle) and 22 rpm (right).

CONCLUSIONS

Analysis of the experimental results allows us to conclude the following.

(i) To decrease the degree of the crystallization front convexity, the geometry of the inductor–crucible system should be chosen so as to locate the bottom part of the crucible in the hottest zone of the crystallization unit.

(ii) An increase in the rotation speed of a crystal facilitates obtaining a planar or close to planar crystallization front; however, the crystal growth at high rotation speeds is accompanied by deformation twisting of the crystals owing to their very perfect cleavage.

(iii) Among the factors affecting the shape of the crystal/melt interface, impurities play an important role as a tool for controlling the radiative heat transfer.

(iv) When free convection in a melt is dominant during the crystal growth, the use of a hydrodynamic insertion in the crucible facilitates the occurrence of forced convection even at relatively low rotation speeds of the crystal.

REFERENCES

1. S. Ch. Atabaev, V. T. Gabrielyan, S. V. Paturyan, *et al.*, Preprint No. 291 (Inst. Probl. Mekh. Akad. Nauk SSSR, Moscow, 1987).
2. S. Ch. Atabaev, V. T. Gabrielyan, S. V. Paturyan, and A. I. Prostomolotov, *Kristallografiya* **39** (1), 124 (1994) [*Crystallogr. Rep.* **39** (1), 110 (1994)].
3. V. T. Gabrielyan, Candidate's Dissertation in Physics and Mathematics (Inst. of Crystallography, USSR Academy of Sciences, Moscow, 1978).
4. Q. Xiao and J. J. Derby, *J. Cryst. Growth* **139**, 147 (1994).
5. V. T. Gabrielyan, O. S. Grunskii, and A. V. Denisov, *Kristallografiya* **50**, 2 (2005).
6. B. Cockayne, *J. Cryst. Growth* **3** (4), 60 (1968).
7. B. Cockayne, M. Chesswas, and D. B. Gasson, *J. Mater. Sci.* **4** (5), 450 (1969).
8. A. A. Kaminskiĭ, *Laser Crystals, Their Physics and Properties* (Nauka, Moscow, 1975; Springer, Berlin, 1981).
9. D. A. Pinnow, *IEEE J. Quantum Electron.* **5**, 223 (1970).

Translated by Yu. Sin'kov

CRYSTAL GROWTH

The $(\text{NH}_4)\text{H}_2\text{PO}_4\text{--KCl--KNO}_3\text{--H}_2\text{O}$ System and Growth of Crystals of the $[(\text{NH}_4),\text{K}]\text{H}_2\text{PO}_4$ Solid Solutions

L. V. Soboleva

Shubnikov Institute of Crystallography, Russian Academy of Sciences,
Leninskii pr. 59, Moscow, 119333 Russia

e-mail: afkonst@ns.crys.ras.ru

Received May 5, 2004

Abstract—On the basis of the known data on the $(\text{NH}_4)\text{H}_2\text{PO}_4\text{--KCl--KNO}_3\text{--H}_2\text{O}$ system, $65.0 \times 9.0 \times 8.0\text{-mm}^3$ -large crystals of the $[\text{K}_{0.75}(\text{NH}_4)_{0.25}]\text{H}_2\text{PO}_4$ solid solutions are grown on seed by the method of temperature decrease. It is shown that the $60.0 \times 17.0 \times 10.0\text{-mm}^3$ -large KH_2PO_4 crystals contain impurities: 6.0×10^{-3} wt % Li and 0.1 wt % Na. © 2005 Pleiades Publishing, Inc.

INTRODUCTION

The solid solutions of dihydrogen phosphates of the elements from the first group of the periodic table are solid phases of variable compositions. They preserve the crystal lattice of dihydrogen phosphate, but their physical properties continuously vary. Obviously, these solid solutions are related to substitutional solid solutions [1].

The solid solutions of two different dihydrogen phosphates with ionic lattices may form solid solutions if their chemical formulas are analogous, their ion charges have the same sign, their ionic radii are close, and their crystal structures are similar [1].

There are the data on the solid solutions of the dihydrogen phosphates $(\text{K},\text{NH}_4)\text{H}_2\text{PO}_4$ [2–7], $(\text{Rb},\text{NH}_4)\text{H}_2\text{PO}_4$ [3, 4, 8–11], and $(\text{Cs},\text{NH}_4)\text{H}_2\text{PO}_4$ [12] formed in different systems, e.g., in $(\text{NH}_4)\text{H}_2\text{PO}_4\text{--MeH}_2\text{PO}_4\text{--H}_2\text{O}$ where $Me = \text{K}, \text{Rb}, \text{or Cs}$. In [13], the formation of $(\text{Cs},\text{NH}_4)\text{H}_2\text{PO}_4$ solid solutions was established in the $\text{KH}_2\text{PO}_4\text{--CsH}_2\text{PO}_4\text{--H}_2\text{O}$ system. However, there are no data on the chemical interactions between the lithium and sodium dihydrogen phosphates with the rubidium, cesium, and ammonium dihydrogen phosphates. It was shown that the $\text{KH}_2\text{PO}_4\text{--MeH}_2\text{PO}_4\text{--H}_2\text{O}$ systems with $Me = \text{Li or Na}$ [14], $\text{RbH}_2\text{PO}_4\text{--NaH}_2\text{PO}_4\text{--H}_2\text{O}$ [14], and $\text{NH}_4\text{H}_2\text{PO}_4\text{--NaH}_2\text{PO}_4\text{--H}_2\text{O}$ [14, 15] systems do not form solid solutions. This may be explained by their different ionic radii, i.e., 0.68 Å for Li, 0.98 Å for Na, 1.33 Å for K, 1.49 Å for Rb, and 1.65 Å for Cs, and the different symmetry classes of their dihydrogen phosphates $Pna2_1$ for LiH_2PO_4 ; $P2_1/C$ for NaH_2PO_4 ; $\bar{1}42d$ for KH_2PO_4 , RbH_2PO_4 , and $(\text{NH}_4)\text{H}_2\text{PO}_4$; and $P2/m$ for CsH_2PO_4 .

The data on synthesis of $[\text{K}_{1-x}(\text{NH}_4)_x]\text{H}_2\text{PO}_4$ solid solutions and some of their physical properties were obtained in [4, 5].

Proceeding from the conditions necessary for formation of solid solutions of dihydrogen phosphates indicated above, the known data, and the results of our studies of daltonide crystals grown proceeding from the solubility phase diagrams of ternary systems [16], we managed to grow solid solutions of dihydrogen phosphates from solutions in the $\text{KH}_2\text{PO}_4\text{--MeH}_2\text{PO}_4\text{--H}_2\text{O}$ systems ($Me = \text{Rb}, \text{Cs}, \text{NH}_4$) and from the solutions in the $\text{NH}_4\text{H}_2\text{PO}_4\text{--MeCl}(\text{NO}_3)\text{--H}_2\text{O}$ systems ($Me = \text{K}, \text{Rb}, \text{Cs}$). It is preferable to use $\text{KCl}(\text{KNO}_3)$ as the starting material and not KH_2PO_4 .

We failed to find any data on synthesis of the solid solution of K and NH_4 dihydrogen phosphates with Li and Na dihydrogen phosphates from the dihydrogen phosphates solutions of these elements.

The present study was undertaken with the aim to grow crystals of the $[(\text{NH}_4),\text{K}]\text{H}_2\text{PO}_4$ solid solutions from the solutions in the $(\text{NH}_4)\text{H}_2\text{PO}_4\text{--KCl--KNO}_3\text{--H}_2\text{O}$ system and to use the $\text{KH}_2\text{PO}_4\text{--NaCl--H}_2\text{O}$ and $\text{KH}_2\text{PO}_4\text{--LiH}_2\text{PO}_4\text{--H}_2\text{O}$ systems to grow the KH_2PO_4 crystals with Na^+ and Li^+ impurities.

EXPERIMENTAL

The conditions for formation of a $[(\text{NH}_4),\text{K}]\text{H}_2\text{PO}_4$ solid solution are fulfilled in the $\text{KCl--KNO}_3\text{--NH}_4\text{H}_2\text{PO}_4\text{--H}_2\text{O}$ system [17, 18] (Fig. 1). In fact, this system is the diagonal section of the five-component aqueous $\text{KCl--KNO}_3\text{--KH}_2\text{PO}_4\text{--NH}_4\text{Cl--NH}_4\text{NO}_3\text{--NH}_4\text{H}_2\text{PO}_4\text{--H}_2\text{O}$ system forming a continuous series of $[(\text{NH}_4),\text{K}]\text{H}_2\text{PO}_4$ solid solutions. To grow crystals of these solid solutions we used sections 1, 2, and 3 of the $\text{KNO}_3\text{--KCl--NH}_4\text{H}_2\text{PO}_4\text{--H}_2\text{O}$ system (Fig. 2). The compositions of the starting solutions are indicated in Table 1. The compositions of the solid phases in the temperature range 35 to 0°C correspond to the compo-

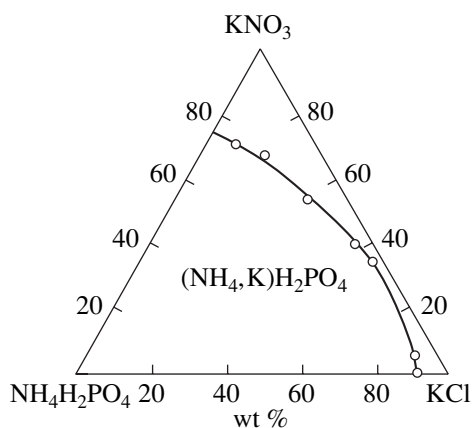


Fig. 1. KCl-KNO₃-NH₄H₂PO₄-H₂O system. Isotherm of a (NH₄,K)H₂PO₄ solid solution at 30°C. Diagonal section of the quinary aqueous KCl-KNO₃-KH₂PO₄-NH₄Cl-NH₄NO₃-NH₄PO₄-H₂O system.

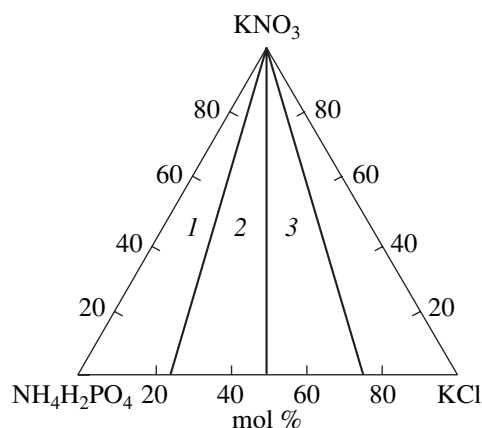


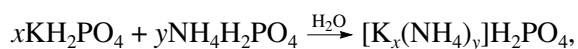
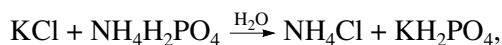
Fig. 2. KNO₃-KCl-NH₄H₂PO₄-H₂O system. Schematic location of sections 1, 2, and 3.

sitions of the [K_x(NH₄)_{1-x}]H₂PO₄ solid solutions ($x = 0.25, 0.50, \text{ and } 0.75$).

The KH₂PO₄-NaCl(LiCl)-H₂O systems have not been studied as yet and, therefore, it was of interest to study the possibilities of growing of [K,Na(Li)]H₂PO₄ solid solutions or KH₂PO₄ crystals with Na⁺ and Li⁺ impurities.

To determine the composition of the starting solutions necessary for growing (K,Na)H₂PO₄ crystals, we used the following compositions: NaCl 25 and 75 mol and KH₂PO₄ 75 and 25 mol (sections 1 and 3) in the NH₄H₂PO₄-KCl-KNO₃-H₂O system (Fig. 2, Table 1). The KH₂PO₄-LiH₂PO₄-H₂O system has not been studied as yet and, therefore, the compositions of the starting solutions used for growth of (K,Li)H₂PO₄ crystals were selected by analogy with the well-known KH₂PO₄-NH₄H₂PO₄-H₂O system [3] (Fig. 3) and are indicated in Table 1, where the compositions NH₄H₂PO₄ are replaced by LiH₂PO₄.

In the solutions of the KCl-NH₄H₂PO₄-KNO₃-H₂O system [17, 18], potassium chloride and ammonium dihydrogen phosphate participate in the exchange reaction with the formation of ammonium chloride and potassium dihydrogen phosphate. During crystallization, the latter reacts with nonreacted ammonium dihydrogen phosphate and forms a continuous series of solid solutions in the temperature range from -10 to 35°C according to the schemes



where x and y are the concentrations of the components in the continuous series of solid solutions.

Proceeding from the above data, we had to establish whether this scheme can also be used to synthesize

some solid solutions of various dihydrogen phosphates of the elements from group 1 of the periodic table.

The starting solutions were prepared from KH₂PO₄ and LiH₂PO₄ single crystals [19, 20], extra pure NH₄H₂PO₄ and NaCl chemicals and KCl obtained by recrystallization of KCl pure for analysis, and twice-distilled water.

The starting solutions were prepared as follows. Taking into account the compositions of the starting solutions indicated in Table 1, we separately dissolved the solution components in water. The solutions thus obtained were heated to 60°C and were gradually (by

Table 1. Compositions of the starting solutions used for crystal growth

[K _x (NH ₄) _y]H ₂ PO ₄					
Compositions of starting solutions, mol			Compositions of starting solutions, g		
KCl	NH ₄ H ₂ PO ₄	H ₂ O	KCl	NH ₄ H ₂ PO ₄	H ₂ O
25	75	1140	18.65	86.25	205.20
50	50	1230	37.30	57.50	221.40
75	25	1330	55.95	28.75	239.40
(K,Na)H ₂ PO ₄					
NaCl	KH ₂ PO ₄	H ₂ O	NaCl	KH ₂ PO ₄	H ₂ O
25	75	1120	14.63	102.10	210.00
75	25	550	43.68	34.03	250.00
(K,Li)H ₂ PO ₄					
LiH ₂ PO ₄	KH ₂ PO ₄	H ₂ O	LiH ₂ PO ₄	KH ₂ PO ₄	H ₂ O
25	75	1023	26.00	102.10	220.00
75	25	520	78.00	34.00	240.00

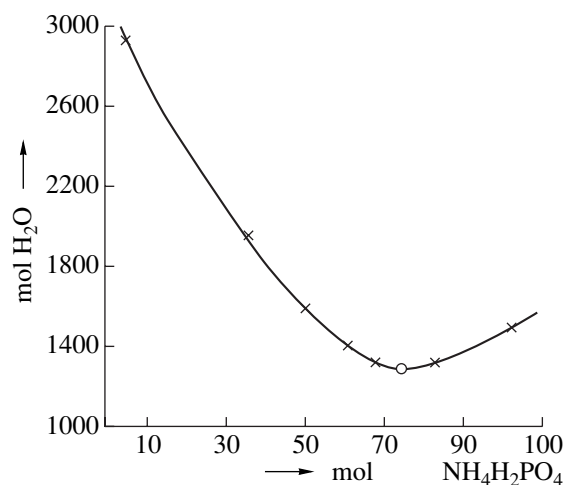


Fig. 3. Isotherm of the $\text{KH}_2\text{PO}_4\text{-NH}_4\text{H}_2\text{PO}_4\text{-H}_2\text{O}$ system at 25°C . o is the composition of the starting solution.

small portions) poured together under constant stirring. The solution thus obtained was filtered through a Shott no. 3 funnel, and poured into a crystallization vessel which was placed into a water thermostat at a given temperature of crystal growth. Growth was performed in the dynamic mode by decreasing the temperature on a point seed. The point seed was obtained by spontaneous crystallization from the starting solutions of the indicated compositions in the temperature range from $\sim 50^\circ\text{C}$ to room temperature. Lowering of the temperature of the solutions used in crystallization was performed only after seed faceting. Table 2 lists the data on growth of crystals of the $[\text{K}_x(\text{NH}_4)_y]\text{H}_2\text{PO}_4$ and KH_2PO_4 solid solutions with Na^+ and Li^+ impurities.

We observed nucleation of parasitic crystals and druses in all the solutions of the systems studied.

It should be indicated that we failed to grow large crystals from cuts 1, 2 in the $\text{NH}_4\text{H}_2\text{PO}_4\text{-KCl-KNO}_3\text{-H}_2\text{O}$ systems. Large crystals were grown from the starting solutions with 75 mol KCl , NaCl , and LiH_2PO_4 and 25 mol $\text{NH}_4\text{H}_2\text{PO}_4$ and KH_2PO_4 , respectively. As a result, we grew the crystals of the compositions $[\text{K}_{0.75}(\text{NH}_4)_{0.25}]\text{H}_2\text{PO}_4$ (Fig. 4a), $(\text{K},\text{Na})\text{H}_2\text{PO}_4$ (Fig. 4b), and $(\text{K},\text{Li})\text{H}_2\text{PO}_4$ (Fig. 4c). The impurity content was determined by the method of emission plasma

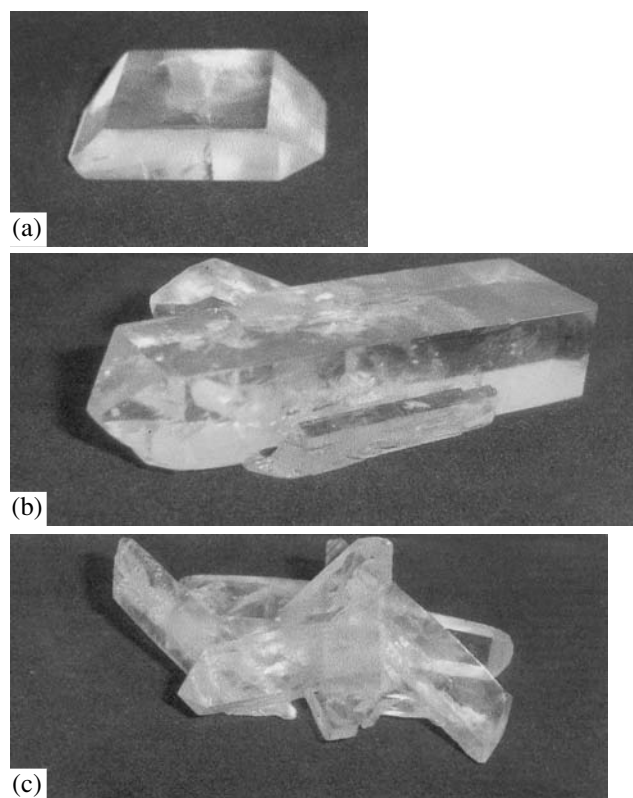


Fig. 4. (a) $[\text{K}_{0.75}(\text{NH}_4)_{0.25}]\text{H}_2\text{PO}_4$, (b) $\text{KH}_2\text{PO}_4 + 0.1 \text{ wt } \% \text{ Na}$, and (c) $\text{KH}_2\text{PO}_4 + 6.0 \times 10^{-3} \text{ wt } \% \text{ Li}$.

spectroscopy as $6 \times 10^{-3} \text{ wt } \% \text{ Li}$ and $0.1 \text{ wt } \% \text{ Na}$. The crystals of the synthesized solid solutions of dihydrogen phosphates are nonhygroscopic.

CONCLUSIONS

The physicochemical characteristics of the solubility diagrams of ternary $(\text{NH}_4)\text{H}_2\text{PO}_4\text{-KCl-KNO}_3\text{-H}_2\text{O}$, $\text{KH}_2\text{PO}_4\text{-NaCl-H}_2\text{O}$, and $\text{KH}_2\text{PO}_4\text{-LiH}_2\text{PO}_4\text{-H}_2\text{O}$ systems are considered with the aim to use these systems for growth of crystals of the $[(\text{NH}_4),\text{K}]\text{H}_2\text{PO}_4$, $(\text{K},\text{Li})\text{H}_2\text{PO}_4$, and $(\text{K},\text{Na})\text{H}_2\text{PO}_4$ solid solutions.

The $50.0 \times 10.0 \times 15.0\text{-mm}^3$ -large $[\text{K}_{0.75}(\text{NH}_4)_{0.25}]\text{H}_2\text{PO}_4$ crystals were grown by the

Table 2. Data on growth of the $[\text{K}_{0.75}(\text{NH}_4)_{0.25}]\text{H}_2\text{PO}_4$, $\text{KH}_2\text{PO}_4 + 0.1 \text{ wt } \% \text{ Na}$, and $\text{KH}_2\text{PO}_4 + 6.0 \times 10^{-3} \text{ wt } \% \text{ Li}$ crystals

System used	Crystal grown		Growth conditions		
	composition	crystal size, mm^3	temperature, $^\circ\text{C}$	rate of temperature decrease, $^\circ\text{C}/\text{day}$	growth time, days
$\text{NH}_4\text{H}_2\text{PO}_4\text{-KCl-H}_2\text{O}$	$[\text{K}_{0.75}(\text{NH}_4)_{0.25}]\text{H}_2\text{PO}_4$	$30.0 \times 20.0 \times 8.0$	45.80–36.50	0.45	30
$\text{KH}_2\text{PO}_4\text{-NaCl-H}_2\text{O}$	$\text{KH}_2\text{PO}_4 + 0.1 \text{ wt } \% \text{ Na}$	$60.0 \times 17.0 \times 10.0$	46.00–34.30	0.40	28
$\text{KH}_2\text{PO}_4\text{-LiH}_2\text{PO}_4\text{-H}_2\text{O}$	$\text{KH}_2\text{PO}_4 + 6 \times 10^{-3} \text{ wt } \% \text{ Li}$	$25.0 \times 10.0 \times 10.0$	35.00–29.10	0.35	37

methods of temperature decrease on a seed from the solutions in the $\text{NH}_4\text{H}_2\text{PO}_4\text{-KCl-KNO}_3\text{-H}_2\text{O}$ system.

The $60 \times 17.0 \times 10.0\text{-mm}^3$ nonhygroscopic KH_2PO_4 crystals with 6.0×10^{-3} wt % Li and 0.1 wt % Na were grown from the $\text{KH}_2\text{PO}_4\text{-LiH}_2\text{PO}_4\text{-H}_2\text{O}$ and $\text{KH}_2\text{PO}_4\text{-NaCl-H}_2\text{O}$ systems.

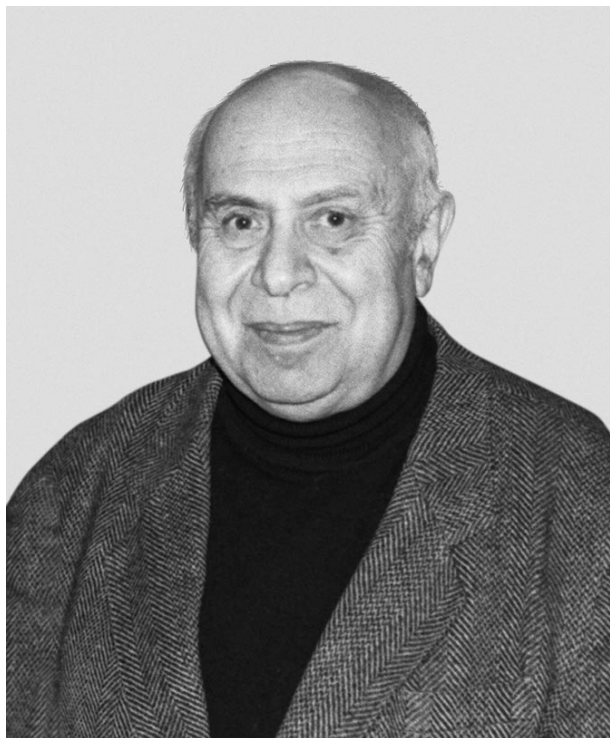
REFERENCES

1. V. A. Anosov and S. A. Pogodin, *Foundations of Physical-Chemical Analysis* (Akad. Nauk SSSR, Leningrad, 1947), p. 311 [in Russian].
2. B. Mattias and W. Mezz, *Helv. Phys. Acta* **20**, 273 (1947).
3. N. S. Kurnakov, A. Ya. Zvorykin, and V. Ya. Ketkovich, *Izv. Sekt. Fiz.-Khim. Anal.* **16** (3), 108 (1948).
4. Y. Ono, T. Hikita, and T. Ikeda, *J. Phys. Soc. Jpn.* **56** (2), 577 (1987).
5. A. I. Baranov, T. Schmidt, and L. A. Chvalov, *Ferroelectrics* **100**, 135 (1989).
6. D. I. Kuznetsov, F. F. Kozhukhovskii, and F. E. Borovaya, *Zh. Prikl. Khim.* **2** (12), 1278 (1948).
7. A. Ya. Zvorykin and V. G. Kuznetsov, *Izv. Akad. Nauk SSSR, Ser. Khim.* 195 (1938).
8. P. Askenasy and F. Nessler, *Z. Anorg. Allg. Chem.* **189**, 305 (1930).
9. G. Brunisholz and M. Bodner, *Helv. Chim. Acta* **49** (2), 347 (1965).
10. F. Ya. Zvorykin and L. S. Vetkina, *Zh. Neorg. Khim.* **6** (11), 2570 (1961).
11. E. Courtens, *Phys. Rev. Lett.* **52** (1), 69 (1984).
12. H. J. Bruckner and E. I. Courtens, *Z. Phys. B: Condens. Matter* **73**, 337 (1988).
13. S. Ya. Shpunt, *Zh. Prikl. Khim.* **13** (1), 9 (1940).
14. A. Ya. Zvorykin and V. D. Ratnikova, *Zh. Neorg. Khim.* **8** (3), 1018 (1963).
15. L. V. Soboleva, *Neorgan. Mater.* **31** (5), 614 (1995).
16. V. A. Polosin and M. I. Shakhparonov, *Zh. Fiz. Khim.* **21** (1), 120 (1947).
17. A. G. Bergman and M. I. Shakhparonov, *Izv. Sekt. Fiz.-Khim. Anal.* **21**, 331 (1952).
18. L. V. Soboleva, *Kristallografiya* **32** (28), 1007 (1996).
19. L. V. Soboleva and I. L. Smol'skii, *Kristallografiya* **42** (4), 762 (1997) [*Crystallogr. Rep.* **42** (4), 700 (1997)].

Translated by L. Man

JUBILEES

Daniel' Moiseevich Kheiker (on the Occasion of His 75th Birthday)



We are celebrating the birthday of Professor Daniel' Moiseevich Kheiker, a remarkable scientist, engineer, and science organizer.

Kheiker is the author of fundamental works on X-ray diffractometry and a well-known expert in X-ray diffraction analysis and instrumentation.

Kheiker was born in Zhitomir, Ukraine, on April 4, 1930. He graduated from high school with a silver medal and, in 1947, entered the Moscow Engineering Physics Institute (MEPhI). In parallel with studies, he started his research work at the Department of Solid State Physics under the guidance of Prof. G.S. Zhdanov and soon published his first articles: "Structure of Semiconductors. X-ray Study of BiPd" and "A Simple Method for Calculating Absorption Factor for Strongly Absorbing Samples in X-ray Diffraction Analysis," in *Zhurnal Eksperimental'noi Teoreticheskoi Fiziki* (the Journal of Experimental and Theoretical Physics). In 1953, Kheiker graduated from MEPhI with distinction and started working as an engineer at the All-Union Research Institute of Asbestos Cement. Soon, Kheiker organized there and headed the Laboratory of physical methods, which was engaged in the development of

various methods for studying materials, including electron microscopy, infrared spectroscopy, thermal analysis, and X-ray diffractometry. The use of various techniques of X-ray diffraction analysis, such as small-angle scattering, precision measurements of unit-cell parameters, and phase analysis, allowed the laboratory headed by Kheiker to solve diverse problems ranging from the study of cements and products of their hydration to the kinetics of formation of copper and lead ferrites and determination of fiber diameter and thickness of the tube walls in chrysotile asbestos. Kheiker was always interested in fundamental scientific problems and, at the same time, also in the development of the experimental methods for their solution. He was an enthusiast of Soviet scientific engineering and managed to unite the efforts of different research organizations. Under his guidance, unique scintillation and proportional counters were created as well as numerous goniometric attachments for industrially manufactured X-ray diffractometers. These instruments formed the basis for design and construction (in cooperation with NPO Burevestnik) of DRON X-ray diffractometers.

In 1958, Kheiker successfully defended his candidate's dissertation dedicated to the diffractometric methods for solving some basic problems of X-ray diffraction analysis. From 1964, the Kheiker's life has been closely related to the Institute of Crystallography of the Russian Academy of Sciences. It is there that he developed highly sensitive precision diffractometric methods for studying polymers; liquid crystals; various single crystals, including biological ones; and polycrystalline materials. He developed original methods used at the preliminary stages of structural studies and in the process of data collection that can be used in diffractometers of various modifications. One of the main directions of his studies is associated with modeling of the size and shape of reciprocal-lattice points in diffractometry studies of single crystals.

In 1972, Kheiker successfully defended his doctoral dissertation dedicated to X-ray diffractometry. He made an enormous contribution to the design and construction of Russian X-ray diffractometers. In cooperation with the Designing Bureau of the Institute of Crystallography and NPO Burevestnik, he developed a DAR automated inclined single-crystal diffractometer, and, in cooperation with the Designing Bureau of the Institute of Crystallography, he developed a four-circle RED diffractometer. The DAR and RED were manufactured industrially. Many X-ray laboratories in Rus-

sia are equipped with these instruments. In the mid-1970s, Kheiker started designing and constructing automated X-ray diffractometers with two-dimensional detectors. He also guided the joint project of the Designing Bureau of the Institute of Crystallography and NPO Burevestnik on the design and construction of a DARK-2.0 multichannel diffractometer for studying proteins. In 1980, Kheiker united the efforts of the Laboratory of High Energy of the Joint Institute for Nuclear Research (JINR) at Dubna and the Designing Bureau of the Institute of Crystallography to design a KARD diffractometer with a two-dimensional detector based on a proportional chamber with 256×256 pixels. This unique instrument has successfully been used for many years in Russia to study hundreds of protein crystals and their derivatives and viruses. At the beginning of the 1990s, the scientists of the Institute of Crystallography developed the method of computing the conventional $I(2\theta)$ curves from the diffraction patterns measured on a KARD-6 diffractometer. Kheiker, in cooperation with the Laboratory of High Energy, JINR, constructed a diffractometer with a focusing collimator and a two-dimensional detector with a spherical entrance window containing 500×500 channels.

In 2003, Kheiker, in cooperation with scientists from the Groningen University (Holland), studied electron-irradiated NaCl crystals on KARD-6 and Bruker-Apex diffractometers with a CCD detector. These studies revealed, for the first time, 100- to 300-Å nanoinclusions of metallic Na with 24 equivalent orientations with respect to the sodium chloride lattice, which corresponded to the Kurdyumov–Sachs relationship.

At present, Kheiker and his colleagues are actively working to create the equipment for two beamlines on a SIBIR'-2 storage ring. One of these beamlines is planned to be used for studying the structure of macro-

molecules. This work is close to the completion. The synchrotron radiation from a bending magnet with $\lambda = 1.5$ Å yields a flux of 10^{11} photons per second with a cross section of 1×1.5 mm². Kheiker is also actively participating in the creation of a beamline for X-ray diffraction analysis of polycrystal samples and small single crystals with nanometer clusters. It has been suggested to use a multipole wiggler as a source of synchrotron radiation.

Kheiker is the head of the Russian school of X-ray diffractometry. His numerous students successfully work in the best national and foreign laboratories. Three monographs written by Kheiker are an indispensable tool for experimenters working in the field of X-ray diffraction analysis. He is the author of more than 200 scientific publications. Kheiker's merits are widely recognized both in Russia and abroad. For many years, Kheiker has been a member of the Commissions on Apparatus and Synchrotron Radiation of the International Union of Crystallography. At present, he is a member of the National Committee of Russian Crystallographers and a member of the Council on Instrumentation of the Presidium of the Russian Academy of Sciences. He has been awarded with the governmental Medal for Valiant Labor, the Veteran of Labor Medal, and six medals of the Exhibition of National Economic Achievements. He has the honorary title of Distinguished Scientist of the Russian Federation. The Editorial Board of *Kristallografiya* and all Kheiker's colleagues and students congratulate Daniel' Moiseevich on his birthday and wish him good health, happiness, and further success in his research.

Translated by L. Man

OBITUARIES

Petr Vasil'evich Klevtsov (July 2, 1930–January 7, 2005)



Petr Vasil'evich Klevtsov, a well-known researcher in the fields of crystal growth, inorganic chemistry, and crystal chemistry; the author of more than 300 scientific publications and 12 inventor's certificates; and one of the leading experts in the preparation of crystalline materials based on tungstates and molybdates and investigation of their structure and properties, died suddenly on January 7, 2005.

Klevtsov was born on July 2, 1930, in the village of Podgornoe, Udmurt ASSR, into a large family. While finishing school, he worked on a collective farm, for which he was awarded the Medal for Valiant Labor in the Great Patriotic War in 1947 and, later, several jubilee medals in honour of the victory in the Great Patriotic War.

From 1947 to 1952, Klevtsov majored in physics at Kazan State University. In 1952, he was appointed a graduate student at the Institute of Crystallography of the USSR Academy of Sciences (USSR AS), where he studied inclusions in crystals under the guidance of

Professor G.G. Lemmleĭn. On the basis of the results obtained, he defended his candidate's dissertation. From 1955 to 1958, Klevtsov worked as a researcher at the Institute of Crystallography and then was invited to Novosibirsk by Corresponding Member of the USSR AS G.B. Bokii. Klevtsov went to the theoretical department (formed by Bokii) of the Institute of Inorganic Chemistry, Siberian Division of the USSR AS, and worked there until the end of his life.

In 1960, Klevtsov organized a laboratory of crystal chemistry and single-crystal growth. The first studies carried out in the new laboratory dealt with the hydrothermal synthesis of rare-earth ferrite garnets; then molybdates and tungstates were chosen as objects of study. First, these investigations were carried out in the interests of the Institute of Catalysis (located nearby), where iron molybdate was used as a catalyst. However, the interest in new laser materials, which greatly increased in the 1960s, gave an impetus to investigation of double molybdates and tungstates of alkaline and rare-earth metals. At that time, several research groups in the Soviet Union, guided by Academician V.I. Spitsyn; Professors V.K. Trunov, M.V. Mokhosoev, A.A. Maĭer; and others, analyzed the phase diagrams, carried out synthesis, and studied physicochemical properties of these compounds. In this field of research, the specific feature of the studies by Klevtsov and his students and colleagues was the aim to solve crystallographic and crystallochemical problems. From the very start, the Novosibirsk researchers intended not only to synthesize new compounds and study polymorphism and the main physicochemical properties but also to investigate their crystal structure. Success was guaranteed to a large extent owing to the direct participation in the structure interpretation by R.F. Klevtsova, a leading researcher and a pupil of Academician N.V. Belov. Particular attention was given to the growth of large single crystals. For example, the widely known promising laser material based on potassium gadolinium tungstate $\text{KGd}(\text{WO}_4)_2$, which is used in practice, was obtained for the first time in the Laboratory of Crystal Growth, headed by Klevtsov.

Klevtsov was always deeply involved in scientific research and continuously devoted to it. He was urged forward by the need for new laser crystals in the 1960s–1970s. The data on molybdates and tungstates obtained during this “golden” period were generalized by Klevtsov and Klevtsova in the well-known review published in *Zhurnal Strukturnoy Khimii* (*Journal of Struc-*

tural Chemistry) in 1977, which has served as a basis for a number of monographs by other authors. Unfortunately, Klevtsov did not compile his results as a doctoral dissertation and did not generalize them in more detailed and extensive publications (although he had all the grounds for this). He considered new investigations of not only his favourite tungstates and molybdates but also other compounds (chromates and complex bismuth oxides) to be more important. Klevtsov was able to transfer his knowledge, researcher's insight, and attitude to science to his pupils and followers. His studies became fundamental in the chemistry and crystal chemistry of molybdates and tungstates and were acknowledged in the Russian and world scientific communities. Under the guidance of Klevtsov, ten of his students defended their candidate's dissertations and then some of them became doctors of science, continuing the cause of their teacher.

Klevtsov was awarded the Medal for Success in the National Economy of the Soviet Union from the Exhibition of National Economic Achievements of the Soviet Union, a diploma of the first degree from the Mendeleev All-Union Chemical Society, the Veteran of Labor Medal, and a Badge of Honor for Work for the Good of the City in honor of the 110th anniversary of Novosibirsk.

The Editorial Board of *Kristallografiya (Crystallography Reports)* and the colleagues and pupils of Petr Vasil'evich Klevtsov will always remember in their hearts this outstanding and remarkable scientist, whose works will be of value to new generations of researchers.

Translated by Yu. Sin'kov